DOKUZ EYLÜL UNIVERSITY
GRADUATE SCHOOL OF NATURAL AND APPLIED SCIENCES

MULTI-TEMPORAL STABILITY INVESTIGATION OF LANDSLIDES IN ÇAĞLAYAN DAM RESERVOIR AREA

by
Tümay KADAKCİ KOCA

January, 2021
İZMİR

MULTI-TEMPORAL STABILITY INVESTIGATION OF LANDSLIDES IN ÇAĞLAYAN DAM RESERVOIR AREA

A Thesis Submitted to the
Graduate School of Natural and Applied Sciences of Dokuz Eylül University
In Partial Fulfillment of the Requirements for the Degree of Doctor of Philosophy in Geological Engineering, Applied Geology Program

by

Tümay KADAKCİ KOCA

January, 2021
İZMİR

Ph.D. THESIS EXAMINATION RESULT FORM

We have read the thesis entitled **"MULTI-TEMPORAL STABILITY INVESTIGATION OF LANDSLIDES IN ÇAĞLAYAN DAM RESERVOIR AREA"** completed by **TÜMAY KADAKCİ KOCA** under supervision of **PROF. DR. M. YALÇIN KOCA** and we certify that in our opinion it is fully adequate, in scope and in quality, as a thesis for the degree of Doctor of Philosophy.

Prof. Dr. M. Yalçın KOCA

Supervisor

Prof. Dr. Yusuf KURUCU

Thesis Committee Member

Assoc. Prof. Dr. Cem KINCAL

Thesis Committee Member

Prof. Dr. Candan GÖKÇEOĞLU

Examining Committee Member

Assoc. Prof. Dr.Alper SEZER

Examining Committee Member

Prof. Dr. Özgür ÖZÇELİK

Director

Graduate School of Natural and Applied Sciences

ACKNOWLEDGEMENTS

This dissertation is dedicated to my beloved father, Necati Kadakçı (1927-1990) who passed away when I was a little girl. I am following his lead throughout my life.

And I am deeply grateful, and I would like to express my thanks to:

My precious mother, the strongest and enthusiastic woman I have ever seen, for always supporting me in my career pursuit and taking care of my son during my everlasting works.

My dearest husband, for giving me help with pleasure in field and laboratory studies and shining his light on the dark days of my Ph.D.

My son, for tolerating the times I can not care with him because of my everlasting studies and for bringing joy to our lives.

M. Yalçın Koca for his skillful supervision and for letting me gain strength, courage, and confidence by every experience in my Ph.D. pursuit.

Assoc. Prof. Dr. Cem Kıncal, Eng. Hakkı Batur Demiray, Dr. Ahmet Turan Arslan, Assoc. Prof. Dr. Doğan Karakuş, Res. Ass. Dr. Aykut Tunçel and our students Samiye İnce, Olca Oflaz, Osman Nuri Erkaya for their effort in helping my field studies.

Res. Asst. Seher Aloğlu Sarı for always giving me moral support and being like a sister.

Prof. Dr. Bahadır Yavuz and Prof. Dr. Candan Gökçeoğlu for their useful criticism in the development of the dissertation.

Assoc. Prof. Dr. Kıvanç Zorlu, Assoc. Prof. Dr. Yılmaz Mahmutoğlu, Prof. Dr. Ahmet Deliormanlı and Res. Asst. Dilek Karakurt for their fruitful collaboration in some of the laboratory tests.

Asst. Prof. Dr. İsmail Işıntek and Prof. Dr. Bilal Sarı for their skillful help in thin-section analyses. Mümtaz Çolak for sharing his excellent expertise in the assessment of peaks of X-ray diffractograms. Res. Asst. Mustafa Çiçek for his precious help in evaluating XRD results and Res. Asst. Zeynep Büçkün for her rigorous work in doing XRD analyses.

Prof. Dr. Yusuf Kurucu for making available to me his expertise in the field of remote sensing techniques and for his interdisciplinary and open mind approach to the landslides.

Assoc. Prof. Dr. Tolga Esetlili and Dr. Fulsen Özen for helping me in GIS and remote sensing software analyses and EMİ Group Information Technologies Corporation for collaboration in DEM generation from historical aerial photographs.

MSc. Eng. Deniz Saffet Karagöz and Muhammet Tunçez for their excellent technical assistance in carrying out UAV flight in my study area and processing UAV data.

Ömer Çağıran from DSI for sharing introductory documentation for my thesis.

Enmersan Marble and Tuntaş Mining for preparing prismatic samples for laboratory tests.

Coordinator of Scientific Research Projects of Dokuz Eylül University for partial financial support as project number 2012.KB.FEN.044.

Tümay KADAKCİ KOCA

MULTI-TEMPORAL STABILITY INVESTIGATION OF LANDSLIDES IN ÇAĞLAYAN DAM RESERVOIR AREA

ABSTRACT

This dissertation includes a multi-temporal slope stability assessment of landslides in the reservoir area of a planned Çağlayan Dam on the Kayacık River, Akhisar, Manisa. The slopes are comprised of Neogene aged clastic and carbonate sedimentary rock intercalations. It was aimed to reveal the multi-temporal evolution and volume of landsides, to determine the effect of triggering factors, and to estimate the future slope conditions. In this study, in-situ geotechnical and geophysical surveys, static and dynamic laboratory testing, photogrammetric analyses with multi-temporal aerial photography, stereographic projection technique and numerical modeling methods were combined. A combination of several photogrammetric techniques to enhance the accuracy of the landslide volume estimation were recommended. It was determined that the reactivations between 1953 and 2017 are the repeated development of the same type of movement in smaller scales and closely related to the triggering factors. A new approach to back analyses to estimate the post-failure strength of joint and rock mass properties using the finite element method (FEM) on geotechnical slope models was developed. Deterministic analyses of future slope stability scenarios were also performed with FEM. It was determined that shallow topsoil and debris cover (0.74 m to 8.55 m) can collapse at the worst conditions (drawdown, seismic activity, and heavy rainfall simultaneously). It can be avoided by trimming the upper weak layers. Although seepage along discontinuities is not expected, the presence of karstic gaps and the intensely faulted rock mass will provide leakage from the dam reservoir.

Keywords: Landslide, weak Neogene aged rocks, multi-temporal photogrammetric analyses, finite element method, back analyses

ÇAĞLAYAN BARAJI GÖL ALANINDAKİ HEYELANLARIN ÇOK ZAMANLI STABİLİTESİNİN İNCELENMESİ

ÖZ

Bu tez çalışması, Manisa, Akhisar'da, Kayacık Nehri üzerinde yapılması planlanan Çağlayan Barajı'nın rezervuar alanındaki heyelanların çok zamanlı duraylılık değerlendirmesini kapsamaktadır. Yamaçlar, zayıf, Neojen yaşlı klastik ve karbonatlı sedimanter kayaç ardalanmalarından oluşmaktadır. Heyelanların çok zamanlı gelişiminin ve hacminin ortaya koyulması, tetikleyici faktörlerin etkisinin belirlenmesi ve gelecek yıllardaki şev koşullarının tahmin edilmesi amaçlanmıştır. Bu çalışmada, yerinde jeoteknik ve jeofizik incelemeler, statik ve dinamik laboratuvar deneyler, çok zamanlı hava fotoğraflarıyla fotogrametrik analizler, stereografik projeksiyon tekniği ve nümerik modelleme yöntemleri birlikte kullanılmıştır. Belirlenen heyelan hacminin doğruluğunu arttırmak için bir kaç fotogrametrik yöntemin birlikte kullanımı önerilmiştir. 1953 ve 2017 arasında meydana gelen yeniden etkinleşmiş kütle hareketlerinin, aynı hareketin daha küçük ölçekli tekrarlarından oluştuğu ve tetikleyici faktörler ile oldukça ilişkili olduğu belirlenmiştir. Kaya kütlesi ve süreksizliklerin yenilme sonrası dayanımlarının belirlenmesi için, jeoteknik şev modellerine sonlu elemanlar yöntemi (FEM) uygulanarak yapılan geri analizlere yeni bir yaklaşım getirilmiştir. Gelecek yıllardaki şev duraylılığı senaryolarının deterministik analizleri, yine FEM kullanılarak yapılmıştır. Sığ toprak örtüsü ve yamaç molozu seviyesinin (0.74 m ile 8.55 m arasında) en kötü koşullarda (su seviyesi düşümü, sismik aktivite, ve şiddetli yağışların birlikte gerçekleşmesi durumu) kayabileceği belirlenmiştir. Sağlam kaya üstündeki zayıf katmanların sıyırılmasıyla bunun önüne geçilebilir. Süreksizlikler boyunca bir su sızıntısı beklenmese de, karstik boşlukların varlığı ve oldukça kırıklı kaya kütlesi, baraj rezervuar alanından su kaçaklarına neden olabilecektir.

Anahtar Kelimeler: Heyelan, zayıf Neojen yaşlı kayaçlar, çok zamanlı fotogrametrik analizler, sonlu elemanlar yöntemi, geri analizler

CONTENTS

Page

Ph.D. THESIS EXAMINATION RESULT FORM ii
ACKNOWLEDGEMENTS iii
ABSTRACT v
ÖZ vi
LIST OF FIGURES xii
LIST OF TABLES xxi

CHAPTER ONE - INTRODUCTION 1

1.1 Location of the Study Area 1
1.2 Scope of the Study 2
1.3 Methodology 2
1.4 Overview of Landslides 5
1.5 Climate, Vegetation, and Hydrology 7
1.6 Seismicity 12

CHAPTER TWO - GEOLOGY OF THE STUDY AREA 17

2.1 Stratigraphy 17
2.1.1 Keçidağ Formation 19
2.1.2 Göcek Formation 21
2.1.3 Yeniköy Formation 23
2.1.4 Küçükderbent Formation 24
2.1.5 Ahmetler Formation 25
2.1.6 Quaternary Alluvium and Slope Debris 25
2.2 Structural Geology 26

CHAPTER THREE - MINERALOGICAL, PETROGRAPHICAL AND GEOCHEMICAL STUDIES 31

3.1 Thin Section Analysis 31

3.2 X-Ray Diffraction Analysis 35

3.3 Geochemical Analysis 36

CHAPTER FOUR- FIELD INVESTIGATIONS 40

4.1 Discontinuity Survey 42

4.1.1 Orientations and Number of Sets of Discontinuities 42

4.1.2 Spacing of Discontinuities 44

4.1.3 Fracture Frequency 46

4.1.4 Volumetric Joint Count 47

4.1.5 Persistence of Discontinuities 49

4.1.6 Roughness of Discontinuity 50

4.1.7 Aperture and Infilling of Discontinuities 54

4.1.8 Weathering 56

4.1.9 Joint Wall Compressive Strength 61

4.2 Borehole Surveying 63

4.3 In-situ Tests 69

4.3.1 Shear Vane Test 69

4.3.2 Standard Penetration Test 71

4.3.3 Lugeon and Permeability Tests 73

4.4 Geophysical Survey 74

4.4.1 Multichannel Analysis of Surface Waves Method 75

4.4.2 Electrical Resistivity Tomography Method 83

CHAPTER FIVE - LABORATORY TESTS 87

5.1 Physical Properties 88

5.2 Static Strength and Deformation Tests 89

5.2.1 Sonic Velocity Test 89

5.2.2 Schmidt Hardness Test 98

5.2.3 Brazilian Test 100

5.2.4 Point Load Test 103

5.2.5 Uniaxial Compressive Strength Test 106

5.2.6 Indirect Estimation of Cohesion and Internal Friction Angle 112

5.2.7 Direct Shear Test 115

5.3 Dynamic Strength and Deformation Tests 136

5.3.1 Dynamic Uniaxial Compressive Strength Test 139

5.3.2 Dynamic Triaxial Compression Strength Test 144

5.3.3 Dynamic Direct Shear Test 147

CHAPTER SIX - ROCK MASS CLASSIFICATION 159

6.1 Various Approaches for Quantitative GSI Rating 161

6.2 Determination of Hoek-Brown Constants 172

6.3 Determination of Rock Mass Modulus 175

6.4 Statistics of the Parameters in the Rock Failure Criterion 178

CHAPTER SEVEN - MULTI-TEMPORAL PHOTOGRAMMETRIC ANALYSES 181

7.1 Aerial Photographs 185

7.2 Data Acquisition by UAV 187
7.3 Interpretation of Aerial Photographs 189
7.4 Digital Elevation Model Generation 191
7.5 Cross-Sectional Analyses 192
7.6 Landslide Volume Estimation 196

CHAPTER EIGHT - MULTI-TEMPORAL SLOPE STABILITY ASSESSMENT 203

8.1 Kinematic Analyses 204
8.2 Geotechnical Model of Landslides 210
8.3 Numerical Modeling with FEM 213
8.4 Back Analysis of the Post-Failure Properties of Landslides 218
8.4.1 Simulation of Structural and Geometrical Condition 222
8.4.2 Simulation of Triggering Factors 224
8.4.3 Landslide-1 228
8.4.4 Landslide-2 230
8.4.5 Landslide-3 233
8.4.6 Landslide-4 236
8.5 Future Slope Stability Scenarios 239
8.5.1 Landslide-1 241
8.5.2 Landslide-2 243
8.5.3 Landslide-3 245
8.5.4 Landslide-4 247
8.5.5 Seepage Analysis 249

CHAPTER NINE - DISCUSSION AND CONCLUSIONS 253

9.1 Type and Evolution of Landslides 255
9.2 Rate of Movement 256
9.3 Triggering Factors of Reactivations 257
9.4 Future Conditions for the Landslides 260

REFERENCES 262

APPENDICES 299

APPENDIX-1: Earthquake Repository 299
APPENDIX-2: 1/10000 Geology Map 305
APPENDIX-3: X-RAY Diffraction Patterns 306
APPENDIX-4: Velocity-Depth Models of MASW Method 313
APPENDIX-5: Laboratory Test Results 319
APPENDIX-6: SRF Values for Future Slope Stability Scenarios 364

LIST OF FIGURES

Page

Figure 1.1 Location map of the study area 1
Figure 1.2 Flowchart of the multi-method approach adapted in this dissertation . 3
Figure 1.3 Landslides observed in the Çağlayan Dam site a. Landslide-1 b. Landslide-2 c. Landslide-3 d. Landslide-4 6
Figure 1.4 The crown and foot of Landslide-3 7
Figure 1.5 Comparison of mean annual precipitation records for the years between 1970 and 2011 8
Figure 1.6 The diagram of the water balance sheet of Manisa 10
Figure 1.7 Watershed boundaries of the landslide-prone area 11
Figure 1.8 The distribution of earthquakes that occurred in the radius of 50 km of the dam site 12
Figure 1.9 The $M_w \geq 4.0$ earthquakes that occurred between 1903 and 2020 13
Figure 1.10 The frequency of magnitudes of earthquakes that occurred in the region between the years 1900 and 2020 13
Figure 1.11 Elastic design acceleration spectra for seismic Zone 1 and local site class Z1 and ZA 16
Figure 2.1 Generalized stratigraphic columnar section of the study area 17
Figure 2.2 Geology map of the study area with shaded relief 18
Figure 2.3 Siltstone interbedded schist of Keçidağ Formation 19
Figure 2.4 The faulted and folded structure of schist unit of Keçidağ Formation 20
Figure 2.5 Light grey colored, fractured, recrystallized limestone around the dam axis 21
Figure 2.6 Mudstone, siltstone, sandstone, conglomerate intercalations of Ilıcak member of Göcek Formation 22
Figure 2.7 Conglomerate with boulders 22
Figure 2.8 Siltstone, cross-bedded sandstone, conglomerate intercalations of Hamit member of Yeniköy Formation 23
Figure 2.9 Faulted and folded structure of siltstone, sandstone, and calcareous mudstone of Yeniköy Formation (15/35, Thrust fault) 24

Figure 2.10 Partly consolidated slope debris with coarse grains of limestone and schist originated gravels that transported into the streambed 25
Figure 2.11 Active faults around the study area 26
Figure 2.12 A strike-slip fault with minor normal fault component 27
Figure 2.13 A thrust fault observed in the study area 28
Figure 2.14 NE-SW trending normal fault observed in the study area 28
Figure 2.15 a. The pole points of nine fault measurements and their representative great circle on the stereographic net b. Rose diagram showing strikes of the discontinuities 29
Figure 2.16 Geological cross-section of A-A′ constructed along the dam axis (taken from 1/10000 scale map) 30
Figure 2.17 Geological cross-section of B-B′ constructed along the Landslide-1 (taken from 1/10000 scale map) 30
Figure 3.1 The photomicrographs of the Neogene aged sedimentary rocks exposed in the study area 32
Figure 3.2 The samples subjected to geochemical analyses 37
Figure 3.3 Disc shape splitting observed in calcareous mudstone samples 38
Figure 4.1 Sampling points shown on the geological shaded relief map 41
Figure 4.2 The contour map of a. Joint b. Bedding planes and great circles of the pole concentration points (equal-area lower hemisphere) 43
Figure 4.3 The illustration of spacing measurement in a discontinuity set 45
Figure 4.4 The histograms of spacing measurement on the slope face for the discontinuity sets a. J-1, J-2, J-3, J-5 b. B-3 c. J-4 d. B-1 e. B-2 46
Figure 4.5 Histogram of the fracture frequency measured on the slope face 47
Figure 4.6 The histograms of persistence measurement for the discontinuity sets a. J-1, J-2, J-3, J-5 and b. B-1 50
Figure 4.7 Typical roughness profiles for JRC range 51
Figure 4.8 An alternative method for estimating JRC from surface roughness amplitude from a straight edge 52
Figure 4.9 Illustration of JRC measurement in the field in four directions with profile comb 53
Figure 4.10 Example of roughness profiles measured by profile comb in the field 53

Figure 4.11 The histograms of aperture measurement for the discontinuity sets a. J-1, J-2, J-3, J-5 b. J-4 c. B-1, B-2 d. B-3 55
Figure 4.12 The effective weathering type in the study area 57
Figure 4.13 a Discoloration around the joints (weathering class II) b Discoloration and disintegration along fault plane (weathering class III) (70/48, normal fault) c (weathering class V)..... 58
Figure 4.14 Discoloration referring to weathering class I-II in some a. KÇ, b. M, c. ÇK, and d. Ç samples..... 60
Figure 4.15 The locations of boreholes drilled in the study area 63
Figure 4.16 The rock blocks slid into the streambed due to the mass movements .. 65
Figure 4.17 The core box of BH-32 between the depth 15 m and 21 m showing the breccia zone 66
Figure 4.18 The histograms of a. RQD (%) and b. λ (m^{-1}) measured on the drill cores 67
Figure 4.19 The in-situ shear vane test 70
Figure 4.20 The MASW and ERT profiles in the study area..... 75
Figure 4.21 S-wave versus depth model of Profile 4 77
Figure 4.22 Rock blocks moved into the stream bed after the mass movements (in front of Landslide-3)..... 77
Figure 4.23 Sub-surface profiles of boreholes BH-11 and BH-36 78
Figure 4.24 V_s-depth model at the midpoint of the profiles obtained using MASW method 79
Figure 4.25 Groundwater levels defined in the boreholes and the ERT profiles..... 85
Figure 4.26 Electrical resistivity tomography results for a. P1 profile, b. P2 profile, c. P3 profile..... 86
Figure 5.1 S-wave velocities were measured by Proceq Pundit PL-200 instrument . 91
Figure 5.2 The variations of $V_{p\text{-}dry}$ with various specimen lengths..... 92
Figure 5.3 The variations of $V_{p\text{-}sat}$ with various specimen lengths 93
Figure 5.4 The variations of $V_{s\text{-}dry}$ with various specimen lengths 93
Figure 5.5 The variations of $V_{s\text{-}sat}$ with various specimen lengths..... 94
Figure 5.6 The apparatus for the Brazilian test 100
Figure 5.7 The rock samples subjected to the Brazilian test..... 102

Figure 5.8 a. Diametral and b. Axial point load test 103
Figure 5.9 The rock samples subjected to point load test 105
Figure 5.10 a. TIRA 28500 Test System b. MTS System Corporation c. ELE ADR 2000 107
Figure 5.11 Stress-strain graphs for the samples examined by Tira 28500 109
Figure 5.12 Schematic representation of different failure modes under uniaxial compression 109
Figure 5.13 The relationship between E_{avg} and n 110
Figure 5.14 The relationship between σ_{ci} and n 111
Figure 5.15 The relationship between the in-situ and laboratory-measured elastic modulus values 111
Figure 5.16 Illustration of determining cohesion and internal friction angle from Mohr-Coulomb Failure envelope with a tension cutoff..... 112
Figure 5.17 GS-1000 shear-box test device in rock mechanics laboratory in Freiberg, Germany..... 118
Figure 5.18 The image of the oncoidal failure surface observed for M-1 119
Figure 5.19 The time-shear stress-shear displacement graph under 5 MPa normal stress for the sample M-1..... 119
Figure 5.20 The shear stress-shear displacement graph under 5 MPa normal stress for the sample M-1..... 120
Figure 5.21 Directions of the applied shear stress during the shear-box test..... 121
Figure 5.22 The image of M-2 after the shear box test..... 121
Figure 5.23 Stress-time-shear displacement graph for M-2 sample under multi-staged normal stress condition (σN: 2, 5, 10 MPa)..... 122
Figure 5.24 The Mohr-Coulomb envelope of the M-2 sample on the shear stress-normal stress graph 123
Figure 5.25 Shear stress-shear displacement graph for M-2 sample under various normal stress conditions (2, 5, and 10 MPa) in four shear directions. 123
Figure 5.26 The image of M-3 after the shear box test..... 124
Figure 5.27 Stress-time-shear displacement graph for M-3 sample under multi-staged normal stress condition (σN: 2, 5, 10 MPa)..... 125

Figure 5.28 The Mohr-Coulomb envelope of the M-3 sample on the shear stress-normal stress graph 125
Figure 5.29 Shear stress-shear displacement graph for M-3 sample under various normal stress conditions (2, 5, and 10 MPa) in four shear directions. 126
Figure 5.30 The image of M-4 after the shear box test 126
Figure 5.31 Stress-time-shear displacement graph for M-4 sample under multi-staged normal stress condition (σN: 2, 5, 10 MPa) 127
Figure 5.32 The Mohr-Coulomb envelope of the M-4 sample on the shear stress-normal stress graph 128
Figure 5.33 Shear stress-shear displacement graph for M-4 sample under various normal stress conditions (2, 5, and 10 MPa) in four shear directions. 128
Figure 5.34 The comparison of average failure envelopes for 3 samples in shear direction-1 132
Figure 5.35 The comparison of average failure envelopes for 3 samples in shear direction-3 133
Figure 5.36 Idealized creep curve showing the stages of creep deformation 134
Figure 5.37 Viscoplastic deformations versus time during the creep test performed on K-14 sample 135
Figure 5.38 The representation of the cyclic loading parameters such as loading level, amplitude, and number loading cycles 139
Figure 5.39 The procedure for calculating dynamic elastic modulus (E_{dyn}) of one loading level (20 MPa) on the stress-strain graph 141
Figure 5.40 The cyclic stress-strain graphs of samples 142
Figure 5.41 The image of the failure surface of the M-50 sample after the dynamic uniaxial compression test 143
Figure 5.42 MTS-815 the triaxial compression test machine and the sample preparation for the test 144
Figure 5.43 Stress-strain curves of triaxial test peformed on M-44 sample with confining stress of 5 MPa 145
Figure 5.44 Stress-strain curves of triaxial test performed on M-47 sample with confining stress of 2 MPa 146
Figure 5.45 The images of M-44 and M-47 after cyclic triaxial compression tests 147

Figure 5.46 Dynamic shear test set up-1 as cyclic loading superimposed on the shear load..... 148
Figure 5.47 Complete stress-displacement-time graph of the M-51 by set up-1 showing various amplitudes of cycles 148
Figure 5.48 Dynamic shear test set up-2 as cyclic loading superimposed on the normal load 149
Figure 5.49 A portion of the stress-displacement-time graph of the M-51 by set up-2 showing different loading levels and frequencies of cycles 150
Figure 5.50 A portion of the normal displacement- shear displacement graph of the M-51 by set up-2 showing contraction and dilation during the early cycles 150
Figure 5.51 A portion of the stress-time graph of the M-51 by set up-2 showing small oscillations on the shear stress curve 151
Figure 5.52 Complete force-shear displacement-time graph of M-2 sample subjected to dynamic loading..... 152
Figure 5.53 Shear stress-shear displacement graph of M-2 sample subjected to dynamic loading..... 153
Figure 5.54 Complete force-shear displacement-time graph of M-3 sample subjected to dynamic loading..... 153
Figure 5.55 Shear stress-shear displacement graph of M-3 sample subjected to dynamic loading..... 154
Figure 5.56 Complete force-shear displacement-time graph of M-4 sample subjected to dynamic loading..... 155
Figure 5.57 Shear stress-shear displacement graph of M-4 sample subjected to dynamic loading..... 155
Figure 5.58 Shear stress-shear displacement graph showing the first 4 cycles of the dynamic excitation of M-2 specimen under 10 MPa normal stress (amplitude of the cyclic load: ±18 kN, loading level: 62 kN~ 1.37 MPa) 156
Figure 5.59 The comparison of average failure envelopes for 3 samples obtained from the shear test, and the empirical Mohr-Coulomb approach for dynamic loading..... 158

Figure 6.1 Size effects on the utilization of GSI 160
Figure 6.2 Quantitative GSI chart proposed by Sönmez&Ulusay (2002) 162
Figure 6.3 Quantitative GSI chart for poor and very poor rock masses proposed by Osgui et al. (2010) 163
Figure 6.4 Classification of the drill cores of weak/disintegrated rock and Göcek Fm. based on the BSTR 164
Figure 6.5 Quantitative GSI chart proposed by Cai et al. (2004) 166
Figure 6.6 Quantitative GSI chart proposed by Russo (2009) 167
Figure 6.7 Quantitative GSI chart proposed by Hoek et al. (2013) 169
Figure 6.8 The variations of elastic modulus values of intact rock and rock mass estimated from different testing methods 178
Figure 7.1 The illustration of the parts of a landslide body 183
Figure 7.2 Dji Phantom 4 Pro drone with an onboard camera 188
Figure7.3 The cross-section of Landslide-1 showing the topography with uncorrected tree heights 189
Figure 7.4 Comparison of landslide areas between the years 1953 and 2017 191
Figure 7.5 The sub-areas in the region to determine the average height error between images 192
Figure 7.6 The cross-section lines taken from the midpoint of the landslide polygons 193
Figure 7.7 Illustration of drawing secondary polygon for accumulation on the plan view of Landslide-4 with respect to the overlapped cross-section profiles of 1970 and 1995 194
Figure 7.8 Illustration of drawing secondary polygon for accumulation and depletion on the plan view of Landslide-4 with respect to the overlapped cross-section profiles of 1953 and 1970 195
Figure 7.9 The cross-sections of Landslide-4 showing the differences in topography between 2012-1995 195
Figure 7.10 The cross-sections of Landslide-4 showing the differences in topography between 2017-2012 196
Figure 7.11 The change in average height difference between two successive DEMs with respect to the number of sub-areas 197

Figure 7.12 The differential DEMs of a. 2012-1995 b. 1995-1970 c. 1970-1953 ... 199
Figure 7.13 The slope maps of each year a. 1953 b. 1970 c. 1995 d. 2012 202
Figure 8.1 Stereographic projection of the critical mean set planes, Landslide-1, and the water flow directions 207
Figure 8.2 Stereographic projection of the critical mean set planes, Landslide-2, and the water flow direction 208
Figure 8.3 Stereographic projection of the critical mean set planes, Landslide-3, and the water flow direction 209
Figure 8.4 Stereographic projection of the critical mean set planes, Landslide-4, and the water flow direction 210
Figure 8.5 The two-block model 211
Figure 8.6 Generalized geotechnical model of the landslides in the study area .. 211
Figure 8.7 The proposed method for back analyses based on the vertical displacement and the location of failure surface (Landslide-1)..... 221
Figure 8.8 The illustration of using the ubiquitous joint tool a. 1953, Landslide-4 b.1970, Landslide-4 223
Figure 8.9 An example of the geometrical and structural design of the slope models in RS2 (Landslide-4, 1995 topography) 224
Figure 8.10 Critical tension crack depth relative to the crest of cut 226
Figure 8.11 The slope models of Landslide-1 in the years of a.1953 b. 1995 c.2012 229
Figure 8.12 The slope models of Landslide-2 in the years of a.1953 b. 1970 c.1995 d.2012 231
Figure 8.13 The comparison of 1970 and 1995 topography of Landslide-2, the harmony of depletion and accumulation areas with SSR result 232
Figure 8.14 The slope models of Landslide-3 in the years of a.1953 b. 1970 c.1995 d.2012 234
Figure 8.15 The comparison of 1970 and 1995 topography of Landslide-3, the harmony of depletion and accumulation areas with SSR result 235
Figure 8.16 The slope models of Landslide-4 in the years of a.1953 b. 1970 c.1995 d.2012 237

Figure 8.17 The comparison of 2012 and 2017 topography of Landslide-4, the harmony of depletion and accumulation areas with SSR result 238
Figure 8.18 The maximum shear stress contours of the worst future scenario for Landslide-1 242
Figure 8.19 The maximum shear stress contours of the worst future scenario for Landslide-2 244
Figure 8.20 The maximum shear stress contours of the worst future scenario for Landslide-3 246
Figure 8.21 The maximum shear stress contours of the worst future scenario for Landslide-4 248
Figure 8.22 The comparison of flow lines and pore pressures a. Before dam construction b. After dam construction with minimum water level (Landslide-4)..... 250
Figure 8.23 The comparison of pore pressures occurred after dam construction with a. Maximum water level b. Minimum water level (Landslide-1)..... 252

LIST OF TABLES

Page

Table 1.1 The climate data of Manisa between 1930 and 2018 7

Table 1.2 Thornthwaite water balance sheet 9

Table 1.3 The selected twenty earthquakes out of 129 to be evaluated in terms of triggering factor 15

Table 3.1 Thin section observations and the assigned names of the carbonate rock samples 33

Table 3.2 Thin section observations and the assigned names of the clastic rock samples 34

Table 3.3 The results of XRD analyses 36

Table 3.4 The whole-rock geochemical analyses (major elements) results 39

Table 4.1 The orientations of dominant bedding and joint sets in Neogene aged sedimentary rocks 44

Table 4.2 Statistics of true spacing values of the discontinuity sets 45

Table 4.3 The J_v of the rock mass from different assumptions 48

Table 4.4 The block shape factor and the corresponding block volumes 49

Table 4.5 Statistics of the persistence of the discontinuity sets 50

Table 4.6 Statistics of the aperture of the discontinuity sets 56

Table 4.7 Descriptions assumed as reference for defining weathering classes 59

Table 4.8 In-situ Schmidt hammer test results performed on limestone and silty sandstone discontinuity surfaces in Göcek Formation 62

Table 4.9 The drilled boreholes in the study area 64

Table 4.10 RQD calculated directly from drill cores and different empirical methods 68

Table 4.11 In-situ shear vane test results 71

Table 4.12 The range of permeability values for the lithological units in the study area 73

Table 4.13 The average weighted P and S-wave velocities for six MASW profiles 81

Table 4.14 The dynamic geotechnical parameters of the four rock mass zone in the dam site 83

Table 5.1 The standards followed in laboratory tests and the number of samples subjected to these tests 87
Table 5.2 The descriptive statistics of effective unit weight (γ), effective porosity (n), water absorption by weight (S_w) of the specimens 88
Table 5.3 The descriptive statistics of V_p and V_s of studied rocks 95
Table 5.4 The descriptive statistics of empirically calculated dynamic elastic properties of the studied rock specimens for dry and saturated conditions 97
Table 5.5 Schmidt hammer rebound values and the corresponding JCS values of the 20x10x10 cm samples 99
Table 5.6 The descriptive statistics of σ_t values of the studied rocks obtained from Brazilian test 101
Table 5.7 The descriptive statistics of $I_{s(50)}$ values for the studied rocks 104
Table 5.8 The descriptive statistics of σ_{ci}, $E_{avg,}$ and υ_i for the investigated rock samples under dry conditions 108
Table 5.9 The descriptive statistics of σ_{ci}, $E_{avg,}$ and υ_i for the investigated rock samples under saturated conditions 108
Table 5.10 The cohesion (c) and the internal friction angle (ϕ) of the intact rock samples calculated based on the Mohr circles of Brazilian and uniaxial compression tests 114
Table 5.11 Static shear test results 129
Table 5.12 The shear stiffness (k_s) values for the samples M-2, 3, and 4 under various normal stress conditions and different shearing directions 130
Table 5.13 The estimated normal and shear stiffness values for the rock samples by using laboratory and in-situ normal and shear modulus values 131
Table 5.14 Creep test results 136
Table 5.15 The parameters used in dynamic tests 138
Table 5.16 Literature review of the comparison between dynamic and static uniaxial compressive strength and elastic modulus 140
Table 5.17 The results of the dynamic uniaxial compressive strength test of sandstone and clayey limestone samples 142
Table 5.18 The results of dynamic triaxial compression tests 145

Table 5.19 Dynamic shear test results 157
Table 6.1 Ranges of rock mass parameters used in GSI estimation and the GSI values estimated from various quantitative methods 171
Table 6.2 Classes of σ_{ci} values obtained by cluster analysis and the GSI values favorable for these classes and the ranges of m_i values 174
Table 6.3 The empirical equations estimating rock mass modulus (E_m) proposed by various researchers based on GSI..... 176
Table 6.4 The E_m values estimated from different empirical equations 177
Table 6.5 The statistics of the intact rock and rock mass properties for Yeniköy Formation 179
Table 6.6 The statistics of the intact rock and rock mass properties for Göcek Formation 179
Table 6.7 The statistics of the intact rock and rock mass properties for very weak rock unit /slope debris 180
Table 7.1 The acquisition parameters of aerial photographs 186
Table 7.2 The landslide areas calculated with respect to the digitized polygons .. 190
Table 7.3 Height differences in differential DEMs before and after image to image coregistration and height adjustment..... 198
Table 7.4 Depleted (cut) and accumulated (fill) volumes for each landslide for the periods 201
Table 8.1 Kinematic analyses results of four landslides with regard to the maximum and overall slope angles 205
Table 8.2 The ranges of the strength and deformation properties of the landslide mass with respect to Generalized Hoek-Brown Criterion..... 216
Table 8.3 The ranges of strength and deformation properties of the soil and rock mass with respect to Mohr-Coulomb Criterion..... 217
Table 8.4 The calculated ϕ_r values based on the static and dynamic ϕ_b values of M-samples, in-situ and laboratory-measured Schmidt hammer rebound values..... 217
Table 8.5 The ranges of strength and stiffness properties of the soil and rock mass with respect to Barton-Bandis Criterion..... 218
Table 8.6 The SRF values for the landslides under ambient conditions..... 220

Table 8.7 The back analyzed properties of the discontinuities 224
Table 8.8 The variations of parameters used in water pressure calculation and the ranges of water pressure used in back analyses 227
Table 8.9 The back analyzed water pressure values 227
Table 8.10 The post-failure strength and deformation properties of the landslide mass at the failure (due to triggering factors) by years obtained from the back analyses (Landslide-1)..... 230
Table 8.11 The post-failure strength and deformation properties of the landslide mass (due to triggering factors) by years obtained from the back analyses (Landslide-2) 233
Table 8.12 The post-failure strength and deformation properties of the landslide mass at the failure (due to triggering factors) by years obtained from the back analyses (Landslide-3)..... 236
Table 8.13 The post-failure strength and deformation properties of the landslide mass at the failure (due to triggering factors) by years obtained from the back analyses (Landslide-4)..... 239
Table 8.14 The strength and deformation values used in the analyses for Landslide-1 241
Table 8.15 The SRF and vertical displacement variations by years and the comparison with the amount of displacement derived from photogrammetric analyses (Landslide-1) 243
Table 8.16 The strength and deformation values used in the analyses for Landslide-2 243
Table 8.17 The SRF and vertical displacement variations by years and the comparison with the amount of displacement derived from photogrammetric analyses (Landslide-2) 245
Table 8.18 The strength and deformation values used in the analyses for Landslide-3 245
Table 8.19 The SRF and vertical displacement variations by years and the comparison with the amount of displacement derived from photogrammetric analyses (Landslide-3) 247

Table 8.20 The strength and deformation values used in the analyses for Landslide-4 247
Table 8.21 The SRF and vertical displacement variations by years and the comparison with the amount of displacement derived from photogrammetric analyses (Landslide-4) 249
Table 8.22 The SRF values of each landslide associated with the seepage analyses 251

CHAPTER ONE
INTRODUCTION

1.1 Location of the Study Area

The study area is covering the Çağlayan Dam reservoir area which is located approximately 22 km southeast of Akhisar town in Manisa, Turkey (Figure 1.1). It is involved in the 1/25000 scale, K20-a4 map sheet. Çağlayan Dam was planned to be built on the Kayacık River. The crest elevation was planned to be 295 m and the talweg elevation is 200 m. The valley shape factor is approximately 5.11 and the dam can be designed to be a concrete faced rockfill dam which is widely preferred for its low-cost and practical construction and for being ideal in earthquake prone areas (Karlsson & Tallberg, 2011). It is estimated that 26 hm^3 water per year will be provided for the use of drinking and industrial purposes to İzmir city. However, the Çağlayan Dam project was recently suspended by The General Directorate of State Hydraulic Works (DSI).

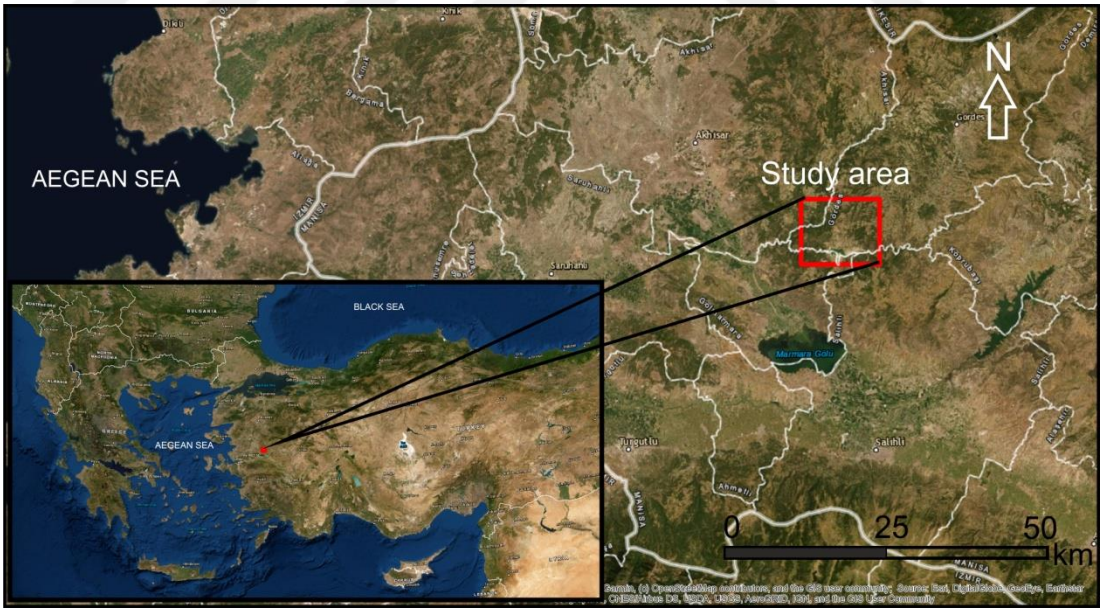


Figure 1.1 Location map of the study area

1.2 Scope of the Study

The landslides in the reservoir area of dam sites necessitate profound geological and geotechnical investigations since any mass movement after dam construction may cause catastrophic damage to the engineering project. Essentially, the volume of earth material transported during a failure and the rate of movement are important parameters. The topography evolves over years by landslides; the geological units also evolve from a geotechnical point of view. In other words, not only the topography changes with mass movements but also the mechanical and elastic properties of the mass change over time; crack formation or crack widening occurs. A reliable geotechnical model facilitates understanding of the landslide evolution in the dam site and gives an opinion for future slope stability conditions. Besides, the operational life of a dam also depends on the volume of material transported by the stream and its tributaries, and the landslide material slid into the reservoir. As the sediments accumulate in the reservoir, the dam gradually loses its storage capacity due to siltation. Therefore, estimating the volume of sliding material into the reservoir is crucial for evaluating the economic feasibility of a dam project.

There are four landslides that have already occurred in the Çağlayan Dam reservoir area. This dissertation aims to (i) determine the multi-temporal topographical evolution (ii) construct a generalized geotechnical model explaining the mechanism of the landslides (iii) estimate the volume and sliding rate of landslides (iv) determine the role of triggering factors (e.g., seismic activity, heavy rainfall, wildfire) in the landslides (v) predict future slope stability conditions of the landslides through several scenarios. This dissertation will also focus on the investigation of the variations in mechanical and deformational properties of the joints and rock units over time by back analyses to fulfill the aims of this study.

1.3 Methodology

In order to achieve the scope of this dissertation, a multi-method approach was adapted (Figure 1.2).

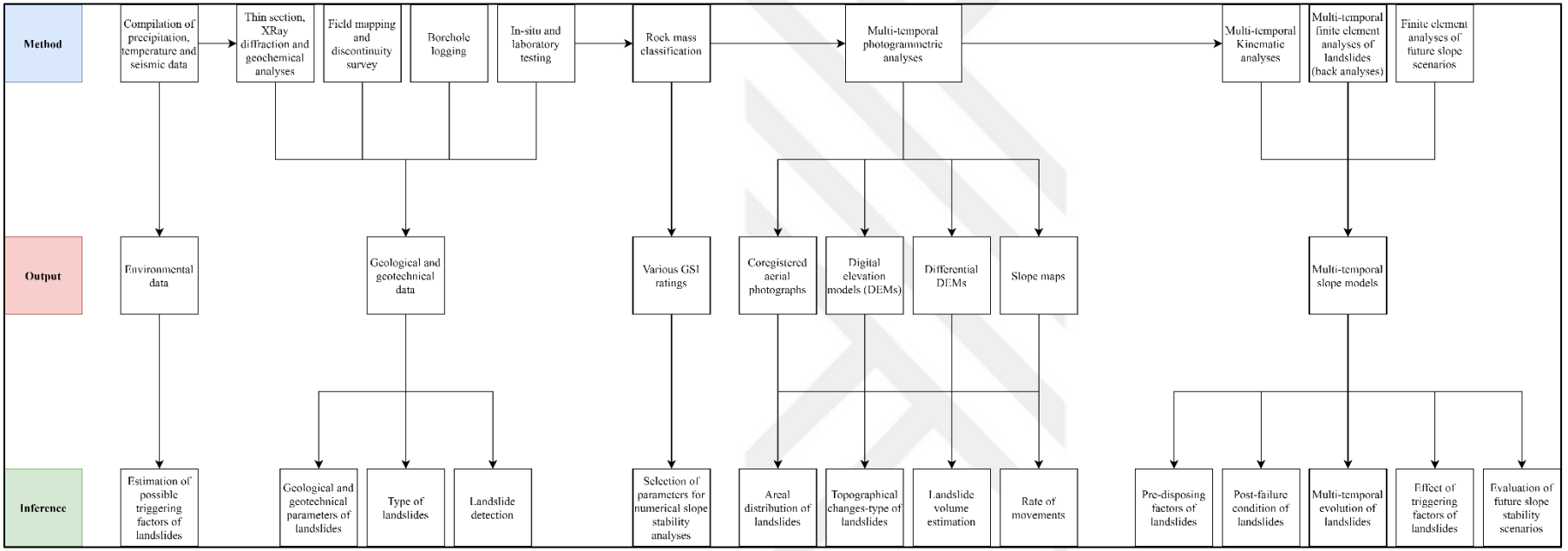


Figure 1.2 Flowchart of the multi-method approach adapted in this dissertation

Initially, published data on geology, seismicity, precipitation, and temperature of the study area were gathered. The core logs of boreholes drilled in the site by the DSI as well as permeability and standard penetration test (SPT) results were reviewed. The climate of the study area was determined by the aid of the Thornthwaite (1948) approach. Afterward, site investigations were performed to obtain detailed geological, geotechnical, geophysical information, and remote sensing data. In this context, a 1/10000 scale geological map was prepared; geotechnical investigations such as discontinuity measurement on scan-lines, Schmidt hammer test, shear vane test; geophysical studies such as multichannel analysis of surface waves (MASW), and electrical resistivity tomography (ERT), and remote sensing image acquisition by unmanned aerial vehicle (UAV) were carried out. In addition, rock blocks were collected from the banks of the reservoir area and cored in the laboratory for laboratory testing. Mineralogical, petrographical, and geochemical investigations of the samples were performed via examining thin sections, whole-rock geochemical analysis, X-Ray diffractometer (XRD) analysis. Several index tests, static and dynamic mechanical tests such as Schmidt hammer, ultrasonic pulse velocity, Brazilian indirect tensile strength, point load, direct shear, uniaxial and triaxial compressive strength tests were performed in the laboratory. Photogrammetric analyses were carried out by processing UAV images as well as multi-temporal aerial photographs of the study area. The landslides have been mapped on the stereographic remote sensing images. Digital elevation models (DEMs) from the stereographic aerial photographs have been constructed to calculate landslide volume (depleted and accumulated volume) and to evaluate topographical changes during 64 years period (1953-2017). The accuracy of the volumetric analyses was improved by image to image coregistration, height adjustment techniques, and cross-sectional analyses. A generalized geotechnical model for the landslides was constructed based on the data derived from above mentioned investigations. Rock mass classification was performed based on Geological Strength Index (GSI). Various quantitative GSI charts were applied to weak, Neogene aged sedimentary rocks in the study area. Thereafter, kinematic analyses and stereographic projections of the four landslides considering the critical discontinuity set orientations and flow directions of the tributaries were made to evaluate the effect of structural features on slope failures.

Finally, multi-temporal back analyses considering the topography of different years (1953, 1970, 1995, 2012) were performed manually by the finite element method (FEM) to estimate realistic post-failure properties of joints and rock mass. Back analyses were based upon a set of parametrical calculations with various combinations of input parameters as well as the triggering factors (seismic activity, heavy rainfall, water pressure on discontinuities, and wildfire). It was aimed to set an optimal combination of input parameters and environmental conditions which reflects the behavior of the slope model close to the real slope behavior that is compatible with the photogrammetric analyses results. In other words, the given set of material properties and structural and environmental conditions that yielded the best harmonizing vertical displacement with the one obtained from photogrammetric analyses were assumed to be the post-failure condition of the slope. In this context, a structurally and mechanically evolving multi-temporal model has been set up for back analyses. In addition, future slope conditions using the topography of the year 2017 were evaluated to obtain the deterministic safety factor and to estimate the volume of depleted material by the effect of seismic, heavy rainfall, seepage, and drawdown under maximum, minimum, and no reservoir water level conditions.

1.4 Overview of Landslides

Landslides close to the study area (minimum: 11.86 km) are classified as old landslides and rarely active landslides (Duman, Çan, & Emre, 2011). The point concentration map of landslide-prone areas in Turkey is very well matched with the active fault map and geological map of Turkey (Gökçe, Özden, & Demir, 2008). Hence, the landslides in the region are strongly related to the fault zones. However, four landslide scarps observed in the Çağlayan Dam site were not mapped in the landslide inventory map of Turkey due to their relatively small areal coverage (Figure 1.3). The right and left banks of the Çağlayan Dam reservoir area were affected by mass movements. The four landslides have been contributing sediment input to the Kayacık streambed. Three of the landslides are on the northern bank (Landslide-1, 2, and 4) and the other one (Landslide-3) is on the southern bank of the reservoir area. Landslide-1 is dominantly composed of sandstone, mudstone,

limestone, and conglomerate; Landslide-2 and Landslide-4 are composed of sandstone, siltstone, conglomerate intercalation, and Landslide-3 dominantly consist of highly fractured clayey limestone with unfilled, opened joints (Figure 1.3). The four slope faces are covered with slope debris and soil derived from the Neogene sedimentary rocks at present.

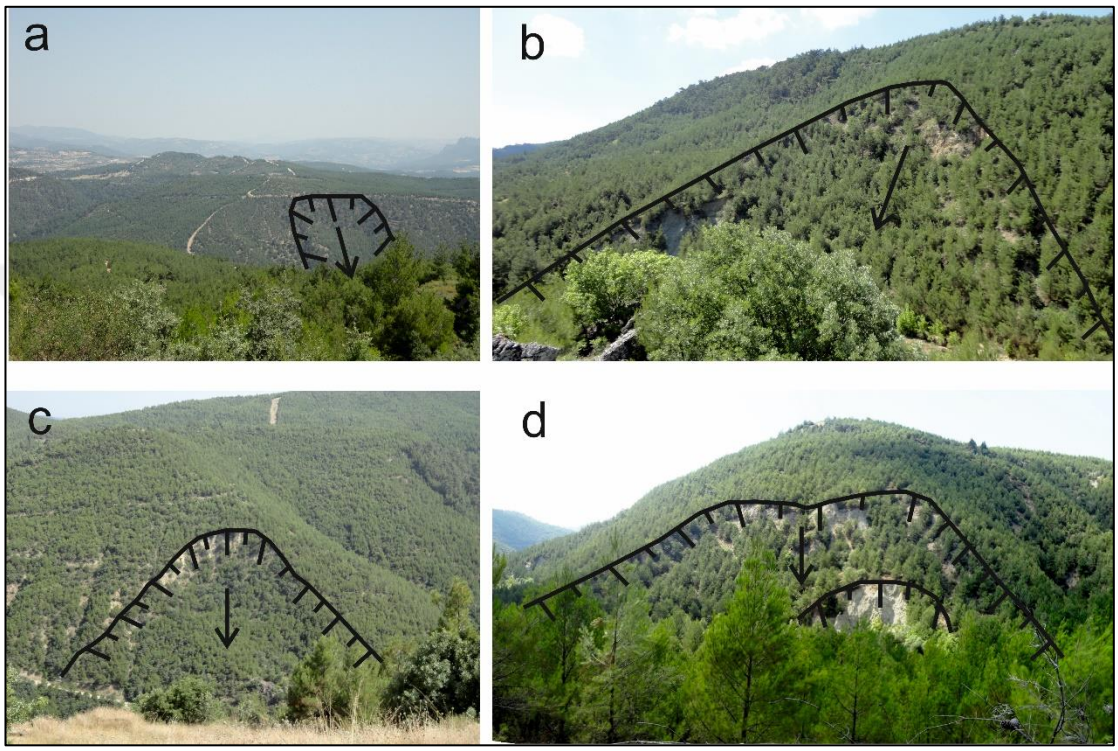


Figure 1.3 Landslides observed in the Çağlayan Dam site a. Landslide-1 b. Landslide-2 c. Landslide-3 d. Landslide-4 (Personal archive, 2012)

The arc-shaped crest and bulging at the foot were observed in the field. Other landslide body parts such as right and left flanks, crown cracks are not possible to be identified due to the dense vegetation and steep slopes. However, minor scarps were observed along Landslide-4 (Figure 1.3d). The crown and foot of Landslide-3 were clearly identified on the photograph acquired by UAV (Figure 1.4).

The altitudes range from 220 m to 480 m in the landslide-prone area. Besides, the slope angles are ranging between 10° and 51°.

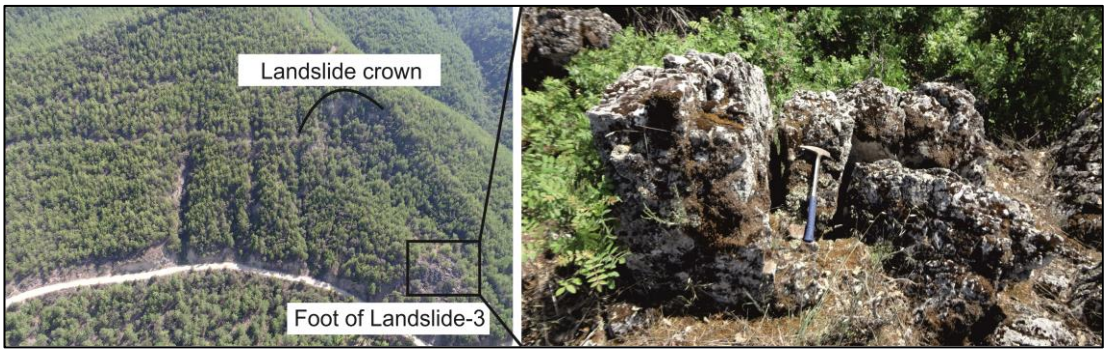


Figure 1.4 The crown and foot of Landslide-3 (Personal archive, 2017)

1.5 Climate, Vegetation, and Hydrology

Precipitation and temperature records were derived from the Turkish State Meteorological Service (MGM) (2019) for the years 1930 to 2018. The mean monthly temperatures ranged from 6.6 °C in January and 27.9 °C in July. The mean monthly precipitation ranges from 5.4 mm to 136.7 mm (Table 1.1).

Precipitation records indicate that %89 of annual precipitation falls between October and April (Figure 1.5). The mean annual precipitation in Manisa city for the period between 1930 and 2018 is 728 mm. The amount of annual precipitation significantly decreases between the years 1989 and 1994. However, an intense daily rainfall (163.5 mm) was also observed on 23 December 1986 which is greater than the mean monthly precipitation value of December. From the slope stability point of view, excessive daily rainfall is playing a more important role as a triggering factor.

Table 1.1 The climate data of Manisa between 1930 and 2018

	Mean of maximum temperature (°C)	Maximum temperature (°C)	Mean of minimum	Minimum temperature (°C)	Mean temperature	Mean of monthly precipitation	No of days precipitated
January	10.8	24.0	2.9	-17.5	6.6	124.6	13.2
February	12.6	26.4	3.7	-10.9	7.8	107.2	11.1
March	16.2	33.5	5.3	-6.7	10.5	78.5	10.0
April	21.4	34.7	8.9	-2.7	15.1	55.6	9.0
May	27.0	39.5	13.3	2.0	20.3	39.7	6.8
June	32.1	42.4	17.5	7.4	25.1	17.6	3.3
July	34.9	45.5	20.3	10.5	27.9	5.9	1.0
August	34.8	44.5	20.3	8.5	27.6	5.4	0.8
September	30.6	40.3	16.1	3.3	23.3	16.4	2.3
October	24.3	37.3	11.7	-0.9	17.8	50.9	5.8
November	17.5	29.9	7.4	-7.3	12.1	89.4	9.4
December	12.2	26.4	4.4	-9.9	8.0	136.7	13.7
Annual	22.9		11.0		16.8	728 (total)	86.4

The amount of annual precipitation passes over the mean value (728 mm) in the following years from 1994 with fluctuations every two years (Figure 1.5).

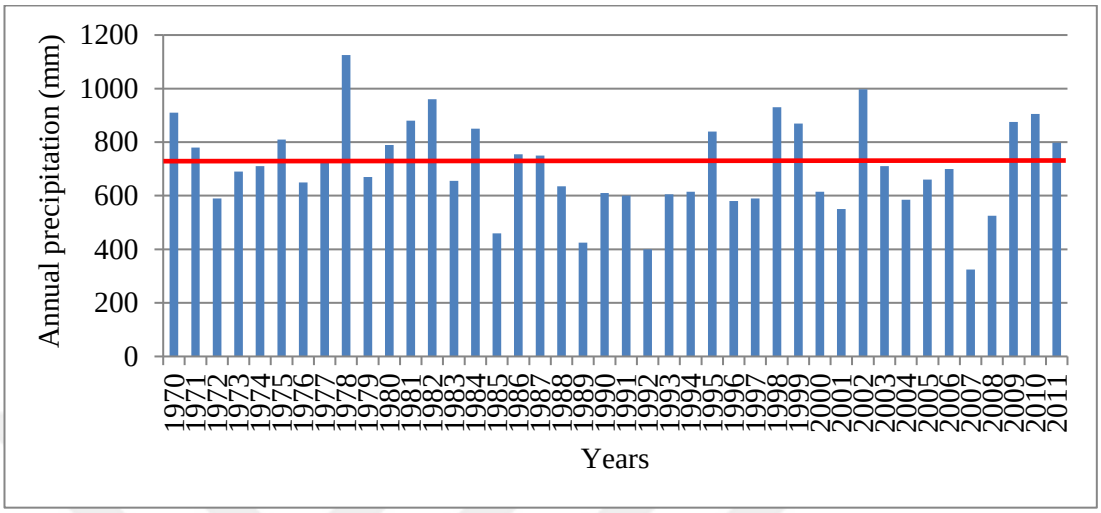


Figure 1.5 Comparison of mean annual precipitation records for the years between 1970 and 2011

The climate of Manisa was defined according to the classification proposed by Thornthwaite (1948). The Thornthwaite classification is based on the relationships between precipitation-evaporation and temperature-evaporation. It is considered that the ground is fully water-saturated in the case precipitation is higher than evaporation. On the contrary, when the precipitation is lower than evaporation, water deficiency in the ground occurs. Firstly, the water balance sheet was constructed according to the mean monthly temperature and precipitation (Table 1.2) and illustrated in Figure 1.6.

Table 1.2 Thornthwaite water balance sheet

Months	MMT (°C)	Temperature indice	Uncorrected PE (mm)	Corrected PE (mm)	Real PE (mm)	MMP (mm)	AWG (mm)	WD (mm)	WE (mm)	Run-off (mm)	HI	VAW
1	6.6	1.56	7.7	3.44	3.44	124.6	100	0	114.0	83.25	33.15	0
2	7.8	2.00	10.5	8.82	8.82	107.2	100	0	100.6	91.96	11.41	0
3	10.5	3.16	23	23.69	23.69	78.5	100	0	58.31	75.13	2.46	0
4	15.1	5.38	45	49.5	49.5	55.6	100	0	8.6	41.87	0.17	0
5	20.3	8.47	82	100.86	100.8	39.7	34.44	0	0	20.93	-0.65	-65.56
6	25.1	11.78	120	148.8	50.94	17.6	0	97.86	0	10.46	-0.89	-34.44
7	27.9	13.65	145	181.25	5.6	5.9	0	175.6	0	5.23	-0.96	0
8	27.6	13.36	140	163.8	4.7	5.4	0	159.1	0	2.61	-0.97	0
9	23.3	10.35	105	109.2	16.5	16.4	0	92.7	0	1.30	-0.84	0
10	17.8	6.95	61	58.56	47.6	50.9	0	10.96	0	0	-0.18	0
11	12.1	3.86	25	21.00	21	89.4	68.5	0	0	0	3.26	68.5
12	8.0	2.23	13	10.79	10.79	136.7	100	0	104.6	52.45	12.64	31.5
Annual	16.8	82.75		879.71	343.4	728		536.2	386.5	385.19		

PE: Evapotranspiration; MMT: Mean monthly temperature; MMP: Mean monthly precipitation; AWG: Accumulated water in the ground; WD: Water deficiency; WE: Water excess; HI: Humidity in; VAW: Variation of accumulated water

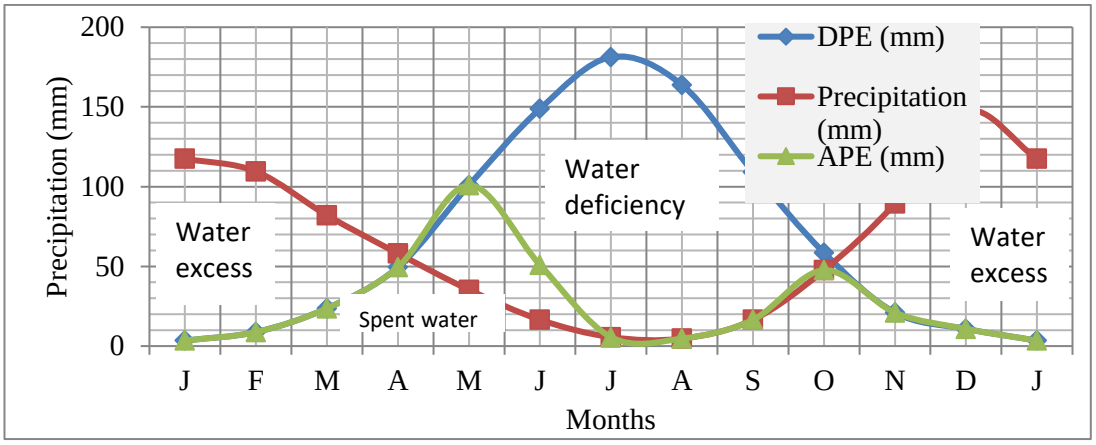


Figure 1.6 The diagram of the water balance sheet of Manisa (DPE: Corrected potential evapotranspiration, APE: real evapotranspiration)

The climate was classified as humid, mesothermal, and large summer efficiency as similarly found by Türkeş (2011) for the surrounding area. Figure 1.6 indicates that in May to October period, water deficiency is present, and the ground is dry and in December to March period, water excess is present.

In brief, the mean annual precipitation in Manisa, Akhisar is 728 mm, and the calculated real evaporation is 343.44 mm. Thus, 47.04% of precipitation is evaporated. In the rainy season (December to April), the water excess is 386.56 mm and 53% of the annual precipitation turns into run-off.

The catchment of the landslide-prone area is approximately 1.22 km^2 (Figure 1.7). The northern part of the catchment has a gentle slope; however, it is steeper in the area where the landslides occur. It should be noted that it is not possible to identify the amount of rainfall within the catchment area unless a station is put in the study area. On the other hand, DSI estimated a maximum water level elevation of 288.73 m in the reservoir after the dam retains water.

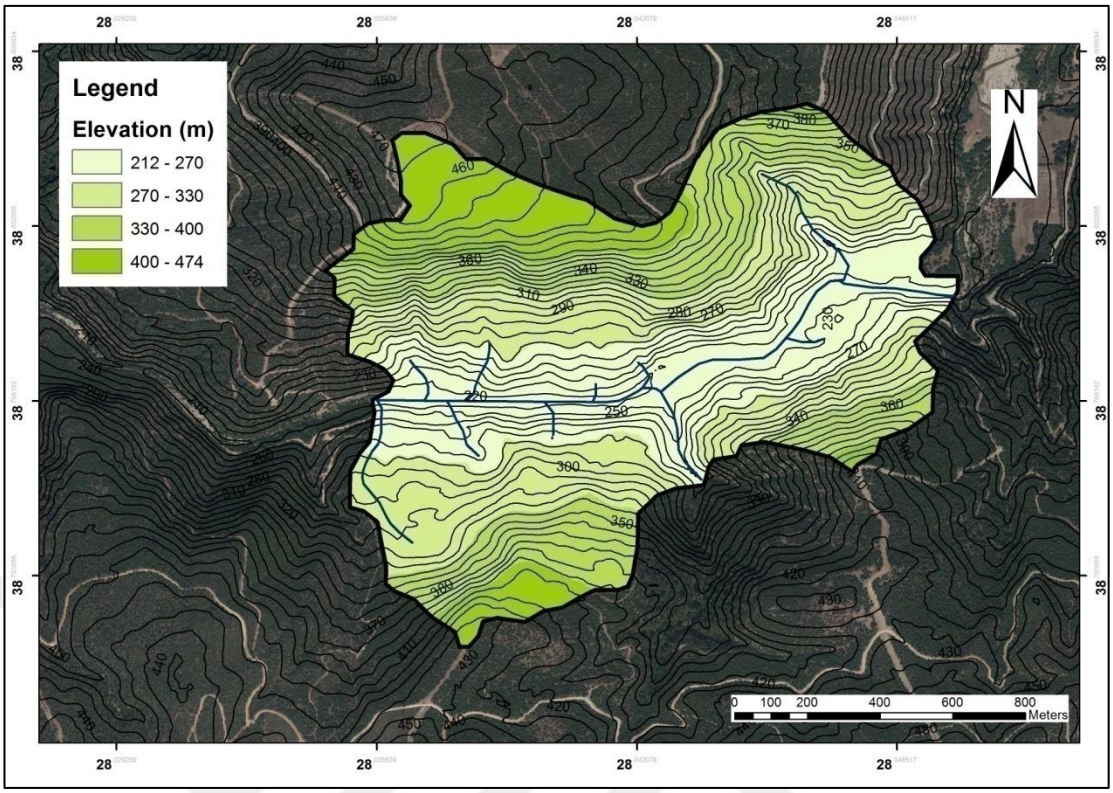


Figure 1.7 Watershed boundaries of the landslide-prone area

The groundwater level is highly variable in the study area due to locally existing karstic drainage in limestones, tectonic, and geological structures such as faults and joints. The seasonal changes in the dam site and its nearby also significantly affect the water table level. The water table level in the banks of the Kayacık River is varying between 7 m and 28 m in June, whereas between 10 and 46 m in October.

Deciduous and coniferous trees, as well as shrubs, characterize the vegetation cover of the study area. Vegetation cover influences the rainfall infiltration and run-off rate and associated erosion rate. Also, root strength directly affects the slope stability as contributing to the shear strength of the soil mantle. Vegetation also contributes to the drying of the slopes by absorbing a portion of groundwater. In 1988 summer, a wildfire had destroyed the vegetation cover on approximately 1190 ha area of the northern and southern hillslopes of Kayacık River (Tezcan Alaca, personal communication, October 10, 2016).

1.6 Seismicity

The city of Manisa is involved in the first-degree earthquake zone according to the Turkish Earthquake zone map (Özmen, Nurlu, & Güler, 1997). Complex structural features of the region indicate that the study area is a seismically active zone. Therefore, earthquakes that occurred in a 50 km radius around the Çağlayan Dam axis between 1900 and 2020 were obtained from the Disaster & Emergency Management Authority (AFAD) Presidential of Earthquake Department earthquake catalog (Figure 1.8).

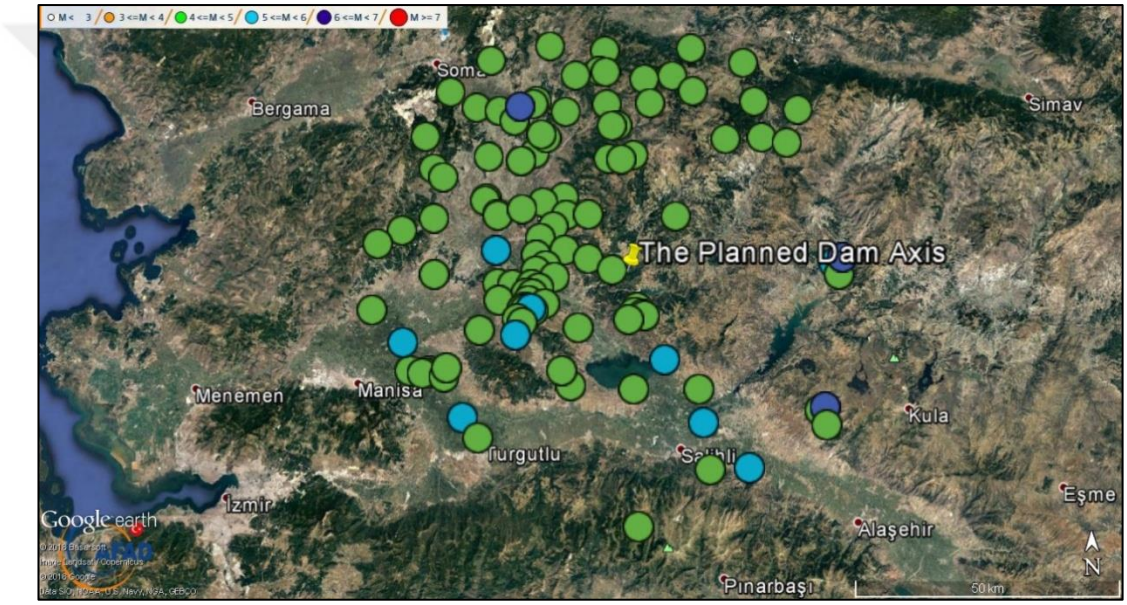


Figure 1.8 The distribution of earthquakes that occurred in the radius of 50 km of the dam site

The moment magnitude (M_w) scale is the best scale for scientific and engineering purposes (Ulusay, Tuncay, Sönmez, & Gökçeoğlu, 2004). However, the recorded earthquakes were not only introduced in the M_w scale but also different (M_s, M_b, M_d, and M_L) scales. Therefore, the recorded magnitudes converted into M_w as suggested by Ulusay et al. (2004). The recorded 129 earthquakes that are greater than M_w: 4.0 are listed in Appendix-1. The distribution of the earthquakes over the past years is illustrated in Figure 1.9.

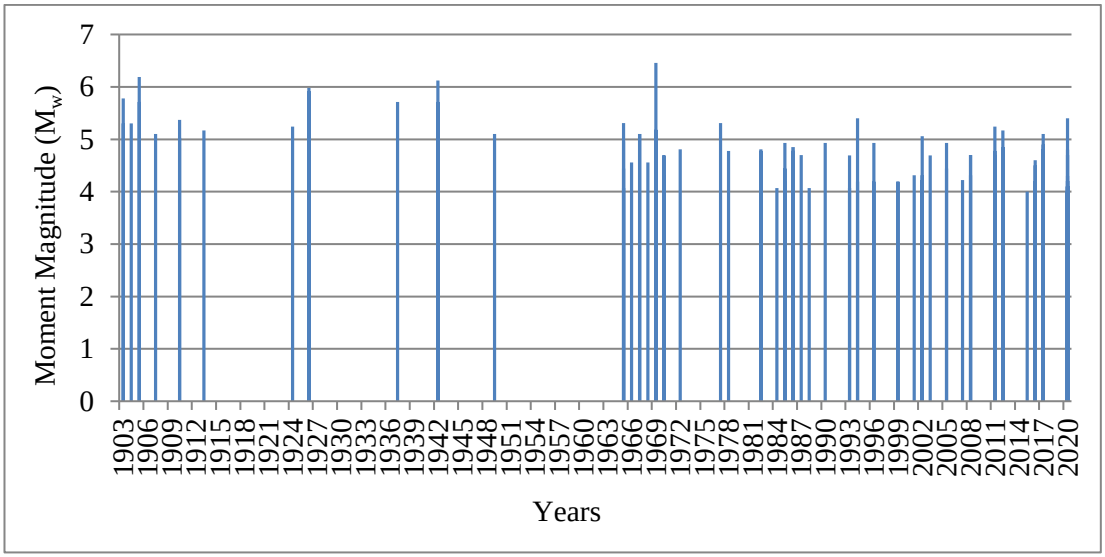


Figure 1.9 The $M_w \geq 4.0$ earthquakes that occurred between 1903 and 2020

The occurred earthquakes mostly have a moment magnitude between 4.0 and 5.0 (Appendix-1). It refers to 76.74% of the recorded 129 earthquakes. It is also indicated from Figure 1.10 that the earthquakes having M_w>6.0 are only 2.33% of the earthquakes that occurred between 1900 and 2020.

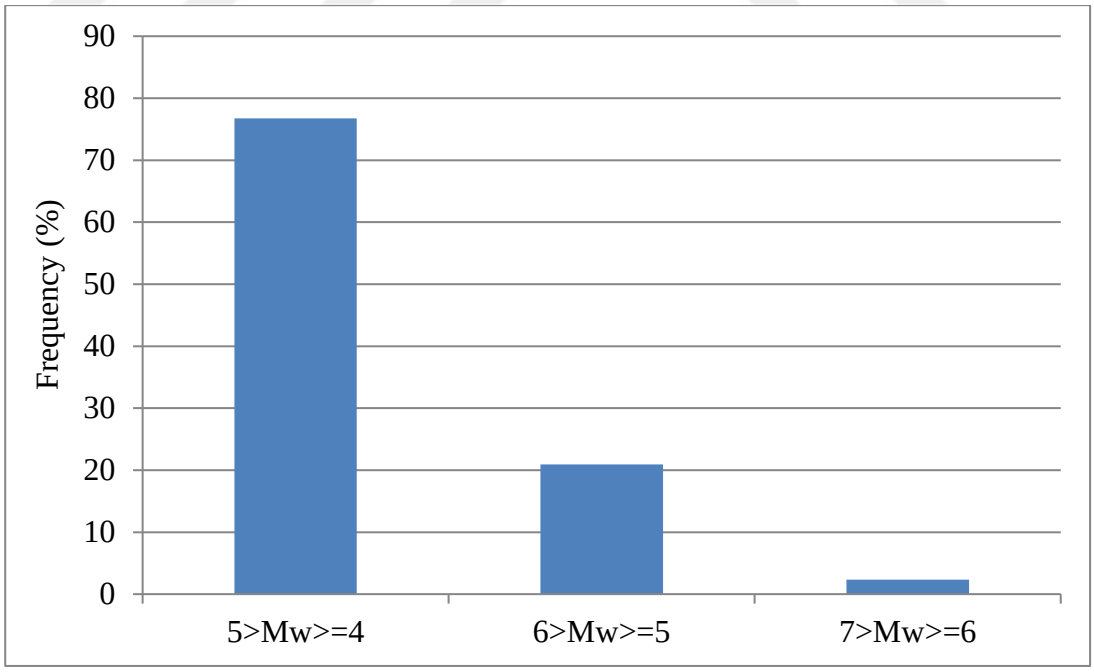


Figure 1.10 The frequency of magnitudes of earthquakes that occurred in the region between the years 1900 and 2020

The greatest earthquake in the region is the Alaşehir Earthquake that occurred on 28 March 1969 with a moment magnitude of 6.5 at 4 km depth. The epicenter of the earthquake is located approximately 40 km southeast of the dam site. According to earthquake attenuation relationships proposed by Ulusay et al. (2004), the peak ground acceleration for the site due to this earthquake is approximately 102.1 gal. This earthquake has produced N70-80W trending surface ruptures of 36 km length. Since 1969, earthquakes that occurred in the region have not caused any surface rupture (Eravcı et al., 2007).

The peak ground acceleration (PGA) is a widely used parameter in pseudo-static slope stability analysis. The distance between the investigated area and the earthquake epicenter as well as the soil type, are used for the determination of the attenuation relationship. In this study, the peak ground acceleration values were calculated according to the attenuation relationship proposed by Ulusay et al. (2004) (Equation 1.1).

$$PGA = 2.18 \times e^{0.0218(33.3Mw - Re + 7.8427S_A + 18.9282S_B)} \quad (1.1)$$

(For rocks; S_A ve S_B is zero.)

Keefer (1984, 2002) argued that a minimum magnitude of M_w:4.0 is generally required to trigger rock slope failures. On the other hand, Hancox, Dellow, & Perrin (1994) argued that a minimum magnitude required for earthquake-induced rockslides in New Zealand is M_w:5.0. The greatest earthquake magnitude around the study area (M_w: 6.5) does not mean that it can be the driver of the landslides in the study area. Earthquakes with smaller magnitude at shallower depths can have a more devastating effect on slopes. Besides, smaller magnitude earthquakes closer to the study area can also trigger landslides. In this manner, twenty earthquakes were selected and investigated considering their depths and distances from the study area (Table 1.3).

Table 1.3 The selected twenty earthquakes out of 129 to be evaluated in terms of triggering factor

Date/Time	Moment Magnitude (M_w)	Distance to the epicenter (R) (km)	Depth (km)	Calculated peak ground acceleration (gal)
28.01.2020 11:26	4.8	27.7	5.08	38.86
22.01.2020 19:22	5.4	10.35	33	53.51
28.05.2017 02:52	4.8	22.8	6.9	43.29
27.05.2017 15:53	5.1	20.2	11.0	56.91
12.09.2016 08:26	4.6	27.7	17.8	33.64
03.08.2012 10:18	5.2	9.0	22.6	75.87
24.12.2005 03:56	4.3	16.9	7.5	36.78
21.09.1996 03:34	4.2	13.0	4	34.64
23.10.1985 06:14	4.4	16.9	12	36.78
18.04.1982 23:56	4.7	14.5	10	48.19
28.03.1969 01:48	6.5	40.0	4	102.1
30.09.1965 19:36	5.0	2.4	10	78.00
19.09.1965 14:03	4.4	13.0	10	40.05
04.01.1949 20:30	5.1	15.7	14	62.76
05.02.1942 01:15	5.7	25.3	10	78.70
23.05.1937 10:57	5.7	24.7	10	79.74
13.01.1926 08:08	5.9	20.0	10	102.1
02.02.1913 06:30	5.2	14.3	10	69.58
14.07.1910 02:35	5.0	18.2	10	55.27
22.06.1907 16:00	5.1	25.2	10	51.02

The idealized response spectrum for seismic Zone 1 and local site class, Z1 was retrieved from TEC (2007) and for seismic Zone 1 and ZA was retrieved from TBEC (2018). The two codes were compared (Figure 1.11). The calculated maximum peak ground acceleration value (0.102g) corresponds to frequency (f) values between 0.2 and 0.33 Hz (f=1/T). Accordingly, the frequency of the dynamic uniaxial loading in the laboratory tests was used as 0.3 Hz. However, the triaxial confining environment is dominant in deeper elevations. As the higher frequency refers to higher peak ground acceleration, 1 Hz frequency was used in triaxial compression and direct shear tests.

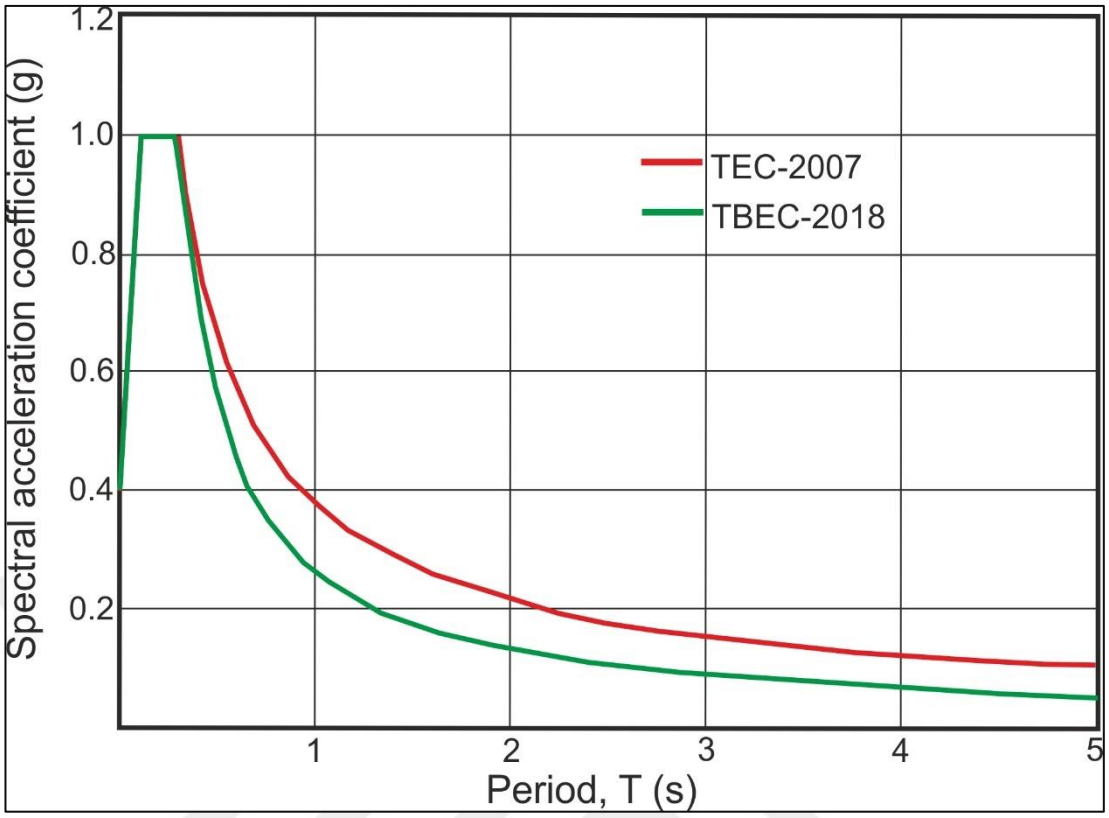


Figure 1.11 Elastic design acceleration spectra for seismic Zone 1 and local site class Z1 and ZA according to TEC-2007 and TBEC-2018, respectively

CHAPTER TWO
GEOLOGY OF THE STUDY AREA

2.1 Stratigraphy

The oldest to the youngest geological units in Çağlayan Dam site and it's nearby are Keçidağ Formation, Göcek Formation, Yeniköy Formation, Küçükderbent Formation, and Ahmetler Formation, respectively. Alluvium and slope debris unconformably overlie the sedimentary and metamorphic basement rocks (Figures 2.1 and 2.2). 1/10000 scale geology map of the study area is given in Appendix-2.

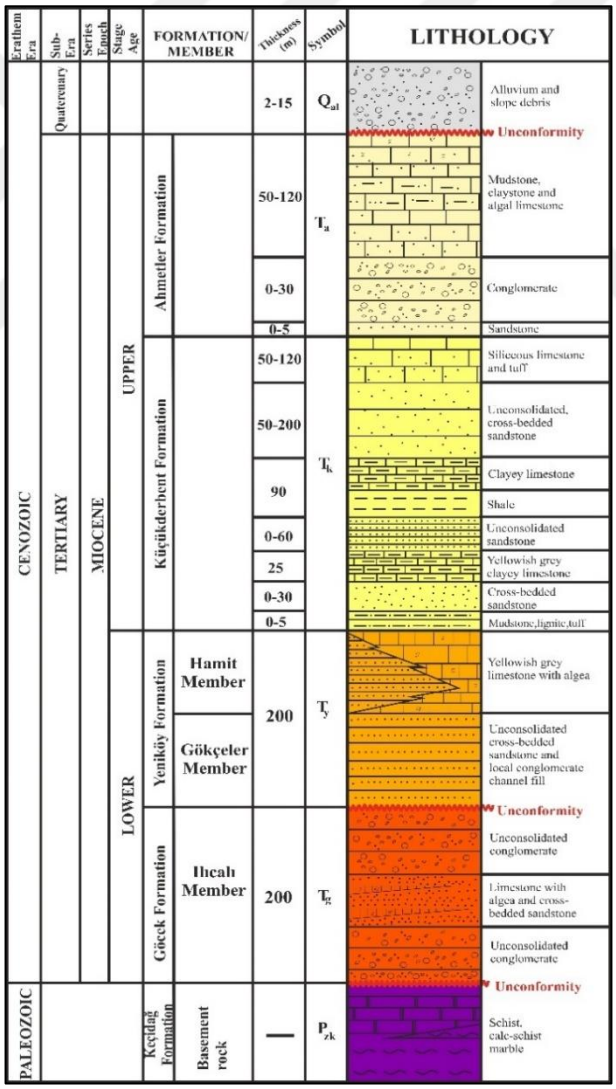


Figure 2.1 Generalized stratigraphic columnar section of the study area (not to scale) (revised from Akgün & Akyol, 1987; Yağmurlu & Baykal, 1989; Emre, 1996)

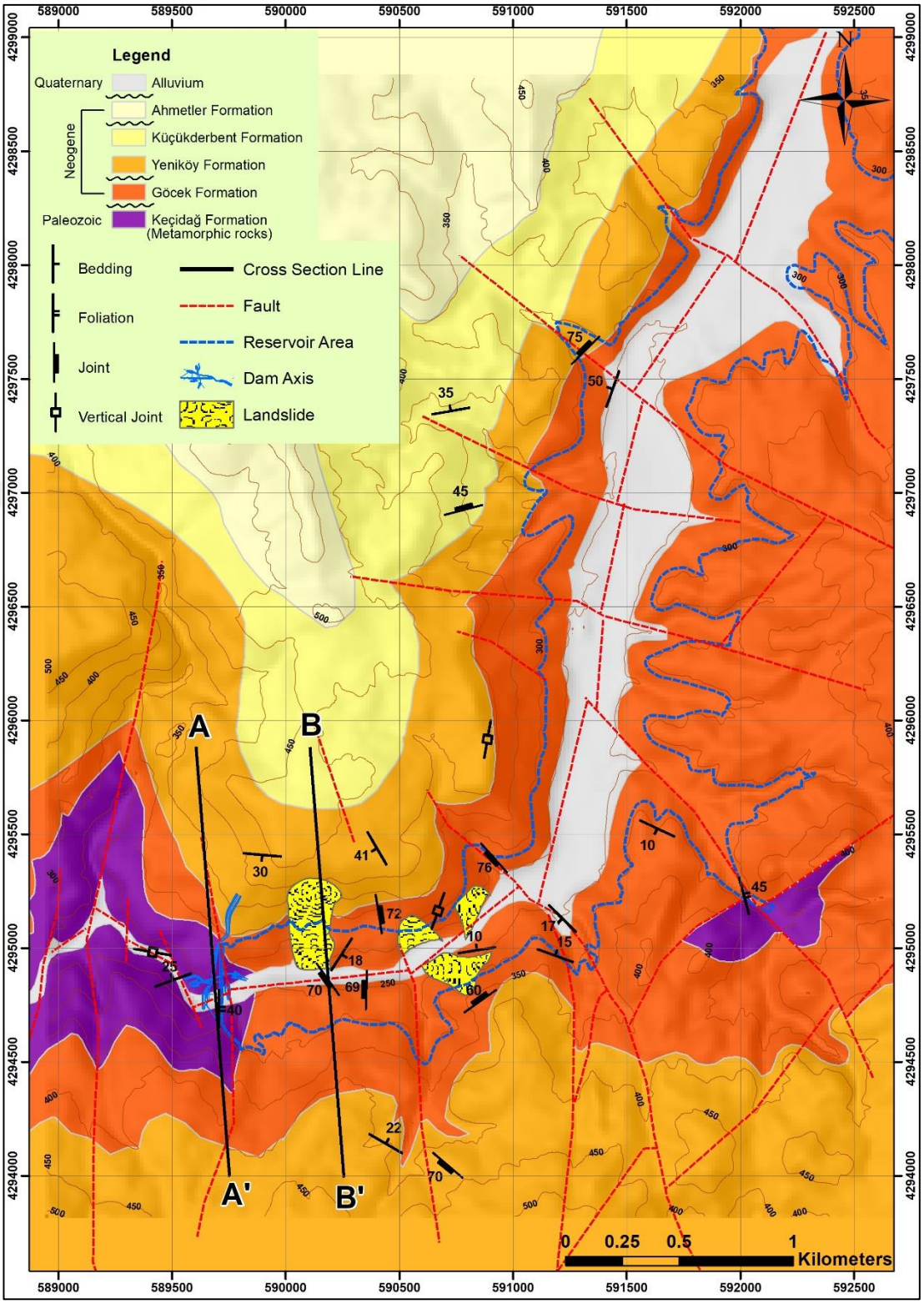


Figure 2.2 Geology map of the study area with shaded relief

2.1.1 Keçidağ Formation

Keçidağ Formation is composed of cover series of Menderes Massif metamorphic rocks and forms the base rock of the dam site (Akdeniz, 1985; Yağmurlu & Baykal, 1989; Konak, 1994; Kılıç, 1997). The cover series of Menderes Massif is composed of schist and marble successions. Well-developed joint systems are present within the marble unit whereas the schist unit has more non-systematic joints. The Schist unit includes marble interlayers. The karstic gaps in the marble unit due to dissolution along open joint systems are observed (Yağmurlu & Baykal, 1989).

Schist is moderate to highly weathered and partly consists of alternating bands of siltstone (Figure 2.3). The thickness of schistosity varies between 1 and 3 cm and is inclined to the southwest.



Figure 2.3 Siltstone interbedded schist of Keçidağ Formation (Personal archive, 2012)

The schist unit is densely faulted and folded (Figure 2.4). Light grey colored recrystallized limestone (marble) outcrop near the dam axis (Figure 2.5). This unit is highly fractured; however, an abandoned quarry is located in the northwest of the study area.



Figure 2.4 The faulted and folded structure of schist unit of Keçidağ Formation (Personal archive, 2012)



Figure 2.5 Light grey colored, fractured, recrystallized limestone around the dam axis (Personal archive, 2012)

2.1.2 Göcek Formation

The Miocene sequence starts with Göcek Formation consisting of the carbonate cemented, rounded, poorly sorted conglomerate; beige-yellow colored sandstone, siltstone, and partly algal limestone intercalations formed in alluvial fan (Yağmurlu, 1982, 1983; Yağmurlu & Karayiğit, 1984; Akgün & Akyol, 1987; Yağmurlu & Baykal, 1989).

Ilıcak member of Göcek Formation outcrops in the study area and mainly consists of non-compacted conglomerate, siltstone, mudstone, cross-bedded sandstone, and limestone with algae (Figure 2.6).



Figure 2.6 Mudstone, siltstone, sandstone, conglomerate intercalations of Ilıcak member of Göcek Formation (Personal archive, 2012)

The grain size of the conglomerate varies between gravel at the bottom and boulders at the top of the sequence (Figure 2.7).

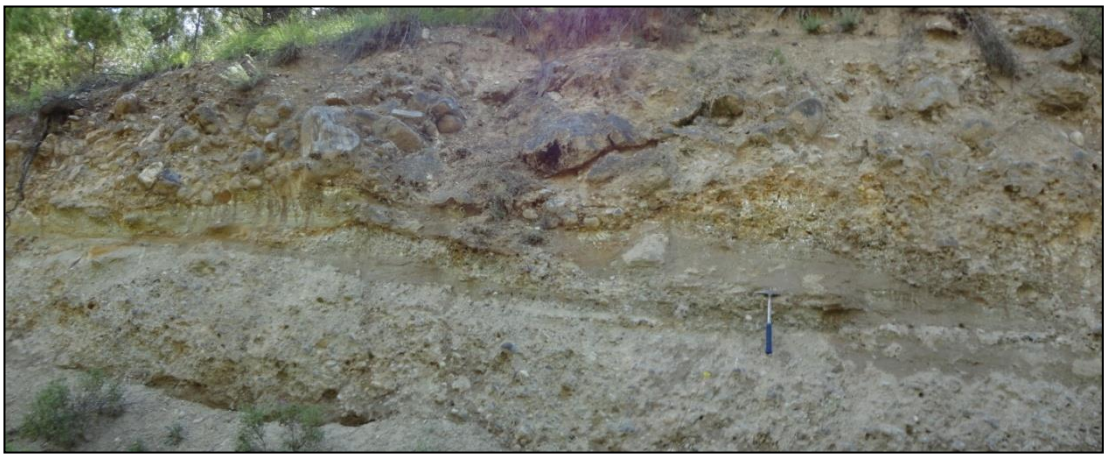


Figure 2.7 Conglomerate with boulders (Personal archive, 2012)

2.1.3 Yeniköy Formation

Middle Miocene aged Yeniköy Formation unconformably overlays the Göcek Formation. It involves cross-bedded sandstone, sandy limestone, mudstone, thickly bedded conglomerate, and siltstone intercalations. Economic coal layers are present at the top of the formation (Yağmurlu, 1982, 1983; Ercan, Türkecan, Dinçel, & Günay, 1983; Yağmurlu & Karayiğit, 1984; Akgün & Akyol, 1987). Hamit member of Yeniköy Formation dominantly outcrops in the study area. It includes sandstone and fewer conglomerate, yellowish-grey colored, sandy, clayey limestone, and mudstone (Figure 2.8). The calcareous mudstones have very thin, and dark grey colored beds of clays.



Figure 2.8 Siltstone, cross-bedded sandstone, conglomerate intercalations of Hamit member of Yeniköy Formation (Personal archive, 2012)

Limestone in Hamit member includes freshwater algae, which indicate the lacustrine environment (Yağmurlu, 1982, 1983). The regional uplift in this period caused folding in Yeniköy Formation and slightly inclined (Ercan et al., 1983) (Figure 2.9).

In contrary to the finding of various researchers, Genç, Altunkaynak, Karacık, Yazman, & Yılmaz (2001) argued that the age of this unit is Upper Miocene-Lower Pliocene.



Figure 2.9 Faulted and folded structure of siltstone, sandstone, and calcareous mudstone of Yeniköy Formation (15/35, Thrust fault) (Personal archive, 2012)

2.1.4 Küçükderbent Formation

Küçükderbent Formation overlies the Yeniköy Formation by conformable and sharp transition contact. It majorly comprises poorly consolidated thin-bedded clayey limestone, calcareous mudstone, sandstone, and minor clastics and tuffaceous unit deposited in lacustrine facies (Yağmurlu, 1982, 1983; Yağmurlu & Karayiğit, 1984; Akgün & Akyol, 1987; Yağmurlu & Baykal, 1989). Ünay & Göktaş (2000) argued that the Küçükderbent Formation is a transgressive deposition which is Lower Miocene aged.

2.1.5 Ahmetler Formation

Ahmetler Formation unconformably overlies the Küçükderbent Formation and mainly consists of conglomerate, sandstone, mudstone, and algal limestone.

According to Yağmurlu (1982, 1983) and Ercan et al. (1983), Ahmetler Formation is composed of fluvial conglomerate, sandstone, tuffite, claystone, marl, and limestone intercalations, and the age of this unit is Pliocene.

2.1.6 Quaternary Alluvium and Slope Debris

Alluvium is consisting of clay, silt, loose sand, and block-sized materials that weathered from the metamorphic basement unit and Neogene aged sedimentary rocks. This unit also consists of lime, clay, and tuffite cemented polygenic gravels (Ercan et al., 1983).

Slope debris consists of a mean of grain size 3-5 cm with a maximum grain size of 22 cm. The gravels are sub-rounded and poorly sorted and partly consolidated (Figure 2.10).



Figure 2.10 Partly consolidated slope debris with coarse grains of limestone and schist originated gravels that transported into the streambed (Personal archive, 2015)

2.2 Structural Geology

The Çağlayan Dam site is in the western part of Turkey, between the Gediz Graben and the Akhisar-Akselendi and Gölmarmara Fault zones. The region is characterized by E-W (e.g., Gediz, Küçük Menderes, and Büyük Menderes Grabens) trending Quaternary basins as a result of N-S extension of the western Anatolia and their basin-bounding active strike-slip and normal faults (Şengör, 1979, 1980; Özkaymak, Sözbilir, & Uzel, 2013; Hakyemez, Göktaş, & Erkal, 2013). These prominent structures commonly dominate the landscape in the region and form a blocky structure (Emre et al., 2005). The closest active fault to the dam site is the Akpınar Fault that is located 2.4 km west of the study area. It is an NW-SE trending strike-slip fault having a length of approximately 18 km (Figure 2.11). On the regional scale, active landslides are generally located on the hanging wall of the normal faults.



Figure 2.11 Active faults around the study area (retrieved from Emre et al., 2013)

Büyük Menderes and Gediz Grabens are the important tectonic features formed within the neotectonic regime in western Anatolia. The NW and NE trending structures are more persistent and dominant in the region (Şaroğlu, Emre, & Boray, 1987; Genç & Yılmaz, 2000) (Figure 2.11).

In the study area, normal faults with low persistence (<3 m) were identified. Some of them are E-W trending and formed due to tensional forces. A strike-slip fault with a minor normal fault component was observed with a rake angle of 10° (Figure 2.12).

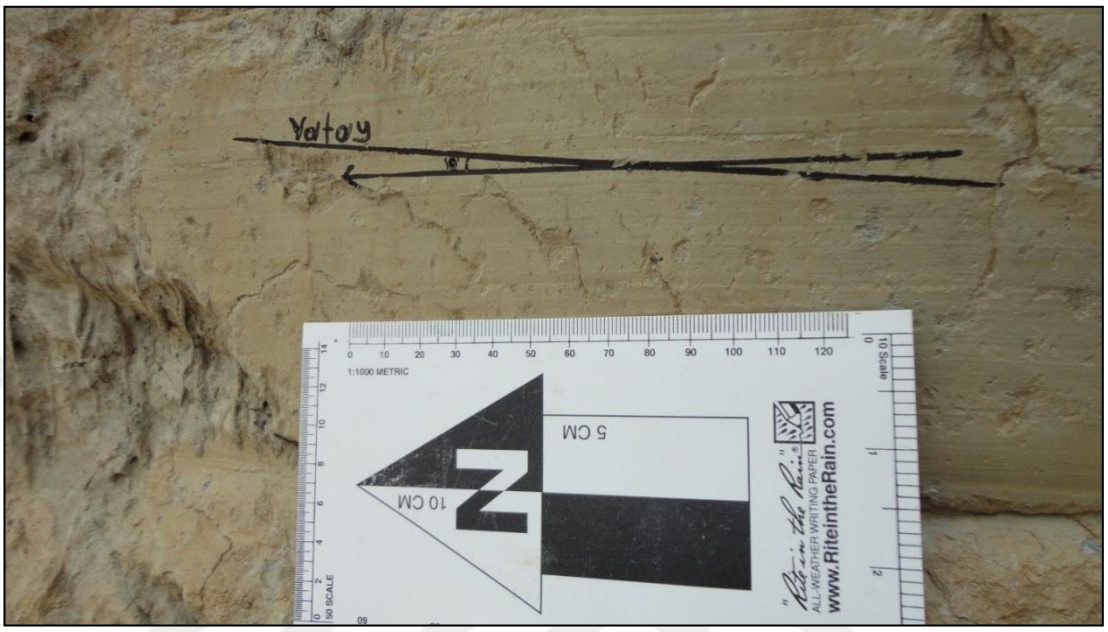


Figure 2.12 A strike-slip fault with minor normal fault component (Personal archive, 2012)

On the other hand, similarly to the tectonics of the Aegean region, NW-SE trending thrust faults (Figure 2.13) and NE-SW trending persistent normal faults were observed in the study area (Figure 2.14).

Stereographic plots of nine fault measurements and a rose diagram of dip direction of discontinuity measurements were prepared via Dips software (Rocscience, 2015) (Figure 2.15). The pole points of the fault measurements and their representative mean great circles are given in Figure 2.15. It was found that the study area has been subjected to a NE-SW trending extension and NW-SE trending compression (Figure 2.15). Therefore, normal and thrust faults were developed parallel and perpendicular to the compression, respectively.

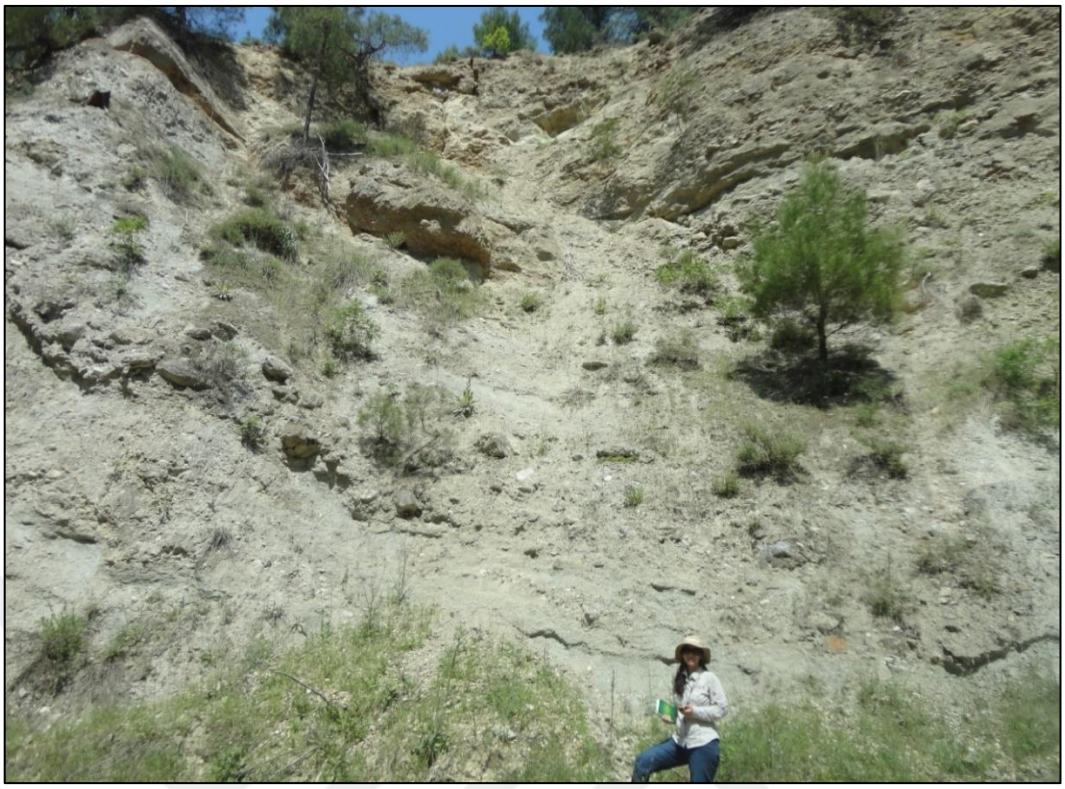


Figure 2.13 A thrust fault observed in the study area (Personal archive, 2012)



Figure 2.14 NE-SW trending normal fault observed in the study area (Personal archive, 2012)

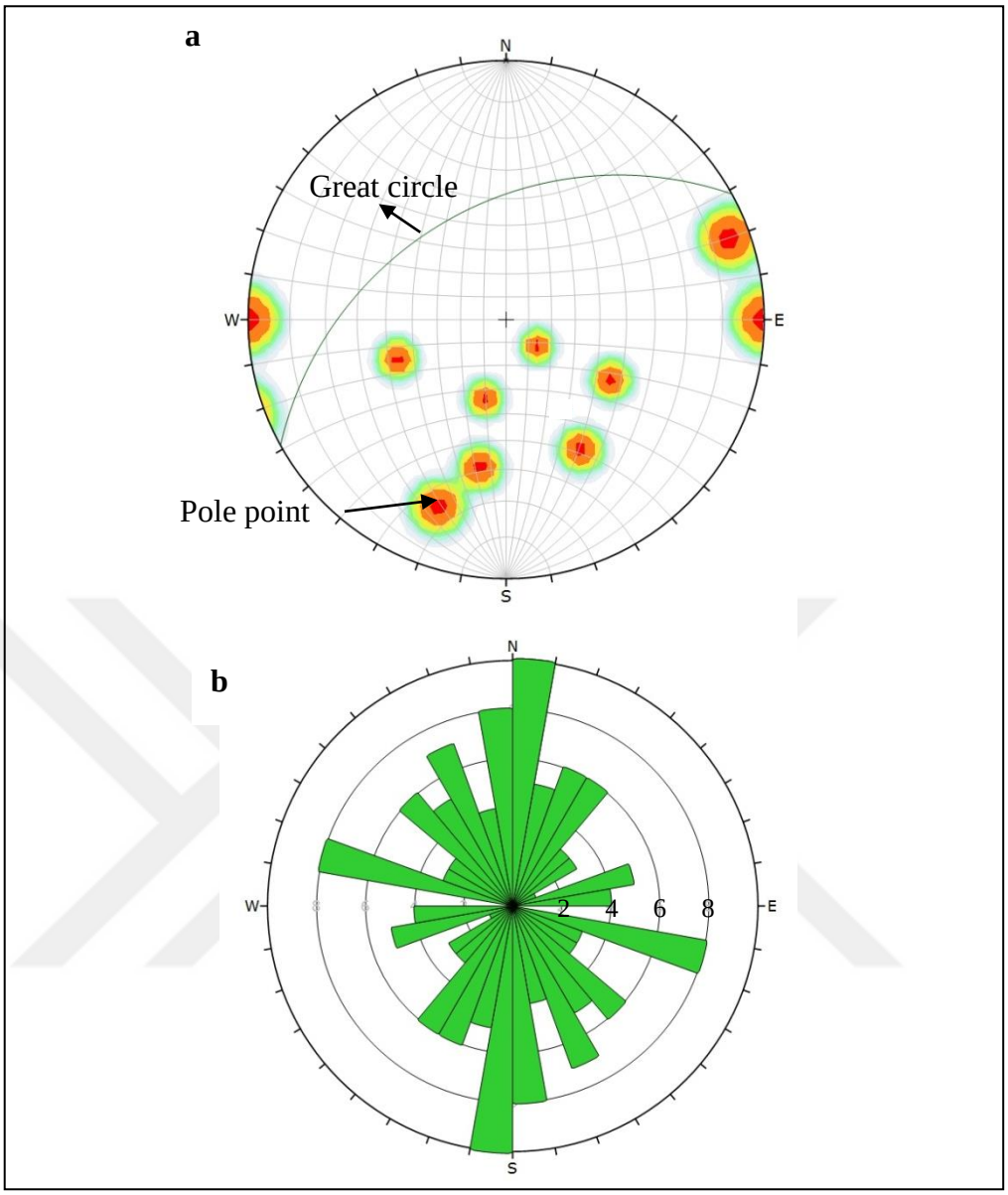


Figure 2.15 a. The pole points of nine fault measurements and their representative great circle on the stereographic net b. Rose diagram showing strikes of the discontinuities

Two geological cross-sections passing through the Landslide-1 and the dam axis were constructed to illustrate the main geostructural features and lithologic framework in the study area (Figures 2.16 and 2.17). The valley of Kayacık River is identified to be formed by the NE-SW trending normal faults.

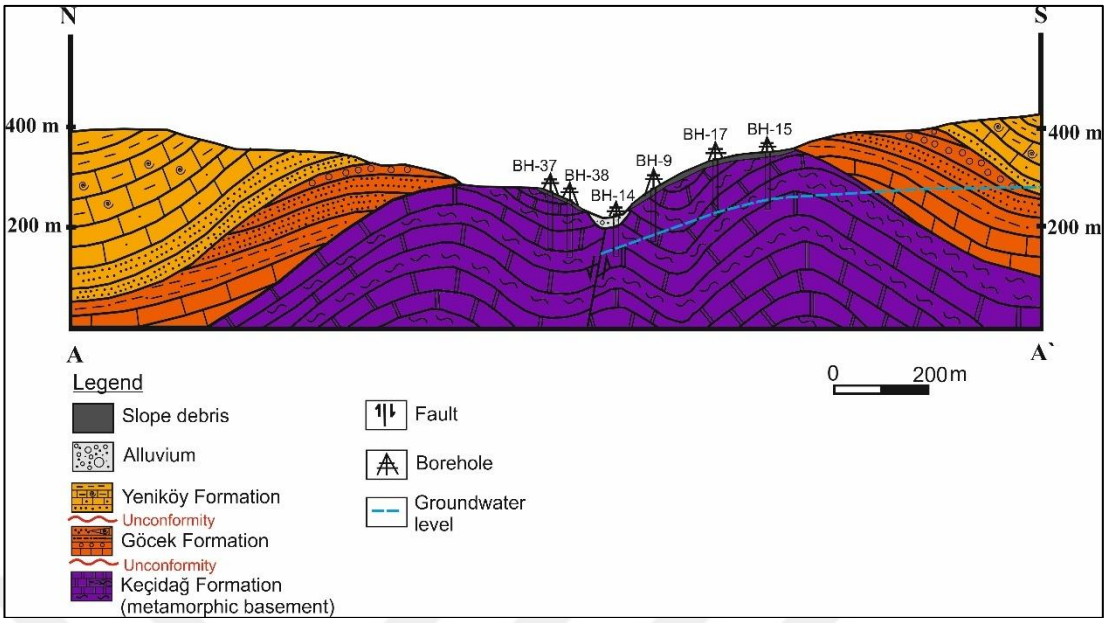


Figure 2.16 Geological cross-section of A-A′ constructed along the dam axis (taken from 1/10000 scale map)

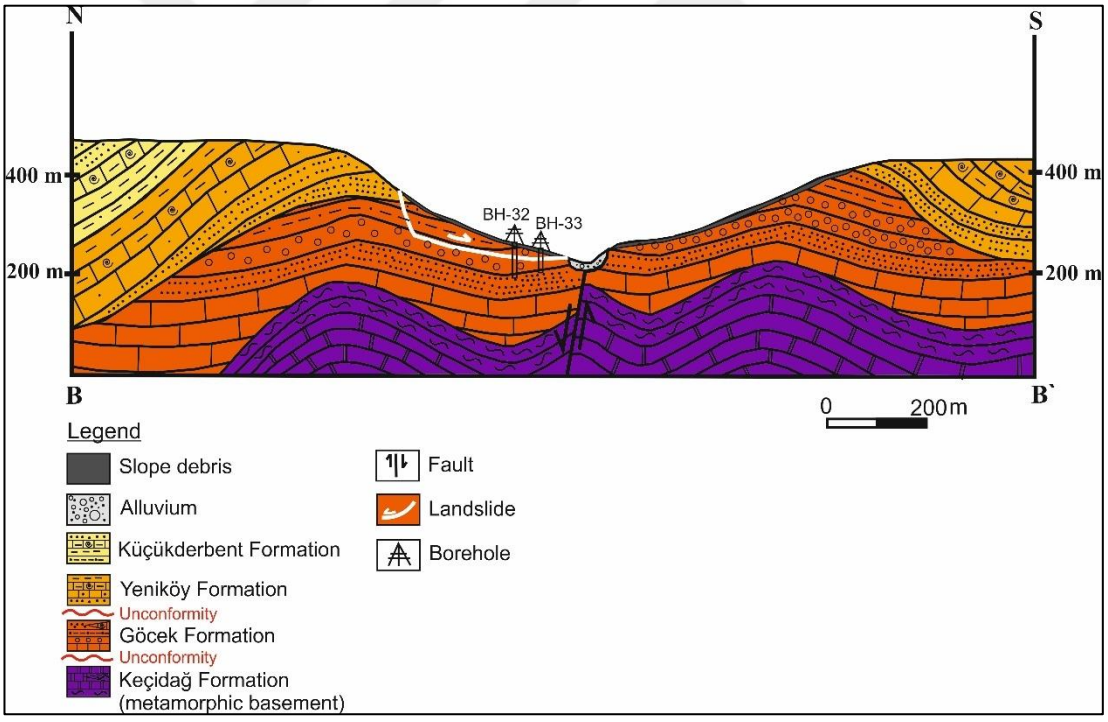


Figure 2.17 Geological cross-section of B-B′ constructed along the Landslide-1 (taken from 1/10000 scale map)

CHAPTER THREE
MINERALOGICAL, PETROGRAPHICAL AND GEOCHEMICAL STUDIES

The inherent characteristics of rock, such as mineralogical composition, texture, grain size, pore size, pore shape, and microfractures are the main factors affecting its strength and elasticity. The type of minerals and their grain size and shape, as well as the amount and type of cement/matrix in sedimentary rocks, are of important parameters. They are not only influencing strength and elasticity but also density, porosity, and permeability (Bell, 1992).

In this study, thin section and geochemical analysis, X-Ray diffraction (XRD) analysis were performed to obtain mineralogical, geochemical content, and petrographic characteristics of rock samples. The powdered rock samples for XRD and geochemical analyses were prepared by a ringed mill (Retsch RS 100).

As the microscopic, macroscopic characteristics, and XRD results are combined, the rock samples were named.

3.1 Thin Section Analysis

Thin sections were prepared from the rock blocks collected from the Göcek and Yeniköy Formations. Fourteen thin sections were examined under a polarized light microscope (Olympus BX50) and a fluorescent microscope (Leica) to describe the mineralogical and textural properties of the samples. The photomicrographs were captured (Figure 3.1).

Microscopic determinations of the carbonate rock samples are presented in Table 3.1.

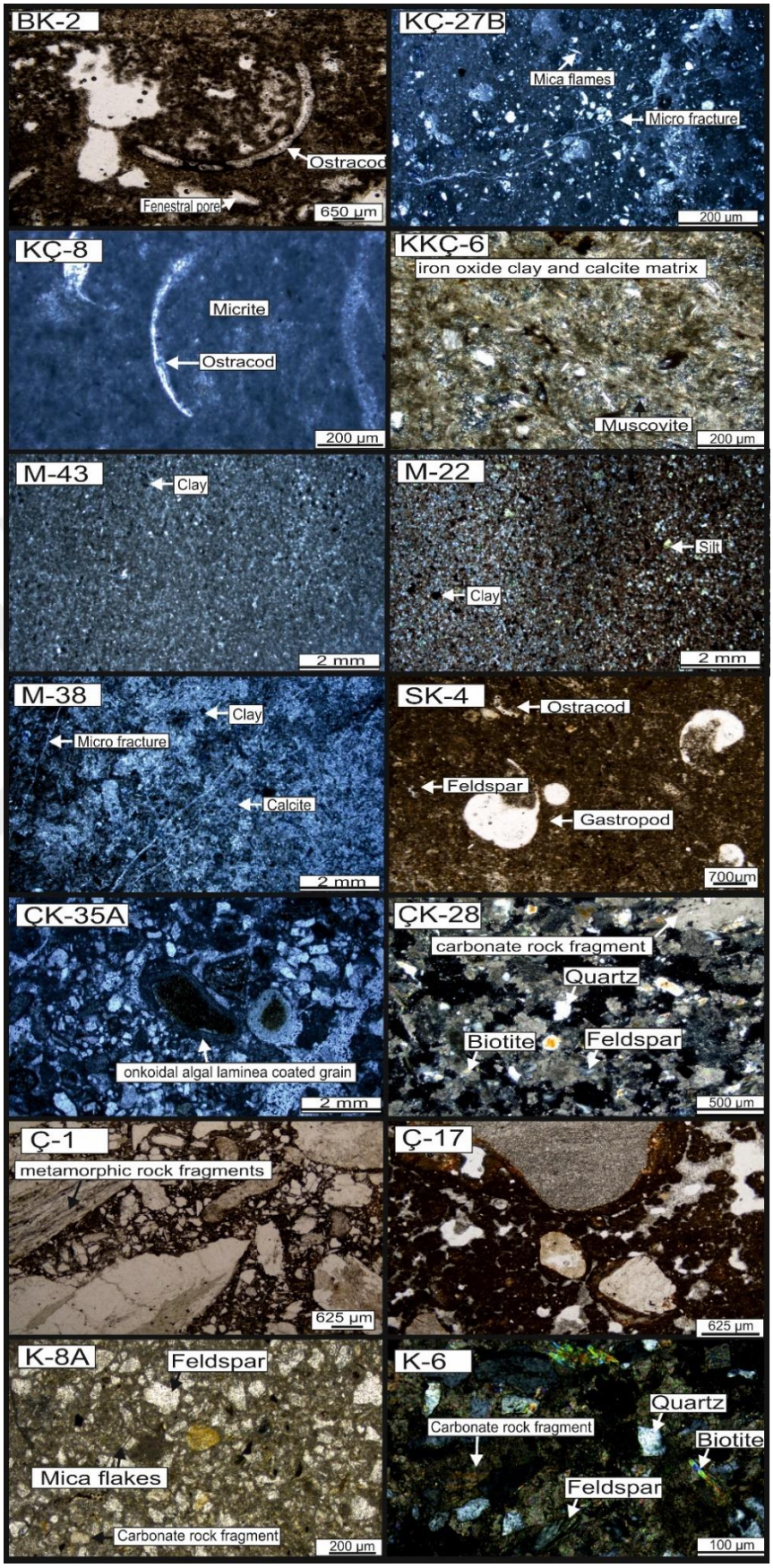


Figure 3.1 The photomicrographs of the Neogene aged sedimentary rocks exposed in the study area

Table 3.1 Thin section observations and the assigned names of the carbonate rock samples

Sample ID	Rock name	Thin section observations
BK-2	Algal biyolithite	Algal framework is recognized. Fenestral pores are partly filled, and pores between algal frames are filled with spar calcite. Fenestral pores indicate a shallow, lacustrine environment.
KÇ-27B	Sandy, silty, clayey micritic limestone	Rare mica flakes and ostracod fossils were identified. The sand, silt, and clay-size mineral content are higher than the sample KÇ-8. The sand and silt-size mineral grains are of metamorphic origin. The sample displays a micritic matrix. It involves microcracks of up to 5 mm in length.
KÇ-8	Micritic limestone with fossils	The percent of allochems (ostracod) in the sample is higher than ten. It displays a matrix-supported texture. It is partly recrystallized.
KKÇ-6	Sandy, clayey micritic limestone	Sand-size mica flakes are identified. The matrix is composed of iron oxide, clay, and calcite. The quartz sand is at the very most 10 percent of the sample. It partly involves microcracks of up to 300 μm in length, and they have <1 μm aperture.
M-43	Clayey limestone	Rare silt-size mica and abundant clay-size mineral grains were observed in the sample. No spar calcite minerals were identified.
M-22	Calcareous mudstone	Silt-size rock fragments and quartz and clay-size mineral grains are dominant in the sample. No coarse calcite minerals were identified. The calcite content is originated from microspar and micrite.
M-38	Clay bearing limestone	The sample involves more calcite and less clay mineral than M-43 and M-22. Sand-size feldspar minerals were identified. Rare silt, sand, and clay-size mineral grains were observed. The recrystallized microspar and micrite were defined.
SK-4	Clay-bearing biomicrite	Gastropod and ostracod fossils were identified. The micritic matrix is extensively recrystallized and transformed into spar. Very rare quartz and feldspar minerals were encountered. The matrix is partly including iron oxide that identified from its brownish-red color.
Ç-17	Pebble bearing algal biyolitite	Microbial algae surround the gravels and the micritic cement displays a pelloidal fabric with iron oxide. The sample was interpreted as consolidated slope debris.

Microscopic determinations of the clastic rock samples were also presented in Table 3.2. Most of the samples are sandstone; however, they have different fractions of mineral components.

Table 3.2 Thin section observations and the assigned names of the clastic rock samples

Sample ID	Rock name	Thin section observations
ÇK-35A	Pebbly, lithic sandstone with calcite cement and micritic matrix	Carbonate and metamorphic rock fragments are abundant. Both grain and matrix supported texture is observed, and it is slightly consolidated. Micrite occupies the space between the sand-size grains and is interpreted as a low energy environment. The grains coated by oncoidal algal laminae are embedded within clayey micrite. The mean grain size is coarse sand.
ÇK-28	Clay-bearing, pebbly sandstone with micritic matrix	Biotite, quartz, and feldspar minerals were identified. Carbonate and metamorphic rock fragments are dominant. Carbonate rock fragments are generally micritic limestone. 50% of the grains are medium-fine sand-size. The texture is partly grain and matrix supported, and the space between the grains is occupied by clayey micrite. The clayey micrite is partly recrystallized, and converted to microspar.
Ç-1	Pebbly, clay matrix bearing lithic sandstone	The sample is matrix supported, and the matrix is composed of clay and silt. The sample is rich in metamorphic rock fragments. The grains are poorly rounded and sorted. The mean grain size is very coarse sand.
K-8A	Lithic sandstone with calcite cement and micritic matrix	Feldspar, quartz, schist, and carbonate rock fragments were identified. Mica flakes are present within the micritic matrix Many of the carbonate grains are unified with calcite cement. The sample has not an ideal grain supported texture, whereas the texture is partly matrix supported. The micritic matrix is recrystallized and converted to microspar. The mean grain size is medium-fine sand.
K-6	Lithic sandstone with calcite cement	Feldspar minerals and more abundant quartz minerals were identified. The sample has not an ideal grain supported texture. Calcite in cement substituted the metamorphic rock fragments. The matrix is largely converted to calcite. The mean grain size is about 100 μm (fine sand).

3.2 X-Ray Diffraction Analysis

Whole-rock X-Ray Diffraction (XRD) analyses of powdered rock materials were performed at room temperature using a Rigaku MiniFlex 600 instrument (having Cu X-Ray tube with a goniometer speed of 2°/min.) with Cu Kα radiation (λ = 1.54059 Å). The accelerating voltage used was 40 kV, and the emission current was maintained at 15 mA. The samples were scanned with a step size of 0.02°, in the 2θ range from 2 to 65°. The peaks in the diffractograms were defined according to the American Society for Testing and Materials (ASTM) (1972) (Appendix-3). The weight percent of the minerals present in the samples were determined by performing quantitative analysis using the Reference Intensity Ratio (RIR) method embedded in the PDXL software (Rigaku, 2016) (Table 3.3). RIR method is based on converting the intensity values to weight percent with regard to a scaling factor. It should be noted that the reliability of the RIR method decreases with the increasing complexity of the mixtures (i.e., the number of component phases and/or unidentified phases, degree of overlap, absorption effects, presence of amorphous and/or preferred orientation effects, etc.) (Altomare et al., 2015). Besides, Toraya (2016) determined that the RIR method applied automatically by the software PDXL yields a slightly high root mean square error (RMSE) of the weight percent estimate. Yet, it is the most commonly used method for calculating the weight percent of minerals.

According to the whole rock analyses of the powdered samples, it is revealed that the fourteen different rock types mainly consist of calcite, and fewer amounts of quartz, clay minerals, mica, and feldspar (Table 3.3). Additionally, trace amounts of dolomite, aragonite, pyrite, cristobalite, and amphibole were also recognized. A considerable amount of ferroan dolomite (ankerite) was defined in KKÇ-6 and SK-4 samples. The presence of oxidized iron matrix in these samples was also determined in thin section analysis. Furthermore, 33.5% margarite was calculated in the ÇK-28 sample. Margarite is commonly considered as a metamorphic mineral. Thus, the relatively high content of margarite in the ÇK-28 sample can be originated from the abundant metamorphic rock fragments (derived from metamorphic basement rock)

that were also defined in thin section analysis. The high calcite content of ÇK-35A and K-6 probably arises from abundant carbonate rock fragments and calcite cement.

Table 3.3 The results of XRD analyses

Sample ID	Whole Rock Analysis									
	Minerals (%)									
	Calcite	Dolomite	Margarite	Ankerite	Quartz	Mica	Amphibole	Pyroxene	Feldspar	Clay
BK-11	99.00	-	-	-	-	0.05	-	-	-	1.12
KÇ-27B	82.40	1.60	-	-	4.30	2.35	-	-	3.43	6.30
KÇ-8	97.00	-	-	-	-	1.10	-	-	-	1.81
KKÇ-6	31.60	-	-	20.00	4.80	6.90	-	-	1.20	35.60
M-43	76.00	-	-	-	-	0.84	-	-	0.20	23.38
M-22	35.75	-	-	0.05	4.58	0.05	-	-	1.90	58.01
M-38	93.00	-	-	-	0.7	2.1	-	-	0.8	0.32
SK-4	66.00	-	-	29.00	-	0.50	-	-	2.10	2.46
Ç-17	98.00	-	-	-	-	0.09	-	-	-	1.79
ÇK-35A	79.00	-	-	-	10.00	8.10	-	-	1.20	1.30
ÇK-28	28.00	1.20	33.50	-	9.80	6.21	3.01	-	12.30	6.10
Ç-1	21.00	-	-	-	46.00	12.00	-	-	15.00	5.60
K-8A	30.00	-	-	1.10	20.00	0.50	-	0.15	44.00	4.94
K-6	55.00	1.90	-	-	30.12	4.40	-	-	4.60	4.00

3.3 Geochemical Analysis

Whole-rock geochemical analyses were performed by Avanta Atomic Absorption Spectrometer (AAS) instrument. M-44, M-45, M-46, M-47, M-49, and M-50 (M-48 excluded) samples are clayey limestone and K-13, K-15, K-16, K-17 (K-14 excluded) samples are clayey sandstone (Figure 3.2).

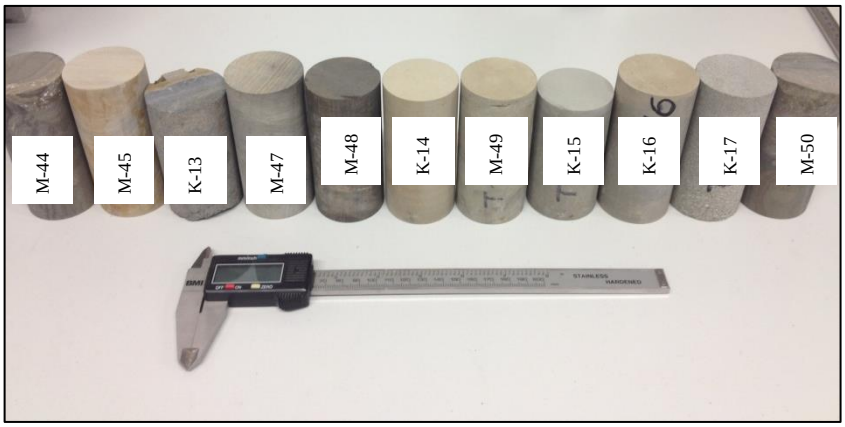


Figure 3.2 The samples subjected to geochemical analyses (Personal archive, 2014)

In the context of whole-rock geochemical analyses, total oxide, and loss on ignition (LOI) values were determined (Table 3.4). LOI values were determined at 1000 °C and they are representing the amount of organic and inorganic carbon in the samples. Salehi, Beni, Harchegani, Borujeni, & Motaghian (2011) suggested that the amount of organic content in the sample can be obtained by measuring the LOI values at 360 °C since inorganic carbon starts to vaporize above 360 °C. As a result of the method proposed by Salehi et al. (2011), the organic content of the samples was determined to be below 5% except for the M-44 sample. It has 5.72% organic content which may significantly affect its mechanical and deformation characteristics. However, the effect of organic content below 5% on the strength and deformability of the rock samples is negligible.

The samples have a SiO_2 content of 1.03 to 57.07 weight percent. The Al_2O_3 content ranges from 0.8 to 15.3 percent and does not vary systematically with SiO_2 content (Table 3.4). The CaO content varies between 4.1 and 46.6 percent and generally declines as SiO_2 increases. The samples which have high CaO content also have high LOI values. Al_2O_3 is demonstrated to be a reliable indicator of clastic input by Scasso, Alonso, Lanes, Villar, & Lafitte (2005). Similarly, the sandstone samples have higher Al_2O_3 content than the mudstone samples in this study. On the other hand, the ratio of SiO_2/Al_2O_3 indicates the presence of siliceous sands (Ojo, Adepoju, & Alhassan, 2014). The SiO_2/Al_2O_3 ratio is varying between 1.8 and 27.9. It indicates that all samples have siliceous sand content, whereas the M-46 sample has the highest siliceous sand input.

Beyhan (2008) stated that if both CaO and SiO_2 content decreases and Al_2O_3, Fe_2O_3, K_2O, TiO_2 increases, the core rock samples split as disc shape (Figure 3.3). As a consequence, the uniaxial compressive strength of the samples reduces, and the variation of clay and carbonate content strongly controls the strength of the specimens.



Figure 3.3 Disc shape splitting observed in calcareous mudstone samples (Personal archive, 2014)

Table 3.4 The whole-rock geochemical analyses (major elements) results

Rock Sample	Weight percents (%)											
	SiO_2	Al_2O_3	$\sum Fe_2O_3$	MgO	CaO	Na_2O	TiO_2	MnO	K_2O	LOI (1000°C)	LOI (360 °C)	Total percent
M-44	31.890	11.946	12.687	4.367	16.376	1.693	0.170	0.194	2.597	15.37	5.72	97.3
M-45	28.625	15.332	8.327	4.535	19.507	1.785	0.028	0.130	0.821	21.70	2.10	100.8
M-46	30.803	1.103	2.367	7.506	20.368	0.252	0.001	0.060	0.127	37.50	1.54	100.1
M-47	1.033	0.807	3.514	4.519	46.606	0.417	0.002	0.402	0.234	42.48	3.48	100.0
M-49	47.615	9.948	12.581	4.219	7.575	0.981	0.002	0.168	3.868	13.02	2.42	100.0
M-50	31.022	3.375	10.279	7.522	14.769	1.175	0.070	0.193	0.631	30.83	2.34	99.9
K-15	47.032	7.110	9.442	5.684	12.401	0.658	0.003	0.210	2.230	15.27	0.98	100.0
K-16	57.070	6.118	12.333	3.178	4.152	0.838	0.007	0.187	3.793	12.32	2.29	100.0
K-17	52.004	6.112	11.586	3.534	10.943	1.918	0.061	0.211	1.409	12.31	1.61	100.1
K-13	50.443	6.370	13.417	2.250	11.911	2.087	0.001	0.334	1.892	11.31	3.22	100.0

CHAPTER FOUR
FIELD INVESTIGATIONS

Field investigations commenced with geological mapping to define the rock types and delineate major structures. Thereafter, the field investigations proceeded with discontinuity survey, examining the borehole logs, permeability test and standard penetration test (SPT) results, performing in-situ tests such as shear vane test, Schmidt hammer test and finally carrying out the geophysical survey by multichannel analysis of surface waves (MASW) method and electrical resistivity tomography (ERT) method. During field works, discontinuity data were collected from 91 different observation points. Block samples were taken from the nine locations out of 91 observation points (Figure 4.1).

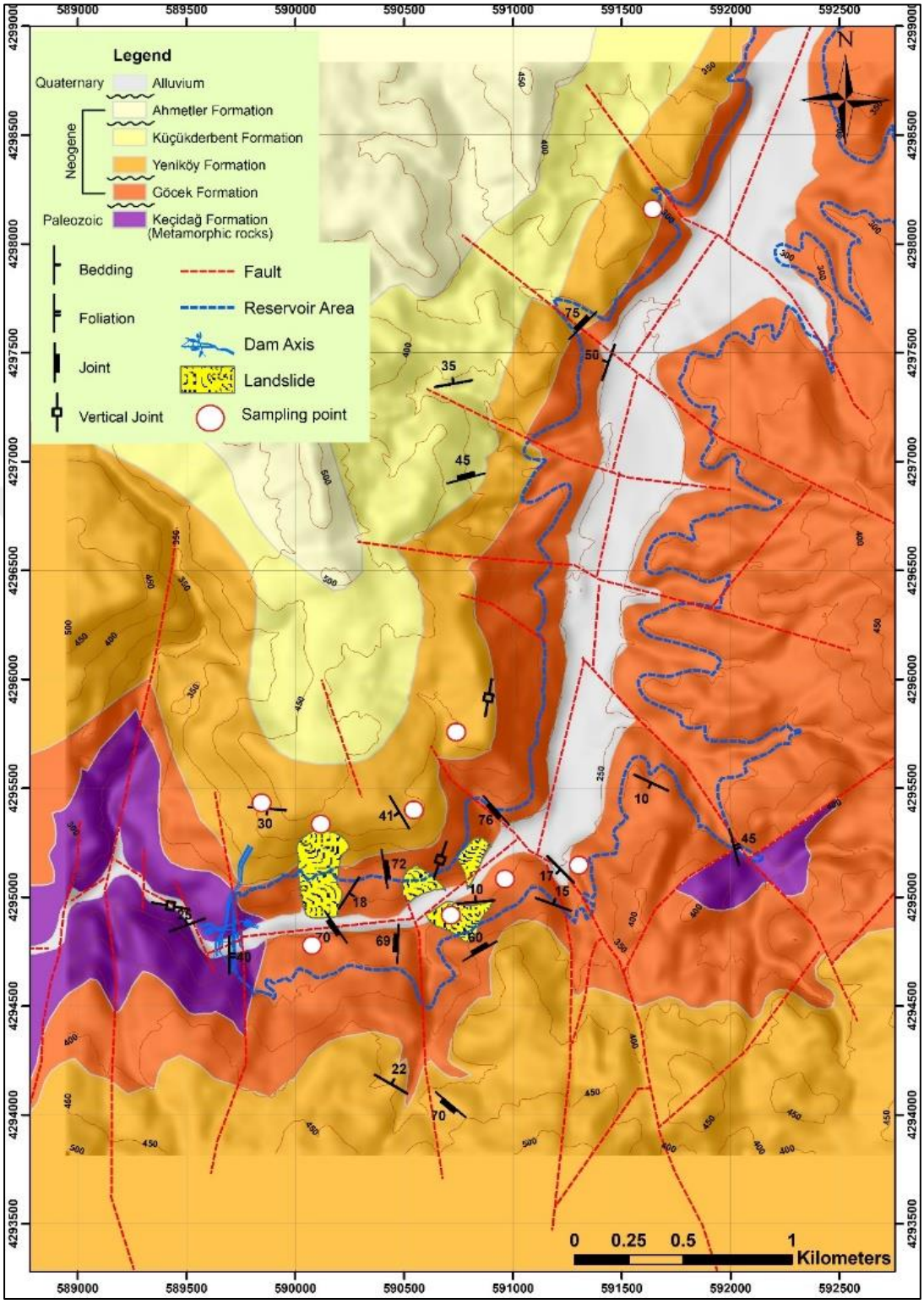


Figure 4.1 Sampling points shown on the geological shaded relief map

4.1 Discontinuity Survey

Detailed discontinuity measurements were carried out to determine dominant discontinuity sets and their physicomechanical properties such as type, orientation and number of sets, spacing, persistence, roughness, aperture, the thickness of infill material, joint wall strength, and weathering state. The significance of discontinuity data lies in the fact that the shear strength of discontinuity is a function of aperture and infilling, roughness, joint wall strength, and weathering (Price, 2009). In addition, the failures in rock masses are generally controlled by the discontinuities, even the heavily fractured rock masses may slide on the complex discontinuity planes. In addition, the shear strength of a rock mass and its deformability are very much influenced by the discontinuity pattern, its geometry, and how well it is developed (Bell, 1992).

It should be noted that the results obtained from the field discontinuity survey have uncertainties due to the spatial variability of the discontinuity properties and difficulty in tracing the discontinuity planes, particularly in moderately weathered and/or disintegrated slope faces.

As a result, ten scan-lines of at least 3 meters were available for proper discontinuity measurements. The definition and classification of discontinuity properties were made along these scan-lines, according to the International Society for Rock Mechanics (ISRM) (2007).

4.1.1 Orientations and Number of Sets of Discontinuities

The geomechanical behavior of a rock mass is strongly influenced by the number of discontinuity sets that intersects since it governs the amount of deformation that the rock mass exhibits (Bell, 1992). All the natural discontinuities have a certain amount of variation in their orientations that result in scatter of the pole plots (Wyllie & Mah, 2004). Therefore, dip direction and dip angle measurements of 198 discontinuities in Miocene aged sedimentary rocks were plotted on Schmidt net

(equal-area projection) with the aid of Dips software (Rocscience, 2015) to readily identify the discontinuity sets that may form potential failure planes (Figure 4.2). Random joints were not taken into account.

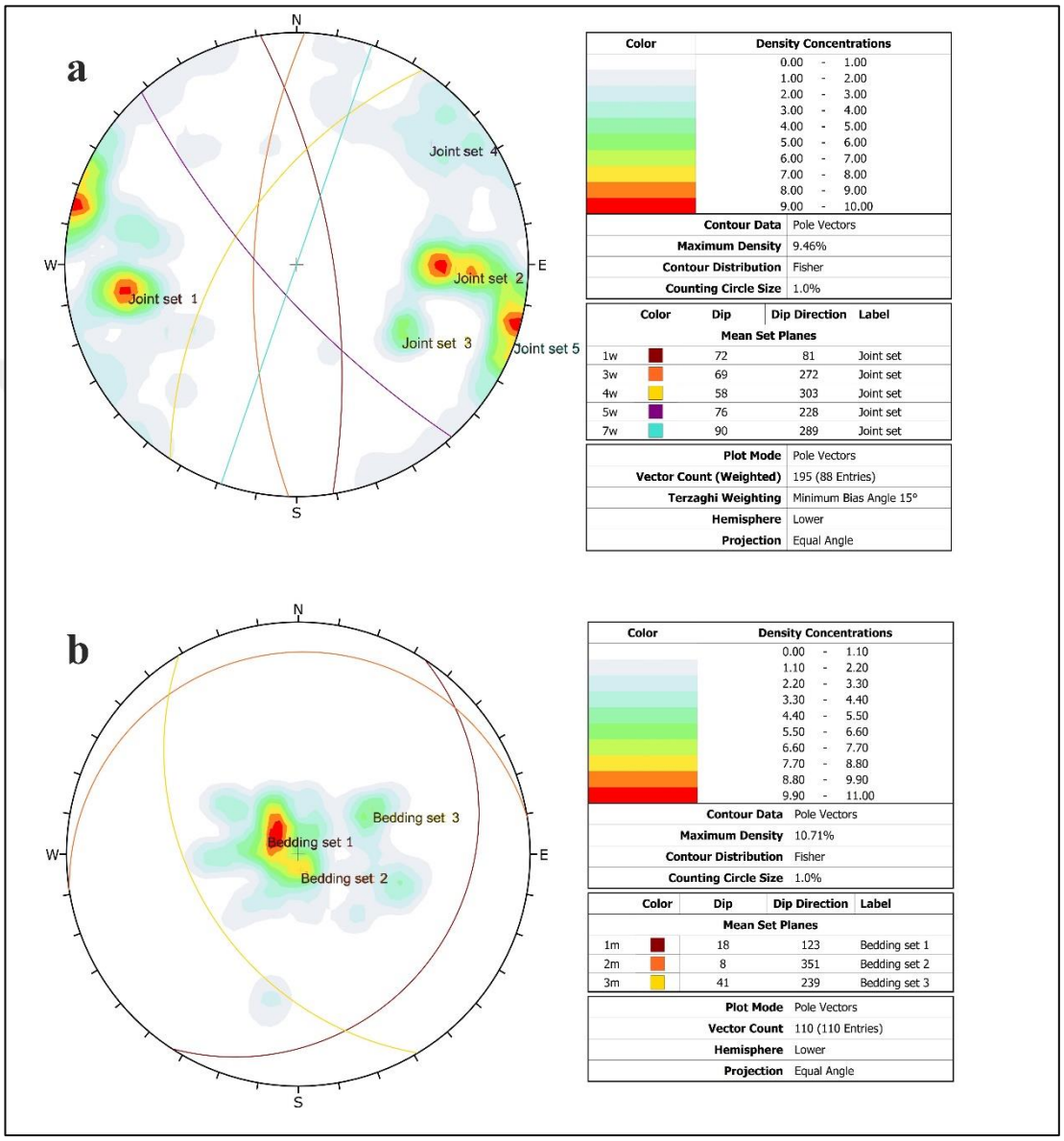


Figure 4.2 The contour map of a. Joint b. Bedding planes and great circles of the pole concentration points (equal-area lower hemisphere)

The contoured poles of discontinuities provided an expression of orientation concentration. As a result of the stereographic projection of 110 bedding plane and 88 joint plane measurements, three and five pole concentration points were obtained, respectively (Table 4.1). Some of the joint and bedding sets do not have a significant weighted percentage among the measurements. Nevertheless, field observations

support that the orientation of sets frequently changes due to folding and stress caused deformations in the rock masses.

Table 4.1 The orientations of dominant bedding and joint sets in Neogene aged sedimentary rocks

Set No	Bedding sets	Set No	Joint sets
B1	123/18	J1	81/72
B2	351/8	J2	272/69
B3	239/41	J3	289/90
		J4	228/76
		J5	303/58

The bedding set-1, 2, and 3 are daylighting on the southern and northern slope faces. J-1, 2, 3, and 5 have a similar strike among the five joint sets identified. While the strikes of J-1, 2, 3, and 5 joint sets are nearly N-S direction, that of J-4 joint set is NW-SE direction (Figure 4.2). Joint sets are oriented nearly perpendicular to the bedding planes. The rock mass can be assumed as heavily jointed since the pole points of discontinuities are widely scattered on the stereonet.

4.1.2 Spacing of Discontinuities

Spacing is the vertical distance (shortest length) between two discontinuity planes. It is one of the most important properties of a discontinuity that is strongly related to the size of blocks in the rock mass when considered together with the persistence of a discontinuity set (Kim, Cai, Kaiser, & Yang, 2007). As discontinuities represent surfaces of weakness, the more closely spaced they are, the more influential they become in reducing the strength of a rock mass (Bell, 1992).

It is almost impossible to lie the scan-line perpendicular to the discontinuity planes to measure the true discontinuity spacing (S). Therefore, the spacing measurements along the scanlines intersecting the discontinuity planes with an acute angle give apparent spacing (S_{app}). The illustration of spacing measurement is given in Figure 4.3.

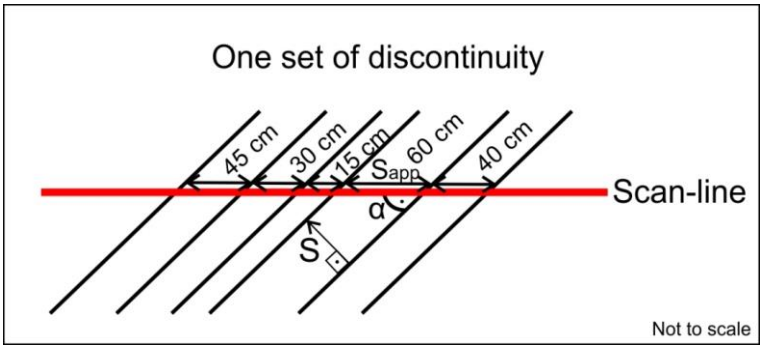


Figure 4.3 The illustration of spacing measurement in a discontinuity set

The mean apparent spacing (S_{mean}) values were converted into true spacing (S) values by Equation 4.1

$$S = S_{app} \times \sin\alpha \quad (4.1)$$

where α is the acute angle between the horizontal scan-line and the discontinuity planes (Figure 4.3). Thereafter, the arithmetic mean of the spacing value of a set was determined. The frequency histogram charts of spacing values for each set were constructed (Figure 4.4).

The mean spacing values of the discontinuity sets refer to extremely close and very close spacing according to ISRM (2007). The statistical properties of spacing values such as mean, maximum (max), minimum (min) values, and standard deviation (SD) values are given in Table 4.2.

Table 4.2 Statistics of true spacing values of the discontinuity sets

Spacing (cm)	Discontinuity sets				
	B-1	B-2	B-3	J-1,2,3,5	J-4
Mean	12.26	38.72	16.81	37.63	14.24
Standard deviation	7.97	10.48	10.21	19.43	5.73
Minimum	1.00	20.00	1.00	4.00	2.00
Maximum	30.00	60.00	36.00	100.00	24.00

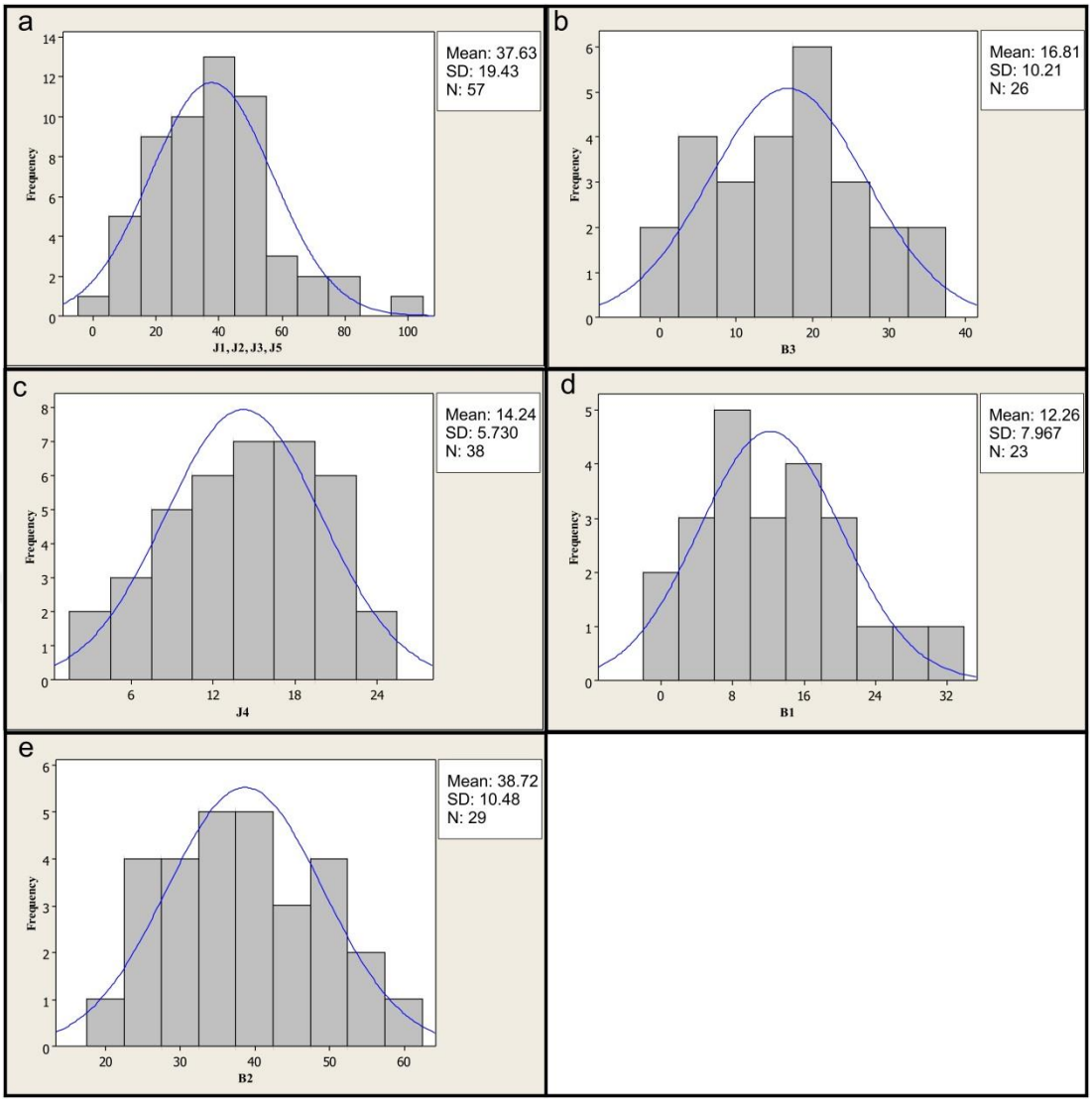


Figure 4.4 The histograms of spacing measurement on the slope face for the discontinuity sets a. J-1, J-2, J-3, J-5 b. B-3 c. J-4 d. B-1 e. B-2

4.1.3 Fracture Frequency

Fracture frequency (λ) is the number of discontinuity per unit length on the scan-line. It should be noted that the scan-line orientation is influencing the number of discontinuities counted. Hudson & Priest (1979) have pointed out that where discontinuities occur in sets, the fracture frequency along a scan-line is a function of scan-line orientation. Since the fracture frequency is the reciprocal of the average spacing value of a discontinuity set, the fracture frequency values were determined from the spacing values of the discontinuity sets as in Figure 4.5.

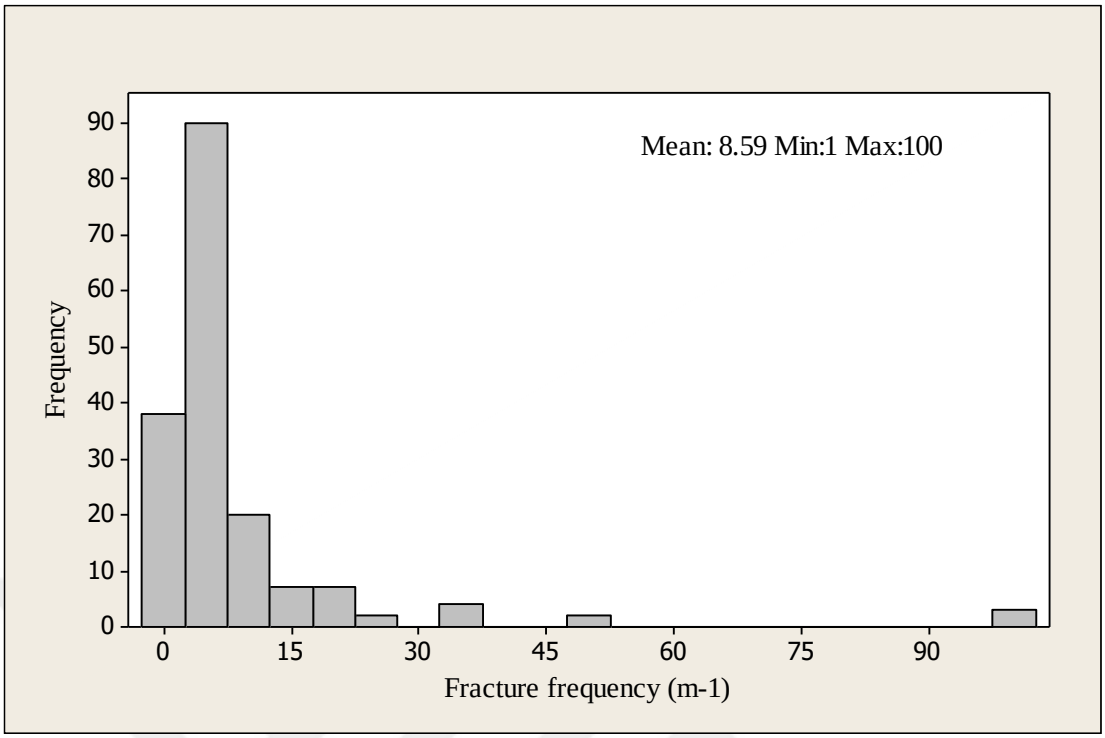


Figure 4.5 Histogram of the fracture frequency measured on the slope face

The mean fracture frequency values indicated a highly fractured, poor quality rock mass (RQD= 25-50%), according to Franklin, Broch, & Walton (1971).

4.1.4 Volumetric Joint Count

The volumetric joint count (J_v) is the sum of the number of discontinuities per unit length for the rock mass. It can be determined from Method-1 (Equation 4.2) proposed by Palmström (1982).

$$J_v = 1/S_1 + 1/S_2 + 1/S_3 \ldots\ldots\ldots\ldots + 1/S_n \quad (4.2)$$

where S is the mean true spacing value, and n is the discontinuity set number. As a result, the Neogene aged sedimentary rocks have a mean J_v value of 34.25 joint/m^3 (Method-1), which corresponds to a block volume of fewer than 0.0002 m^3 (very small blocks) according to the classification proposed by Anon (1977). Even though Method-1 gives reasonable J_v for mean value, it yields extremely high values for the very closely spaced discontinuities.

Since the heavily jointed rock masses can be assumed to be homogeneous and isotropic, Sönmez & Ulusay (2002) suggested calculating J_v by counting the faces of individual rock blocks represented as Method-2 (Equation 4.3)

$$J_v = D_n (1/S) \quad (4.3)$$

where D_n is the number of joint sets. For example, a prismatic block has six faces, three pairs of them are perpendicular to each other, which corresponds to three joint sets. Hence, D_n is used as 3. However, in highly jointed rock masses and if the faces are not perpendicular to each other, D_n is directly used as the defined number of joint sets. It was therefore assumed as eight in this study. The S value was assumed to be the spacing values measured on the slope face.

On the other hand, there are both disintegrated and extremely crushed rock units in the slope faces. Thus, Method-2 was also used considering the thickness of the rock particles (mean: 9.6 cm, minimum: 8 cm, maximum: 12.8 cm) from drill cores of the extremely crushed zone (Method-3).

The J_v values calculated from different methods are given in Table 4.3.

Table 4.3 The J_v of the rock mass from different assumptions

J_v (joint/m^3)	Mean	Minimum	Maximum
Method-1	34.25	16	355
Method-2	27.58	11.63	160
Method-3	83	62.5	100

Method-3 gave representative values for the very weak rock units, whereas Method-1 and Method-2 represent the relatively stronger Neogene units.

Additionally, the block volume (V_b) was also calculated by Equation 4.4.

$$V_b = \beta \times J_v^{-3} \quad (4.4)$$

where V_b is the block volume in m^3; β is the block shape factor. Palmström (1995) proposed Equation 4.5 also for estimating the block shape factor (β);

$$\beta = \frac{(a_{2+}\, a_2\ a_{3+}\, a_3\ )3}{(a_2 \times a_3\ )2} \tag{4.5}$$

where a_2: $\frac{S_2}{S_1}$; a_3: $\frac{S_3}{S_1}$; S_1 , S_2 , S_3 : Mean spacings of discontinuities approximately perpendicular to each other ($S_3 > S_2 > S_1$). As the mean, minimum, and maximum J_v values from Method-1 and Method-2 were considered; the mean, maximum, and minimum block volumes were calculated, respectively (Table 4.4). The calculated block volumes correspond to small and very small size blocks according to Anon (1977).

Table 4.4 The block shape factor and the corresponding block volumes

Statistical values	Mean	Minimum	Maximum
β	42.96	175.76	38.36
V_b (m^3) (Method-I)	0.00107	0.004×10^{-3}	0.009
V_b (m^3) (Method-II)	0.002047	0.04×10^{-3}	0.024

4.1.5 Persistence of Discontinuities

The persistence of discontinuity refers to its extent in the rock mass. It is often difficult to trace the discontinuity length on the exposures. In the case of two discontinuity sets intersecting each other, one of the sets will terminate against other joints and assumed as a continuous joint. In addition, another set may terminate in intact rock and can be termed as discontinuous joints.

The measurement of discontinuity persistence was generally unavailable for siltstone and conglomerate outcrops due to the soil cover. The best lateral persistence measurements were obtained for the units of sandstone and limestone dominated

outcrops. The size-frequency histograms of the discontinuity persistence mainly in the direction of dip are given in Figure 4.6.

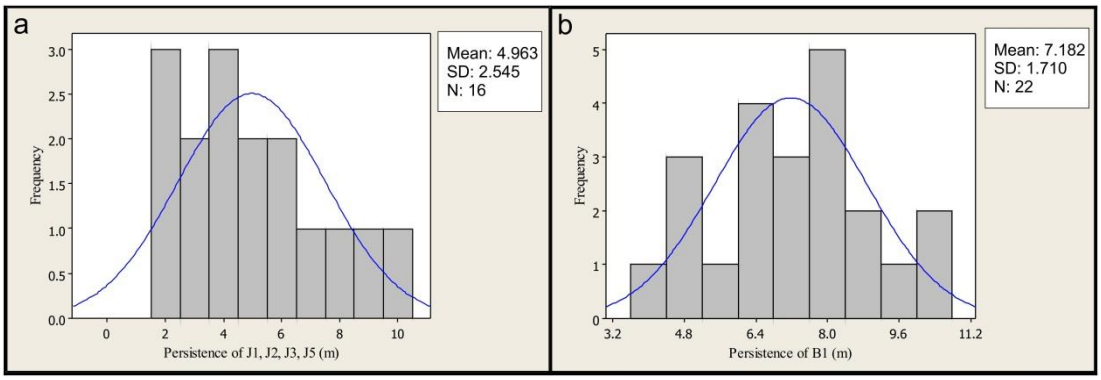


Figure 4.6 The histograms of persistence measurement for the discontinuity sets a. J-1, J-2, J-3, J-5 and b. B-1

Principally the joint sets vary in direction. Hence, the mean persistence of joint and bedding planes is 4.96 and 7.18 m, respectively (Table 4.5). Thus, the mean trace lengths were described as “medium persistence” according to ISRM (2007).

Table 4.5 Statistics of the persistence of the discontinuity sets

Persistence (m)	Discontinuity sets	
	B-1	J-1,2,3,5
Mean	7.18	4.96
Standard deviation	1.71	2.54
Minimum	4.00	1.50
Maximum	10.00	10.00

4.1.6 Roughness of Discontinuity

The surface roughness/irregularity of rock joints has a profound influence on the shear strength of joints, especially in the case of unfilled joints. Generally, the shear strength of the joint surface increases with increasing surface roughness (Nguyen, 2013). In other words, as the smoother joint surfaces are, the more easily can movement take place along them. The discontinuity surface can be described as wavy, rough, or smooth. The waviness and roughness can be differentiated by their

effect on the shear strength of the discontinuity surface. Waviness is the first-order asperity that appears as undulations of the joint surface, which is unlikely to be sheared-off, whereas roughness is small-sized second-order asperity, which is easier to be sheared-off (Beavis, 1985).

There are many techniques for determining the roughness of discontinuity surfaces, such as profile combs and profilometry methods, as well as photogrammetry, image processing, and laser scanning methods. The profile combs and profilometry methods are more commonly used due to being cheap and easy.

The joint roughness coefficient (JRC) is a commonly used measure of joint roughness in rock engineering practice. The JRC value of a rock joint can be estimated qualitatively by comparing it with the ten standard JRC profiles proposed by Barton & Choubey (1977) (Figure 4.7).

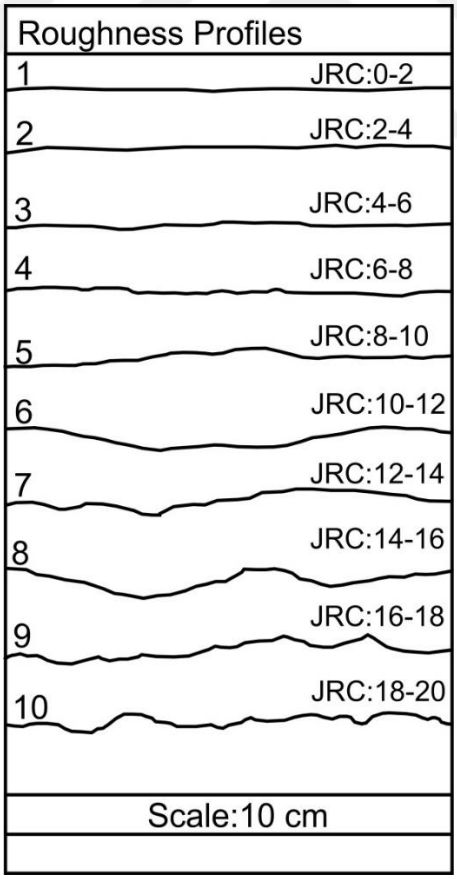


Figure 4.7 Typical roughness profiles for JRC range (Barton & Choubey, 1977)

Alternatively, the diagram illustrated by Barton & Bandis (1982) can be used to estimate JRC values for various profile lengths (Figure 4.8).

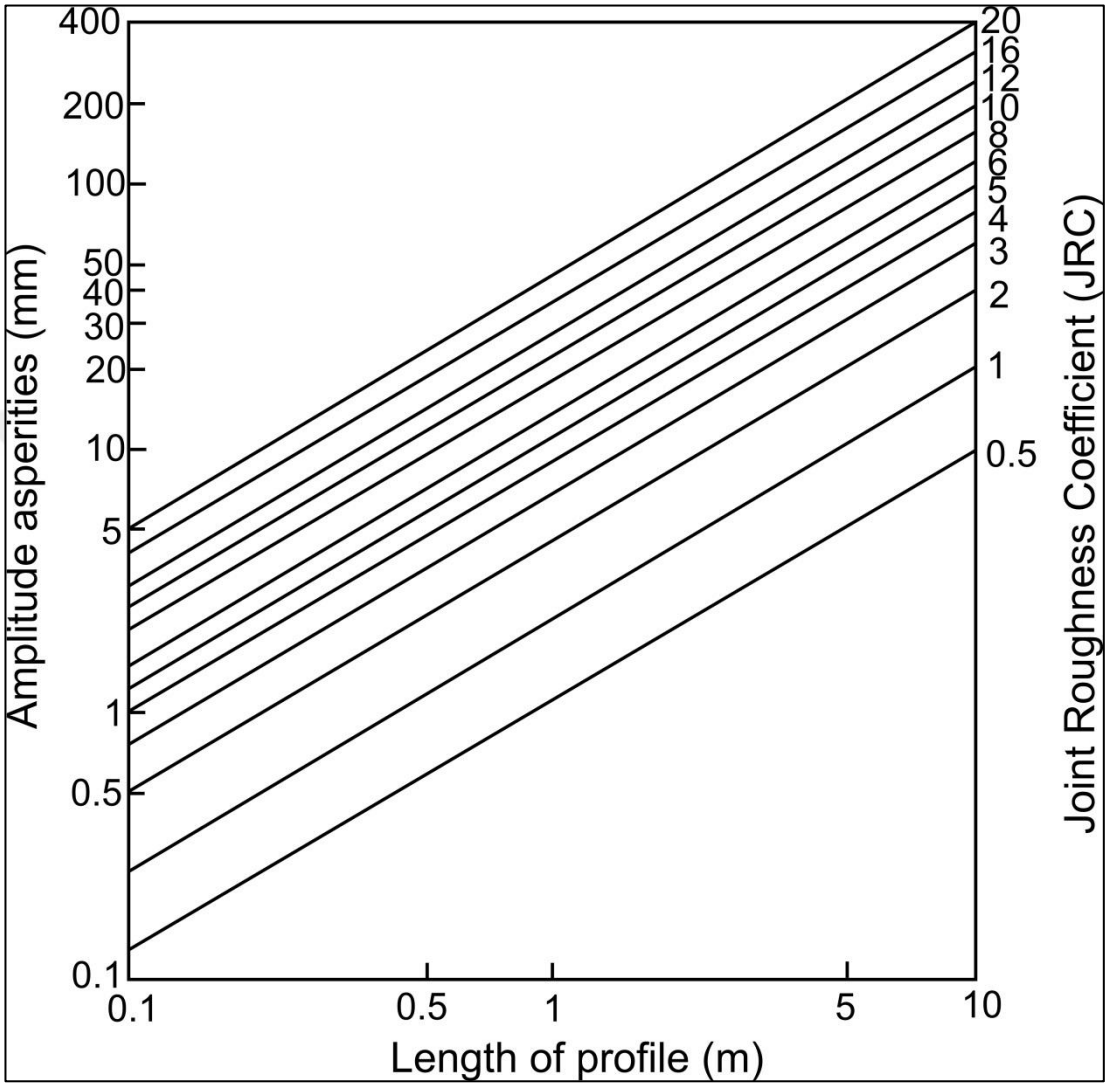


Figure 4.8 An alternative method for estimating JRC from surface roughness amplitude from a straight edge (retrieved from Barton & Bandis, 1982)

In this study, a Meister profile comb having 15 cm length was used in the field, and the JRC values were estimated according to Barton & Choubey (1977). In order to reduce the effect of anisotropy in the roughness profile, JRC profiles were produced in four different directions, as illustrated in Figure 4.9. The measurements were carried out on discontinuity surfaces at ten observation points.

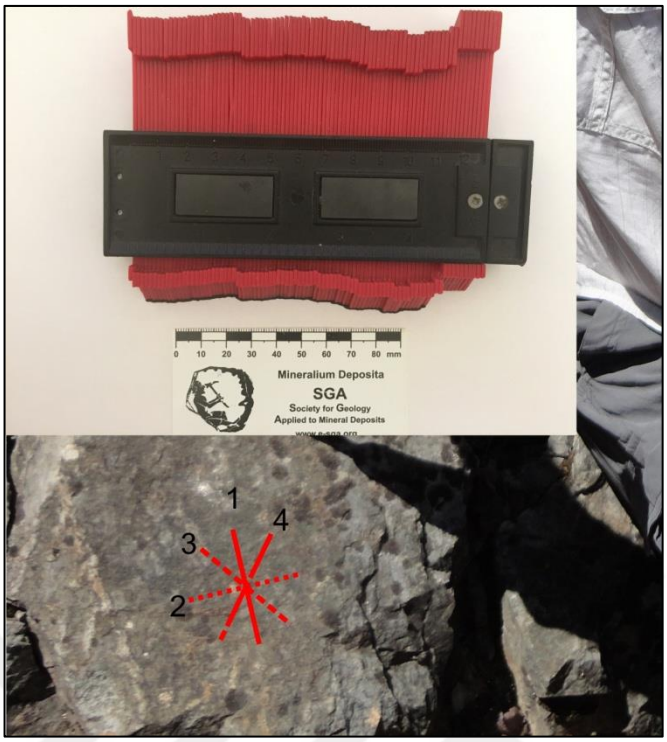


Figure 4.9 Illustration of JRC measurement in the field in four directions with profile comb (Personal archive, 2016)

The JRC values were estimated based on the surface profile sketches as given in Figure 4.10.

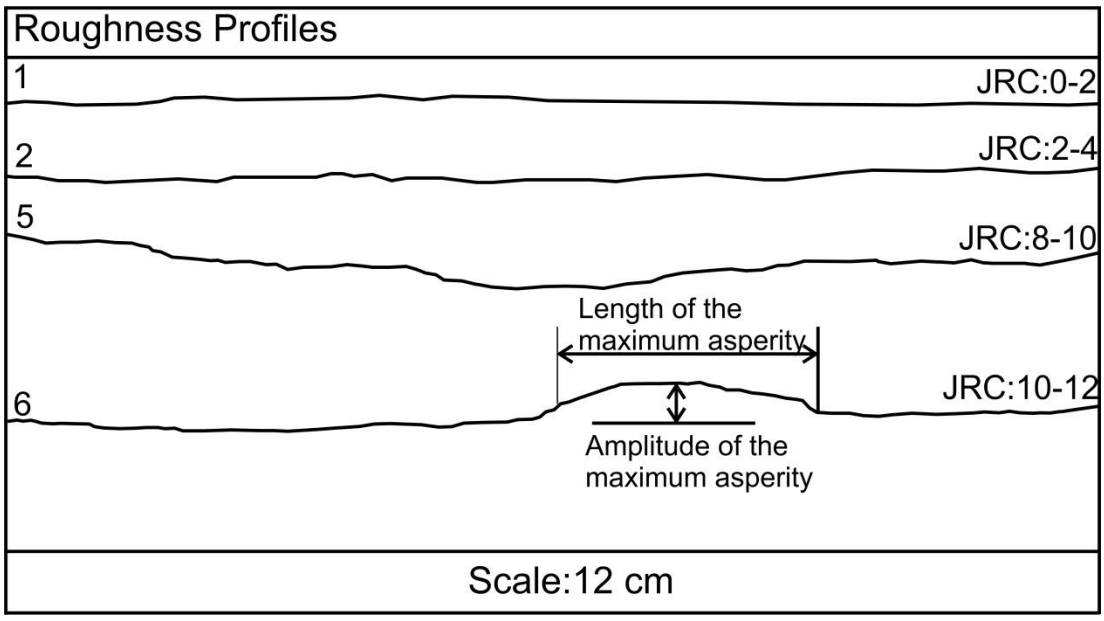


Figure 4.10 Example of roughness profiles measured by profile comb in the field

The arithmetic mean values of JRC measured in four directions at ten locations were obtained as 9 and 3 for joint sets and bedding sets, respectively. The mean amplitude of the asperities is 5.52 mm, and the length between the maximum amplitudes is 20 mm, which has been measured on the sketch from the profile comb.

It should be kept in mind that the roughness of rock joints is scale-dependent. Bandis, Luumsden, & Barton (1981) investigated scale effects and found that the peak shear strength of rock joint decreases with increasing size of the specimen (increase in roughness) as similarly found by Tatone & Grasselli (2013). Therefore, a scale correction proposed by Barton & Bandis (1982) for JRC values were applied in this study (Equation 4.6).

$$JRC_n = JRC_0 \left(\frac{L_n}{L_0}\right)^{-0.02JRC_0} \quad (4.6)$$

where JRC_o is the JRC value of L_o (length) of 100 mm length sample, and JRC_n and L_n refer to in-situ block size. The maximum spacing value, which is corresponding to the discontinuity surface length was considered (L_n=40 cm). Consequently, the corrected JRC values are 7, 2.3 for joint sets and bedding sets, respectively.

4.1.7 Aperture and Infilling of Discontinuities

Below the zone of weathering, discontinuities are usually tight due to the state of stress in the rock mass, including confining pressure (Beavis, 1985). The stress release due to excavation, natural weathering, and erosional unloading results in the opening of joint walls. Discontinuities may be open or closed. How open they are is of importance in relation to the overall strength and permeability of a rock mass. Therefore, the discontinuity aperture is assumed to become tighter towards depth and open at the surface with various grades. The aperture between discontinuities imports the rock mass a secondary permeability and also reduces the stability with increasing width. In addition, the apertures may be filled with weathering products, minerals transported by water flow or hydrothermal fluids, and rock gouges due to shearing

and/or faulting. If the thickness of the infill material is greater than the amplitude of the roughness, the type of infill material mainly controls the shear strength of the discontinuity.

The frequency histograms of aperture measurements in this study are given in Figure 4.11.

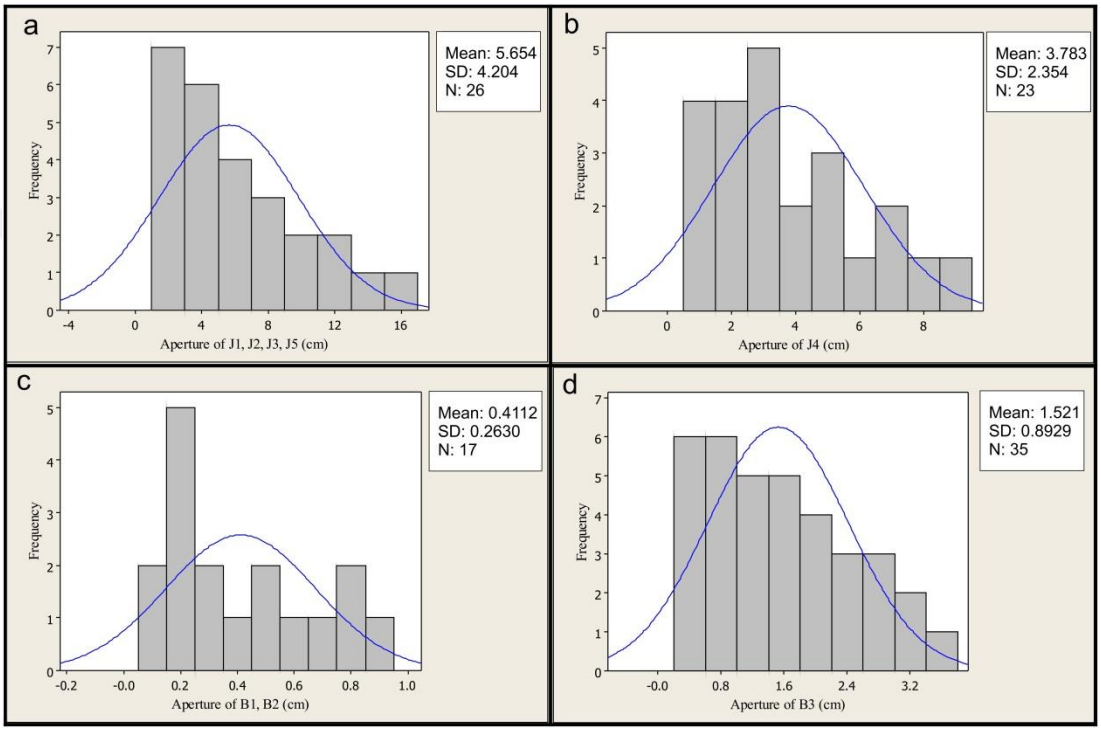


Figure 4.11 The histograms of aperture measurement for the discontinuity sets a. J-1, J-2, J-3, J-5 b. J-4 c. B-1, B-2 d. B-3

The aperture of the bedding and joint sets are mainly unfilled, whereas partly filled with disintegrated material having particles of coarse sand and fine gravel in limestone dominated outcrops. In addition, decomposed material having particles of silt and clay in argillaceous limestone as well as sandstone, siltstone dominated outcrops were observed as infill material. The infill materials were dry, and no seepage was observed in the summer season. The thickness of the infill material is changing between 0.1 cm to 3 cm. Since the mean roughness amplitudes (mean: 6 cm) observed in the field are greater than the thickness of the infill material, it was assumed that the infill material do not affect the shear strength of the discontinuity

planes. The statistics of the aperture of the discontinuity sets are given in Table 4.6. The maximum aperture of the joints was measured on Landslide-3 which is related to the disturbed rock mass. Hence, these extremely wide, open features were neglected in evaluating the rock mass behavior.

Table 4.6 Statistics of the aperture of the discontinuity sets

Aperture (cm)	Discontinuity sets			
	B-1, 2	B-3	J-1,2,3,5	J-4
Mean	0.41	1.52	5.65	3.78
Standard deviation	0.26	0.89	4.20	2.35
Minimum	0.10	0.30	1.00	1.00
Maximum	0.9	3.50	15.00	9.00

4.1.8 Weathering

Weathering is a process of physical disintegration and chemical decomposition of rocks that occurs at the surface and/or subsurface. Physical and chemical weathering can work together in an area or vice versa. As a result of weathering, rocks become more porous, mineral grains are weakened, and bonding between grains is lost. Therefore, permeability may change depending on the degree of weathering and the amount of weathering products within fractures, pores, or at grain boundaries. The most significant consequence of weathering is the decrease in strength and the increase in deformability of rock material. The overall strength and permeability of a rock mass often depend largely on the amount of weathering which the rocks have suffered. In addition, if the effects of weathering have penetrated deeply into a joint, a wide weak zone may be present.

The slope failures are sometimes strongly related to the climatic conditions and degree of weathering. The relationship between rock weathering grade and slope instabilities were studied by several researchers (Deere & Patton, 1971; Hencher, Massey, & Brand, 1984; Gullà & Nicoletti, 1996; Gullà et al., 2004; Valley, Thuro, Eberhardt, & Raetzo, 2004). Borrelli, Greco, & Gulla (2007) stated that the weathering of rock masses can be assumed as a predisposing factor for slope

instabilities. Therefore, the interaction between climate and weathering was examined by the classification proposed by Peltier (1950) (Figure 4.12). Peltier's classification is based on the mean annual precipitation value and temperature. According to Figure 4.12, the city of Manisa is prone to "slight weathering" due to mean annual precipitation (728 mm) and mean annual temperature (16.8 °C). However, qualitative and quantitative weathering indices were utilized to determine the weathering grades in the field.

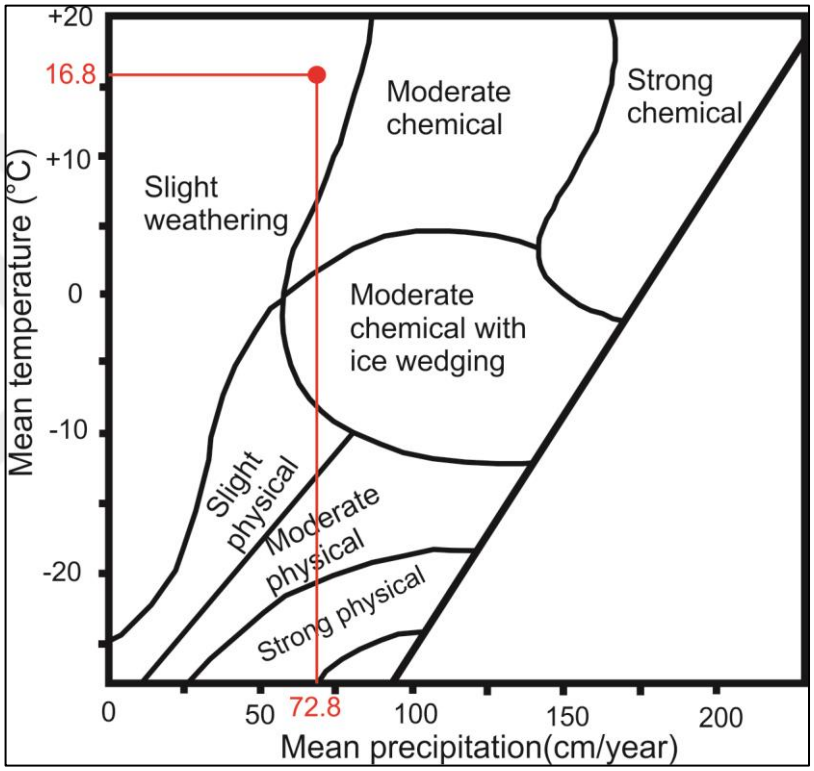


Figure 4.12 The effective weathering type in the study area (Peltier, 1950)

Slight and moderate discoloration and disintegration of the rock mass (highly weathered) near or along joint and fault planes, the decomposed and/or disintegrated rock mass has various thicknesses from 20 cm to 6 m at the top of the ground indicate the grades of weathering in the study area (Figure 4.13).

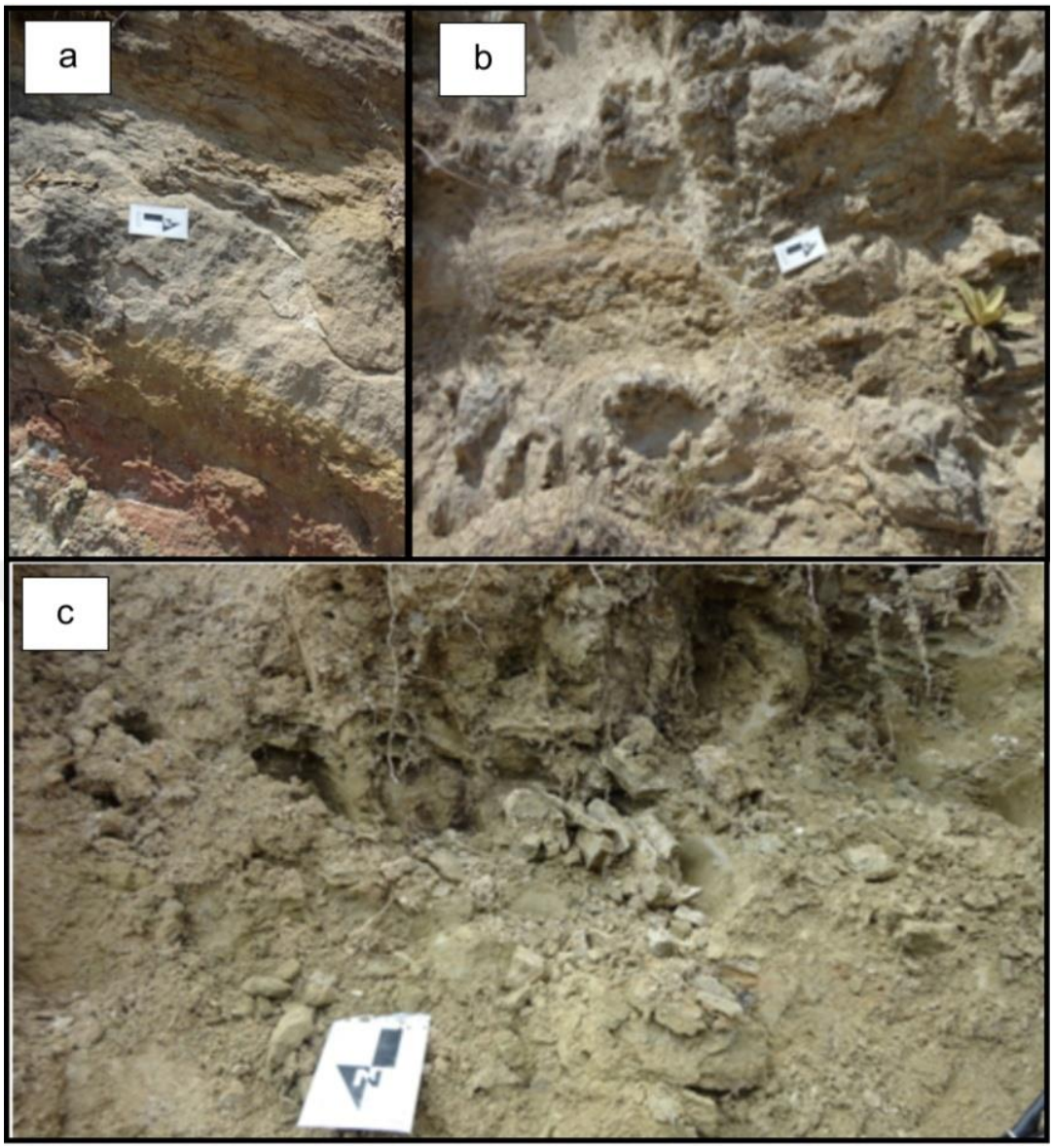


Figure 4.13 a. Discoloration around the joints (weathering class II) b. Discoloration and disintegration along fault plane (weathering class III) (70/48, normal fault) c. (weathering class V) (Personal archive, 2015)

On the basis of field observation, the weathering degree of the rock mass was described qualitatively. The descriptions used as a reference for the field observations are reported in Table 4.7, which are proposed by Dearman (1976) and Anon (1981). As a consequence, the Miocene aged sedimentary rocks outcrop in the study area refer to the II, III, and V weathering classes.

Table 4.7 Descriptions assumed as reference for defining weathering classes (Dearman, 1976; Anon, 1981)

Term	Description	Grade
Fresh	No visible sign of rock material weathering; perhaps slight discoloration on major discontinuity surfaces	I
Slightly weathered	Discoloration indicates the weathering of rock material and discontinuity surfaces. All the rock material may be discolored by weathering.	II
Moderately weathered	Less than half of the rock material is decomposed or disintegrated into soil. Fresh and discolored rock is present either as a continuous framework or as corestones.	III
Highly weathered	More than half of the rock material is decomposed or disintegrated into soil. Fresh and discolored rock is present either as a discontinuous framework or as corestones.	IV
Completely weathered	All rock material is decomposed and/or disintegrated into soil. The original mass structure is still largely intact.	V
Residual soil	All rock material is converted to soil. The mass structure and material fabric are destroyed. There is a large change in volume, but the soil has not been significantly transported.	VI

The weathering degree of the rock mass was also classified based on the weathering coefficient (W_c) proposed by Gökçeoğlu & Aksoy (2000) (Equation 4.7).

$$W_c = R_{fresh\ (lab)} / R_{weathered\ (in\text{-}situ)} \quad (4.7)$$

where $R_{fresh\ (lab)}$ is the Schmidt hammer rebound value measured on the fresh samples in the laboratory (will be given in Chapter 5), $R_{weathered\ (in\text{-}situ)}$ is the Schmidt hammer rebound value measured in-situ. There are four weathering classes (1, 2, 3, 4) in this classification which corresponds to fresh, slightly weathered, moderately weathered, and completely weathered, respectively. The weathering classes according to this classification are given in the next section, in Table 4.8. According to Table 4.8, it can be said that the W_c classification is comparing well with the qualitative weathering classification proposed by Anon (1981).

On the other hand, indicators of weathering were also observed in samples cored in the laboratory. Weathering of the iron-bearing carbonate rocks causes limonitic staining in or near the veins, as given in Figure 4.14. Calcite-cemented sandstone samples also showed some discoloration. These are classified as Grade I-II according to Table 4.7.

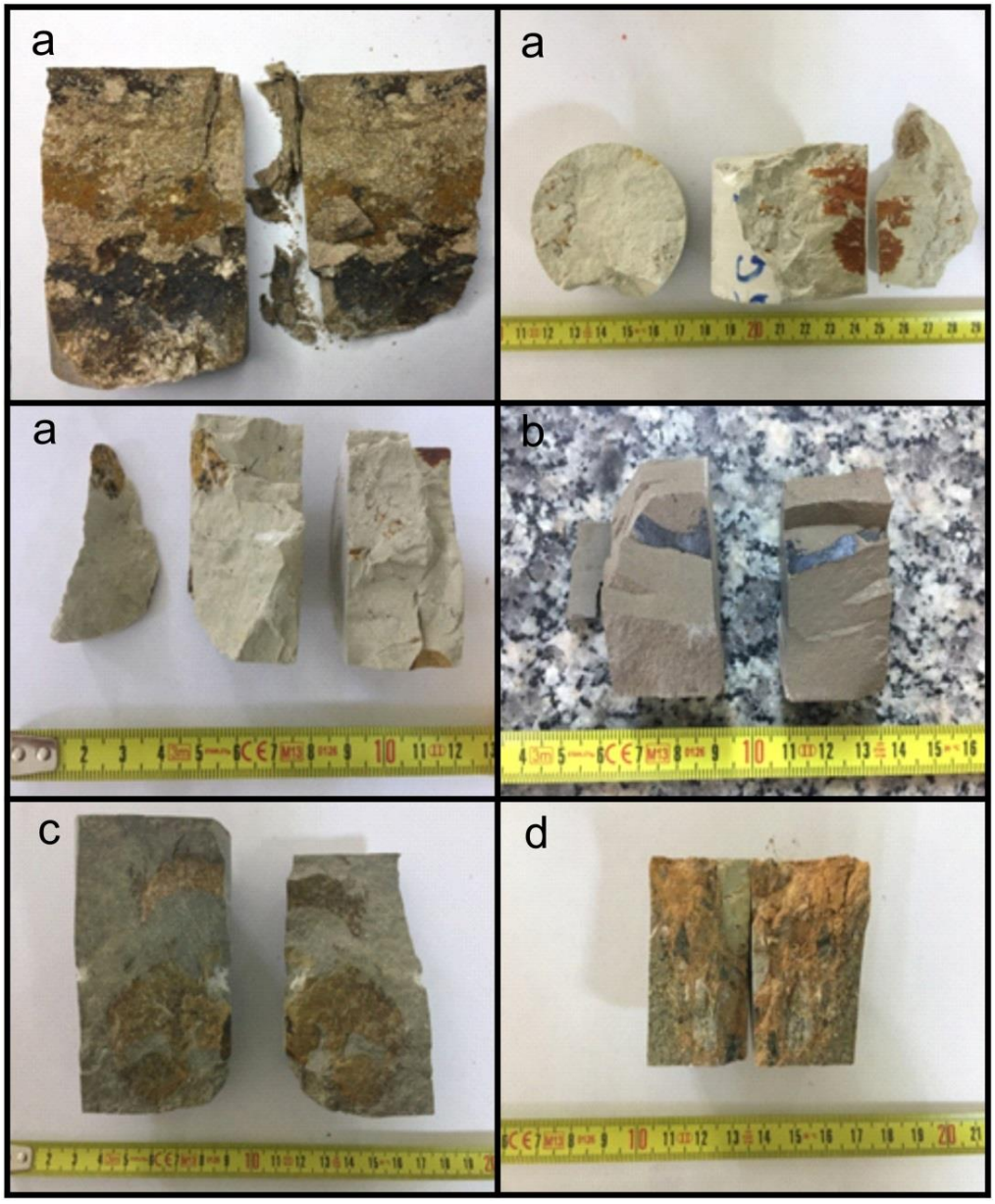


Figure 4.14 Discoloration referring to weathering class I-II in some a. KÇ, b. M, c. ÇK, and d. Ç samples (Personal archive, 2018)

4.1.9 Joint Wall Compressive Strength

The mainly unfavorable sets which are dipping out of the slope and those are cutting them perpendicularly were considered, and Schmidt hammer tests were conducted to estimate the compressive strength of discontinuity surface or joint wall strength (JCS). The standard L-type Schmidt hammer can generate different levels of impact energy of 0.735 Nm. and is recommended to use in heterogeneous and low strength rock medium (Aydın & Basu, 2005; Karakul, 2017). ISRM (2007) suggests recording 20 rebound values from single impacts separated by at least a plunger diameter and averaging the upper ten rebound values.

L-type Schmidt hammer was used during field measurements on limestone and sandstone discontinuity planes. Mostly smooth and crack-free surfaces were chosen for the test, according to ISRM (2007). The Schmidt hammer was perpendicularly aligned to the surface and the test was conducted on 20 points on each discontinuity surface. The lowest 10 readings were omitted and the mean rebound value of the remaining ten readings was calculated. The mean value of Schmidt rebound values (R) and the rock unit weight (γ) for the discontinuity surface of interest were used to estimate the JCS, as suggested by Miller (1965) (Equation 4.8).

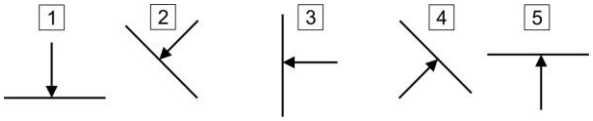
$$\log JCS = 0.0008\gamma R + 1.01 \text{ (MPa)} \quad (4.8)$$

The test results and estimated uniaxial compressive strength (σ_c) values are given in Table 4.8. Table 4.8 indicates that the discontinuity walls are high to low strength rocks according to Anon (1981).

Table 4.8 In-situ Schmidt hammer test results performed on limestone and silty sandstone discontinuity surfaces in Göcek Formation

Location	Rock group	Weathering grade Anon (1981)	Position of hammer *	Mean R	γ (kN/m^3)	$JCS_{in\text{-}situ}$ (MPa)	W_c (Gökçeoğlu & Aksoy, 2000)
589672 4294922	K	I-II	2	43.5	24.29	87.06	0.95 (1)**
589653 4294931	K	I-II	4	43.9	24.29	88.79	0.94 (1)
589616 4294978	M	I-II	2	36.7	23.02	56.68	1.28 (2)
589597 4295010	K	II	2	40.6	24.29	75.48	1.11 (2)
592242 4295316	Ç	III	2	13	23.09	18.80	1.81 (3)
591369 4294594	Ç	III	2	15.8	23.09	21.43	1.49 (2-3)
591947 4294587	Ç	II	1	27.2	24.87	40.30	1.22 (2)

*



**W_c classes

It should be noted that JCS is supposed to be equal to the uniaxial compressive strength of rock material (σ_{ci}), while the joint wall is unweathered. However, the JCS value may be reduced up to 75% when the walls of the joint are weathered (Bell, 2007). Already, Barton (1973) have stated that a ratio of JCS/σ_{ci} equal to 1/4 can be used for weathered rocks when no direct measurements are available. On the other hand, Singh & Goel (1999) suggest not to use Schmidt hammer rebound values for JCS in the case of rough joints.

4.2 Borehole Surveying

The information derived from the discontinuity survey was gathered with the measurements along with the drill cores. Additionally, the core logs of 25 boreholes drilled by the DSI were used to provide more information about subsurface lithologies in the dam site.

Core borings were made to recover rock core specimens by using the rotary system. NX diameter was used in exploratory borings for rock identification. In fractured rock and breccia zone, core recovery improves with larger diameters. HX size was used in these zones along the profiles. In the site, 25 vertical boreholes were drilled; the depths are changing between 15 and 100 m (Table 4.9).

Six boreholes out of 25 boreholes are located in the streambed; six boreholes are on the northern bank of the reservoir area and seven boreholes on the southern bank. Six boreholes were drilled along the planned dam axis. The locations of the boreholes are given in Figure 4.15.

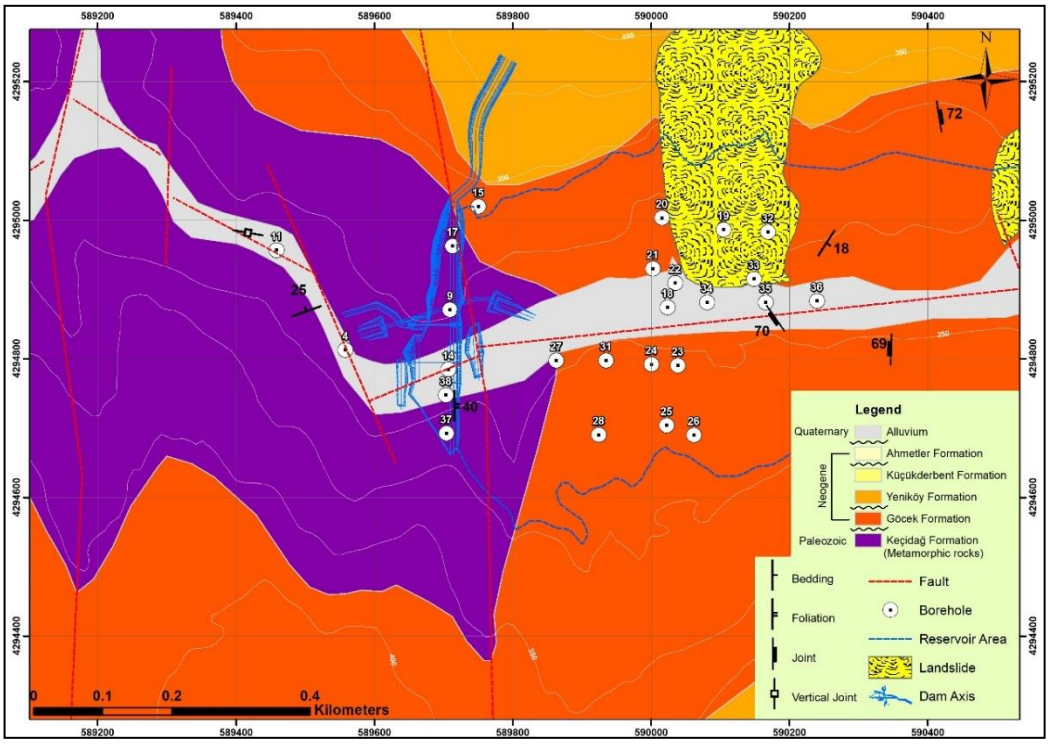


Figure 4.15 The locations of boreholes drilled in the study area

Table 4.9 The drilled boreholes in the study area

No	Borehole No	Location	Elevation (m)	Depth (m)	WTL * (m)	WTL ** (m)
1	19	Reservoir Northern Bank	238.81	15	6.5	-
2	20	Reservoir Northern Bank	237.88	15	7.1	10.38
3	21	Reservoir Northern Bank	234.15	15	-	-
4	22	Reservoir Northern Bank	218.51	15	9.6	10.6
5	32	Reservoir Northern Bank	248.68	45	13	32.05
6	33	Reservoir Northern Bank	221.78	50	28.5	46.75
7	23	Reservoir Southern Bank	256.47	15	-	-
8	24	Reservoir Southern Bank	256.21	30	13.9	-
9	25	Reservoir Southern Bank	279.77	30	27.15	-
10	26	Reservoir Southern Bank	280.82	30.5	19.25	-
11	27	Reservoir Southern Bank	238.73	21	19.25	-
12	28	Reservoir Southern Bank	278.98	30	22.3	-
13	31	Reservoir Southern Bank	255.89	26	23.5	-
14	18	Reservoir Streambed	213.22	15	9.9	10.05
15	34	Reservoir Streambed	215.44	29	9.8	19.05
16	35	Reservoir Streambed	215.32	36	11.45	29.07
17	36	Reservoir Streambed	215.56	26	1.7	1.4
18	9	Dam axis	255.03	60	58.6	-
19	14	Dam axis	209.66	55	42.8	43
20	15	Dam axis	292.72	100	93.7	-
21	17	Dam axis	275.16	90	85.3	-
22	37	Dam axis	269.85	100	-	-
23	38	Dam axis	236.44	60	-	-
24	11	Downstream Streambed	207.00	20	17.9	18.12
25	4	Downstream Streambed	208.33	55	38.65	41.00

*Groundwater level measured in June, 2011

** Groundwater level measured in October, 2011

The thickness of alluvium in the river section is changing between 4.5 and 6 m with a maximum grain size of 20-30 cm. It consists of medium-dense to dense, particularly cohesionless materials.

The first 6 m depth from the ground surface level also comprises embedded rock blocks, which were moved as a result of mass movements that occurred in the past. Some of the rock blocks remain on the stream bed (Figure 4.16).



Figure 4.16 The rock blocks slid into the streambed due to the mass movements (Personal archive, 2016)

On the other hand, unconsolidated slope debris material with a thickness of 1.3 m to 15 m in the southern bank and 2 to 6 m in the northern bank were defined in the boreholes. A residual soil cover was partly encountered at the top of the rock units with a thickness of 1 to 7 m.

Three boreholes (BH-19, BH-32, and BH-33) are located in the lower part of Landslide-1 (Figure 4.15). Breccia zone was intersected between the depths 5 m and

8 m below the ground surface level in BH-19; between 9 m and 16 m in BH-33; between 15 m and 23 m in BH-32 (Figure 4.17). Complex layering in the landslide mass indicates that the weakest layer has a significant role in the slope failures.



Figure 4.17 The core box of BH-32 between the depth 15 m and 21 m showing the breccia zone (Personal archive, 2012)

The groundwater level is changing between 1.4 m to 46.75 m (Table 4.9). However, in fourteen boreholes, no groundwater level is detected even at 100 m depth in October. This was referred to due to karstic gaps and faulting. This case indicates that the groundwater flows to the lower elevations along the faults and into the karstic gaps.

The rock quality designation (RQD%) and fracture frequency (λ) that measured along the drill cores were evaluated. Limestone layers within the Neogene sedimentary units gave high RQD values, whereas the siltstone, mudstone, and poorly consolidated sandstone samples gave very low even zero RQD values. The RQD value depends on the quality of the rock concerned; in poor quality rock such as siltstone and mudstone is likely to be lost during drilling. The frequency histograms of the RQD and λ values measured on the drill cores are given in Figure 4.18.

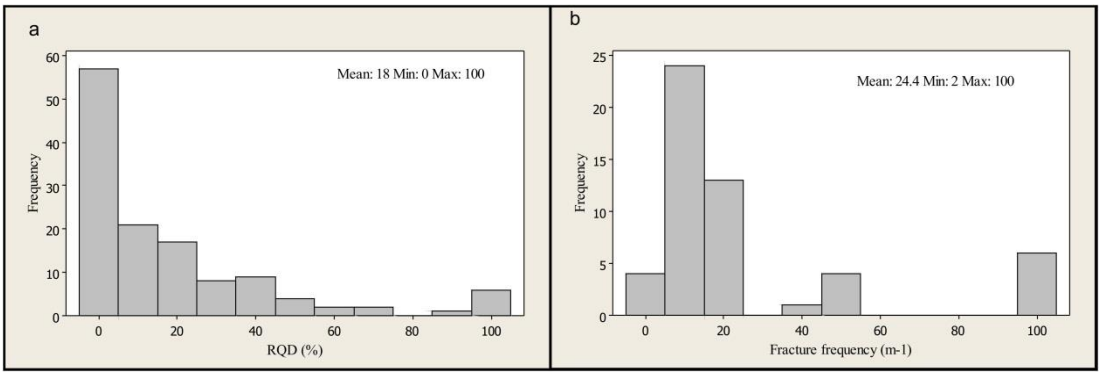


Figure 4.18 The histograms of a. RQD (%) and b. λ (m^{-1}) measured on the drill cores

RQD value is fundamentally proposed to represent the in-situ rock mass quality. However, RQD is a directionally dependent parameter, and it yields variable values depend on the borehole orientation. Pells, Bieniawski, Hencher, & Pells (2017) suggested using volumetric joint to reduce the directional dependence of RQD value. Zhang (2016) deeply investigated the utilization of RQD in engineering calculations and pointed to the importance of considering the effect of sampling length and direction on RQD while determining RQD. Since the use of RQD in rock mass classifications are questionable due to being vulnerable to different errors and being unrepresentative for the quality of the rock. For this reason, RQD values were also estimated from three different empirical equations for comparison with the ones directly measured on the drill cores.

The empirical equation proposed by Priest & Hudson (1976) was used to estimate the RQD value from fracture frequency measurement made along scan-lines and along drill cores (Equation 4.9). It should be noted that the equation is valid for the scan-lines having at least 1 m length.

$$RQD = 100\, e^{-0.1\lambda}\,(0.1\lambda+1) \tag{4.9}$$

The J_v value can also be correlated with the rock quality designation (RQD) value as suggested by Palmström (2005) (Equation 4.10).

$$RQD = 110 - 2.5\, J_v \tag{4.10}$$

The use of volumetric joint count for estimating RQD quite reduces the directional dependence of RQD that is calculated from core boring (Zhang, 2016). The RQD values were calculated by considering the minimum, maximum, and mean J_v values, and therefore maximum, minimum, and mean RQD values were obtained, respectively (Table 4.10).

Finally, Deere, Hendron, Patton, & Cording (1967) proposed Equation 4.11 to estimate RQD value from in-situ and laboratory-measured P-wave velocities (V_p).

$$RQD = (V_{p\text{-insitu}} / V_{p\text{-lab}}) \times 100 \quad (4.11)$$

Table 4.10 RQD calculated directly from drill cores and different empirical methods

Method	RQD (%)		Mean	Min.	Max.
Direct	From drill cores		18	0	100
Equation 4.9	From λ measured on drill cores		30	0	98
Equation 4.9	From λ measured on slope face		79	0	99
Equation 4.10	From J_v measured on slope face	Method-I	24	0	60
		Method-II	41	0	81
Equation 4.11	From ultrasonic wave velocity ratios	V_p ratios	20	-	-
		V_s ratios	28	-	-

The RQD values calculated from Equation 4.9 using drill core fracture frequency values are well matching with the RQD values directly measured from drill cores. However, the maximum RQD value (100%) measured on the drill cores was not obtained from Equation 4.10. One reason is that the J_v=4 can not be calculated (which yields RQD=100% according to Equation 4.10) for the rock masses having more than three discontinuity sets. Another possible reason is that the RQD values at greater depths are higher than the ones on ground contacts due to stress relaxation.

Hence, if the RQD value is estimated from the measurements on the slope face, it can sometimes be underestimated. While considering the all RQD values measured directly on drill cores and estimated by several empirical methods match well except the ones estimated from Equation 4.9 using slope face-measured λ.

It should be noted that the discontinuity properties change with depth. Due to this fact, spacing, infilling, and aperture measured on the slope face and the drill cores would vary. In this study, the physical and mechanical properties of discontinuities measured on the slope face were used in rock mass classifications. On the other hand, the values of RQD measured on drill cores and estimated ones from various empirical relationships were compared to determine the upper and lower limit of the RQD values. It should also be noted that RQD=100% does not indicate a rock mass without discontinuities such as an intact rock. Despite, RQD=100% means almost massive rock with extremely wide-spaced discontinuities.

4.3 In-situ Tests

Together with the laboratory tests, the in-situ tests such as shear vane test, standard penetration test, Lugeon and permeability tests, and geophysical measurements provide quantitative information required to properly assess the relevant geotechnical properties of rock and soil units.

4.3.1 Shear Vane Test

In-situ shear vane test is commonly used to determine the strength of clays; however, Blight (1968) argued that the test can also be used for silty soils. In this manner, shear strength of silty clayey soils derived from Neogene sedimentary rocks was determined from rapid field vane tests (ASTM D2573-08, 2008) to avoid the drainage of soil (Figure 4.19). It has been stated that the values of undrained shear strength from field vane tests are likely to be higher than can be mobilized in practice (Bjerrum, 1972, 1973). It is referred to the combination of anisotropy of the soil and the rapid shear rate during the vane shear test.



Figure 4.19 The in-situ shear vane test (Personal archive, 2012)

Four in-situ shear vane tests were conducted at two locations (5932096/4299760 and 591783/4297698) in the residual soil (silty clayey soil) in the dry season. Residual soil was encountered particularly at the toe and lower parts of the landslide body. The following equations were used to calculate the in-situ undrained shear strength (c_u), and the results are given in Table 4.11.

$$c_u = T / K \quad (kg/ cm^2) \tag{4.12}$$

$$K = \frac{\pi D^2 H}{2}\left[1 + \frac{D}{3H}\right] \tag{4.13}$$

T: The torque required to shear the soil (kg.m)

K: Coefficient for the shape and dimensions of the vane (cm^3)

D: The width of the vane (cm)

H: the height of the vane (cm)

Table 4.11 In-situ shear vane test results

Location	T (kg.m)	H (cm)	D (cm)	K	c_u (MPa)
1	100	10	6	678.24	0.0147
1	98	10	6	678.24	0.0144
2	200	10	6	678.24	0.0295
2	190	10	6	678.24	0.0280

As a result, the mean undrained shear strength of the disturbed, residual soil was determined as 0.022 MPa. Since the clayey soils soften while saturated, the c_u values can be slightly lower in the wet season. However, the use of undrained shear strength leads to a safer design, especially in pseudo-static analyses.

4.3.2 Standard Penetration Test

Standard Penetration Test (SPT) is the most commonly used in-situ test for estimating particularly cohesionless soil properties (ASTM D1586-11, 2011). The tests were performed by a donut type free falling hammer. Since the project is in the preliminary stage, there is a limited number of SPT results. One test was carried out in alluvium in BH-4 between elevations 1.5 and 1.95 m. The other three tests were performed in residual soil derived from Neogene sedimentary rocks in BH-34 between the elevations 2 m and 10 m. The blows (N) required for the hammer to penetrate soil 30 cm are counted, and the N_{30} value is recorded. There is a wide range of empirical equations based on the SPT blow value to estimate the elastic modulus of soil (E_s). Bowles (2001) compiled several equations that estimating elastic modulus. Equation 4.14 proposed for gravelly sand was used to estimate the elastic modulus of the alluvium consist of silt, sand, and gravel-size particles.

$$E_s = 1200(N_{55} + 6) \tag{4.14}$$

On the other hand, the three SPT-N_{30} values of stiff to very stiff residual soil are 25, 46, and 37. The elastic modulus of clayey sands in kN/m^2 can be estimated from Equation 4.15 proposed by Bowles (2001).

$$E_s = 320(N_{55} + 15) \quad (4.15)$$

Bowles (2001) suggested using N_{55} value, which is the corrected value of the N_{30} to obtain a standard energy ratio. N_{55} can be readily calculated by the equation below.

$$N_{55} = N \frac{Er}{55} \quad (4.16)$$

where N is the in-situ counted blow, and E_r is the rod energy ratio for the method used in the test. E_r value is considered as 45 for the donut type hammers in Turkey. As the N_{30}=50 is obtained for alluvium, N_{55} is calculated as 41. Relevantly, E_s of the alluvium is 56.4 MPa. The Poisson's ratio of the partially permeable alluvium can be chosen between 0.3 and 0.4 based on the chart proposed by Bowles (2001). The internal friction angle (ϕ) of the alluvium can be also estimated between 33˚- 44˚ from the chart proposed by Koloski, Schwarz, & Tubbs (1989).

If the mean N_{30} value is considered as 36, according to Equation 4.15, the E_s is calculated as 14.22 MPa for the residual soil. However, the typical elastic modulus value for stiff to very stiff clayey soils is between 10 MPa and 30 MPa based on the data compiled by Obrzud & Truty (2012). The Poisson's ratio can be chosen between 0.3-0.35 for silty clayey soils. Besides, the ϕ value can be chosen between 27˚-34˚ from the chart proposed by Carter & Bentley (1991). However, the ϕ value can be as low as 17° for high plasticity clayey soils. These values will be back-calculated in numerical analyses.

4.3.3 Lugeon and Permeability Tests

During core drilling, water pressure tests were carried out, and the permeability is expressed in terms of Lugeon (LU) values. Ghafoori, Lashkaripour, & Tarigh Azali (2011) stated that to describe or estimate the permeability of the jointed rock, the result of the water pressure test should be converted to permeability coefficient (k) value instead of LU value. Considering a homogenous and isotropic condition, one Lugeon is equal to 1.3 x 10^{-5} cm/sec. Since the rock discontinuities affect the hydraulic conductivity of the rock mass, the Lugeon values can also be used for evaluating the conditions of discontinuities. LU value was measured as higher than 25 for the metamorphic rock unit (schist and marble) in the boreholes drilled under the dam axis (for example, BH-14 LU: 63). On the other hand, the weathered schist layers have lugeon values as low as 1 LU due to the clay content as a weathering product. The typical ranges of permeability values for the geological units in the study area are given in Table 4.12.

Table 4.12 The range of permeability values for the lithological units in the study area

Units	Permeability coefficient (k) (cm/sec)		Description (Anon, 1979)
	Maximum	Minimum	
Alluvium	$1.89x10^{-2}$	$1.00\ x10^{-9}$	Highly to very slightly permeable
Slope debris-weak rock	$1.03x10^{-2}$	$1.21x10^{-4}$	Highly to moderately permeable
Neogene aged rocks	$1.62x10^{-3}$	$1.00\ x10^{-9}$	Highly to very slightly permeable
Very stiff soil	$1.00x10^{-9}$	$4.30x10^{-9}$	Very slightly permeable
Metamorphic rock unit	$1.00x10^{-3}$	$1.30x10^{-5}$	Moderately to slightly permeable

The Neogene aged sedimentary rocks are commonly impermeable according to the classification of Anon (1979) due to the clayey interlayers and partially highly permeable due to limestone interlayers. The permeability values rise with low rock quality. The unconsolidated slope debris and weak rock layers are highly permeable. As indicated earlier by Kayabaşı (2017), the Lugeon values higher than 25

corresponds to blocky-disturbed and disintegrated rock mass type on the Geological Strength Index (GSI) chart (Hoek & Brown, 1997).

On the other hand, a rough estimate of the permeability can be made based on the frequency of discontinuities. For instance, the rocks with very closely to extremely closely spaced discontinuities can be defined as, highly to very highly permeable rocks.

Due to the fact that the slip surfaces are commonly impervious and retain the surface water and groundwater until the slip surface daylights on the ground surface, the high permeability of slope debris and weak rock layers causes the underlying rock layers to be saturated after prolonged rainfalls. Thus, a favorable surface for sliding is provided.

Rock slope stability is commonly performed considering the effective stress conditions of the rock mass which provides undrained conditions. Reliable stability analysis of a slope and/or landslide requires the shear strength parameters, joint-water pressure, and sliding mechanisms to be specified.

4.4 Geophysical Survey

In-situ geophysical methods are increasingly used for the investigation of near-surface landslides. Most of the researchers have studied landslides via electrical methods (McCann & Forster, 1990; Hack, 2000; Godio & Bottino, 2001; Le Roux et al., 2011; Perrone, Lapenna, & Pisticell, 2014;). On the other hand, Cardarelli, Cercato, & De Donno (2014) investigated a dam site by a combination of methods such as Multichannel Analysis of Surface Waves (MASW) and P and S wave tomography. Donohue et al. (2012) studied landslides on quick clays by correlating stratigraphical data with geophysical data obtained by MASW.

The geophysical surveys such as MASW and Electrical Resistivity Tomography (ERT) were carried out in this study to (i) differentiate the lithological units, (ii)

calculate dynamic deformation and shear moduli, and Poisson's ratio of these units (iii) determine the groundwater level (iv) detect the embedded landslide material in the streambed (v) detect heavily fractured zones. The MASW and ERT profiles are given in Figure 4.20.

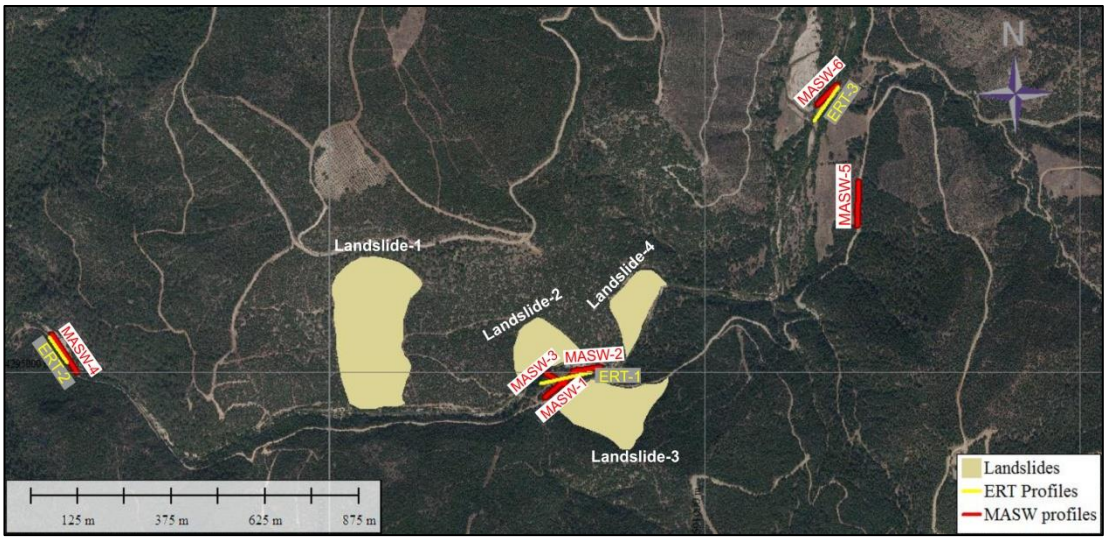


Figure 4.20 The MASW and ERT profiles in the study area

4.4.1 Multichannel Analysis of Surface Waves Method

Multichannel Analysis of Surface Waves (MASW) method is a geophysical technique that can be used for geotechnical characterization of near-surface geological units by obtaining seismic shear wave velocity (V_s) (Miller, Xia, Park, & Ivanovo, 1999; Park, Miller, & Xia, 1999; Xia, Miller, & Park, 1999). The MASW method was introduced by Park et al. (1999). They explained that MASW is an active-source technique requiring an impulsive signal that surface waves are generated by various tools such as sledgehammer, weight drop, and swept vibratory signal. V_s is obtained from the fundamental mode Rayleigh wavefield generated by the source. In their study, phase velocities are directly determined from MASW data after transforming seismic data to the phase velocity-frequency domain.

The estimated V_s profile of sediments deposited over geological basement from MASW measurement is essential for earthquake hazard zonation as well as for

geotechnical investigations (Miller et al., 1999). MASW field study was performed along with six profiles, as shown in Figure 4.20. The geological units along the boreholes were correlated with the MASW results.

For Profiles 1, 4, and 5; 24 geophones were employed with a geophone spacing of 5 m. For the other profiles, geophone spacing was 3 m due to the limited availability of fields in the study area. The data sets were created using a Geometrics Geode Seismic receiver, 24 geophones of 4.5 Hz resonant frequency, and a 100 lb hydraulic hammer as the energy source. The sample interval was utilized as 0.5 ms and the recording time was 2 s. The MASW method provided information about shear (S) and compressive (P) wave velocities of the sub-surface ground profile.

The soil and rock were distinguished according to the threshold value of 700 m/s for shear wave velocity (V_s). S-wave velocities lower than 700 m/s were considered to represent soil and/or hard soil-very weak rock transition, and the higher ones represent weak and hard rock mass. According to the obtained Vs-depth graph, Vs values of the ground changes both laterally and vertically. The shear wave velocities of geological units were found to be between 300 and 1200 m/s. There is a low-velocity zone for the first 10 m. depth. The shear velocities are between 300 and 400 m/s for the first 10 m from the ground surface level and the mean values of shear velocities of alluvial units can be assumed as 350 m/s. On the contrary, in Profile 4, for the first 8 m from the ground surface, V_s values are higher (Vs >700 m/s) than the other profiles due to the rock blocks embedded in alluvium (Figure 4.21). However, Profile 4 is in the downstream area, and no clear indication of embedded rock blocks is obtained along the other MASW profiles in the reservoir area. The NE-SW trending normal fault dipping north which is forming the Kayacık valley was clearly identified in Profile-3 (Appendix-4).

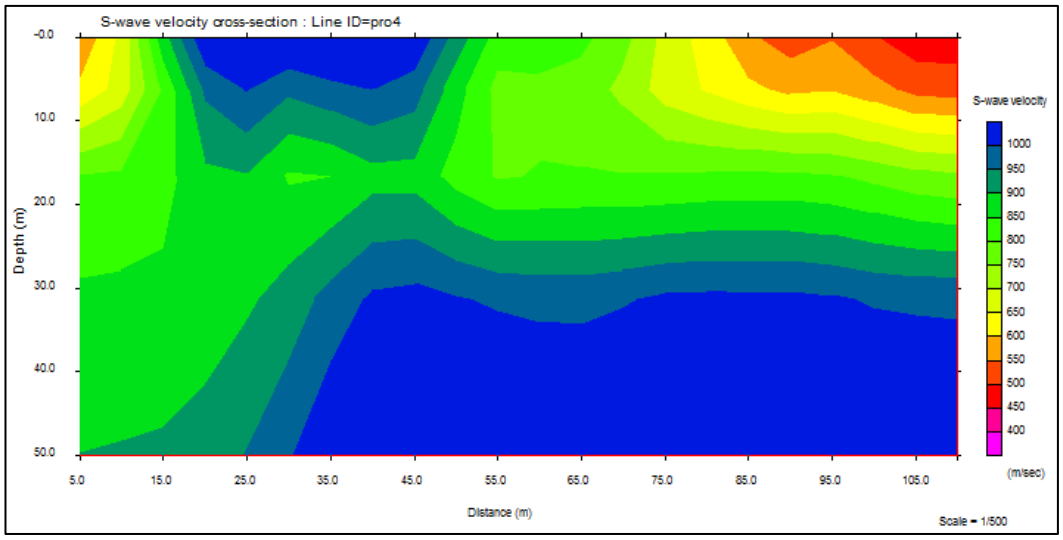


Figure 4.21 S-wave versus depth model of Profile 4

On the other hand, several rock blocks were encountered in the stream bed during the field studies on the toe of the pre-failed slopes, as well. The materials transported and deposited by the landslide range from gravel to several meter-sized blocks of limestone at the toe of Lanslide-3 (Figure 4.22).



Figure 4.22 Rock blocks moved into the stream bed after the mass movements (in front of Landslide-3) (Personal archive, 2015)

The V_s profiles obtained from six profiles were compared with the geological units intersected along two boreholes (BH-11, BH-36). BH-36 is located near the intersection of two normal faults trending in E-W and NW-SE directions. As a consequence, highly fractured breccia and karstic limestone with clay filling, highly fractured, and slightly weathered limestone units were intersected in the following depths. The thickness of heavily fractured conglomerate, sandstone, siltstone, and limestone intercalation was encountered below the alluvium is 6.2 m. Very poor core recovery was acquired in this heavily fractured zone. In BH-11, mainly disintegrated and highly fractured, slightly to moderately weathered limestone of Neogene unit was intersected along the depths between 6 m and 19 m. Core recovery of the limestone was generally 100%. Paleozoic aged calcschist (belonging to the Menderes Massif) was intersected at the last 1 m of drilling (Figure 4.23).

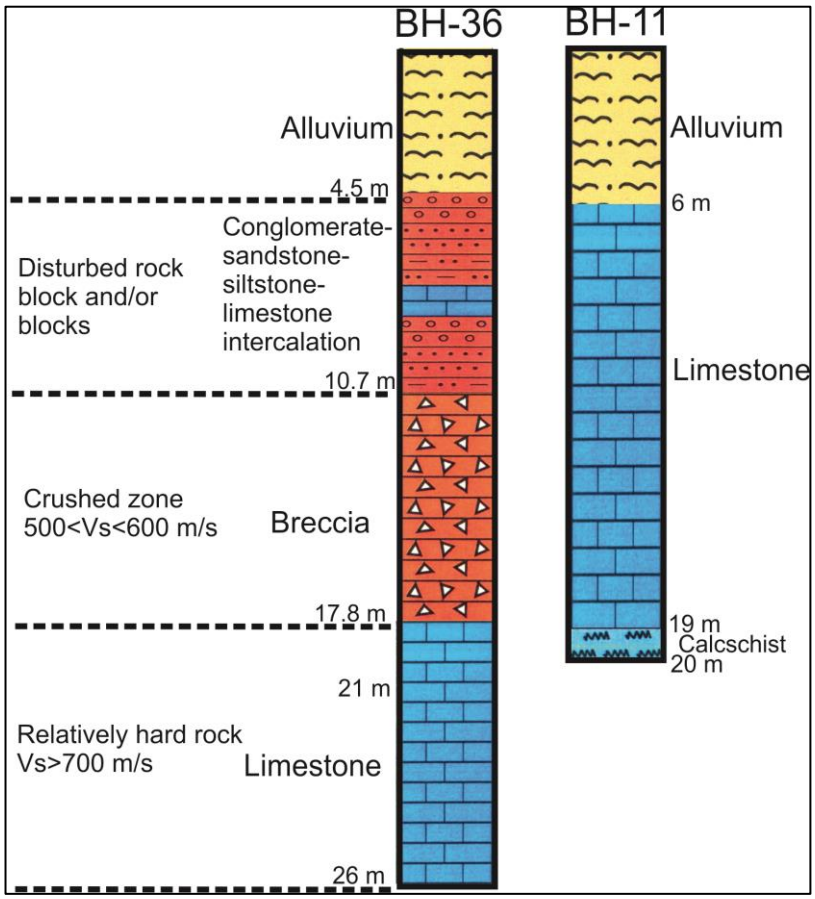


Figure 4.23 Sub-surface profiles of boreholes BH-11 and BH-36

Afterward, V_s-depth model was graphed for six profiles to investigate the V_s-depth changes in a 2D cross-section. For longer profiles (1, 4, and 5) the research depth is 50 m, but it is 35 m for Profiles 2, 3, and 6 which have shorter profile length (Figure 4.24).

The seismic profiles were sub-divided into four zones regarding the V_s values (Figure 4.24). The V_s values of 400-1200 m/s at deeper levels are well matching with the borehole logs and local geological units consisting of Neogene aged conglomerate, sandstone, siltstone, and limestone intercalations. The highly heterogeneous rock units are the reason for deriving a wide variety of seismic velocities. Following the depth of 30 m, more homogeneous, moderately fractured Paleozoic rocks (metamorphic basement) were verified.

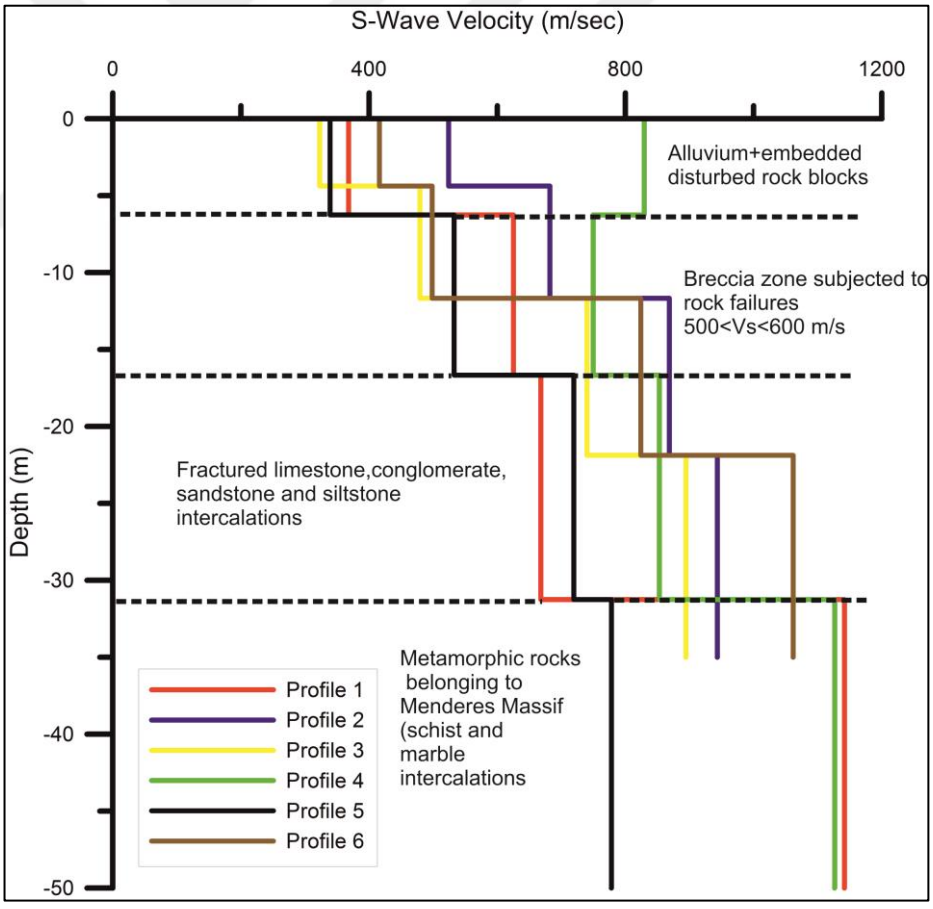


Figure 4.24 V_s-depth model at the midpoint of the profiles obtained using MASW method

The weighted average of P-wave velocity ($V_{p\text{-in-situ}}$) and also S-wave velocity ($V_{s\text{-in-situ}}$) values of each differentiated zone were calculated. The weighted average velocity values of the four zones (I, II, III, IV) beneath the 6 seismic refraction profiles were calculated by Equation 4.17.

$$V_s \text{ (zone-I)} = \frac{\sum_{i=1}^{i=6} Hi}{\sum_{i=1}^{i=6} \frac{Hi}{Vsi}} \quad (4.17)$$

where H is the thickness of the differentiated zone in the profile, and V_s (zone) is the S-wave velocity of the relevant zone in the profile. The same formula was also applied for calculating the average weighted V_p, and the results are given in Table 4.13.

Table 4.13 The average weighted P and S-wave velocities for six MASW profiles

Zone	$V_{p\text{-in-situ}}$ (m/s)	$V_{s\text{-in-situ}}$ (m/s)
(I) Alluvium+ Disintegrated rock zone	1686.0	363.0
	1624.0	524.0
	1620.0	322.5
	1709.0	500.0
	1683.0	483.0
	1726.0	416.5
Average weighted value	1690.0	450.0
(II) Heavily fractured rock+breccia zone subjected to rock failures	2113.0	620.0
	1676.0	680.0
	1820.0	480.0
	1954.0	747.0
	1900.0	533.0
	1804.0	500.0
Average weighted value	1890.0	590.0
(III) Heavily fractured limestone, conglomerate, sandstone, and mudstone intercalations	2000.0	663.0
	1868.0	858.0
	2040.0	740.0
	2318.0	854.0
	2073.0	720.0
	1673.0	823.5
Average weighted value	1990.0	760.0
(IV) Metamorphic rocks belonging to Menderes Massif (schist and marble intercalations)	2318.0	1141.0
	2204.0	941.0
	2280.0	890.0
	2432.0	1127.0
	2100.0	775.0
	2313.0	1061.0
Average weighted value	2270.0	970.0

It is seen from Table 4.13 that both $V_{p\text{-}in\text{-}situ}$ and $V_{s\text{-}in\text{-}situ}$ increase towards the stronger rock (metamorphic rocks). It can also be inferred from Table 4.13 that the ultrasonic wave velocities are increasing as the depth increases.

In order to estimate the dynamic geotechnical parameters of the rock mass, seismic wave velocities derived from geophysical methods are widely used. The dynamic geotechnical parameters of rock mass such as density (γ), modulus of elasticity (E), shear modulus (G), Poisson's ratio (υ), were calculated from the $V_{p\text{-}in\text{-}situ}$ and $V_{s\text{-}in\text{-}situ}$. The above-mentioned parameters of the rock mass, which are essential inputs in numerical slope stability analyses were calculated with the aid of equations proposed by Bowles (1988). However, it should be taken into account that the dynamic elastic constants derived from the seismic wave velocities are commonly higher than the in-situ measured deformation modulus values from pressuremeter, dilatometer, and plate loading tests (Table 4.14).

$$E_{in\text{-}situ} = \gamma V_s^2 \left[(3V_p^2 - 4 V_s^2)/ (V_p^2 - V_s^2) \right] \quad (4.18)$$

$$\upsilon_{in\text{-}situ} = (V_p^2 - 2 V_s^2)/ 2(V_p^2 - V_s^2) \quad (4.19)$$

$$G_{in\text{-}situ} = \gamma V_s^2 \quad (4.20)$$

$$\gamma_{in\text{-}situ} = 0.44 V_s^{0.25} \quad (4.21)$$

Table 4.14 The dynamic geotechnical parameters of the four rock mass zone in the dam site

$\gamma_{in\text{-}situ}$ (kN/m^3)	$E_{in\text{-}situ}$ (GPa)	$G_{in\text{-}situ}$ (GPa)	$\upsilon_{in\text{-}situ}$	Zone
19.91	1.22	0.42	0.46	(I) Alluvium+ Disintegrated rock zone
21.19	2.15	0.74	0.45	(II) Heavily fractured rock+breccia zone subjected to rock failures
22.66	3.82	1.35	0.41	(III) Heavily fractured limestone, conglomerate, sandstone, and mudstone intercalations
24.13	6.45	2.32	0.39	(IV) Metamorphic rocks belonging to Menderes Massif (schist and marble intercalations)

4.4.2 Electrical Resistivity Tomography Method

Electrical resistivity (or conductivity), which is an easy geophysical parameter to measure in the field, exhibits a wide range of values in nature, from 1 ohm.m in clay or contaminated soil to more than 104 ohm.m in rocks like limestone or granite (Reynolds, 1997). Recent developments in data acquisition allowed interpretation of the data in the form of electrical resistivity tomography (ERT) with multi-electrode resistivity equipment (Göktürkler, Balkaya, Erhan, & Yurdakul, 2008). Electrical resistivity tomography has various applications in landslide studies, groundwater explorations, investigations in waste disposal areas, defining physical properties of soil, and detection of faults (Steeples, 2001). Heavily fractured zones can be clearly identified by this method.

The resistivity distribution of the subsurface may help to identify structural features, fluid content, and sub-surface fluid movement (Göktürkler et al., 2008). The main components of the system are a multicore cable, a switching unit, and a resistivity meter (Griffiths & Barker, 1993). The method is based on recording the electrical potential difference between two certain electrodes generated by current injected utilizing the other two certain electrodes.

Two-dimensional electrical imaging surveys were performed along three profiles (Profiles 1, 2, and 3) in the different sections of the study area. The profiles are located both on the upstream and downstream areas and overlapping with the MASW profiles (Figure 4.20).

Two multicore cables which having 30 take-outs, a manual switching unit, and a resistivity meter. The profile lengths were variable. P1 profile was about 140 m, P2 profile was about 84 m, and P3 was about 112 m. Data acquisition was performed by a Wenner–Schlumberger array using a 29-electrode cable with changing (5 m for P1, 3 m for P2, and 4 m for P3) electrode spacing.

The measured apparent resistivity data were inverted using the smoothness-constrained least-squares inversion method of the Res2Dinv software (Loke & Barker, 1996). This method attempts to find the subsurface resistivity by trying to fit the measured and calculated data iteratively. The Jacobian matrix was recalculated for all the iteration steps, and a homogeneous half-space, which is derived from the average value of the apparent resistivities, was used for the initial model.

Electrical resistivity values mainly depend on water saturation, whereas the degree of water saturation of geological units has almost no effect on the V_s. Therefore, ERT was used to define the water table level. The groundwater levels in the drill holes BH-11, BH-18, BH-34, and BH-35 are 17.9 m, 30.65 m, 9.90 m, 9.8 m, and 11.45 m, respectively. These are well correlated with the estimated groundwater levels from the ERT method (Figure 4.25).

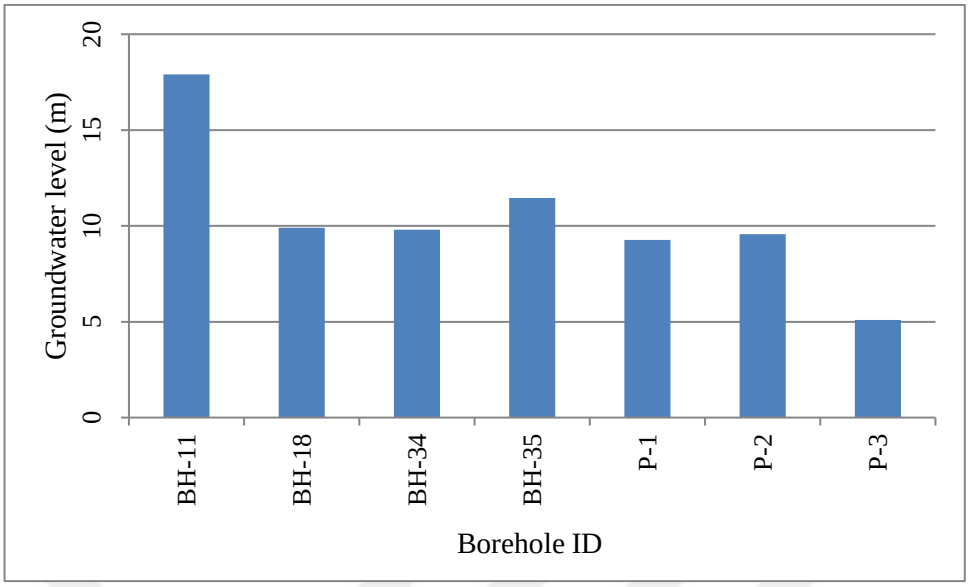


Figure 4.25 Groundwater levels defined in the boreholes and the ERT profiles

According to the obtained resistive tomography results, there is a very low-resistivity layer after about 5-10 m depth for three profiles. It can be said that the water content of this layer is high, and the water table level is taking place after these depths. As the varying water table level, the faulted/disturbed rock mass, and the presence of karstic gaps are considered, it can be interpreted that the stream may discharge along the fault zones and karstic gaps. According to the ERT results, the resistivity values of P1 and P3 profiles are changing in the vertical direction, and the geological units are horizontally layered. On the contrary, lateral changes are observed around 50 meters on the P2 profile which coincides with the MASW Profile 4. In this profile, the upper layers are sharply interrupted by a relatively low resistivity body (Figure 4.26b). It can be assumed that high-resistivity rock blocks embedded in alluvium that was also detected in MASW results.

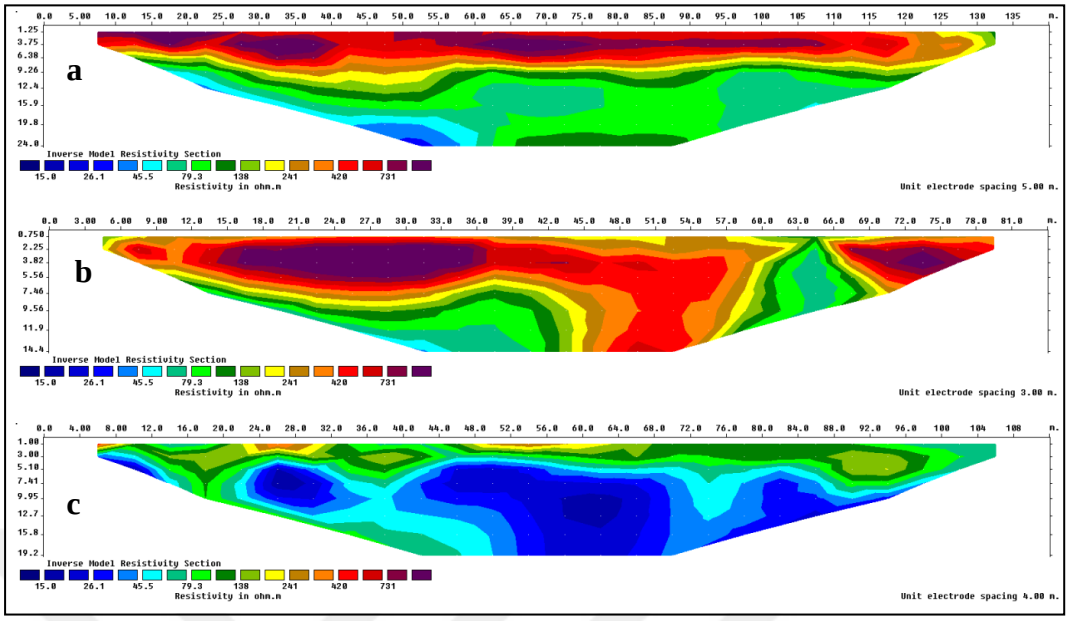


Figure 4.26 Electrical resistivity tomography results for a. P1 profile, b. P2 profile, c. P3 profile

CHAPTER FIVE
LABORATORY TESTS

The laboratory tests carried out on intact rock specimens were discussed in this chapter. In addition to the in-situ data measured on rock mass; the physical, index, mechanical, and deformation properties of intact rock can serve as a base for performing slope stability analyses. Core and prismatic samples were extracted from the blocks collected from the field. The standards for laboratory tests employed on these rock specimens are summarized in Table 5.1. The laboratory test results are given in Appendix-5.

Table 5.1 The standards followed in laboratory tests and the number of samples subjected to these tests

Laboratory Test		Number of samples (N)	Standard
Physical properties (unit weight, porosity, etc.)		208	ISRM (2007)
Uniaxial compressive strength (static)		72	ASTM D7012-14e1 (2014)
Uniaxial compressive strength (dynamic)		5	-
Point Load		67	ISRM (2007)
Brazilian		63	ISRM (2007)
Shear box (static)		3	ASTM D5607-16 (2016)
Shear box (dynamic)		3	-
Uniaxial creep		1	ASTM D7070-16 (2016)
Triaxial (dynamic)		2	-
Ultrasonic pulse velocity	P-wave velocity	196	ISRM (2007)
	S-wave velocity	91	ISRM (2007)
Schmidt hammer		17	ISRM (2007)

5.1 Physical Properties

Effective porosity (n), water absorption by weight (S_w), and unit weight (γ) of specimens were calculated by using saturation and buoyancy techniques (Table 5.2). The core samples were saturated by immersing the sample in distilled water at approximately 22 °C until the sample reaches a stable weight. Yavuz & Topal (2007, 2016) suggested that drying the specimens at 60 °C is ideal for calcite bearing rocks due to anisotropic thermal expansion and contraction of calcite minerals. For this reason, the drying process was performed in the oven under 65 °C and then allowed to cool for 40 minutes in the desiccator.

Table 5.2 The descriptive statistics of effective unit weight (γ), effective porosity (n), water absorption by weight (S_w) of the specimens

Rock Group		SK	KÇ	ÇK	KKÇ	M	BK	K	Ç
Formation		Yeniköy Fm.					Göcek Fm.		
n (%)	Mean	6.43	5.09	6.60	25.02	9.82	7.44	5.83	5.82
	SD (±)	2.93	1.26	3.27	1.31	3.41	6.82	2.30	2.45
	Min	3.43	2.06	2.17	23.21	3.85	1.39	2.25	1.62
	Max	11.69	6.89	12.73	27.01	16.19	19.44	8.74	9.26
γ_{dry} (kN/m^3)	Mean	24.29	24.93	24.98	19.79	21.55	23.02	24.29	24.87
	SD (±)	1.10	0.24	1.02	0.40	0.97	1.65	1.45	1.41
	Min	22.38	24.42	22.99	19.19	19.95	19.60	21.76	23.09
	Max	25.42	25.29	26.46	20.56	23.35	24.73	26.36	27.09
γ_{sat} (kN/m^3)	Mean	24.92	25.43	25.63	22.24	22.41	23.75	25.58	25.44
	SD (±)	0.82	0.22	0.72	0.31	0.64	1.65	0.63	1.18
	Min	23.53	25.02	24.16	21.84	21.36	21.50	24.81	23.94
	Max	25.77	25.75	26.67	22.84	23.45	24.92	26.58	27.25
S_w (%)	Mean	2.65	2.01	2.64	12.42	4.56	3.39	2.32	2.35
	SD (±)	1.33	0.51	1.39	0.87	1.69	0.17	0.97	1.09
	Min	1.32	0.81	0.80	11.07	1.65	0.56	0.84	0.59
	Max	5.13	2.74	5.31	13.81	7.49	9.71	3.53	3.85
N		19	30	37	10	47	27	19	19

The values of n (%) and γ (kN/m^3) were classified according to the classification of Anon (1979) as medium to high porosity and low to high-density rocks, respectively.

5.2 Static Strength and Deformation Tests

In-situ measurements of rock properties are desirable for practical rock mechanics; however, field tests commonly require high costs (Rahn, 1996). For this reason, laboratory tests on intact rock samples, which are assumed to be free from fractures, are used to measure the compressive, tensile, and shear strength as well as deformation (elastic and shear modulus, Poisson's ratio, stiffness, etc.) and time-dependent properties (creep). In this context, static uniaxial compression, direct shear box, and creep tests were performed. Index tests such as sonic velocity, point load, Schmidt hammer, and Brazilian tests were used for the classification of rock material and estimation of strength and elastic properties.

5.2.1 Sonic Velocity Test

Ultrasonic non-destructive testing of core rock samples is practical and time-saving in providing a preliminary estimation of the physical properties, strength, and deformability of rock samples.

P-wave velocity (V_p) depends on the elastic properties of the rock material (Goodman, 1989) as well as its mineralogical composition, unit weight, porosity, microfractures, strength; and weathering (Guyader & Denis, 1986; Kossev, 1970). In brief, it can be said that the ultrasonic velocity is governed by the mineral composition, density, porosity, elasticity, and degree of fracturing within a rock (Mavko, Mukerji, & Dvorkin, 2003; Kahraman & Yeken, 2008; Yang, Duan, & Zhu, 2019).

Many researchers have used ultrasonic wave velocities to obtain dynamic elastic properties of rock (Deere & Miller, 1966), microcrack intensity (King, 1983; Kuster

& Toksöz, 1974; Toksöz, Cheng, & Timur, 1976), to estimate rock grout efficiency (Türk & Dearman, 1987), strength and deformability of rock mass (Gladwin, 1982; Onodera, 1963), weathering grade (Karpuz & Paşamehmetoğlu, 1997), rock mass characterization (Türk & Dearman, 1986; Boadu, 1997), rock quality index and fissurity classification (Fourmaintraux, 1976; Goodman, 1989). On the other hand, many factors are influencing the ultrasonic wave velocities which can be categorized as internal and external factors (Türk & Dearman, 1987). External factors include porewater, water content, compressive and confining pressure, temperature, sample size, and pore fluid properties (Gregory, 1976; Lama & Vutukuri, 1978). Internal factors mentioned above can be summarized as; rock type and related mineralogy, grain size and shape, density, porosity, weathering, anisotropy, micro and macro cracks (Kahraman, 2001; Yaşar & Erdoğan, 2004; Sharma & Singh, 2008). It should be noted that ultrasonic wave velocities do not depend on all the above-mentioned factors individually; some of these factors interact with each other. For this reason, correlations between these factors and ultrasonic wave velocities can be poor. In that case, the effect of more than one factor should be examined.

Karaman, Cihangir, Ercikdi, & Kesimal (2010) suggested the length to diameter ratio for the ultrasonic wave velocity test to be between 1.1 and 2 for clayey limestones. Furthermore, Karaman, Kaya, & Kesimal (2015) determined that the threshold core length for dry and saturated V_p measurement as 109 mm for limestone samples. On the other hand, Ercikdi et al. (2016) suggested that a core length of 75 mm can be interpreted as the optimum core sample length for the dry and saturated V_p test. In accordance, 54 mm-diameter core samples were extracted in the laboratory from the rock blocks that are collected from the field. The V_p and V_s were measured on 184, and 91 cylindrical core specimens under dry and fully water-saturated conditions, respectively. Pundit Lab ultrasonic instrument was used to determine the V_p, however, V_s was measured by the Proceq Pundit PL-200 instrument (Figure 5.1). In order to provide better transmission between the transmitter and receiver, a standard ultrasound coupling gel and S-wave couplant were used for V_p and V_s measurements, respectively. The sample lengths are in the range between 26 mm and 110 mm and satisfying the ISRM (2007) standard for the

ultrasonic test. The end surfaces of core rock samples were smoothened to provide good coupling during ultrasonic tests. The samples which do not have any macroscopic fractures and cracks were chosen to eliminate their effect on ultrasonic wave transmission. The clastic rock samples have grain sizes in the range of clay to coarse sand except for the sample types Ç and ÇK, which have a maximum grain size of 5 mm and 10 mm, respectively, which are also consistent with the ISRM (2007) standard.

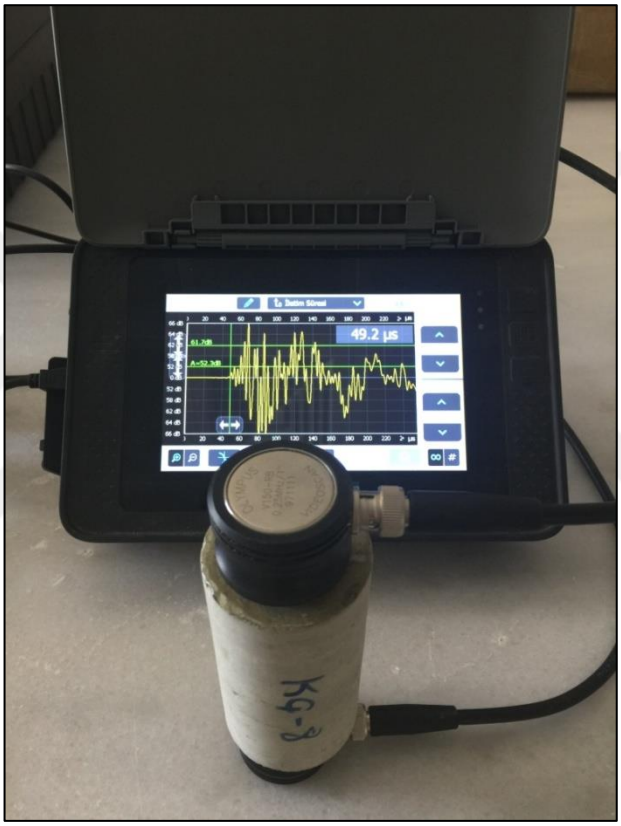


Figure 5.1 S-wave velocities were measured by Proceq Pundit PL-200 instrument (Personal archive, 2018)

Türk & Dearman (1987) and Vasconcelos, Lourenço, Alves, & Pamplona (2008) observed that the effect of pulse frequency on the ultrasonic wave velocities is less significant than the other factors such as physical, mechanical, elastic properties of the rock and environmental conditions. In this study, sinusoidal P and S waves were transmitted with frequencies of 200 and 250 kHz, respectively. These frequencies are corresponding to a wavelength of about 1.5 mm and 1.2 mm, respectively.

Consequently, the minimum diameter of the specimen (15 mm and 12 mm) suggested by ISRM (2007) was satisfied.

In addition, as the heterogeneity of the rock samples influences the propagation of the ultrasonic wave, to reduce scattering and poorly defined first arrivals at the receiver, the transmitter was designed to generate wavelengths higher than the average grain size of the rock (ISRM 2007). Particularly for pebbly sandstones and conglomerates, lower frequencies (54 kHz) were also used. Approximately 10 N/cm^2 stress was applied on the end surfaces of the specimen by compressing with hand even for S-wave velocity measurement since the shear wave transducers (Olympus V150-RB Videoscan) do not require any additional load. Moreover, no further stress is required for the samples taken from the ground surface. The waveform that is transmitted through the specimen can be observed on the instrument or the pc linked to the Pundit device. The S- wave first arrivals were manually triggered. Ultrasonic wave velocities are then calculated by dividing the path length by the time required for the pulse to pass through the specimen.

The ultrasonic wave velocities under dry ($V_{p\text{-}dry}$, $V_{s\text{-}dry}$) and saturated ($V_{p\text{-}sat}$, $V_{s\text{-}sat}$) conditions were firstly examined based on sample length (Figures 5.2, 5.3, 5.4, and 5.5).

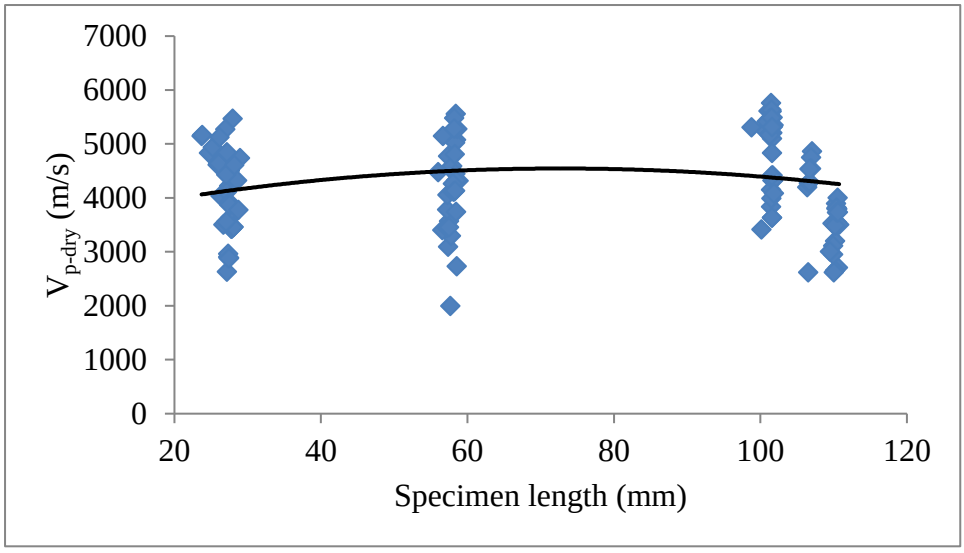


Figure 5.2 The variations of $V_{p\text{-}dry}$ with various specimen lengths

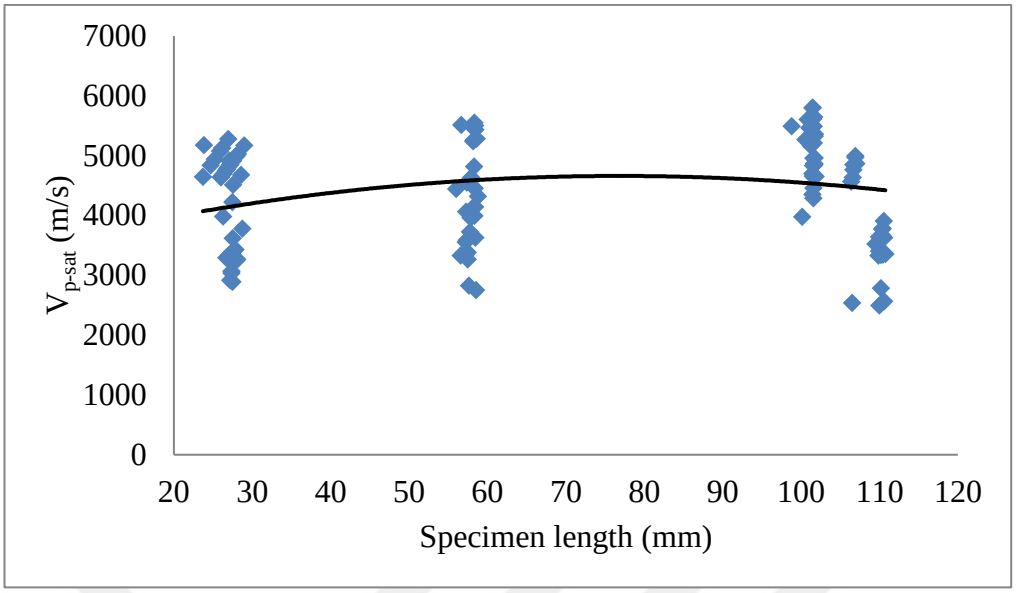


Figure 5.3 The variations of $V_{p\text{-}sat}$ with various specimen lengths

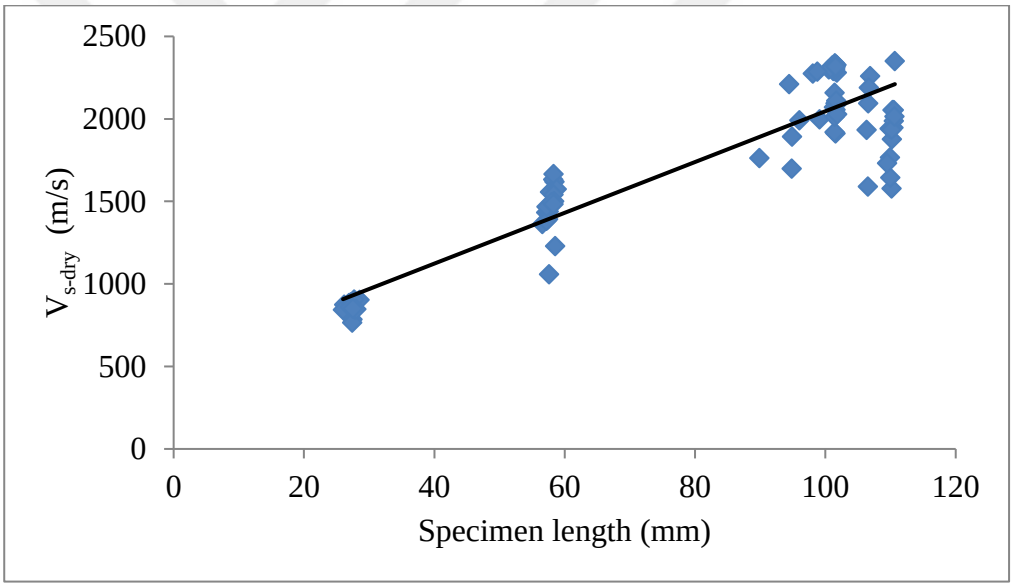


Figure 5.4 The variations of $V_{s\text{-}dry}$ with various specimen lengths

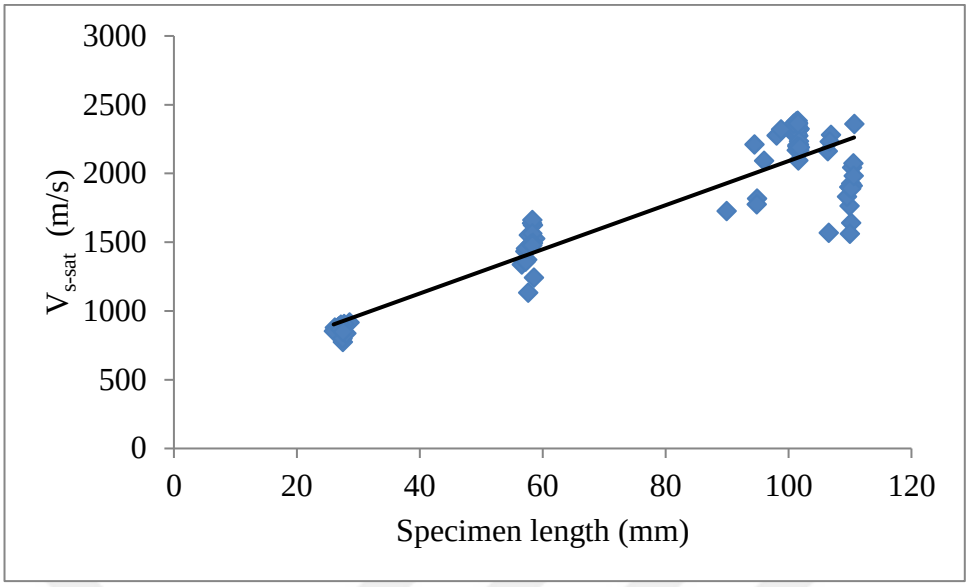


Figure 5.5 The variations of V_{s-sat} with various specimen lengths

It is obvious from Figure 5.2 and Figure 5.3 that V_p is not significantly affected by sample length, whereas there is a polynomial relationship between sample length and V_p. On the other hand, V_s is much more affected by the specimen length (Figure 5.4 and Figure 5.5). V_s significantly decreases as the specimen length is shorter than 57 mm, and thus enormous V_p/V_s ratio is derived, which is also unusual. As a result, the samples having a length of 94 mm and higher (53 samples out of 91) were considered for the evaluation of V_s values. Accordingly, basic statistics (mean, minimum, maximum, and standard deviation) of the V_p and V_s of 53 specimens were taken into consideration for further analyses (Table 5.3).

The highest standard deviation in ultrasonic wave velocities was observed in pebbly specimens as expected. The scattering regimes of ultrasonic waves for these specimens are mainly dominated by grains of extraordinarily large size along the wave propagation path.

Table 5.3 The descriptive statistics of V_p and V_s of studied rocks

Rock Group		SK	KÇ	ÇK	KKÇ	M	BK	K	Ç
Formation		Yeniköy Fm					Göcek Fm		
$V_{p\text{-}dry}$ (km/s)	Mean	5.21	4.78	3.73	2.63	3.62	5.07	5.17	4.60
	SD	0.070	0.050	0.056	0.021	0.013	0.064	0.051	0.037
	Min	5.10	4.20	2.95	2.62	3.48	3.89	4.23	4.22
	Max	5.32	5.47	4.42	2.66	3.79	5.61	5.63	4.92
$V_{p\text{-}sat}$ (km/s)	Mean	5.27	4.95	4.25	2.60	3.45	5.06	5.33	4.91
	SD	0.064	0.031	0.058	0.015	0.015	0.070	0.054	0.025
	Min	5.16	4.56	3.40	2.49	3.32	3.76	4.44	4.66
	Max	5.33	5.44	4.86	2.78	3.62	5.61	5.79	5.19
$V_{s\text{-}dry}$ (km/s)	Mean	2.27	2.14	1.93	1.60	1.96	2.25	2.23	2.16
	SD	0.080	0.012	0.013	0.035	0.033	0.011	0.014	0.012
	Min	2.09	1.93	1.73	1.57	1.93	2.05	1.99	2.07
	Max	2.32	2.27	2.10	1.64	2.01	2.32	2.33	2.34
$V_{s\text{-}sat}$ (km/s)	Mean	2.29	2.22	2.04	1.58	1.92	2.27	2.28	2.22
	SD	0.016	0.046	0.018	0.043	0.037	0.012	0.013	0.090
	Min	2.27	2.16	1.76	1.56	1.88	2.04	2.04	2.16
	Max	2.31	2.27	2.23	1.63	1.92	2.34	2.38	2.35
N		7	7	10	3	5	9	8	4

Furthermore, the dynamic Young's modulus ($E_{i\text{-}dyn}$) and shear modulus ($G_{i\text{-}dyn}$) and dynamic Poisson's ratio (ν_{dyn}) of the rock specimens were calculated by the Equations 4.18, 4.19, and 4.20 given in Chapter 4 based on laboratory-measured V_p, V_s, and γ (Table 5.4).

It should be noted that the $E_{i\text{-}dyn}$ is generally higher than the elastic modulus values obtained from the stress-strain loading curve because of the presence of small cracks that affect stress-strain loading curves more than seismic measurements (Kuster & Toksöz, 1974; Toksöz et al., 1976; King, 1983; Rahn, 1996). On the other hand, seismic velocities are more sensitive to mineralogical content, such as slight variations in the composition cause drastic changes in the seismic velocities (Tandon & Gupta, 2015).

It was determined that the laboratory-measured V_p and V_s values are 2.61 and 3.29 times higher than the in-situ-measured values, respectively. This comparison was made by considering the average in-situ velocities for Zone II and III identified in MASW analyses. The velocities of specimens that were chosen as representing Zone II and Zone III were compared with the average in-situ velocities for these zones.

Table 5.4 The descriptive statistics of empirically calculated dynamic elastic properties of the studied rock specimens for dry and saturated conditions

Rock Group		SK	KÇ	ÇK	KKÇ	M	BK	K	Ç
Formation		Yeniköy Fm.					Göcek Fm.		
$E_{i\text{-}dyn\text{-}dry}$ (GPa)	Mean	36.75	32.06	25.98	12.54	21.36	32.95	36.18	33.08
	SD	2.45	3.92	5.01	0.50	1.01	6.02	5.72	2.50
	Min	31.33	25.57	19.05	11.95	20.51	22.09	26.92	30.98
	Max	38.48	36.77	32.35	12.83	22.62	37.26	39.90	36.25
$E_{i\text{-}dyn\text{-}sat}$ (GPa)	Mean	38.07	34.96	30.22	13.81	21.24	34.25	38.55	35.89
	SD	5.91	1.60	6.08	1.40	1.32	5.68	5.49	1.53
	Min	37.13	32.58	21.24	12.97	20.22	23.67	29.22	34.56
	Max	38.73	37.08	36.93	15.44	22.96	38.10	42.50	38.02
$G_{i\text{-}dyn\text{-}dry}$ (GPa)	Mean	13.30	11.69	9.90	5.20	8.27	11.97	13.05	12.19
	SD	9.49	1.38	1.57	0.25	0.32	1.96	1.98	0.87
	Min	11.20	9.36	7.61	4.94	8.00	8.44	9.76	11.52
	Max	13.92	13.17	11.96	5.45	8.73	13.34	14.35	13.40
$G_{i\text{-}dyn\text{-}sat}$ (GPa)	Mean	13.76	12.73	11.20	5.74	8.34	12.48	13.89	13.09
	SD	2.15	0.521	2.11	0.44	0.41	1.78	1.86	0.53
	Min	13.4	12.02	8.07	5.47	8.02	9.16	10.69	12.68
	Max	14.01	13.52	13.53	6.25	8.92	13.65	15.29	13.87
$\nu_{i\text{-}dyn\text{-}dry}$ (GPa)	Mean	0.38	0.37	0.30	0.21	0.29	0.37	0.38	0.36
	SD	0.01	0.02	0.05	0.03	0.01	0.03	0.01	0.02
	Min	0.37	0.34	0.22	0.18	0.28	0.31	0.36	0.34
	Max	0.40	0.40	0.35	0.23	0.31	0.40	0.40	0.38
$\nu_{i\text{-}dyn\text{-}sat}$ (GPa)	Mean	0.38	0.37	0.35	0.20	0.27	0.37	0.39	0.37
	SD	0.00	0.02	0.03	0.03	0.02	0.04	0.01	0.01
	Min	0.38	0.35	0.31	0.18	0.26	0.29	0.36	0.36
	Max	0.39	0.39	0.38	0.23	0.30	0.39	0.40	0.38
N		7	7	10	3	5	9	8	4

5.2.2 Schmidt Hammer Test

The instructions for measuring the Schmidt hammer value and calculating the corresponding JCS value were discussed in detail in Chapter 4. Therefore, this information will not be given in this chapter.

Schmidt hammer test was employed on the intact rock samples having 20x10x10 cm dimensions, smooth and fresh surfaces in the laboratory. The measured Schmidt rebound values and corresponding uniaxial compressive strength of the rock are given in Table 5.5. It should be kept in mind that the Schmidt hammer is not a satisfactory method for the determination of very soft or very hard rocks.

The studied samples have moderate strength according to the classification suggested by Anon (1981) except the samples Ç-21, KÇ-27, and M-5.

Table 5.5 Schmidt hammer rebound values and the corresponding JCS values of the 20x10x10 cm samples

Formation	Rock ID	Position of hammer	Mean R	Unit weight (kN/m^3)	$JCS_{(lab)}$ (MPa)
Göcek Formation	K-7	1	40.7	24.33	76.10
	K-8	1	41.4	24.53	80.07
	K-9	1	45.2	24.13	93.30
	K-10	1	36.8	24.33	62.79
	K-11	1	39.4	24.43	71.93
	Ç-20	1	33.3	24.82	54.61
	Ç-21	1	23.5	24.82	33.36
Yeniköy Formation	ÇK-33	1	43.9	24.62	91.46
	ÇK-34	1	44.3	24.43	91.68
	ÇK-35	1	39	24.43	70.52
	SK-20	1	38.5	24.33	68.27
	KÇ-27	1	26.1	24.82	38.02
	M-1	1	40.3	23.39	69.10
	M-2	1	47.1	20.58	72.95
	M-3	1	45	20.29	65.09
	M-4	1	45.2	20.36	66.04
	M-5	1	35.6	21.83	49.92

5.2.3 Brazilian Test

Several researchers found that the overall tensile strength is directly related to crack initiation and propagation, because the first cracking that occurs in intact rock is locally tensile in nature, even under globally compressive loading conditions (Murrell, 1963; Eberhardt, 1998; Diederichs, 2007).

The Brazilian test is a simple indirect testing method to obtain the tensile strength of brittle material such as concrete, rock, and rock-like materials (Li & Wong, 2013). The measurements were carried out as given in Figure 5.6 under flat loading platens, according to ISRM (2007). ISRM (2007) recommends that the specimen diameter should not be less than NX core size (54 mm diameter) and that the length should be approximately equal to the radius of the specimen. The length to diameter ratio of the rock specimens is approximately 0.5.

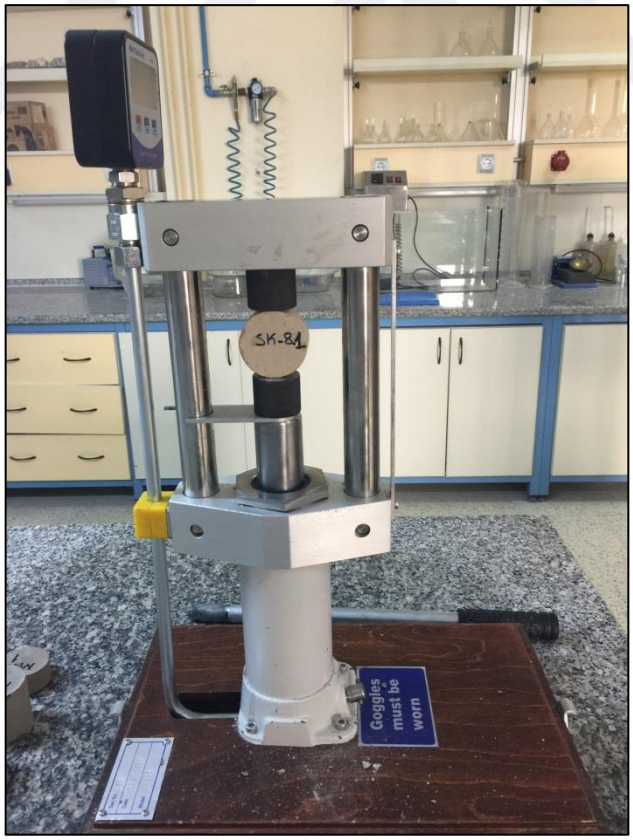


Figure 5.6 The apparatus for the Brazilian test (Personal archive, 2018)

The peak load at the time of failure was recorded from the digital loading gauge, and the tensile strength (σ_t) was calculated as proposed by ISRM (2007).

$$\sigma_t = \frac{0.636\ x\ P}{D\ x\ L} \tag{5.1}$$

where P is the peak load at the time of failure; D and L are the diameter and length of the specimen, respectively.

Due to the grain size variation in pebbly samples, even in the same rock group, the variations of porosity and composition lead to the high standard deviation in the tensile strength (σ_t) values (Table 5.6).

Table 5.6 The descriptive statistics of σ_t values of the studied rocks obtained from Brazilian test

Rock group		SK	KÇ	KKÇ	M	ÇK	BK	K	Ç
Formation		Yeniköy Fm.					Göcek Fm.		
σ_t (MPa)	Mean	8.40	2.65	0.86	3.05	2.83	2.05	1.84	3.84
	SD	1.84	1.05	0.37	2.32	2.34	0.82	0.53	2.06
	Min	4.83	0.95	0.36	0.40	0.80	0.89	1.16	1.52
	Max	10.57	4.33	1.24	4.34	7.92	3.16	2.62	7.59
N		7	12	6	8	10	7	6	7

Particularly, KÇ and SK rock groups exhibited “central multiple” failure mode, whereas the other samples generally showed a “central” failure type as also indicated by Basu, Mishra, & Roychowdhury (2013) (Figure 5.7).



Figure 5.7 The rock samples subjected to the Brazilian test (the first column is before and the second column is after the test) (Personal archive, 2018)

5.2.4 Point Load Test

The point load test was applied to classify the rocks which did not allow extracting core samples having appropriate length for uniaxial compression tests. The diametral point load test was performed on the rock specimens having a length (W) to diameter (D) ratio equal to approximately one (Figure 5.8a). On the other hand, the samples having a length to diameter ratio lower than one were subjected to the axial test as proposed by ISRM (2007) (Figure 5.8b).

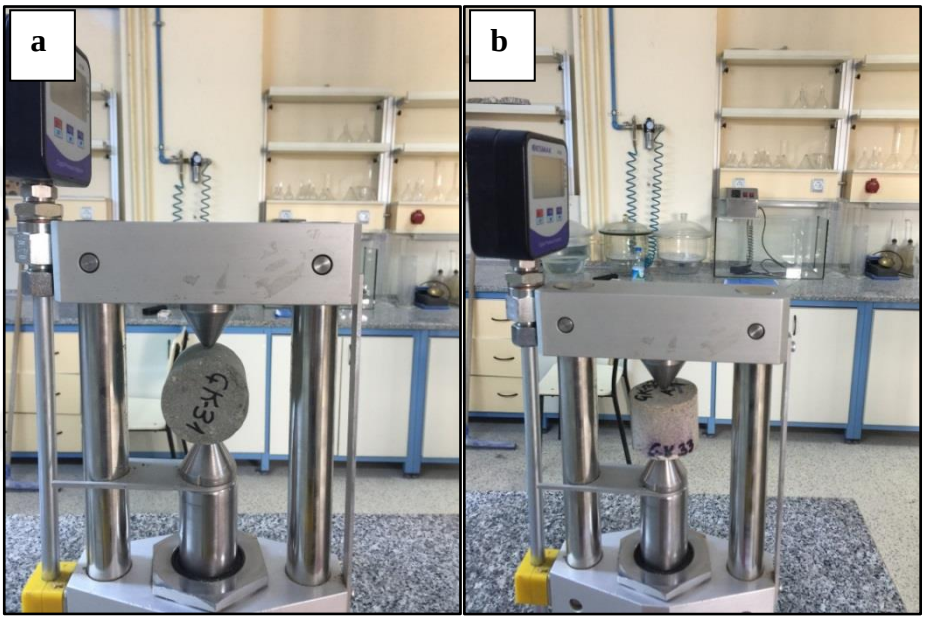


Figure 5.8 a. Diametral and b. Axial point load test (Personal archive, 2018)

The peak load (load at failure) was recorded from the digital loading gauge. After that, the point load index (I_s) values were calculated and corrected for 50 mm diameter ($I_{s(50)}$) by the equations given below and presented in Table 5.7.

$$I_s = P / De^2 \quad (5.2)$$

where P is the peak load at the time of failure; De is the equivalent core diameter of the specimen.

for diametral test, De is;

$$De^2 = De^2 \quad (5.3)$$

and for the axial test, De is;

$$De^2 = 4A/\pi \ (A= WxD) \quad (5.4)$$

where A is the minimum cross-sectional area of a plane through the platen contact points.

$$I_{s(50)} = I_s \times K \quad (5.5)$$

$$K=(De/50)^{0.45} \quad (5.6)$$

where K is the size correction factor.

Table 5.7 The descriptive statistics of $I_{s(50)}$ values for the studied rocks

Rock Group		SK	KÇ	M	ÇK	BK	K	Ç
Formation		Yeniköy Fm.				Göcek Fm.		
I_{s50} (MPa)	Mean	2.26	2.02	1.15	0.61	1.67	1.27	1.41
	SD	0.77	0.62	0.48	0.39	0.65	0.69	0.63
	Min	1.13	0.57	0.51	0.11	0.29	0.34	0.40
	Max	3.84	3.07	2.08	1.53	2.49	2.79	2.50
N		7	11	9	12	10	8	10

Table 5.7 indicates widely variable point load index values. Clay bearing biomicrite (SK) showed the highest $I_{s(50)}$ values (1.13-3.84 MPa) and the pebbly sandstones (ÇK) the lowest. The classification proposed by Broch & Franklin (1972) was used together with Anon (1981) to classify the strength of rock samples based on the mean $I_{s(50)}$ values. Accordingly, the studied samples were classified as low to high strength rocks.

The samples showed a failure surface along a single plane, which refers to a single extensional plane containing the line of loading under axial and diametral

loading, as previously indicated by Basu et al. (2013). The triple-junction type of failure plane, which represents a failure along three extensional planes (dihedral angle ≈120°) containing the line of loading was rarely observed (Figure 5.9).

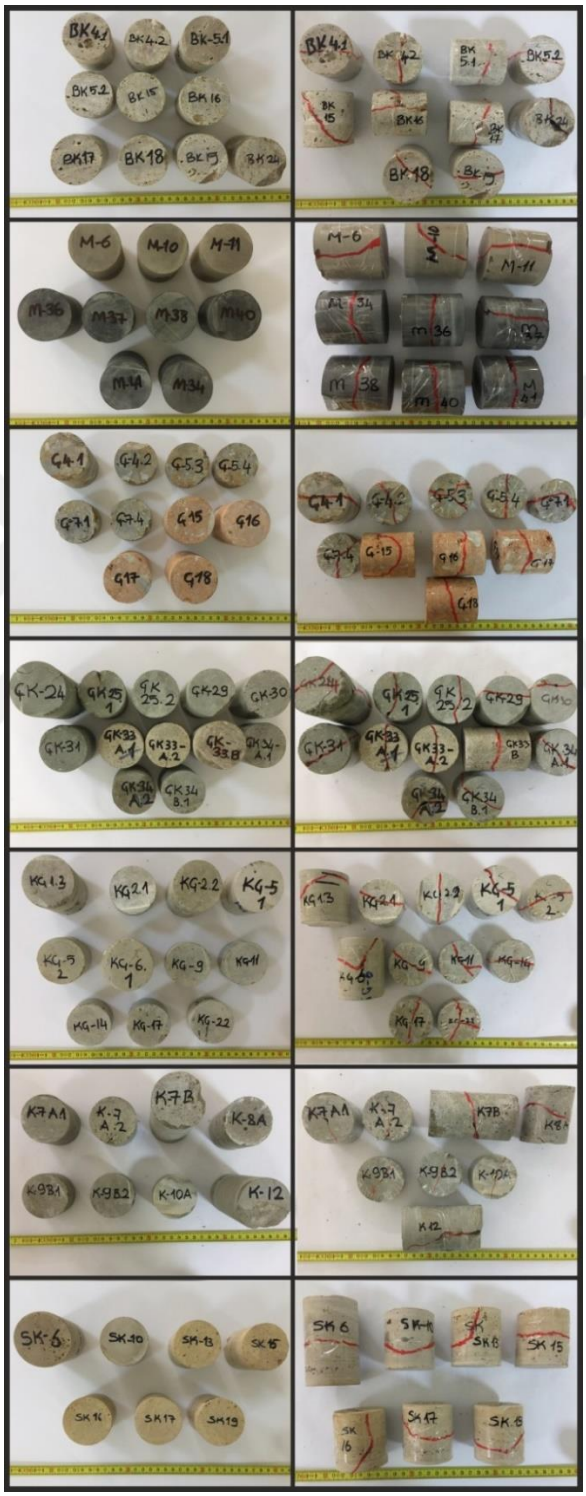


Figure 5.9 The rock samples subjected to point load test (the first column is before and the second column is after the test) (Personal archive, 2018)

5.2.5 Uniaxial Compressive Strength Test

Three uniaxial compressive strength tests were performed by the TIRA 28500 Test System illustrated in Figure 5.10a. The system can perform static and dynamic compression tests, has a compressive loading capacity of 500 kN, a piston stroke length of 1300 mm, and a maximum loading velocity of 100 mm/min. The external measuring system that consists of vertical and radial strain gauges is shown in Figure 5.10a. The deformation rate was applied as 0.05 mm/min. Uniaxial compressive strength (σ_{ci}), average elastic modulus (E_{avg}), and Poisson's ratio (υ_i) were obtained.

Thirty-five tests were performed with a closed-loop servo-controlled stiff testing machine of MTS System Corporation (Figure 5.10b). The device is capable of performing compression tests at a constant strain rate. The strain rate can be arranged with a span adjustment for a stroke motion and requiring time for the desired strain rate can be selected before testing. A linear variable displacement transducer (LVDT) was employed for the measurement of axial strain. The applied strain rate was 10^{-5} s^{-1} with a maximum allowed axial deformation of 3 mm. The σ_{ci} and E_{avg} were calculated.

Thirty-four tests were performed with the ELE ADR 2000 machine, which has an automatic hydraulic press having a maximum load limit of 200 tons (Figure 5.10c). The applied loading rate was 2 kN/s. Solely the σ_{ci} values were measured.

During the uniaxial compressive strength testing, ASTM D7012-14e1 (2014) standard was followed. It recommends the length to diameter ratio of the core specimen as higher than 2.0 and the diameter as at least 47 mm. The measured uniaxial compressive strength values were corrected for the specimens, which have a length to diameter ratio below 2.0 using the equation proposed by ASTM (1994).

$$\sigma_{ci} = \frac{\sigma_c}{0.88 + 0.24\,\frac{D}{L}} \tag{5.7}$$

where σ_c and σ_{ci} are measured and corrected uniaxial compressive strength values, respectively. The test results and corrected values can be found in Appendix-5.

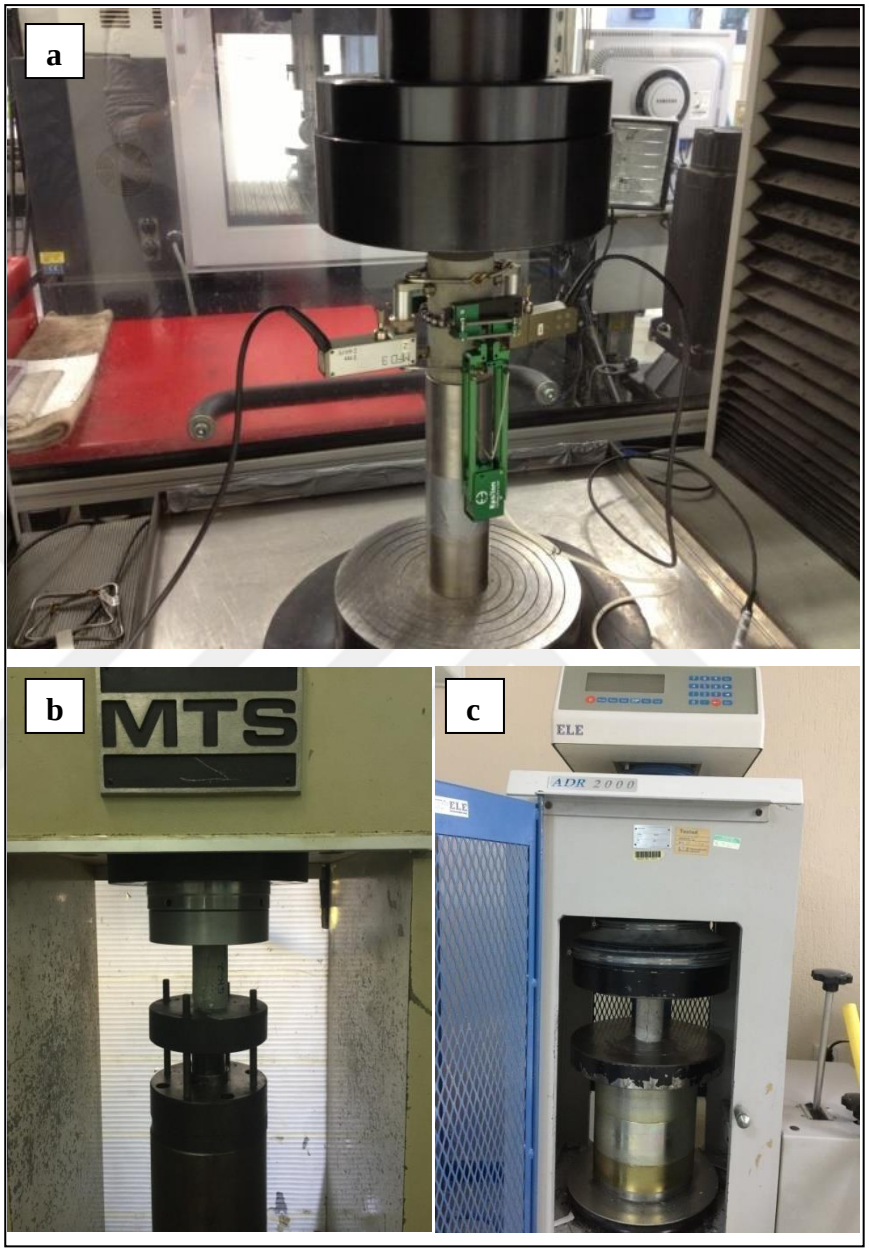


Figure 5.10 a. TIRA 28500 Test System b. MTS System Corporation c. ELE ADR 2000 (Personal archive, 2018)

The samples from Göcek Formation showed a variety of strength classes, such as from low to high rock strength. Similarly, the samples from Yeniköy Formation have a sizeable amount of standard deviation under dry conditions (Table 5.8).

Table 5.8 The descriptive statistics of σ_{ci}, $E_{avg,}$ and υ_i for the investigated rock samples under dry conditions

Rock Group		SK	KÇ	KKÇ	M	ÇK	BK	K	Ç
Formation		Yeniköy Fm.					Göcek Fm.		
σ_{ci} (MPa)	Mean	57.49					53.23		
	SD	27.63					38.77		
	Min	20.80					19.18		
	Max	117.02					146.56		
E_{avg} (MPa)	Mean	7132.54					8145.39		
	SD	3875.311					2773.659		
	Min	1726.56					4776.83		
	Max	14561.67					11299.67		
υ_i		0.34					0.28		
N		25					14		

As the dry and saturated strength and elastic properties are compared, it can be said that rock samples rapidly lose their strength and elasticity under saturated conditions (Table 5.9).

Table 5.9 The descriptive statistics of σ_{ci}, $E_{avg,}$ and υ_i for the investigated rock samples under saturated conditions

Rock Group		SK	KÇ	KKÇ	M	ÇK	BK	K	Ç
Formation		Yeniköy Fm.					Göcek Fm.		
σ_{ci} (MPa)	Mean	49.82					40.07		
	SD	34.52					24.38		
	Min	6.13					10.28		
	Max	133.73					105.37		
E_{avg} (MPa)	Mean	5715.83					5313.939		
	SD	4370.28					2991.364		
	Min	1180.18					591.48		
	Max	13754.5					10593.22		
υ_i		0.44					-		
N		18					15		

Stress-strain graphs of dry and saturated samples showed that the sandstone samples gained a ductile behavior. The higher the strength, the higher the brittle behavior is observed in the samples (Figure 5.11). The stress-strain graphs of the other samples are given in Appendix-5.

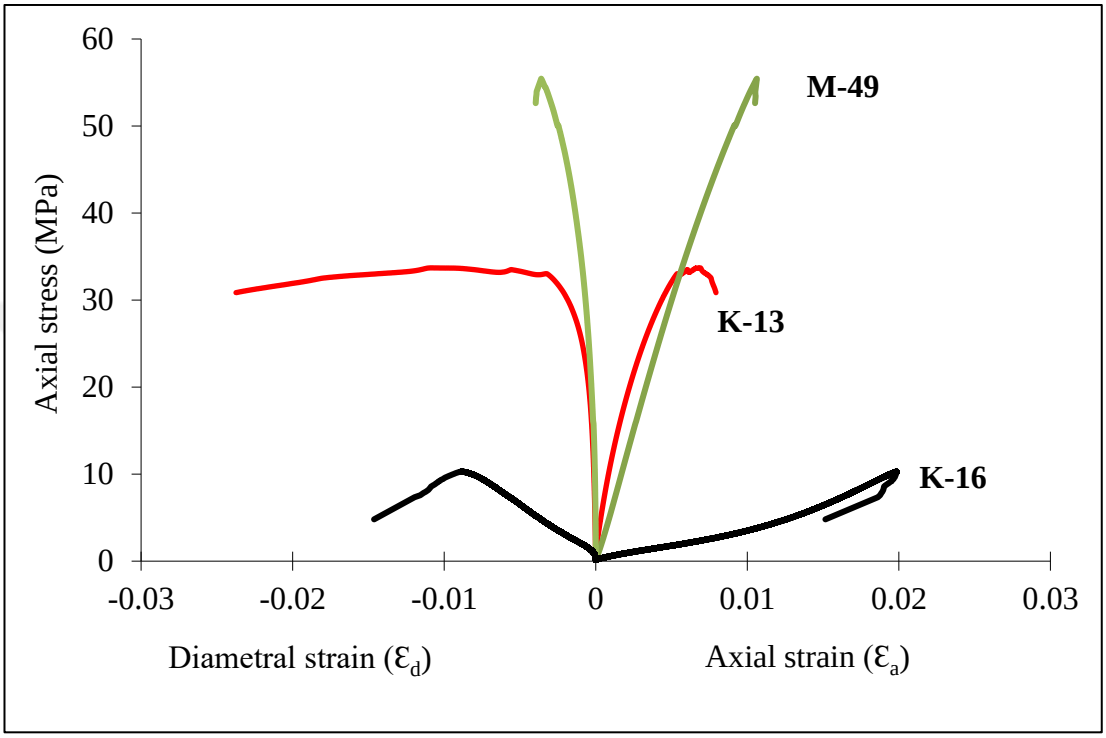


Figure 5.11 Stress-strain graphs for the samples examined by Tira 28500

The four types (axial splitting, shearing along a single plane, double shear, and multiple fracturing) out of the failure modes given in Figure 5.12 were observed on the investigated samples.

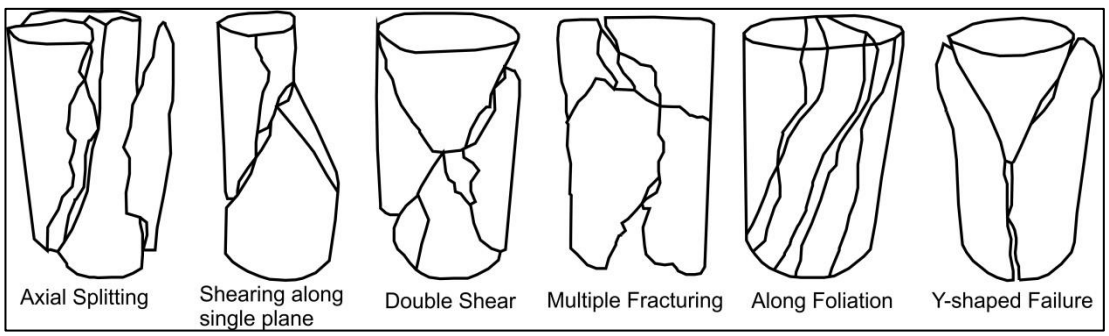


Figure 5.12 Schematic representation of different failure modes under uniaxial compression (from Basu et al., 2013)

Pores and joints are the weakest and most deformable elements in the rock. (Abdulhadi & Barghouthi, 2012). Porosity has a remarkable effect on strength and elasticity. The relationship between porosity and uniaxial compressive strength, as well as the elastic modulus illustrated in Figures 5.13 and 5.14. Since different rock groups have different trends; the plot seems to be widespread. For this reason, the correlations between n, σ_{ci}, E_{avg} are very poor. It indicates that the effect of other parameters (textural, mineralogical properties of the rocks, etc.) are also significant in these samples. However, it is observed that as the porosity increases strength and elasticity decrease.

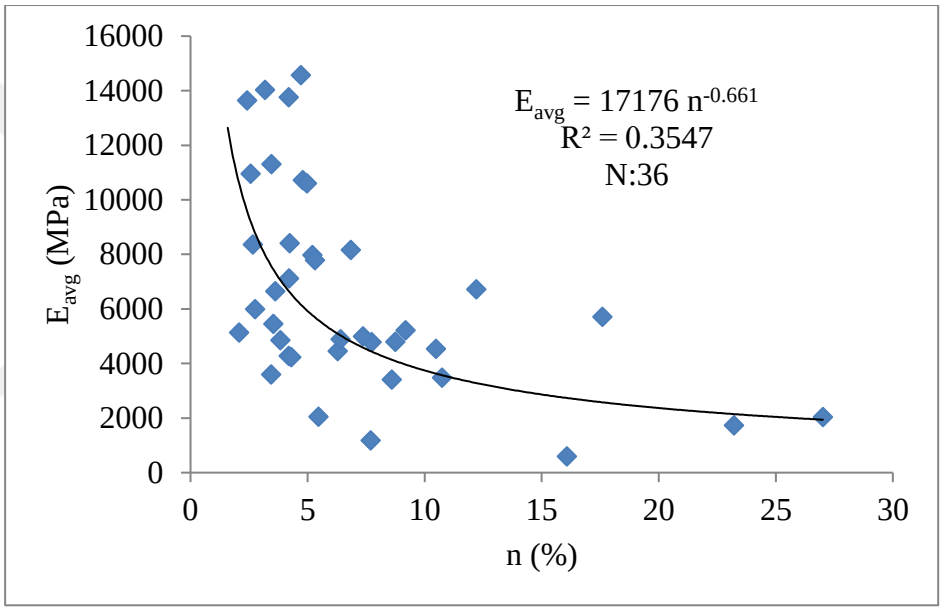


Figure 5.13 The relationship between E_{avg} and n

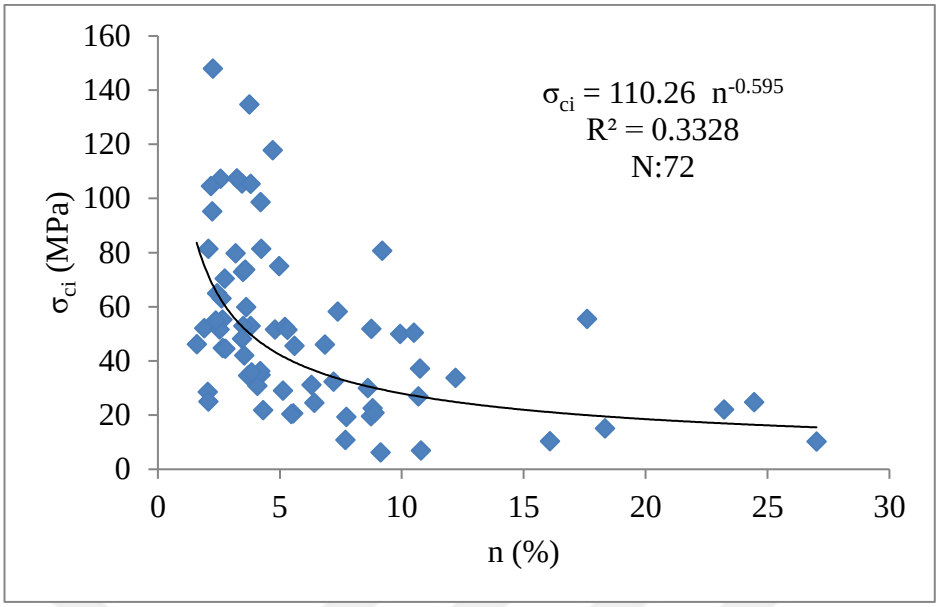


Figure 5.14 The relationship between σ_{ci} and n

The laboratory measured static E_{avg} values under water-saturation were also correlated with the elastic modulus values calculated from average seismic waves of Zone II and III along six MASW profiles (for example, MASW Profile I and Zone II abbreviated as P-1.2) and illustrated in Figure 5.15. The two elastic modulus values are fairly compared.

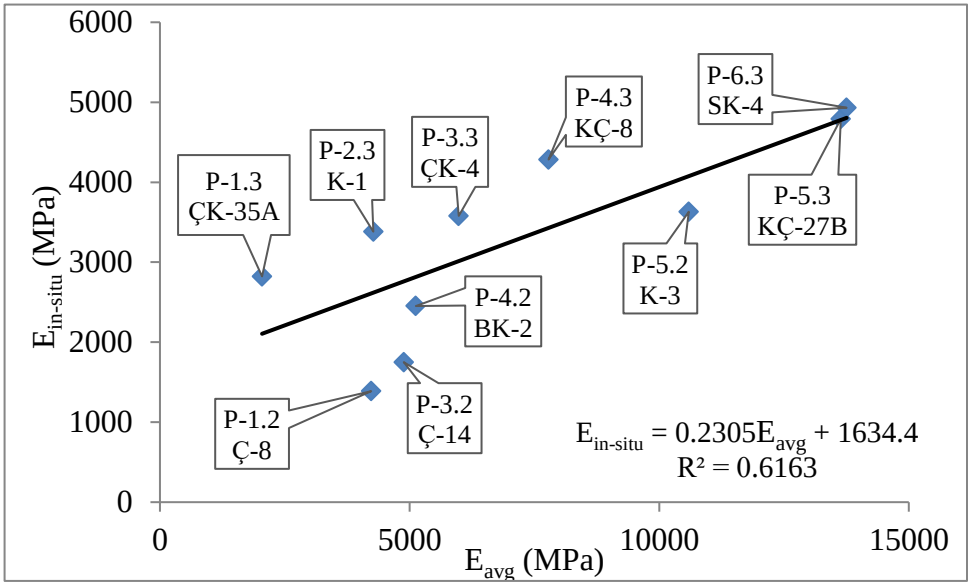


Figure 5.15 The relationship between the in-situ and laboratory-measured elastic modulus values

5.2.6 Indirect Estimation of Cohesion and Internal Friction Angle

The shear strength parameters of the intact rock, cohesion, and internal friction angle were estimated from the Mohr-Coulomb Failure envelope with tension cutoff using Brazilian and static uniaxial compression test results. The tension cutoff criterion is a combination of criteria for tensile and shear failure and is illustrated in Figure 5.16.

The representation of the Brazilian tensile strength on the failure envelope was achieved based on the theoretical relationship proposed by Fairhurst (1964), Goodman (1989), Chen, Pan, & Amadei (1998). According to the researchers, in the Brazilian test, the radial compressive stress obtained at the center of the disc specimen is three times the maximum tensile stress for an isotropic Griffith material at failure.

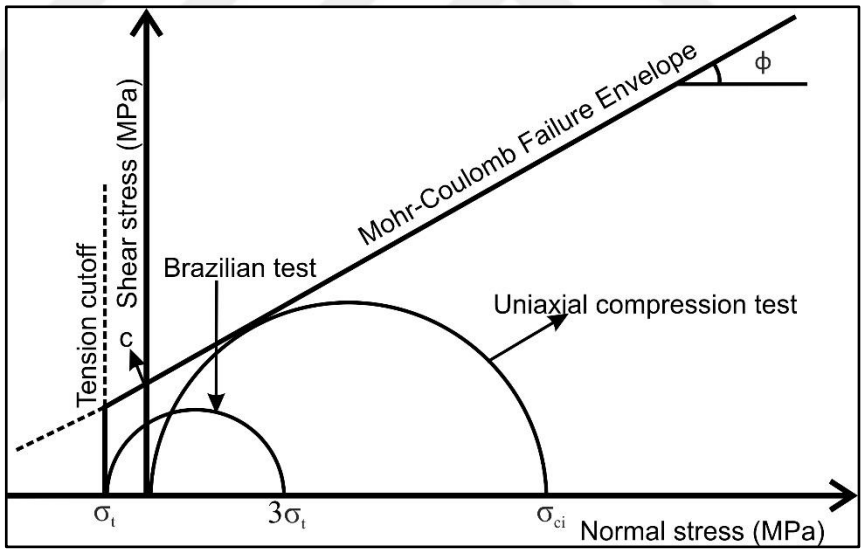


Figure 5.16 Illustration of determining cohesion and internal friction angle from Mohr-Coulomb Failure envelope with a tension cutoff (Goodman, 1989)

The cohesion and internal friction angles were determined on the shear stress-normal stress graph, as illustrated in Figure 5.16, and given in Table 5.10. The mean cohesion values are 10.19 MPa and 5.70 MPa for Yeniköy and Göcek Formations, respectively. On the other hand, internal friction angle values were found to be very

high. This finding is in agreement with the results of Karaman, Cihangir, & Kesimal (2013). For this reason, an equation proposed by Karaman et al. (2013) was used to estimate the internal friction angle values. This equation is based on the statistical correlation of laboratory-measured internal friction angle under triaxial compression and the uniaxial compressive strength.

$$\phi = 0.05\ \sigma_{ci} + 40.23 \qquad (5.8)$$

The internal friction angle values calculated from Equation 5.8 are termed as corrected ϕ. Both the ϕ values and the cohesion values are given in Table 5.10. Hence, the mean ϕ values are 43.27°, 41.85°, and 39.99° for Yeniköy and Göcek Formations, and very weak rock, respectively.

Table 5.10 The cohesion (c) and the internal friction angle (ϕ) of the intact rock samples calculated based on the Mohr circles of Brazilian and uniaxial compression tests

Rock Group	σ_t (MPa)	σ_{ci} (MPa)	σ_{ci}/σ_t	c (MPa)	ϕ (°)	Corrected ϕ (°)
SK	8.08	80.82	10.00	15.25	47.0	44.27
	9.74	104.63	10.74	18.00	50.0	45.46
	10.57	117.02	11.07	20.50	50.0	46.08
KÇ	3.82	46.06	12.06	8.50	48.0	42.53
	2.74	28.47	10.39	5.50	47.5	41.65
	4.33	52.53	12.13	8.50	50.0	42.86
BK	3.16	51.31	16.24	7.00	55.0	42.80
	2.78	34.56	12.43	6.25	51.5	41.96
	1.98	28.37	14.33	4.25	53.0	41.65
K	1.44	19.18	13.32	3.62	48.0	41.19
	1.67*	10.28	6.16	2.75	38.0	-
Ç	3.58	32.26	9.01	7.00	42.5	41.84
	2.77	20.45	7.38	4.80	43	41.25
	4.47	41.78	9.35	8.00	45.5	42.32
	2.08*	19.34	9.30	3.75	45.0	41.20
ÇK	7.92	103.92	13.12	16.00	55.0	45.43
	4.36	45.18	10.36	8.45	47.0	42.49
	4.89	59.48	12.16	10.00	52.0	43.20
	1.28*	10.82	8.45	2.5	44	40.77
KKÇ	1.11	21.70	19.55	2.50	60.0	41.32
	1.19	24.80	20.84	2.75	60.0	41.47
M	4.34	55.44	12.77	9.00	52.5	43.00
	3.51	49.91	14.22	7.50	54.0	42.73

*Very weak rock samples separated from the relatively stronger samples

The σ_{ci}/σ_t ratios are changing between 6.16 and 20.84. Griffith (1921) suggested that the uniaxial compressive strength (σ_{ci}) is eight times the σ_t of intact rock based on the two-dimensional theory of brittle failure. On the other hand, the three-dimensional extension of this assumption by Murrell (1963) predicts the uniaxial compressive strength as 12 times the σ_t of intact rock. Some of the samples in rock groups BK, K, KKÇ, and M, have σ_{ci}/σ_t ratios higher than 12. The high σ_{ci}/σ_t ratios

mostly coincide with the samples having low strength and relatively high clay bearing rocks.

5.2.7 Direct Shear Test

The shear strength of the discontinuity surface mainly depends on the roughness, normal stress, JCS, and ϕ of the discontinuity wall. In the case of the presence of water, water pressure decreases the normal stress acting on the discontinuity surface ($\sigma_N' = \sigma_N - u$). As a consequence, a reduction in normal stress leads to a reduction in the effect of friction on the shear strength. Thus, the probability of failure increases. However, as the normal stress increases, shear strength also increases.

During the direct shear test, shear strength reaches a peak value (τ_{peak}), then as the asperities are sheared and degraded, shear strength value decreases to a residual value (τ_{res}) and remains constant while the shear displacement (δ) continues. The relationship between the peak shear strength and the normal stress is represented regarding the Mohr-Coulomb Criterion is expressed as;

$$\tau_{peak} = c + \sigma_N \tan \phi \tag{5.9}$$

where c is cohesion, ϕ is internal friction angle, σ_N is the normal stress acting on the surface. On the other hand, residual shear strength is a function of residual ϕ (ϕ_r) and σ_N, c is practically zero and can be expressed as;

$$\tau_{res} = \sigma_N \tan \phi_r \tag{5.10}$$

where ϕ_r expresses the internal friction angle after failure. The base friction angle (ϕ_b) also serves as a fundamental parameter for assessing the shear strength of the planar discontinuity surface and it is widely used for long-term slope stability analysis. The internal friction angle for the saw-cut surface is also found as ϕ_b. Therefore, Equation 5.10 is transformed into Equation 5.11 for planar, smooth surfaces.

$$\tau_{res} = \sigma_N \tan \phi_b \quad (5.11)$$

After that, Barton & Choubey (1977) developed a non-linear failure criterion using unfilled, variously weathered rock samples.

$$\tau_{peak} = \sigma_N \tan [\phi_r + JRC \log_{10} (JCS/ \sigma_N)] \quad (5.12)$$

where JRC is the joint roughness coefficient, which can be selected from the graph proposed by Barton & Bandis (1982) (Chapter 4); JCS is the joint wall compressive strength which can be estimated from the Schmidt Hammer test.

In this study, as the M-2, M-3, and M-4 samples are fresh (unweathered), JCS values measured by the Schmidt Hammer test were used in the peak shear strength equation.

ϕ_r can be assumed to be equal to the ϕ_b measured on the saw-cut planar surfaces if the discontinuity surface is dry, planar, and unweathered according to Barton & Choubey (1977). Thus, Equation 5.12 is transformed into;

$$\tau_{peak} = \sigma_N \tan [\phi_b + JRC \log_{10} (JCS/ \sigma_N)] \quad (5.13)$$

However, if the discontinuity surface is weathered, ϕ_r can be calculated from ϕ_b considering the ratio of in-situ Schmidt hammer rebound value on smooth, natural, weathered and wet joint surface (r) to laboratory-measured Schmidt hammer rebound value on smooth, fresh, unweathered, and dry joint surface (or sawn-cut surface) (R).

$$\phi_r = (\phi_b - 20) + (20 \times \frac{r}{R}) \quad (5.14)$$

Barton's model is valid when JCS is higher than normal stress acting on joint, the τ_{peak} calculated from Barton's model is always higher than that from Mohr-Coulomb Failure Criterion (Sainoki & Mitri, 2014).

On the other hand, a new method for shear strength determination of unfilled, unweathered rock joint was proposed by Jang & Jang (2014) more recently by testing the replica joints as follows;

$$\tau_{peak} = \sigma_N^{B} \tan [\phi_b + \phi_j + s_n] \quad (5.15)$$

where B is the regression coefficient, ϕ_j is the joint roughness angle, and s_n is the shear component. These parameters can be found from the equations below;

$$\phi_j = \tan^{-1} (Z_2^{+}) \text{ while } Z_2 = (JRC+11.44)/51.16)^{1.883239171} \quad (5.16)$$

where Z_2 is a parameter related to roughness.

$$s_n = 0.18377\sigma_j + 0.4519\ \phi_j + 0.9774 \quad (5.17)$$

where, σ_j is the equivalent of joint wall compressive strength (JCS), and

$$B = 0.00062\ \sigma_j - 0.01085\ \phi_j + 0.90331 \quad (5.18)$$

In order to determine the shear strength of intact rock and the discontinuity surface, direct shear tests were performed on the clayey limestone (M) samples. These tests were conducted by GS1000 machine, which applies forces up to 1000 kN (Figure 5.17).

A horizontal LVDT measures shear displacement with high accuracy ($\pm$0.001 mm), which is attached to the bottom part of the direct shear. The normal displacement is measured by four vertical LVDTs, which were positioned at the four corners of the upper part of the direct shear. Load-cells measure normal and shear loads with a sampling rate of 100 Hz (Konietzky, Frühwirt, & Luge, 2012).

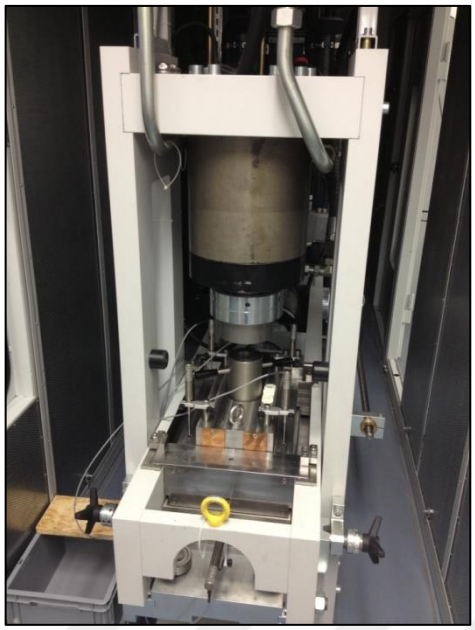


Figure 5.17 GS-1000 shear-box test device in rock mechanics laboratory in Freiberg, Germany (Personal archive, 2014)

CNL boundary condition is applied during the tests. CNL means that the normal load is kept constant during the shearing process. Shear testing under CNL boundary condition is only suitable for cases such as non-reinforced rock slopes, where the surrounding rock mass enables the joint to shear, which allows unrestricted dilation (Nguyen, 2013). At that time, the normal load on the shear plane is constant during the shear process (Ulusay & Gerçek, 2017).

The tests were performed under the normal stresses of 2, 5, 10 MPa. The specimen size is 20x10x10 (length/width/height). Consequently, stress-time-shear displacement and shear stress-shear displacement, and shear stress-normal stress relations were derived.

Firstly, intact, clayey limestone sample M-1 was subjected to the shear forces under 2 MPa and after 5 MPa and 10 MPa normal stresses. It was aimed to create a naturally occurred shear joint surface by the first test. Cohesion and internal friction angle of the rock material would also be evaluated. After that, the naturally occurred surface will again be sheared under 2, 5, and 10 MPa normal stresses. However, the test was terminated where the recorded data become disrupted. It was due to the

oncoidal shape of the failure surface, and it was unable to shear this kind of surface (Figure 5.18).

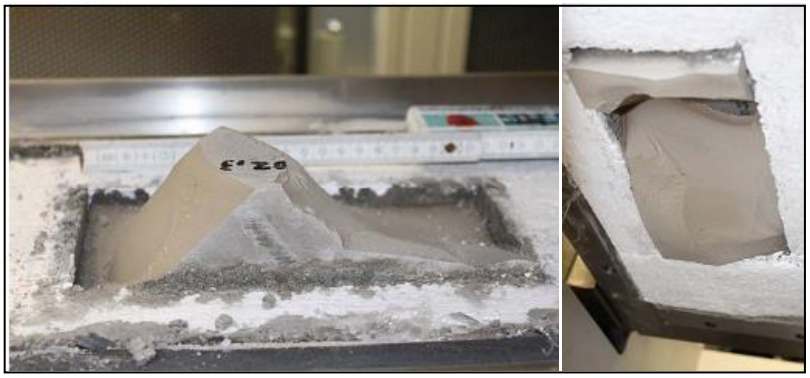


Figure 5.18 The image of the oncoidal failure surface observed for M-1 (Personal archive, 2014)

The stress-displacement-time graph for M-1 under 5 MPa normal stress is given in Figure 5.19.

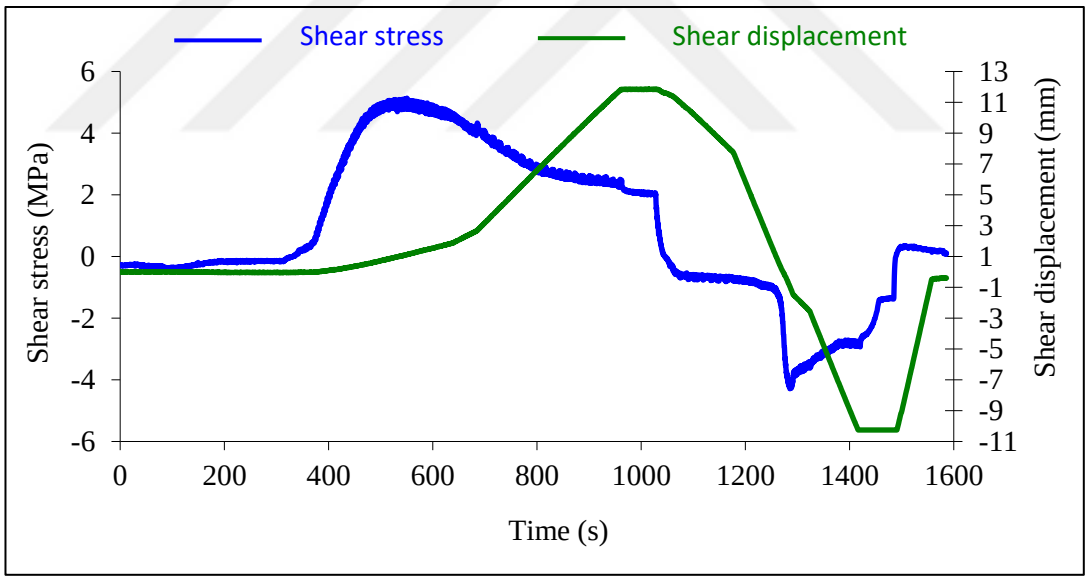


Figure 5.19 The time-shear stress-shear displacement graph under 5 MPa normal stress for the sample M-1

The shear stress-shear displacement graph is also given in Figure 5.20. The peak and residual shear strength can be observed on the graph, and the plot is incomplete since the test was terminated at that time. Thus, it was impossible to calculate the intact cohesion and internal friction angle of the sample M-1.

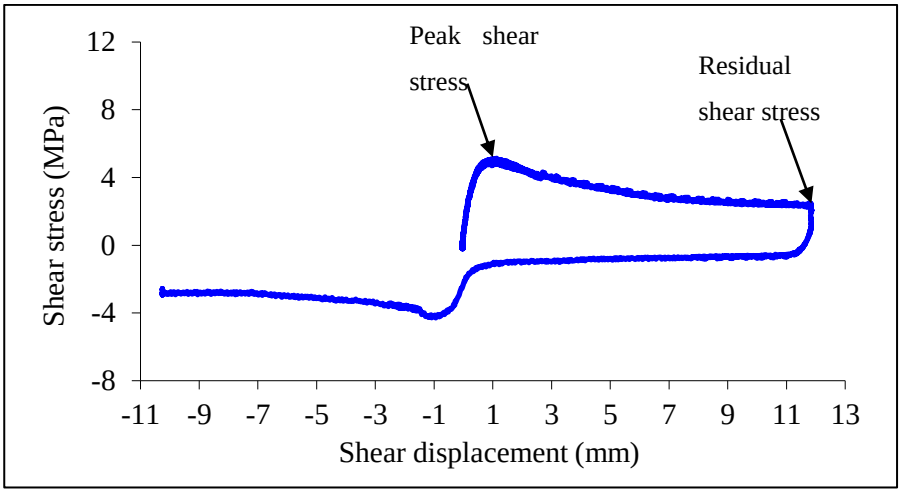


Figure 5.20 The shear stress-shear displacement graph under 5 MPa normal stress for the sample M-1

After the shear test on the M-1 sample, the other samples (M-2, M-3, and M-4) were not tested to find their intact shear strength parameters and to derive the naturally occurred discontinuity surfaces. It was decided to cut the samples in parallel to their length to obtain saw-cut surfaces on which shear test can be performed. As mentioned earlier, the cohesion will be zero since the saw cut surfaces are planar, smooth, and unweathered. The ϕ_r and ϕ_b values will be similar for the same reason. According to Barton&Choubey's (1977) approach, the saw-cut surfaces correspond to JRC values 0 to 4. ϕ_b values were found by shear strength envelope obtained from the shear strength versus normal stress graphs.

The saw-cut surfaces were sheared in four different directions, in which the peak shear stresses can be measured. These directions are forward-advance, forward-return, backward-advance, and backward-return (Figure 5.21). In other words, the sheared surface in the forward direction is again exposed to shear forces in the reverse direction. The same surface is sheared four times in opposite directions. Even though the surfaces are saw-cut and planar, higher-order asperities can lead to slight differences in the peak shear strength measured in different directions. Tatone & Grasselli (2010) have also revealed that τ_{peak} in different directions can vary due to anisotropy in shear directions.

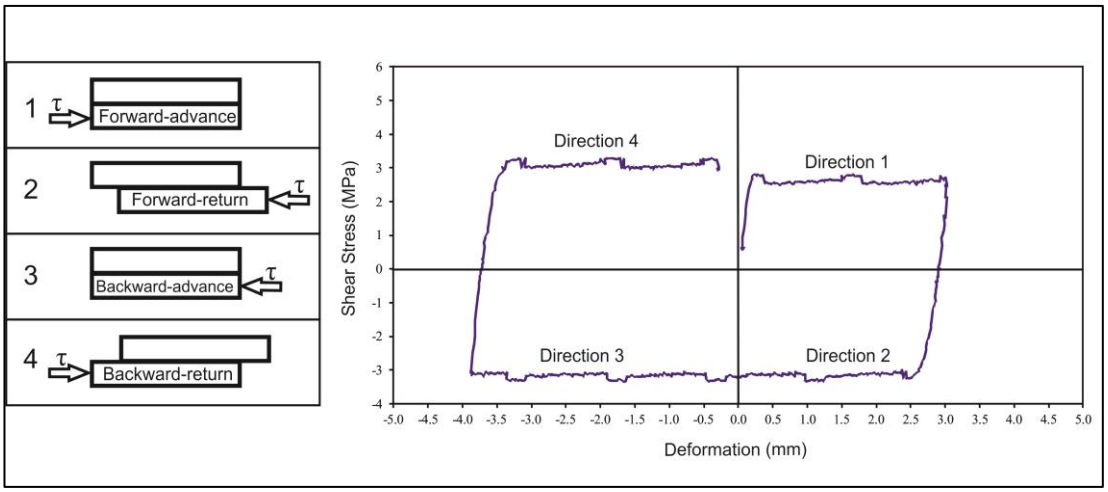


Figure 5.21 Directions of the applied shear stress during the shear-box test

Since the shear-box test is performed on the saw-cut surfaces, no initial roughness can be measured, whereas secondary or higher-order roughness can still affect the stress-strain characteristics. Nevertheless, the changes in normal displacement are negligible due to the planar (saw-cut) surface.

Three stages of normal stress (2, 5, and 10 MPa) were applied on the saw-cut surface of M-2. The image of the M-2 after the test is shown in Figure 5.22.

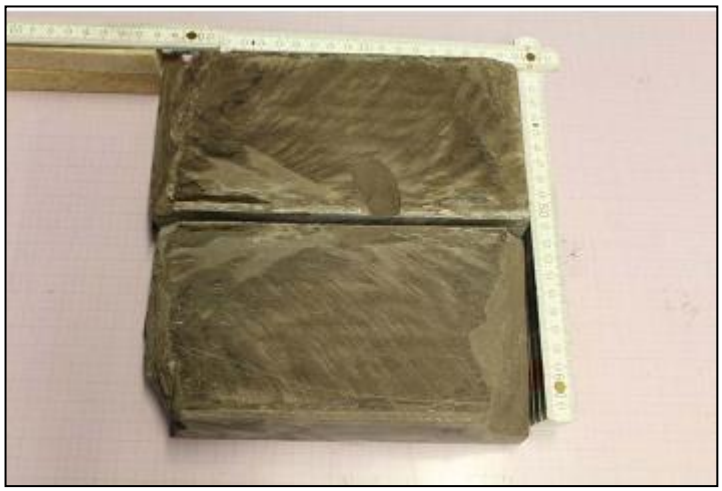


Figure 5.22 The image of M-2 after the shear box test (Personal archive, 2014)

At different normal stresses, the shear stress firstly increases rapidly while the shear displacement increases slowly. After that, the shear displacement curve shows

a sharp increase than the curve of shear stress. As the shear stress reaches the peak value, it means that shear failure has occurred on the discontinuity surface, and the shear stress will not vary much after that point, whereas the shear displacement continues increasing (Figure 5.23).

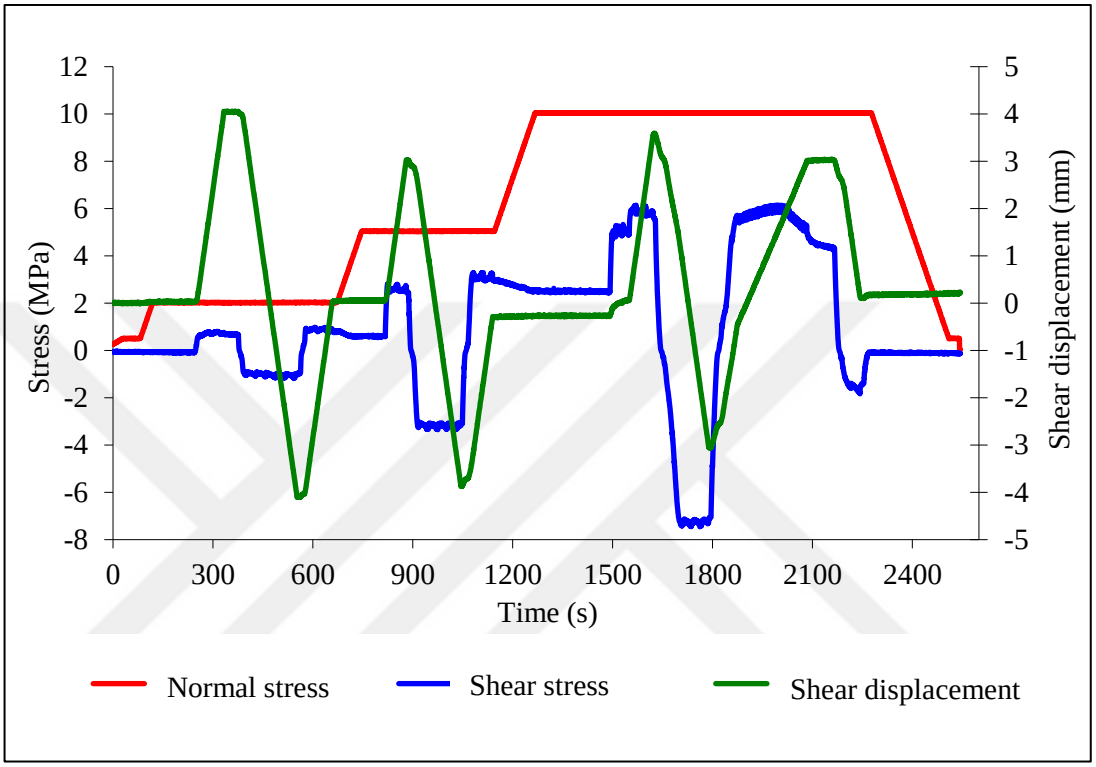


Figure 5.23 Stress-time-shear displacement graph for M-2 sample under multi-staged normal stress condition (σ_N: 2, 5, 10 MPa)

The failure envelope of the M-2 sample was derived, considering the peak shear stresses in directions 1 and 3. The inclination of the envelope gave the base friction angle as 33.8° (Figure 5.24). The Mohr-Coulomb equation of the envelope is given as $\tau_{peak}= 0.6682\sigma_N$ in Figure 5.24.

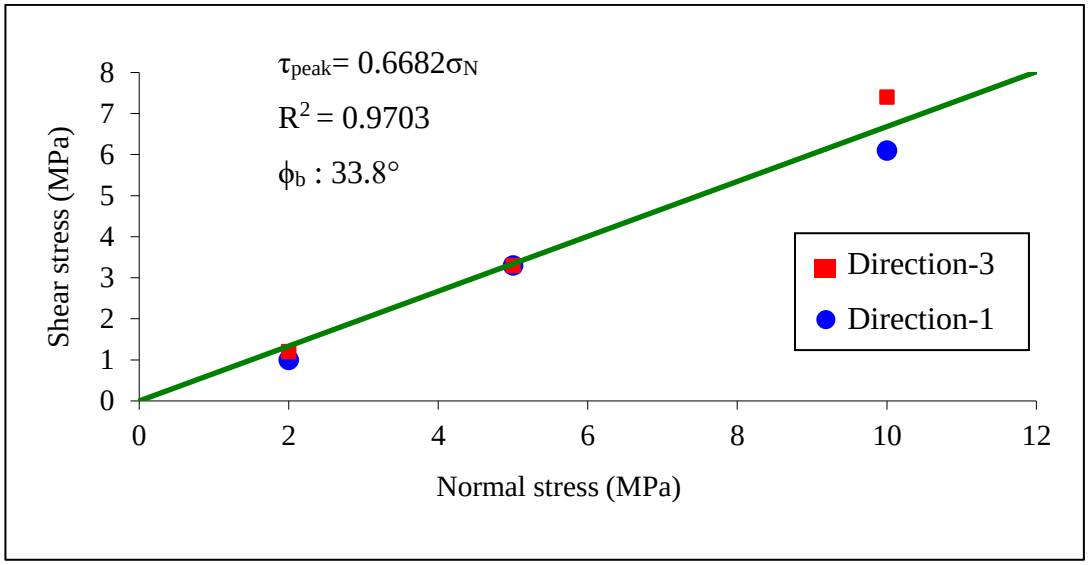


Figure 5.24 The Mohr-Coulomb envelope of the M-2 sample on the shear stress-normal stress graph

The small oscillations observed on the shear stress-shear displacement graph are most probably due to the gradual failure of microscopic/macroscopic higher-order asperities present on the discontinuity surface (Figure 5.25). Figure 5.25 also indicates that as the normal stress increases, the peak shear stress also increases.

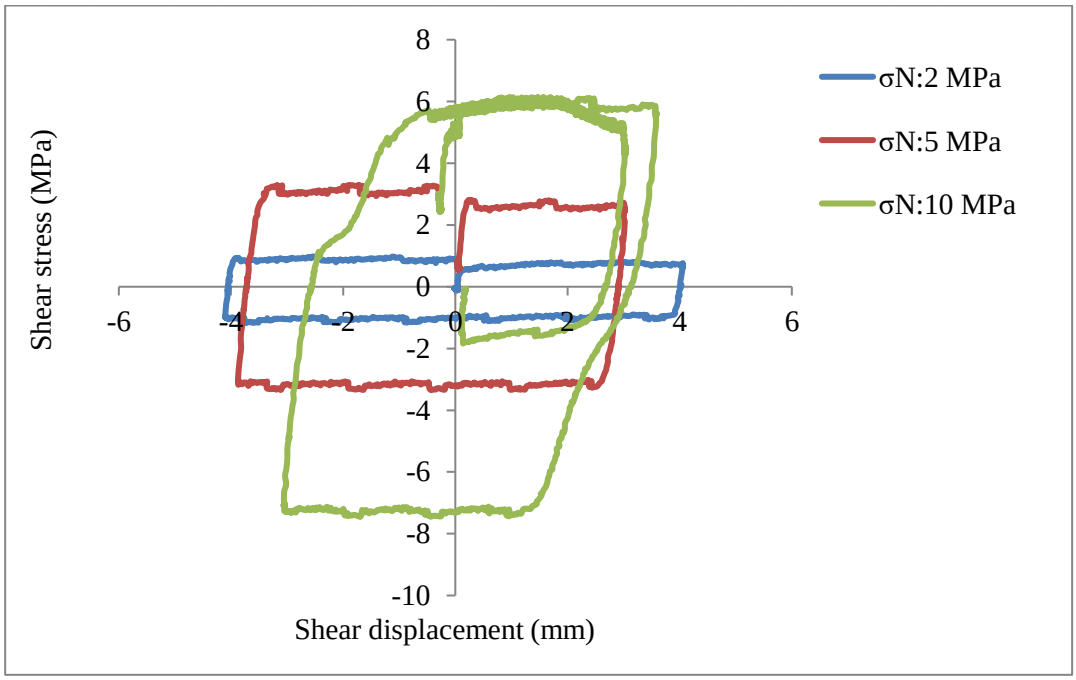


Figure 5.25 Shear stress-shear displacement graph for M-2 sample under various normal stress conditions (2, 5, and 10 MPa) in four shear directions

Three stages of normal stress (2, 5, and 10 MPa) were applied on the saw-cut surface of M-3. The image of the M-3 after the test is shown in Figure 5.26.



Figure 5.26 The image of M-3 after the shear box test (Personal archive, 2014)

At 10 MPa normal stresses, the shear displacement increases as rapidly as the shear stress unlike the M-2 sample; however, 10 MPa normal stress is applied for less time to the sample than the M-2 sample (Figure 5.27).

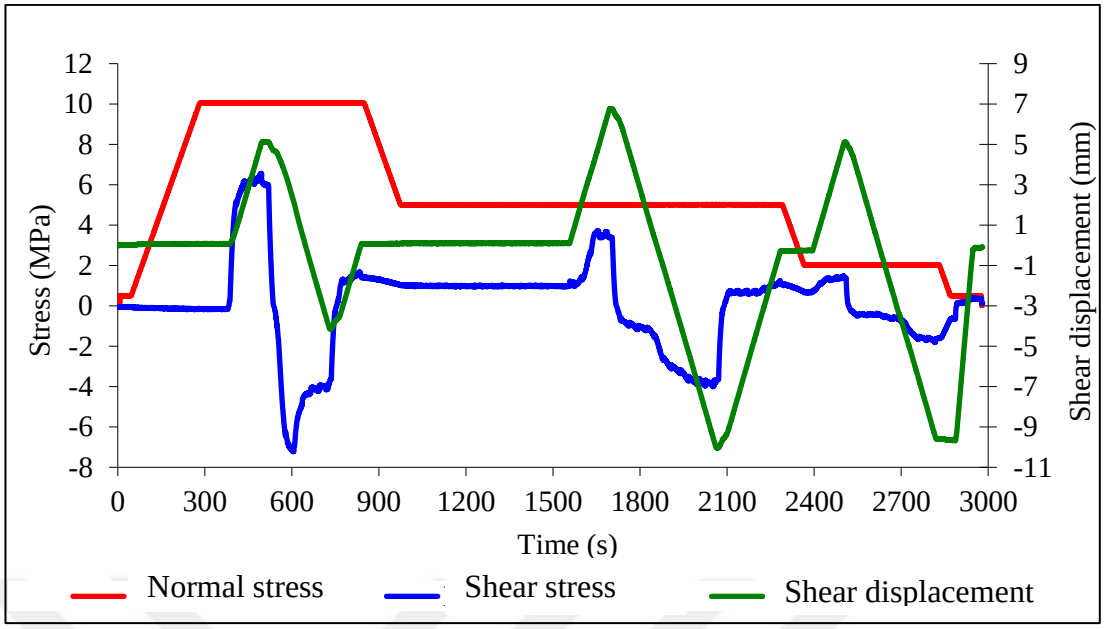


Figure 5.27 Stress-time-shear displacement graph for M-3 sample under multi-staged normal stress condition (σN: 2, 5, 10 MPa)

The failure envelope of the M-3 sample was derived considering the peak shear stresses in directions 1 and 2. The inclination of the envelope gave the base friction angle as 35.4° (Figure 5.28). The Mohr-Coulomb equation of the envelope is given as $\tau_{peak} = 0.7066\sigma_N$ in Figure 5.28.

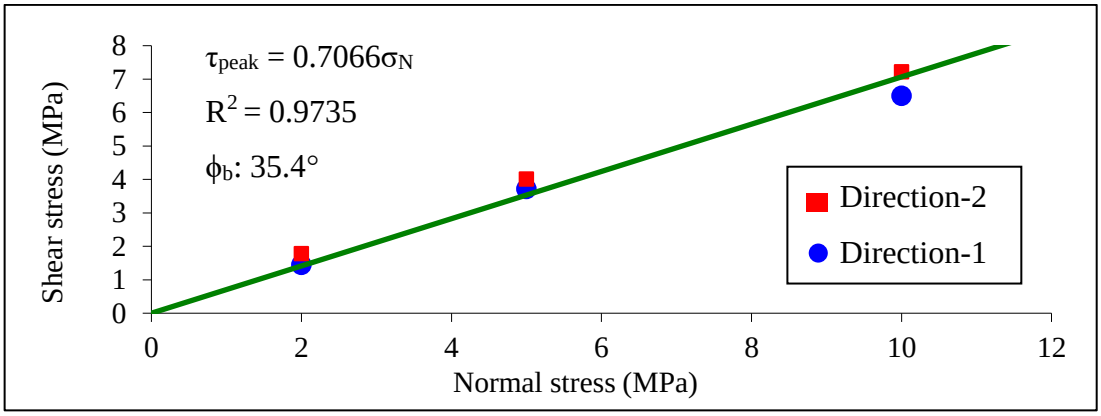


Figure 5.28 The Mohr-Coulomb envelope of the M-3 sample on the shear stress-normal stress graph

The difference between the peak and residual shear stress under 10 MPa normal stress is more observable on sample M-3 along direction-2 (Figure 5.29).

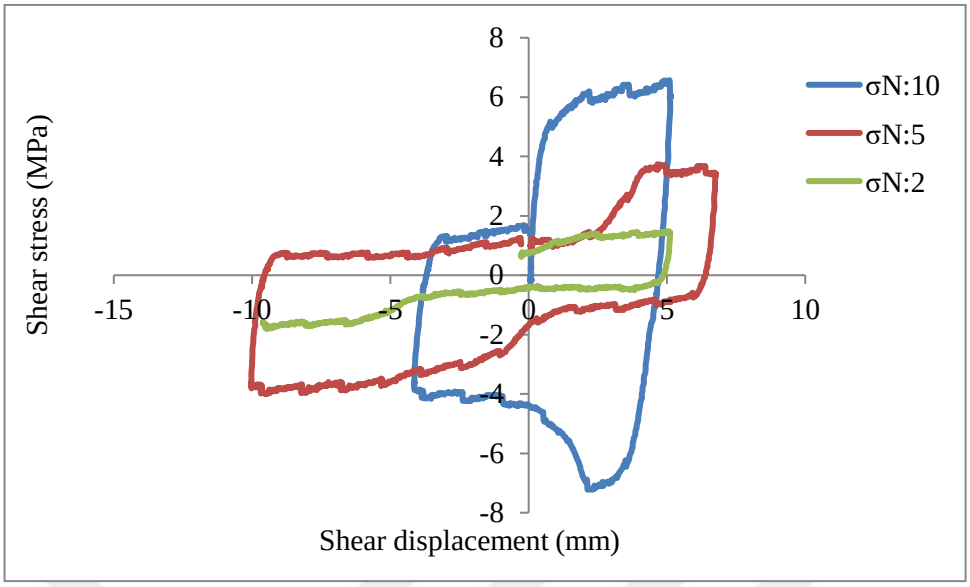


Figure 5.29 Shear stress-shear displacement graph for M-3 sample under various normal stress conditions (2, 5, and 10 MPa) in four shear directions

Three stages of normal stress (2, 5, and 10 MPa) were applied on the saw-cut surface of M-4. The image of M-4 after the test is shown in Figure 5.30.



Figure 5.30 The image of M-4 after the shear box test (Personal archive, 2014)

The difference between the peak shear strength values in different directions is significant in the M-4 sample. The duration of the test is less than the other tests (Figure 5.31).

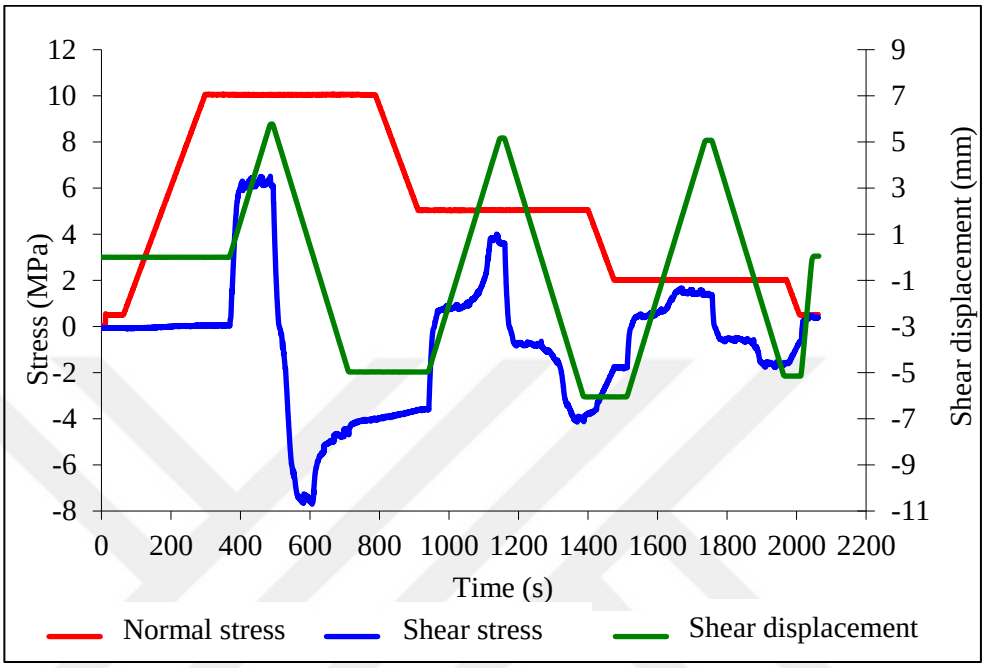


Figure 5.31 Stress-time-shear displacement graph for M-4 sample under multi-staged normal stress condition (σ_N: 2, 5, 10 MPa)

The failure envelope of the M-4 sample was derived considering the peak shear stresses in directions 1 and 2. The inclination of the envelope gave the base friction angle as 35.6° (Figure 5.32). The Mohr-Coulomb equation of the envelope is given as $\tau_{peak} = 0.7155\sigma_N$ in Figure 5.32.

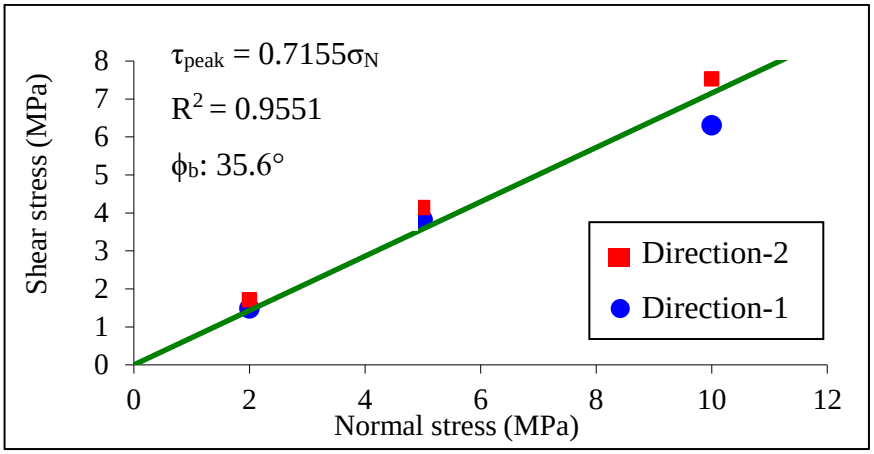


Figure 5.32 The Mohr-Coulomb envelope of the M-4 sample on the shear stress-normal stress graph

The linear and non-linear phases of the shear stress-shear displacement graph for the M-4 sample, particularly under 5 MPa normal stress are more slowly advances (Figure 5.33).

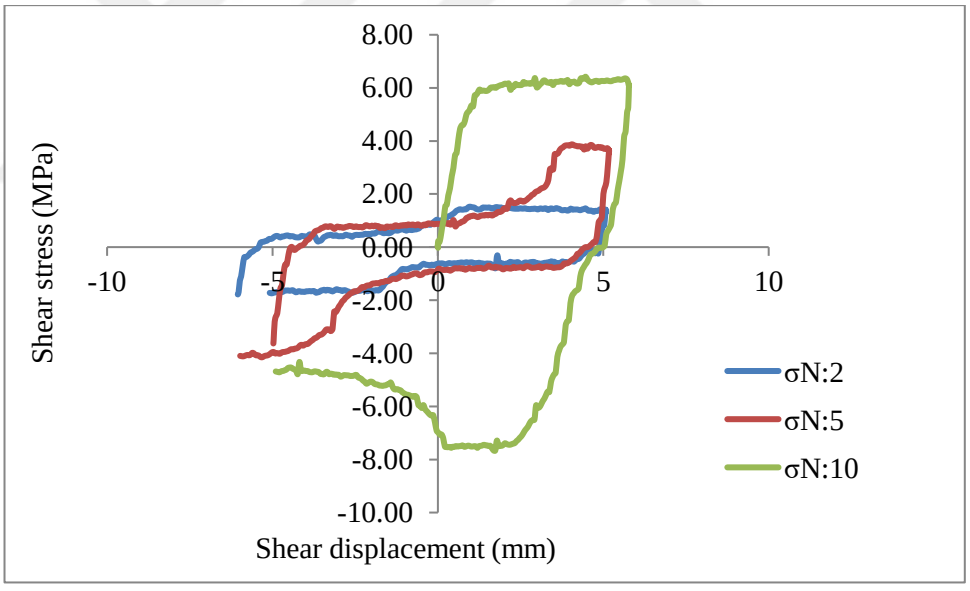


Figure 5.33 Shear stress-shear displacement graph for M-4 sample under various normal stress conditions (2, 5, and 10 MPa) in four shear directions

The measured τ_{peak} values are presented in Table 5.11. The τ_{peak} values in backward-advance (3) or forward-return (2) values are higher than the ones in forward-advance (1) direction as 1.5% to 18.3%. Hence, the JRC values were assumed to be 1 under 2 and 5 MPa normal stresses. JRC values were assumed to be 0 under 10 MPa normal stress conditions for direction-1 because of degradation of

asperities under high normal stress. However, the JRC values were assumed to be 3 for all normal stress conditions in directions 2 and 3.

As given in Table 5.11, with increasing normal stress, the peak shear stress is increasing, and shear displacement (δ) is slightly decreasing. It suggests that the shear displacement value is not significantly changing. Because the tests with different normal stresses were performed on the already sheared surface. Once the surface is sheared, even the peak shear stress is increased with the increasing normal stress; maximum shear displacement (δ_{max}) is not significantly affected.

Table 5.11 Static shear test results

Sample ID	σ_N (MPa)	τ_{peak} (MPa)	δ_{max} (mm)	τ_{peak} (MPa)	δ_{max} (mm)	Static ϕ_b (°)
Direction		1	1	2-3	2-3	
M-2	2	0.98	4.023	1.16	4.080	33.75
	5	3.29	2.977	3.34	3.872	
	10	6.14	2.545	7.45	3.090	
M-3	2	1.48	5.062	1.82	9.920	35.24
	5	3.73	4.651	4.01	9.501	
	10	6.5	5.093	7.2	4.136	
M-4	2	1.66	5.054	1.77	6.045	35.58
	5	3.80	5.036	4.14	5.000	
	10	6.51	5.636	7.70	4.927	

Since the changes in normal displacement are negligible with regard to different normal stress values, only the shear stiffness (k_s) value of the discontinuity surface could be measured. The k_s is the resistance to deformation under shear stresses. It is found from the slope of the shear stress to the shear displacement graph. Stiffness values were calculated as the ratio of peak shear stress to shear displacement at peak shear stress (δ_i). The mean k_s value was found to be 1619.81 MPa/m (Table 5.12).

Table 5.12 The shear stiffness (k_s) values for the samples M-2, 3, and 4 under various normal stress conditions and different shearing directions

Sample ID	Direction	σ_N (MPa)	k_s (MPa/m)	τ_{peak} (MPa)	δ_i (mm)
M-2	1	2.00	384.77	0.98	2.55
	1	5.00	1734.32	3.29	1.90
	1	10.00	4171.20	6.14	1.47
	2	2.00	310.16	1.16	3.74
	2	5.00	999.40	3.34	3.34
	2	10.00	4382.35	7.45	1.70
M-3	1	2.00	292.37	1.48	5.06
	1	5.00	801.98	3.73	4.65
	1	10.00	1288.04	6.56	5.09
	2	2.00	183.47	1.82	9.92
	2	5.00	422.06	4.01	9.50
	2	10.00	3234.90	7.23	2.24
M-4	1	2.00	222.85	1.66	7.45
	1	5.00	392.81	4.00	10.18
	1	10.00	1283.77	6.51	5.07
	2	2.00	292.37	1.77	6.05
	2	5.00	772.24	4.14	5.36
	2	10.00	7987.55	7.70	0.96
		Mean	1619.81	4.05	4.79

As the normal stiffness values could not be estimated from the direct shear tests on saw-cut surfaces. Another method for determining the shear and normal stiffness values was applied by using the empirical equations proposed by Barton (1972).

$$k_n = \frac{Ei\ Em}{L\ (Ei - Em)} \tag{5.19}$$

$$k_s = \frac{Gi\ Gm}{L\ (Gi - Gm)} \tag{5.20}$$

where E_i is the intact rock elastic modulus which can be derived from the slope of the stress-strain curve of the rock specimen subjected to uniaxial compressive strength test (E_{avg}). E_m is the rock mass elastic modulus and the $E_{in\text{-}situ}$ values estimated from the in-situ seismic velocities can be used as E_m. G_m is the rock mass shear modulus and $G_{in\text{-}situ}$ values estimated from the in-situ seismic velocities can be used to calculate it. L is the mean joint spacing and used as 40 cm (mean joint spacing). G_i is the intact rock shear modulus (rigidity) and can be calculated from the equation below,

$$G_i = \frac{Ei}{2(1+\nu)} \tag{5.21}$$

The other parameters to calculate k_n and k_s values are given in Table 5.13. Abdulhadi & Barghouthi (2012) found that the stiffness values calculated from ultrasonic pulse velocities are more reasonable than any other empirical equation estimating the stiffness.

Table 5.13 The estimated normal and shear stiffness values for the rock samples by using laboratory and in-situ normal and shear modulus values

Parameter	Minimum	Maximum
E_i (E_{avg}) (MPa)	5711.34	6710.55
E_m ($E_{in\text{-}situ}$) (MPa)	1517.19 (Zone II)	2452.44 (Zone III)
G_i (MPa)	2131.10	2621.31
G_m (MPa)	520.16 (Zone II)	843.98 (Zone III)
ν (ν_i)	0.34	0.28
k_n (MPa/m)	5165.04	9662.28
k_s (MPa/m)	1720.29	3111.88

The joint stiffness ratio (k_n/k_s) was found to be approximately 3. The minimum k_s value estimated from Equation 5.20 (1720.29 MPa/m) agrees well with the mean laboratory-measured k_s (1619.81 MPa/mm). On the other hand, the maximum k_s value (3111.88 MPa/m) is more correlating with the k_s values measured under 10 MPa normal stress. This finding also supports the knowledge of the dependency of

shear stiffness on normal stress. Since the laboratory-measured k_s values show significant variability, the range of k_s values in Table 5.13 that is also within limits of the laboratory-measured values was considered in the numerical slope stability analyses. The range of k_n values shown in Table 5.13 was also used as a base in the slope stability analyses.

The failure envelopes obtained from static direct shear tests and the empirical approaches such as Barton & Choubey (1977) and Jang & Jang (2014) were compared. For the peak shear strength in shear direction-1, JRC was set to 1 under 2 MPa and 5 MPa normal stresses. JRC was set to zero for the 10 MPa normal stress condition (Figure 5.34). It should be noted that Barton&Choubey's shear strength model with JRC=0 corresponds to Mohr-Coulomb Failure Criterion. Laboratory-measured JCS values on M-2, 3, and 4 samples by the Schmidt hammer test, ϕ_b from the static shear tests were used. The best fit between the empirical and experimental results was made with the above-given parameters.

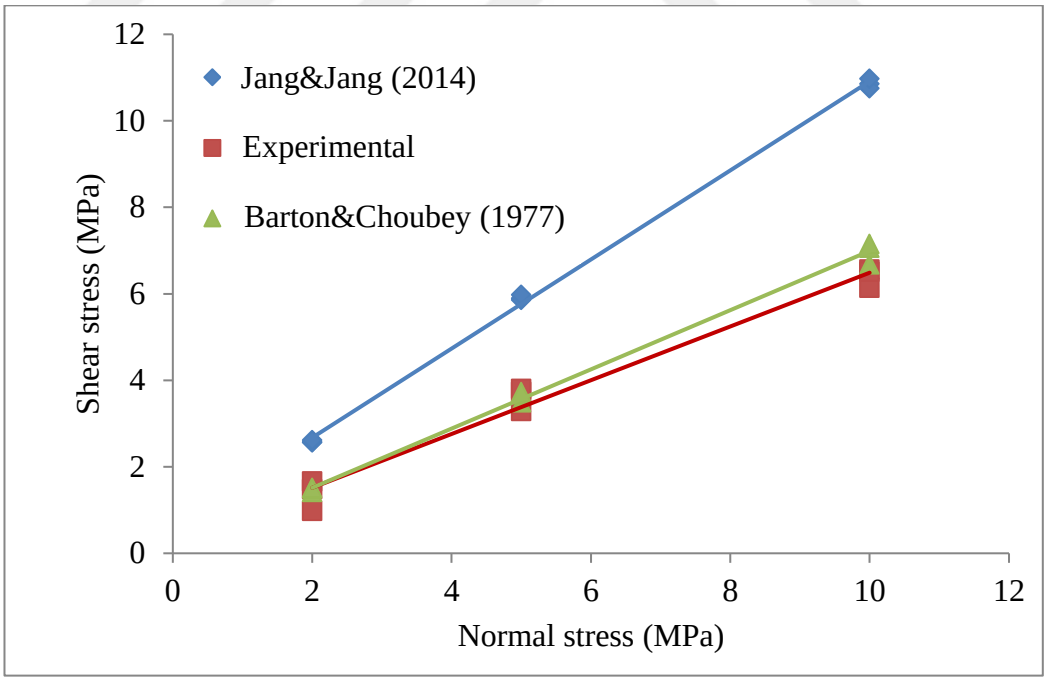


Figure 5.34 The comparison of average failure envelopes for 3 samples in shear direction-1

Figure 5.34 indicated that as normal stress increases, the experimental and Barton's τ_{peak} values slightly diverge from each other. The average Mohr-Coulomb

failure envelope of 3 investigated samples (M-2, 3, 4) is lying below the average Barton & Choubey (1977) failure envelope. In other words, Barton&Choubey's (1977) empirical approach slightly overestimates the τ_{peak} values, particularly at higher normal stresses (Figure 5.34). A similar relationship was found by Özvan, Dinçer, Acar, & Özvan (2014) for granites. Özvan et al. (2014) also argued that the JCS value and the weathering degree are more effective on the τ_{peak} than the JRC value. On the other hand, Jang & Jang (2014) yielded significantly overestimated τ_{peak} values for the samples investigated in this study. It was referred to a possible inconsistency in this empirical approach between saw-cut, smooth surfaces, and very low JRC values.

On the other hand, for the peak shear strength in shear direction-3 for M-3 and M-4 and direction-2 for M-2, JRC was set to 3 for all normal stress conditions (Figure 5.35).

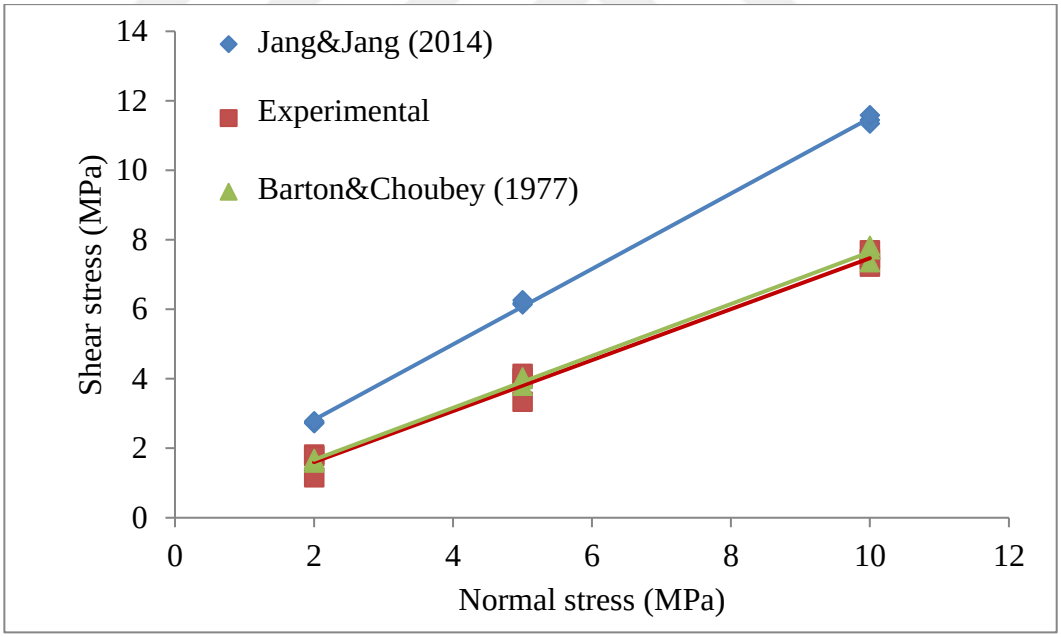


Figure 5.35 The comparison of average failure envelopes for 3 samples in shear direction-3

Figure 5.35 indicated that the experimental and Barton&Choubey's τ_{peak} values match well for all normal stress values in shear direction-2 and direction-3. On the other hand, Jang & Jang (2014) again yielded significantly overestimated τ_{peak} values, particularly for high normal stress conditions.

5.2.8 Creep tests

Creep is the type of rock behavior in which the strain continues to increase under applied constant stress. A creep test provides the time-dependent behavior of the rock sample under constant stress for a given time. Besides, it is essential to find out whether creep type deformation contributes to the landslide occurrence (Fabre & Pellet, 2006). The mathematical theory of this type of behavior is known as viscoelasticity.

During the creep test, three stages can be observed: (1) a primary creep stage, also termed as transient creep, where the strain rate decreases and the delayed deformation stabilizes over a long period, (2) a secondary creep stage, or steady-state creep, where the strain increases linearly with time, strain rate stabilizes (3) a tertiary creep stage where the creep curve turn upwards, an increase in strain rate due to the progressive rock damage (rupture) (Figure 5.36). During the tertiary creep stage, rock may fail under dilatational deformation (Hunsche, 1993; Özarslan, Geniş, Bilir, & Özkan, 2007).

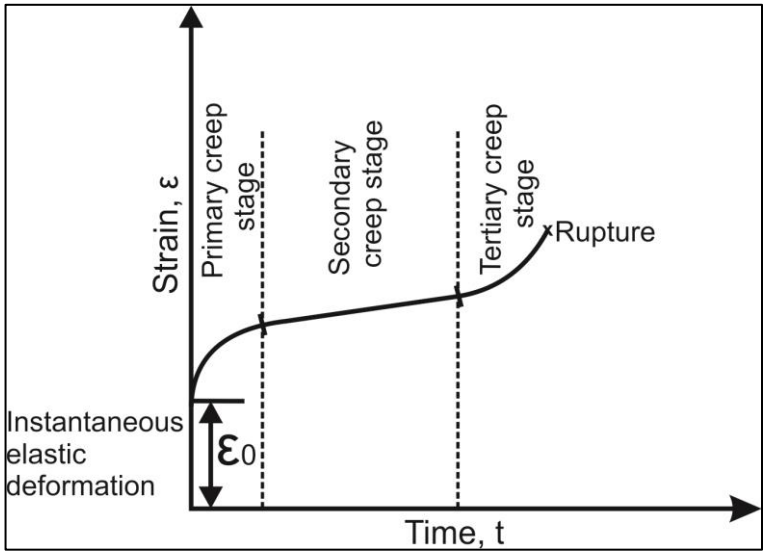


Figure 5.36 Idealized creep curve showing the stages of creep deformation

A cylindrical rock core sample (K-14) was used to determine the creep behavior of Neogene sandstone under uniaxial stress conditions. The length to diameter ratio

of the specimen was 2.12, confirming the ISRM (2007). A long-term (14 days- 336 hours) creep test was carried out by MTS 20/M creep machine under uniaxial compression at 25 °C constant temperature. The sandstone sample was loaded to constant stress as 50% of its σ_{ci} (24 MPa). The deformation (ε) versus time (t) graph of the creep test indicated that the deformation rapidly increases at the elastic and primary creep stage (Figure 5.37). Thereafter, at the secondary creep stage, the steady-state strain rate is reached, and the plastic deformation slowly increases. The secondary creep is initiated approximately at the 52nd hour. It was observed that, after 216 hours from the beginning of the test, the strain rate slows down, and the creep curve becomes almost horizontal. Figure 5.37 also indicates that most of the deformation occurs in a short time after the test begins, and the later deformation is negligible. The tertiary creep phase could not be observed. The test ended before any overall rock damage, and it only contributed to the crack growth. Thus, the failure under constant stress after steady-state creep deformation was not observed (Figure 5.37).

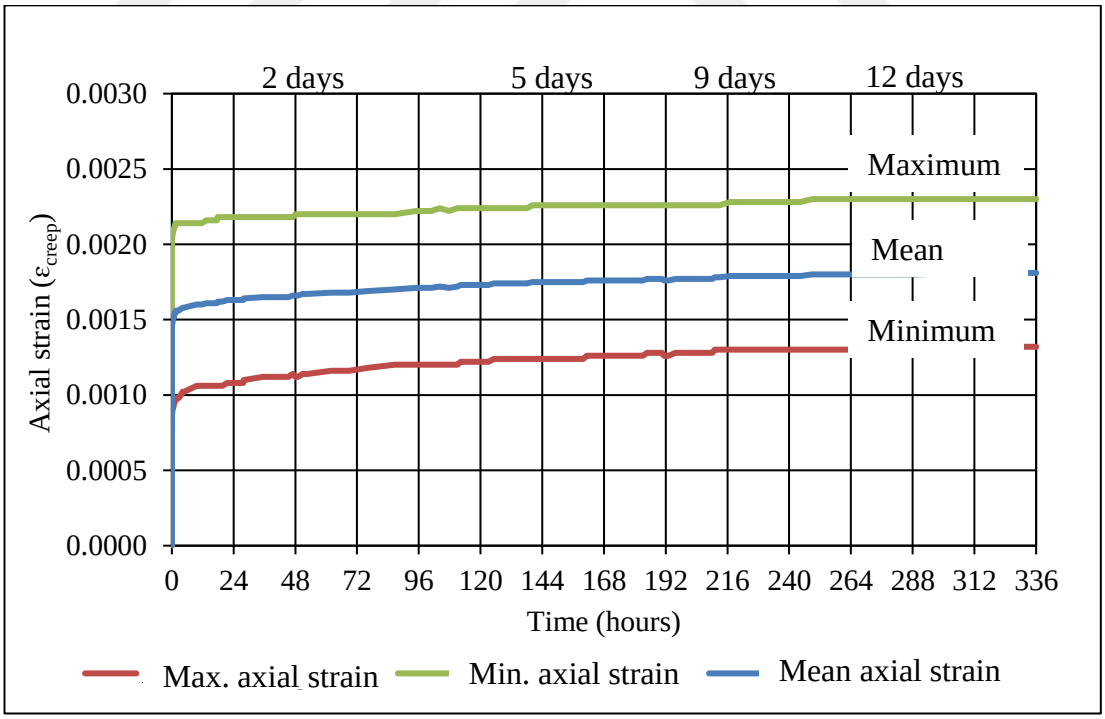


Figure 5.37 Viscoplastic deformations versus time during the creep test performed on K-14 sample

The minimum, maximum, and mean axial creep strain values are given in Table 5.14. The contribution of the creep phenomenon of the sandstone sample to a complete failure was found to be insignificant.

Table 5.14 Creep test results

Statistics	Uniaxial Stress (MPa)	Axial ε_{creep}
Maximum	24	0.0023
Minimum	24	0.0013
Mean	24	0.0018

5.3 Dynamic Strength and Deformation Tests

A better understanding of the dynamic behavior of rock can be helpful in the design of safe structures in rock. Besides, in long-term stability analysis, it is crucial to determine the dynamic response of rock to cyclic loading. Previous studies have shown that the dynamic strength of intact rock varies according to the rock type (mineralogy, micro-fracturing, grain size, rock fabric, quartz content, etc.) and dynamic testing parameters (loading rate, strain rate frequency, amplitude, number of cycles, waveform). The cyclic loading conditions influence not only the strength but also the cracking behavior of rocks (Zou & Wong, 2014). Thus, failure modes and even the location of the maximum damage in the specimens under cyclic loadings are different from those under static loadings (Ishizuka, Abe, & Kodama, 1990; Chen, 1995; Zhao, Li, Wu, & Li, 1999; Demirdağ, Tüfekçi, Kayacan, Yavuz, & Altındağ, 2010; Mohd Salim, Mohamed, & Berhan, 2013; Vaneghi, Ferdosi, Okoth, & Kuek, 2017).

There is a great number of studies focused on the effect of dynamic testing parameters on the fatigue strength of a wide variety of rocks from hard rocks to soft rocks. It was argued that as the loading rate, strain rate, and frequency increases, the dynamic σ_{ci} also increases (Burdine, 1963; Haimson & Kim, 1972; Attewell & Farmer, 1973; Tien, Lee, & Juang, 1990; Ray, Sarkar, & Singh, 1999; Zhao, 2000;

Li, Zhang, Chen, & Swoboda, 2003; Bagde & Petroš, 2005a, 2009; Huang & Liu, 2013; Zhang & Zhao, 2014; Zou, Wong, Lo, & Gan, 2016). On the other hand, as the number of cycles and amplitude increases, the dynamic σ_{ci} decreases (Burdine, 1963; Singh, 1989; Li, Chen, Zhang, & Swoboda, 2001; Fuenkajorn & Phueakphum, 2010). A ramp waveform is less damaging, whereas the square waveform is the most damaging (Zhenyu & Haihong, 1990; Bagde & Petroš 2005b, 2009). Since there is no clear standard for choosing dynamic testing parameters, it is recommended to consider roughly the half of static σ_{ci} of the rock for choosing the loading level and the seismic properties of the study area for choosing the frequency of the cyclic loads.

In the dynamic tests, the rock samples were firstly loaded under static conditions and then subjected to cyclic loads (unloading-reloading) for a predefined number of cycles. In other words, the tests were performed with partial cyclic loading during the loading path to reveal the fact that small dynamic oscillations on the big stress-strain curve change its slope with changing stress. Some of the samples failed before reaching the maximum predefined number of dynamic loading cycles while some of the samples having relatively higher strength failed much after the cycles ended.

In this study, clayey sandstone and clayey limestone samples were subjected to dynamic uniaxial and triaxial compression and dynamic shear box tests in the rock mechanics laboratory of TU Bergakademie Freiberg Institut Für Geotechnik. The dynamic testing parameters applied to the samples are presented in Table 5.15 and shown in Figure 5.38.

Table 5.15 The parameters used in dynamic tests

Type of Test	Frequency (Hz)	Loading levels	Amplitude	Dynamic strain/loading rate	Static strain rate	No of loading cycle
Uniaxial compression test	0.3	20-28 MPa	± 10 MPa	0.20 mm/s	0.05 mm/min	5 load levels with 50 cycles for each
Triaxial compression test	1.0	20-38 MPa	± 8.25 MPa	0.50 MPa/min	0.05 mm/min	10 load levels with 10 cycles for each
Shear box test	1.0	28-82 kN	± 18 kN	3 mm/min	3 mm/min	10 load levels with 120 cycles for each

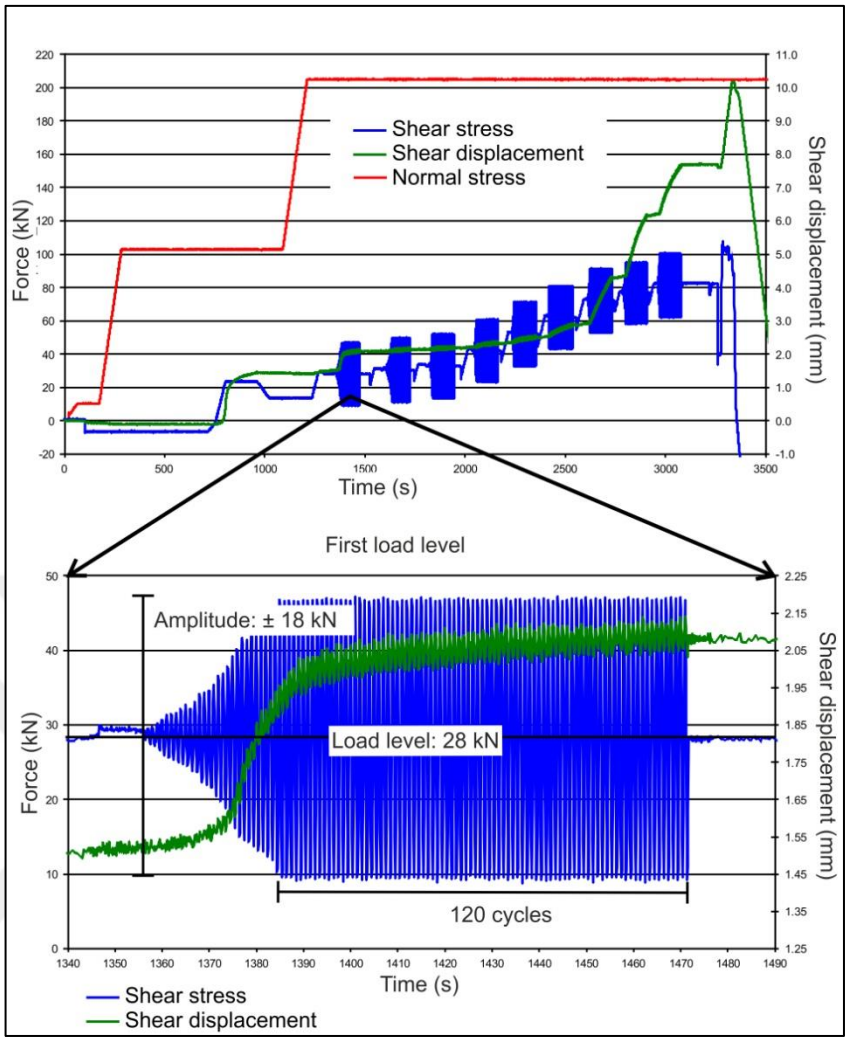


Figure 5.38 The representation of the cyclic loading parameters such as loading level, amplitude, and number loading cycles

5.3.1 Dynamic Uniaxial Compressive Strength Test

Several researchers argued that some of the materials become stronger and more brittle, while others become weaker and more ductile under dynamic loading (Attewell & Farmer, 1973; Stavrogin & Tarasov, 2001). These two cases are both reported in the literature (Table 5.16).

Table 5.16 Literature review of the comparison between dynamic and static uniaxial compressive strength and elastic modulus

Reference	Finding
Burdine (1963)	$\sigma_{dyn} = 0.74 \times \sigma_{st}$
Haimson & Kim (1972)	$\sigma_{dyn} = (0.50\text{-}0.77) \times \sigma_{st}$
Attewell &Farmer (1973)	$\sigma_{dyn} = (0.50\text{-}0.70) \times \sigma_{st}$
Singh (1989)	$\sigma_{dyn} = 0.87 \times \sigma_{st}$ $\sigma_{dyn} = 1.29 \times \sigma_{st}$
Ishizuka et al. (1990)	$\sigma_{dyn} = (0.35\text{-}0.85) \times \sigma_{st}$
Tien et al. (1990)	$\sigma_{dyn} = (1.18\text{-}2.85) \times \sigma_{st}$
Zhenyu & Haihong (1990)	$\sigma_{dyn} < \sigma_{st}$
Bagde & Petroš (2005c)	$\sigma_{dyn} = 0.70 \times \sigma_{st}$ $E_{dyn} = 0.80 \times E_{st}$
Fuenkajorn & Phueakphum (2010)	$\sigma_{dyn} = 0.70 \times \sigma_{st}$
Demirdağ et al. (2010)	$\sigma_{dyn} > \sigma_{st}$
Mohd Salim et al. (2013)	$\sigma_{dyn} = 0.70 \times \sigma_{st}$ σ_{dyn} (weathered) > σ_{dyn} (fresh)
Zou et al. (2016)	$\sigma_{dyn} = 3.8 \times \sigma_{st}$ $E_{dyn} = >3.8 \times E_{st}$

σ_{dyn}: Dynamic uniaxial compressive strength; E_{dyn}: Dynamic elastic modulus; σ_{st}: Static uniaxial compressive strength; E_{st}: Static elastic modulus

In this study, dynamic uniaxial compression strength tests were carried out to determine the dynamic behavior of the sandstone and clayey limestone samples having L/D ratios between 1.92 and 2.14. While four tests were performed under dry conditions, one test was under saturated conditions. Tira Test 28500 equipment with a loading frame, an axial loading system, and a data acquisition system was used. The axial cyclic load was applied in the sinusoidal waveform with a strain rate of 0.20 mm/s. The accuracy of the displacement transducers is 0.001 mm. The static σ_{ci} values of the same rock groups were used as a base for choosing the load levels. Five loading levels (20, 22, 24, 26, 28 MPa) approximately correspond to the 50 % of the static σ_{ci} with an amplitude of ±10 MPa were employed. The maximum predefined number of cycles is 250 (5 load levels with 50 cycles for each). The overall time for

cyclic loading is approximately 750 seconds. The test includes sequential static and cyclic loading until failure occurs.

For this reason, both the static and dynamic elastic modulus ($E_{avg\text{-}dyn}$) can be calculated on the same stress-strain graph of a sample. The average and secant elastic modulus (E_{avg}, E_{sec}) values were calculated. E_{sec} was calculated regarding 50% of the uniaxial compressive strength. On the other hand, the dynamic elastic modulus value was measured for each loading level, as illustrated in Figure 5.39. However, it was determined that the E_{dyn} is not significantly varying for different load levels.

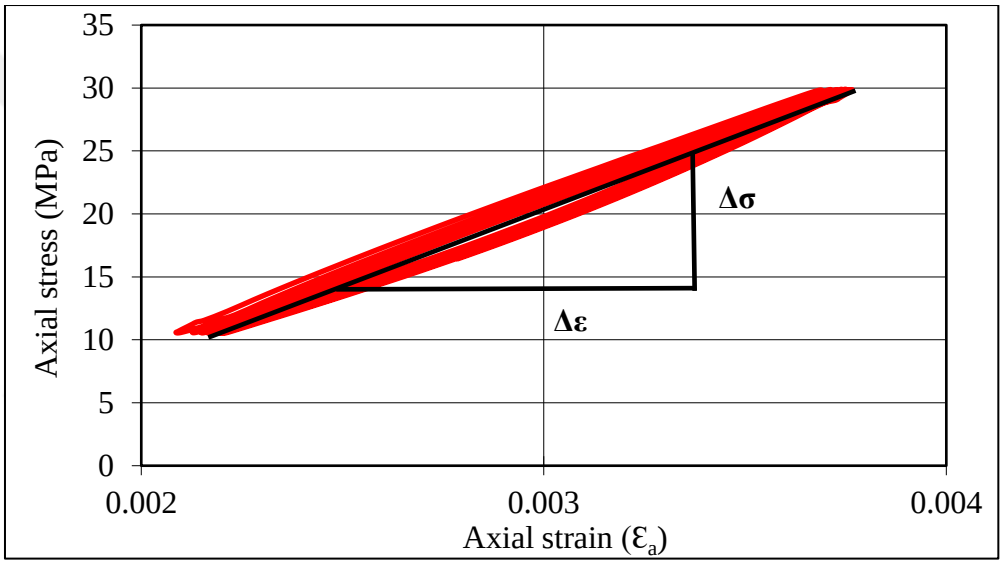


Figure 5.39 The procedure for calculating dynamic elastic modulus (E_{dyn}) of one loading level (20 MPa) on the stress-strain graph

The five stress-strain graphs were derived as given in Figure 5.40. The sandstone samples showed higher strength reduction in dynamic tests than clayey limestone samples. The uniaxial compressive strength of the sandstone samples reduced up to 34% under cyclic loading ($\sigma_{ci\text{-}dyn}$). On the other hand, dynamic elastic modulus values increased for both sandstone and clayey limestone samples. The rock samples exhibited strain hardening and a tendency for ductile behavior after cyclic loading. It can clearly be inferred that elastic modulus and Poisson's ratio increase in cyclic loading conditions, whereas the σ_{ci} commonly tends to decrease (Table 5.17). While the sample exhibits a high amount of CaO and a low amount of NaO_2, and FeO_2

(e.g., M-45, M-46) σ_{ci} tends to increase in cyclic loading. Besides, the high siliceous sand content also gives M-46 sample a higher strength. As the CaO content increases, the strength of the rock increases. However, strength is inversely proportional to the clay content. A similar finding was reported by Beyhan (2008) for marl samples. For this reason, the effect of loading level and the number of loading cycles on the dynamic strength become less notable.

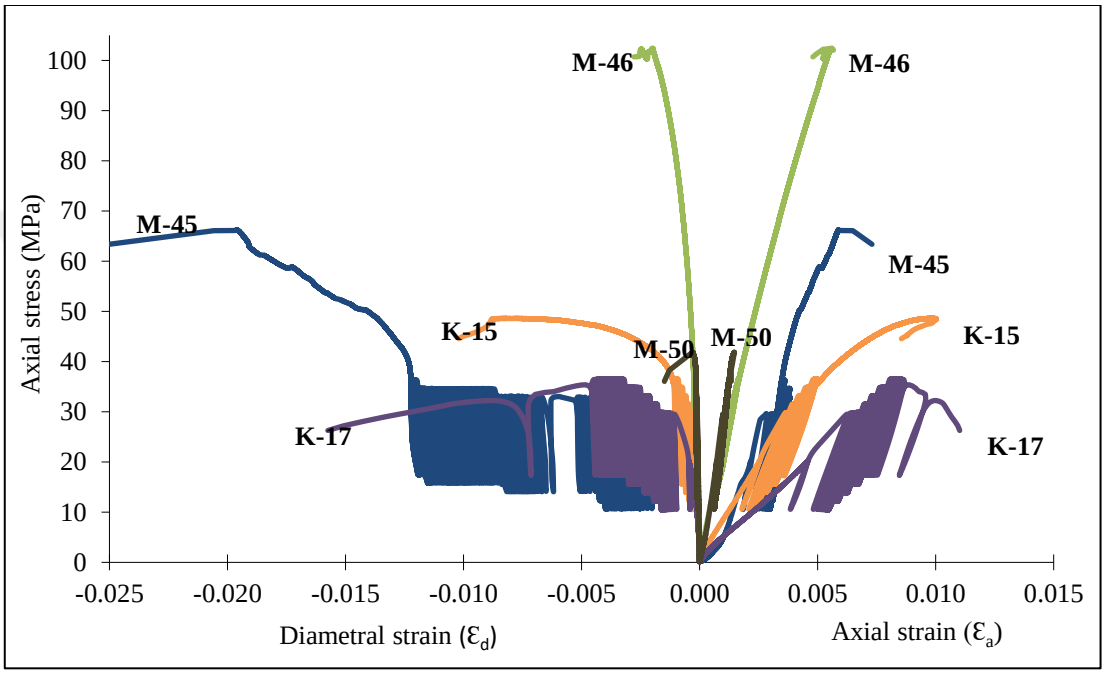


Figure 5.40 The cyclic stress-strain graphs of samples

Table 5.17 The results of the dynamic uniaxial compressive strength test of sandstone and clayey limestone samples

Sample ID	$\sigma_{ci\text{-}dyn}$ (MPa)	E_{avg} (GPa)	E_{sec} (GPa)	$E_{avg\text{-}dyn}$ (GPa)	υ_{dyn}
K-15	48.35	8.00	8.55	12.68	0.41
K-17	36.56	4.34	4.44	16.00	0.48
M-46	102.43	20.00	19.91	26.28	0.35
M-50	41.84	30.06	28.20	36.78	0.30
M-45 (saturated)	66.27	10.64	10.00	26.83	0.48

Deformability, like strength, depends mostly on the mineral composition, porosity, and the degree of fracturing of the rock material. However, it was found that elastic modulus is much more affected by cyclic loading than strength as found earlier by Zou et al. (2016). Interestingly, M-45 and K-17 samples gave a Poisson's ratio of approximately equal to rubber, which indicates that they gained a very ductile behavior. Bagde & Petroš (2005a) stated that lateral deformation develops faster than axial deformation during cyclic loading. Therefore, the higher lateral deformation makes the Poisson's ratio higher. Another reason for higher ductility for M-45 is assumed to be the water saturation, whereas the reason can be low-strength for the K-17 sample. It can be concluded that the more the sample is weak and/or water-saturated, the more gains ductility and strain hardening under cyclic loading. Mohd Salim et al. (2013) referred to the higher dynamic strength of weathered samples than the fresh ones to the high energy absorption capability of the altered minerals such as clay and feldspar minerals.

A considerable variation in strength and elastic properties is a result of the difference in mineralogy, porosity, and microstructure even in the same rock group. A similar finding was also reported by Bagde & Petroš (2009) and Beyhan (2008). In addition, the thin layers of clay within the specimens are interpreted to be responsible for the shape of the failure plane (Figure 5.41).



Figure 5.41 The image of the failure surface of the M-50 sample after the dynamic uniaxial compression test (Personal archive, 2014)

5.3.2 Dynamic Triaxial Compression Strength Test

Like the static loading condition, as the confining pressure increases, the compressive strength increases under dynamic loading conditions (Li, Zhao, & Li, 1999; Zhao, 2000; Liu & He, 2012). Mohr-Coulomb Criterion can estimate the dynamic triaxial strength under low confining stress, whereas Hoek-Brown Criterion is applicable for both low and high confining stresses. Hence the dynamic triaxial stress can be estimated by the equation given in Zhao (2000).

$$\sigma_{1\text{-dyn}} = \sigma_3 + \sigma_{st}\,(m\,\sigma_3 / \sigma_{st} + 1.0)^{0.5} \qquad (5.22)$$

where σ_{st} is the static uniaxial compressive strength of the intact rock and m is the Hoek-Brown constant, which can be derived from static triaxial tests or the charts proposed by Hoek, Kaiser, & Bawden (1995) or several quantitative methods.

Two levels of confining pressure (2 MPa and 5 MPa) were applied during axial cyclic loading at a 1.0 Hz frequency using an MTS-815 Rock and Concrete Test System (Figure 5.42).

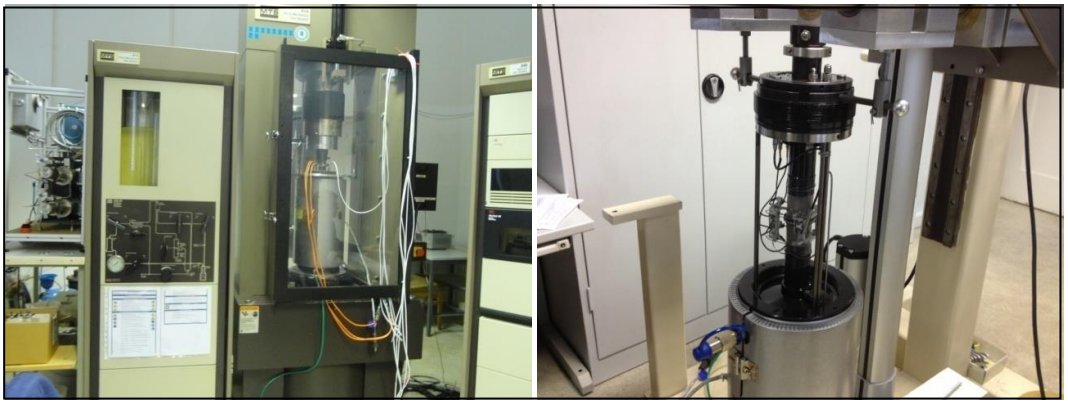


Figure 5.42 MTS-815 the triaxial compression test machine and the sample preparation for the test (Personal archive, 2014)

Ten loading levels (approx. 20, 22, 24…..,38 MPa), including ten cycles for each, were applied to the samples. The strain rate of 0.05 mm/min and loading rate of 0.5 MPa/min were applied during the static and dynamic portions of the test,

respectively. The test results of two saturated clayey limestone samples (M-44 and M-47) are given in Table 5.18.

Table 5.18 The results of dynamic triaxial compression tests

Sample ID	σ_3 (MPa)	Max. deviator stress ($\sigma_1 - \sigma_3$) (MPa)	E_{dyn} (MPa)	υ_{dyn}
M-44	5	35.89	2.45	0.29
M-47	2	52.85	17.21	0.21

E_{dyn}: elastic modulus under confining pressure; υ_{dyn}: Poisson's ratio under confining pressure; σ_3: confining pressure

M-44 sample failed after the 2nd cycle of the 8th loading level (82nd cycle). The stress-strain graph of the sample under 5 MPa confining stress is given in Figure 5.43.

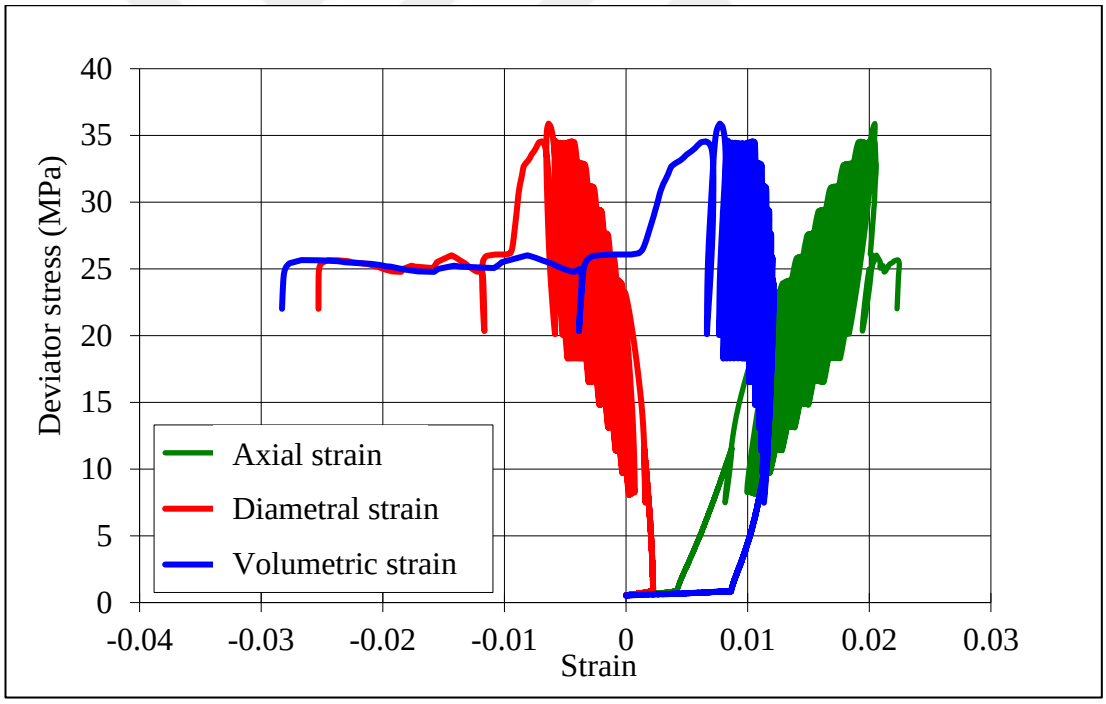


Figure 5.43 Stress-strain curves of triaxial test performed on M-44 sample with confining stress of 5 MPa

M-47 sample failed after cyclic loading ended and loaded additionally under static load for further 350 seconds. The stress-strain graph of the sample under 2 MPa

confining stress is given in Figure 5.44. As the confining stress decreased, axial and volumetric strains at failure also reduced.

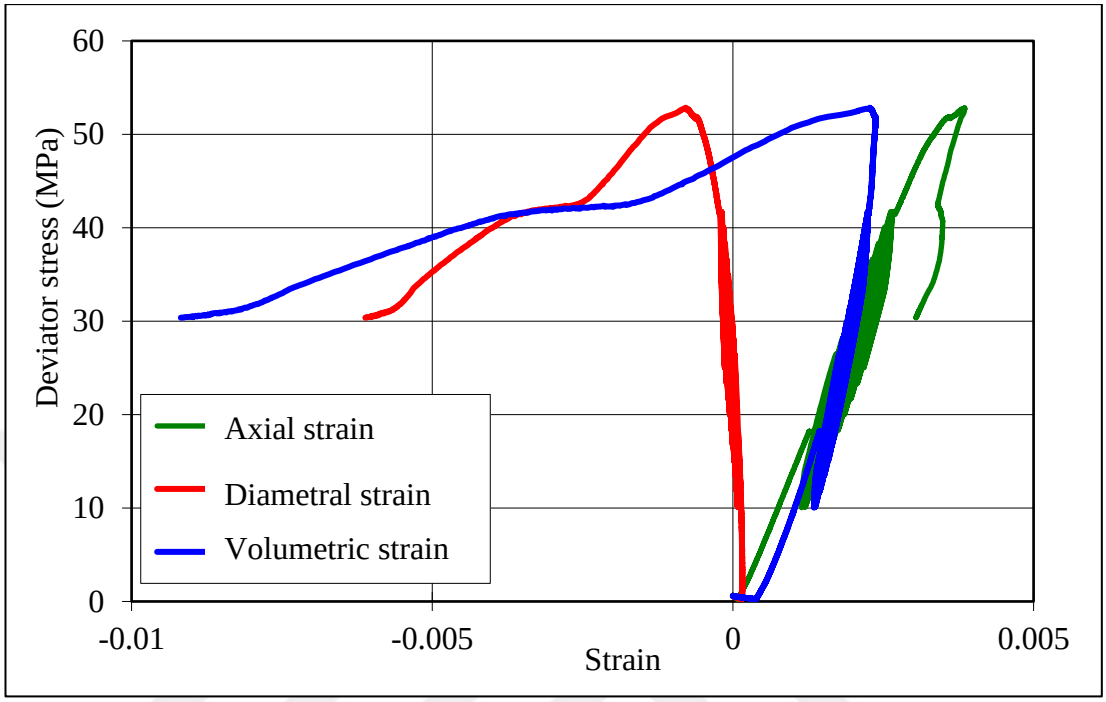


Figure 5.44 Stress-strain curves of triaxial test performed on M-47 sample with confining stress of 2 MPa

According to Equation 5.22, $\sigma_{1\text{-dyn}}$ for σ_3:2 MPa and σ_3:5 MPa were calculated as 50.32 MPa and 66.32 MPa, respectively. Although the test under 2 MPa yielded a well-harmonizing result with the empirical estimation of $\sigma_{1\text{-dyn}}$, the test under 5 MPa has yielded a very low σ_1 than the one obtained from the empirical equation. M-44 sample seems to fail following the thin clay layers (>1mm) and the M-47 sample has a less distinct failure surface (Figure 5.45). It was concluded that very weak rocks may fail before reaching the peak deviatoric stress value under high confining pressure as occurred in the M-44 sample. Another possible explanation is that the organic content of M-44 samples is higher than 5% (Table 3.4) which can significantly affect its mechanical characteristics.



Figure 5.45 The images of M-44 and M-47 after cyclic triaxial compression tests (Personal archive, 2014)

5.3.3 Dynamic Direct Shear Test

The deformation of jointed rock mass surrounding an excavation may result from dynamic loadings due to blasting or earthquake excitations (Nguyen, 2013). Therefore, the dynamic effects on jointed rock need to be evaluated. The shear behavior of joints under dynamic conditions have been studied by many researchers (Barla, Barbero, Scavia, & Zaninetti, 1990; Jing, Stephansson, & Nordlund, 1993; Ahola, Hsiung, & Kana, 1996; Barbero, Barla, & Zaninetti, 1996; Zhao, 2000; Lee, Park, Cho, & You, 2001; Jafari, Amini Hosseini, Pellet, Boulon, & Buzzi, 2003; Konietzky et al., 2012; Dang, Konietzky, & Frühwirt, 2016).

The GS-1000 apparatus was used to investigate the dynamic shear behavior of discontinuity surfaces. Firstly, it was aimed to find the appropriate loading condition for the test. In this context, the M-51 sample was tested under different frequencies, amplitudes, loading levels. The dynamic impulse was applied both on normal and shear loads.

Initially, the intact specimen was mounted in the testing machine. Static shearing at a constant normal load of 1 MPa was maintained until the intact specimen fails. Thus, a natural discontinuity surface is expected to be obtained. Afterward, sinusoidal cyclic loading with 1 Hz frequency was superimposed parallel to the shear direction with three different amplitudes of shear displacement (± 0.3, 0.15, 1.5 mm). The normal load was kept constant at 0.5 MPa during cyclic loading (Figure 5.46).

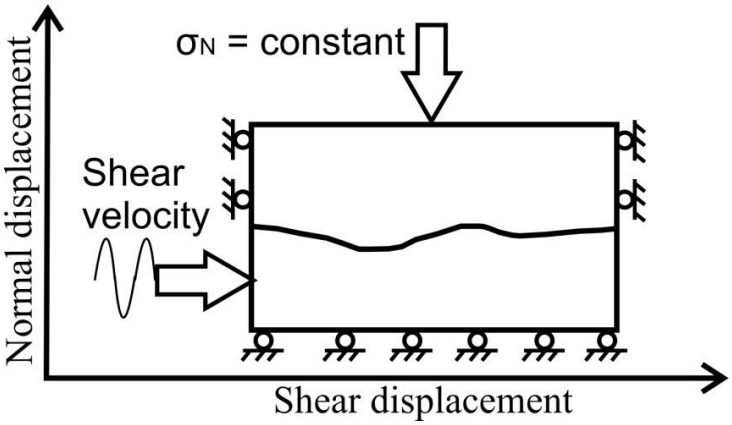


Figure 5.46 Dynamic shear test set up-1 as cyclic loading superimposed on the shear load

Dilation occurred at first cycles with 1 Hz frequency and amplitude of ± 0.3 mm and then contracted during cycles with 1 Hz frequency and amplitude of ± 1.5 mm (Figure 5.47). As the amplitude of the cyclic input increases, shear displacement sharply increases, which indicates the rapid degradation of surface roughness.

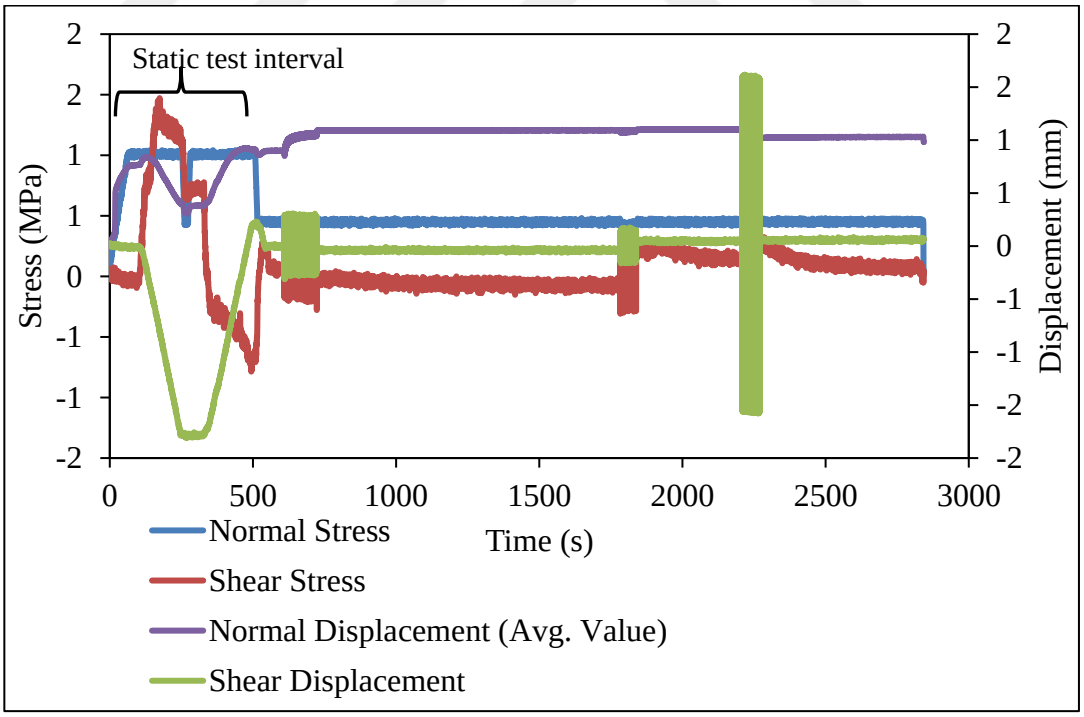


Figure 5.47 Complete stress-displacement-time graph of the M-51 by set up-1 showing various amplitudes of cycles

Secondly, the same sample was further examined under different cyclic loading conditions. This time, shear stress was kept constant at 5 MPa, and the normal stress was 15 MPa. Cyclic loading was superimposed on the normal load with an amplitude of ± 3 MPa (Figure 5.48).

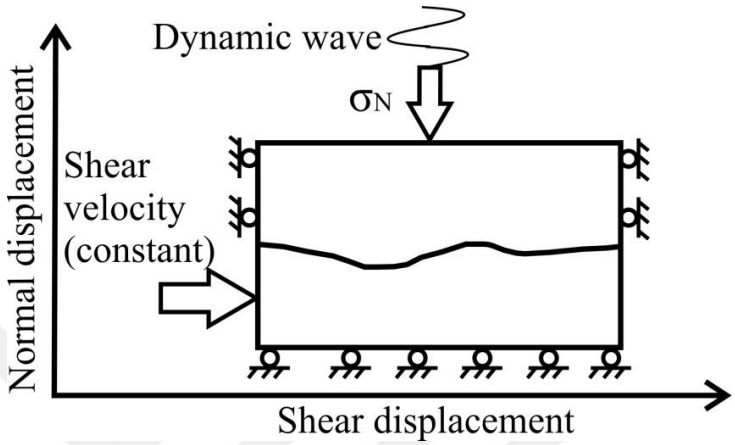


Figure 5.48 Dynamic shear test set up-2 as cyclic loading superimposed on the normal load

The normal loading level gradually reduced until a slip occurs during cycles. As a result, thirteen loading levels (15, 14.5, 14.0, 13.5,… 9.0 MPa) were achieved. On each loading level, various frequencies (20, 10, 5, 2, 1, 0.5, respectively) were applied (Figure 5.49).

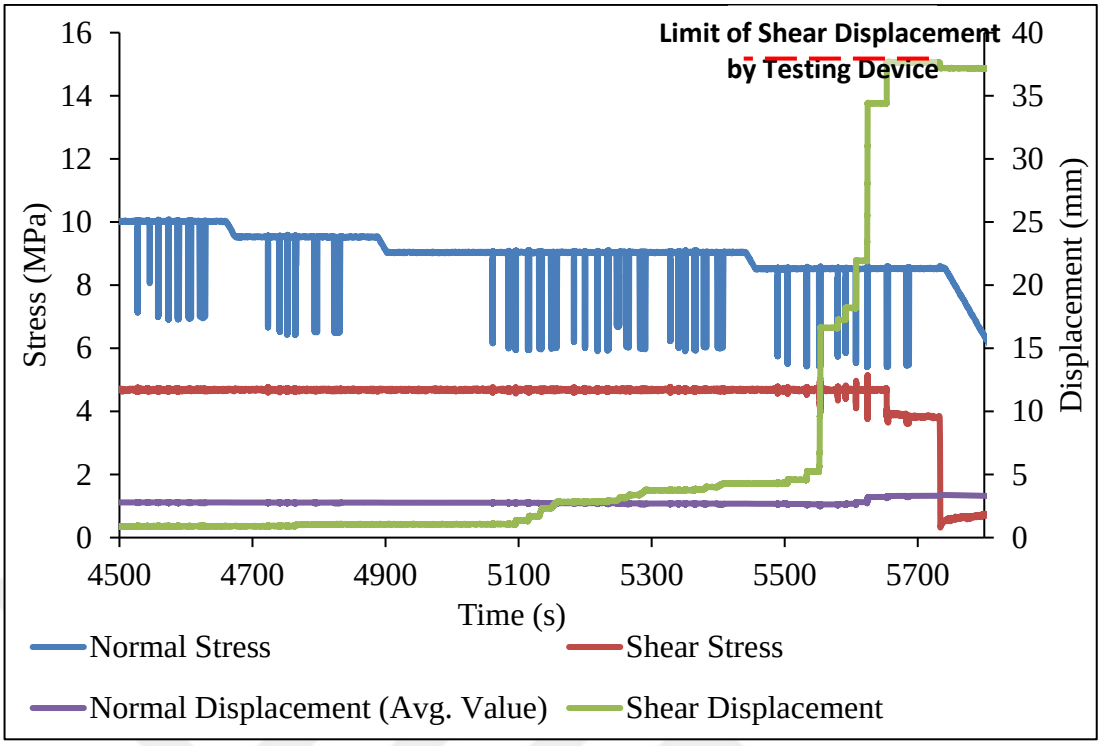


Figure 5.49 A portion of the stress-displacement-time graph of the M-51 by set up-2 showing different loading levels and frequencies of cycles

The initial dynamic loading cycles lead to compaction of the sample, and as the normal load is reduced gradually, the sample tended to dilate slightly (Figure 5.50).

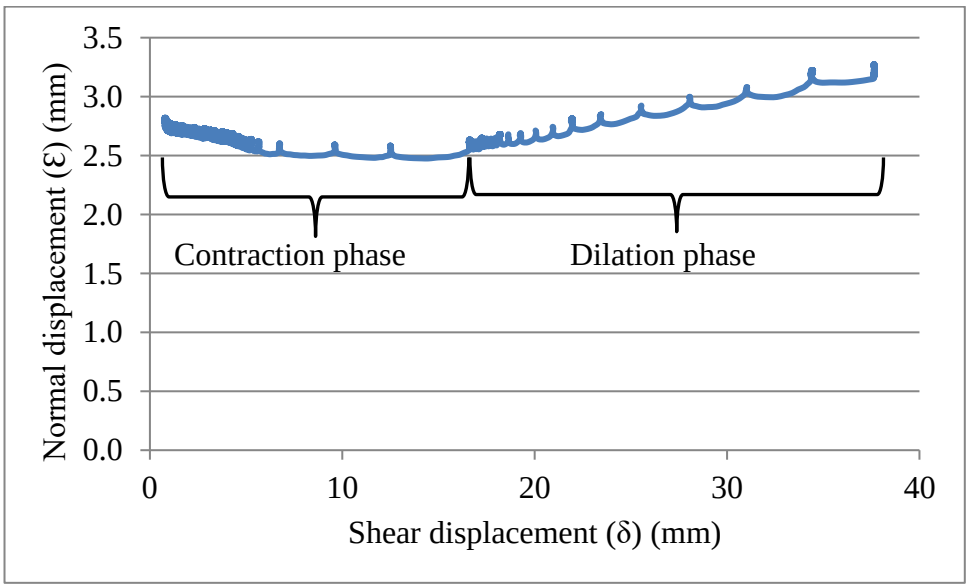


Figure 5.50 A portion of the normal displacement- shear displacement graph of the M-51 by set up-2 showing contraction and dilation during the early cycles

As the frequency decreased, shear displacement increased. On the other hand, as the loading level reduced, shear displacement decreased. Small oscillations in the shear stress curve indicated stick-slip movements as determined earlier by Dang et al. (2016). The joint stick-slip behavior leads to permanent deformation on the surface (Figure 5.51).

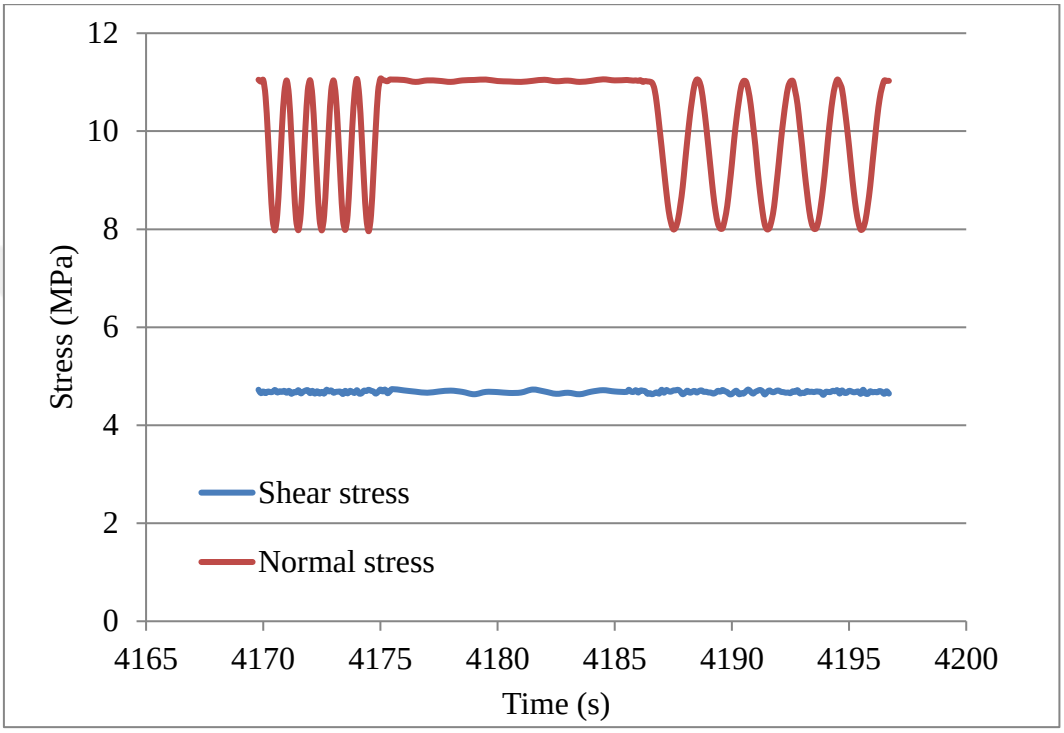


Figure 5.51 A portion of the stress-time graph of the M-51 by set up-2 showing small oscillations on the shear stress curve

According to the findings of the experimental test on the M-51 sample, the pre-sheared (under static conditions) saw-cut surfaces of M-2, 3, and 4 were again used for dynamic testing with the selected cyclic loading parameters. The cyclic loading was applied as a dynamic excitation in parallel to the applied shear stress, while constant normal stress of 5 and 10 MPa was simultaneously applied on the surface. The applied normal stress was maintained constant at 5 MPa for M-3 and M-4 samples and 10 MPa for the M-2 sample (Figures 5.52, 5.54, and 5.56). The amplitude of dynamic impulse on shear stress was ± 18kN with a 1 Hz frequency. The samples were subjected to dynamic loading at ten loading levels, each of which includes 120 cycles. As a result, the shear stress, shear displacement variations were

investigated. Since the surfaces are saw-cut, normal displacement (<1 mm) was ignored as under static loading.

At the point in time of about 1400 s, a dynamic impulse superimposed on the shear load with an amplitude of ± 18 kN to M-2 sample. The duration of the cyclic test phase was about 1763 s. During cyclic loading, the normal stress was constant at 10 MPa (Figure 5.52).

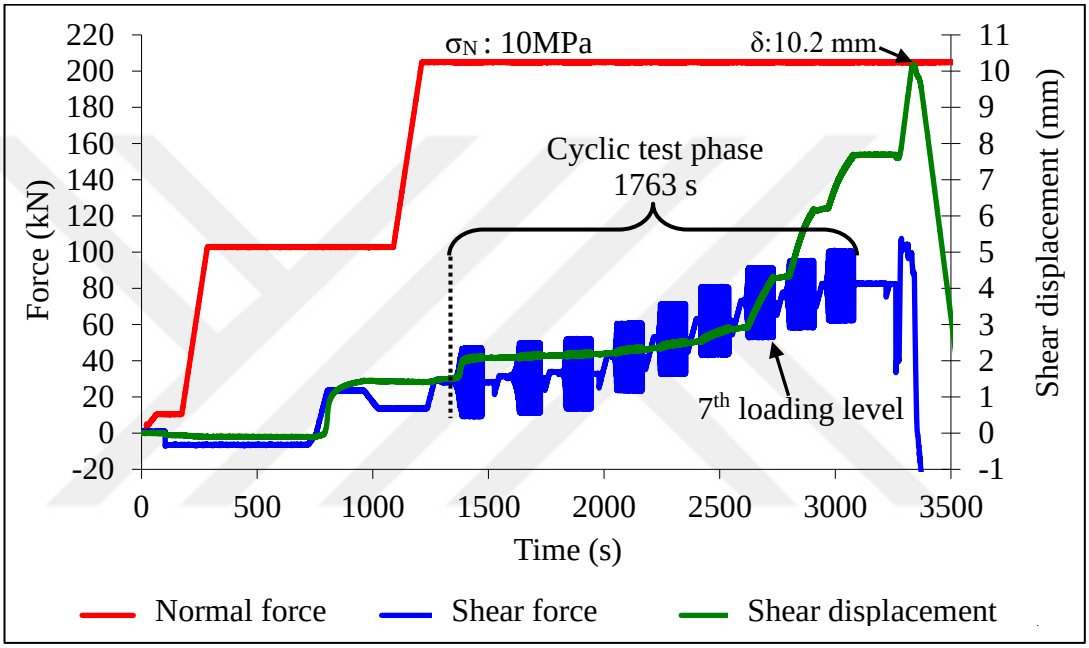


Figure 5.52 Complete force-shear displacement-time graph of M-2 sample subjected to dynamic loading

The increase in shear displacement is more pronounced at the beginning of dynamic loading then gradually stabilizes with continued cycling (Figure 5.53). However, the shear displacement again accelerates after the 70th cycle and continues until reaching the peak shear stress. The shear displacement at failure was measured as 10.2 mm. The specimen failed at the 9th loading level (approx. 90th cycle) of the cyclic loading. The loading levels were 28, 30, 32, 42, 52, 62, 72, 77, and 82 kN.

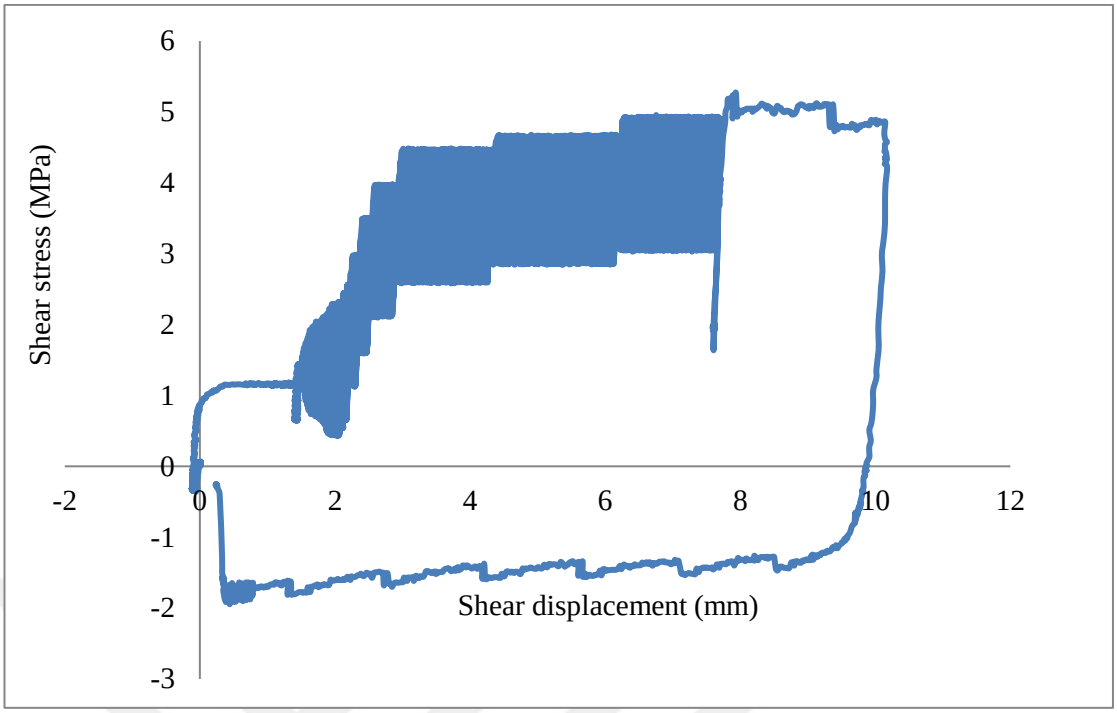


Figure 5.53 Shear stress-shear displacement graph of M-2 sample subjected to dynamic loading

At the point in time of about 630 s, a dynamic impulse superimposed on the shear load with an amplitude of ± 18 kN. The duration of the cyclic test phase was about 174 s. During cyclic loading, the normal stress was constant at 5 MPa (Figure 5.54).

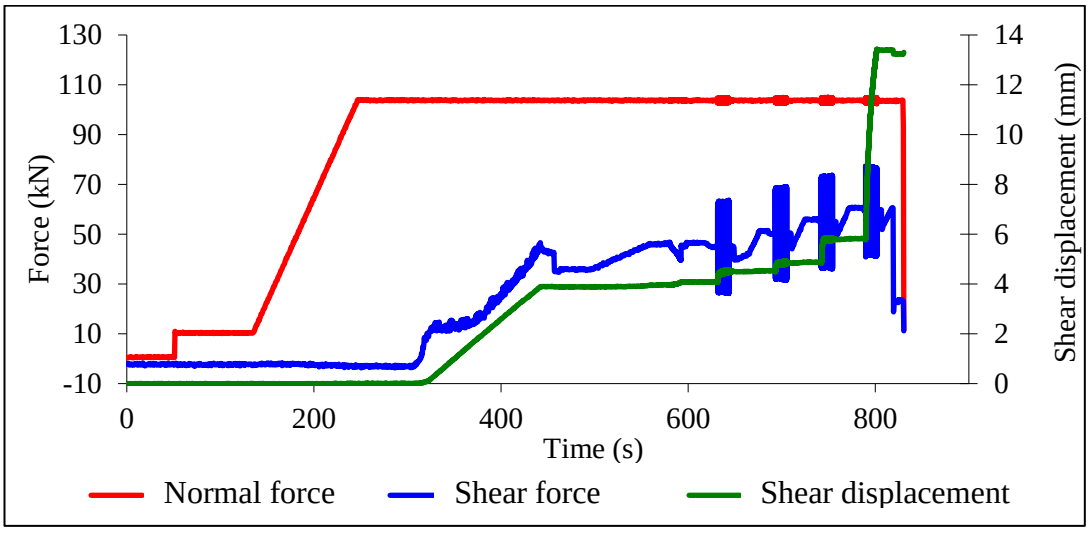


Figure 5.54 Complete force-shear displacement-time graph of M-3 sample subjected to dynamic loading

The shear displacement increased with the increasing shear stress and then stabilized before cyclic loading. As the cyclic loading started, the shear displacement again accelerated and increased with nearly constant shear stress. The shear displacement at failure was measured as 13.3 mm (Figure 5.55). The specimen failed at the 4th loading level (approx. 40th cycle) of the cyclic loading. The loading levels were 45, 50, 55, and 60 kN.

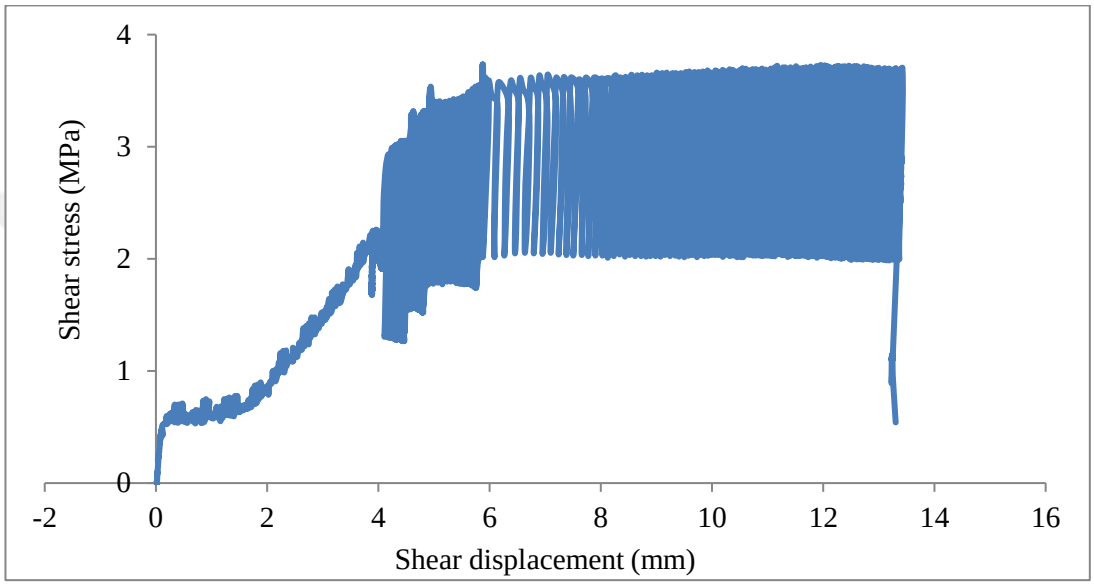


Figure 5.55 Shear stress-shear displacement graph of M-3 sample subjected to dynamic loading

At the point in time of about 671 s, a dynamic impulse superimposed on the shear load with an amplitude of ± 18 kN. The duration of the dynamic test phase was about 190 s. During cyclic loading, the normal stress was constant at 5 MPa (Figure 5.56).

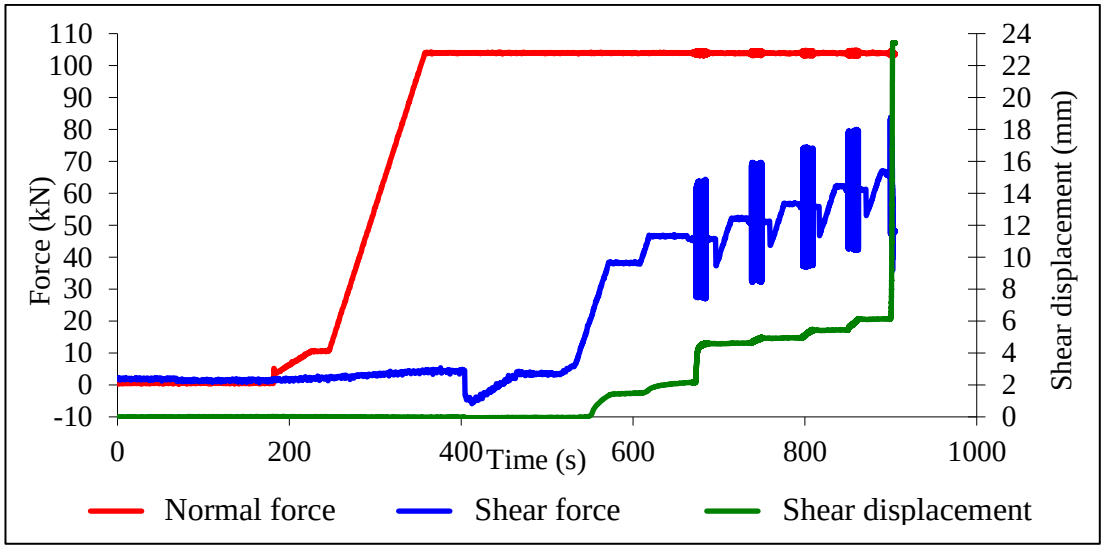


Figure 5.56 Complete force-shear displacement-time graph of M-4 sample subjected to dynamic loading

A sharp increase in shear displacement at the initial loading cycles was determined. Then shear displacement increased with the increasing loading cycles. The specimen failed at the 5th loading level (approx. 50th cycle) of the cyclic loading. During the last loading level, shear displacement rapidly increased and reached 23.4 mm (Figure 5.57). The loading levels were 45, 50, 55, 60, and 65 kN.

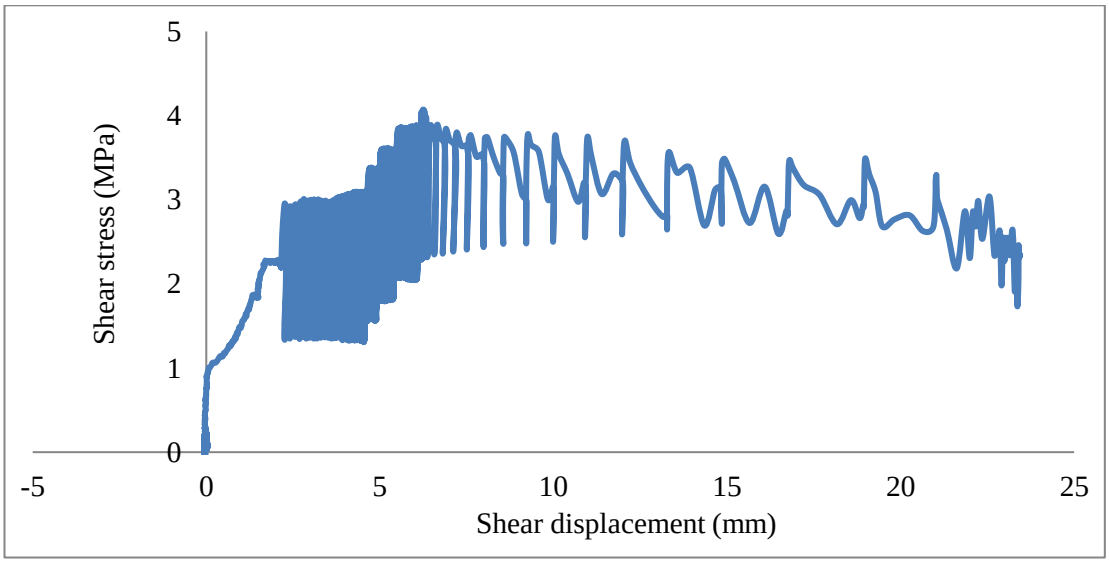


Figure 5.57 Shear stress-shear displacement graph of M-4 sample subjected to dynamic loading

The first four cycles applied to the M-2 sample are illustrated in Figure 5.58. Figure 5.58 indicates that the peak shear stress among the cycles does not change

significantly; however, the ongoing cycles mainly affect the amount of shear displacement.

The peak dynamic friction angle (ϕ_{dyn}) was calculated based on the ratio between peak shear and normal stresses.

$$\phi_{dyn} = \arctan (\tau / \sigma_N') \quad (5.23)$$

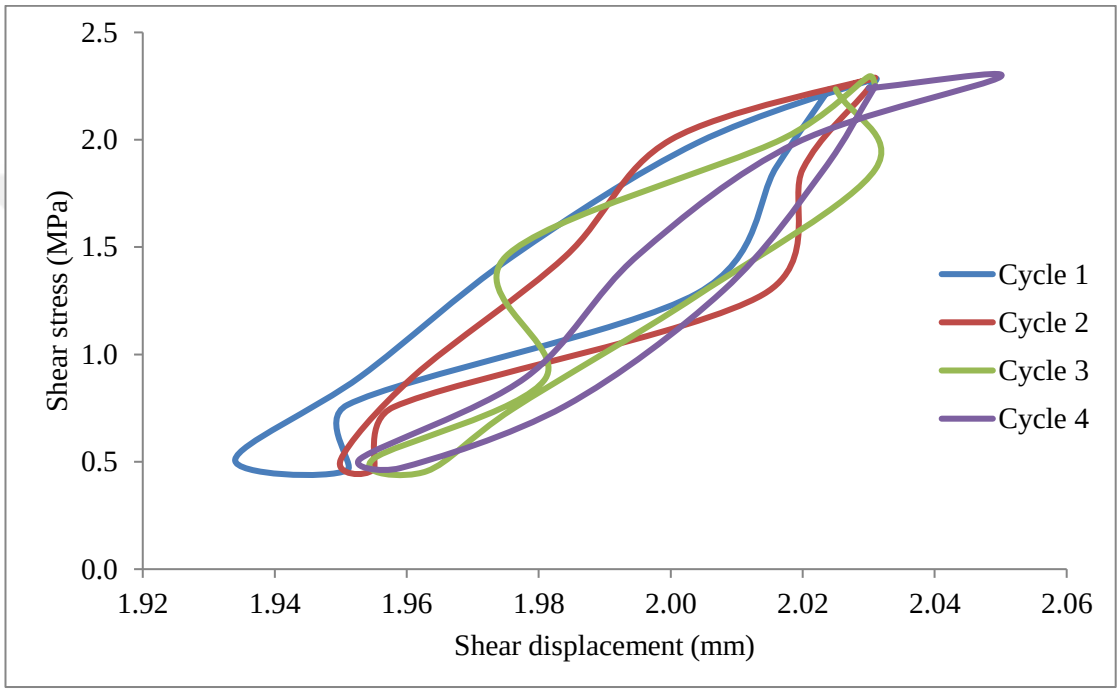


Figure 5.58 Shear stress-shear displacement graph showing the first 4 cycles of the dynamic excitation of M-2 specimen under 10 MPa normal stress (amplitude of the cyclic load: ±18 kN, loading level: 62 kN~ 1.37 MPa)

In this study, each sample was first subjected to a static shear test to determine the static shear strength, and then the dynamic tests were performed on the same surfaces. As normal stress increases, the dynamic effect on the samples reduces. For this reason, the M-2 sample loaded by normal stress of 10 MPa, the dynamic shear strength (τ_{dyn}) of M-2 decreased by 14.2%. The peak shear strength was unchanged for the M-3 sample and increased 7.1% for the M-4 sample relative to static shear strength (τ_{st}) (Table 5.19). Nguyen (2013) also reported that the dynamic peak shear stress is approximately 30% higher than the static one for rough schistose rock surfaces. Barla et al. (1990) and Barbero et al. (1996) have studied saw-cut samples

under static and dynamic conditions. They also found that the dynamic shear strength is greater than the static shear strength. They mainly refer this finding to the higher shear stress rate being applied. Barla et al. (1990) revealed that the dynamic shear strength is highly dependent on the strain rate, particularly at low normal stresses. Barbero et al. (1996) also noted that the ratio of dynamic to static shear strength becomes closer to unity as the mobilized strength increases. As all the samples have an initial mobilized strength, the ratio of dynamic to static shear strength (τ_{dyn}/τ_{st}) becomes closer to unity (M-3, M-4). Mobilized shear strength indicates the level of shear stress applied in static conditions to the saw-cut surface prior to the onset of dynamic shear displacement. On the other hand, the static base friction angle (ϕ_{st}) value of M-2 decreased as 17.27%, and ϕ_{st} value of M-3 and M-4 value increased by 4.2% and 10.73%, respectively, under dynamic loading. It was inferred from Table 5.19 that the shear strength is not significantly affected by cyclic loading while the effect of cyclic loading on ϕ is more pronounced. It is possible that the M-2 sample is slightly strong (JCS: 72.95 MPa) than the other samples which enabled a more significant change in ϕ. It can also be said that the higher normal stress during cyclic loading leads to a significant reduction in ϕ, while leads to a slight increase under 5 MPa. On the other hand, the most explicit finding is that the shear displacement was considerably increased for both samples under dynamic conditions.

Table 5.19 Dynamic shear test results

Sample ID	σ_N (MPa)	k_s (MPa/m)	τ_{dyn} (MPa)	τ_{dyn}/τ_{st}	Shear displacement (mm)	ϕ_{dyn} (°)
M-2	10	659.33	5.27	0.86	10.2	27.92
M-3	5	634.35	3.73	1	13.3	36.72
M-4	5	651.41	4.07	1.07	23.4	39.40

The Mohr-Coulomb empirical assumption for estimating the dynamic peak shear strength was compared with the dynamic shear test results. As the static shear tests were performed on the same surfaces prior to the dynamic shear tests, the JRC is reduced to 0 for estimating dynamic shear strength (Figure 5.59). It should be noted

that Barton&Choubey's shear strength model with JRC=0 corresponds to Mohr-Coulomb Failure Criterion. It is evident from Figure 5.59 that Mohr-Coulomb's empirical assumption fits the laboratory test results well.

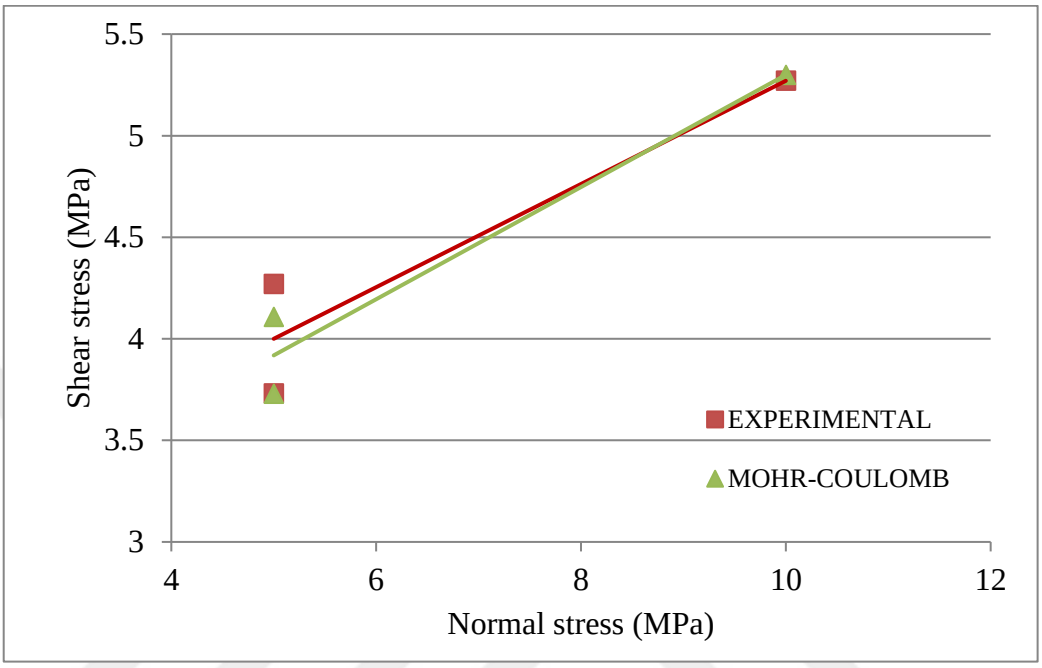


Figure 5.59 The comparison of average failure envelopes for 3 samples obtained from the shear test, and the empirical Mohr-Coulomb approach for dynamic loading

CHAPTER SIX
ROCK MASS CLASSIFICATION

The laboratory intact rock characteristics significantly differ from the in-situ rock characteristics due to the structural differences and scale factors. The main reason for using the rock mass classifications is to estimate the in-situ rock behavior. Bell (1992) defines rock mass classification schemes as a quantitative tool to rock engineering problems. The first steps of engineering classification of rock masses were started with Terzaghi (1946), and subsequently, Wickham, Tiedemann, & Skinner (1972), Bieniawski (1973) and Barton, Lien, & Lunde (1974), Hoek & Brown (1980) proposed classifications for jointed rock masses based on the several properties of both intact rock and rock mass. Their objective was to obtain rock mass ratings that can be practically used for design purposes.

More recently, the Geological Strength Index (GSI) was introduced into the Hoek-Brown Criterion by Hoek et al. (1995). GSI has gained great attention. It was revisited by its authors and other researchers and revisions were made (Hoek, Carranza-Torres, & Corkum, 2002; Sönmez & Ulusay, 1999, 2002; Cai, Kaiser, Uno, Tasaka, & Minami, 2004; Russo, 2009; Osgoui, Ulusay, & Ünal, 2010; Hoek, Carter, & Diederichs, 2013; Vásárhelyi & Bögöly, 2019). For this reason, GSI is the most widely used rock mass classification, principally for slope stability problems. The original GSI chart is based on the descriptive categories of rock mass structure (interlockness degree of the rock blocks) and the discontinuity surface conditions (infilling, roughness, weathering degree). It has a rating interval of 10 to 85 and it is used in the Hoek-Brown Failure Criterion as a parameter to estimate the rock mass strength. Its authors always mention that unless the GSI is well understood and applied correctly, the reliability of the estimated rock mass properties will be questionable. They also do not recommend using the GSI system to the rock masses in which there is a clearly defined dominant structural orientation. Hoek & Brown (2019) illustrated the size effects in rock mass characterization and the validity of the utilization of GSI (Figure 6.1).

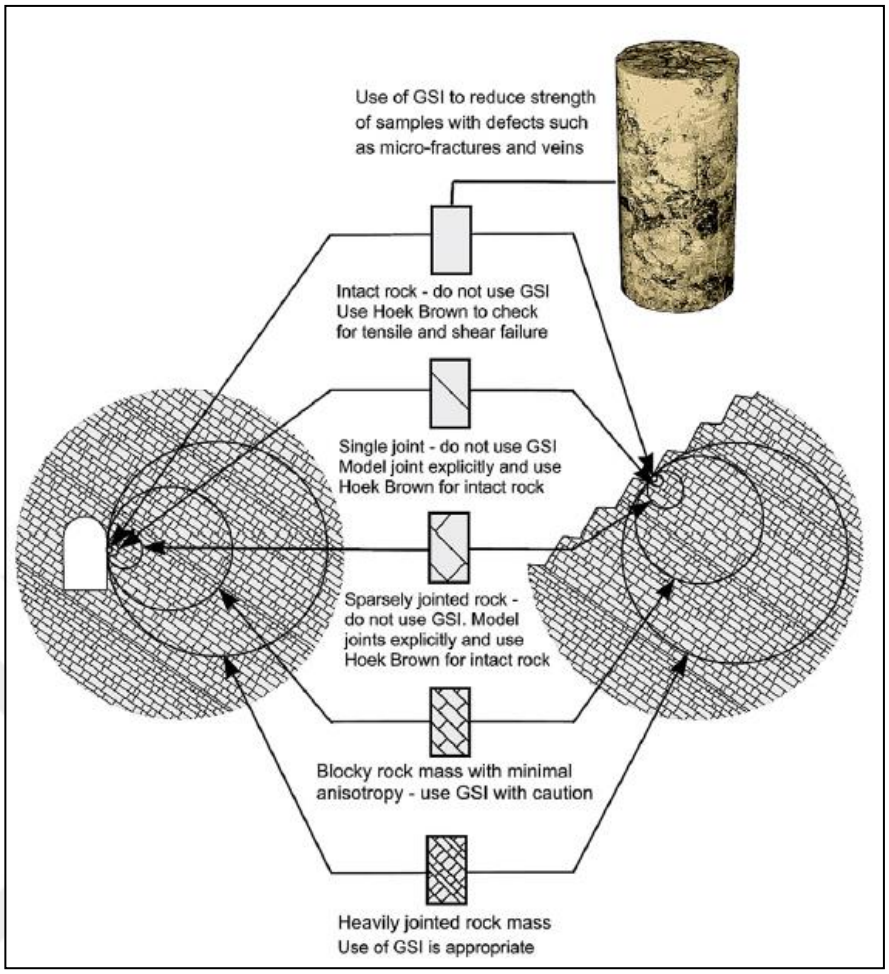


Figure 6.1 Size effects on the utilization of GSI (Hoek & Brown, 2019)

As it is, GSI was reworked by many researchers for different rock masses, and different quantitative methods to obtain a GSI rating were proposed. Several researchers have also compared these quantitative GSI methods (Thomas, Ayemin, & Neilsen, 2015; Vásárhelyi, Somodi, Krupa, & Kovács, 2016; Somodi, Krupa, Kovács, & Vásárhelyi, 2018). They found that there are significant differences between GSI ratings obtained from different methods.

In this study, the rock mass exposed in the reservoir area of a planned Çağlayan Dam is partly unconsolidated, folded, faulted, and fractured Neogene clastic and carbonate sedimentary rocks. As a consequence, the poor rock mass, which is highly disintegrated (Zone I) were classified according to Osgoui et al. (2010). On the other hand, the densely lithified, relatively stronger rocks with a significant number of fractures were classified according to Cai et al. (2004), Russo (2009), Hoek et al.

(2013), and Vásárhelyi & Bögöly (2019). Hence, different quantitative aspects were considered in determining the GSI value. Afterward, the revisions of Sönmez & Ulusay (1999) and Sönmez & Ulusay (2002) made to the Generalized Hoek-Brown Failure Criterion (Hoek et al. 2002) to determine the rock mass properties such as m_b, s, and a.

6.1 Various Approaches for Quantitative GSI Rating

Somodi et al. (2018) found that the difference between the GSI values determined from different methods decreases in the case of better rock mass quality and increases in the case of lower GSI values. They also noted that other rock mass classification systems do not work sufficiently in weak rock masses (GSI < 35). Hence, this deficiency brings some uncertainty to the rock mass classifications. Similarly, Budetta, & Nappi (2011) explained that as the heterogeneity increases such as the presence of frequent alternations of hard and weak strata, it poses uncertainties to the GSI. They suggested using a range of GSI values representing the rock mass rather than a single value. Marinos & Carter (2018) also stated that in tectonic areas, GSI values might be considerably reduced, due to the intense fracturing in rock mass which frequently behaves in a more ductile manner (e.g., mudstones, shales, or siltstones). Zhai, Canbulat, Hebblewhite, & Zhang (2017) emphasized being cautious of using empirical approaches for low strength, young sedimentary rocks which are frequently poorly lithified (σ_{ci}: 0.5-25 MPa). They subdivided weak rock mass into three categories as 1) low strength rock mass 2) highly fractured decomposed rock mass 3) tectonically disturbed rock mass. As the low strength rock mass (young sedimentary rocks) is expected to behave close to intact rock if the intact rock strength is low enough, the GSI system is likely to underestimate the rock mass strength. Osgoui et al. (2010) brought that case a step further and proposed a method to quantify the poor and very poor rock masses in the GSI system. Vásárhelyi et al. (2016) concluded that there is no exact method for estimating GSI value; thus, a visual judgment by an experienced engineering geologist is the best way to solve rock engineering problems.

A quantitative GSI chart proposed by Sönmez & Ulusay (2002) was firstly applied in this study. It is based on the surface condition rating (SCR), and structure rating (SR). These parameters can be calculated by the equations below;

$$SR: -17.5 \times \ln(J_v) + 79.8 \quad (6.1)$$

where J_v is the volumetric joint count.

$$SCR: R_r + R_w + R_f \quad (6.2)$$

where R_r, R_w, and R_f are the roughness rating, weathering rating, and infilling rating, respectively. The ratings of these surface condition properties are similar to the ratings of the RMR system (Bieniawski, 1989). The corresponding GSI value can be defined on the chart (Figure 6.2)

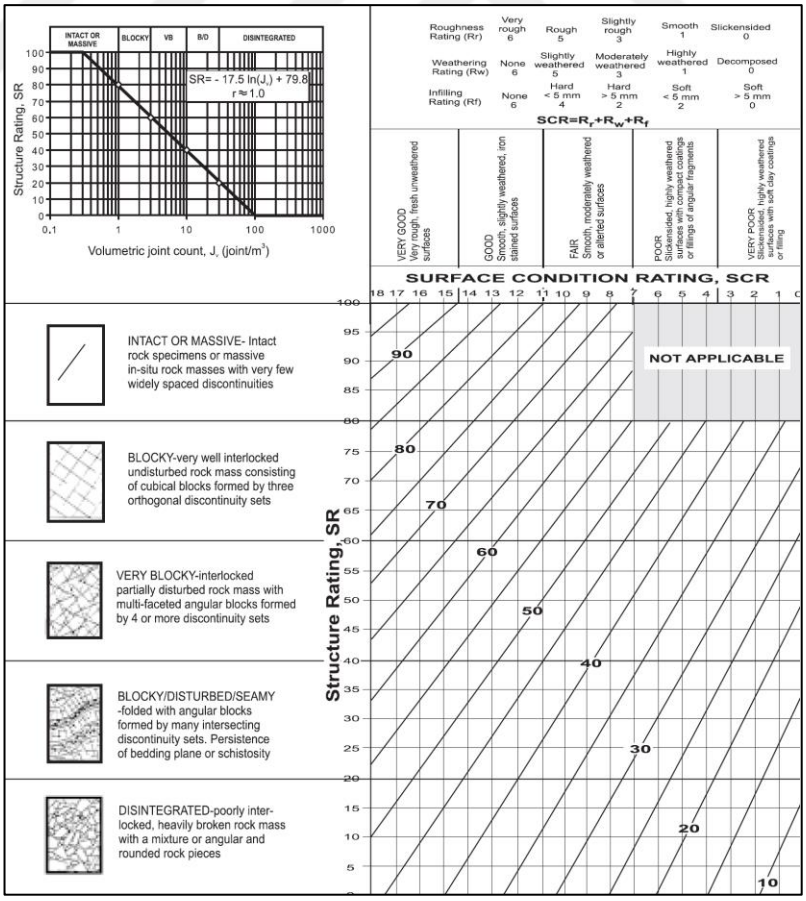


Figure 6.2 Quantitative GSI chart proposed by Sönmez & Ulusay (2002)

Osgoui et al. (2010) and Sönmez & Ulusay (2002) have SR in common; however, SR is estimated with the different empirical equation given below;

$$SR: -15.58 \ln (Jv) + 74.62 \quad (6.3)$$

Osgoui et al. (2010) added a qualitative parameter BSTR (broken structural domain), quantitative parameters as Ijc (joint condition index) instead of SCR, and ICR (intact rock recovery). They defined ICR as the ratio of the total length of cylindrical cores having length greater than 2 cm to the length of the core-run. ICR fits well with the qualitative assessment of BSTR. They recommend using their modified GSI for poor and very poor rock masses that have a GSI rating lower than 27, otherwise, they recommend using the above-mentioned other quantifications (Figure 6.3). They excluded RQD from the system since RQD in very poor rock is mostly zero or hard to estimate.

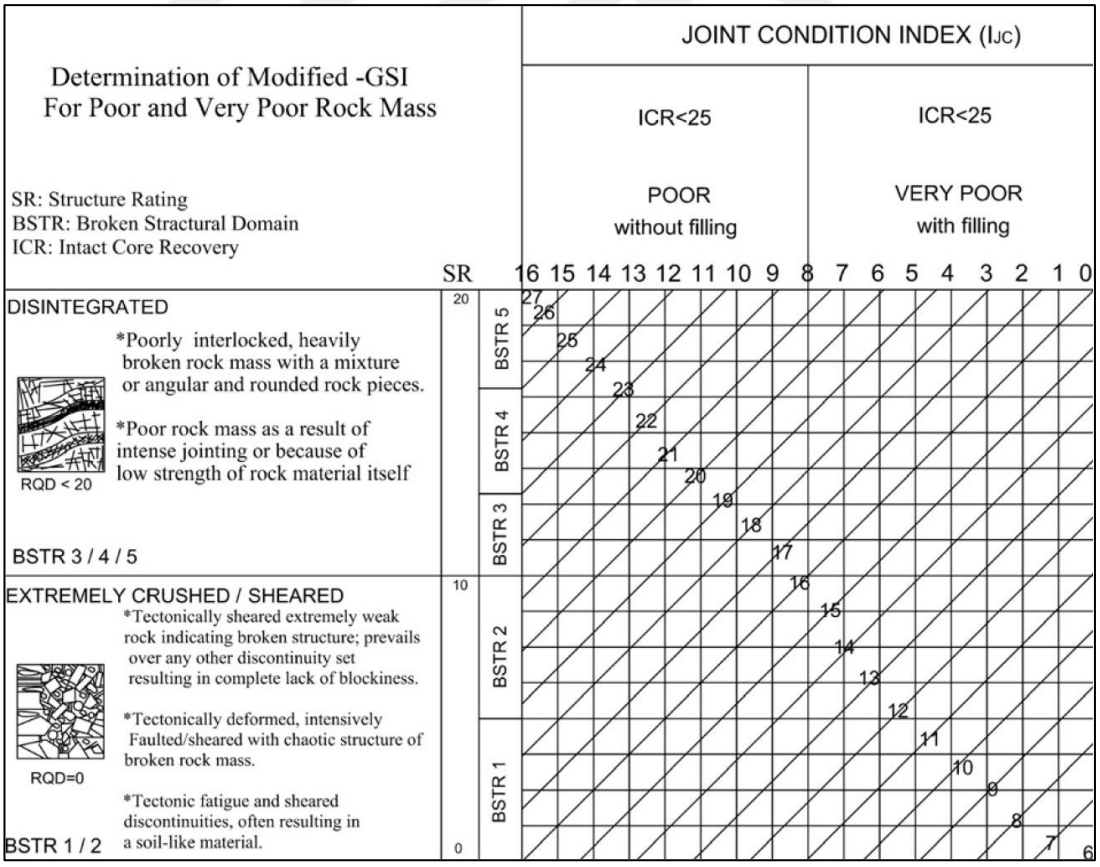


Figure 6.3 Quantitative GSI chart for poor and very poor rock masses proposed by Osgoui et al. (2010)

$$I_{JC} = (bs) + (W/2) + 4 \quad (6.4)$$

where bs is rated based on the BSTR class of the core rock pieces, W is the weathering degree and defined qualitatively, according to ISRM (2007).

The BSTR classifications were made on drill cores of the weak rock to Neogene rock transition considering the instructions suggested by Osgoui et al. (2010). A representative example is given in Figure 6.4.

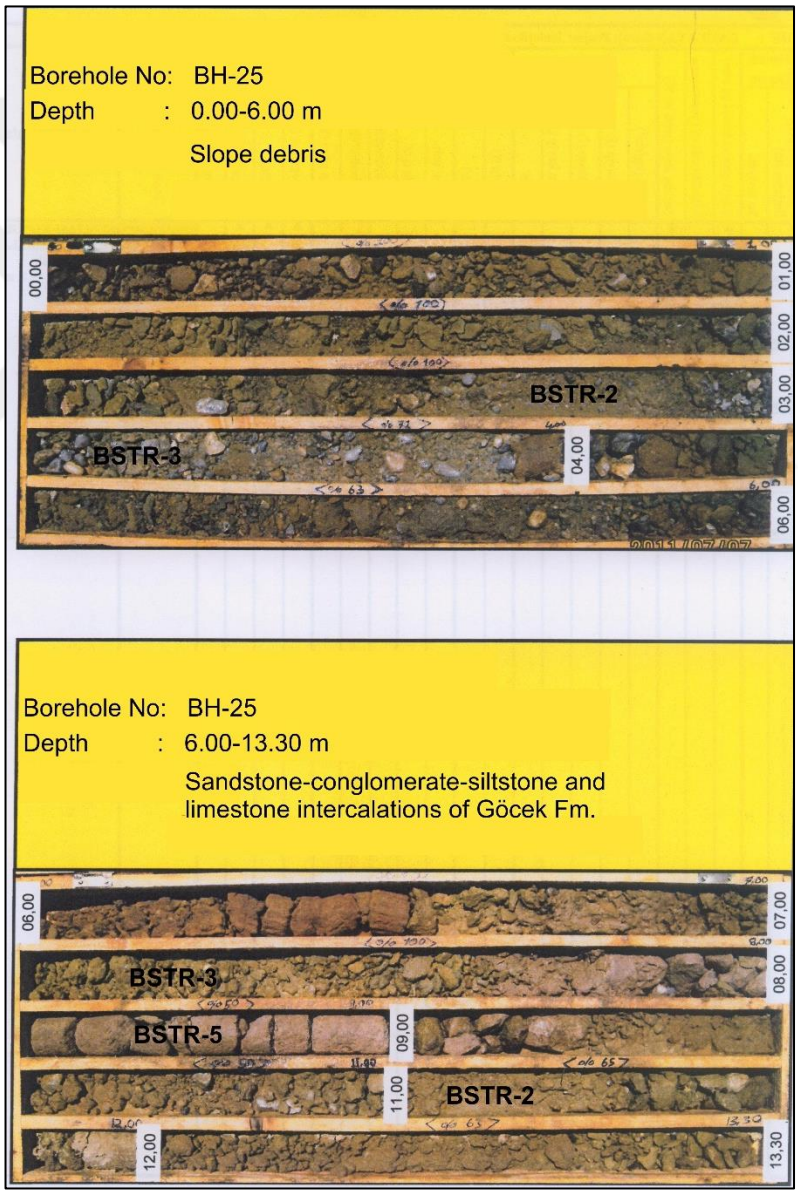


Figure 6.4 Classification of the drill cores of weak/disintegrated rock and Göcek Fm. based on the BSTR (Personal archive, 2012)

Cai et al. (2004) reported that the cohesion, internal friction angle, and elastic modulus of the rock mass calculated using the GSI rating by the way they proposed are in good agreement with the in-situ measured data. They suggest calculating GSI as given in Equation.

$$GSI = \frac{26.5 + 8.79lnjC + 0.9lnV_b}{1 + 0.015lnjC - 0.0253lnV_b} \quad (6.5)$$

where jC is the joint condition factor (dimensionless), V_b is the block volume in cm^3. jC can be defined as given in Equation 6.6.

$$jC = \frac{jW\ x\ jS}{jA} \quad (6.6)$$

where jW is the rating for waviness, jS is the rating for smoothness, and jA is the joint alteration factor. Both of them were chosen from the charts proposed by Palmström (1995). Solely, jL is assumed to be one. For this reason, this quantitative GSI approach may slightly overestimate if the joint length is classified as discontinuous or if the joint is less persistent.

The quantitative GSI chart based on jC and block volume proposed by Cai et al. (2004) is given in Figure 6.5.

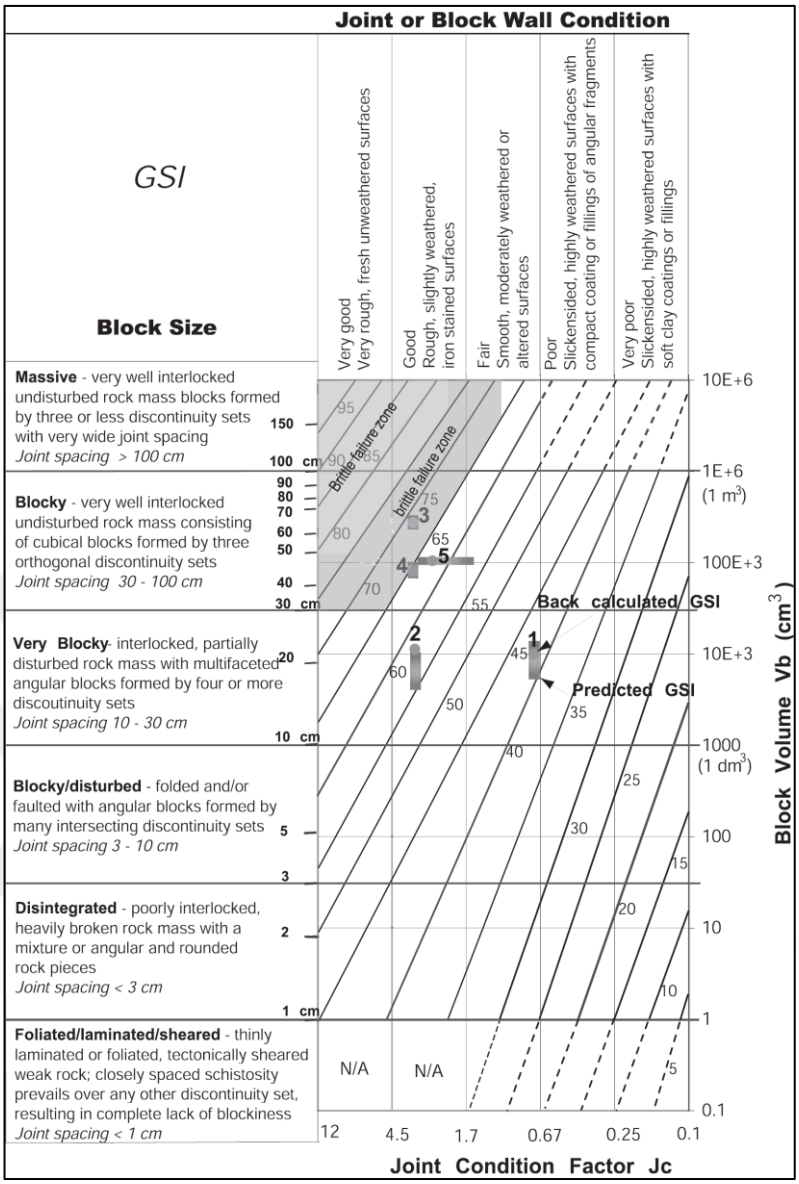


Figure 6.5 Quantitative GSI chart proposed by Cai et al. (2004)

Russo (2009) argues that the integration of GSI to RMi (Palmström, 1995) is a promising way to estimate GSI rating (Eq). Since the original GSI chart accounts for the interlockness degree of the rock blocks, the elementary block volume does not necessarily cause a change in the assigned GSI rating. However, the ratio of block volume to the engineering opening is an important parameter. Thus, Russo (2009) uses block volume in the proposed quantification.

$$GSI = 153 - \frac{165}{1 + \frac{jP}{0.19}^{0.44}} \quad (6.7)$$

where jP is the jointing parameter and can be found as;

$$jP = 0.2jC^{0.5}V_b^{D} \tag{6.8}$$

where V_b is block volume and coefficient D can be derived as;

$$D= 0.37\ jC^{-0.2} \tag{6.9}$$

where jC is the joint condition factor used in RMi classification and the value of D depends on the factor of jC in this method (Figure 6.6). Russo (2009) explained that jL might play an important role in avoiding too cautious assumptions about jC, and the simplified assumption jL = 1, which was made by Cai et al. (2004) is not realistic for some cases. Even though Russo (2009) provides a better estimation of rock mass class, block volume has a significant effect on the calculated GSI value. For this reason, block volume should be precisely estimated.

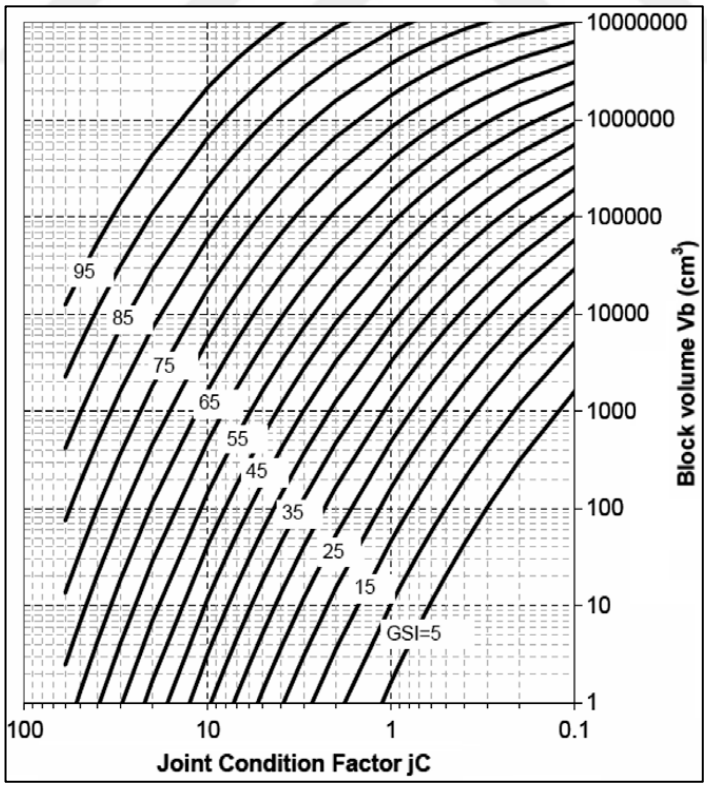


Figure 6.6 Quantitative GSI chart proposed by Russo (2009)

Hoek et al. (2013) proposed two quantitative methods to estimate the GSI rating. Even though they found that RQD is out of date and questionable from different aspects, due to the ongoing popularity of RQD, they proposed Equation 6.10.

$$GSI = 1.5\ J_{cond89} + 0.5RQD \tag{6.10}$$

where J_{cond89} is the joint condition factor rated in the rock mass rating system (RMR) (Bieniawski, 1989). In the second equation, J_r and J_a parameters from Q system (Barton et al. 1974) are used as an alternative to J_{cond89}.

$$GSI = \frac{52(\frac{J_r}{J_a})}{1+(\frac{J_r}{J_a})} + 0.5RQD \tag{6.11}$$

One limitation of Hoek et al. (2013) assumption is that it is not suggested for the slopes higher than 20 m, otherwise, the authors suggest reducing GSI. The quantitative GSI chart proposed by Hoek et al. (2013) is presented in Figure 6.7.

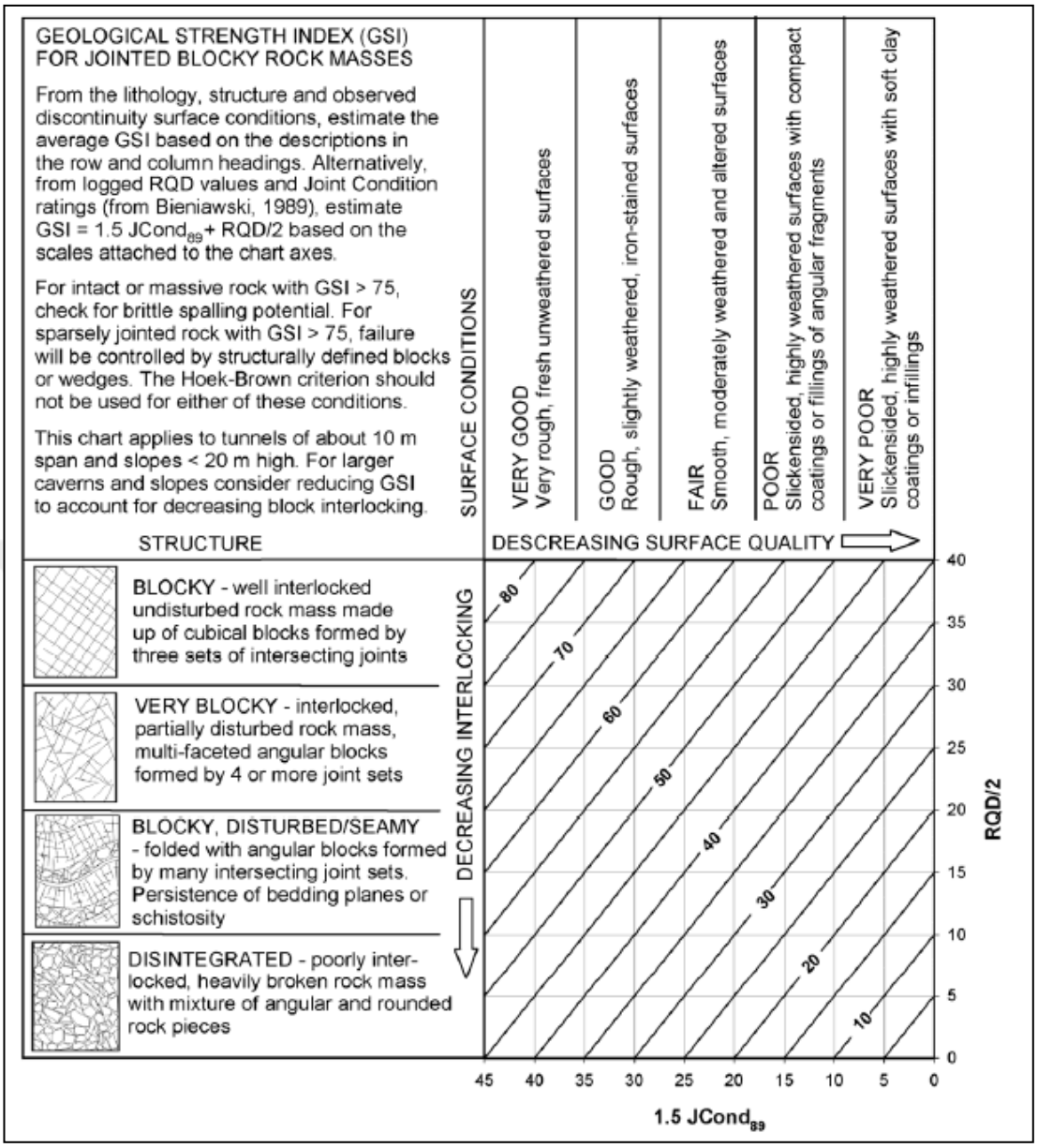


Figure 6.7 Quantitative GSI chart proposed by Hoek et al. (2013)

Vásárhelyi & Bögöly (2019) recently proposed an integral geometric method to estimate GSI rating. They aimed to eliminate the limitations of RQD. Their approach characterizes the rock mass with the unit area of the discontinuities.

$$t = \frac{2N_i}{(h_b - h_a)} \quad (m^{-1}) \tag{6.12}$$

where N_i is the number of joints along the investigated distance (from h_a to h_b depth of the borehole). However, in the case of poor rock (RQD <50%), they suggested finding t as;

$$RQD = -10 \ln(t) + 70 \quad (6.13)$$

Finally, the GSI can be estimated from;

$$GSI = 1.5\, J_{cond89} - 5\ln(t) + 35 \quad (6.14)$$

The quantitative approach of Vásárhelyi & Bögöly (2019) is fundamentally very similar to Hoek et al. (2013) assumption. RQD value has a significant role in both approaches.

The minimum and maximum GSI ratings calculated from different quantitative methods presented in detail above are given in Table 6.1.

The lowest GSI ratings (min:14, max:18) calculated from Osgoui et al. (2010) represents the disintegrated weak rock layers from upper levels of Göcek Formation and slope debris. The other GSI ratings are changing between 29 and 39, which can be used for more lithified, relatively stronger parts within the rock units.

Table 6.1 Ranges of rock mass parameters used in GSI estimation and the GSI values estimated from various quantitative methods

Zone	Reference	Parameter	Ratings	
			Min.	Max.
I	Osgoui et al. (2010)	I_{JC} (BSTR-2 and 3)	9	11
		Jv	62.5	83
		W	6	6
		GSI ratings	14	18
II-III	RMi (Palmström, 1995)	jR	2.25	2.25
		jA	4	4
		jL	1	2
		jC	0.5625	1.125
		V_b (cm^3)	1070	2000
	Q (Barton et al., 1974)	J_r	1.5	1.5
		J_a	3	3
	RMR (Bieniawski, 1989)	Persistence	2	2
		Aperture	0	0
		Roughness	3	3
		Filling	2	2
		Weathering	5	5
		RQD (%)	24	41
	Sönmez & Ulusay (2002)	SCR	10	10
		SR	19.14	21.80
		GSI	35	36
	Cai et al. (2004)		34	35
	Russo (2009)		31	34
	Hoek et al. (2013)		29	39
	Vásárhelyi & Bögöly (2019)		30	39

6.2 Determination of Hoek-Brown Constants

Hoek & Brown (1980) proposed the "Hoek and Brown Failure Criterion" for estimating the strength of jointed rock masses. They also made several modifications to provide the requirements due to limitations of criterion. The final form of the criterion is named Generalized Hoek-Brown Criterion by its authors. It defines the non-linear relationship between the minor and major principal stresses and the shear strength for jointed rock masses (Hoek et al., 2002). The empirical relationship for the Generalized Hoek-Brown Failure Criterion for jointed rock masses is presented in Equation 6.15.

$$\sigma_1' = \sigma_3' + \sigma_{ci} \left[m_b . \frac{\sigma_3}{\sigma_{ci}} + s\right]^a \quad (6.15)$$

The intact rock pieces that make up the rock mass, is defined by;

$$\sigma_1' = \sigma_3' + \sigma_{ci} \left[m_i . \frac{\sigma_3}{\sigma_{ci}} + s\right]^{0.5} \quad (6.16)$$

where σ_1' and σ_3' are the maximum and minimum effective principal stresses at failure. The m_i is a Hoek-Brown constant that represents the rock material, m_b is the reduced value of material constant m_i that represents the rock mass. The s and a are constants that depend upon the rock mass characteristics, σ_{ci} is the uniaxial compressive strength of the intact rock.

The rock mass constants are found with the aid of GSI and disturbance factor (D). The following equations represent the relationship between GSI and the Hoek-Brown constants (Hoek et al., 2002).

$$m_b/m_i = \exp\left(\frac{GSI-100}{28-14D}\right) \quad (6.17)$$

$$s = \exp\left(\frac{GSI-100}{9-3D}\right) \quad (6.18)$$

$$a = 1/2 + 1/6 \left(e^{-GSI/15} - e^{-20/3}\right) \quad (6.19)$$

where D is a factor that depends on the degree of disturbance due to blast damage and stress relaxation. It is obvious that the appearance of a rock face that has been excavated by controlled blasting and a face that has been damaged by bulk blasting show differences. The rating of D varies between 0 to 1, representing the undisturbed in situ rock masses and very disturbed rock masses, respectively. The m_i and m_b depend on the rock type, the size, geometry, and interlocking degree of the rock-forming grains.

m_i value can be directly found from the triaxial tests in which the confining pressure is applied in the range as $0<\sigma_3< 0.5\sigma_{ci}$. Instead, it can be selected from the proposed guidelines (Hoek & Brown, 1980; Hoek, 2007). Many researchers have also suggested using R index which is the ratio of the uniaxial compressive strength σ_{ci} to the tensile strength σ_t, as an alternative way to assess m_i values in the absence of triaxial test data (Hoek & Brown, 1980; Mostyn & Douglas, 2000; Cai, 2010; Sarı, 2010; Read & Richards, 2011, 2014.) Besides, there are other m_i estimation methods such as σ_{ci} based (Shen & Karakuş, 2014; Vásárhelyi et al., 2016), TS based (Wang & Shen, 2017), crack initiation stress-based models (Cai, 2010). Zuo & Shen (2020) reviewed all the above-mentioned methods and suggest using the R index method for sandstone and limestone samples for m_i estimation. Sarı (2010) showed that there is a negligible difference between using uniaxial, biaxial tensile, or Brazilian tensile strength in the R index. Hence, m_i can be estimated from,

$$m_i = \sigma_{ci}/\sigma_t \quad (6.20)$$

The calculated m_i values can be found in Table 5.10 in Chapter 5. The m_i values will further be used directly in calculating m_b and hence major principal stress conditions according to Hoek-Brown Criterion. The m_i value for the weak rock and relatively stronger rocks unit varies between 7 and 20. Besides, GSI values (between 14 and 39) and the σ_{ci} values (between 10 and 117 MPa) for each sample were

classified by K-means cluster analysis by SPSS software (IBM, 2006) to obtain GSI value classes representing the σ_{ci} values. Four clusters of σ_{ci} values were obtained. Afterward, the GSI values estimated from different methods were assigned to the corresponding σ_{ci} value, as presented in Table 6.2. On the other hand, m_i values calculated from the R index have no distinct relationship between GSI values.

Table 6.2 Classes of σ_{ci} values obtained by cluster analysis and the GSI values favorable for these classes and the ranges of m_i values

Classes	Ranges of σ_{ci} (MPa)	Ranges of m_i	Ranges of GSI
1	10-19	7-9	14-18
2	19-42	9-20	29-34
3	45-50	10-16	35-37
4	80-117	10-13	38-39

One of the Hoek-Brown rock mass constants, s value, varies between 0 and 1 and depends on the interlocking degree of the grains in the rock mass, s = 0 indicates a very weak rock that has approximately zero cohesion and tensile strength. The Hoek-Brown parameters can also define the uniaxial compressive strength of the rock mass (σ_{cm}) by setting $\sigma_3' = 0$ in Equation 6.21 (Hoek et al., 2002);

$$\sigma_{cm} = \sigma_{ci}. s^a \quad (6.21)$$

Sönmez & Ulusay (2002) have shown that the parameter s and, consequently, the σ_{cm} suddenly drop to zero when GSI<25. Even though the Hoek et al. (2002) edition to the criterion provided a smooth continuous transition at GSI=25, Sönmez & Ulusay (2002) suggests calculating the "a" value with a switch value of GSI=30

$$a = 0.5 \text{ if } GSI \geq 30 \quad (6.22)$$

$$a = 0.65 - GSI/200 \text{ if } GSI < 30 \quad (6.23)$$

In addition, s and m_b value can be calculated as follows regardless of any switch for GSI value;

$$s = \exp\left(\frac{GSI-100}{b_s}\right) \tag{6.24}$$

where b_s is a unitless parameter ranging between 6 and 9. The b_m is ranging between 14 and 28.

$$m_b/m_i = \exp\left(\frac{GSI-100}{b_m}\right) \tag{6.25}$$

where b_m and b_s coefficients are calculated by a different disturbance factor (d_f) depending on the method of excavation proposed by Sönmez & Ulusay (2002). They recommended using d_f since it can be selected as any value between 0.8 and 1.

$$b_m = 3.14 \ln\left(\frac{d_f}{d_f+340(1-d_f)}\right) +28 \tag{6.26}$$

$$b_s = 0.67 \ln\left(\frac{d_f}{d_f+340(1-d_f)}\right) +9 \tag{6.27}$$

6.3 Determination of Rock Mass Modulus

Fundamentally, jointed rock masses do not behave elastically; however, the elastic modulus is widely used in geotechnical investigations. The elastic modulus of the rock mass can be estimated from empirical equations based on the GSI value proposed by various researchers. These empirical equations are given in Table 6.3.

Table 6.3 The empirical equations estimating rock mass modulus (E_m) proposed by various researchers based on GSI

Reference	Equation	Equation No
Hoek & Brown (1997)	$E_m = (\sigma_{ci}/100)^{0.5}\, 10^{(GSI-10)-40}$	6.28
Hoek et al. (2002)	$E_m = (1- D/2)\sqrt{(\sigma_{ci}/100)}\, 10^{(GSI-100)/40}$ can be used for $\sigma_{ci} \leq 100$ MPa	6.29
Gökçeoğlu, Sönmez & Kayabaşı (2003)	$E_m = 0.1451e^{0.0654GSI}$	6.30
Hoek (2004) in Zhang (2016)	$E_m = 0.33e^{0.064GSI}$	6.31
Hoek & Diederichs (2006)	$E_m = E_i \left(0.02 + \frac{1-(D/2)}{1+ e^{((60+15D-GSI)/11)}}\right)$	6.32
Işık, Doyuran, & Ulusay (2008)	$E_m = 5.67GSI$	6.33

The upper and lower bound of the GSI ratings from different quantitative methods were taken into consideration while selecting a proper GSI value for each different rock deformation zone (Zone-I, II, III). Afterward, the average GSI values were used to estimate the rock mass deformation modulus (E_m) based on different empirical relationships using three samples representative of the zones (Table 6.4).

Table 6.4 The E_m values estimated from different empirical equations

Zone*	Sample ID	σ_{ci} (MPa)	E_i (GPa)	GSI	Equations					
					6.28 (GPa)	6.29 (GPa)	6.30 (GPa)	6.31 (GPa)	6.32 (GPa)	6.33 (GPa)
I	ÇK-28	10.8	1.18	18	0.521	0.339	0.471	1.440	0.03	0.102
II	BK-11	51.3	10.19	35	3.021	1.963	1.431	3.099	0.48	0.198
III	KÇ-28A	78.1	14.02	37	4.181	2.718	1.631	3.523	0.69	0.209

*1= Disintegrated-weak rock zone (classified according to Osgoui et al. (2010))

2= Heavily fractured rock+ breccia zone subjected to rock failures

3=Heavily fractured limestone, conglomerate, sandstone, and mudstone intercalations

It is obvious from Table 6.4 that Işık et al. (2008) equation (Equation 6.33) yields extremely low E_m values than $E_{in\text{-}situ}$. Because their regression equation is constructed by the E_m values derived from in-situ pressuremeter and plate loading tests. It is a well-known fact that dynamic E_m calculated from seismic velocities is always higher than the other methods. The Hoek & Diederichs (2006) equation (Equation 6.32) also has a conservative estimation of E_m. Nevertheless, the Hoek et al. (2002) equation (Equation 6.29) seems to be fitting $E_{in\text{-}situ}$ values obtained from seismic velocities more than other equations.

Lastly, E_m estimated from Equation 6.29, the $E_{in\text{-}situ}$ as well as the E_{avg} values and $E_{i\text{-}dyn}$ values calculated from the laboratory ultrasonic pulse velocities of ten samples were compared by a bar graphic given in Figure 6.8. Laboratory-measured static elastic modulus values do not accord well with the laboratory dynamic elastic modulus determined from ultrasonic pulse velocities. It is obvious from this finding that the laboratory-measured seismic velocities are significantly overestimating elastic modulus values. However, the E_m calculated from Hoek et al. (2002) and $E_{in\text{-}situ}$ values compare well.

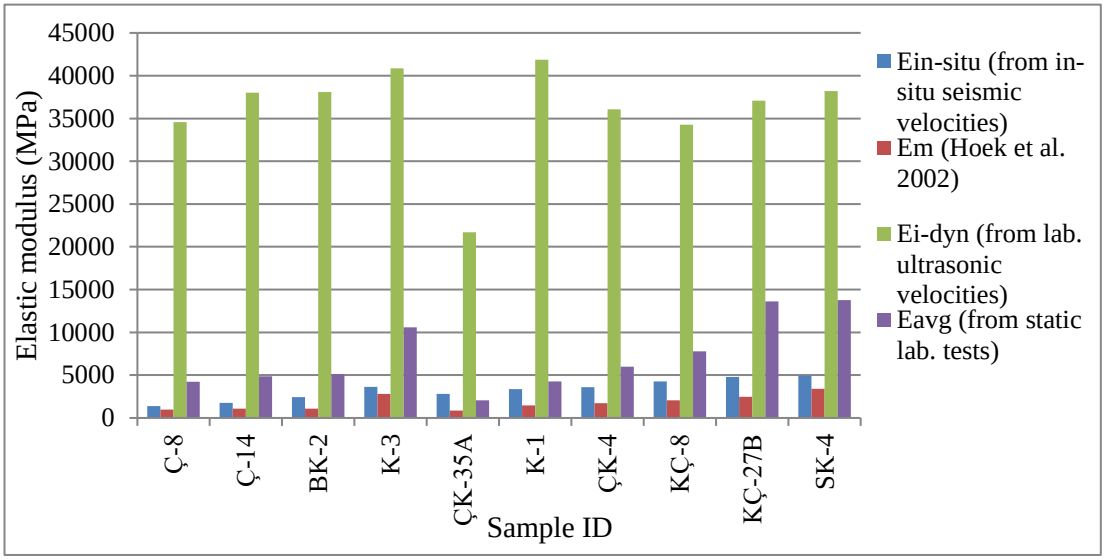


Figure 6.8 The variations of elastic modulus values of intact rock and rock mass estimated from different testing methods

6.4 Statistics of the Parameters in the Rock Failure Criterion

The Hoek-Brown constants such as m_b, s, a, and E_m were calculated for Yeniköy and Göcek Formations and the very weak rock/slope debris materials, considering 13, 7, and 3 samples, respectively. The statistical data of these parameters are given in Tables 6.5, 6.6, and 6.7.

Table 6.5 The statistics of the intact rock and rock mass properties for Yeniköy Formation

Sample	σ_{ci} (MPa)	GSI	m_i	m_b	s	a	E_m (MPa) by Hoek et al. (2002)
SK	80.82	38	10	0.473	0.000220	0.500	2928.69
	104.63	39	10.74	0.534	0.000252	0.500	3529.73
	117.02	39	11.07	0.551	0.000252	0.500	3732.87
KÇ	46.06	35	12.06	0.493	0.000147	0.500	1860.27
	28.47	32	10.39	0.366	0.000097	0.500	1230.57
	52.53	36	12.13	0.521	0.000168	0.500	2104.35
ÇK	103.92	39	13.12	0.653	0.000252	0.500	3517.73
	45.18	35	10.36	0.423	0.000147	0.500	1842.41
	59.48	37	12.16	0.548	0.000192	0.500	2371.91
KKÇ	21.7	30	19.55	0.625	0.000074	0.500	957.51
	24.8	31	20.84	0.699	0.000085	0.500	1084.27
M	55.44	37	12.77	0.576	0.000192	0.500	2289.94
	49.91	35	14.22	0.580	0.000147	0.500	1936.45
Mean	60.77	36	13.00	0.542	0.000171	0.500	2260.52
Max	117.02	39	20.80	0.699	0.000252	0.500	3732.87
Min	21.70	30	10.00	0.366	0.000074	0.500	957.51
SD	31.48	3	3.40	0.091	0.000063	0.000	932.10

D:0.7, df:0.97, b_m:20.33, b_s:7.37

Table 6.6 The statistics of the intact rock and rock mass properties for Göcek Formation

Sample	σ_{ci} (MPa)	GSI	m_i	m_b	s	a	E_m (MPa) by Hoek et al. (2002)
BK	51.31	36	16.24	0.697	0.000168	0.500	2079.77
	34.56	33	12.43	0.460	0.000112	0.500	1436.15
	28.37	32	14.33	0.505	0.000097	0.500	1228.41
K	19.18	29	13.32	0.405	0.000065	0.505	849.84
Ç	32.26	33	9.01	0.334	0.000112	0.500	1387.54
	20.45	29	13.45	0.409	0.000065	0.505	877.53
	41.78	34	9.35	0.364	0.000128	0.500	1672.62
Mean	32.56	32	12.60	0.453	0.000107	0.501	1361.69
Max	51.31	36	16.20	0.697	0.000168	0.505	2079.77
Min	19.18	29	9.00	0.334	0.000065	0.500	849.84
SD	11.43	3	2.60	0.122	0.000036	0.002	434.49

D:0.7, df:0.97, b_m:20.33, b_s:7.37

Table 6.7 The statistics of the intact rock and rock mass properties for very weak rock unit /slope debris

Sample	σ_{ci} (MPa)	GSI	m_i	m_b	s	a	E_m (MPa) by Hoek et al. (2002)
Very weak rock (Ç- K-ÇK)	19.34	18	9.29	0.164451	0.0000146	0.560	453.05
	10.28	14	6.16	0.089565	0.000008	0.580	262.37
	10.82	15	8.45	0.129057	0.000010	0.575	285.12
Mean	13.48	16	8.0	0.128	0.0000109	0.572	333.51
Max	19.34	18	9.3	0.164	0.0000146	0.580	453.05
Min	10.28	14	6.2	0.090	0.0000085	0.560	262.37
SD	5.08	2	1.6	0.037	0.0000032	0.010	104.14

D:0.7, df:0.97, b_m:20.33, b_s:7.37

CHAPTER SEVEN
MULTI- TEMPORAL PHOTOGRAMMETRIC ANALYSES

The landslides in a dam reservoir area have caused severe damages in history. Therefore, a detailed geological and geotechnical investigation of reservoir slopes and generating DEM of landslide affected area (Yu, Huang, Xu, Guo, & Dai, 2016) is crucial for hazard mitigation. Volume estimation of old landslides in the dam reservoir area is also essential to anticipate the potential of a possible future hazard. In this context, remote sensing data were processed with photogrammetric techniques to identify the evolution of landslides and to calculate the volumes of depleted (collapsed/cut) and accumulated (fill) material.

The scale of the images used in determining spatial distribution and evolution of landslides has significant importance. Mantovani, Soeters, & Van Westen (1996) and Metternicht, Hurni, & Gogu (2005) suggested that 1:15000 scale imagery is an optimum scale for landslide mapping. Singhroy (2002) stated that a smaller scale than 1:25000 does not permit evaluating the failure type and causes of a mass movement.

Landslide volume determination is a difficult task that requires information on the surface and sub-surface geometries of the slope failure (Guzzetti et al., 2009). A considerable amount of literature has been published on estimating the volume of a landslide. Cruden & Varnes (1996) and Marchesini, Cencetti & De Rosa (2009) have used the ellipsoid approach to determine the volume of rotational landslides. This method assumes a regular-shaped landslide body that is being a portion of an ellipsoid. Nikolaeva, Walter, Shirzaei, & Zschau (2014) revised the ellipsoid approach and adapted it to rock slides that having translational components. All the above procedures require information on the depth of the rupture surface or the depth of displaced material, which can only be provided from in-situ methods such as borehole and inclinometric measurements or geophysical investigations. Gathering this information is expensive, time-consuming, and maybe very challenging due to steep slopes (Malamud, Turcotte, Guzzetti, & Reichenbach, 2004).

Conversely, the information on the area of the landslides can be rapidly and simply provided from aerial photographs or satellite images. Several studies thus far have linked the volume to the area of landslides (Malamud et al., 2004; Guzzetti et al., 2009; Larsen, Montgomery, & Korup, 2010; Fuller, Riedler, Bell, Marden, & Glade, 2016; Amirahdi, Pourhashami, Karami, & Akbari, 2016). They found that there is an unambiguous relationship between the area (A) and the volume (V) of displaced material independent from the local physiographical setting (Equation 7.1).

$$V = \alpha \times A^{\gamma} \tag{7.1}$$

where α and γ are empirical constants.

Larsen et al. (2010) stated that small differences in γ lead to substantial variance in volume estimations. Besides, there is no general agreement about selecting a proper scaling exponent (γ) for landslides involving both debris material and rock. In the case of reactivations that occur in different portions of the initial landslide body, the areal extension of the reactivated portion may not be detected on the aerial photograph. In that case, the empirical equations and the ellipsoid approach can not be used.

Unlike the conventional methods based on geometrical assumptions and empirical equations, subtracting the DEMs of two successive years is a useful tool to obtain the volume of landslides. The latter DEM is subtracted from the former one, and the resultant differential DEMs can be evaluated in terms of the negative and positive height differences. The positive values refer to increment in height and thus the accumulated (fill) volume, whereas the negative values indicate a decrease in height and hence the depleted (cut) volume.

De Bari, Lapenna, Angela, Puglisi & Sdao (2011) combined the ellipsoid approach with results from differential DEMs. They have argued that the ellipsoid volume refers to the volume of depleted (collapsed) mass since there is a part in the

landslide body named “filling up” volume that no elevation change is detected (Figure 7.1).

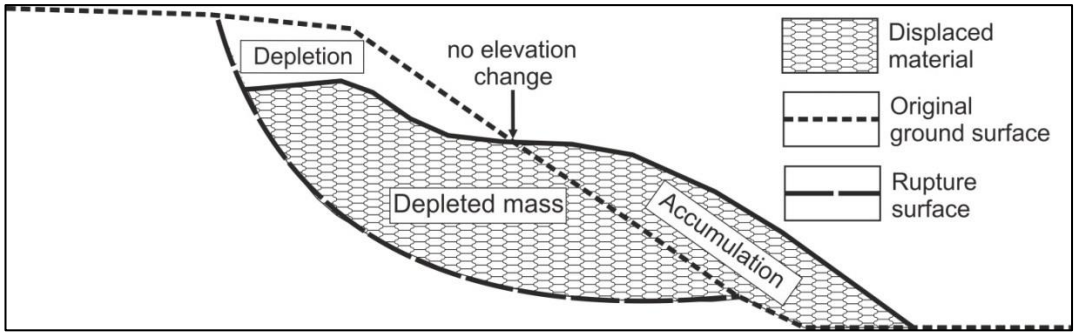


Figure 7.1 The illustration of the parts of a landslide body (modified after De Bari et al., 2011)

Therefore, De Bari et al. (2011) suggested that the total volume of displaced material can only be obtained by adding the depleted and accumulated material volume calculated from differential DEMs to the ellipsoid volume. However, the term, displaced material, has been defined by International Association of Engineering Geology (IAEG) Commission on Landslides (1990) as the material displaced from its original position on the slope by movement in the landslide, and it is referred to the sum of depleted mass and the accumulation. Hence, adding ellipsoid volume to the depleted and accumulated material volume calculated from differential DEMs does not meet the term of displaced material proposed by the IAEG Commission on Landslides (1990).

Several researchers have used Height Difference Model (HDM) for estimating volume from differential DEMs. HDM is based on merely the multiplication of elevation differences and the corresponding pixel sizes (Coe, Glancy, & Whitney, 1997; Van Westen, & Getahun 2003; Tsutsui et al., 2007; Du & Teng, 2007; Corsini et al., 2009). The volume can be calculated as follows;

$$V = \frac{A}{n} \sum_{i=1}^{n} \Delta z_i \qquad (7.2)$$

where V is volume, A is the area, n is the number of pixels within the area, and Δz_i is the elevation difference value of the i^{th} pixel.

It should be noted that HDM enables the calculation of only depleted and accumulated material volumes and does not take into account the depleted mass. One major limitation of HDM is that the errors in the plane positions and height value and height baseline difference between two DEMs may reduce the accuracy of the results produced by this model (Chen, Zhang, Han, Zuo, & Zhang, 2014). A broader perspective has been adopted by Chen et al. (2006), who improved the HDM to minimize the height errors between two DEMs. The new method was referred to as the Advanced Height Difference Model (AHDM) by Chen et al. (2014). This model assumes that if there is no height error between two DEMs, the elevation difference should be zero outside the landslide-prone area. In this context, sub-areas outside the landslide-prone area are selected to control the elevation differences between the two DEMs. The average height differences in the sub-areas are considered to be systematic height errors between successive DEMs. Subsequently, the differential DEMs are adjusted for the average height differences. According to Chen et al. (2014), standards do not exist for the way of choosing sub-areas; however, the average height adjustment value obtained from sub-areas has a significant effect on the volume calculations. Chen et al. (2014) further improved the AHDM to Mass Balance Model (MBM), which is based on the mass balance principle. They argued that MBM provides more accuracy on volume estimation where there is no material loss, and there is no "filling up volume". However, the mass balance between depletion and accumulation is not provided for a wide range of landslides, particularly for landslides along riverbanks.

The volume of displaced material is not necessary when dealing with the inrush volume into the reservoir of the dam. It is obvious that only a portion of the whole landslide body slides into the reservoir, whereas the depleted mass remains on the rupture surface (Figure 7.1). A portion of the accumulated material volume is washed out of the landslide-prone area due to fluvial erosion. However, after the dam construction, the loss in accumulated volume due to fluvial erosion will be captured by the dam. In this study, the volume estimation of mainly the depleted material that

will contribute to siltation was aimed. The AHDM was therefore applied to the landslides observed in the reservoir area of the Çağlayan Dam.

There may be two different causes of errors in landslide volume calculations: 1) the shifts in-plane positions between two images and systematic height differences between two DEMs 2) the misinterpretation of the aerial photograph while identifying the limits of landslide body when the size of the landslide is small when compared to the scale of aerial photographs (Mantovani et al., 1996; Metternicht et al., 2005; Singhroy, 2002; Guzzetti et al., 2012). Therefore, the errors in identifying the limits and parts of the landslide body due to the scale, date, and quality of the aerial photograph were eliminated by examining depletion and accumulation zones through cross-section profiles extracted from DEMs. The shifts in-plane positions between two images and systematic height differences between two DEMs were minimized by image to image coregistration and height adjustment, respectively. The effect of the image to image coregistration and height adjustment on the reliability of differential DEMs was examined. The ambiguity in choosing sub-areas for height adjustment was investigated.

7.1 Aerial Photographs

Four sets of multi-temporal, stereo aerial photographs (1953, 1970, 1995, and 2012) were used to quantify the surface area of landslides over time and to generate digital elevation models (DEMs). The available acquisition parameters for the historical aerial photographs and the digital photograph are given in Table 7.1.

Table 7.1 The acquisition parameters of aerial photographs

Date	Camera	Focal Length (mm)	Color	Scale/Resolution
1953	Unknown	99.91	Black and white	1/35000
1970	RC5/RC8	151.86	Black and white	1/20000
1995	RC10	153.29	Black and white	1/20000
2012	Multispectral camera (UltracamEagle)	79800	Digital, colored	0.3x0.3 m

Initially, the aerial photographs were georeferenced to a common base map (1/25000 topographical map) individually. Each photograph was adapted to the Universal Transverse Mercator (UTM) map projection (Zone 35N), the World Geodetic System (WGS) 1984 horizontal datum, and the WGS 1984 ellipsoid. Following the georeferencing process, orthorectification was performed via the ortho engine module of PCI Geomatica software (PCI Geomatics, 2012). The orthorectification process requires acquisition parameters that are rarely available for historical photographs. The unknown acquisition parameters cause misregistration between the orthorectified images to be compared (Ayoub, Leprince & Avouac, 2009). In this context, a 2012 aerial photograph with a spatial resolution of 0.3 m was selected as a base image. The acquisition parameters of warp images (1953, 1970, 1995) were improved by optimizing with respect to the base image (2012). Image to image coregistration was therefore performed by manually identifying the common points (tie points) in both images such as individual trees, pathway intersections, and corners of farmlands. As a result of the image to image coregistration, the pixel sizes of the warp images were the same as those of the base image.

Polygons of four landslide bodies were digitized through the interpretation of aerial photographs by using ArcGIS software (Environmental Systems Research Institute (ESRI), 2015). The main scarps of landslides were identified on aerial photographs with the aid of brighter and white-colored pixels, which are indicating exposed fresh rock due to landslides. The lateral edges were estimated according to the differences or lineation in vegetation and drainage patterns. The toes of the slopes bounded by the streambed. Thereafter, the areas of the polygons were rapidly calculated by ArcGIS software (ESRI, 2015).

7.2 Data Acquisition by UAV

Small unmanned aerial vehicles (UAV) known as drones have gained attention for landslide monitoring in recent years. UAV is a promising tool for low-cost, fast, and high-resolution orthophoto acquisition on a local scale. The UAV images of bare terrain or terrain with individual trees can be reliably used in landslide monitoring. Furthermore, high-resolution DEMs generated from overlapped orthophotos taken by UAV provide detailed information for landslide investigation. The accuracy of these DEMs have been defined by comparing with the DEMs from GPS survey, total station survey, airborne Lidar scanning, terrestrial laser scanners (TLS) and resolved to be consistent by various researchers (Carvajal, Agüera, & Pérez, 2011; Niethammer, James, Rothmund, Travelletti, & Joswig, 2012; Turner, Lucieer, & De Jong, 2015; Rusnak, Sladek, Busa, & Greif, 2016; Balek & Blahut, 2017). However, Niethammer et al. (2012) revealed that vegetation affects the accuracy of DEM generated from UAV images significantly. Clapuyt, Vanacker, & Van Oost (2016) deduced that vegetation leads to errors in elevation models derived from UAV images. Furthermore, Hugenholtz et al. (2013) recommend using UAV in barely vegetated areas. The height correction of vegetation is most commonly done with the Lidar or TLS point cloud data since trees, stumps and bushes are easily identifiable in the point clouds and can be removed manually without any automatic filtering (Niethammer et al., 2012). Unless the vegetation height is corrected, it will be difficult to achieve a proper DEM from UAV, and therefore, landslide volume will be overestimated.

In 2017, overlapped photographs of the study area (122 ha area) were acquired by Dji Phantom 4 Pro drone. The Dji Phantom 4 Pro small drone weighs 1.39 kg, has a cruising speed of 8 m/s, maximum flight duration is 30 minutes unless the weather is stable (Figure 7.2). It can fly by remote control or autonomously with the aid of its GPS receiver and its waypoint navigation system and is equipped with a 20-megapixel camera.

The flight altitude was 100 m above the starting point (428 m) and kept constant during the flight. The image acquisition route was planned before the flight. Seven hundred sixteen images with 77% longitudinal and 60% transversal overlaps were acquired. UAV images were transformed into georeferenced orthophoto, a digital surface model (DSM), and a point cloud using Agisoft (2016), which is a widely used software for UAV photogrammetry. The resultant orthophoto and DSM have pixel sizes of 0.07 m and 0.26 m, respectively. The point cloud data was composed of points per 3 cm. UAV point cloud data can not penetrate the dense vegetation and capture the actual terrain. Therefore, the cross-sections include vegetation heights and show rough topography (Figure 7.3).



Figure 7.2 Dji Phantom 4 Pro drone with an onboard camera (Personal archive, 2017)

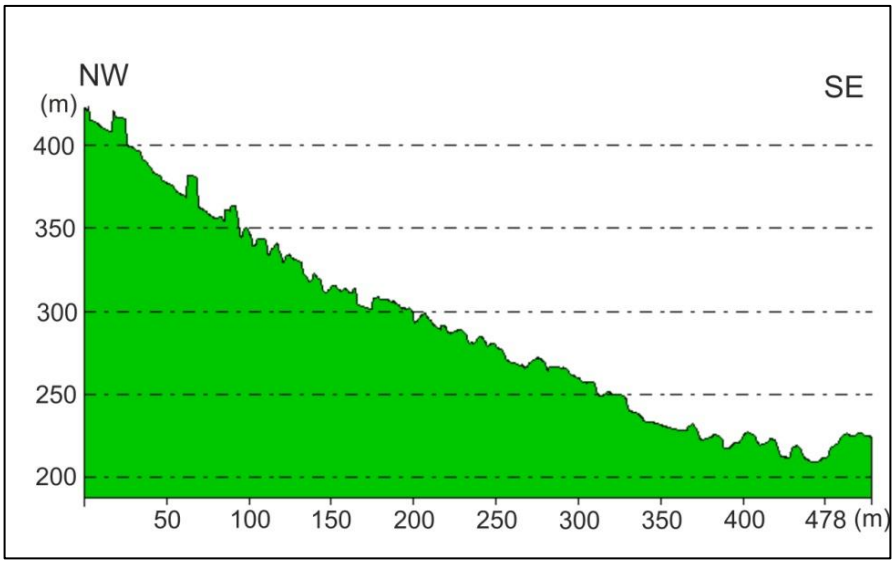


Figure 7.3 The cross-section of Landslide-1 showing the topography with uncorrected tree heights

A filtering process to eliminate the height of trees converts the DSM to DEM data. In this context, the height of the trees was trimmed via computer software based on the cross-section method. However, this process led to large data gaps in the DEM. The data gaps can be filled by entering ground control points or point cloud from TLS/lidar manually for interpolation. Nevertheless, it is unavailable to assign points for interpolation since ground control points can not be taken due to steep slopes and dense vegetation.

As a consequence, volumetric analyses were not performed on DEM that was generated from UAV images, however, the landslides were evaluated by taking cross-sections and orthophoto interpretation for the year 2017. In this context, the four landslide bodies were digitized on UAV orthophoto and their dimensions were compared with the ones from multi-temporal aerial photos. Cross-sections along landslide bodies were constructed to define the topographical changes.

7.3 Interpretation of Aerial Photographs

The main scarps of Landslide-2 and Landslide-4 were clearly identified by the aid of exposed, partly vegetated terrain, whereas the main scarps of Landslide-1 and Landslide-3 were densely vegetated and could only be identified by the lineation of

the vegetation as well as the height differences and convexities. The main scarps were even identified in the oldest aerial photo which showed that the first occurrence of landslides (initial failure) is before 1953. However, it is unknown at which moment the landslides reactivated and which triggering factors featured in reactivations (secondary failures) after 1953.

All surface features indicated a rotational type of movement (arc-shaped scarp, bulging at the foot, etc.). Landslides with surface areas of 1.55 $x10^4$ to 7.37$x10^4$ m^2 were digitized as polygons on each photograph. The area of landslide polygons provided information about the areal extension of slope failures quantitatively (Table 7.2 and Figure 7.4). According to Table 7.2, minor changes in the area of the landslides between 1953 and 2012 were determined. It can, therefore, be said that the main landslide body is always active in the lower order of the initial failure and is not extending from its initial area. However, minor scarps were not recognized on aerial photographs except for the 2012 photograph. 2012 digital photograph partly allowed identifying the reactivated parts in the downslope of landslides. Nevertheless, the precise limits of reactivations could not be identified.

Table 7.2 The landslide areas calculated with respect to the digitized polygons

Years	Area (m^2)			
	Landslide-1	Landslide-2	Landslide-3	Landslide-4
2017	73742	18473	31695	16631
2012	72909	18785	31800	16640
1995	65226	17511	31290	15544
1970	63086	16484	29889	16460
1953	72334	18842	30092	16366

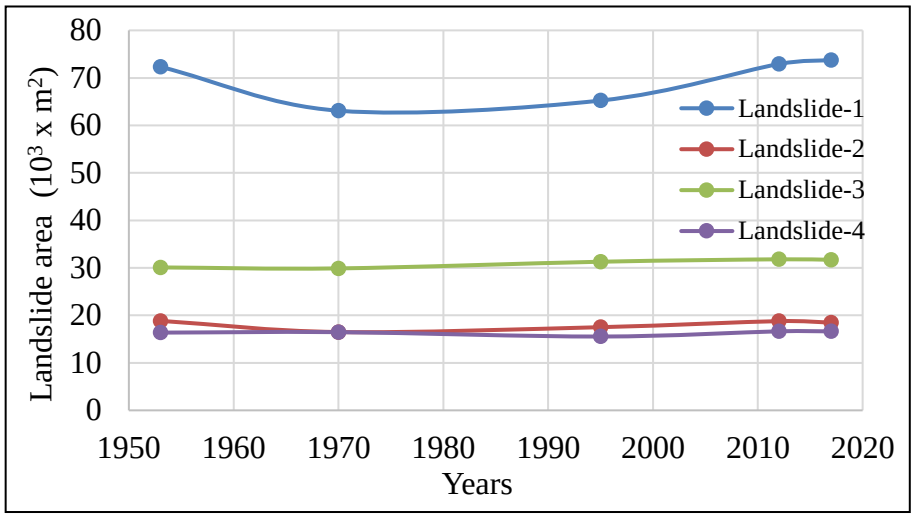


Figure 7.4 Comparison of landslide areas between the years 1953 and 2017

7.4 Digital Elevation Model Generation

Digital elevation models were produced by the software Inpho MATCH-T DSM (Trimble, 2009) using the coregistered stereo pairs of aerial photographs and automatically collected ground control points. The resultant pixel size of 1953, 1970, 1995, and 2012 DEMs are 10 m, 20 m, 10 m, 10 m, respectively. The DEM of 1970 partially includes Landslide-1. Therefore, Landslide-1 was evaluated for the two periods between 1995 to 2012 and 1953 to 1995.

Differential DEMs were produced by subtracting the successive DEMs. The differential DEMs were then adjusted for the systematic height differences between successive DEMs, according to AHDM proposed by Chen et al. (2006). In contrast to the original AHDM, eleven sub-areas with various sizes (1284 m^2 to 34785 m^2) from different locations (residential areas, farmlands) outside the landslide-prone area were selected (Figure 7.5). The height differences between sub-areas on successive DEMs were obtained. The histogram of the height difference data provided the average value. The average height differences were considered to be systematic height errors between successive DEMs. As a consequence, different orders of average error were obtained for the years between 1970-1953, 1995-1970, 1995-1953, and 2012-1995. The differential DEMs were then adjusted for these

average height differences with the aid of minus/plus tools in ArcGIS software (ESRI, 2015).

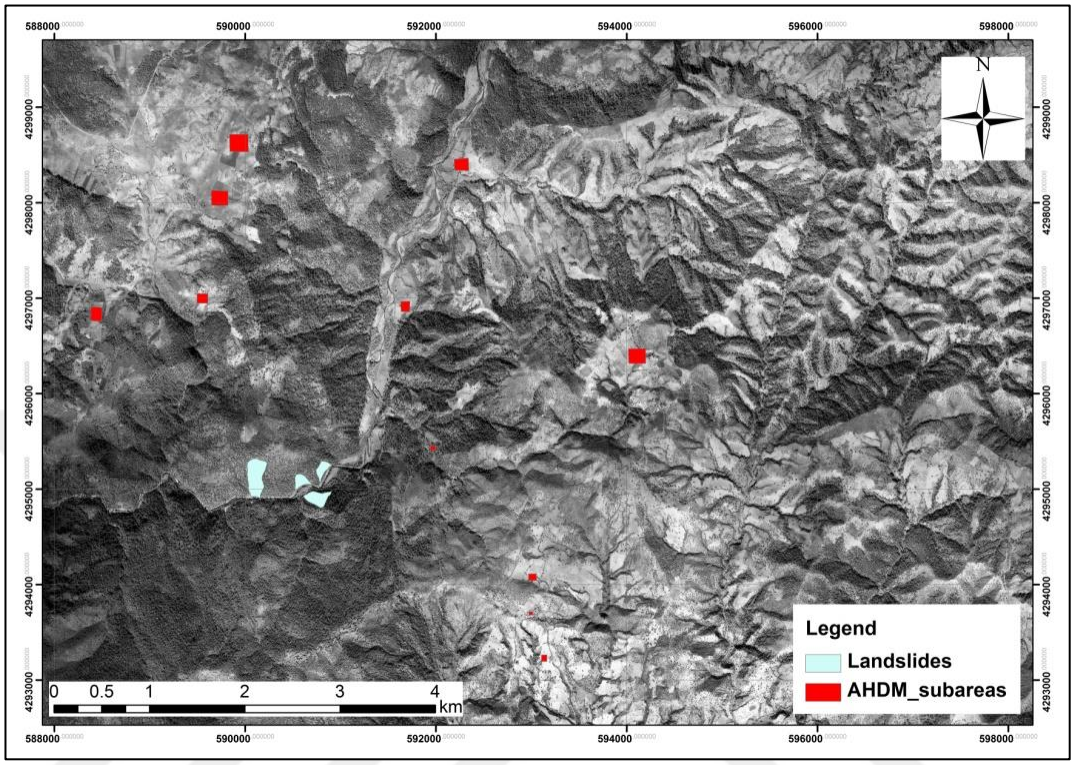


Figure 7.5 The sub-areas in the region to determine the average height error between images

7.5 Cross-Sectional Analyses

As the acquisition date, camera type, scale, and the scanner resolution of film-based aerial photographs have an impact on the accuracy of interpretation of landslides, and further methods are required to interpret the landslide body on the aerial photographs. Revegetation also inhibits identifying the secondary scarps related to reactivations on the aerial photographs. Thus, identification of the depletion and accumulation zone of the initial landslide body is prone to errors due to the misleading effect of vegetation and poor resolution and shadows in the aerial photograph. It is, therefore, necessary to construct overlapped cross-sections to check the limits of the landslide boundary before employing AHDM to estimate the volume of a landslide more precisely. Hence, cross-sectional analyses were performed to control the accuracy of digitized landslide polygon boundaries on aerial photographs.

In this context, longitudinal cross-sections passing through the digitized polygons, as shown in Figure 7.6 for each year were extracted by Global Mapper software (Blue Marble Graphics, 2016). Two successive cross-section profiles were overlapped each other for three periods (2012-1995, 1995-1970, 1970-1953) for each landslide. The average error values obtained from the AHDM were also used to adjust the height values in cross-section profiles. The overlapped cross-section profiles provided information on the limits of the landslide body, which is indiscernible on aerial photographs.

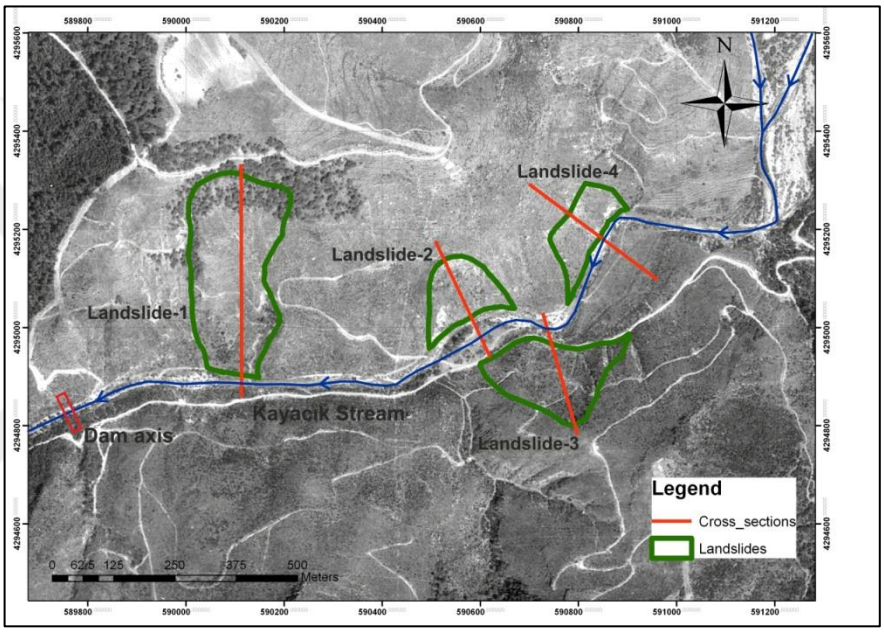


Figure 7.6 The cross-section lines taken from the midpoint of the landslide polygons

Prior to volume calculations, the overlapped cross-section profiles of 1953 and 1970, as well as 1995 and 1970, indicated that the accumulation zone of Landslide-4 is not involved within the digitized polygon (Figure 7.7). Accordingly, no accumulated material volume can be calculated for Landslide-4. For this reason, the polygon of the landslide should be extended in the direction of movement to involve the accumulation zone detected in overlapped cross-section profiles. In this context, a secondary polygon at the toe of Landslide-4 was digitized (Figure 7.7). The secondary polygon at the toe showed both negative and positive changes in height. There is a strong possibility that the negative changes in height are due to fluvial erosion. Therefore, only the positive changes in height (accumulated volume) were

considered within the secondary polygon. Otherwise, the depleted material volume within the whole polygon can be overestimated.

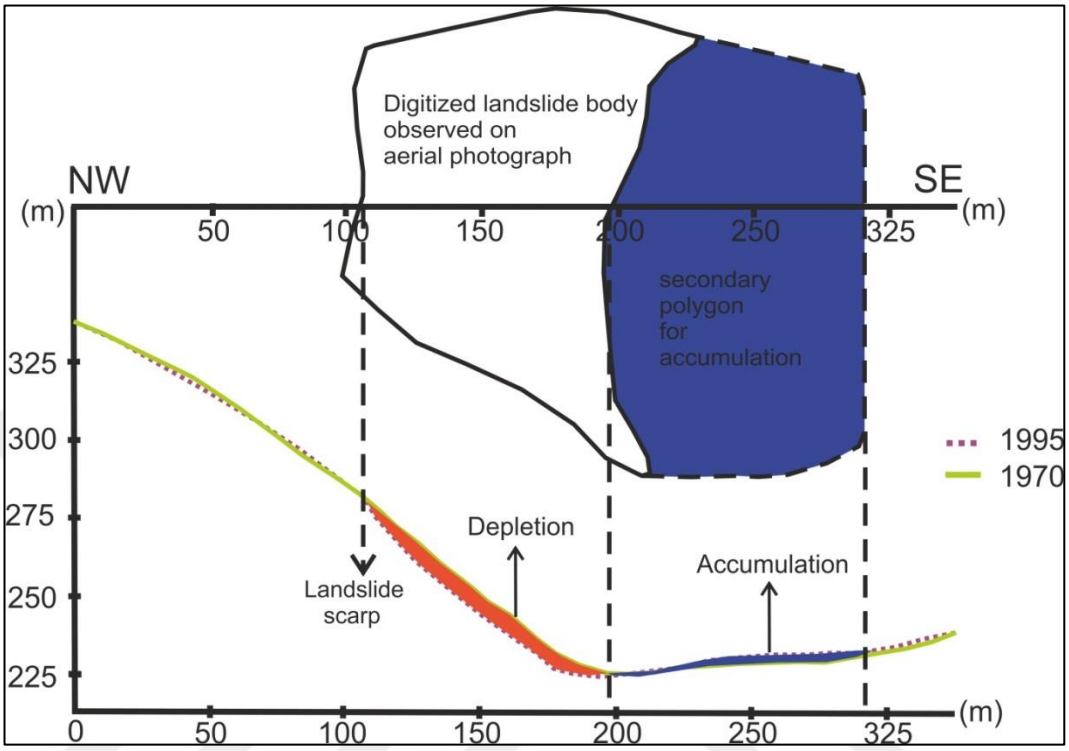


Figure 7.7 Illustration of drawing secondary polygon for accumulation on the plan view of Landslide-4 with respect to the overlapped cross-section profiles of 1970 and 1995

The overlapped cross-section profiles of 1995 and 1970 also indicated that the reactivations are the repeated development of the same type of movement, which occurs in different scarps within the main landslide body. In other words, reactivations are independent movements of small portions of the initial displaced mass.

A topographical comparison between 1953 and 1970 for Landslide-4 also revealed that there is another scarp 63 m behind the main scarp that was observed on the aerial photograph (Figure 7.8). Another distinct (secondary) polygon was digitized for the depletion zone, as shown in Figure 7.8. In this case, only the depleted material volume within the secondary polygon was taken into account.

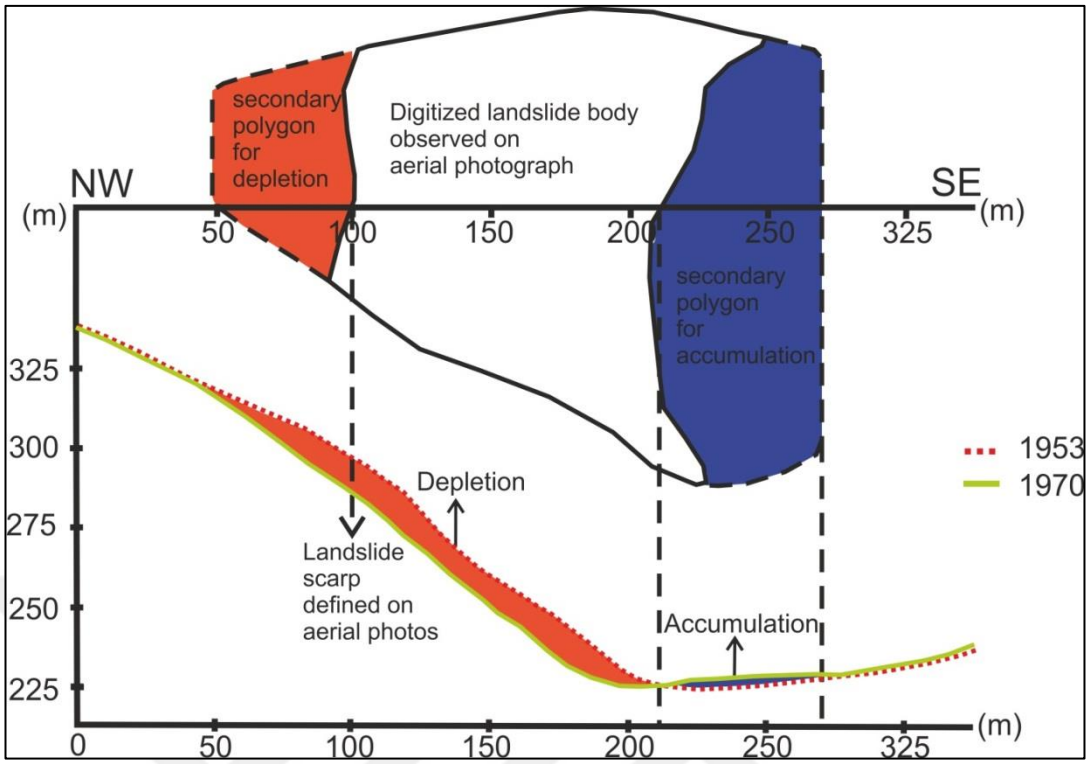


Figure 7.8 Illustration of drawing secondary polygon for accumulation and depletion on the plan view of Landslide-4 with respect to the overlapped cross-section profiles of 1953 and 1970

The topographical changes between 1995 and 2012 for Landslide-4 highlighted that the heaving in the toe may refer to a possible mass movement (Figure 7.9).

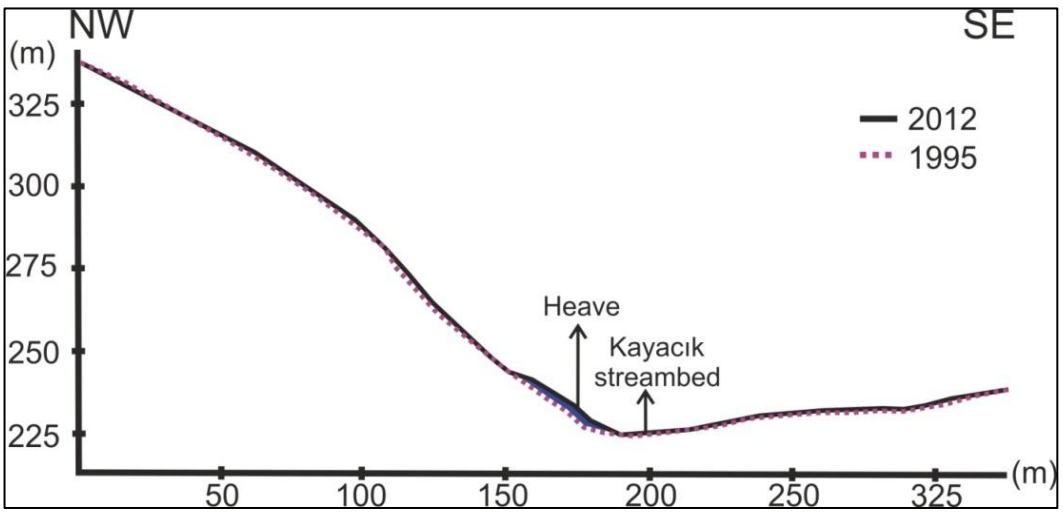


Figure 7.9 The cross-sections of Landslide-4 showing the differences in topography between 2012-1995

Furthermore, 2012 and 2017 cross-sections of Landslide-4 were compared (Figure 7.10). Figure 7.10 indicates that a maximum of 2.3-3 m thick slope material moved downslope over the five years. This movement only includes sliding of shallow debris on the bedrock and can be differentiated from the previous slides.

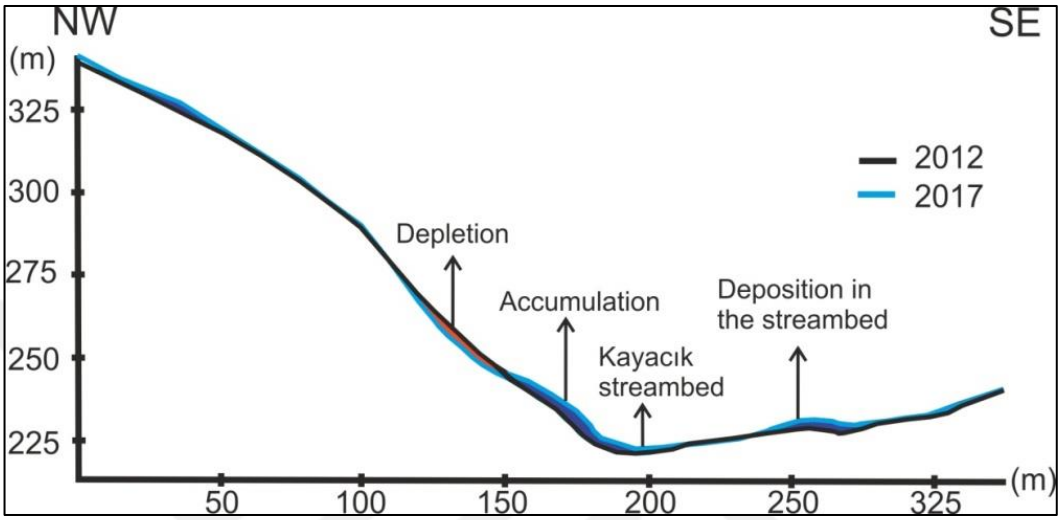


Figure 7.10 The cross-sections of Landslide-4 showing the differences in topography between 2017-2012

Even though cross-section profiles enabled identifying more precise accumulation and depletion zones, the major limitation of using this method is being subjective in drawing the lateral limits of secondary polygons on the aerial photographs.

7.6 Landslide Volume Estimation

The volume of landslide material slid into the dam reservoir area, which is corresponding to depleted/collapsed material volume was determined based on AHDM proposed by Chen et al. (2006). Despite the original AHDM, average height errors were determined from the increased number of sub-areas on successive DEMs. The height adjustment values were obtained from the average error between two successive DEMs based on the control sub-areas located outside the landslide-prone area. The variety in the number and location of the sub-areas were reported to be affecting the average height adjustment value (Chen et al., 2014). Thus, choosing the ideal elevation control sub-areas is a problem. Various numbers of sub-areas from

different locations (residential areas, farmlands) were examined to obtain an optimum number of sub-areas (Figure 7.11).

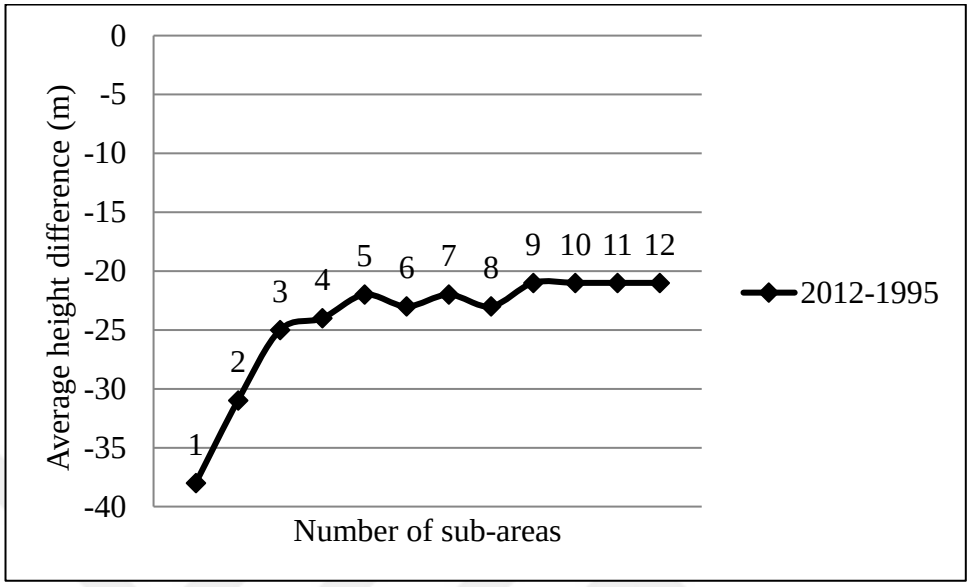


Figure 7.11 The change in average height difference between two successive DEMs with respect to the number of sub-areas

Figure 7.11 shows that eleven sub-areas can provide accurate height adjustment value independent of their size and location for the DEMs used in this study. The average systematic errors for the periods 1970-1953, 1995-1970, 1995-1953 and 2012-1995 were obtained as +25, -15, -5 and +21, respectively. The differential DEMs were then adjusted for these average errors.

The image to image coregistration, as well as the height adjustment processes, improved the accuracy of the differential DEMs. Table 7.3 shows that both methods have a significant effect on differential DEMs and thus on volume estimation. It can, therefore, be assumed that the combination of the two methods is a reliable tool for landslide volume estimation as well as cross-sectional analyses mentioned previously.

Table 7.3 Height differences in differential DEMs before and after image to image coregistration and height adjustment

	Height Difference (m)					
	Before image to image coregistration		After image to image coregistration		After height adjustment	
Period	Min.	Max.	Min.	Max.	Min.	Max.
2012-1995	-38	23	-30	-13	-9	8
1995-1970	-32	13	-3	23	-18	8
1970-1953	-64	30	-46	-12	-21	13

The corrected differential DEMs are given in Figure 7.12. It was deduced from Figure 7.12 that the reactivations occurred in the different portions of the initial landslide body.

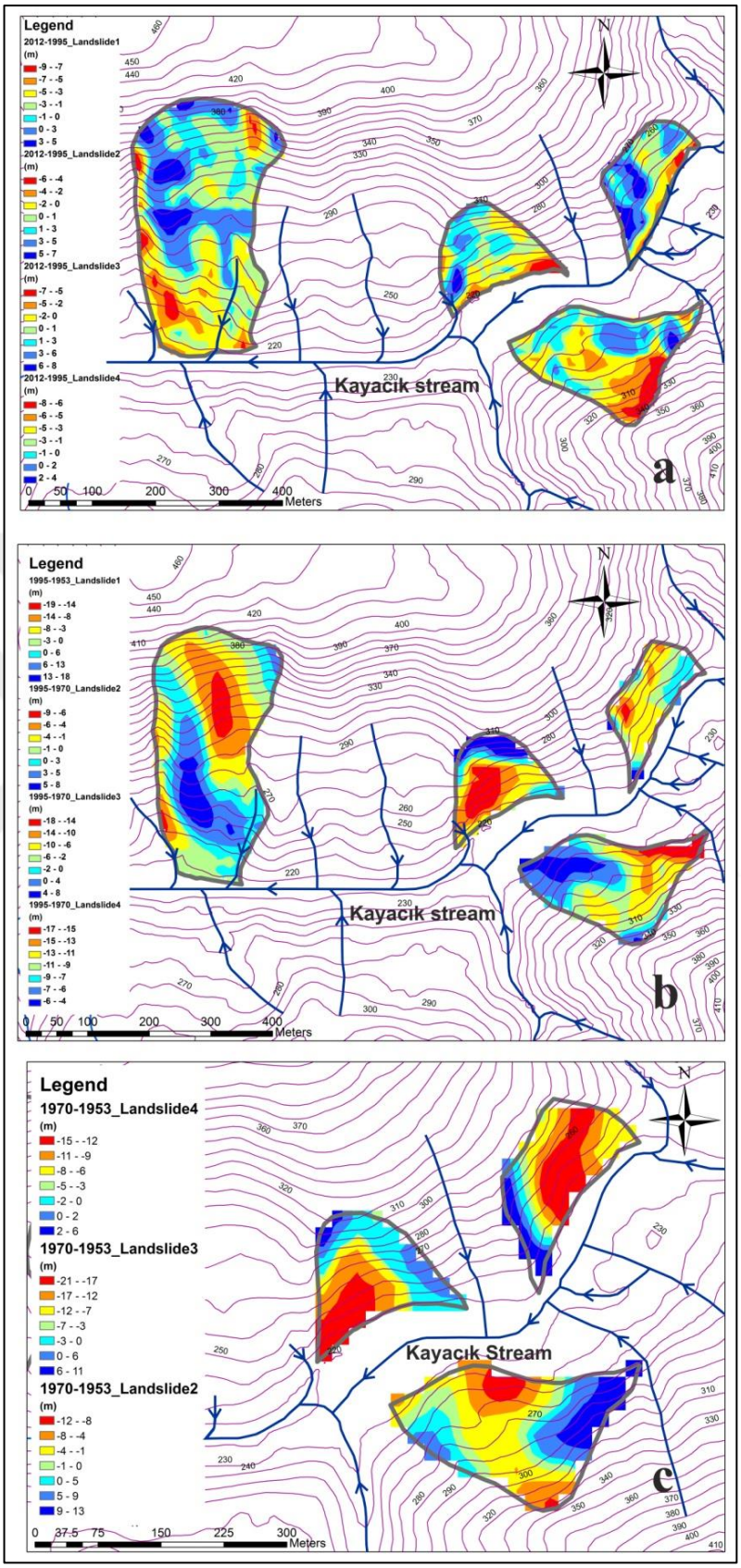


Figure 7.12 The differential DEMs of a. 2012-1995 b. 1995-1970 c. 1970-1953

Afterward, the four landslide polygons were cropped from the adjusted differential DEMs. The depleted and accumulated material volumes within the landslide polygons were calculated by the "measure cut and fill" command in Global Mapper software (Blue Marble Graphics, 2016). The principle of the calculation is simple, and it is time-saving. The negative (cut) and positive (fill) elevation difference values of each pixel were multiplied by the pixel area via software automatically. As a result, the depleted and accumulated material volumes were estimated for each landslide polygon and secondary polygons for the periods 1970-1953, 1995-1970, and 2012-1995. The depleted (cut) material volume was considered to be the volume of material slid into the reservoir. It was determined that a total of 121.78×10^4 m^3 material depleted, and 68.50×10^4 m^3 material accumulated between the years 1953 and 2012.

The total cut and fill volumes preliminary indicated that the mass balance is not reached. In other words, the volume of depleted material is not equal to the accumulated volume. The total cut volume is commonly greater than the fill volume due to fluvial erosion, whereas the order of the difference between cut and fill volumes varies in different periods (Table 7.4). These results also showed that the long term (1953-2012) annual average (1953-2012) of 2.06×10^4 m^3 landslide material has slid into the reservoir area (annual average = total cut volume (121.78×10^4 m^3)/59 years). However, some fluctuations in sliding rate (2012-1995: 1.37×10^4 m^3/year, 1995-1953: 2.34×10^4 m^3/year) due to different behavior of rock mass to different triggering factors can be observed.

Table 7.4 Depleted (cut) and accumulated (fill) volumes for each landslide for the periods

	Landslide-1		Landslide-2		Landslide-3		Landslide-4	
	Volume (x 10^4 m^3)							
Period	Cut	Fill	Cut	Fill	Cut	Fill	Cut	Fill
2012-1995	15.07	11.35	1.42	2.01	3.96	3.24	2.81	3.45
1995-1970	-	-	5.24	2.27	14.63	3.13	12.6	4.92
1970-1953	-	-	6.25	3.17	20.18	3.94	15.66	7.52
1995-1953	23.96	17.3						
Mean slope of streambed (°)	8.97		5.21		11.3		6.67	

Except for the period 1995 to 2012, the accumulated (fill) volume was defined to be considerably less than depleted (cut) volume. The depleted material deposited in the streambed was assumed to be eroded and transported by the streamflow at various rates. In addition, this fluvial erosion may also contribute to the instability of slopes in the long-term period due to the undercutting phenomenon, as similarly stated by Lacroix, Berthier & Maquerhua (2015). The slope of the accumulation area that involves the streambed is another controlling factor for the amount of material transported by the streamflow. As the slope of the streambed increases, the amount of transportation also increases. Accordingly, the lowest amount of accumulation was calculated for the Landslide-3, where the slope of the streambed is 11.3° (Table 7.4). The lowest amount of material depleted in the years between 1995 and 2012, whereas the accumulated material volume is proportionally higher than the other periods. A similar result was obtained in both Van Westen & Getahun (2003) and Chen et al. (2006). Van Westen & Getahun (2003) explained the greater accumulation volume than the depletion volume by a reduction of accumulation area. On the other hand, Chen et al. (2006) refer the excess volume to decompaction.

Slope maps generated from DEMs also highlighted the landslide scarps and partly the release surfaces (Figure 7.13). The steep main scarps and lateral edges of landslides are well correlated with the slope angle of 40-50°. On the other hand, a geological differentiation can be made between the landslides based on the critical

slope angle. The mean critical overall slope angle determined from cross-sections for Landslide-1, 2, and 4, which are formed of unconsolidated conglomerate, sandstone, siltstone, and mudstone alternations was found to be 33°. Besides, Landslide-3 is mainly composed of highly fractured clayey limestone, which allows rapid infiltration of water during intense rainfalls. Therefore, this slope fails even though the slope angle is lower than 33°.

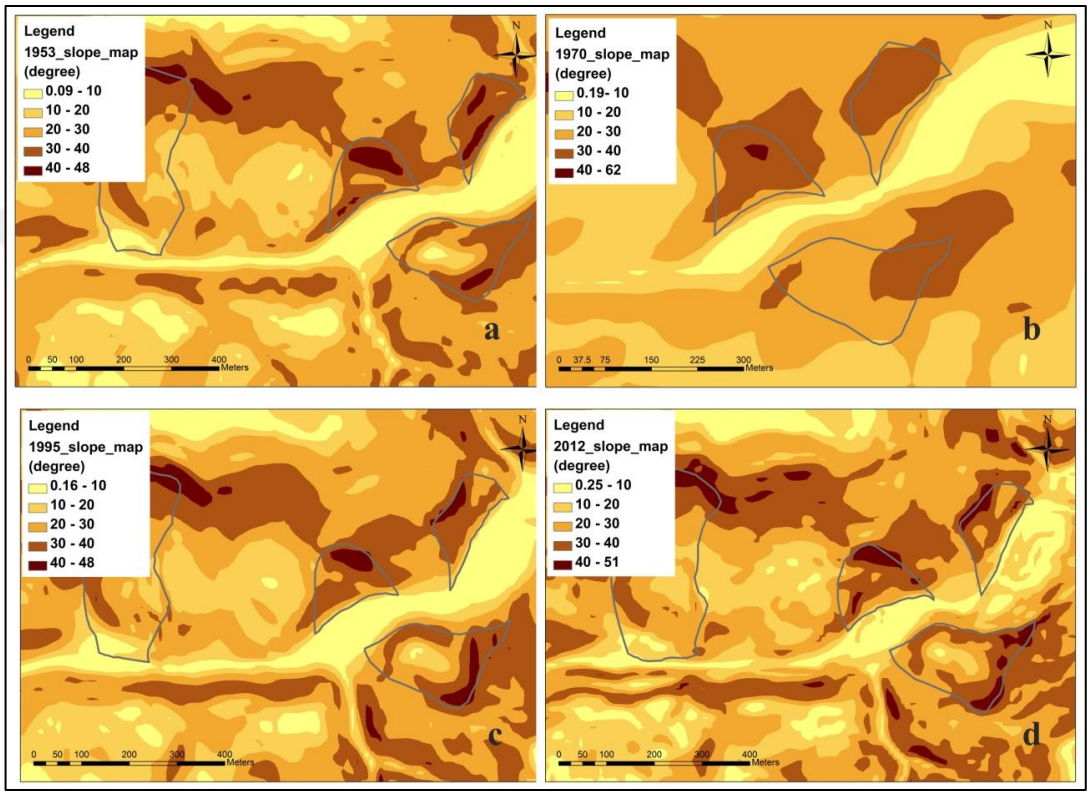


Figure 7.13 The slope maps of each year a. 1953 b. 1970 c. 1995 d. 2012

CHAPTER EIGHT
MULTI-TEMPORAL SLOPE STABILITY ASSESSMENT

The slope stability problems are mainly affected by the anisotropy and non-homogeneity of the rock mass, whereas the deformation analyses are less affected by them. Therefore, a better simulation of a slope depends on the better input of the geological setting regarding the mechanical properties of rocks (Zaruba & Mencl, 1982).

As stability of rock slopes is predominately governed by discontinuities, the failure of intact rock strength is not expected unless rock bridges are present. For this reason, the strength of discontinuity walls plays an important role in the shear strength and deformability of rock mass, where the small shear displacement of individual joints may lead actual stresses to exceed the compression strength of the rock wall material (Pantelidis, 2009).

In the case of non-structurally controlled slopes where traces of rock joints are not obvious and have no or little effect on the stability, mainly external factors (e.g., rainfall, weathering, seismicity) influence the stability condition of the rock slope (Basahel & Mitri, 2017).

Hydrologic properties as well as the physical, geotechnical, mineralogical, and geomorphic properties of the rock mass even the root strength, fundamentally define the depth, type, and sliding rate of the failure (Sidle & Bogaard, 2016).

In this study, slope stability evaluations were made by multi-temporal kinematic and numerical analyses. The effect of triggering factors was also evaluated by numerical analyses.

8.1 Kinematic Analyses

Kinematic analyses allow identification of the possibility of slope instability likely to occur due to the orientation and internal friction angle of the structural features (predisposing factors such as joint, bedding sets, etc.). It is a fast and practical analysis of the preliminary slope design. However, it should be kept in mind that, while the kinematic analysis is a good indicator of potential slope instability, external forces (earthquake forces, water pressures, etc.) on the slope as well as the height of the slope and unit weight of the rock material are not taken into consideration. It is better to use kinematic analysis prior to detailed slope stability analysis since it facilitates understanding the failure mechanism and guides for selecting the appropriate type of numerical slope stability analysis.

The rock masses which are complexly jointed and bedded can exhibit plane sliding, wedge sliding, and toppling simultaneously or successively with failure through rock bridges by flexure, shear, or splitting (Goodman, 1989). Unless the rock mass consists of well-defined and regular sets of discontinuities, kinematic analysis is not essential. However, stereographic projection of the mean joint set planes and slopes can refer to a block sliding.

In this study, the critical mean discontinuity set planes and the slope planes and their pole points are projected on the stereographic net with the aid of Dips software (Rocscience, 2015). The maximum and overall slope angles along the cross-sections of four landslides in different years (1953, 1970, 1995, 2012, 2017) were investigated by considering the mean friction angle as 34.8° (Table 8.1).

Table 8.1 Kinematic analyses results of four landslides with regard to the maximum and overall slope angles

Landslide-1	Years				
Dip direction of slope: 180	1953	1970	1995	2012	2017
Max. slope angle	40	-	44	47.5	44
Possible failure type	Wedge	-	Wedge	Wedge	Wedge
Overall slope angle	30	-	26	27	27
Possible failure type	None	-	None	None	None
Landslide-2	Years				
Dip direction of slope: 155	1953	1970	1995	2012	2017
Max. slope angle	41	41	44.5	45	44
Possible failure type	None	None	None	Wedge	None
Overall slope angle	31	32	32	32	32
Possible failure type	None	None	None	None	None
Landslide-3	Years				
Dip direction of slope: 347	1953	1970	1995	2012	2017
Max. slope angle	40	32	44.5	48	50
Possible failure type	Wedge	None	Wedge	Wedge	Wedge
Overall slope angle	32	27	30	30	30
Possible failure type	None	None	None	None	None
Landslide-4	Years				
Dip direction of slope: 126	1953	1970	1995	2012	2017
Max. slope angle	42	36.5	46	50	51
Possible failure type	Toppling	Toppling	Toppling	Toppling Wedge	Toppling Wedge
Overall slope angle	27	29	31	31	32
Possible failure type	None	Toppling	Toppling	Toppling	Toppling

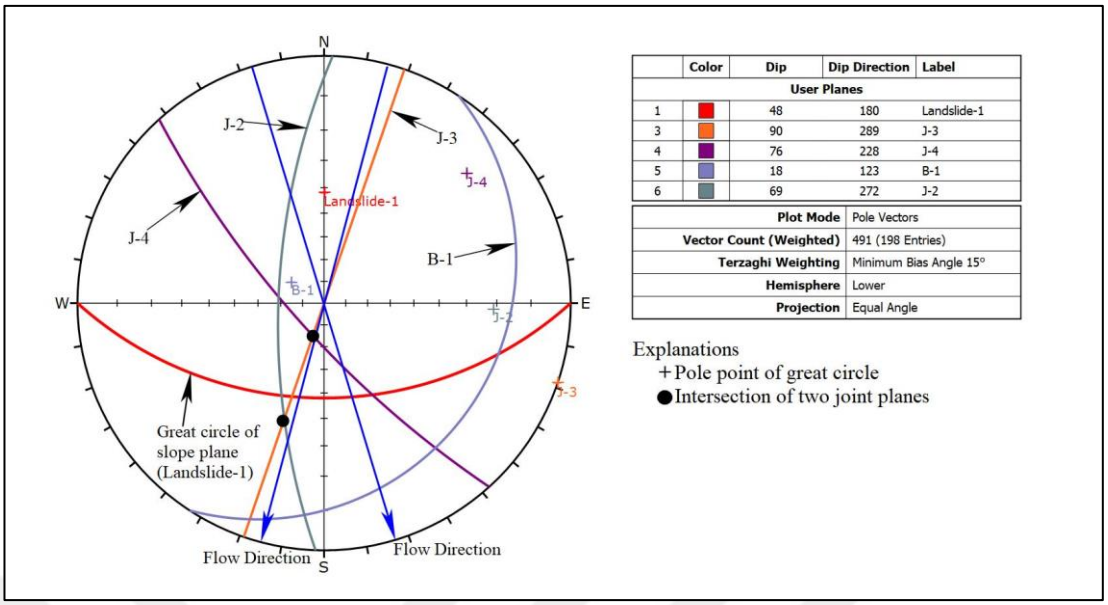
Even though the interpretation of the aerial photographs indicated a rotational failure character, stereographic projection showed that the role of discontinuity sets in defining the failure mode is not negligible. However, these findings will be a matter while benching during the dam construction as a bench-scale failure. An overall slope instability due to structural features is not expected except Landslide-4. For this reason, structural features forming blocks and flow directions of the

tributaries that may affect slope instabilities were further investigated on the stereographic projection net considering the maximum slope angles along the cross-section of the landslides.

Stereographic projections indicated that flow directions of tributaries are mainly coinciding with the dip direction of bedding planes and/or trend of the intersection of two discontinuity planes. It can, therefore, be evaluated that the surface water or groundwater is flowing into the landslide body along these discontinuity planes or intersections.

The blocks are formed by the steeply dipping joint sets and their intersections with the gently dipping bedding planes (B-1 and B-2). The steep joint sets also work as lateral release surfaces of the sliding blocks.

For landslide-1, the trend of the intersection of J-3 and J-4 (steep plunge$\approx 72°$) is relatively the same as the dip direction of B-1. Hence, the intersection line of J-3 and J-4 with B-1 form a block together. The flows of tributaries are restricting the Landslide-1 area from west and east. Water flow directions are coinciding with the plane of J-3. Water flows into the landslide mass, particularly during and after heavy rainfall. The overall slope angle is known as changing between 26° and 30° for the period between 1953 and 2017 regarding the cross-sections taken from multi-temporal DEMs. The steeper parts ($\approx 48°$) of the overall slope (along the cross-section) may exhibit complex failure modes involving wedge (J-2 and J-3) in conjunction with sliding (Figure 8.1).



	Color	Dip	Dip Direction	Label
User Planes				
1		48	180	Landslide-1
3		90	289	J-3
4		76	228	J-4
5		18	123	B-1
6		69	272	J-2

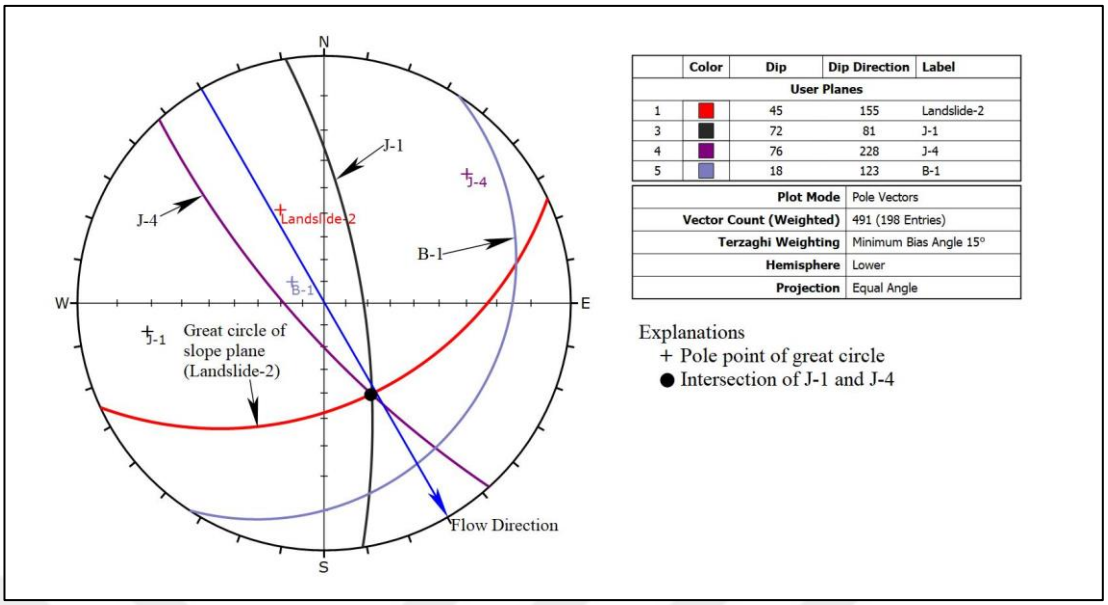
Plot Mode	Pole Vectors
Vector Count (Weighted)	491 (198 Entries)
Terzaghi Weighting	Minimum Bias Angle 15°
Hemisphere	Lower
Projection	Equal Angle

Figure 8.1 Stereographic projection of the critical mean set planes, Landslide-1, and the water flow directions

For Landslide-2, the trend of the intersection of J-1 and J-4 (plunge ≈ 44°) is almost the same as the dip direction of the slope. Hence, the intersection line of J-1 and J-4 with B-1 form a block together. The flow of a tributary is affecting the Landslide-2 area from the west. It works as a pathway for water flow into the landslide mass, particularly during and after heavy rainfall. The overall slope angle is changing between 31° and 32° for the period between 1953 and 2017. The steeper parts (≈45°) of the overall slope are prone to complex failure modes involving wedge (J-1 and J-4) in conjunction with sliding (Figure 8.2). As the value of the wedge factor (K) as a function of wedge geometry increases, wedge potential in the slope decreases. K value changes proportional to the angle of the wedge (angle between the two joint planes) and angle of tilt (β).

$$K = \sin\beta / \sin(\xi/2) \quad (8.1)$$

As the angle of the wedge (ξ) increases, the K value increases. In Landslide-2, the K factor is greater than 2.0 (ξ: 45°, β: 87°) which makes the slope unfavorable for wedge sliding. On the other hand, the direction of flow overlaps the trend of the intersection of J-1 and J-4 and the dip direction of the slope.

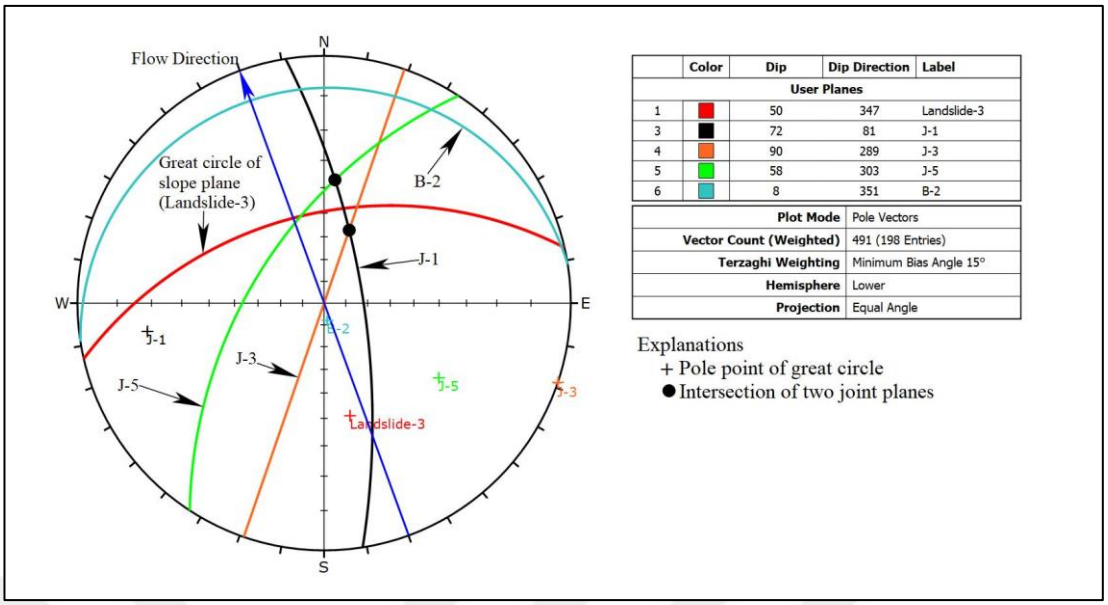


	Color	Dip	Dip Direction	Label
User Planes				
1		45	155	Landslide-2
3		72	81	J-1
4		76	228	J-4
5		18	123	B-1

Plot Mode	Pole Vectors
Vector Count (Weighted)	491 (198 Entries)
Terzaghi Weighting	Minimum Bias Angle 15°
Hemisphere	Lower
Projection	Equal Angle

Figure 8.2 Stereographic projection of the critical mean set planes, Landslide-2, and the water flow direction

For Landslide-3, the trend of the intersection of J-1 and J-3 (plunge ≈ 56°) is fairly the same as the dip direction of B-2. Hence, the intersection line of J-1 and J-3 with B-2 form a block together. The flow of a tributary is affecting the Landslide-3 area from the west. The direction of flow is coinciding with the dip direction of B-2, which works as a pathway for water flow into the landslide mass, particularly during and after heavy rainfall. The overall slope angle is changing between 27° and 32° for the period between 1953 and 2017. The steeper parts (≈50˚) of the overall slope are prone to complex failure modes involving wedge (J-1 and J-5) in conjunction with sliding (Figure 8.3). The potential of wedge failure in the steeper parts of Landslide-3 is greater than the one at Landslide-2 due to the decreasing K factor and the plunge angle of the joints' intersection.

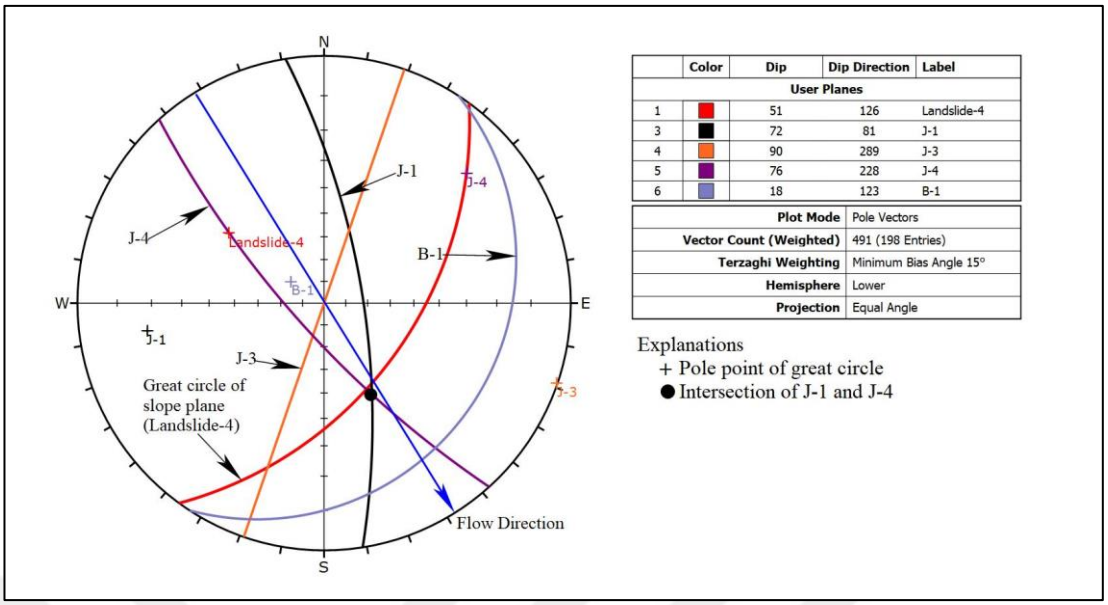


	Color	Dip	Dip Direction	Label
User Planes				
1		50	347	Landslide-3
3		72	81	J-1
4		90	289	J-3
5		58	303	J-5
6		8	351	B-2

Plot Mode	Pole Vectors
Vector Count (Weighted)	491 (198 Entries)
Terzaghi Weighting	Minimum Bias Angle 15°
Hemisphere	Lower
Projection	Equal Angle

Figure 8.3 Stereographic projection of the critical mean set planes, Landslide-3, and the water flow direction

For Landslide-4, the dip direction of J-3 (dip ≈ 90°) is nearly the same as the dip direction of B-1 (Figure 8.4). Hence, the J-3 and B-1 from a block together. In such a case, the failure surface is very steep at the upper parts of the landslide and turning almost parallel towards the toe of the slope. This finding is consistent with the field observations and the cross-sections taken from DEMs. The flow of a tributary is affecting the Landslide-4 area from the southeast. The direction of flow is coinciding with the trend of the intersection of J-1 and J-4 which works as a pathway for water flow into the landslide mass particularly during and after heavy rainfall. The steeper parts (≈51˚) of the overall slope and the overall slope (dip ≤29˚) are prone to complex failure modes involving potential flexural toppling (J-3) in conjunction with sliding (Figure 8.4).



	Color	Dip	Dip Direction	Label
User Planes				
1		51	126	Landslide-4
3		72	81	J-1
4		90	289	J-3
5		76	228	J-4
6		18	123	B-1

Plot Mode	Pole Vectors
Vector Count (Weighted)	491 (198 Entries)
Terzaghi Weighting	Minimum Bias Angle 15°
Hemisphere	Lower
Projection	Equal Angle

Figure 8.4 Stereographic projection of the critical mean set planes, Landslide-4, and the water flow direction

8.2 Geotechnical Model of Landslides

As the kinematic conditions for overall slopes are not favorable for planar, wedge, or toppling failures in complexly fractured rocks, sliding along two different planes (combined failure with two planar surfaces) can occur. In such a mechanism, two intersecting structural features form a block that can slide along a steeply dipping set at the crest and follows a less inclined surface to the toe of the slope as explained in Goodman (1989). It should be noted that this type of failure only occurs if the dip angle of the upper part of the failure surface is greater than the internal friction angle (Figure 8.5). It should also be noted that this type of failure shows some rotational character due to the failure of weak rock layers at the point where the shear stress is the greatest along the failure surface.

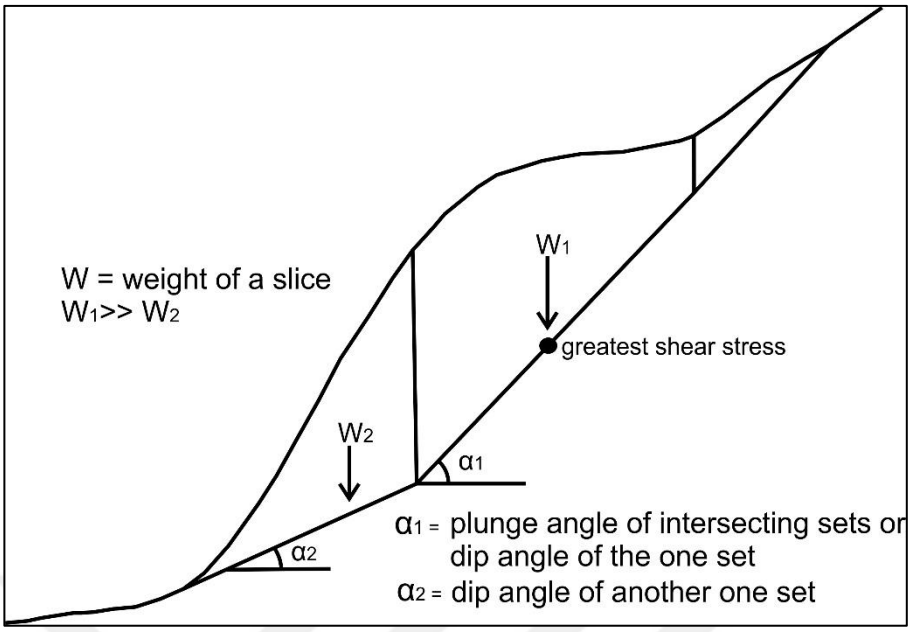


Figure 8.5 The two-block model (Goodman, 1989)

In parallel with the mechanism proposed by Goodman (1989), a generalized geotechnical model was constructed for the landslides in the study area (Figure 8.6).

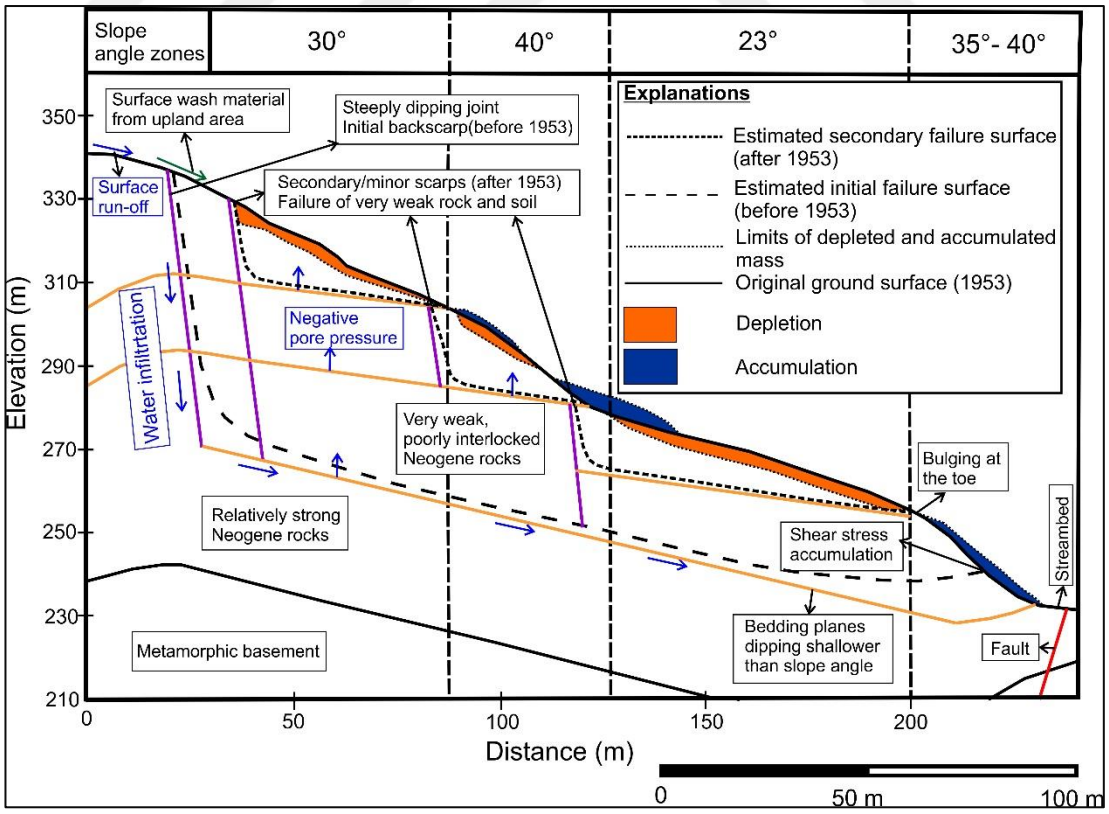


Figure 8.6 Generalized geotechnical model of the landslides in the study area

The initial movement was defined to have occurred before 1953 from remote sensing data. The initial failure surface is estimated to be formed by multiple planes with two or more weakness planes. The failure initiates from the steeply dipping joint or fault plane. It explains the steep back scarp observed in the field and defined on the slope maps. Since the slip surface tends to seek out the weakest path, the rupture follows the joint surface and breaks through the very weak rock material until approximately 30 m deep. Afterward, the rupture surface follows the gently dipping bedding plane which is probably the contact between the very weak and relatively stronger Neogene units. And finally, bulges at the toe. As mentioned earlier by Goodman (1989), the accumulation of shear stress at the toe transmitted from the upper slope exceeds the friction along the flat basal surface at the toe (Figure 8.6).

On the other hand, shallow secondary failures (1953-2017) within the pre-failed slope mass involve the movement of a very weak Neogene unit and soil layer covering this unit. Sometimes, only the soil and debris material move downwards. The average slope angle of the region involving the initial movement is approximately 30° (Figure 8.6). The depleted material reaches relatively lower slope angles, whereas the accumulated material forms a steeper slope up to 40° (Figure 8.6). The minor or secondary failures can be defined as the repeated development of the same type of movement in smaller scales which indicates an overlapping successive movement. These secondary failures do not share the same rupture surface but do share the same displaced material (Figure 8.6). At the toe, the slope angle of the stream terrace is approximately 35°-40°. It is necessary to say that complex failure mechanism is involved in the multi-temporal model. Hence, it is also possible that new failure surfaces may be formed due to the failure of intact rock bridges over time. In addition, the surface run-off and water infiltration along discontinuities facilitate the shear strength breakdown.

Considering the geotechnical model proposed, the four landslides in the study area were simulated based on the environmental and topographic conditions for the years 1953, 1970, 1995, 2012, and 2017. The cross-sections were constructed along the

center of the landslides using the DEMs of the successive years. Hence, a multi-temporal evaluation of slope stability problems was made.

8.3 Numerical Modeling with FEM

Rock masses are generally jointed and may be faulted, and are generally anisotropic (Barton, 2013). Hence, rock masses presumably fail through intact rock and by the controls of joints. Nevertheless, heavily fractured, highly weathered, or poorly unconsolidated rock slopes can be assumed to obey the equivalent continuum, which considers isotropic, homogeneous media (Hoek et al., 2002). Goodman (1989) also stated that pervasively fractured rock slopes may represent an equivalent continuum condition and exhibit combinations of failure modes.

In the study area, multiple sets of discontinuities enable the material to show an equivalent near-isotropic behavior. The only exception to this general statement is when one of the joints becomes much more weaker than the others as previously stated by Hoek & Brown (1980), Brown (1970).

An appropriate numerical method to evaluate slope stability should be chosen with regard to the presence of structural factors controlling the stability. There are three main numerical methods such as; 1) continuum-based methods (finite element method (FEM), finite difference method (FDM), boundary element method (BEM)), 2) discontinuum-based methods (discrete element method (DEM), discontinuous deformation analysis (DDA), particle flow codes) and 3) coupled continuum/discontinuum based methods which can also be termed as hybrid methods (LEM+FEM, particle flow code+FDM, etc.)

Continuum methods assume the material is continuous throughout the body. In these methods, discontinuities can be treated as special cases by introducing interfaces between continuum bodies (Wyllie & Mah, 2004). Jointed rock masses can also be simulated by continuum modeling. The strength of discontinuities is included in the analyses. Even though simulation of the detachment of the discrete blocks may

be required, Hammah, Yacoub, Corkum, Wibowo, & Curran (2007), Kadakci Koca & Koca (2019) have shown that discrete element modeling and finite element modeling gave consistent results for several cases.

Even in the case of the heavily fractured rock mass, failure may start from a weak discontinuity plane and then pass through the very weak rock mass. Because the shear strength of rock material and the discontinuity plane may both breakdown if the low strength rock material itself is accompanying the poor rock mass as a result of intense jointing. Hence, discontinuity controlled failure would not be expected and continuum modeling answers the purpose.

The most commonly used continuum-based finite element method (FEM) was firstly introduced by Turner, Clough, Martin, & Topp (1956). Since the stability of a slope is evaluated by a FOS value which is the ratio of driving forces to resisting forces, Zienkiewicz, Humpheson, & Lewis (1975) firstly used the SSR technique, which enables calculating FOS in FEM analysis. The SSR technique is based on reducing Mohr-Coulomb (c' and ϕ') and Hoek-Brown strength parameters (m_b, s, a) by a "strength reduction factor" (SRF) until non-convergence occurs within a specified number of iterations and tolerance. The reduction of Mohr-Coulomb shear strength parameters by an SRF is simple since the Mohr-Coulomb envelope is linear. On the other hand, lowering the non-linear Hoek-Brown envelope is not straightforward. The non-linear shear strength envelope of the rock mass is reduced in an automated process in the software, as introduced in Hammah, Yacoub, Corkum, & Curran (2005a).

In FE analysis, the sliding body is discretized into a number of sub-elements termed mesh. Iterative solutions process for the nodes which link the sub-elements. The lack of convergence in the numerical iterations indicates that stress and displacement distributions that satisfy equilibrium conditions can not be determined. Thus, the critical SRF, which corresponds to the point at the last convergence state, is equal to the critical safety factor. The calculation of stress and deformation is performed through nodes without any assumption of the depth or location of the

failure surface. Therefore, the failure surface can be estimated from the incremental shear strain and plastic zone contours. The SRF value can be manually increased to indicate more than one slip surface. The detected failure surfaces may have not a simple and regular shape.

The equivalent continuum approach was adopted to simulate the rock mass in the study area using a commercially available elastoplastic finite element stress analysis program, RS2 (Rocscience, 2019) based on the Shear Strength Reduction (SSR) technique. The folded and faulted nature of the area results in closely spaced discontinuities and slickensided surfaces that the rock mass reaches its residual strength values. For this reason, elastic-perfectly plastic material behavior for poor quality rock masses (Göcek Fm. and Yeniköy Fm.) was used by considering the Generalized Hoek-Brown Criterion (GHBC), which expresses the shear strength with a non-linear envelope. The mechanical behavior of soil, alluvium, and Keçidağ Fm. unit was represented by the Mohr-Coulomb Criterion. The mechanical properties of Keçidağ Fm. were taken from Uslu & Koca (2019). As the discontinuity sets play an essential role in forming the lateral release surfaces and back scarp of the landslide body, joint and bedding sets were modeled with respect to the geotechnical model proposed in this study. In the jointed model, the mechanical behavior of joints was represented by Barton & Bandis (1982) Criterion. The deterministic computation of FOS was carried out by RS2 software. A non-associated flow rule (dilation parameter=0, no volume change) was considered. Boundary limit conditions were extended to the lateral and vertical sides until the numerical solutions are not significantly affected by the limits of the model. The mesh configuration was set to six noded triangular elements with 2000 mesh elements since the number of mesh elements has little impact on FOS values (Hammah, Yacoub, Corkum, & Curran, 2005b).

The ranges of the required parameters for the numerical analyses were chosen based on the laboratory and in-situ tests. The values representing the post-failure conditions were found by back analysis. The range of the parameters used for Hoek-Brown and Mohr-Coulomb materials is given in Tables 8.2 and 8.3.

Table 8.2 The ranges of the strength and deformation properties of the landslide mass with respect to Generalized Hoek-Brown Criterion

Parameters	Göcek Fm. N:7	Yeniköy Fm. N:13	Very weak rock N:3
	Generalized Hoek-Brown Failure Criterion		
GSI	29-36 (mean:32)	30-39 (mean:36)	14-18
σ_{ci} (MPa)	19.18-51.31	21.70-117.02	10.28-19.34
E_{avg} (MPa)	5446.43-10719.07	1726.56-14561.67	591.48-4776.83
E_m (MPa)	849.84-2079.77	957.51-3732.87	262.37-453.05
m_i	9-16	10-21	7-9
m_b	0.334-0.697	0.366-0.699	0.09-0.164
s	$6.5x10^{-5}$ -$16.79x10^{-5}$	$7.4x10^{-5}$ -$25.2x10^{-5}$	$8.5x10^{-6}$ -$1.46x10^{-5}$
a	0.500-0.505	0.500	0.560-0.580
df	0.97	0.97	0.97
υ	0.28	0.34	0.30-0.35
γ (kN/m^3)	23.45-25.89	19.81-26.48	19.91-22.17

Table 8.3 The ranges of strength and deformation properties of the soil and rock mass with respect to Mohr-Coulomb Criterion

Parameters	Alluvium	Residual Soil	Keçidağ Fm.*
	Mohr-Coulomb Failure Criterion		
σ_t	0	0	0
ϕ (°)	33-44	17-34	26
c (MPa)	0	0-0.022	1.5
υ	0.30-0.4	0.3-0.35	0.2
γ (kN/m^3)	19.0-21.0	17.0-18.0	25.4
E_m (MPa)	30-80	10-30	1536.83

***** The mechanical properties of Keçidağ Fm. were taken from Uslu & Koca (2019).

In-situ measured JCS values for all types of discontinuities were considered for back analyses (Table 8.4). For this reason, no scale effect correction was made on JCS values as proposed by Barton & Bandis (1982). Due to variations of weathering grade, ϕ_r was calculated from ϕ_b and Schmidt hammer rebound values according to Equation 5.13 (Table 8.4).

Table 8.4 The calculated ϕ_r values based on the static and dynamic ϕ_b values of M-samples, in-situ and laboratory-measured Schmidt hammer rebound values

Condition	R (lab)	r (in-situ)	ϕ_b (°)	r/R	W_c	ϕ_r (°)
Static	47.1	36.7	33.75	0.78	1.28	29.33
	47.1	36.7	35.24	0.78	1.28	30.82
	47.1	36.7	35.58	0.78	1.28	31.16
Dynamic	47.1	36.7	27.92	0.78	1.28	23.50
	47.1	36.7	36.72	0.78	1.28	32.30
	47.1	36.7	39.4	0.78	1.28	34.98

Back analyses were performed for discontinuities considering all the types (bedding, joint, tension crack) are having the same range of mechanical and stiffness properties (Table 8.5).

Table 8.5 The ranges of strength and stiffness properties of the soil and rock mass with respect to Barton-Bandis Criterion

Parameters	Joints	Bedding	Tension crack
	Barton & Bandis (1982) Criterion		
ϕ_r (°)	23.50-34.98	23.50-34.98	23.50-34.98
JRC	3-7	3-7	3-7
JCS (MPa)	18.80-88.79	18.80-88.79	18.80-88.79
k_n (MPa/m)	5165.04-9662.2	5165.04-9662.2	5165.04-9662.2
k_s (MPa/m)	1720.29-3111.88	1720.29-3111.88	1720.29-3111.88

8.4 Back Analysis of the Post-Failure Properties of Landslides

Pre-failed slopes are commonly subjected to back analysis to determine or estimate the shear strength, water pressure on discontinuities, or other conditions at the time of failure. However, Duncan & Wright (2005) pointed out the inefficacy of this simple method for complex failure cases. Deschamps & Yankey (2006) also argued that back analysis is only reliable when the slope models and assumptions are accurately representing the real case. Nevertheless, back analyses are essential to deal with the uncertainty in input parameters for slope stability modeling. Back analyses can be done by considering known conditions, such as failure surfaces, displacement, or simply find out the combination of material properties satisfying the limit equilibrium (FOS:1) (Sönmez, Ulusay, & Gökçeoğlu, 1998; Duncan & Wright, 2005; Jiang & Yamagami, 2008). If multiple sets of slope stability parameters have to be back-analyzed simultaneously under uncertainty, back analysis is performed in a probabilistic assumption (Zhang, Tang, & Zhang, 2010). Advanced methods for back analysis such as optimization techniques (Zhang et al., 2010; Fatty & Li, 2018), various artificial intelligence techniques (Zhu, Zhao, & Zhao, 2014), and progressive deformation (creep) assumption (Bozzano, Martino, Montagna, & Prestininzi, 2012; Sandøy, 2012) were developed in the literature. The displacement-based back analysis was also used by many researchers (Okui, Tokunaga, Shinji, & Mori, 1997; Zhu et al., 2014; Lv, Liu, & Yang, 2017; Saroglou et al., 2018;). However, these studies are mainly focused on the pre-failure or failure time. FOS:1 is used in back

analyses because FOS:1 represents the theoretical critical stability condition (critical balance) which reflects the conditions at the time of failure. However, in the FEM, the SRF is the factor that input strength parameters were divided by it. In this manner, while the SRF increases, the input shear strength parameters decrease until failure occurs. Thus, if one searches for the pre-failed model until giving critical SRF:1, it means that the slope is at the edge of instability. However, in the real case, the model has already failed, and a certain amount of displacement has occurred, and the material properties were reduced to residual. In addition, the critical SRF is corresponding to the maximum SRF for which the model remains stable.

There are two recent studies that are correlating displacements derived from slope monitoring methods with the numerical models. Conte, Pugliese, & Troncone (2019, 2020) used back analyses for post-failure characteristics which can be preferred for better understanding the complex mechanical processes of landslides. They argued that since the in-situ displacements are generally recorded after the main failure event that has already occurred; the back analyzed values depending on these displacement values do not reflect the strength at the time of failure but the post-failure characteristics.

Despite the studies on displacement-based back analysis mentioned above, a structurally and mechanically evolving multi-temporal model has not been made by back analyses. In other words, in this study, the geomechanical properties of rock mass and joints and the structural design of the same slope evolves/changes regarding the movements during the years and due to triggering factors, and these conditions were all considered in multi-temporal numerical slope models.

Since the failure has already occurred in the study area, the back analyses were performed for the models giving lower critical SRF values than 1. It is known that the numerical analyses were performed for not only one SRF value but different SRF values. Thus, the model giving an SRF value lower than 1 was evaluated for the "SRF=1 tab" which means that the input strength parameters are divided by "1". In other words, the stress and displacement values in the SRF:1 tab are the results of

exactly the input parameters. For this reason, the amount of vertical displacement in this tab is expected to be similar to the amount of vertical displacement (depletion) derived from photogrammetric analyses as well as the shape of the failure surface. It should also be noted that the displacements calculated by FEM are viewed on the interpret model is based on a referenced stage. In other words, by default settings, the software shows the displacement values relative to a reference iteration. Commonly, it is SRF:1 and varies case by case. In order to view the absolute displacement values, one should not use a reference value, otherwise, the displacements will be zero at that referenced stage. Many cases were searched manually until obtaining an amount of vertical displacement, shape and depth of depletion matching well with the photogrammetric results.

Prior to back analyses, multi-temporal slope geometries that were extracted from the DEMs of 1953, 1970, 1995, and 2012 were evaluated for ambient conditions (non-triggered conditions). Almost all cases were found to be stable; however, some of the slopes were at the edge of instability (SRF: 1.00-1.10) (Table 8.6).

Table 8.6 The SRF values for the landslides under ambient conditions

	Ambient condition SRF			
	1953	1970	1995	2012
Landslide-1	1.64	-	1.80	1.86
Landslide-2	1.08	1.50	1.50	1.25
Landslide-3	1.10	1.11	1.81	2.32
Landslide-4	1.07	1.26	1.49	1.23

Afterward, the same cross-sections were used for back analyses. The crest of the movements and amount of vertical displacement obtained from the photogrammetric analyses were used as a reference to find the most realistic slope conditions. The models were based upon a set of parametrical calculations with various combinations of input parameters as well as the triggering factors (seismic activity, heavy rainfall, water pressure on discontinuities, wildfire). It was aimed to set an optimal combination of input parameters and environmental conditions which determines the

behavior of the slope model close to the real slope behavior based on the photogrammetric analysis results.

Consequently, following the methodology described above, the best harmonizing vertical displacements and location of depletion with the photogrammetric results for the given material properties and structural conditions were assumed to be the post-failure condition of the slope. The secondary failures after 1953 within the initial displaced material were evaluated. For example; Landslide-1 yielded a maximum of 4.58 m depletion in numerical analyses and 5.67 m has been found by comparing the aerial photograph of 2012 and UAV-based 2017 topographies (Figure 8.7).

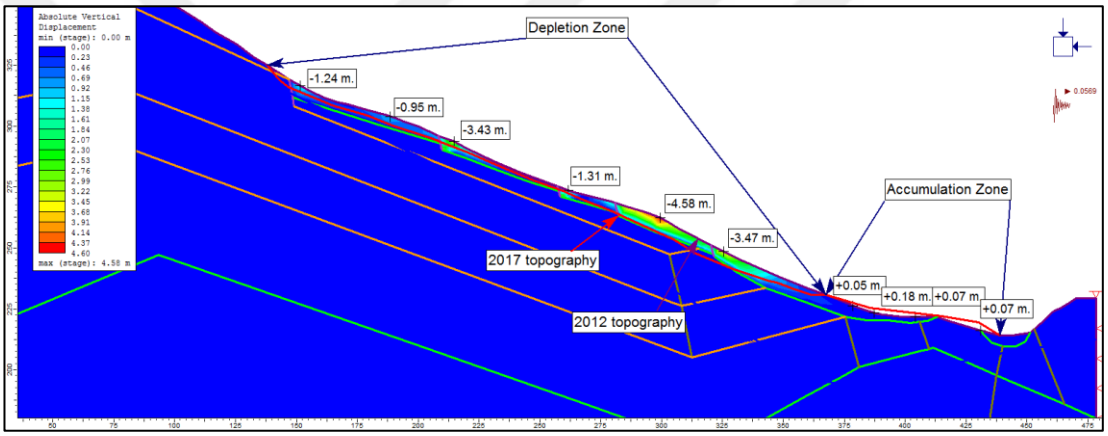


Figure 8.7 The proposed method for back analyses based on the vertical displacement and the location of failure surface (Landslide-1)

The back analyses of the four cross-section lines cutting the landslide mass provided the post-failure mechanical properties of rock mass and joints, as well as the structural geometry contributing to the failures. Back analyses also allowed us to determine the variation in mechanical characteristics with triggering factors over years.

The results confirm the assumption that the topography evolves during years by landslides; the geological units also evolve from a geotechnical point of view. In other words, not only the topography changes with mass movements but also the mechanical and elastic properties of the mass decrease due to triggering factors and time; crack formation or crack widening occurs. For example, the cohesion and

internal friction angle of the surface soil cover material decreases over time since the slope movements lead to the loosening of the soil material. On the other hand, as the very weak rock unit fails and is transported to the downslope, the underlying relatively stronger layers of Neogene units are exposed on the upper slope faces.

8.4.1 Simulation of Structural and Geometrical Condition

The slope models were constructed considering the generalized geotechnical model constructed in this study based on the orientation of critical structural features derived from the stereographic projection, field observations, and borehole information. In order to simulate the structurally evolving multi-temporal slope model, ubiquitous joints representing tension cracks formed after an event were searched in the interpret window of the slope model and imported to the slope model of the following year as illustrated in Figure 8.8. Herein, it is important to choose the ubiquitous joints that failed in tension. In this manner, a user-defined slip condition (Barton-Bandis Failure Criterion) and orientation for a random plane (inclination: 90°) can be searched in a calculated slope model to determine whether this plane fails in tension or shear stresses. It is a post-processing tool in FE analyses. The search for ubiquitous joints was limited within the range of mechanical properties given in Table 8.5. If the normal stress on this investigated ubiquitous joint plane is tensile, the shear strength (and the strength factor) for the joint is automatically set to zero. As seen in Figure 8.8a, the blue-contoured areas are dominated by tension stresses adjacent to or in conjunction with the shear stresses. In Figure 8.8b, red areas represent the tension stresses for the given slip condition of a ubiquitous joint.

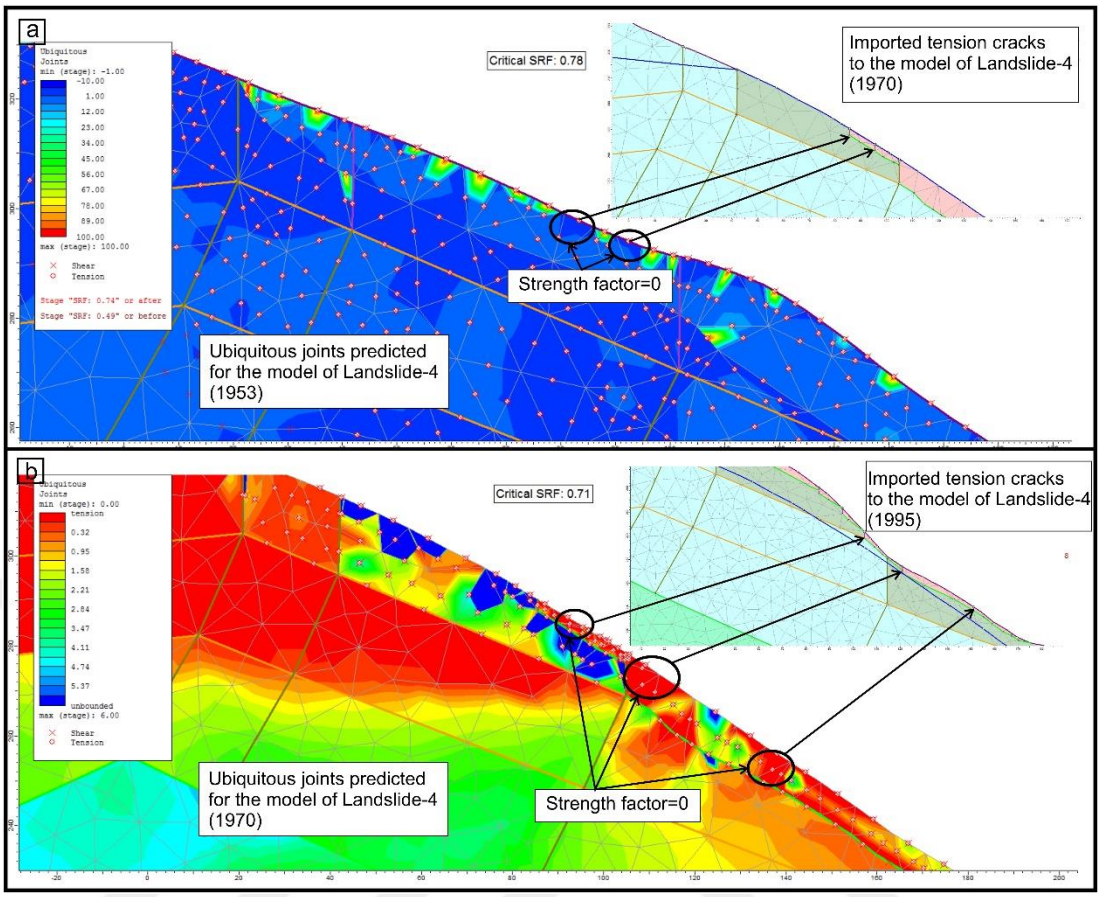


Figure 8.8 The illustration of using the ubiquitous joint tool a. 1953, Landslide-4 b.1970, Landslide-4

The thickness of the geological units was estimated from the drill cores and the geophysical investigation. The main folds were designed in a large-scale manner (Figure 8.9). The tension cracks were imported to the models after 1953. Because the identified failures (between 1953 and 2017) caused tension failures in some points along the cross-section. These points reflected by the ubiquitous joint tool were considered as the location of tension cracks in the slope model of the successive year.

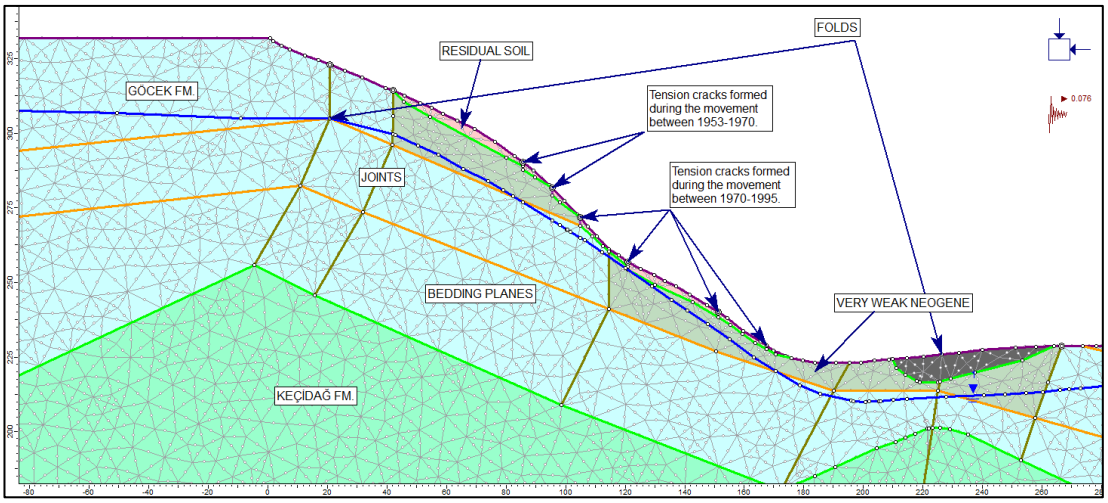


Figure 8.9 An example of the geometrical and structural design of the slope models in RS2 (Landslide-4, 1995 topography)

Consequently, the back analyzed properties of joint and bedding planes and tension crack were obtained (Table 8.7).

Table 8.7 The back analyzed properties of the discontinuities

Parameters	Joints	Bedding	Tension crack
	Barton & Choubey (1977) Criterion		
ϕ_r (°)	31.2	30	26.2
JRC	7	3	3
JCS (MPa)	40.3	21.43	21.43
k_n (MPa/m)	9662.2	5165.04	5165.04
k_s(MPa/m)	3111.88	1720.29	1720.29

8.4.2 Simulation of Triggering Factors

Wu & Sidle (1995) and Riestenberg & Sovonick-Dunford (1983) found that vegetation root systems contribute to soil strength by providing additional cohesion. Secci, Calcina, Ranieri, & Uras (2014) determined that the shear strength of the burned surface material (topsoil layer) is reduced due to wildfires. Wildfires also

decrease the infiltration rates and therefore advance the hillslope sediment transport by runoff processes. Due to the loss of vegetation roots and organic cover, the decrease in soil shear strength, and the changes in hydrologic properties, non-cohesive surface material becomes vulnerable to erosion (Gabet, 2003). For this reason, the wildfire that occurred in 1988 was simulated by reducing the cohesion of the thin soil layer on the top of the rock units. Since the slope was observed to be still bare in 1995, the weakening effect of wildfire was imported to the slope models of 1970 and 1995.

Rainfall is a common trigger for landslides on both natural and engineered slopes (Cai & Ugai, 2004; Martinović, Gavin, Reale, & Mangan, 2018; Wang, Vardon, & Hicks, 2018). Rainfall infiltration leads to a rise of groundwater level and pore water pressure and thus reduces the effective stress and the shear strength of earth material that may result in rainfall-induced slope failures. Various researchers stated that high-intensity rainfalls increase the possibility of relative landslides (Bai, Wang, Thiebes, Cheng, & Yang, 2014; Vardon, 2015). On the other hand, extreme rainfalls during a short time may not totally infiltrate and cause run-off. Run-off affects both the weathering process and the stability of rock masses. Iwahashi, Kamiya, & Yamagishi (2012) found that rainfall-induced landslides commonly occur at a slope gradient of 30°, however, the frequency of earthquake-induced landslides increases exponentially with the slope gradient. They also argued that the attributes of surface convexity and concavity, and the slope gradient to be effective factors for rainfall-induced landslides, whereas earthquake-induced landslides are mainly related to slope steepness.

The SRF values may readily decrease to below 1.0 due to excessive and prolonged rainfall. The highest rainfall recorded during the 1930-2018 period is 163.5 mm in one day (23 December 1986). Thus, the rainfall as a triggering factor was imported to the models of 1970. The water table level was raised to ground level to simulate such heavy rainfall, and to consider the effect of surface run-off. Additional water pressures were imported to bedding and joint planes and tension cracks.

The ranges of expected water pressures were calculated. Prior to the calculation, a simple and practical chart for defining the critical tension crack depth proposed by Wyllie & Mah (2004) was used. The tension cracks are expected to be formed within the 6 to 15 m thick very weak rock zone in which the secondary failures occur. Hence, the critical depth of the tension crack is obtained as varying between 0.6 m to 5 m according to Figure 8.10.

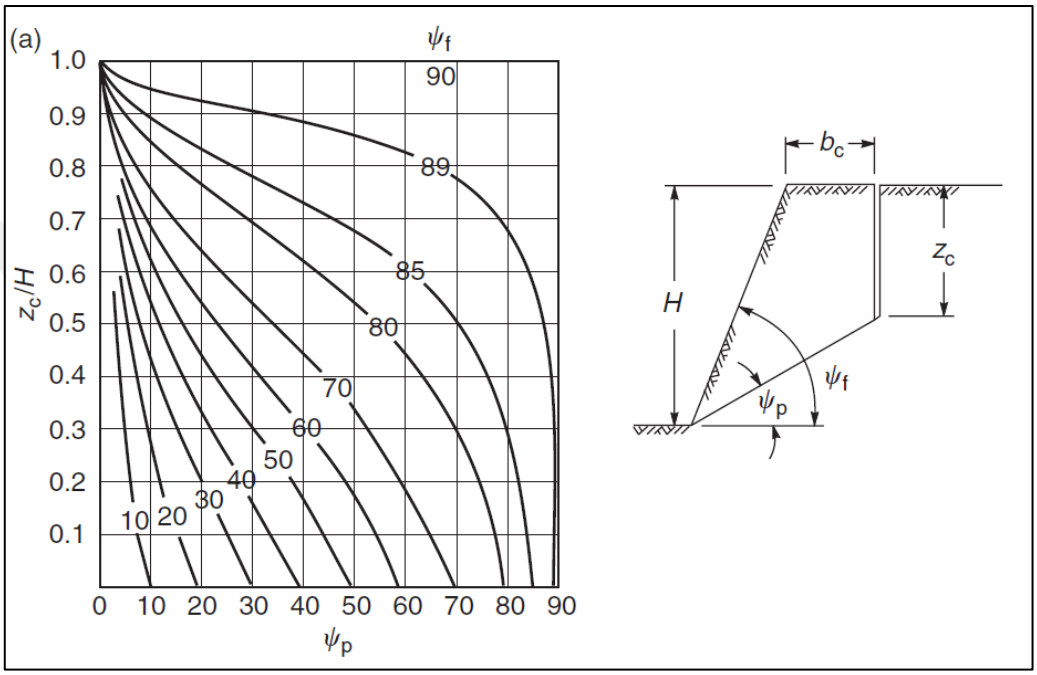


Figure 8.10 Critical tension crack depth relative to the crest of cut (Wyllie & Mah, 2004)

Thereafter, the exerted water pressure on the tension crack (V) can be found by Equation 8.2.

$$V = 0.5 \times \gamma_w \times z_w^2 \qquad (8.2)$$

where γ_w is the unit weight of water and z_w is the depth of water in the tension crack. z_w was assumed to be equal to the depth of tension crack (z) in this study which means that the tension crack is full of water. As a result, the minimum and maximum water pressure on the tension crack were calculated as 0.0018 MPa and 0.122 MPa, respectively.

On the other hand, water pressure on the joint or bedding planes (U) was calculated by Equation 8.3.

$$U = 0.5 \times \gamma_w \times z_w [(H-z) \times \text{cosec}\alpha] \quad (8.3)$$

where H is the slope height (the thickness of the zone that is prone to failure) and α is the inclination of the discontinuity. The minimum and maximum water pressures that may occur on the joint and bedding planes were calculated regarding the combinations of the data given in Table 8.8.

Table 8.8 The variations of parameters used in water pressure calculation and the ranges of water pressure used in back analyses

	Bedding	Joint
z_w (m)	0.6, 2, 3, 4, 5	
H (m)	6, 9, 15	
α (°)	8, 18	60, 80
Minimum water pressure (MPa)	0.051	0.017
Maximum water pressure (MPa)	1.762	0.249

The ranges of the water pressures were added to simulate water infiltration along the discontinuities. In addition, the values of E_m, c, and ϕ of the soil and very weak rock unit were reduced slightly, whereas the unit weight and Poisson's ratio were slightly increased to better simulate the effect of water on shear strength and elasticity. After many simulations, the back analyzed water pressure values were obtained (Table 8.9).

Table 8.9 The back analyzed water pressure values

Discontinuity	Water pressure (MPa)
Bedding	0.11
Joint	0.09
Tension crack	0.11

Seismic events are well known to trigger both small and large landslides. While the shear strength of the sub-surface soil or rock masses is reduced due to

weathering, extensive rainfall, and wildfire, an earthquake can trigger the failure (Hack, Alkema, Kruse, & Leenders, 2007). Seismic waves lead to a great water pressure in the groundmass. Hence, heavy seismic damage tends to occur in water-saturated slopes at a lower horizontal seismic intensity (Lu, Wang, Song, & Arai, 2015). Keefer (1984, 2002) argued that a minimum magnitude of M_w: 4.0 can trigger rock slope failures.

Seismic forces were applied as a pseudo-static load on all the slope models considering the highest M_w of the earthquakes that occurred within the investigated period (Table 1.3). For example, the seismic coefficient was used as 0.102g, 0.048g, 0.076g, and 0.0569g for the slope models belonging to the years 1953, 1970, 1995, and 2012, respectively. It was found from the laboratory test results that elastic modulus and internal friction angle values commonly increases under cyclic loading conditions. However, elastic modulus values possess residual values due to strain fatigue. On the other hand, strength has different trends under cyclic loading and generally decreases. These findings were also considered in simulating the earthquake effect in numerical models. More than one triggering factor most probably influenced the slopes in the area successively or simultaneously.

8.4.3 Landslide-1

Landslide-1 is the only landslide observed in the study area involving both the Yeniköy and Göcek Formations. These two formations have similar strength and deformation properties. Thus, the failure surface intersects both of these formations at one time. The intersection line of J-3 and J-4 and B-1 were expected to form rock blocks of very weak Neogene (Figure 8.1). The slope models of Landslide-1 in the years 1953, 1995, and 2012 are presented in Figure 8.11. The groundwater level (GWL) was estimated according to borehole data and ERT measurements. The GWL in the past years was also modeled as coherent with the current estimation.

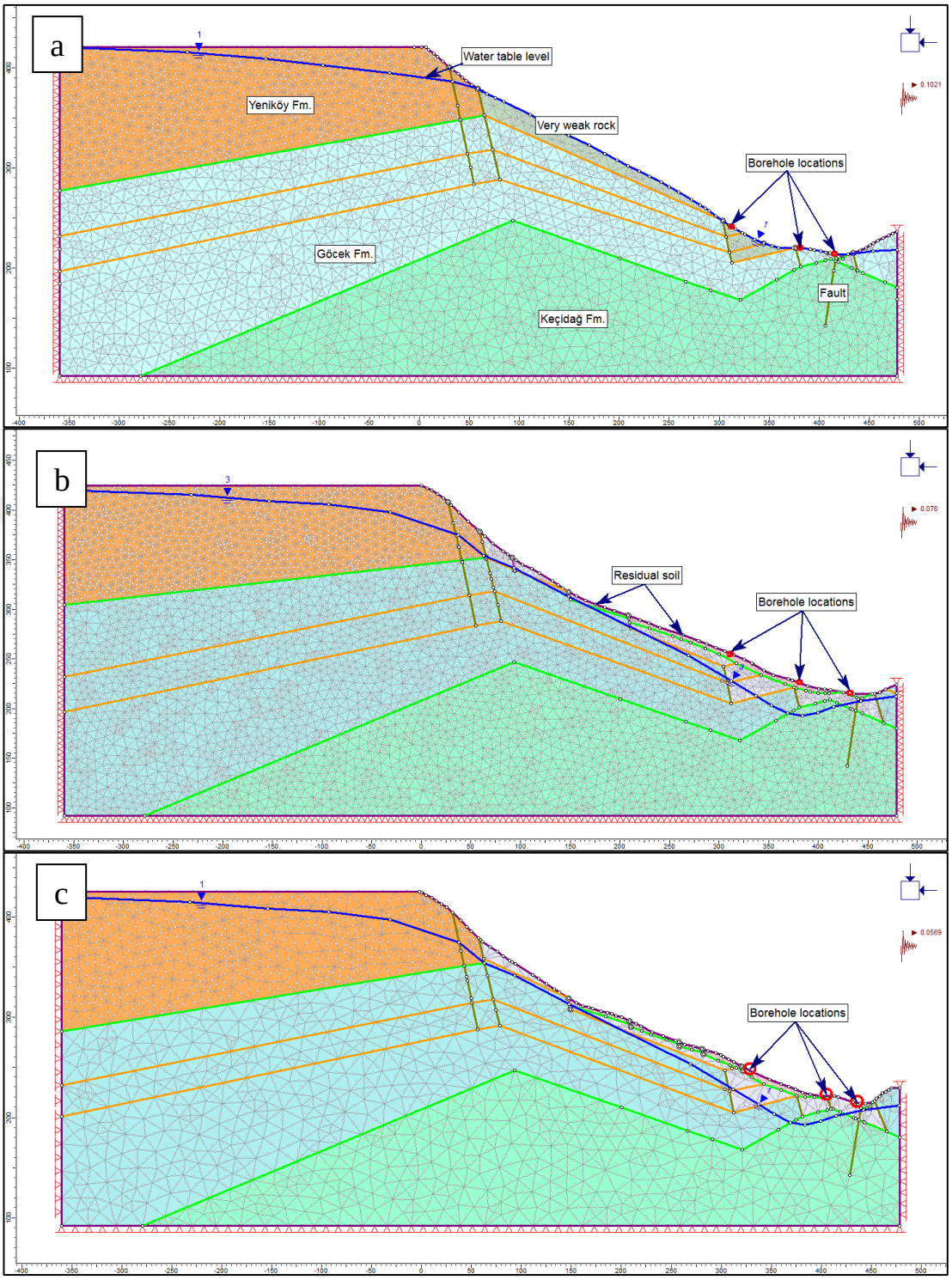


Figure 8.11 The slope models of Landslide-1 in the years of a.1953 b. 1995 c.2012

The back analyses provided post-failure physical, mechanical, and deformation properties of Landslide-1 (Table 8.10).

Table 8.10 The post-failure strength and deformation properties of the landslide mass at the failure (due to triggering factors) by years obtained from the back analyses (Landslide-1)

Years	Unit	Parameter								
		ɣ (kN/m^3)	E_m (MPa)	E_r (MPa)	υ	m_b	s	a	c (MPa)	ϕ (°)
1953	Alluvium*	19.91	56.4	-	0.3	-	-	-	0	41
	Very weak rock	20.20	350	300	0.4	0.124	0	0.56	-	-
	Göcek Fm.*	24.06	1358.24	-	0.28	0.435	10.66 x 10^{-5}	0.501	-	-
	Yeniköy Fm.*	23.11	2260.52	-	0.34	0.542	17.12 x10^{-5}	0.50	-	-
	Keçidağ Fm.*	25.40	1536.83	-	0.20	-	-	-	1.5	26
1995	Very weak rock	21.00	350	-	0.35	0.124	1.46 x 10^{-5}	0.56	-	-
	Residual soil	18.00	25	-	0.35	-	-	-	0.0007	23.5
2012	Very weak rock	20.20	350	-	0.35	0.124	1.46 x 10^{-5}	0.56		
	Residual soil	18.00	24	-	0.35	-	-	-	0.001	22

*The properties of alluvium, Göcek, Yeniköy, and Keçidağ Fm. were only given for the first year, they were the same for all the analyses**.**

8.4.4 Landslide-2

Landslide-2 is composed of solely Göcek Formation. The sandstone, siltstone, and fossiliferous clayey limestone units are dominant in this area. The intersection line of J-1 and J-4 and B-1 were expected to form a block of very weak Neogene (Figure 8.2). The slope models of Landslide-2 in the years 1953, 1970, 1995, and 2012 are presented in Figure 8.12. The groundwater level (GWL) was estimated according to borehole data and ERT measurements. The GWL in the past years was also modeled as coherent with the current estimation. However, the GWL in the slope model of 1970 was raised to ground surface level to simulate the heavy rainfall effect.

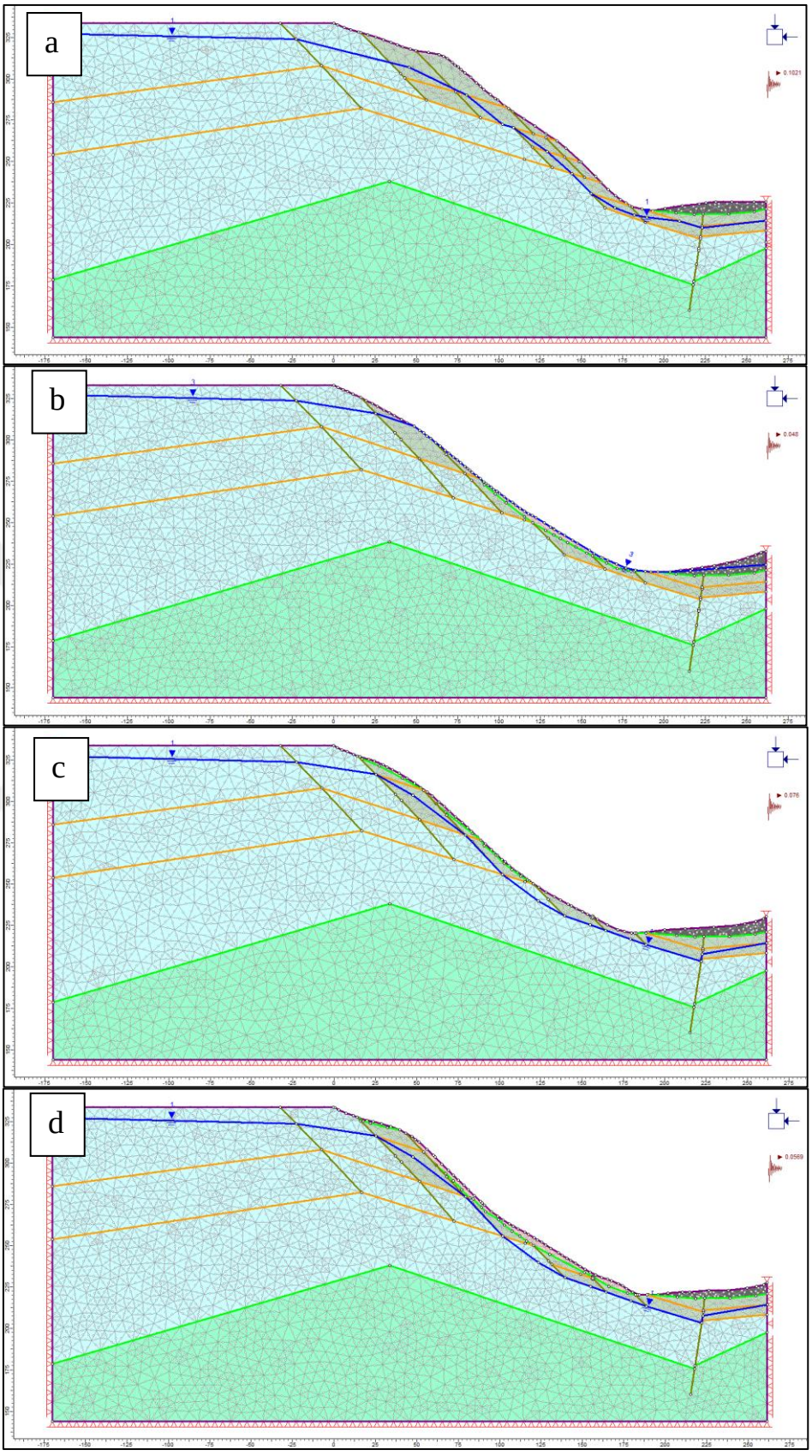


Figure 8.12 The slope models of Landslide-2 in the years of a.1953 b. 1970 c.1995 d.2012

The numerical solutions for Landslide-2 are fitting very well the photogrammetric analyses results considering both vertical displacement and the location failure surface (Figure 8.13). The soil cover on the top of the rock mass between the elevations 290 and 320 m was estimated to be transported by erosional processes from upper slopes after the wildfire and heavy rainfall.

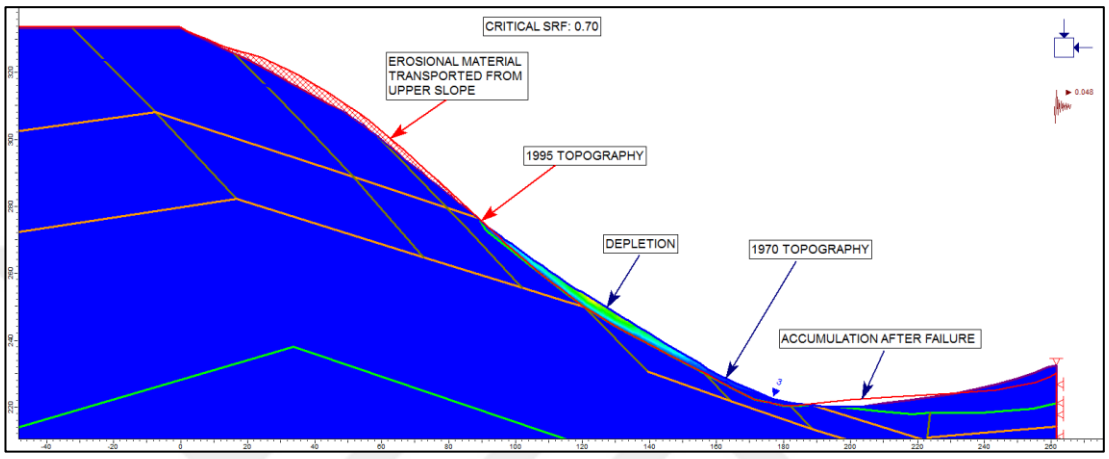


Figure 8.13 The comparison of 1970 and 1995 topography of Landslide-2, the harmony of depletion and accumulation areas with SSR result

The back analyses provided post-failure physical, mechanical, and deformation properties of Landslide-2 (Table 8.11). After the secondary failures occurred during 1953-1995, the majority of the very weak material has displaced, and the underlying rock layers were exposed in the upper parts of the slope which are relatively well-interlocked but still in the range of very weak rock. Due to this fact, the mechanical properties were slightly increased (Table 8.11). The changes in elastic modulus can be clearly seen in Table 8.11 that as the very weak material displaced, the underlying rock units having the values of 370 MPa and 1013.13 MPa elastic modulus are exposed.

Table 8.11 The post-failure strength and deformation properties of the landslide mass (due to triggering factors) by years obtained from the back analyses (Landslide-2)

Years	Unit	Parameter								
		ɣ (kN/m^3)	E_m (MPa)	E_r (MPa)	υ	m_b	s	a	c (MPa)	ϕ (°)
1953	Alluvium*	19.91	56.4	-	0.3	-	-	-	0	41
	Very weak rock	21.00	350	300	0.4	0.124	1.46×10^{-5}	0.56	-	-
	Göcek Fm.*	24.06	1358.24	-	0.28	0.435	10.66×10^{-5}	0.501	-	-
	Keçidağ Fm.*	25.40	1536.83	-	0.20	-	-	-	1.5	26.0
1970	Very weak rock	20.20	370	-	0.28	0.159	1.46×10^{-5}	0.56	-	-
	Residual soil	18.00	24	-	0.35	-	-	-	0	23.6
1995	Very weak rock	20.20	1013.13	-	0.30	0.159	1.46×10^{-5}	0.56	-	-
	Residual soil	18.00	24	-	0.35	-	-	-	0.0037	23.5
2012	Very weak rock	20.20	1013.13	-	0.28	0.159	1.46×10^{-5}	0.56	-	-
	Residual soil	17.00	24	-	0.35	-	-	-	0.0035	24.0

*The properties of alluvium, Göcek, and Keçidağ Fm. were only given for the first year, they were the same for all the analyses.

8.4.5 Landslide-3

Landslide-3 is the only landslide resting on the southern slope of the reservoir area. The dominant lithology is also differing from the other landslides. It is mainly composed of fossiliferous limestone with open fractures. The sandstone and siltstone intercalations are underlying this unit. The intersection line of J-1 and J-3 and B-2 were expected to form a block of very weak Neogene (Figure 8.3). Despite the other landslides, due to the abundant open fracture type in the limestones, additional water pressure of 0.09 MPa was imported on the joint planes not only for the 1970 slope model but also for 1953, 1995, and 2012 slope models. The slope models of Landslide-3 in the years 1953, 1970, 1995, and 2012 are presented in Figure 8.14.

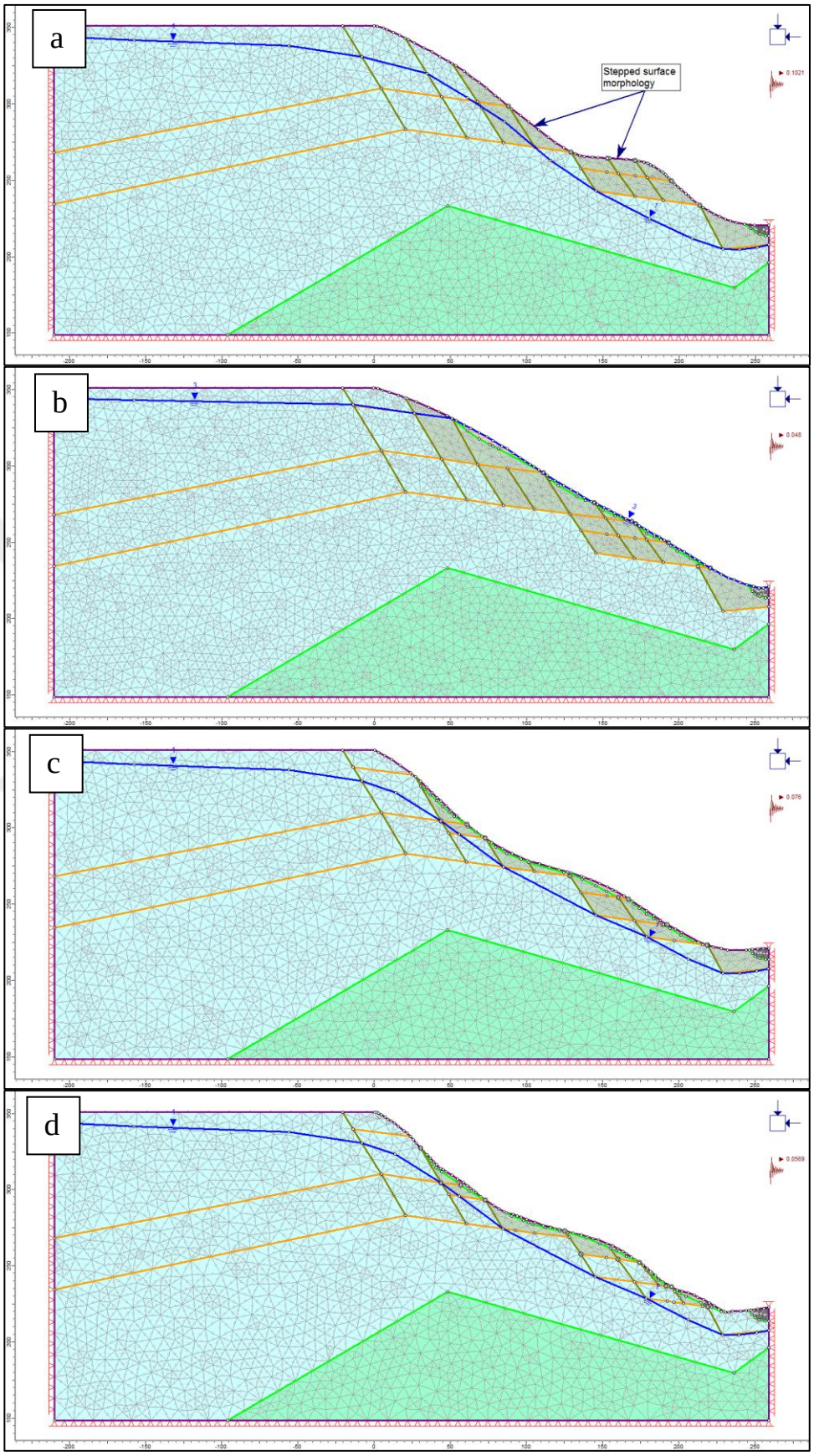


Figure 8.14 The slope models of Landslide-3 in the years of a.1953 b. 1970 c.1995 d.2012

The numerical solutions for Landslide-3 are fitting very well the photogrammetric analyses results considering both vertical displacement and the failure surface (Figure 8.15). It should also be noted that shear displacement is much more difficult along the failure surface with undulations than on the planar surface. However, movements have occurred along the surface with undulations in the past. This case indicates that water is an effective factor in the media and the very weak rock zone is also effective in the shape of the failure surface.

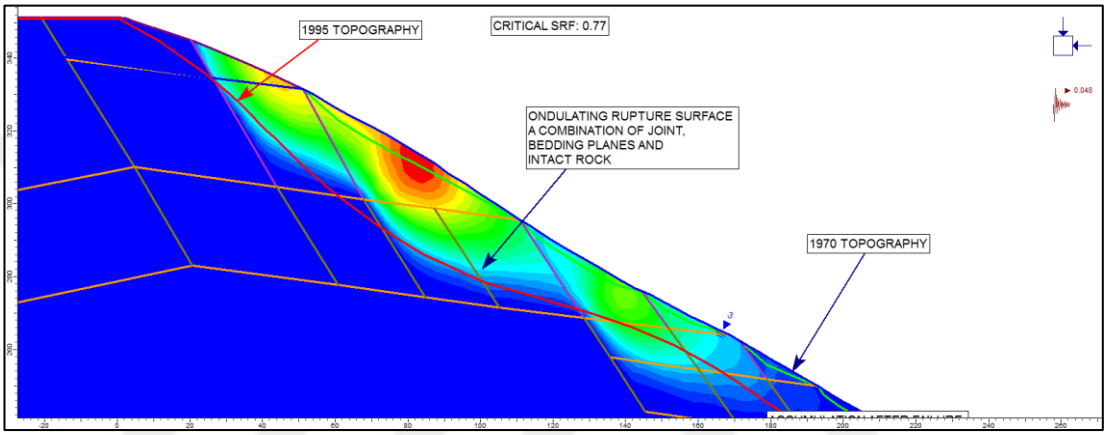


Figure 8.15 The comparison of 1970 and 1995 topography of Landslide-3, the harmony of depletion and accumulation areas with SSR result

The back analyses provided post-failure physical, mechanical, and deformation properties of Landslide-3 (Table 8.12).

Table 8.12 The post-failure strength and deformation properties of the landslide mass at the failure (due to triggering factors) by years obtained from the back analyses (Landslide-3)

Years	Unit	Parameter								
		ɣ (kN/m^3)	E_m (MPa)	E_r (MPa)	υ	m_b	s	a	c (MPa)	ϕ (°)
1953	Alluvium*	19.91	56.4	-	0.3	-	-	-	0	41
	Very weak rock	21.00	350	300	0.40	0.124	1.46 x 10^{-5}	0.56	-	-
	Göcek Fm.*	24.06	2079.77	-	0.28	0.697	16.79 x 10^{-5}	0.50	-	-
	Keçidağ Fm.*	25.40	1536.83	-	0.20	-	-	-	1.5	26.0
1970	Very weak rock	20.20	350	-	0.35	0.159	1.46 x 10^{-5}	0.56	-	-
	Residual soil	17.00	25	-	0.30	-	-	-	0.022	33.0
1995	Very weak rock	20.20	370	-	0.4	0.159	1.46 x 10^{-5}	0.56	-	-
	Residual soil	18.00	24	-	0.35	-	-	-	0.004	28
2012	Very weak rock	20.20	370	-	0.4	0.159	1.46 x 10^{-5}	0.56		
	Residual soil	18.00	24	-	0.35	-	-	-	0.0012	23.5

*The properties of alluvium, Göcek, and Keçidağ Fm. were only given for the first year, they were the same for all the analyses**.**

8.4.6 Landslide-4

Landslide-4 is the landslide resting on the east. An NW-SE trending thrust fault is adjacent to its northeastern lateral wall. For this reason, even the surface area of this landslide calculated by photogrammetric analyses is lower than the other landslides, the vertical displacement is relatively higher. The J-3 and B-1 were expected to form a block of very weak Neogene (Figure 8.4). The slope models of Landslide-4 in the years 1953, 1970, 1995, and 2012 are presented in Figure 8.16.

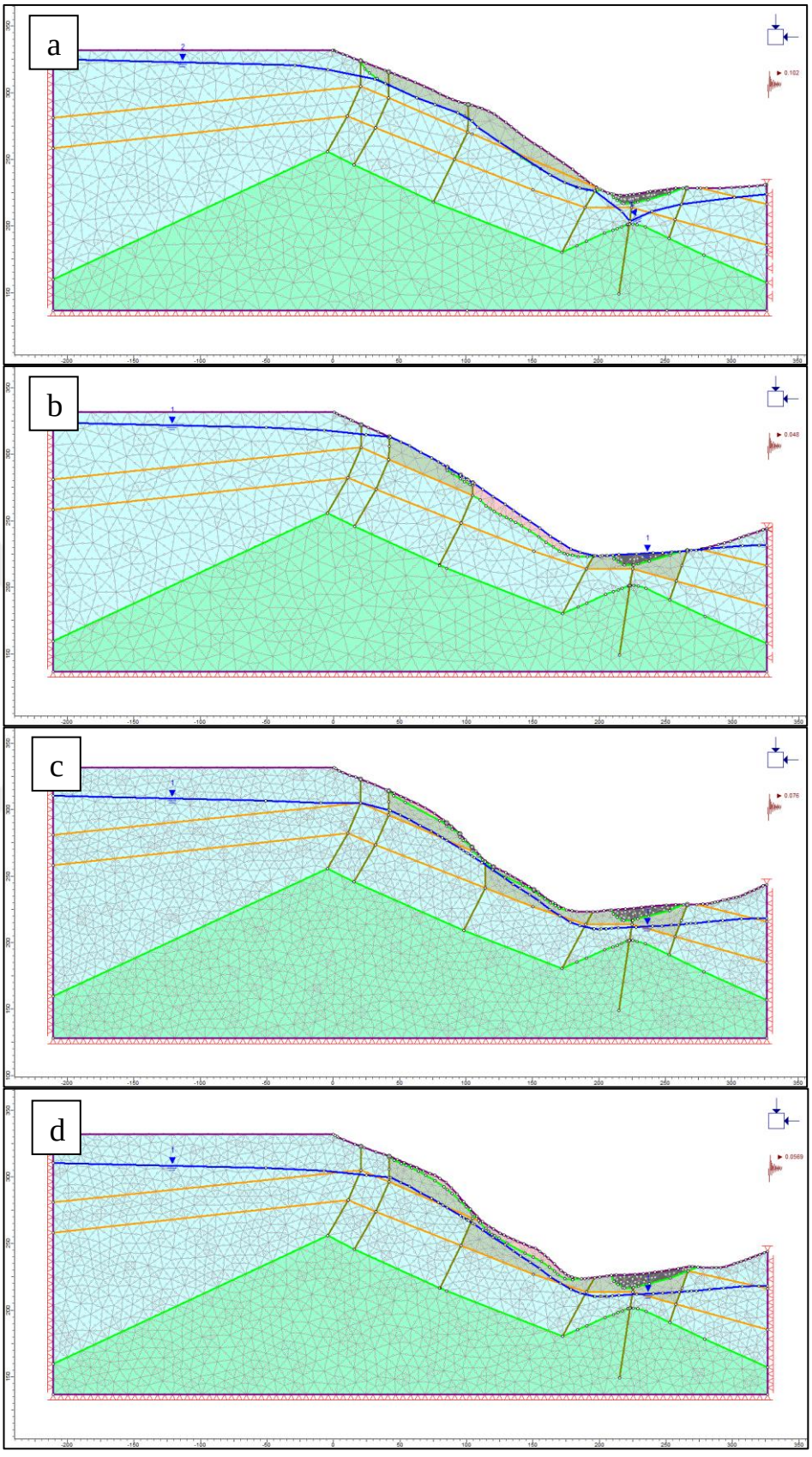


Figure 8.16 The slope models of Landslide-4 in the years of a.1953 b. 1970 c.1995 d.2012

The numerical solutions for Landslide-4 are also fitting very well the photogrammetric analyses results considering both vertical displacement and the failure surface (Figure 8.17).

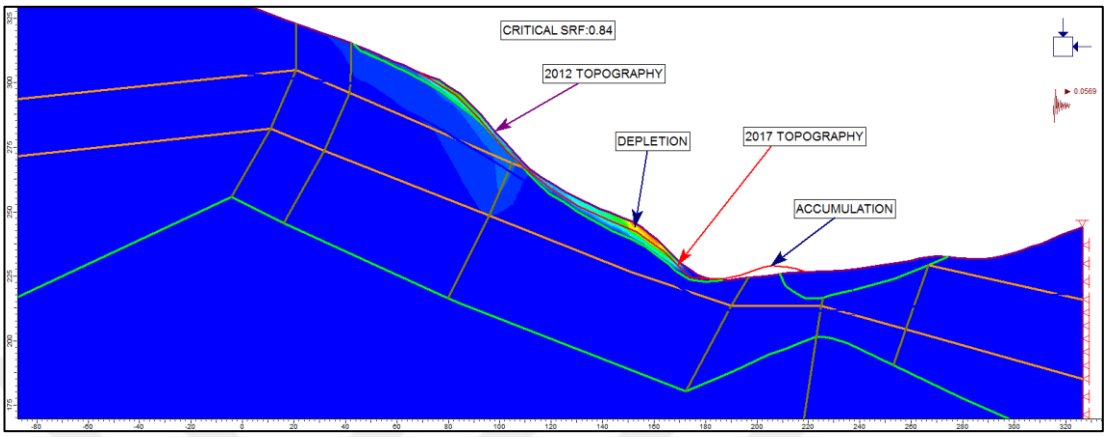


Figure 8.17 The comparison of 2012 and 2017 topography of Landslide-4, the harmony of depletion and accumulation areas with SSR result

The back analyses provided post-failure physical, mechanical, and deformation properties of Landslide-4 (Table 8.13). After the secondary failures occurred during 1953-1970, the majority of the very weak material has displaced, and the underlying rock layers were exposed which are relatively well-interlocked but still in the range of very weak rock. Due to this fact, the mechanical properties were slightly increased (Table 8.13).

Table 8.13 The post-failure strength and deformation properties of the landslide mass at the failure (due to triggering factors) by years obtained from the back analyses (Landslide-4)

Years	Unit	Parameter								
		ɣ (kN/m^3)	E_m (MPa)	E_r (MPa)	υ	m_b	s	a	c (MPa)	ϕ (°)
1953	Alluvium*	19.91	56.4	-	0.3	-	-	-	0	41
	Very weak rock	21.00	350	300	0.40	0.124	1.46 x 10^{-5}	0.56	-	-
	Göcek Fm.*	24.06	1358.24	-	0.28	0.435	10.66 x 10^{-5}	0.501	-	-
	Keçidağ Fm.*	25.40	1536.83	-	0.20	-	-	-	1.5	26.0
1970	Very weak rock	20.20	1013.13	-	0.28	0.159	1.46 x 10^{-5}	0.56	-	-
	Residual soil	17.00	25	-	0.30	-	-	-	0.002	33.0
1995	Very weak rock	20.20	1013.13	-	0.28	0.159	1.46 x 10^{-5}	0.56	-	-
	Residual soil	17.00	25	-	0.35	-	-	-	0.0025	22.0
2012	Very weak rock	20.20	1013.13	-	0.28	0.159	1.46 x 10^{-5}	0.56	-	-
	Residual soil	17.00	25	-	0.35	-	-	-	0.005	22.0

*The properties of alluvium, Göcek, and Keçidağ Fm. were only given for the first year, they were the same for all the analyses**.**

8.5 Future Slope Stability Scenarios

The recent slopes were investigated by FE analyses for future conditions such as before and after dam construction with minimum and maximum retained water level as well as fully water-saturated, pseudo-static, drawdown, and seepage conditions (Appendix-6). The four slope models of the year 2017 were constructed using the cross-sections extracted from the DEM generated from UAV orthophotos. The worst future scenario was represented based on the lowest SRF and the highest amount of displacement.

The results of the photogrammetric analyses indicate that the Alaşehir earthquake that occurred in 1969 had imported a great earthquake force that played an important role in the reactivations of the landslides in the study area between 1953 and 1970. There is no standard for choosing probable peak ground accelerations or duration of shaking of a future earthquake for any given site (Rahn, 1996). Thus, a design earthquake was chosen based on a maximum M_w generated on the nearby fault which is located approximately 2.4 km northwest of the study area. An M_w:5.9 earthquake corresponds to 149.91 gal according to the attenuation relationships proposed by Ulusay et al. (2004) which is equal to a seismic coefficient of approximately 0.15g.

A fully water-saturated condition was used for simulating the effect of prolonged rainfalls in the analyses. The maximum and minimum reservoir water levels were simulated.

The effect of drawdown was also taken into account during the FE analyses. The retained water level in the dam reservoir will gradually increase once the dam construction is completed. The water pressure acting on the rupture surface affects the shear strength distinctly in the case of an empty and filled reservoir. The shear strength along the sliding surface is greater when the reservoir is empty. However, even the shear strength along the sliding surface decreases once the water is retained, the water level produces water pressure that originated from the self-weight of the water. It works as a resisting force towards the slope face. In the case of a drawdown, this resistive force is lost. The water inside the pores of the ground will not drain immediately and the high pore pressures in the fully saturated ground will lead to a reduction in the shear strength. Hence, there will be an increased driving force.

The drawdown phenomenon was simulated as the maximum water level (288.73 m) was reduced to the minimum water level (246.882 m) corresponding to a drawdown ratio (L/H; L: the reduction in water level, H: the initial water level) of 0.145. Fully-drained conditions were considered in which zero excess pore pressure is expected and the drawdown is relatively slow rather than undrained conditions. The slope stability analyses are performed through the steady-state finite element analyses.

The combinations of the above-mentioned triggering factors were applied to the slope models of 2017.

The strength and deformation values for ambient (non-triggered) and the disturbed (triggered) conditions based on back analyses were used in 2017 topographic models.

8.5.1 Landslide-1

Landslide-1 has the biggest area when compared to others; however, it is the most stable one in the present time. The physical, mechanical, and elastic properties for Landslide-1 under ambient and triggered conditions are given in Table 8.14.

Table 8.14 The strength and deformation values used in the analyses for Landslide-1

Condition	Unit	Parameter							
		ɣ (kN/m^3)	E_m (MPa)	υ	m_b	s	a	c (MPa)	ϕ (°)
Ambient	Very weak rock	20.2	370	0.3	0.124	$1.46x10^{-5}$	0.56	-	-
	Soil	17.0	25	0.3	-	-	-	0.004	30
Triggered	Very weak rock	21.0	350	0.4	0.124	$1.46x10^{-5}$	0.56	-	-
	Soil	18.0	24	0.35	-	-	-	0.001	22

The worst future condition for Landslide-1 was determined to be a seismic event and a drawdown occurring successively when the slope is fully saturated (SRF:0.83). The landslide was started with the movement of soil material on the upper slope surface and followed by a deeper failure at the toe. However, the extent of this type of failure depends on the rate of water lowering (Figure 8.18).

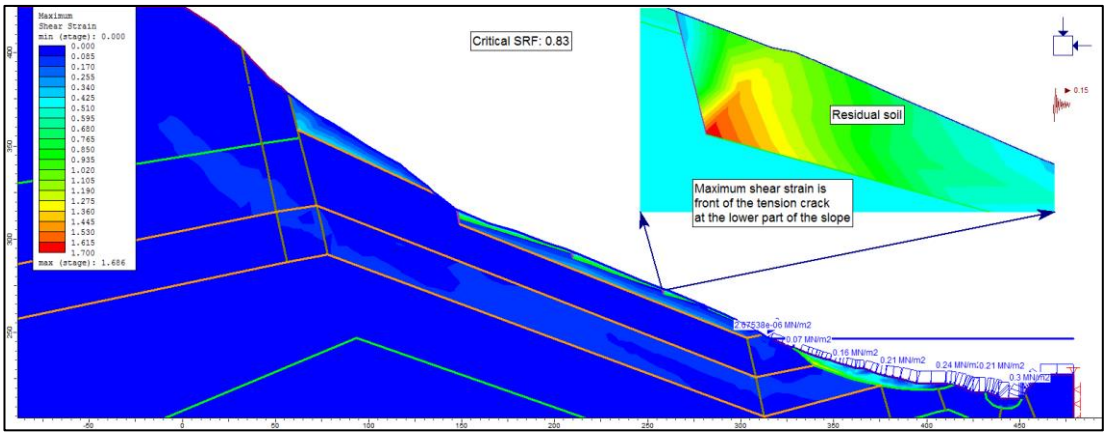


Figure 8.18 The maximum shear stress contours of the worst future scenario for Landslide-1

A general SRF and vertical displacement comparison for Landslide-1 between ambient and triggered conditions and photogrammetric analyses (Table 8.15). According to Table 8.15, for the worst condition, 8.55 m vertical displacement can occur along the cross-section line which is approximately 28.30% of the total vertical displacement (30.21 m) obtained from photogrammetric analyses for the 1953-2012 period. The total cut volume for Landslide-1 is 39.03×10^4 m^3 regarding the photogrammetric analyses (Table 7.4). Based on this knowledge, it can be said that 11.045×10^4 m^3 (=39.03x 28.3%) material can be depleted at most for the worst future scenario.

Table 8.15 The SRF and vertical displacement variations by years and the comparison with the amount of displacement derived from photogrammetric analyses (Landslide-1)

Year	Non-triggered (Ambient)		Triggered		Photogrammetric analyses
	SRF	Vertical displacement (cm)	SRF	Vertical displacement (m)	Max. depletion along cross-section line (m)
1953	1.64	13.49	0.99	11.63	19.00
1970	-	-	-	-	-
1995	1.80	14.12	1.00	3.97	5.54
2012	1.86	14.06	0.86	4.57	5.67
2017 (scenario)	1.87	14.13	0.83	8.55	-

8.5.2 Landslide-2

Landslide-2 is the landslide that its numerical solutions match very well with the photogrammetric analysis results. The physical, mechanical, and elastic properties for Landslide-2 under ambient and triggered conditions are given in Table 8.16.

Table 8.16 The strength and deformation values used in the analyses for Landslide-2

Condition	Unit	Parameter							
		ɣ (kN/m^3)	E_m (MPa)	υ	m_b	s	a	c (MPa)	ϕ (°)
Ambient	Very weak rock	20.2	1013.13	0.28	0.159	$1.46x10^{-5}$	0.56	-	-
	Soil	17.0	25	0.3	-	-	-	0.004	30
Triggered	Very weak rock	21.0	1013.13	0.28	0.159	$1.46x10^{-5}$	0.56	-	-
	Soil	18.0	24	0.35	-	-	-	0.0035	23

The worst future condition for Landslide-2 was determined to be a seismic event when the slope is fully saturated while the reservoir level is at maximum (SRF:0.75) (Figure 8.19). The maximum shear strain contours were concentrating within the thin soil layer lying at a 31° slope angle. However, Göcek Formation on the higher elevations with approximately 44° slope angle stays stable under these circumstances.

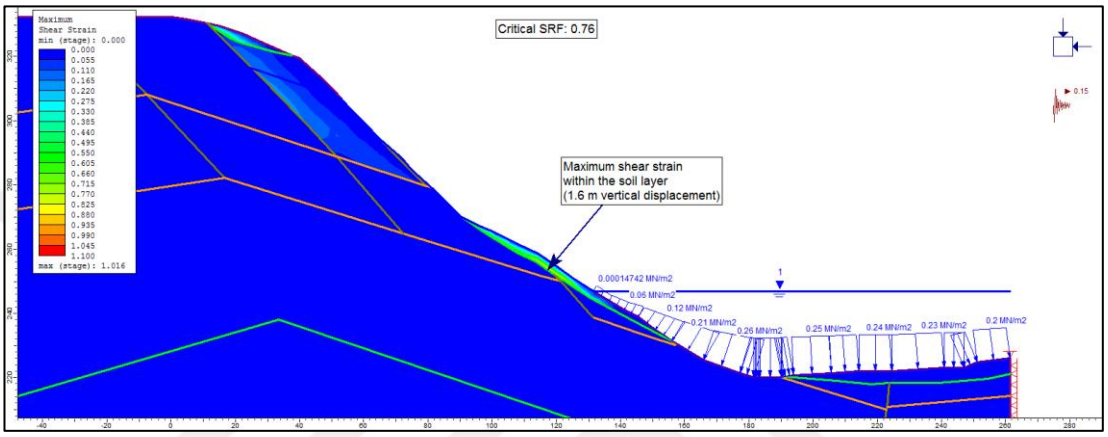


Figure 8.19 The maximum shear stress contours of the worst future scenario for Landslide-2

A general SRF and vertical displacement comparison for Landslide-2 between ambient and triggered conditions and photogrammetric analyses (Table 8.17). According to Table 8.17, for the worst condition, 1.60 m vertical displacement can occur along the cross-section line which is approximately 7.53% of the total vertical displacement (21.25 m) obtained from photogrammetric analyses for the 1953-2012 period. The total cut volume for Landslide-2 is 12.91×10^4 m^3 regarding the photogrammetric analyses (Table 7.4). Based on this knowledge, it can be said that 0.97×10^4 m^3 (=12.91x 7.53%) material can be depleted at most for the worst future scenario.

Table 8.17 The SRF and vertical displacement variations by years and the comparison with the amount of displacement derived from photogrammetric analyses (Landslide-2)

Year	Non-triggered (Ambient)		Triggered		Photogrammetric analyses
	SRF	Vertical displacement (cm)	SRF	Vertical displacement (m)	Max. depletion along cross-section line (m)
1953	1.08	5.12	0.69	7.75	8.54
1970	1.50	4.87	0.70	5.91	6.66
1995	1.50	4.99	0.995	2.35	2.48
2012	1.25	12.41	0.61	3.55	3.57
2017 (scenario)	1.50	4.89	0.76	1.60	-

8.5.3 Landslide-3

Landslide-3 yielded the lowest displacements for future scenarios when compared to other landslides (Table 8.18). It indicates that Landslide-3 has gained a stable condition. The physical, mechanical, and elastic properties for Landslide-3 under ambient and triggered conditions are given in Table 8.18.

Table 8.18 The strength and deformation values used in the analyses for Landslide-3

Condition	Unit	Parameter							
		γ (kN/m^3)	E_m (MPa)	υ	m_b	s	a	c (MPa)	ϕ (°)
Ambient	Very weak rock	20.2	370	0.3	0.1593	$1.46x10^{-5}$	0.56	-	-
	Soil	17.0	25	0.3	-	-	-	0.004	30
Triggered	Very weak rock	21.0	370	0.4	0.159	$1.46x10^{-5}$	0.56	-	-
	Soil	18.0	24	0.35	-	-	-	0.0012	23.5

The worst future condition for Landslide-3 was determined to be a seismic event and a drawdown occurring successively when the slope is fully saturated (SRF:1.00) (Figure 8.20). The very thin soil layer overlying the very weak rocks at a slope angle of 41° is showing slight displacement. However, it may initiate a deeper failure along the cross-section (approximately 1.6 m according to the increased SRF condition) progressively.

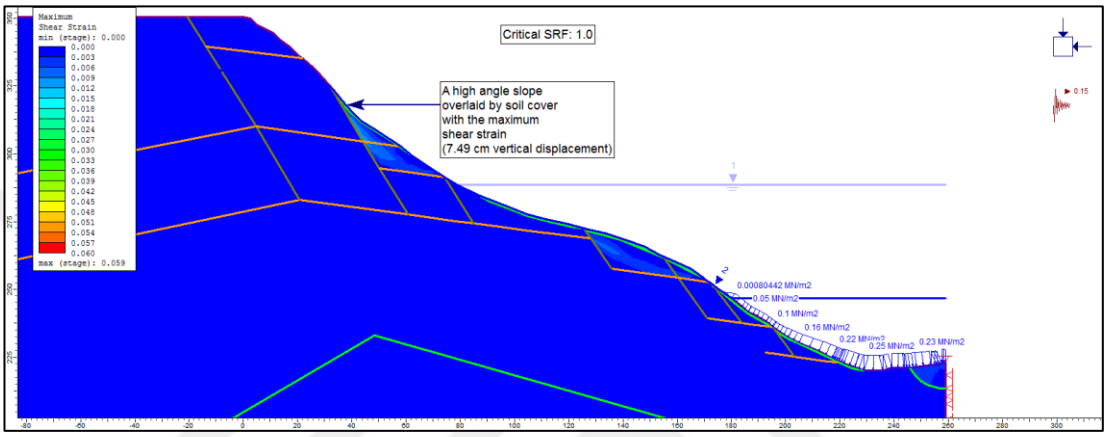


Figure 8.20 The maximum shear stress contours of the worst future scenario for Landslide-3

A general SRF and vertical displacement comparison for Landslide-3 between ambient and triggered conditions and photogrammetric analyses (Table 8.19). According to Table 8.19, for the worst condition, 0.74 m vertical displacement can occur along the cross-section line which is approximately 1.72% of the total vertical displacement (42.96 m) obtained from photogrammetric analyses for the 1953-2012 period. The total cut volume for Landslide-3 is 38.77×10^4 m^3 regarding the photogrammetric analyses (Table 7.4). Based on this knowledge, it can be said that 0.66×10^4 m^3 (=38.77x 1.72%) material can be depleted at most for the worst future scenario.

Table 8.19 The SRF and vertical displacement variations by years and the comparison with the amount of displacement derived from photogrammetric analyses (Landslide-3)

Year	Non-triggered (Ambient)		Triggered		Photogrammetric analyses
	SRF	Vertical displacement (cm)	SRF	Vertical displacement (m)	Max. depletion along cross-section line (m)
1953	1.10	4.69	0.78	9.94	21.93
1970	1.11	5.34	0.77	6.84	10.53
1995	1.81	4.31	0.57	2.69	7.37
2012	2.32	4.09	0.57	2.03	3.13
2017 (scenario)	2.5	4.38	1.00	0.74	-

8.5.4 Landslide-4

Landslide-4 yielded the lowest SRF for its recent slope condition when compared to other landslides (Table 8.20). It indicates that Landslide-4 is the most vulnerable for mass movements. The physical, mechanical, and elastic properties for Landslide-4 under ambient and triggered conditions are given in Table 8.20.

Table 8.20 The strength and deformation values used in the analyses for Landslide-4

Condition	Parameter								
	Unit	γ (kN/m^3)	E_m (MPa)	υ	m_b	s	a	c (MPa)	ϕ (°)
Ambient	Very weak rock	20.2	1013.13	0.28	0.1593	$1.46x10^{-5}$	0.56	-	-
	Soil	17.0	25	0.3	-	-	-	0.004	30
Triggered	Debris	21.0	1013.13	0.28	0.159	$1.46x10^{-5}$	0.56	-	-
	Soil	18.0	24	0.35	-	-	-	0.004	22

The worst future condition for Landslide-4 was determined to be a seismic event when the slope is fully saturated before dam construction (SRF:0.72) (Figure 8.21).

As mentioned before, this landslide is located near a thrust fault zone trending in the NW-SE direction and prone to shallow or deep failures depend on the intensity of the triggering factors.

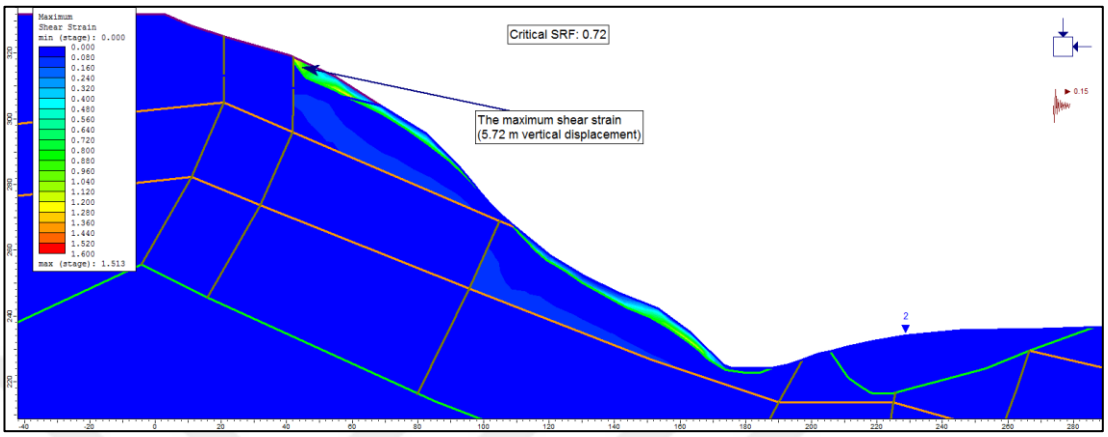


Figure 8.21 The maximum shear stress contours of the worst future scenario for Landslide-4

A general SRF and vertical displacement comparison for Landslide-4 between ambient and triggered conditions and photogrammetric analyses (Table 8.21). According to Table 8.21, for the worst condition, 5.72 m vertical displacement can occur along the cross-section line which is approximately 14.82% of the total vertical displacement (38.6 m) obtained from photogrammetric analyses for the 1953-2012 period. The total cut volume for Landslide-4 is 31.07×10^4 m^3 regarding the photogrammetric analyses (Table 7.4). Based on this knowledge, it can be said that 4.60×10^4 m^3 (=31.07x 14.82%) material can be depleted at most for the worst future scenario.

Table 8.21 The SRF and vertical displacement variations by years and the comparison with the amount of displacement derived from photogrammetric analyses (Landslide-4)

Year	Non-triggered (Ambient)		Triggered		Photogrammetric analyses
	SRF	Vertical displacement (cm)	SRF	Vertical displacement (m)	Max. depletion along cross-section line
1953	1.07	4.06	0.78	11.35	15.20
1970	1.26	4.55	0.66	10.04	13.37
1995	1.49	4.94	0.70	2.92	6.93
2012	1.23	4.94	0.85	1.87	3.20
2017	1.28	4.95	0.72	5.72	-

8.5.5 Seepage Analysis

Seepage analysis was performed considering the effective stress conditions for the four slopes in the reservoir area where the slope movements have occurred. It was aimed to evaluate the discharge rates and the variation of groundwater level within the model. The in-situ measured mean permeability values during the drilling process were assigned for the geological units in the model. Seepage analyses have also included the SSR technique, which gives SRF value for the investigated condition. The conditions before dam construction and after dam construction with maximum and minimum water levels were evaluated (Figure 8.22).

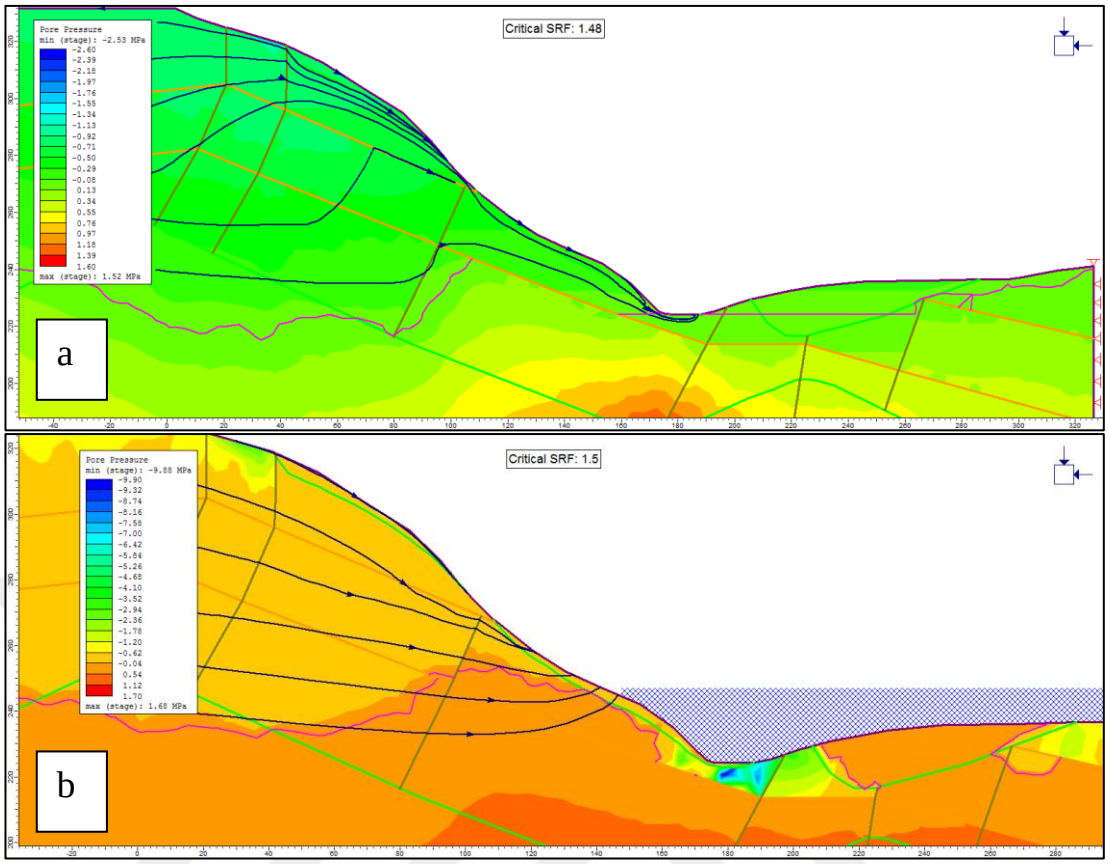


Figure 8.22 The comparison of flow lines and pore pressures a. Before dam construction b. After dam construction with minimum water level (Landslide-4)

Flow lines are strongly affected by the structural geometry and mainly follow the bedding planes and cause run-off for fully saturated conditions. The pink line in the Figure 8.22 represents the estimated static water table level; however, ponded water levels can be expected during the winter season. The water flow model confirmed that the water flows towards the streambed. However, the core drilling has revealed that the karstic and fractured structure of mainly the limestones lead to instantaneous drops in the water table level.

It was found that discharge rates are slightly increasing as the retained water level is increasing. Besides, pore pressures due to seepage do not induce slope instability. For this reason, the SRF values are high (Table 8.22)

Table 8.22 The SRF values of each landslide associated with the seepage analyses

	SRF values		
	Before dam construction	After dam construction	
		Max. water level: 288.73 m	Min. water level: 246.882 m
Landslide-1	2.01	1.90	1.89
Landslide-2	1.75	1.89	1.75
Landslide-3	2.74	2.84	2.57
Landslide-4	1.48	1.49	1.50

The mean total discharge rates are 4.002 $x10^{-7}$, 3.445 $x10^{-7}$, 1.36 $x10^{-6}$ m^3/sec for before dam construction, after construction with minimum and maximum water levels, respectively. On the other hand, negative pore pressures (suction) are present above the water table level. The negative pore pressure exerted into the rock masses at various degrees. The negative pore pressure leads to an increase in the effective stress and therefore in the shear strength of the mass. However, after prolonged rainfalls, negative pore pressures may tend to be zero, which will be positive due to the increasing groundwater level. Such a change in pore pressure causes a significant reduction in shear strength. However, in finite element groundwater analyses, negative pore pressures do not affect SRF values unless unsaturated shear strength values are imported into the model.

No excess pore pressure was obtained for the investigated conditions. However, very high negative pore pressures were determined at the back of the open tension cracks (Figure 8.23).

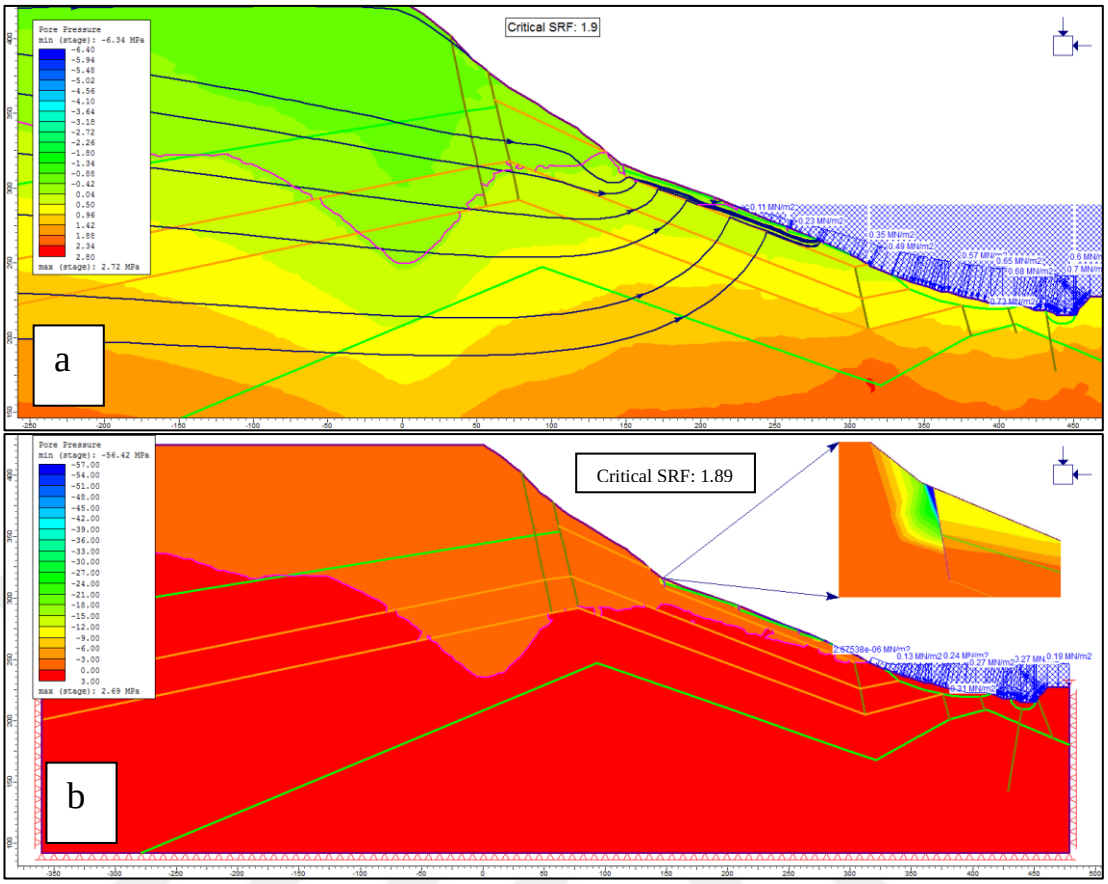


Figure 8.23 The comparison of pore pressures occurred after dam construction with a. Maximum water level b. Minimum water level (Landslide-1)

CHAPTER NINE
DISCUSSION AND CONCLUSIONS

Rock units outcropped in the dam site and its nearby were differentiated and a 1/10000 scale geological map of the study area was prepared. Two geological cross-sections in the N-S directions transversely crossing the streambed were constructed to reveal the main geostructural features and lithologic framework. It was determined that the oldest geological unit Keçidağ Formation which is composed of marble and schist forms the base rock of the dam site. The unconformably overlying Miocene sedimentary rock units are composed of clastic and carbonate rock intercalations. The discontinuity survey revealed that the study area has been subjected to NE-SW trending extension and NW-SE trending compression. The valley of Kayacık River on which the Çağlayan Dam will be built, identified to be formed by NE-SW trending normal faults. There are landslide areas on both flanks of the planned dam (Çağlayan Dam) on the Kayacık River. For this reason, it was aimed to determine the evolution of the landslides, type and rate of the movements, to find out the triggering factors and their effect on the mechanical properties of the geological units. In this manner, a multi-method slope stability assessment has been performed.

Numerical modeling of slopes is a useful tool to corroborate or develop the interpretation of slope behavior; however, a proper evaluation of the field observations, geological and hydrological data, as well as the physical, mechanical, and deformation properties of the rock mass is the key issue for realistic slope model. In this manner, static and cyclic laboratory tests and in-situ tests were performed. Several quantitative methods estimating GSI ratings and different empirical equations estimating E_m values were compared. The best-fitting approaches were selected to represent the rock mass properly. It is also well-known that the results from numerical modeling should be correlated with the in-situ measurements or remote sensing data in order to approximate the real slope conditions. Due to this fact, previously proposed photogrammetric and numerical techniques in the literature were revised and adapted to the failed slopes in the study area. For example, the AHDM proposed by Chen et al. (2014) was revised by increasing the number of sub-areas for the calculation of depleted (depleted) and accumulated materials. The

volumetric calculations were also improved by image to image coregistration. Cross-sectional analyses were also recommended to obtain more precise limits of landslide bodies on historical aerial photographs which indeed affects the accuracy of volume calculations. On the other hand, a multi-temporal approach for back analysis of joint and mass properties was proposed to estimate the post-failure strength. This method is based on the comparison of the depletion (vertical displacement) obtained from photogrammetric analyses with the vertical displacement calculated by the FEM model as well as the comparison between the location of depletion and accumulation zones. The most realistic multi-temporal landslide models (mechanically and structurally evolving) with the corresponding post-failure properties were obtained. As a result, the possibility of a mass movement for similar triggering conditions can be more precisely achieved. However, a detailed database on the possible triggering factors such as the relationship between rainfall and groundwater level variations, surface run-off, or displacement measurements of pre-event and post-event conditions is required to provide threshold values for triggering factors. Nevertheless, the hypotheses on the inherent parameters of the rock mass and the triggering conditions were validated by the back analyses based on the comparison of displacements obtained from photogrammetric and numerical analyses.

The topographical, hydrogeological, geological, and geotechnical conditions were extensively evaluated. A generalized geotechnical model was constructed for the landslides in the area. The results of the numerical analysis are consistent with the photogrammetric analysis results. It should be noted that back analyses were performed manually for trial sets of mechanical and structural parameters until reaching the vertical displacement that is best harmonizing with the photogrammetric results. For this reason, it was not a time-effective process.

9.1 Type and Evolution of Landslides

A generalized geotechnical model was constructed for the landslides in the study area based on the inferences from field observations, geophysical investigations, cored boreholes, photogrammetric analysis, and stereographic projection.

It was determined that the landslides involve sandstone, conglomerate, mudstone, claystone, and limestone intercalations, which have inherent anisotropy and heterogeneity. The failures are not composed of one failure plane but a complex surface consisting of joints/faults, bedding planes, and intact rock bridges. The rupture surface starts from the steeply dipping joints or faults and follows gently dipping bedding planes to slide on while it may gain a rotational character at the deepest portion of the failure surface. The secondary failures (reactivations) are successive movements of the same type of failure occurring within the initial (before 1953) displaced material. The displaced material of secondary failures involves both the highly fractured, weak, poorly interlocked rock mass and the overlying soil and debris material. The high permeability of the upper layers of the slope face leads the underlying layers to become fully saturated which may have weakened these layers over time or instantaneously.

The mechanical evolution of rock and soil units during continuous mass movement over years was revealed by the aid of back analyses in FEM. Very weak and poorly interlocked Neogene sedimentary rocks which transported to downslope were modeled as evolving to crushed soil-like material due to the disturbance by slope movements and environmental effects. However, as the very weak rock unit is transported to the downslope, the underlying relatively stronger layers of Neogene units are exposed in the upper slope faces. These exposed layers have relatively higher mechanical properties. For example, the uniaxial compressive strength increases from 10 MPa to 19 MPa. Elastic modulus value also increases from 370 MPa to 1013.13 MPa. On the other hand, the cohesion and internal friction angle of the surface soil material decreases over time because the slope movements lead to the loosening of the soil material. For example, the cohesion of upper soil cover gradually drops from 0.022 MPa to 0.004 MPa (81.8% reduction) within the period

1953-2017. The internal friction angle (ϕ) reduces from 34° to 30° (11.8% reduction). These changes in mechanical properties are due to continuous mass movements and landform processes (fluvial and surface erosions). This approach for estimating the evolving mechanical properties due to continuous movement reveals progressive accumulation of rock weakening (strain softening) as earlier mentioned by Sandøy (2012). Besides, structural evolution can be simulated by assuming new tension cracks are formed after each movement.

In brief, the topographical evolution together with the mechanical and structural evolution of rock and soil units derived from back analyses gave the insight to understand the multi-temporal evolution of slope materials in a geotechnical manner. The failure has not occurred on a single plane; it rather followed multiple planes and intact rock bridges. It is also possible that new failure surfaces may be formed due to the failure of intact rock bridges over time due to strain softening. The main assumption in such heavily fractured and weak rock masses is that discontinuities and the intact rock material itself have very low strength and elastic properties. Hence, complex failure occurs both on discontinuity planes and in intact rock bridges. In these circumstances, the rock mass is favorable for numerical model solutions for isotropic media. It is also very hard to survey the discontinuities on slope faces formed by partially disintegrated and weak rock units which are commonly covered with dense vegetation. Nevertheless, the discontinuities affected the shape and the location of the failure plane. The surface run-off and water infiltration along discontinuities most probably facilitated the shear strength breakdown.

9.2 Rate of Movement

A combination of several photogrammetric techniques was used to estimate the depleted and accumulated volumes of the four landslides in the Çağlayan Dam reservoir area. Stereographic aerial photographs, differential DEMs and overlapped cross-section profiles revealed that the first occurrence of landslides was determined to be before 1953 and reactivated with varying rates in the investigated periods. Soil

and rock materials have been depleted from the four slopes between 1953 and 2012 with an average mobilization rate of 2.06 $x10^4$ m^3/year. Hence, the landslides in the study area can be characterized by continuous movement with fluctuations in sliding rate (2012-1995: 1.37$x10^4$ m^3/year, 1995-1953: 2.34$x10^4$ m^3/year) due to different triggering factors. The shifts in-plane positions between two aerial photographs and systematic height differences between two DEMs were minimized by image to image coregistration, height adjustment model, respectively. Additionally, cross-sectional analyses were recommended for more accurate volumetric calculations. Nevertheless, historical aerial photographs of 1953 still have shifts in-plane positions while compared to the recent photographs. As a result, the depletion calculated from photogrammetric methods is slightly biased from the amount of vertical displacement calculated from FE slope models of 1953. It can be useful to import radar interferometric data into the multi-method approach proposed in this study to obtain more precise DEMs; however, these data may not be available for the historical time. Nevertheless, it is known that radar microwaves penetrate deeper into the vegetation than optical wavelengths and can be more effective in densely vegetated areas.

9.3 Triggering Factors of Reactivations

The varying landslide volumes calculated from successive DEMs were evaluated with respect to the triggering factors such as precipitation, fire, and earthquake.

The landslide volumes are fluctuating due to rainfall, earthquake, and wildfire. However, it is unknown if the reactivations have occurred right after the events or the rock mass gradually comes to the edge of failure. Besides, there is no apparent single reason for the reactivations (secondary failures) within the initial landslide body.

Results indicated that the largest volume of material removed from 1953 to 1970, which can be relevant to the Alaşehir earthquake, occurred in 1969 with a moment magnitude of 6.5 at approximately 40 km south of the dam site. The peak ground acceleration for the site due to this earthquake was approximately 0.102g. It should be noted that the landslides due to this earthquake can not be evaluated as co-seismic

or post-seismic. On the other hand, the drainage pattern indicates that the failure planes of Landslide-1 and 4 are controlled by the local normal faults, which are limiting the landslide from both sides. It is also meaningful that the repeated seismic loading can be influential in reducing shear strength and loosening the rock mass.

The lowest amount of material depleted in the years between 1995 and 2012, whereas the accumulated material volume is proportionally higher than the other periods. The volume of accumulated material can probably be greater than that of the depleted material due to decompaction and related increase in porosity. The increase in volume for failed rock mass can be up to 30% of the initial volume. Another possible explanation for the highest percentage of accumulation can be the transportation of eroded surface material (surface wash material) into the landslide body from upper parts of the slope due to a wildfire that occurred in 1988. Delong, Youberg, Delong, & Murphy (2018) have a similar argument that the accumulated volume can be greater than the depleted volume since surface material that came from farther up in the catchment can be transported through the study area. In this study, the amount of eroded material was considered to be increased by the removal of vegetation by the wildfire since the shear strength of the burned surface material is reduced (Secci et al., 2014), and the root strength of woody vegetation is lost (Riestenberg & Sovonick-Dunford, 1983). As a result, the rate of erosion increases (Rengers et al., 2020). Sidle & Bogaard (2016) found that the maximum susceptibility to landslides due to harvesting is three to eight years after losing the vegetation and at least nine years are required to root strength regrowth. In addition, excessive daily precipitation of 163.5 mm in 1986 was thought to be an additional factor for decreasing the resistance of the thin soil layer to erosion. In other words, wildfires lead to increased susceptibility to landslides triggered by rainfall. On the other hand, similar to the finding of Rengers et al. (2020), Landslide-3 which is facing towards the north has recovered vegetation more quickly that resulted in a significant reduction in cut volume in the 2012-1995 period (Table 7.4). Besides, Beullens, Van de Velde, & Nyssen (2014) found that the slope aspect has also an important effect on the magnitude of rill erosion due to its strong relationship with the direction of hydrological rainfall.

Lastly, the effect of the triggering factors on the mechanical properties of the geological units was investigated with the aid of back analyses using FEM. It was found that the elastic modulus of the very weak rock unit (370-350 MPa) is slightly decreasing (~5.4%) after heavy rainfall, whereas slightly increasing during earthquakes with strain fatigue (E_m: 350; $E_{residual}$: 300 MPa). On the other hand, Poisson's ratio (0.4-0.3) is increasing after heavy rainfall and during earthquakes (~16.6 to 42.8%). The cohesion of soil (0-0.022 MPa) reduces after heavy rainfall (~96.8 to 100%) and wildfire. The internal friction angle of soil (33°-22°) decreases after heavy rainfall (~0.3 to 30.8%), whereas remains the same or slightly increases after the wildfire. Unit weight is increasing by approximately 4%-6% after heavy rainfall. As a result of back analyses, heavy rainfall was determined to provide additional water pressures along open joint and bedding planes and tension cracks as 0.09 MPa and 0.11 MPa, respectively. The amount of depletion derived from the photogrammetric analysis was determined to be consistent with the results of the numerical analysis.

In brief, the reactivations are closely related to seismic activity, heavy rainfall, and wildfire. However, the volumetric calculations indicated that the most effective triggering factor is the seismic event that occurred in 1969, which induced movement of the largest amount of material. However, the complex hydrodynamic forces occurred under seismic loading if the slope is fully saturated can play a great role in the failures. In addition, the flow direction of the tributaries coincides with the discontinuity planes and enables water flow along these planes. Hence, the succession of the two or more triggering factors may be responsible for the slope instabilities in both flanks of the Kayacık River. The results of the numerical model supported that assumption and gave very well matching vertical displacement values with the photogrammetric analysis. These triggering factors caused degradation in the mechanical properties of soil and rock units. However, a shorter period of differential DEMs that coinciding pre-event and post-event is required for a more precise estimation of triggering factors. Hence, the landslides due to the triggering factors can not be evaluated as co-event or post-event.

9.4 Future Conditions for the Landslides

Geotechnical parameters calculated from P and S-wave velocities obtained from the MASW method indicated that if the soil (alluvium and breccia zone) is excavated beneath the dam axis, the rock basement (metamorphic basement) has desirable elastic properties in terms of being a dam foundation rock. Thus, if the upper 17 m from the ground level, which includes the alluvium and breccia zone is excavated, the foundation rock beneath that depth will be favorable for the dam site if only there is no seepage problem. The very weak and poorly interlocked Neogene aged sedimentary rock units are commonly impermeable due to the significant amount of clayey layers. In-situ permeability test results, the numerical seepage analysis results as well as the dominant orientation of the discontinuities indicate no seepage problems. However, the faulted/disturbed and karstic structure of the lithological units gives secondary permeability to the rock mass. Therefore, fault zones and karstic gaps will probably lead to considerable leakage from the reservoir. This inference is supported by the very deep or absence of groundwater level in boreholes.

On the other hand, the slopes in the reservoir area of the dam are stable in ambient conditions in present; however, they may fail by triggering factors due to fluctuations in the dam reservoir level (drawdown) and extensive rainfalls together with seismic activities. As the main scarps of landslide bodies are expected to remain below or partly above the estimated maximum water level of the dam lake, a drawdown may result in slope failure due to losing the resisting effect of the retained water and the low shear strength of the rock and soil units depending on the drawdown rate.

In brief, the main landslide body was always active in the lower order of the initial failure. However, a thin layer of soil and debris were only affected by mass movement after 2012. Thus, a deep landslide is not expected in the future. $11.045x10^4$, $0.97x10^4$, $0.67x10^4$, $4.60x10^4$ m^3 material can collapse at the worst (most conservative) future slope stability conditions (drawdown + seismic activity + heavy rainfall simultaneously) for Landslide-1, Landslide-2, Landslide-3 and Landslide-4, respectively. Based on these predicted depletion volumes, future landslides will not

have a destructive effect on the dam structure. The dam itself will not be destroyed, but the depleted material will contribute to siltation and thus lead to loss of storage and shorten the operational life of the dam. However, future mass movements can be avoided by trimming the topsoil and debris cover. It is noteworthy to mention that a considerable quantity of leakage due to the faulted and karstic structure of the rock units under the dam axis should be precluded.

REFERENCES

Abdulhadi, N. O., & Barghouthi, A. F. (2012). Measurement of stiffness of rock from laboratory and field tests. In *Proceedings of the 5th Jordanian International Civil Engineering Conference*, Amman, 1-12.

AgiSoft (2016). *PhotoScan Professional* (Version 1.2.6) [Computer software]. http://www.agisoft.com/downloads/installer/

Ahola, M. P., Hsiung, S., & Kana, D. D. (1996). Experimental study on dynamic behavior of rock joints. In *Developments in Geotechnical Engineering*, *79*, 467-494.

Akdeniz, N., (1985). *Geology of Akhisar-Gölmarmara-Gördes-Sındırgı*. PhD Thesis, İstanbul University, İstanbul.

Akgün, F., & Akyol, E. (1987). Palynologie examination of the Akhisar (Çıtak) coal deposits. *Bulletin of the Geological Society of Turkey*, *30*, 35-50.

Altomare, A., Corriero, N., Cuocci, C., Falcicchio, A., Moliterni, A., & Rizzi, R. (2015). QUALX2.0: A qualitative phase analysis software using the freely available database POW-COD. *Journal of Applied Crystallography*, *48*, 598-603.

American Society for Testing and Materials (ASTM) (1972). *Inorganic index to the powder diffraction file. Joint committee on powder diffraction standards*. Philedelphia: ASTM International.

American Society for Testing and Materials (ASTM) (1994). *Annual book of ASTM standards* (Volume 04.08). Philadelphia: ASTM International.

American Society for Testing and Materials (ASTM) D1586-11 (2011). *Standard test method for standard penetration test (SPT) and split-barrel sampling of soils*. West Conshohocken: ASTM International.

American Society for Testing and Materials (ASTM) D2573-08 (2008). *Standard test method for field vane shear test in cohesive soil*. West Conshohocken: ASTM International.

American Society for Testing and Materials (ASTM) D5607-16 (2016). *Standard test method for performing laboratory direct shear strength tests of rock specimens under constant normal force*. West Conshohocken: ASTM International.

American Society for Testing and Materials (ASTM) D7012-14e1 (2014). *Standard test methods for compressive strength and elastic moduli of ıntact rock core specimens under varying states of stress and temperatures*. West Conshohocken: ASTM International.

American Society for Testing and Materials (ASTM) D7070-16 (2016). *Standard test methods for creep of rock core under constant stress and temperature*. West Conshohocken: ASTM International.

Amirahdi, A., Pourhashami, S., Karami, M., & Akbari, E. (2016). Modeling of landslide volume estimation. *Open Geoscience, 8*, 360-370.

Anon (1977). The description of rock masses for engineering purposes. *Quarterly Journal of Engineering Geology, 10*, 355-388.

Anon (1979). Classification of soils and rocks for engineering geological mapping. Part I Rock and soil materials. *Bulletin of the International Association of Engineering Geology, 19*, 364-371.

Anon (1981). Basic geotechnical description of rock masses. *International Journal of Rock Mechanics Mining Sciences & Geomechanics Abstracts, 18*, 85-110.

Attewell, P. B., & Farmer, I. W. (1973). Fatigue behaviour of rock. *International Journal of Rock Mechanics and Mining Sciences, 10*, 1-9.

Aydın, A., & Basu, A. (2005). The Schmidt hammer in rock material characterization. *Engineering Geology, 81*, 1-14.

Ayoub, F., Leprince, S., & Avouac, J. (2009). Co-registration and correlation of aerial photographs for ground deformation measurements. *ISPRS Journal of Photogrammetry and Remote Sensing, 64*, 551-560.

Bagde, M. N., & Petroš, V. (2005a). Fatigue properties of intact sandstone samples subjected to dynamic uniaxial cyclical loading. *Journal of Rock Mechanics and Mining Sciences, 42* (2), 237-250.

Bagde, M. N., & Petroš, V. (2005b). Waveform effect on fatigue properties of ıntact sandstone in uniaxial cyclical loading. *Rock Mechanics and Rock Engineering, 38* (3), 169-196.

Bagde, M. N., & Petroš, V. (2005c). The effect of machine behaviour and mechanical properties of intact sandstone under static and dynamic uniaxial cyclic loading. *Rock Mechanics and Rock Engineering, 38* (1), 59-67.

Bagde, M. N., & Petroš, V. (2009). Fatigue and dynamic energy behavior of rock subjected to cyclical loading. *International Journal of Rock Mechanics and Mining Sciences, 46*, 200-209.

Bai, S., Wang, J., Thiebes, B., Cheng, C., & Yang, Y. (2014). Analysis of the relationship of landslide occurrence with rainfall: A case study of Wudu County, China. *Arabian Journal of Geosciences, 7* (4), 1277-1285.

Balek, J., & Blahut, J. (2017). A critical evaluation of the use of an inexpensive camera mounted on a recreational unmanned aerial vehicle as a tool for landslide research. *Landslides*, *14*, 1217-1224.

Bandis, S. Lumsden, A. C. & Barton, N. (1981). Experimental studies of scale effects on the shear behaviour of rock joints. *International Journal of Rock Mechanics and Mining Sciences & Geomechanics Abstracts*, *18*, 1-21.

Barbero, M., Barla, G., & Zaninetti, A. (1996). Dynamic shear strength of rock joints subjected to impulse loading. *International Journal of Rock Mechanics and Mining Sciences*, *33* (2) 141-151.

Barla, G., Barbero, M., Scavia, C., & Zaninetti, A. (1990). Direct shear testing of single joints under dynamic loading. In *Proceedings of Rock Joints-International Symposium*, Norway, 447-454.

Barton, N. R (1973). Review of a new shear strength criterion for rock joints. *Engineering Geology*, *7*, 287-332.

Barton, N. R. (1972). A model study of rock-joint deformation. *International Journal of Rock Mechanics and Mining Sciences & Geomechanics Abstracts*, *9* (5), 579-582.

Barton, N. R. (2013). Shear strength criteria for rock, rock joints, rock fill and rock masses: Problems and some solutions. *Journal of Rock Mechanics and Geotechnical Engineering*, *5*, 249-261.

Barton, N. R., & Bandis, S. (1982). Effects of block size on the shear behaviour of jointed rock. In *Proceedings of 23rd U.S. Symposium on Rock Mechanics*, USA, 739-760.

Barton, N. R., & Choubey, V. (1977). The shear strength of rock joints in theory and practice. *Rock Mechanics, 10* (1-2), 1-54.

Barton, N. R., Lien, R. & Lunde, J. (1974). Engineering classification of rock masses for the design of tunnel support. *Rock Mechanics, 6* (4), 189-239.

Basahel, H., & Mitri, H. (2017). Application of rock mass classification systems to rock slope stability assessment: A case study. *Journal of Rock Mechanics and Geotechnical Engineering, 9*, 993-1009.

Basu, A., Mishra, D. A., & Roychowdhury, K. (2013). Rock failure modes under uniaxial compression, Brazilian, and point load tests. *Bulletin of Engineering Geology and the Environment, 72*, 457-475.

Beavis, F. C. (1985). *Engineering geology*. Melbourne: Blackwell.

Bell, F. G. (1992). *Engineering in rock masses*. Oxford: Butterworth-Heinemann.

Bell, F. G. (2007). *Engineering geology* (2nd ed.). Burlington: Butterworth-Heinemann.

Beullens, J., Van de Velde, D., & Nyssen, J. (2014). Impact of slope aspect on hydrological rainfall and on the magnitude of rill erosion in Belgium and northern France. *Catena, 114* (1), 129-139.

Beyhan, S. (2008). *The determination of G.L.I and E.L.I marl rock material properties depending on triaxial compressive strength*. PhD Thesis, Eskişehir Osmangazi University, Eskişehir.

Bieniawski, Z. T. (1973). Engineering classification of jointed rock masses. *South African Institution of Civil Engineers, 15*, 335-344.

Bieniawski, Z. T. (1989). *Engineering rock mass classifications*. New York: Wiley.

Bjerrum, L. (1972). Embankments on soft ground. *Proceedings of ASCE Specialty Conference on Performance of Earth and Earth-Supported Structures, 2*, 1-54.

Bjerrum, L. (1973). Problems of soil mechanics and construction on soft clays and structurally unstable soils. In *Proceedings of 8th International Conference on Soil Mechanics and Foundation Engineering*, Russia, 111-159.

Blight, G. E. (1968). A note on field vane testing on silty soils. *Canadian Geotechnical Journal, 5* (3), 142-149.

Blue Marble Geographics (2016). *Global Mapper* (Version 18) [Computer software]. https://www.bluemarblegeo.com/products/global-mapper.php

Boadu, F. (1997). Rock properties and seismic attenuation: Neural network analysis. *Pure and Applied Geophysics, 149,* 507-524.

Borrelli, L. R., Greco, R., & Gullà, G. (2007). Weathering grade of rock masses as a predisposing factor to slope instabilities: Reconnaissance and control procedures. *Geomorphology, 87* (3), 158-175.

Bowles, J. E. (1988). *Foundation analysis and design* (4th ed.). Singapore: McGraw-Hill.

Bowles, J. E. (2001). *Foundation analysis and design* (5th ed.). New York: McGraw-Hill.

Bozzano, F., Martino, S., Montagna, A., & Prestininzi, A. (2012). Back analysis of a rock landslide to inferrheological parameters. *Engineering Geology, 131-132*, 45-56.

Broch, E., & Franklin, J. A. (1972). The point load strength test. *International Journal of Rock Mechanics and Mining Sciences, 9*, 669-697.

Brown, E. T. (1970). Strength of models of rock with intermittent joints. *Journal of the Soil Mechanics and Foundations Division*, *96* (6), 1935-1949.

Budetta, P., & Nappi, M. (2011). Heterogeneous rock mass classification by means of the geological strength index: the San Mauro formation (Cilento, Italy). *Bulletin of Engineering Geology and the Environment*, *70* (4), 585-593.

Burdine, N. T. (1963). Rock failure under dynamic loading conditions. *Society of Petroleum Engineers Journal*, *3*, 1-8.

Cai, F., & Ugai, K. (2004). Numerical analysis of rainfall effects on slope stability. International Journal of Geomechanics, *4* (2), 69-78.

Cai, M. (2010). Practical estimates of tensile strength and Hoek-Brown strength parameter mi of brittle rocks. *Rock Mechanics and Rock Engineering*, *43* (2), 167-184.

Cai, M., Kaiser, P.K., Uno, H., Tasaka, Y., & Minami, M. (2004). Estimation of rock mass deformation modulus and strength of jointed hard rock masses using the GSI system. *International Journal of Rock Mechanics and Mining Sciences*, *41* (1), 3-19.

Cardarelli, E., Cercato, M., & De Donno, G. (2014). Characterization of an earth-filled dam through the combined use of electrical resistivity tomography, P- and S-wave seismic tomography and surface wave data. *Journal of Applied Geophysics*, *106*, 87-95.

Carter, M., & Bentley, S. (1991). *Correlations of soil properties*. London: Penetech Press.

Carvajal, F., Agüera, F., & Pérez, M. (2011). Surveying a landslide in a road embankment using unmanned aerial vehicle photogrammetry. In *Proceedings of Conference on Unmanned Aerial Vehicle in Geomatics*, Switzerland, 201-206.

Chen, R. F., Chang, K. J., Angelier, J., Chan, Y. C., Deffontaines, B., Lee, C. T., et al. (2006). Topographical changes revealed by high-resolution airborne LiDAR data: The 1999 Tsaoling landslide induced by the Chi-Chi earthquake. *Engineering Geology*, *88*, 160-172.

Chen, C. S., Pan, E., & Amadei, B. (1998). Determination of deformability and tensile strength of anisotropic rock using Brazilian tests. *International Journal of Rock Mechanics and Mining Sciences*, *35* (1), 43-61.

Chen, E. P. (1995). Dynamic brittle material response based on a continuum damage model. In R. C., Barta, A. K. Mal, & G. P. MacSithigh, (Eds.). *Impact waves and fracture* (21-34). New York: American Society of Mechanical Engineers.

Chen, Z., Zhang, B., Han, Y., Zuo, Z., & Zhang, X. (2014). Modeling accumulated volume of landslides using remote sensing and DTM data. *Remote Sensing*, *6*, 1514-1537.

Clapuyt, F., Vanacker, V., & Van Oost, K. (2016). Reproducibility of UAV-based earth topography reconstructions based on structure-from-Motion algorithms. *Geomorphology, 260*, 4-15.

Coe, J., Glancy, P., & Whitney, J. (1997). Volumetric analysis and hydrologic characterization of a modern debris flow near Yucca Mountain, Nevada. *Geomorphology*, *20*, 11-28.

Conte, E., Pugliese, L., & Troncone, A. (2019). Post-failure stage simulation of a landslide using the material point method. *Engineering Geology*, *253*, 149-159.

Conte, E., Pugliese, L., & Troncone, A. (2020). Post-failure analysis of the Maierato landslide using the material point method. *Engineering Geology*, *277*, 105788.

Corsini, A., Borgatti, L., Cervi, F., Dahne, A., Ronchetti, F., & Sterzai, P. (2009). Estimating mass-wasting processes in active earth slides-earth flows with time-series of high-resolution DTMs from photogrammetry and airborne LiDAR. *Natural Hazards Earth System Sciences*, *9*, 433-439.

Cruden, D. M., & Varnes, D. J. (1996). Landslide types and processes. In A. K. Turner, R. L. Schuster, (Eds.). *Landslides: Investigation and Mitigation* (36-75). Washington: National Academy Press.

Dang, W., Konietzky, H., & Frühwirt, T. (2016). Direct shear behavior of a plane joint under dynamic normal load (DNL) conditions. *Engineering Geology, 213*, 133-141.

De Bari, C., Lapenna, V., Angela, P., Puglisi, C., & Sdao, F. (2011). Digital photogrammetric analysis and electrical resistivity tomography for investigating the Picerno landslide (Basilicata region, southern Italy). *Geomorphology, 133*, 34-46.

Dearman, W. R. (1976). Weathering classification in the characterisation of rock: A revision. *Bulletin of the International Association of Engineering Geology*, 13, 123-127.

Deere, D. U., & Miller, R. P. (1966). *Engineering classification and index properties for intact rock*. Technical Report No: AFWL-TR-65-116, University of Illinois.

Deere, D. U., & Patton, F. D. (1971). Slope stability in residual soils. In *Proceedings of 4th Pan American Conference on Soil Mechanics and Foundation Engineering*, Puerto Rico, 87-170.

Deere, D. U., Hendron, A. J., Patton, F. D., & Cording, E. J. (1967). Design of surface and near surface construction. In *Proceedings of 8th U.S. Symposium on Rock Mechanics-Failure and Breakage of Rock*, USA, 237-302.

DeLong, S. B., Youberg, A. M., DeLong, W. M., & Murphy, B. P. (2018). Postwildfire landscape change and erosional processes from repeat terrestrial lidar in a steep headwater catchment, ChiricahuaMountains, Arizona, USA. *Geomorphology, 300*, 13-30.

Demirdağ, S., Tüfekçi, K., Kayacan, R., Yavuz, H., & Altındağ, R. (2010). Dynamic mechanical behavior of some carbonate rocks. *International Journal of Rock Mechanics and Mining Sciences, 47*, 307-312.

Deschamps, R., & Yankey, G. (2006). Limitations in the back-analysis of strength from failures. *Journal of Geotechnical and Geoenvironmental Engineering, 132*, 532-536.

Diederichs, M. S. (2007). The 2003 Canadian Geotechnical Colloquium: Mechanistic interpretation and practical application of damage and spalling prediction criteria for deep tunnelling. *Canadian Geotechnical Journal, 44* (9), 1082-1116.

Donohue, S., Long, M., O'Connor, P., Helle, T. E., Pfaffhuber, A. A., & Romoen, M. (2012). Multi-method geophysical mapping of quick clay. *Near Surface Geophysics, 10*, 207-219.

Du, J. C., & Teng, H. C. (2007). 3D laser scanning and GPS technology for landslides earthwork volume estimation. *Automation in Construction, 16*, 657-663.

Duman, T. Y., Çan, T., & Emre, Ö. (2011). 1/1.500.000 Turkey landslide inventory map. In *General Directorate of Mineral Research and Exploration Special Publications Series*, 27. Ankara, Turkey.

Duncan, J. M. & Wright, S. G. (2005). *Soil strength and slope stability* (2nd ed.). New Jersey: John Wiley and Sons.

Eberhardt, E. (1998). *Brittle rock fracture and progressive damage in uniaxial compression*. PhD Thesis, University of Saskatchewan, Saskatoon.

Emre, Ö., Duman, T. Y., Özalp, S., Elmacı, H., Olgun, Ş., & Şaroğlu, F. (2013). 1/1.250.000 Turkey active fault map. In *General Directorate of Mineral Research and Exploration Special Publications*. Ankara, Turkey.

Emre, Ö., Özalp, S., Doğan, A., Özaksoy, V., Yıldırım, C., & Göktaş, F. (2005). *Active faults of İzmir and its nearby and their earthquake potential*. General Directorate of Mineral Research and Exploration (MTA) Report No: 10754, Geological Prospection Department.

Emre, T. (1996). Geology and tectonics of Gediz Graben. *Turkish Journal of Earth Sciences, 5*, 171-185.

Environmental Systems Research Institute (ESRI) (2015). *ArcGIS* (Version 10.4.1) [Computer software]. https://desktop.arcgis.com/en/

Eravcı, B., Yaman, M., Tepeuğur, E., Erkmen, C., Aktan, T., Albayrak, H., et al. (2007). *Final report on the paleoseismology in the East Anatolian Fault zone.* Report No: DPT 2002 K 120050, Ministry of Public Works, General Directorate of Natural Disasters, Earthquake Research Department.

Ercan, T., Türkecan, A., Dinçel, A., & Günay, E. (1983). The geology of Kula-Selendi (Manisa) region. *Geological Engineering, 17*, 3-28.

Ercikdi, B., Karaman, K., Cihangir, F., Yılmaz, T., Aliyazıcıoğlu, Ş., & Kesimal, A. (2016). Core size effect on the dry and saturated ultrasonic pulse velocity of limestone samples. *Ultrasonics, 72*, 143-149.

Fabre, G., & Pellet, F. (2006). Creep and time-dependent damage in argillaceous rocks. *International Journal of Rock Mechanics and Mining Sciences, 43*, 950-960.

Fairhurst, C. (1964). On the validity of the Brazilian test for the brittle materials. *International Journal of Rock Mechanics and Mining Sciences, 1* (4), 535-546.

Fatty A., Li A. J. (2018). Back analysis algorithm based on particle swarm optimization. In W. Wu, & H. S. Yu, (Eds.). *Proceedings of China-Europe Conference on Geotechnical Engineering. Springer Series in Geomechanics and Geoengineering* (1470-1473). Austria: Springer.

Fourmaintraux, D. (1976). Characterization of rocks; laboratory tests: Chapter IV. In *La Mechanique des roches applique auxouvr ges du genie civil by Marc Panet et al.* Ecole Nationale des Ponts et Chaussees.

Franklin, J. A., Broch, E., & Walton, G. (1971). Logging the mechanical character of rock. *Transaction of Institute of Mining and Metallurgy*, *80* (770), 1-9.

Fuenkajorn, K., & Phueakphum, D. (2010). Effects of cyclic loading on mechanical properties of Maha Sarakham salt. *Engineering Geology*, *112* (1-4), 43-52.

Fuller, J. C., Riedler, A. R., Bell, R., Marden, M., & Glade, T. (2016). Landslide-driven erosion and slope channel coupling in steep, forested terrain, Ruahine Ranges, New Zealand, 1946-2011. *Catena, 142*, 252-268.

Gabet, E. J. (2003). Post-fire thin debris flows: sediment transport and numerical modelling. *Earth Surface Processes and Landforms*, *28*, 1341-1348.

Genç, C., Altunkaynak, Ş., Karacık, Z., Yazman, M., & Yılmaz, Y. (2001). The Çubukludağ Graben, south of İzmir: Its tectonic significance in the Neogene geological evolution of the Western Anatolia. *Geodinamica Acta*, *14*, 45-55.

Genç, Ş. C., & Yılmaz, Y. (2000). The geology and neotectonic of Aliağa and its nearby. In *Proceedings of the seismicity of the Western Anatolia (BADSEM)*, Turkey, 152-159.

Ghafoori, M., Lashkaripour, G. R., & Tarigh Azali, S. (2011). Investigation of the geological and geotechnical characteristics of Daroongar Dam, Northeast Iran. *Geotechnical and Geological Engineering, 29*, 961-975.

Gladwin, M. T. (1982). Ultrasonic stress monitoring in underground mining. *International Journal of Rock Mechanics and Mining Sciences, 19*, 221-228.

Godio, A., & Bottino, G. (2001). Electrical and electromagnetic investigation for landslide characterization. *Physics and Chemistry of the Earth, 26* (9), 705-710.

Goodman, R. E. (1989). *Introduction to rock mechanics*. New York: Wiley.

Gökçe, O., Özden, S., & Demir, A. (2008). *The inventory of the spatial and statistical distribution of natural disasters*. Ankara: Ministry of Intrior Disaster and Emergency Management Presidency.

Gökçeoğlu, C., & Aksoy, H. (2000). New approaches to the characterization of clay-bearing, densely jointed and weak rock masses. *Engineering Geology, 58*, 1-23.

Gökçeoğlu, C., Sönmez, H., & Kayabaşı, A. (2003). Predicting the deformation moduli of rock masses. *International Journal of Rock Mechanics and Mining Sciences, 40* (5), 701-710.

Göktürkler, G., Balkaya, Ç., Erhan, Z., & Yurdakul, A. (2008). Investigation of a shallow alluvial aquifer using geoelectrical methods: a case from Turkey. *Environmental Geology, 54*, 1283-1290.

Gregory, A. R. (1976). Fluid saturation effects on dynamic elastic properties of sedimentary rocks. *Geophysics, 41*, 721-895.

Griffith, A. A. (1921). The phenomena of rupture and flow in solids. *Philosophical Transactions of the Royal Society of London*, *221*, 163-198.

Griffiths, D. H., & Barker, R. D. (1993). Two-dimensional resistivity imaging and modelling in areas of complex geology. *Journal of Applied Geophysics*, *29*, 211-226.

Gullà, G., & Nicoletti, P. G. (1996). Rock weathering and discontinuity network in a Sackung in the Aspromonte Massif (Calabria, Italy). In *Proceedings of 7th International Symposium on Landslides*, Norway, 971-976.

Gullà, G., Antronico, L., Terranova, O., Aceto, L., Niceforo, D., Cilento, M., et al. (2004). Failure and post failure conditions of a landslide involving weathered and degraded rocks. In *Proceedings of 9th International Symposium On Landslides*, Brazil, 1241-1246.

Guyader, J., & Denis, A. (1986). Wave propagation in anisotropic rocks under stress evaluation of the quality of slates. *Bulletin of Engineering Geology and the Environment*, *33*, 49-55.

Guzzetti, F., Ardizzone, F., Cardinali, M., Galli, M., Rossi, M., & Valigi, D. (2009). Landslide volumes and landslide mobilization rates in Umbria, central Italy. *Earth and Planetary Science Letters*, *279*, 222-229.

Guzzetti, F., Mondini, A. C., Cardinali, M., Fiorucci, F., Santangelo, M., & Chang, K. T. (2012). Landslide inventory maps: new tools for an old problem. *Earth Science Reviews*, *112*, 42-66.

Hack, H., Alkema, D., Kruse, G., & Leenders, N. (2007). Influence of earthquakes on the stability of slopes. *Engineering Geology*, *91*, 4-15.

Hack, R. (2000). Geophysics for slope stability. *Surveys in Geophysics*, 21, 423-448.

Haimson, B. C., & Kim, C. M. (1972). Mechanical behaviour of rock under cyclic fatigue. In E. J. Cording, (Ed.). *Stability of rock slopes: Proceedings of 13. Symposium on Rock Mechanics (*845-863). New York: American Society of Civil Engineering (ASCE).

Hakyemez, H. Y., Göktaş, F., & Erkal, T. (2013). Quaternary geology and evolution of the Gediz Graben. *Geological Bulletin of Turkey, 56* (2), 1-26.

Hammah, R. E., Yacoub, T. E., Corkum, B., & Curran, J. H. (2005b). A comparison of finite element slope stability analysis with conventional limit-equilibrium investigation. In *Proceedings of 58th Canadian Geotechnical and 6th Joint IAH-CNC and CGS Groundwater Specialty Conferences*, Canada, 1-8.

Hammah, R. E., Yacoub, T. E., Corkum, B., & Curran, J.H. (2005a). The shear strength reduction method for the Generalized Hoek-Brown Criterion. In *Proceedings of 40th U.S. Symposium on Rock Mechanics*, Alaska, 1-6.

Hammah, R. E., Yacoub, T. E., Corkum, B., Wibowo, F., & Curran, J. H. (2007). Analysis of blocky rock slopes with finite element shear strength reduction analysis. In *Proceedings of 1st Canada U.S. Rock Mechanics Symposium*, Canada, 329-334.

Hancox, G. T., Dellow, G. D., & Perrin, N. D. (1994). *Wellington Regional Council: Earthquake-induced slope failure hazard study in the Wellington Region -Review of historical records of earthquake-induced slope failures*. Client Report 353905.26, Institute of Geological and Nuclear Sciences.

Hencher, S. R., Massey, J. B., & Brand, E. W. (1984). Application of back analysis to some Hong Kong landslides. In *Proceedings of 4th International Symposium on Landslides*, Canada, 631-638.

Hoek E., & Brown, E. T. (2019). The Hoek–Brown Failure Criterion and GSI-2018 edition. *Journal of Rock Mechanics and Geotechnical Engineering*, *11* (3), 445-463.

Hoek E., Carter, T. G., & Diederichs, M. S. (2013). Quantification of the Geological Strength Index chart. In *Proceedings of 47th US Rock Mechanics/Geomechanics Symposium*, USA, 1-9.

Hoek, E. & Diederichs, M. S. (2006). Empirical estimation of rock mass modulus. *International Journal of Rock Mechanics and Mining Sciences*, *43*, 203-215.

Hoek, E. (2007). *Practical rock engineering*, Retrieved November 16, 2016, from https://www.rocscience.com/learning/hoek-s-corner.

Hoek, E., & Brown, E. T. (1980). Empirical strength criterion for rock masses. *Journal of Geotechnical and Engineering Division*, *GT9*, 1013-1035.

Hoek, E., & Brown, E. T. (1997). Practical estimates or rock mass strength. *International Journal of Rock Mechanics and Mining Sciences*, *34* (8), 1165-1186.

Hoek, E., Carranza-Torres, C., & Corkum, B. (2002). Hoek-Brown Criterion-2002 edition. In *Proceedings of North American Rock Mechanics Symposium*, Canada, 267-273.

Hoek, E., Kaiser, P. K., & Bawden, W. F. (1995). *Support of underground excavations in hard rock*. Rotterdam: AA Balkema.

Huang, B., & Liu, J. (2013). The effect of loading rate on the behavior of samples composed of coal and rock. *International Journal of Rock Mechanics and Mining Sciences*, *61*, 23-30.

Hudson J. A., & Priest, S. D. (1979). Discontinuities and rock mass geometry. *International Journal of Rock Mechanics and Mining Science & Geomechanics Abstracts, 16*, 339-362.

Hugenholtz, C. H., Whitehead, K., Brown, O. W., Barchyn, T. E., Moorman, B. J., LeClair, A., et al. (2013). Geomorphological mapping with a small unmanned aircraft system (sUAS): Feature detection and accuracy assessment of a photogrammetrically-derived digital terrain model. *Geomorphology, 194*, 16-24.

Hunsche, U. (1993). Effect of humidity and confining pressure on creep of rock salt. In *Proceedings of the 3rd conference of mechanical behavior of salt,* Germany, 237-247.

IBM (2006). *SPSS Statistical package for social sciences* (Version 16.0.1) [Computer software]. https://www.ibm.com/tr-tr/products/spss-statistics

International Association of Engineering Geology (IAEG) Commission on Landslides (1990). Suggested nomenclature for landslides. *Bulletin of the International Association of Engineering Geology, 41* (1), 13-16.

International Society for Rock Mechanics (ISRM) (2007). R. Ulusay, & J. A. Hudson, (Eds.). *The complete ISRM suggested methods for rock characterization, testing and monitoring: 1974-2006*. Suggested methods prepared by the Commission on Testing Methods, ISRM. Compilation arranged by the ISRM Turkish National Group, Ankara: Kozan Ofset.

Ishizuka, Y., Abe, T., & Kodama, J. (1990). Fatigue behaviour of granite under cyclic loading. In Brumer R., (Ed.). *ISRM International Symposium—Static and Dynamic Considerations in Rock Engineering*, 139-146.

Işık, N., Doyuran, V. & Ulusay, R. (2008). Assessment of deformation modulus of weak rock masses from pressuremeter tests and seismic surveys. *Bulletin of Engineering Geology and the Environment*, *67* (3), 293-304.

Iwahashi, J., Kamiya, I. & Yamagishi, H. (2012). High-resolution DEMs in the study of rainfall- and earthquake-induced landslides: Use of a variable window size method in digital terrain analysis. *Geomorphology*, *153-154*, 29-38.

Jafari, M. K., Amini Hosseini, K., Pellet, F., Boulon, M., & Buzzi, O. (2003). Evaluation of shear strength of rock joints subjected to cyclic loading. *Soil Dynamics and Earthquake Engineering*, *23*, 619-630.

Jang, H.S., & Jang, B. A. (2014). New method for shear strength determination of unfilled, unweathered rock joint. *Rock Mechanics and Rock Engineering*, *48*, 1515-1534.

Jiang, J., & Yamagami, T. (2008). A new back analysis of strength parameters from single slips. *Computers and Geotechnics*, *35* (2), 286-291.

Jing, L., Stephansson, O., & Nordlund, E. (1993). Study of rock joints under cyclic loading conditions. *Rock Mechanics and Rock Engineering*, *26* (3), 215-232.

Kadakci Koca, T., & Koca, M. Y. (2019). The continuum and discontinuum modelling of a rock slope in Aydın, Turkey. In *Proceedings of International Earth Science Colloquium on the Aegean Region (IESCA)*, Turkey, 176-179.

Kahraman, S. (2001). A correlation between P-wave velocity, number of joints and Schmidt hammer rebound number. *International Journal of Rock Mechanics and Mining Sciences*, *38*, 729-733.

Kahraman, S., & Yeken, T. (2008). Determination of physical properties of carbonate rocks from P-wave velocity. *Bulletin of Engineering Geology and the Environment*, *67*, 277-281.

Karakul, H. (2017). Investigation of saturation effect on the relationship between compressive strength and Schmidt hammer rebound. *Bulletin of Engineering Geology and the Environment*, *76* (3), 1143-1152.

Karaman, K., Cihangir, F., & Kesimal, A. (2013). Investigation of cohesion and internal friction angle of rock materials by indirect methods. *Mehmet Akif Ersoy University, Journal of Graduate School of Natural and Applied Sciences, 4* (2), 13-19.

Karaman, K., Cihangir, F., Ercikdi, B., & Kesimal, A. (2010). The effect of specimen length on ultrasonic P-wave velocity in clayey-carbonate rocks. *Mining*, *49* (4), 37-45.

Karaman, K., Kaya, A., & Kesimal, A. (2015). Effect of the specimen length on ultrasonic P wave velocity in some volcanic rocks and limestones. *Journal of African Earth Sciences, 112*, 142-149.

Karlsson, T., & Tallberg, J. (2011). *Concrete face rock-fill dam compared to roller compacted concrete dam*. MSc Thesis, Chalmers University of Technology, Sweden.

Karpuz, C., & Paşamehmetoğlu, A. G. (1997) Field characterization of weathered Ankara andesite. *Engineering Geology*, *46* (1), 1-17.

Kayabaşı, A. (2017). The Geological Strength Index chart assesment for rock mass permeability. *Bulletin of the Earth Sciences Application and Research Centre of Hacettepe University, 38* (3), 295-309.

Keefer, D. K. (1984). Landslides caused by earthquakes. *Geological Society of America Bulletin*, *95* (4), 406-421.

Keefer, D. K. (2002). Investigating landslides caused by earthquakes-a historical review. *Surveys of Geophysics, 23* (6), 473-510.

Kılıç, A. M. (1997). *Stratigraphy of Lower Mesozoic sediments of Akhisar (Manisa) region*. MSc Thesis, Cumhuriyet University, Sivas.

Kim B. H., M. Cai, P. K. Kaiser, & H. S. Yang (2007). Estimation of block sizes for rock masses with non-persistent joints. *Rock Mechanics and Rock Engineering*, *40* (2), 169-192.

King (1983). Static and dynamic elastic properties of rocks from the Canadian Shield. *International Journal of Rock Mechanics and Mining Sciences & Geomechanics Abstracts*, *20* (5), 237-241.

Koloski, J. W., Schwarz, S. D., & Tubbs, D. W. (1989). Geotechnical properties of geologic materials. *Washington Division of Geology and Earth Resources Bulletin*, *78*, 19-24.

Konak, N. (1994). A general review of Menderes Massif. In *Proceedings of 47. Turkey Geological Congress*, Turkey, 126.

Konietzky, H., Frühwirt, T., & Luge, H. (2012). A new large dynamic rock mechanical direct shear box device. *Rock mechanics and Rock Engineering*, *45* (3), 427-432.

Kossev, V. N. (1970). Corelation between the physical and mechanical properties of rocks and degree of their weathering. In *Proceedings of 2nd Conference of International Society of Rock Mechanics*, Serbia, 1-67.

Kuster G. T., & Toksöz M. N. (1974). Velocity and attenuation of seismic waves in two-phase media: Part I. Theoretical formulations. *Geophysics*, *39*, 587-606.

Lacroix, P., Berthier, E., & Maquerhua, E. T. (2015). Earthquake-driven acceleration of slow-moving landslides in the Colca valley, Peru, detected from Pléiades images. *Remote Sensing Environment*, *165*, 148-158.

Lama, R. D., & Vutukuri, V. S. (1978). *Handbook on mechanical properties of rocks Volume II*. Germany: Trans. Tech. Publications.

Larsen, I. J., Montgomery, D. R., & Korup, O. (2010). Landslide erosion controlled by hillslope material. *Natural Geosciences, 3*, 247-251.

Le Roux, O., Jongmans, D., Kasperski, J., Schwartz, S., Potherat, P., Lebrouc, V., et al. (2011). Deep geophysical investigation of the large Séchilienne landslide (Western Alps, France) and calibration with geological data. *Engineering Geology, 120*, 18-31.

Lee H., Park, Y., Cho, T., & You, K. (2001). Influence of asperity degradation on the mechanical behavior of rough rock joints under cyclic shear loading. *International Journal of Rock Mechanics and Mining Sciences, 38* (7), 967-980.

Li, D., Wong, L.N.Y. (2013). The Brazilian Disc Test for rock mechanics applications: Review and new insights. *Rock Mechanics and Rock Engineering, 46*, 269-287.

Li, H. B., Zhao, J., & Li, T. J. (1999). Triaxial compression tests on a granite at different strain rates and confining pressures. *International Journal of Rock Mechanics and Mining Sciences, 36* (8), 1057-1063.

Li, N., Chen, Y., Zhang, P., & Swoboda, G. (2001). The mechanical properties and fatigue damage model for jointed rock masses subjected to dynamic cyclical loading. *International Journal of Rock Mechanics and Mining Sciences, 38*, 1071-1079.

Li, N., Zhang, P., Chen, Y., & Swoboda, G. (2003). Fatigue properties of cracked, saturated and frozen sandstone samples under cyclic loading. *International Journal of Rock Mechanics and Mining Sciences, 40*, 145-150.

Liu, E., & He, S. (2012). Effects of cyclic dynamic loading on the mechanical properties of intact rock samples under confining pressure conditions. *Engineering Geology*, *125*, 81-91.

Loke, M. H., & Barker, R.D. (1996). Rapid least-squares inversion of apparent resistivity pseudo sections by a quasi-Newton method. *Geophysical Prospecting*, *44*, 131-152.

Lu, L., Wang, Z. J., Song, M. L., & Arai, K. (2015). Stability analysis of slopes with ground water during earthquakes. *Engineering Geology*, *193*, 288-296.

Lv, Q., Liu, Y., & Yang, Q. (2017). Stability analysis of earthquake-induced rock slope based on back analysis of shear strength parameters of rock mass. *Engineering Geology*, *228*, 39-49.

Malamud, B. D., Turcotte, D. L., Guzzetti F., & Reichenbach, P. (2004). Landslides, earthquakes, and erosion. *Earth Planetary Science Letters*, *229*, 45-59.

Mantovani, F., Soeters, R., & Van Westen, C. J. (1996). Remote sensing techniques for landslide studies and hazard zonation in Europe. *Geomorphology*, *15*, 213-225.

Marchesini, I., Cencetti, C., & De Rosa, P. (2009). A preliminary method for the evaluation of the landslides volume at a regional scale. *Geoinformatica*, 13(3), 277-289.

Marinos, V., & Carter, G. T. (2018). Maintaining geological reality in application of GSI for design of engineering structures in rock. Engineering Geology, *239*, 282-297.

Martinović, K., Gavin, K., Reale, C., & Mangan, C. (2018). Rainfall thresholds as a landslide indicator for engineered slopes on the Irish Rail network. *Geomorphology*, *306*, 40-50.

Mavko, G., Mukerji, T., & Dvorkin, J. (2003). *The rock physics handbook*. United Kingdom: Cambridge University Press.

McCann, D. M., & Forster, A. (1990). Reconnaissance geophysical methods in landslide investigations. *Engineering Geology*, *29*, 59-78.

Metternicht, G., Hurni, L., & Gogu, R. (2005). Remote sensing of landslides: An analysis of the potential contribution to geo-spatial systems for hazard assessment in mountainous environments. *Remote Sensing of Environment*, *98*, 284-303.

Miller, R. P. (1965). *Engineering classification and index properties for intact rock.* PhD Thesis, University of Illinois, Champaign.

Miller, R. D., Xia, J., Park, C. B., & Ivanovo, J. M. (1999). Multichannel analysis of surface waves to map bedrock. *The Leading Edge*, *18* (12), 1392-1396.

Mohd Salim, N. A. M., Mohamed, Z., & Berhan, M. N. (2013). Behaviour of weathered granite under cyclic loading. *International Refereed Journal of Engineering and Science*, *2* (2), 7-22.

Mostyn, G. R., & Douglas, K. J. (2000). Strength of intact rock and rock masses. In C. Haberfield et al., (Eds.). *Proceedings of international conference on geotechnical and geological engineering, volume I* (1389-1421). Lancaster: Technomic Publishing.

Murrell, S. A. F. (1963). A criterion for brittle fracture of rock under triaxial stress and the effect of pore pressure on the criterion. In C. Fairhurst, (Ed.). *Rock Mechanics* (563-577). Oxford: Pergamon Press.

Nguyen, V. M. (2013). *Static and dynamic behaviour of joints in schistose rock: Lab testing and numerical simulation*. PhD Thesis, Technische Universität Bergakademie, Freiberg.

Niethammer, U., James, M. R., Rothmund, S., Travelletti, J., & Joswig, M. (2012). UAV-based remote sensing of the Super-Sauze landslide: Evaluation and results. *Engineering Geology, 128*, 2-11.

Nikolaeva, E., Walter, T. R., Shirzaei, M., & Zschau, J. (2014). Landslide observation and volume estimation in central Georgia based on L-band InSAR. *Natural Hazards Earth System Sciences, 14*, 675-688.

Obrzud, R., & Truty, A. (2012). *The hardening soil model - a practical guidebook z soil*. Report PC 100701.

Ojo, O. J., Adepoju, S. A., & Alhassan, N. (2014). Geochemical and mineralogical studies of kaolinitic clays in parts of ılorin, southwestern basement rock area, Nigeria. *Universal Journal of Geoscience, 2* (7), 212-221.

Okui, Y., Tokunaga, A., Shinji, M., & Mori, S. (1997). New back analysis method of slope stability by using field measurements. *International Journal of Rock Mechanics and Mining Sciences, 34* (3-4), 234.e1-234.e16.

Onodera, T. F. (1963). Dynamic investigation of foundation rocks, in situ. In *Proceedings of the 5th US Symposium on Rock Mechanics*, America, 517-533.

Osgoui, R. R., Ulusay, R., & Ünal, E. (2010). An assistant tool for the Geological Strength Index to better characterize poor and very poor rock masses. *International Journal of Rock Mechanics and Mining Sciences, 47*, 690-697.

Özarslan, A., Geniş, M., Bilir, M. E., & Özkan, İ. (2007). Stability analysis of the solution mining underground storage caverns. In *Proceedings of 20th International Turkish Mining Congress*, Turkey, 49-58.

Özkaymak, Ç., Sözbilir, H., & Uzel, B. (2013). Neogene-Quaternary evolution of the Manisa Basin: Evidence for variation in the stress pattern of the İzmir-Balıkesir Transfer Zone, western Anatolia. *Journal of Geodynamics, 65*, 117-135.

Özmen, B., Nurlu, M., & Güler H. (1997). Inspection of earthquake zones of Turkey with geographical information systems. In *Disaster & Emergency Management Authority (AFAD), Presidential of Earthquake Department Report*.

Özvan, A., Dinçer, İ., Acar, A., & Özvan, B. (2014). The effects of discontinuity surface roughness on the shear strength of weathered granite joints. *Bulletin of Engineering Geology and the Environment, 73*, 801-813.

Palmström, A. (1982). The volumetric joint count- a useful and simple measure of the degree of jointing. In *Proceedings of the 4th International Congress of IAEG*, India, 221-228.

Palmström, A. (1995). *RMi-a rock mass characterization system for rock engineering purposes*. PhD Thesis, University of Oslo, Norway.

Palmström, A. (2005). Measurements of and correlations between block size and rock quality designation (RQD). *Tunnels and Underground Space Technology, 20*, 362-377.

Pantelidis, L. (2009). Rock slope stability assessment through rock mass classification systems. *International Journal of Rock Mechanics and Mining Sciences, 46* (2), 315-325.

Park, C. B., Miller, R. D., & Xia, J. (1999). Multi-channel analysis of surface waves. *Geophysics, 64*, 800-808.

PCI Geomatics (2012). *PCI Geomatica* (Version 12.0.1) [Computer software]. https://www.pcigeomatics.com/software/geomatica/education

Pells, P., Bieniawski, Z., Hencher, S., & Pells, S. (2017). RQD: Time to rest in peace. *Canadian Geotechnical Journal*. *54* (6), 825-834.

Peltier, L. C. (1950). The geographic cycle in periglacial regions as it is related to climatic geomorphology. *Annals of the Assocaition of American Geographers, 40,* 214-236.

Perrone, A., Lapenna, V., & Piscitell, S. (2014). Electrical resistivity tomography technique for landslide investigation: A review. *Earth-Science Reviews, 135,* 65-82.

Price, D.G. (2009). *Engineering geology principles and practice*. M. H. Freitas (Ed.), London: Springer.

Priest, S. D., Hudson, J. A. (1976). Discontinuity spacings in rock. *Journal of Rock Mechanics & Mining Science and Geomechanics Abstracts, 13,* 135-148.

Rahn, P. (1996). *Engineering geology an environmental approach* (2nd ed.). New Jersey: Prentice Hall.

Ray, S. K., Sarkar, M., & Singh, T. N. (1999). Effect of loading and strain rate on the mechanical behaviour of sandstone. *International Journal of Rock Mechanics and Mining Sciences, 36* (4), 543-549.

Read, S. A. L., & Richards, L. (2011). A comparative study of mi, the Hoek-Brown constant for intact rock material. In Proceedings of *12th ISRM Congress, International Society for Rock Mechanics,* Portugal, 1-6.

Read, S. A. L., & Richards, L. (2014). Correlation of direct and indirect tensile tests for use in the Hoek-Brown constant mi. In *Rock engineering and rock mechanics: Structures in and on rock masses*. London: Taylor and Francis.

Rengers, F. K., McGuire, L.A., Oakley, N. S., Kean, J. W., Staley, D. M., & Tang, H. (2020). Landslides after wildfire: Initiation, magnitude, and mobility. *Landslides, 17,* 2631-2641.

Reynolds, J. (1997). *An introduction to applied and environmental geophysics*. Chichester: Wiley.

Riestenberg, M. M. & Sovonick-Dunford, S. (1983). The role of woody vegetation on stabilizing slopes in the Cincinnati area. *Geologic Society of America Bulletin, 94*, 504-518.

Rigaku (2016). *PDXL Integrated X-ray powder diffraction* (Version 2.6.1.2) [Computer software]. http://www.rigaku.com/service/software/pdxl

Rocscience (2015). *Dips- graphical and statistical analysis of orientation data* (Version 6.017) [Computer software]. https://www.rocscience.com/software/dips

Rocscience (2019). *RS2- Two-dimensional finite element analysis program* (Version 10.012) [Computer software]. https://www.rocscience.com/software/rs2

Rusnak, M., Sladek, J., Busa, J., & Greif, V. (2016). Suitability of digital elevation models generated by UAV photogrammetry for slope stability assessment (case study of landslide in Svätý Anton, Slovakia). *Acta Scientiarum Polonorum Formatio Circumiectus, 15* (4), 439-450.

Russo, G. (2009). A new rational method for calculating the GSI. *Tunnelling and Underground Space Technology, 24* (1), 103-111.

Sainoki, A., Mitri, H. S. (2014). Dynamic modelling of fault-slip with Barton's shear strength model. *International Journal of Rock Mechanics and Mining Sciences, 67*, 155-163.

Salehi, M. H., Beni, O. H., Harchegani, H. B., H., Borujeni, I. E., & Motaghian, H. R. (2011). Refining soil organic matter determination by loss-on-ignition. *Pedosphere*, *21* (4), 473-482.

Sandøy, G. (2012). *Back-analysis of the 1756 Tjellefonna rockslide, Langfjorden*. MSc Thesis, Norwegian University of Science and Technology, Norway.

Sarı, M. (2010). A simple approximation to estimate the Hoek-Brown parameter mi for intact rocks. In J. Zhao, V. Labiouse, J. P. Dudt, & J. F. Mathier, (Eds.). *Proceedings of Rock Mechanics in Civil and Environmental Engineering (EUROCK)* (169-172). London: Taylor & Francis.

Saroglou, C., Asteriou, P., Zekkos, D., Tsiambaos, G., Clark, M., & Manousakis, J. (2018). UAV-based mapping, back analysis and trajectory modeling of a coseismic rockfall in Lefkada island, Greece. *Natural Hazards and Earth System Sciences*, *18*, 321-333.

Scasso, R. A., Alonso, M. S., Lanés, S., Villar, H. J., & Laffitte, G. (2005). Geochemistry and petrology of a Middle Tithonian limestone-marl rhythmite in the Neuquén Basin, Argentina: Depositional and burial history. *Geological Society Special Publications*, *252*, 207-229.

Secci, R., Calcina, S. V., Ranieri, G., & Uras, G. (2014). Analysis of the stability variation of a slope crossed by forest fire. *International Journal of Civil Engineering*, *3* (1), 41-50.

Sharma, P. K., & Singh, T. N. (2008). A correlation between P-wave velocity, impact strength index, slake durability index and uniaxial compressive strength. *Bulletin of Engineering Geology and the Environment*, *67*, 17-22.

Shen, J., & Karakuş, M. (2014). Simplified method for estimating the Hoek-Brown constant for ıntact rocks. *Journal of Geotechnical and Geoenvironmental Engineering*, *140*, 04014025-1-8.

Sidle, R. C., & Bogaard, T. A. (2016). Dynamic earth system and ecological controls of rainfall-initiated landslides. *Earth-Science Reviews*, *159*, 275-291.

Singh, B., & Goel, R. K. (1999). *Rock Mass Classification: A Practical Approach in Civil Engineering*. Amsterdam: Elsevier.

Singh, S. K. (1989). Fatigue and strain hardening behaviour of graywacke from the flagstaff formation, New South Wales. *Engineering Geology, 26,* 171-179.

Singhroy, V. (2002). Landslide hazards: CEOS, the use of earth observing satellites for hazard support: Assessments and scenarios. In *Committee on Earth Observing Systems (CEOS) Disaster Management Support Group* (Final report). Maryland, America.

Somodi, G., Krupa, Á., Kovács, L., & Vásárhelyi, B. (2018). Comparison of different calculation methods of Geological Strength Index (GSI) in a specific underground construction site. *Engineering Geology, 243,* 50-58.

Sönmez, H., & Ulusay, R. (1999). Modification to the Geological Strength Index (GSI) and their applicability to stability of slopes. *International Journal of Rock Mechanics and Mining Sciences, 36,* 743-760.

Sönmez, H., & Ulusay, R. (2002). A discussion on the Hoek-Brown Failure Criterion and suggested modifications to the criterion verified by slope stability case studies. *Bulletin of Earth Sciences Application and Research Centre of Hacettepe University, 26,* 77-99.

Sönmez, H., Ulusay, R., & Gökçeoğlu, C. (1998). A practical procedure for the back analysis of slope failures in closely jointed rock masses. *International Journal of Rock Mechanics and Mining Sciences, 35* (2), 219-233.

Stavrogin, A. N., & Tarasov, B. G. (2001). *Experimental physics and rock mechanics: Results of Laboratory Studies*. Lisse: Balkema.

Steeples, D.W. (2001). Engineering and environmental geophysics at the millennium. *Geophysics, 66*, 31-35.

Şaroğlu, F., Emre, Ö., & Boray, A. (1987). The active faults of Turkey and their seismicity. In *General Directorate Of Mineral Research And Explorations* (Report No: 8174). Ankara.

Şengör, A. M. C. (1979). The North Anatolian Transform Fault: Its age, offset and tectonic significance. *Journal of the Geological Society, 136,* 269-282.

Şengör, A. M. C. (1980). *Principles of the Neotectonism of Turkey*. Ankara: Geological Society of Turkey.

Tandon, R. S. & Gupta, V. (2015). Estimation of strength characteristics of different Himalayan rocks from Schmidt hammer rebound, point load index, and compressional wave velocity. *Bulletin of Engineering Geology and the Environment, 74* (2), 521-533.

Tatone, B. S. A., & Grasselli, G. (2013). An investigation of discontinuity roughness scale dependency using high-resolution surface measurements. *Rock Mechanics and Rock Engineering, 46*, 657-681.

Tatone, B. S. A., Grasselli, G. (2010). A new 2D discontinuity roughness parameter and its correlation with JRC. *International Journal of Rock Mechanics and Mining Sciences, 47* (8), 1391-1400.

TBEC (Turkish Building Earthquake Code) (2018). *Specifications for building design under earthquake effects*. Ankara: Ministry of Public Works and Settlement Government of Republic of Turkey.

TEC (Turkish Earthquake Code) (2007) *Specification for buildings to be built in seismic zones*. Ankara: Ministry of Public Works and Settlement Government of Republic of Turkey.

Terzaghi, K. (1946). Rock defects and loads on tunnel supports. In R. V. Proctor, & T. L. White, (Eds.). *Rock Tunneling with Steel Supports*. Youngstown: Commercial Shearing and Stamping Company.

Thomas, R., Ayemin, K., & Neilsen, J. M. (2015). Quantification of the Geological Strength Index- effects on open pit slope design. In *Proceedings of International Symposium on Slope Stability in Open Pit Mining and Civil Engineerin,* South Africa, 1-14.

Thornthwaite, C. W. (1948). An approach toward a rational classification of climate. *Geographical Review*, *38* (1), 55-94.

Tien, Y. M., Lee, D. H., & Juang, C. H. (1990). Strain, pore pressure and fatigue characteristics of sandstone under various load conditions. *Journal of Rock Mechanics and Mining Science & Geomechanics Abstracts*, *27* (4), 283-289.

Toksöz, M. N., Cheng, C. H., & Timur A. (1976). Velocities of seismic waves in porous rocks. *Geophysics*, *41*, 621-645.

Toraya, H. (2016). A new method for quantitative phase analysisusing X-ray powder diffraction: Direct derivation of weight fractions from observed integrated intensities and chemical compositions of individual phases. *Journal of Applied Crystallography*, *49*, 1508-1516.

Trimble (2009). *Inpho Match-T DSM* (Version 5.2) [Computer software]. https://geospatial.trimble.com/products-and-solutions/inpho

Tsutsui, K., Rokugawa, S., Nakagawa, H., Miyazaki, S., Cheng, C., Shiraishi, T., et al. (2007). Detection and volume estimation of large-scale landslides based on elevation-change analysis using DEMs extracted from high-resolution satellite stereo imagery. *IEEE Transactions on Geoscience and Remote Sensing*, *45* (6), 1681-1696.

Turkish State Meteorological Service (MGM) (2019). *Statistical precipitation and temperature records,* Retrieved October 18, 2019 from https://www.mgm.gov.tr/veridegerlendirme/ilveilceleristatistik.aspx?k=A&m=MANISA

Turner, D., Lucieer, A., & De Jong, M. (2015). Time series analysis of landslide dynamics using an unmanned aerial vehicle (UAV). *Remote Sensing, 7,* 1736-1757.

Turner, M. J., Clough, R. W., Martin, H. C., & Topp, L. J. (1956). Stiffness and deflection analysis of complex structures. *Journal of the Aeronautical Sciences, 23* (9), 805-823.

Türk, N., & Dearman, W.R. (1986). A suggested approach to rock characterization in terms of seismic velocities. In H. L. Hartman, (Ed.). *Rock Mechanics: Key to Energy Production Proceedings of 27th U.S. Symposium on Rock Mechanics* (168-175). Colorado: Society of Mining Engineers.

Türk, N., & Dearman, W.R. (1987). Assessment of grouting efficiency in a rock mass in terms of seismic velocities. *Bulletin of the International Association of Engineering Geology, 36,* 101-108.

Türkeş, M. (2011). Hydroclimatological and time-series analysis of variations in precipitation and aridity index series of the Akhisar and Manisa districts and geographical synthesis of their consequences with respect to desertification. *Turkish Journal of Geographical Sciences, 9* (1), 79-99.

Ulusay, R., & Gerçek, H. (2017). Introductory longer review for rock mechanics testing methods. In X. Feng, (Ed.). *Rock Mechanics and Engineering Volume 2: Laboratory and Field Testing*. London: CRC Press.

Ulusay, R., Tuncay, E., Sönmez, H., & Gökçeoğlu, C. (2004). An attenuation relationship based on Turkish strong motion data and iso-acceleration map of Turkey. *Engineering Geology*, *74* (3–4), 265-291.

Uslu, S., & Koca, M. Y. (2019). Determination of the deformability, modulus ratios and anisotrophic behavior of the micaschists; A case study from Burgaz Dam Site, İzmir-Turkey. *Journal of Geological Engineering*, *43* (2), 155-185.

Ünay, E., & Göktaş, F. (2000). Small mammal biochronology of the early Miocene lignitifeous sediments around Kınık (Gördes): Preliminary results. *Geological Bulletin of Turkey*, *43* (1), 1-5.

Valley, B., Thuro, K., Eberhardt, E., & Raetzo, H. (2004). Geological and geotechnical investigation of a shallow translational slide along a weathered rock/soil contact for the purpose of model development and hazard assessment. In *Proceedings of 9th International Symposium on Landslides*, Brazil, 385-391.

Van Westen, C., & Getahun, F. (2003). Analyzing the evolution of the Tessina landslide using aerial photographs and digital elevation models. *Geomorphology*, *54*, 77-89.

Vaneghi, R. G., Ferdosi, B., Okoth, A. D., & Kuek, B. (2017). Strength degradation of sandstone and granodiorite under uniaxial cyclic loading. *Journal of Rock Mechanics and Geotechnical Engineering*, *10* (1), 117-126.

Vardon, P. J. (2015). Climatic influence on geotechnical infrastructure: A review. *Environmental Geotechnics*, *2* (3), 166-174.

Vásárhelyi, B., & Bögöly, G. (2019). New method for determining the Geological Strength Index (GSI) value of boreholes. In *Proceedings of Geotechnical Challenges in Karst ISRM Specialised Conference*, Croatia, 425-430.

Vásárhelyi, B., Somodi, G., Krupa, Á., & Kovács, L. (2016). Determining the Geological Strength Index, GSI using different methods. In *Proceedings of Rock Mechanics and Rock Engineering (EUROCK)*, Turkey, 1049-1054.

Vasconcelos, G., Lourenço, P. B., Alves, C.A. S., & Pamplona, J. (2008). Ultrasonic evaluation of the physical and mechanical properties of granites. *Ultrasonics*, *48*, 453-466.

Wang, B., Vardon, P. J., & Hicks, M. A. (2018). Rainfall-induced slope collapse with coupled material point method. *Engineering Geology*, *239*, 1-12.

Wang, W., & Shen, J. (2017). Comparison of existing methods and a new tensile strength based model in estimating the Hoek-Brown constant mi for intact rocks. *Engineering Geology*, *224*, 87-96.

Wickham, G. E., Tiedemann, H. R. & Skinner, E. H. (1972). Support determination based on geologic predictions. In K. S. Lane, & L. A. Garfield, (Eds.). *Proceedings of North American Rapid Excavation & Tunneling Conference* (43-64). New York: Society of Mining Engineers, American Institute of Mining, Metallurgical, and Petroleum Engineers.

Wu, T. H., & Sidle, R. C. (1995). A distributed slope stability model for steep forested basins *Water Resources Research*, *31*, 2097-2110.

Wyllie, D. C., & Mah, C. W. (2004). *Rock slope engineering civil and mining* (4th ed.). New York: Spon Press.

Xia, J., Miller, R. D., & Park, C. B. (1999). Estimation of near-surface shear-wave velocity by inversion of Rayleigh wave. *Geophysics*, *64*, 691-700.

Yağmurlu, F. (1982). Geology and coal potential of Çıtak (Akhisar) coal deposits. In *Bulletin of Turkey 3th Coal Congress* (39-61). Zonguldak: Chamber of Mining Engineering.

Yağmurlu, F. (1983). *Geology and coal potential of the Neogene sediments in the east of Akhisar*. PhD Thesis, Dokuz Eylül University, İzmir.

Yağmurlu, F., & Baykal, H. (1989). Fundamental geological properties of Gördes Dam and its surrounding. *Geological Bulletin of Turkey, 32* (1-2), 1-7.

Yağmurlu, F., & Karayiğit, A. İ. (1984). Petrographical properties of Çıtak (Akhisar) lignites. In *Proceedings of Turkey 4th Coal Congress*, Turkey, 111-122.

Yang, H., Duan, H. F., & Zhu, J. B. (2019). Ultrasonic P-wave propagation through water-filled rock joint: An experimental investigation. *Journal of Applied Geophysics*, *169*, 1-14.

Yaşar, E., & Erdoğan, Y. (2004). Correlating sound velocity with the density, compressive strength and Young's modulus of carbonate rocks. *International Journal of Rock Mechanics and Mining Sciences*, *41*, 871-875.

Yavuz, A. B., & Topal, T. (2007). Thermal and salt crystallization effects on marble deterioration: Examples from Western Anatolia, Turkey. *Engineering Geology*, *90* (1), 30-40.

Yavuz, A. B., & Topal, T. (2016) Effects of different drying temperatures on the physical and mechanical properties of some marbles (Muğla, Turkey) during salt crystallization tests. *Environmental Earth Sciences*, *75*, 982.

Yu, M., Huang, Y., Xu, Q., Guo, P., & Dai, Z. (2016). Application of virtual earth in 3D terrain modeling to visual analysis of large-scale geological disasters in mountainous areas. *Environmental Earth Sciences*, *75* (7), 1-7.

Zaruba, Q., & Mencl, V. (1982). *Landslides and their control: Development in geotechnical engineering*. Amsterdam: Elsevier.

Zhai, H., Canbulat, İ., Hebblewhite, B., & Zhang, C. (2017). Review of current empirical approaches for determination of the weak rock mass properties. *Procedia Engineering, 191*, 908-917.

Zhang, J., Tang, W., & Zhang, L. (2010). Efficient probabilistic back-analysis of slope stability model parameters. *Journal of Geotechnical and Geoenvironmental Engineering*, *136* (1), 99-109.

Zhang, L. (2016). Determination and applications of rock quality designation (RQD). *Journal of Rock Mechanics and Geotechnical Engineering*, *8* (3), 389-397.

Zhang, Q., & Zhao, J. (2014). A review of dynamic experimental techniques and mechanical behaviour of rock materials. *Rock Mechanics and Rock Engineering, 47,* 1411-1478.

Zhao, J. (2000). Applicability of Mohr-Coulomb and Hoek-Brown Strength Criteria to the dynamic strength of brittle rock. *International Journal of Rock Mechanics and Mining Sciences, 37,* 1115-1121.

Zhao, J., Li, H. B., Wu, M. B., & Li, T. J. (1999). Dynamic uniaxial compression tests on a granite. *International Journal of Rock Mechanics and Mining Sciences, 36* (2), 273-277.

Zhenyu, T., & Haihong, M. (1990). An experimental study and analysis of the behaviour of rock under cyclic loading. *Journal of Rock Mechanics and Mining Science & Geomechanics Abstracts, 27* (1), 51-56.

Zhu, C., Zhao, H., & Zhao, M. (2014). Back analysis of geomechanical parameters in underground engineering using artificial bee colony. *The Scientific World Journal,* ID 693812.

Zienkiewicz, O. C., Humpheson, C., 6 Lewis, R. W. (1975). Associated and non-associated visco-plasticity and plasticity in soil mechanics. *Geotechnique*, *25* (4), 671-689.

Zou, C., & Wong, L. N. Y. (2014). Experimental studies on cracking processes and failure inmarble under dynamic loading. *Engineering Geology*, *173*, 19-31.

Zou, C., Wong, L. N. Y., Lo, J. J., & Gan, B. S. (2016). Different mechanical and cracking behaviors of single-flawed brittle gypsum specimens under dynamic and quasi-static loadings. *Engineering Geology*, *201*, 71-84.

Zuo, J., & Shen, J. (2020). *The Hoek-Brown Failure criterion—From theory to application*. Singapore: Springer.

APPENDICES

APPENDIX-1: Earthquake Repository

Table A1.1 The recorded 129 earthquakes greater than Mw: 4.0

Date/Time	Latitude	Longitude	Depth (km)	Type	Magnitude	Converted to M_w
28.01.2020 20:10	39.01	27.87	5.08	M_w	4.7	4.7
28.01.2020 14:53	39.08	27.82	7.0	M_w	4.1	4.1
28.01.2020 11:26	39.10	27.84	6.98	M_w	4.8	4.8
25.01.2020 17:49	39.02	27.84	7.84	M_w	4.1	4.1
24.01.2020 21:16	39.05	27.86	9.59	M_w	4.0	4.0
23.01.2020 00:45	39.03	27.86	6.98	M_w	4.2	4.2
22.01.2020 22:39	39.02	27.84	7.86	M_w	4.2	4.2
22.01.2020 21:52	39.07	27.85	7.01	M_w	4.1	4.1
22.01.2020 21:30	39.04	27.84	7.29	M_w	4.0	4.0
22.01.2020 21:24	39.05	27.86	6.98	M_w	4.0	4.0
22.01.2020 20:17	39.06	27.86	6.95	M_w	4.3	4.3
22.01.2020 20:17	39.07	27.82	7.0	M_w	4.1	4.1
22.01.2020 19:25	39.07	27.85	7.01	M_w	4.1	4.1
22.01.2020 19:22	39.04	27.84	10.35	M_w	5.4	5.4
11.11.2017 08:56	38.86	27.47	18.09	M_w	4.4	4.40
19.07.2017 04:42	38.76	27.82	11.36	M_w	4	4.00
05.07.2017 07:26	38.62	27.62	10.26	M_w	4.1	4.10
22.06.2017 08:56	38.63	27.54	16.53	M_w	4	4.00
28.05.2017 11:04	38.74	27.80	7.21	M_w	4.8	4.80
28.05.2017 08:49	38.73	27.80	7.1	M_w	4.1	4.10

Table A1.1 continues

Date/Time	Latitude	Longitude	Depth (km)	Type	Magnitude	Converted to M_w
28.05.2017 07:34	38.78	27.78	7.21	M_w	4.1	4.10
28.05.2017 04:38	38.74	27.81	9.78	M_w	4.5	4.50
28.05.2017 02:52	38.71	27.80	6.9	M_w	4.8	4.80
28.05.2017 02:50	38.72	27.78	8.64	M_w	4.6	4.60
28.05.2017 02:16	38.74	27.85	4.44	M_w	4	4.00
28.05.2017 02:14	38.74	27.80	9.17	M_w	4.4	4.40
27.05.2017 15:53	38.74	27.82	11.03	M_w	5.1	5.10
21.04.2017 14:12	38.63	27.59	13.2	M_w	4.9	4.90
19.04.2017 11:23	38.64	27.63	21.92	M_w	4.2	4.20
04.04.2017 13:00	38.63	27.58	18.4	M_w	4	4.00
02.04.2017 05:32	38.63	27.57	12.56	M_w	4.3	4.30
15.10.2016 02:51	38.93	27.72	9.8	M_w	4.2	4.20
15.10.2016 02:49	38.93	27.72	8.14	M_w	4.1	4.10
09.10.2016 06:21	39.01	27.73	14.07	M_w	4	4.00
12.09.2016 09:29	38.90	27.74	17.24	M_w	4.5	4.50
12.09.2016 08:26	38.91	27.75	17.78	M_w	4.6	4.60
03.07.2016 18:05	38.76	27.81	9.82	M_w	4	4.00
02.12.2015 15:52	39.15	28.15	10.85	M_w	4	4.00
05.09.2012 15:49	38.97	27.62	20.71	M_L	4.1	4.78
25.08.2012 07:24	38.71	28.03	17.4	M_L	4.1	4.78
07.08.2012 23:57	38.72	28.05	22.21	M_L	4.2	4.85
07.08.2012 23:17	38.73	28.05	18.05	M_L	4	4.70

Table A1.1 continues

Date/Time	Latitude	Longitude	Depth (km)	Type	Magnitude	Converted to M_w
04.08.2012 02:23	38.72	28.07	22.94	M_L	4.2	4.85
03.08.2012 10:18	38.72	28.07	22.61	M_L	4.6	5.17
08.02.2012 19:57	39.21	27.87	6.99	M_L	4.2	4.85
08.10.2011 22:10	39.01	28.06	25.38	M_L	4	4.70
10.06.2011 22:47	39.10	28.34	34.38	M_L	4.7	5.24
01.05.2011 15:04	39.06	28.02	24.88	M_L	4.1	4.78
13.07.2008 14:30	38.92	27.85	10	M_L	4	4.70
15.03.2008 15:34	39.04	27.86	2.5	M_L	4	4.70
15.03.2008 11:52	39.05	27.85	11.8	M_b	4.2	4.31
10.12.2007 21:50	38.78	27.74	21.43	M_d	4	4.22
24.12.2005 03:56	38.78	27.82	7.5	M_b	4.3	4.44
13.01.2005 11:00	39.19	27.73	8.9	M_L	4.3	4.93
22.06.2003 23:46	39.00	28.03	15.1	M_b	4.5	4.69
06.06.2002 05:09	39.06	28.01	8	M_b	4.2	4.31
01.03.2002 12:01	38.36	28.04	26.8	M_d	4	4.22
21.01.2002 14:34	38.63	27.88	26.2	M_b	4.8	5.06
19.01.2001 04:38	39.16	27.93	7.3	M_d	4.1	4.31
26.09.1999 06:38	39.09	27.91	10.8	M_b	4.1	4.19
17.06.1999 04:24	38.55	28.45	7.7	M_b	4.1	4.19
21.09.1996 03:34	38.84	27.89	4	M_b	4.1	4.19
14.03.1996 09:28	39.05	27.58	12	M_L	4.3	4.93
06.02.1994 01:15	38.74	27.46	5	M_b	4.1	4.19

Table A1.1 continues

Date/Time	Latitude	Longitude	Depth (km)	Type	Magnitude	Converted to M_w
28.01.1994 15:45	38.68	27.53	16.5	Mw	5.4	5.40
26.08.1993 19:50	39.10	27.83	5	M_b	4	4.07
31.03.1993 18:20	39.15	28.09	15	M_b	4.5	4.69
19.12.1990 09:46	38.59	28.04	6.7	M_b	4.7	4.93
23.04.1988 17:54	39.10	28.10	33	M_b	4	4.07
23.07.1987 07:07	38.73	27.82	10	M_L	4	4.70
30.11.1986 05:29	38.75	27.74	14	M_b	4.3	4.44
29.09.1986 17:38	39.07	27.79	11	M_L	4.1	4.78
23.09.1986 08:41	39.09	27.75	14	M_L	4.2	4.85
30.08.1986 04:47	39.11	27.84	10	M_L	4.1	4.78
27.05.1986 04:44	38.88	27.53	10	M_L	4	4.70
23.10.1985 06:14	38.80	27.83	12	M_b	4.3	4.44
17.10.1985 19:15	38.77	27.83	10	M_b	4.1	4.19
14.03.1985 11:35	38.51	27.69	15	M_b	4.7	4.93
07.11.1984 11:39	38.91	27.80	10	M_b	4	4.07
27.12.1982 19:55	39.01	27.83	17	M_L	4.1	4.78
02.11.1982 05:58	38.52	28.46	31.4	M_b	4.6	4.81
18.04.1982 23:56	38.89	28.15	10	M_L	4	4.70
31.03.1982 01:15	38.59	28.18	10	M_L	4.1	4.78
19.01.1978 12:08	38.93	27.90	10	M_L	4.1	4.78
24.02.1977 20:47	38.55	27.66	20	M_b	5	5.31
03.09.1972 08:38	39.16	27.98	30.4	M_b	4.6	4.81

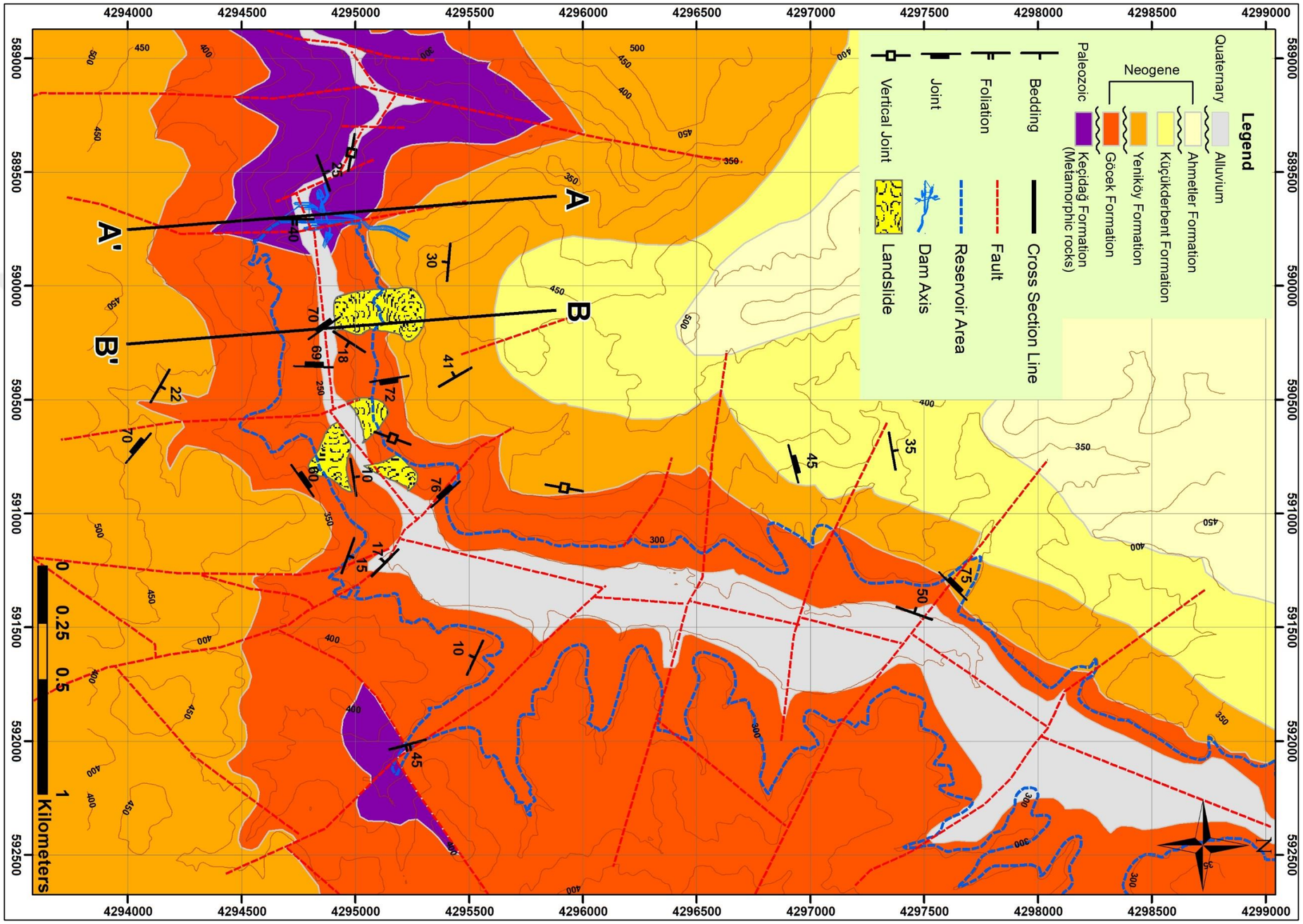
Table A1.1 continues

Date/Time	Latitude	Longitude	Depth (km)	Type	Magnitude	Converted to M_w
07.04.1970 10:55	39.00	27.80	48	M_b	4.2	4.31
29.03.1970 14:40	38.82	27.95	43.2	M_b	4.5	4.69
29.03.1970 14:37	38.81	27.85	52.3	M_b	4.5	4.69
23.03.1970 07:56	39.20	28.20	26	M_b	4.1	4.19
01.05.1969 01:14	39.10	28.00	10	M_S	4.1	4.83
20.04.1969 04:59	39.20	28.00	10	M_b	4.1	4.19
28.03.1969 01:48	38.55	28.46	4	M_S	6.5	6.46
27.03.1969 18:07	39.12	28.20	51	M_b	4.5	4.69
26.03.1969 03:31	39.03	28.27	37	M_b	4.6	4.81
25.03.1969 17:51	39.16	28.00	44	M_b	4.4	4.56
25.03.1969 16:13	39.08	28.44	42	M_b	4.7	4.93
25.03.1969 13:37	39.00	28.00	10	M_S	4	4.76
25.03.1969 13:28	38.78	28.51	40	M_b	4.8	5.06
25.03.1969 13:21	39.03	28.35	29.3	M_b	4.9	5.18
25.03.1969 10:05	38.75	27.81	35	M_b	4.3	4.44
24.03.1969 08:13	39.02	28.41	43	M_b	4.7	4.93
23.03.1969 00:15	39.17	28.32	12	M_b	4.4	4.56
17.02.1969 22:49	38.90	27.60	10	M_S	4	4.76
21.03.1968 09:42	38.80	27.60	52	M_S	4.4	4.56
29.01.1967 19:47	38.99	27.60	33	M_S	4.5	5.10
22.05.1966 07:37	38.70	27.92	23	M_b	4.4	4.56
18.10.1965 14:32	38.83	27.83	36	M_b	4	4.07

Table A1.1 continues

Date/Time	Latitude	Longitude	Depth (km)	Type	Magnitude	Converted to M_w
30.09.1965 19:36	38.80	28.00	10	M_S	4.3	4.96
19.09.1965 14:03	38.90	27.95	10	M_b	4.3	4.44
02.03.1965 22:00	38.45	28.29	41	M_b	5	5.31
04.01.1949 20:30	38.90	27.90	14	M_S	4.5	5.10
28.10.1942 02:22	39.10	27.80	50	M_S	6	6.12
12.08.1942 21:52	39.10	27.70	17	M_S	4.8	5.30
12.08.1942 20:38	39.13	27.64	50	M_S	4.8	5.30
05.02.1942 01:15	38.84	27.74	10	M_S	5.4	5.71
23.05.1937 10:57	38.69	27.78	10	M_S	5.4	5.71
13.01.1926 08:08	38.53	28.19	10	M_S	5.7	5.92
13.01.1926 01:47	38.64	28.11	50	M_S	5.8	5.98
14.04.1924 00:00	39.00	27.80	10	M_S	4.7	5.24
02.02.1913 06:30	38.79	27.87	10	M_S	4.6	5.17
27.07.1910 14:51	38.88	27.87	10	M_S	4.9	5.37
14.07.1910 02:35	38.86	27.84	10	M_S	4.4	5.03
22.06.1907 16:00	38.60	27.90	10	M_S	4.5	5.10
02.05.1905 00:00	38.80	28.50	10	M_S	5.4	5.71
30.04.1905 16:01	38.81	28.52	10	M_S	6.1	6.19
01.12.1904 00:00	38.70	27.70	20	M_S	4.8	5.30
04.04.1903 00:00	39.00	28.00	20	M_S	5.5	5.78
13.01.1903 23:00	38.45	28.20	10	M_S	4.8	5.30

APPENDIX-2: 1/10000 Geology Map



APPENDIX-3: X-RAY Diffraction Patterns

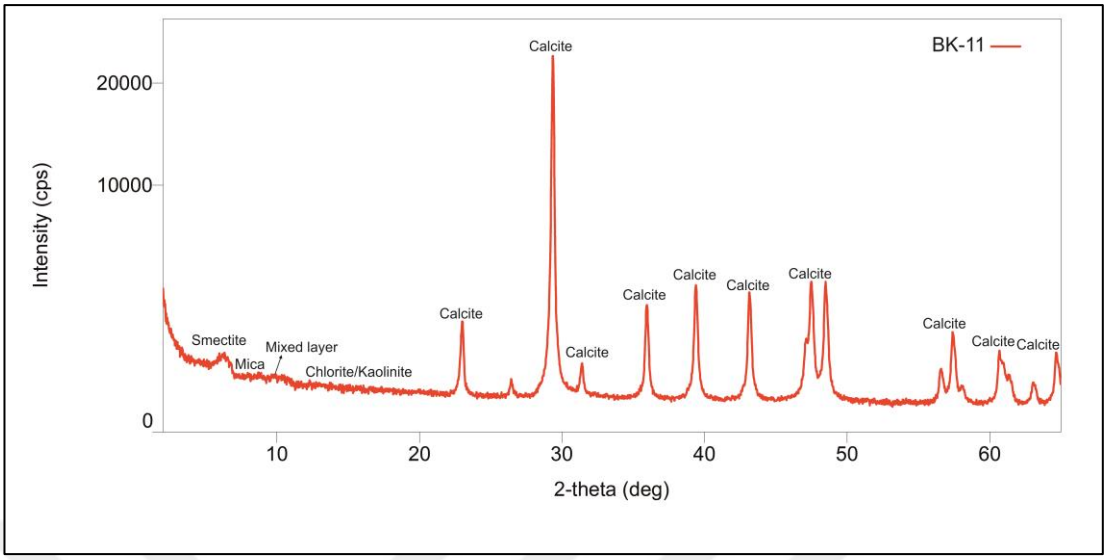


Figure A3.1 X-Ray diffraction pattern of BK-11

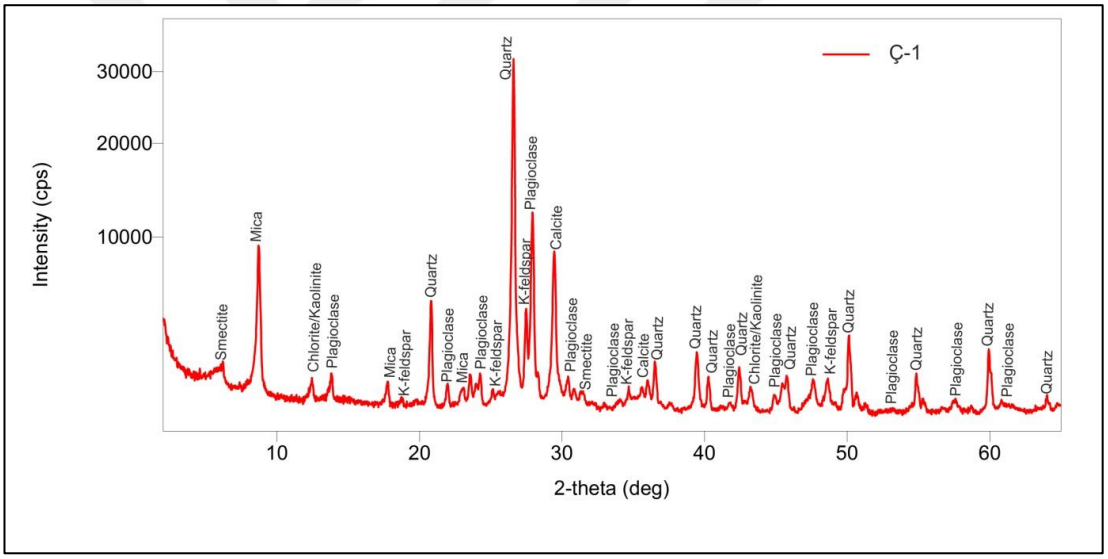


Figure A3.2 X-Ray diffraction pattern of Ç-1

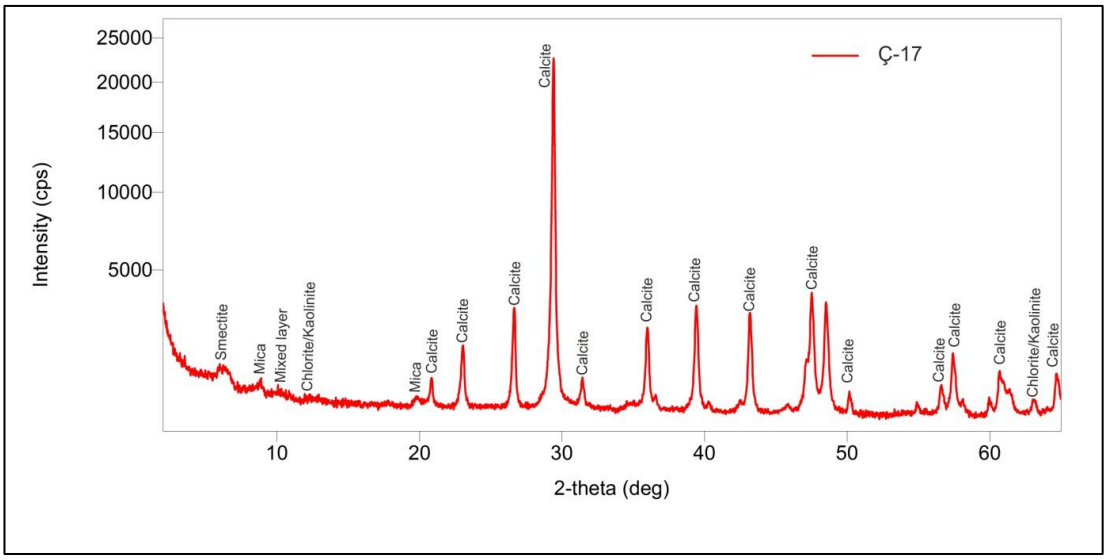


Figure A3.3 X-Ray diffraction pattern of Ç-17

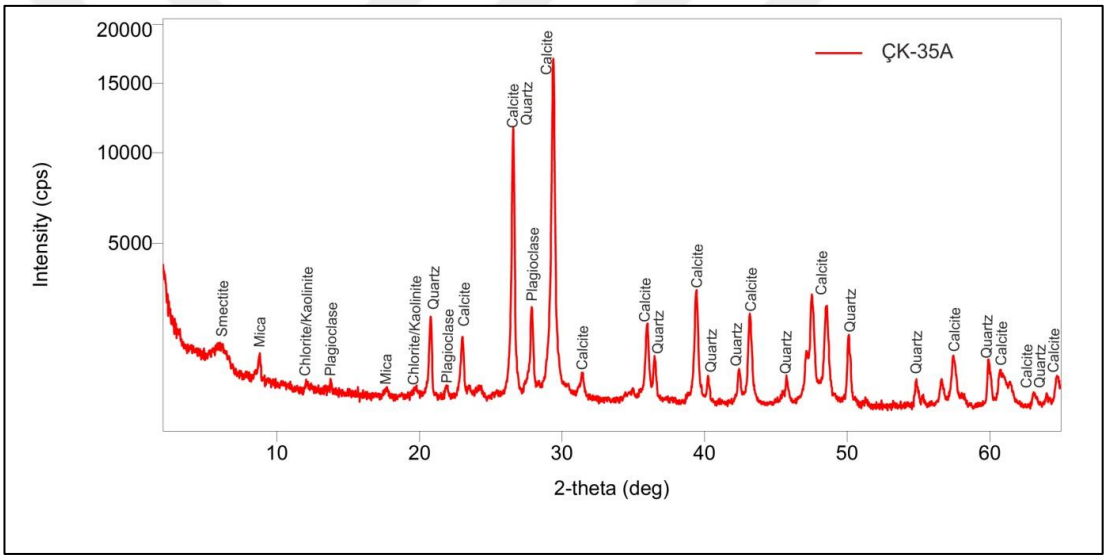


Figure A3.4 X-Ray diffraction pattern of ÇK-35A

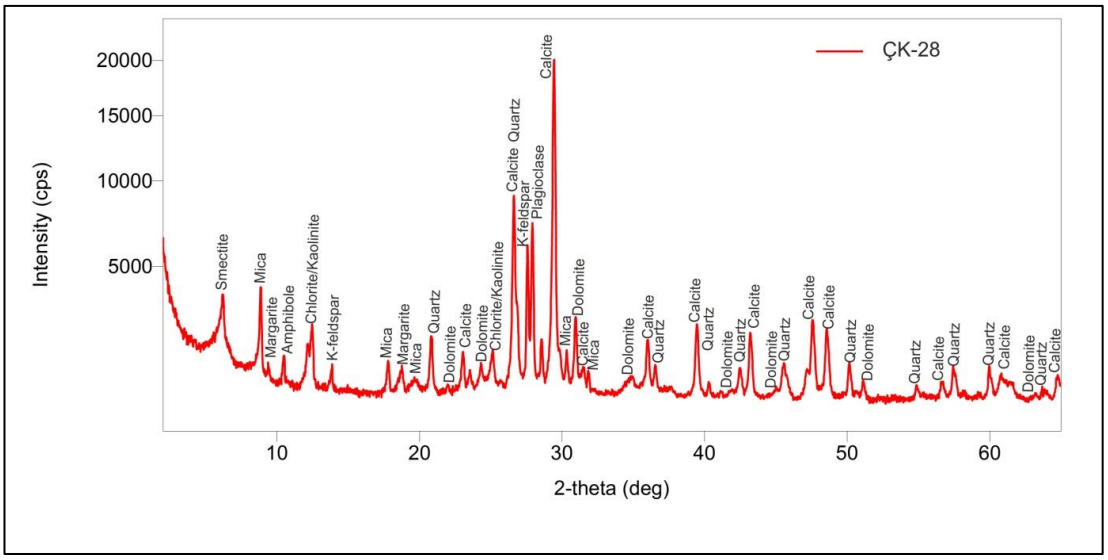


Figure A3.5 X-Ray diffraction pattern of ÇK-28

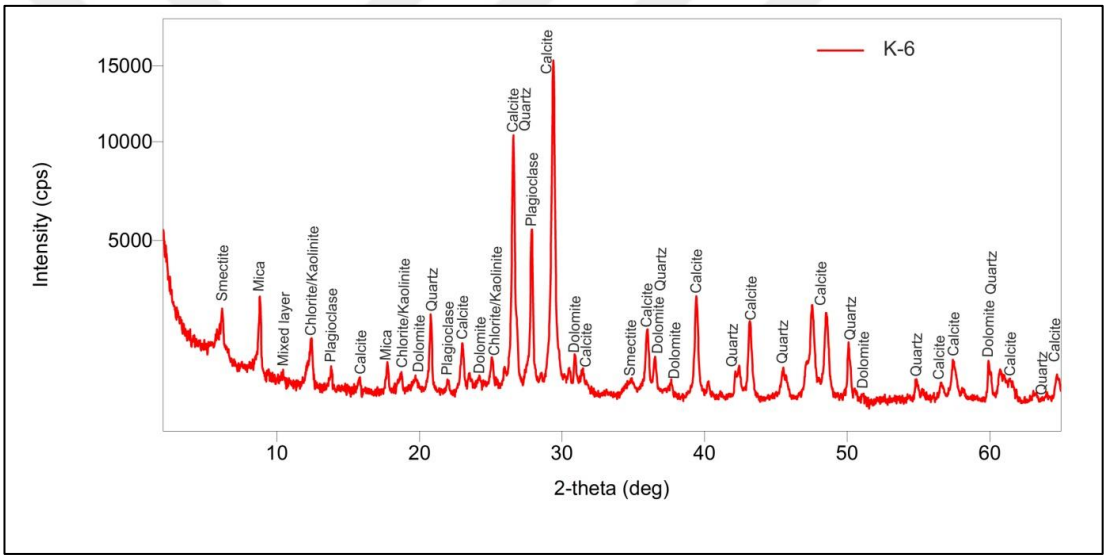


Figure A3.6 X-Ray diffraction pattern of K-6

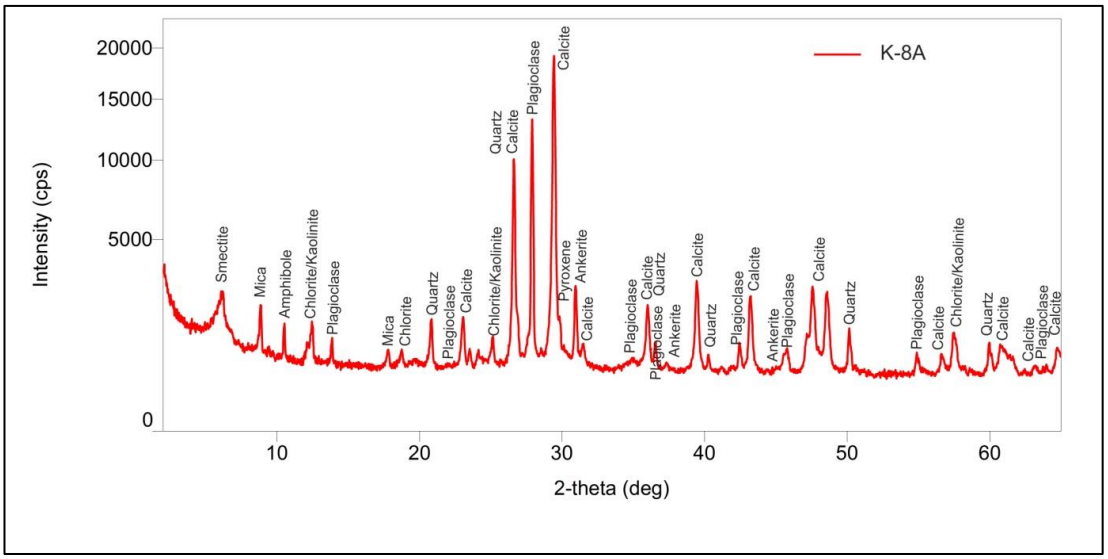


Figure A3.7 X-Ray diffraction pattern of K-8A

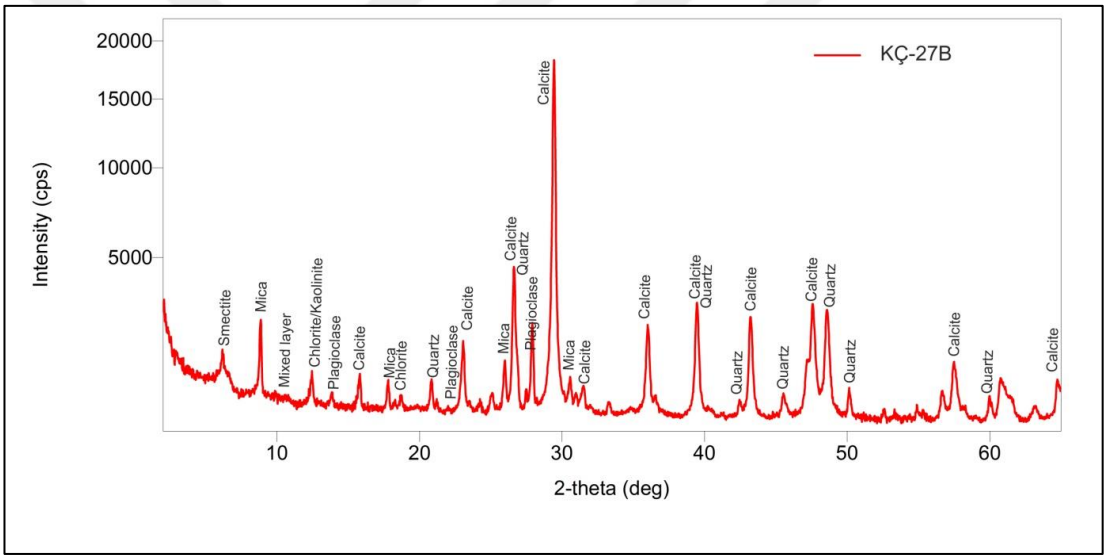


Figure A3.8 X-Ray diffraction pattern of KÇ-27B

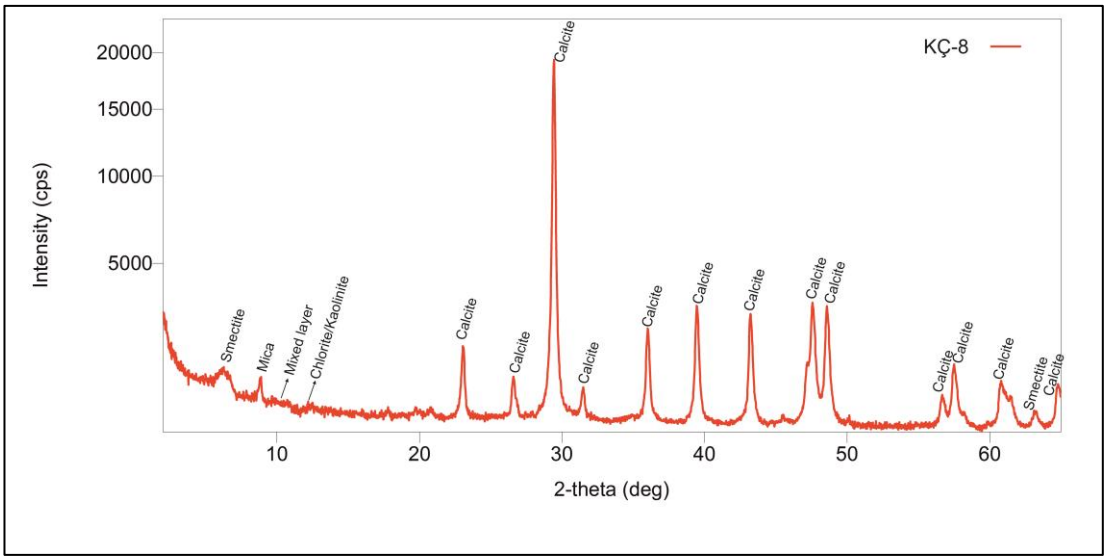


Figure A3.9 X-Ray diffraction pattern of KÇ-8

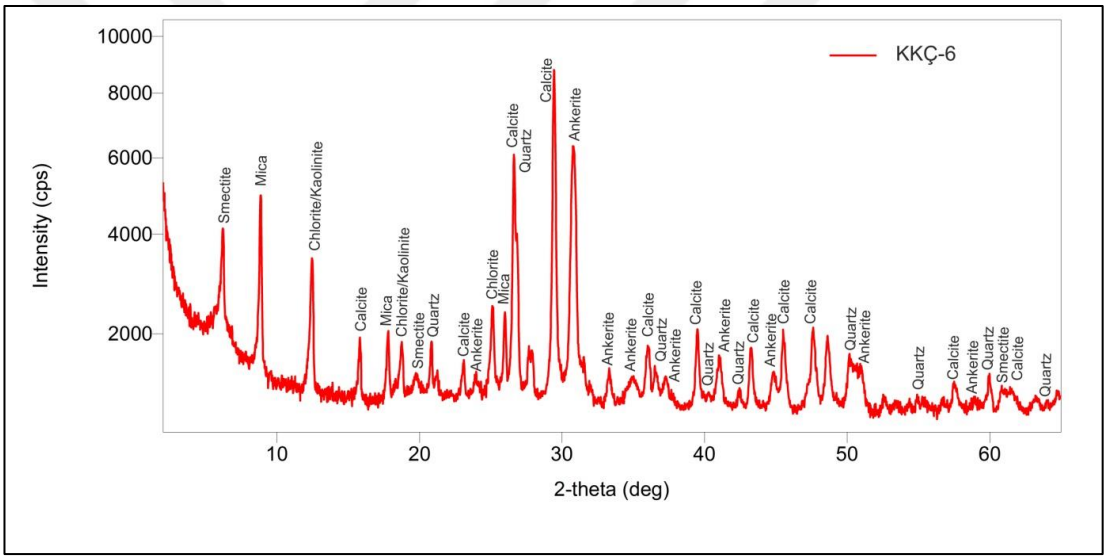


Figure A3.10 X-Ray diffraction pattern of KKÇ-6

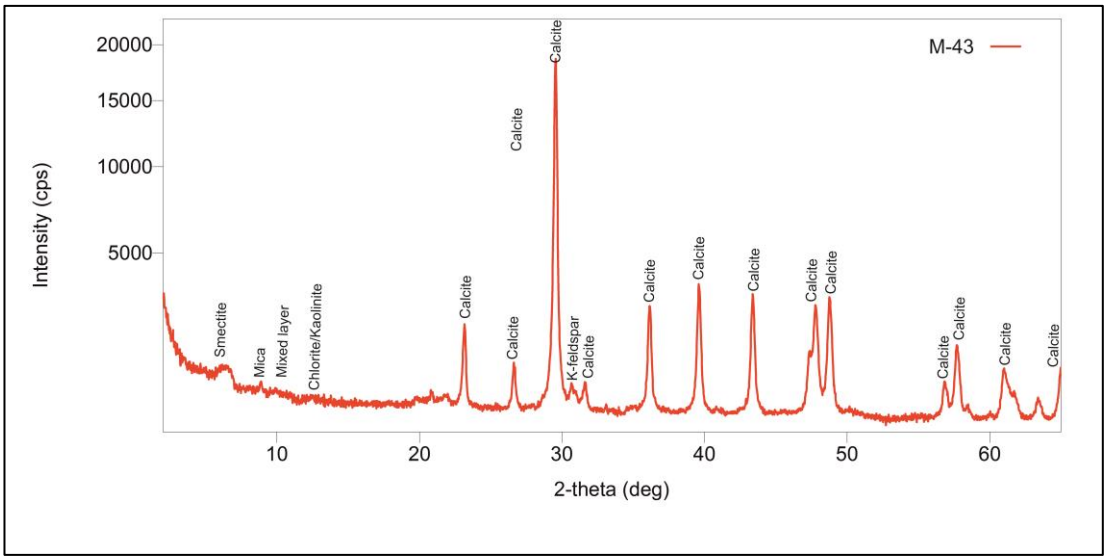


Figure A3.11 X-Ray diffraction pattern of M-43

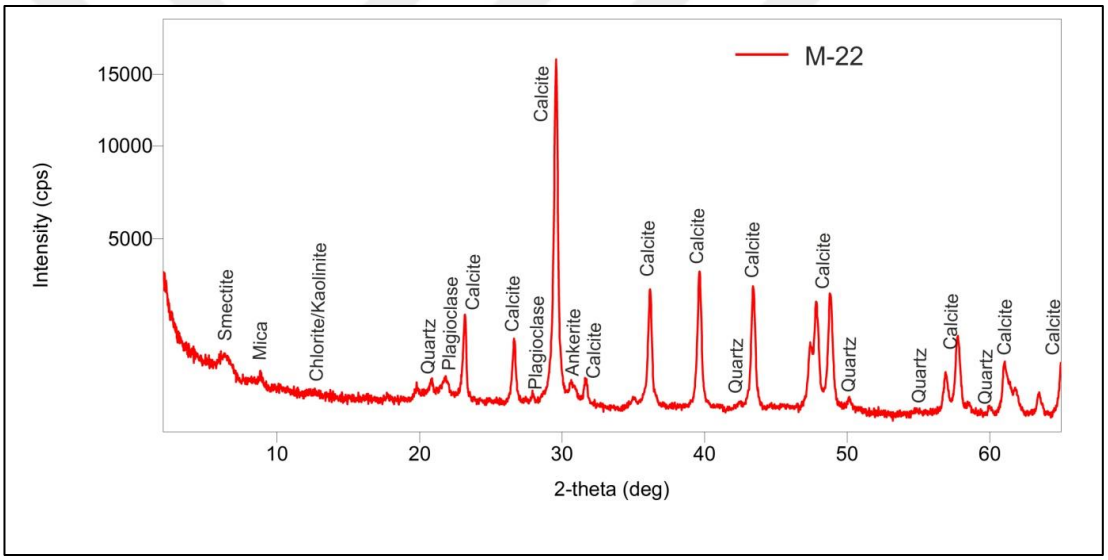


Figure A3.12 X-Ray diffraction pattern of M-22

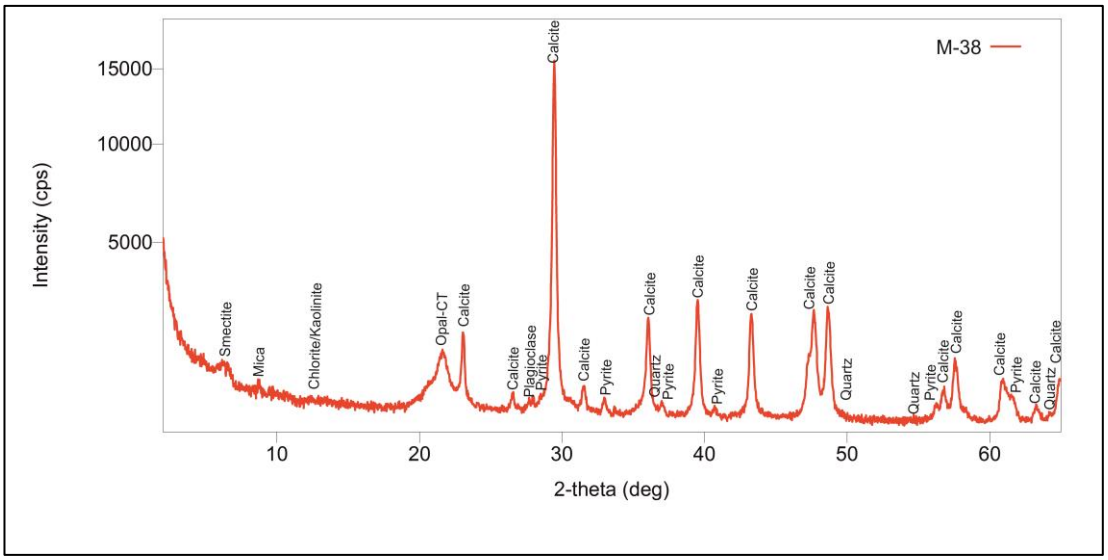


Figure A3.13 X-Ray diffraction pattern of M-38

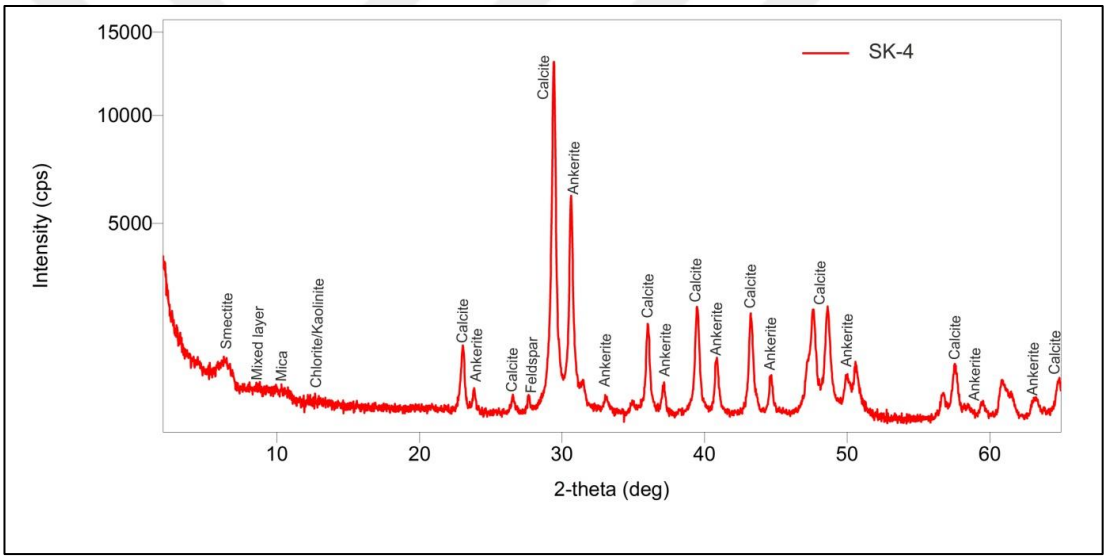


Figure A3.14 X-Ray diffraction pattern of SK-4

APPENDIX-4: Velocity-Depth Models of MASW Method

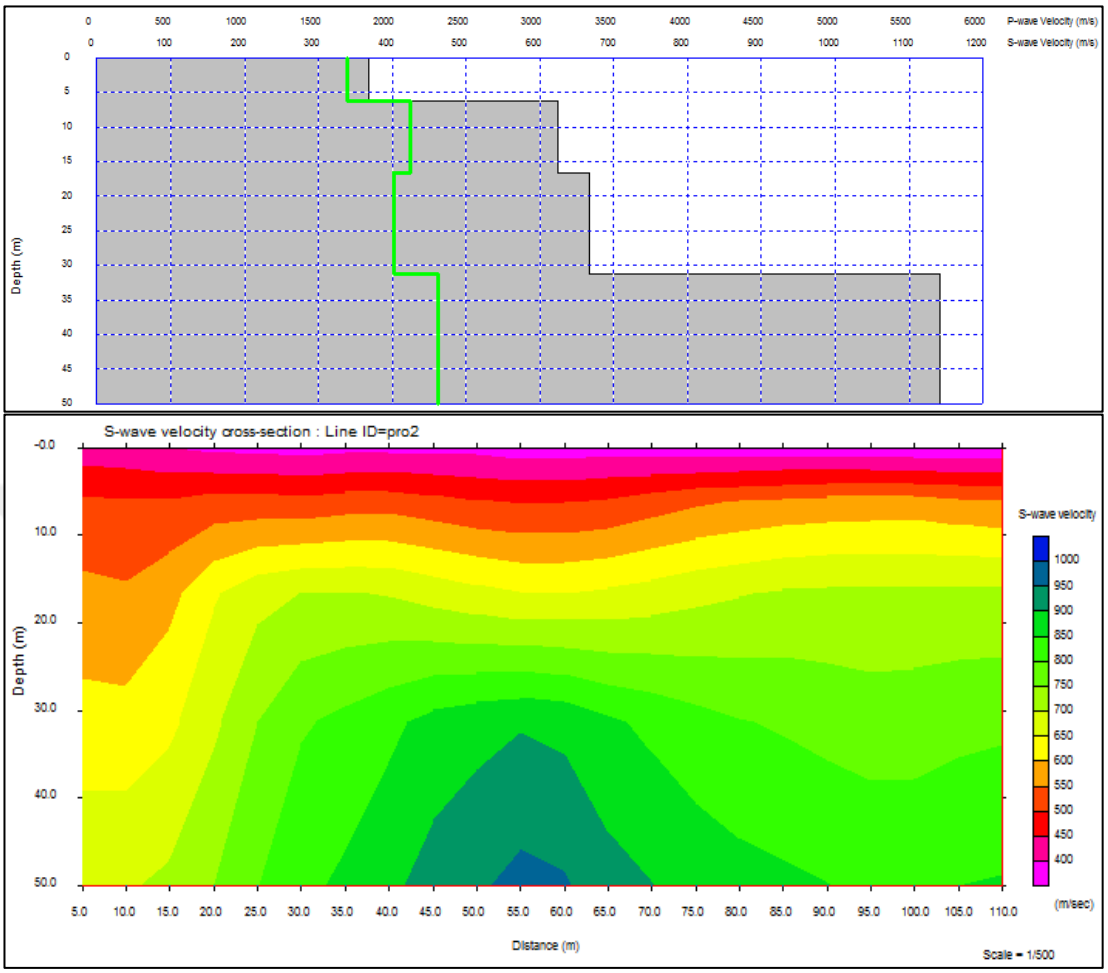


Figure A4.1 Two dimensional V_p and V_s-depth graph for Profile 1

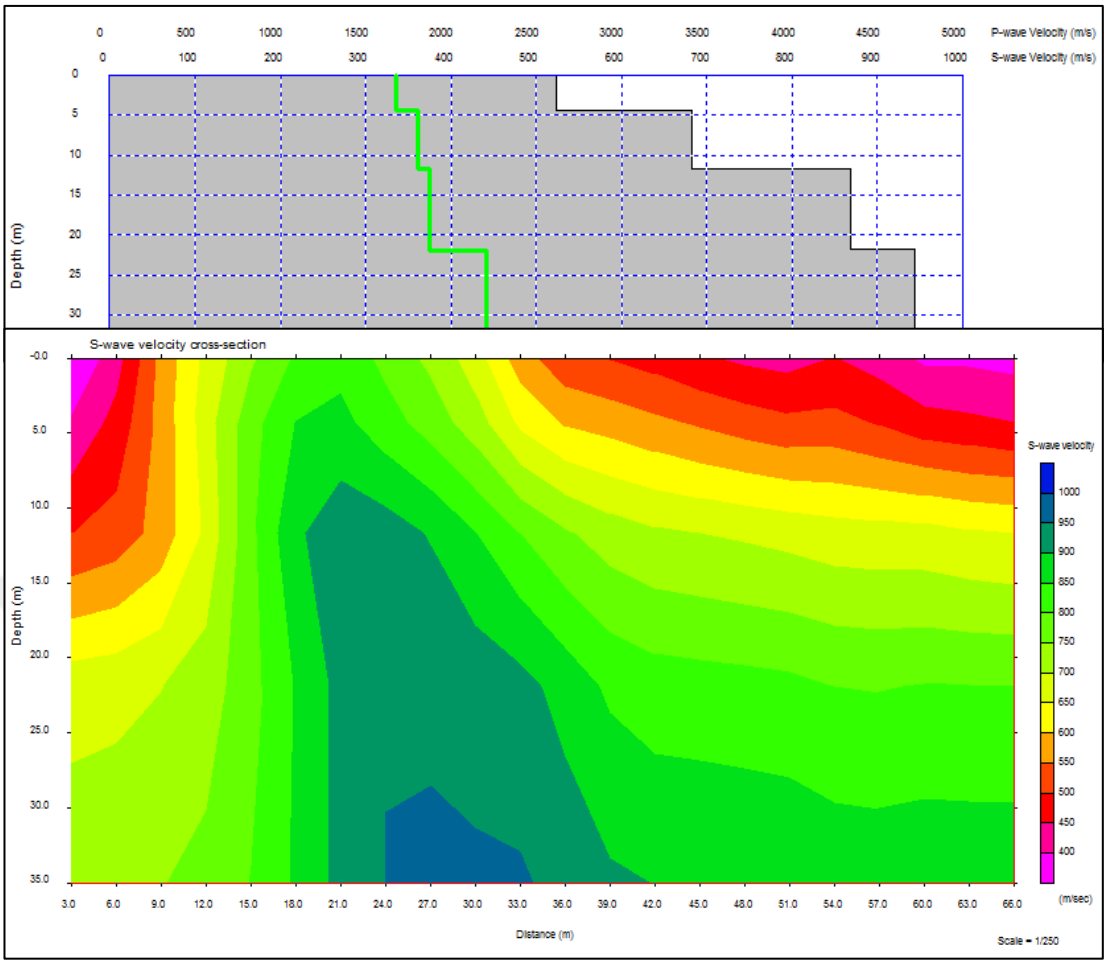


Figure A4.2 Two dimensional V_p and V_s-depth graph for Profile 2

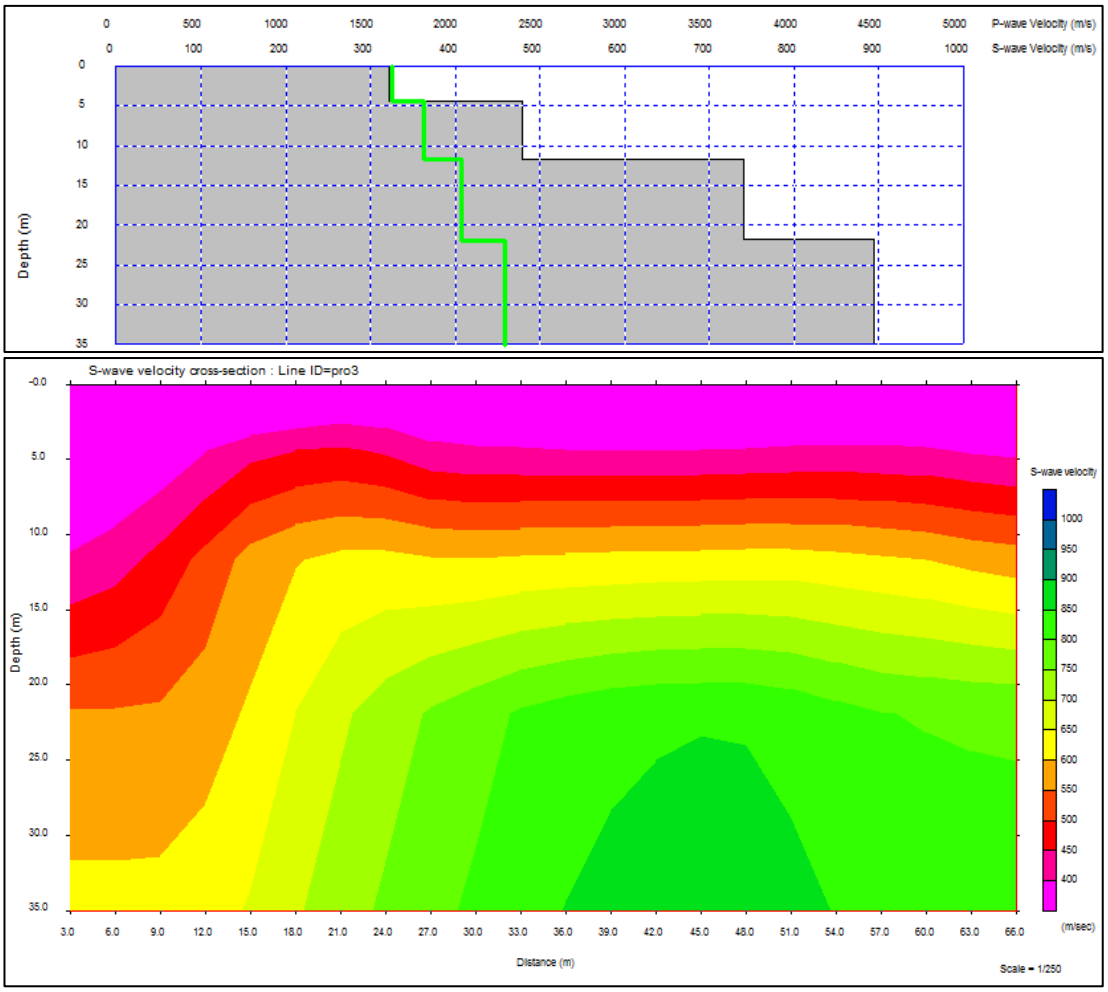


Figure A4.3 Two dimensional V_p and V_s-depth graph for Profile 3

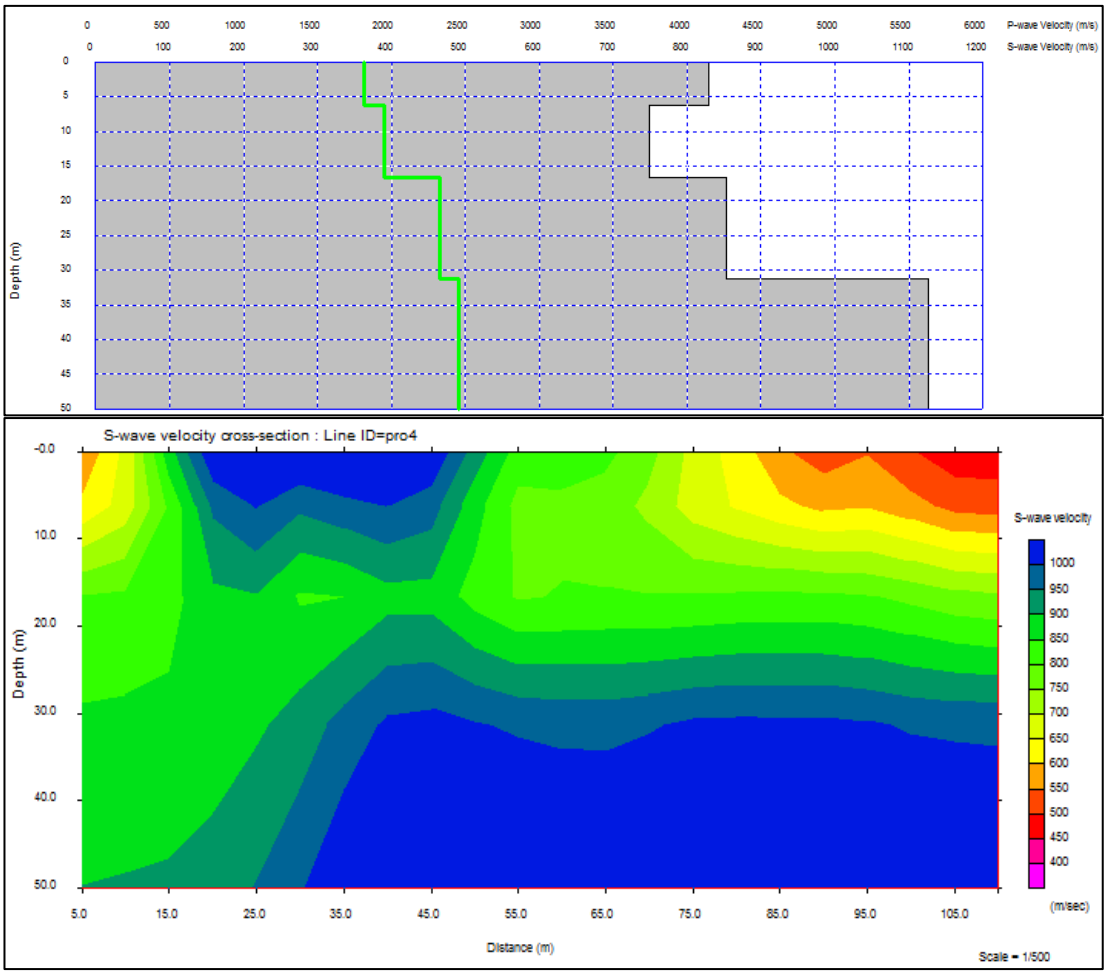


Figure A4.4 Two dimensional V_p and V_s-depth graph for Profile 4

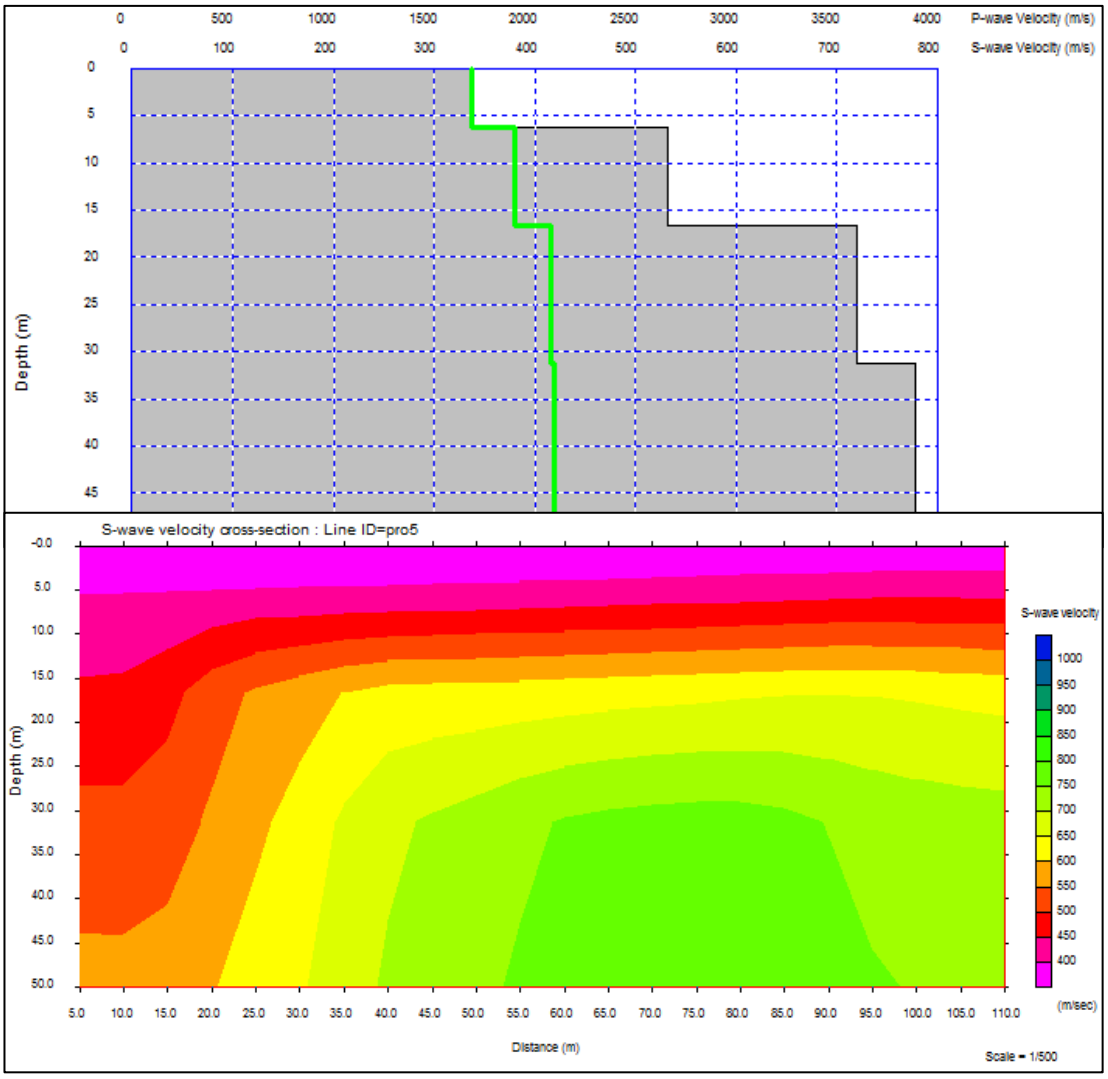


Figure A4.5 Two dimensional V_p and V_s-depth graph for Profile 5

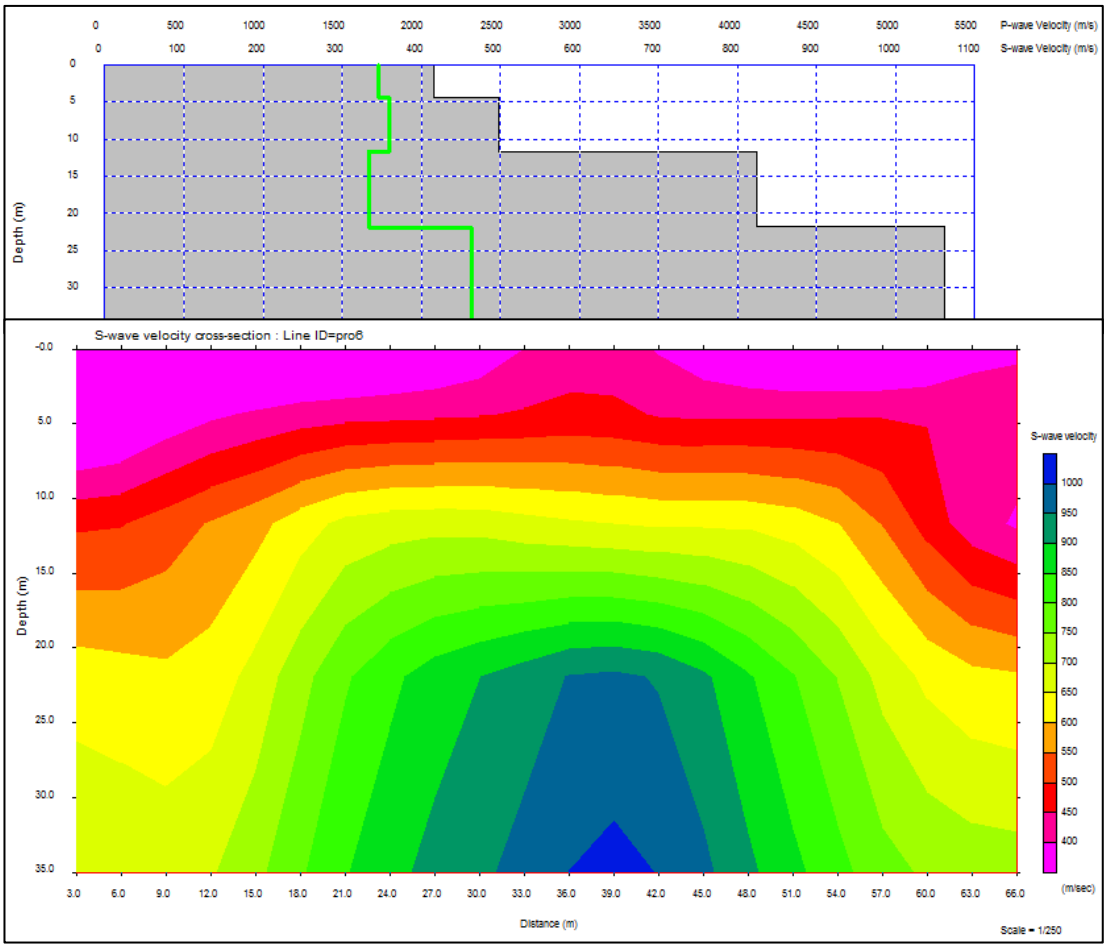


Figure A4.6 Two dimensional V_p and V_s-depth graph for Profile 6

APPENDIX-5: Laboratory Test Results

Table A5.1 The length and diameter of the test specimens

Sample	D_{mean} (mm)	L_{mean} (mm)	L/D
BK-1	53.39	100.98	1.89
BK-2	53.51	101.13	1.89
BK-3	53.39	101.60	1.90
BK-4.1	53.37	51.16	0.96
BK-4.2	53.66	48.77	0.91
BK-5.1	53.50	58.76	1.10
BK-5.2	53.37	40.14	0.75
BK-6	53.38	101.45	1.90
BK-7	53.39	101.65	1.90
BK-8	53.41	101.55	1.90
BK-9	53.36	101.42	1.90
BK-10	53.36	101.69	1.91
BK-11	53.41	101.54	1.90
BK-12	53.38	100.77	1.89
BK-13	53.42	101.68	1.90
BK-14	53.35	27.50	0.52
BK-15	53.41	58.14	1.09
BK-16	53.31	58.35	1.09
BK-17	53.38	57.69	1.08
BK-18	53.44	58.31	1.09
BK-19	53.41	56.47	1.06
BK-20	53.35	27.29	0.51
BK-21.1	53.15	31.13	0.59
BK-22	53.22	110.59	2.08
BK-23.1	53.27	28.97	0.54
BK-23.2	53.64	30.83	0.57
BK-24	53.24	56.83	1.07
BK-25	53.34	27.33	0.51
BK-26	53.41	27.20	0.51
BK-27	53.25	27.44	0.52
SK-1	53.56	101.60	1.90
SK-2	53.52	100.75	1.88
SK-3	53.54	101.61	1.90
SK-4	53.54	101.13	1.89
SK-5	53.55	101.18	1.89
SK-6	53.52	101.15	1.89
SK-7	53.50	101.17	1.89
SK-8.1	53.55	28.73	0.54
SK-8.2	53.63	26.14	0.49
SK-9.1	53.70	29.11	0.54
SK-9.2	53.73	27.17	0.51
SK-10	53.54	58.16	1.09
SK-12	53.54	27.28	0.51
SK-13	53.52	58.22	1.09
SK-14.1	53.53	26.30	0.49
SK-14.2	53.66	27.69	0.52
SK-15	53.48	58.61	1.10
SK-16	53.52	58.07	1.09
SK-17	53.53	58.33	1.09
SK-19	53.53	58.30	1.09
KÇ-1.1	53.30	15.69	0.29
KÇ-1.2	53.33	28.73	0.54
KÇ-1.3	53.29	55.69	1.05
KÇ-2.1	53.36	29.78	0.56
KÇ-2.2	53.37	49.47	0.93
KÇ-3	53.32	106.51	2.00
KÇ-4	53.28	106.77	2.00
KÇ-5.1	53.33	50.15	0.94
KÇ-5.2	53.44	37.11	0.69
KÇ-6.1	53.32	68.34	1.28
KÇ-7	53.36	106.53	2.00
KÇ-8	53.28	101.31	1.90
KÇ-9	53.28	27.98	0.53
KÇ-11	53.34	23.98	0.45
KÇ-13	53.28	26.97	0.51
KÇ-14	53.29	24.73	0.46
KÇ-15	53.34	26.59	0.50
KÇ-16	53.25	26.09	0.49
KÇ-17	53.30	28.64	0.54
KÇ-18	53.29	26.35	0.49
KÇ-19	53.34	26.06	0.49
KÇ-20	53.37	26.10	0.49
KÇ-21	53.28	27.08	0.51
KÇ-22	53.37	24.65	0.46
KÇ-24	53.29	28.49	0.53
KÇ-25	53.26	25.92	0.49
KÇ-26	53.28	27.36	0.51
KÇ-27.A	53.22	96.18	1.81
KÇ-27.B	53.71	97.55	1.82
KÇ-28.A	53.88	94.14	1.75

Table A5.1 continues

Sample	D_{mean} (mm)	L_{mean} (mm)	L/D
KÇ-28.B	53.48	99.63	1.86
Ç-1	53.42	101.45	1.90
Ç-2	53.37	101.37	1.90
Ç-3	53.38	101.63	1.90
Ç-4.1	53.41	52.12	0.98
Ç-4.2	53.72	22.98	0.43
Ç-5.1	53.61	27.37	0.51
Ç-5.2	53.56	24.75	0.46
Ç-5.3	53.49	22.50	0.42
Ç-5.4	53.48	22.80	0.43
Ç-6	53.39	101.49	1.90
Ç-7.1	53.49	22.67	0.42
Ç-7.2	53.47	24.10	0.45
Ç-7.3	53.61	24.96	0.47
Ç-7.4	53.43	18.70	0.35
Ç-8	53.38	101.69	1.90
Ç-9	53.39	27.61	0.52
Ç-10	53.38	27.36	0.51
Ç-11	53.42	27.68	0.52
Ç-12	53.33	110.31	2.07
Ç-13	52.91	110.75	2.09
Ç-14	53.32	110.47	2.07
Ç-15	53.24	57.38	1.08
Ç-16	53.33	56.98	1.07
Ç-17	53.37	57.18	1.07
Ç-18	53.36	57.52	1.08
Ç-19	53.24	27.52	0.52
K-1	53.39	101.45	1.90
K-2	53.39	101.56	1.90
K-3	53.39	101.21	1.90
K-4	53.39	98.95	1.85
K-5	53.40	101.44	1.90
K-6	53.40	101.38	1.90
K-7A.1	53.74	47.47	0.88
K-7A.2	53.71	44.09	0.82
K-7B	53.58	97.32	1.82
K-9B.1	53.74	29.93	0.56
K-9B.2	53.77	31.25	0.58
K-9B.3	53.67	28.71	0.53
K-8A	53.68	62.55	1.17
K-8B	53.79	94.31	1.75
K-9A.1	53.86	28.32	0.53
K-9A.2	53.68	26.17	0.49
K-9A.3	53.81	27.35	0.51
K-10A	53.81	29.23	0.54
K-11A	53.62	94.30	1.76
K-11B.1	53.83	28.51	0.53
K-11B.2	53.88	29.40	0.55
K-11B.3	53.90	27.25	0.51
K-12	53.52	90.07	1.68
K-12	53.52	90.07	1.68
K-13	47.10	89.50	1.90
K-14	46.90	99.70	2.13
K-15	46.80	89.70	1.92
K-16	46.70	101.20	2.17
K-17	46.80	99.50	2.13
KKÇ-2	53.31	110.18	2.07
KKÇ-4	53.30	106.35	2.00
KKÇ-6	53.35	109.93	2.06
KKÇ-7.1	53.51	27.59	0.52
KKÇ-7.2	53.62	27.82	0.52
KKÇ-8	53.29	27.49	0.52
KKÇ-9	53.26	27.43	0.51
KKÇ-10	53.29	27.36	0.51
KKÇ-11	53.29	27.48	0.52
ÇK-1	53.34	100.07	1.88
ÇK-2	53.41	101.50	1.90
ÇK-4	53.41	101.61	1.90
ÇK-5	53.44	101.58	1.90
ÇK-6	53.42	101.55	1.90
ÇK-7	53.36	101.53	1.90
ÇK-8	53.47	101.62	1.90
ÇK-9	53.33	101.42	1.90
ÇK-10	53.46	101.50	1.90
ÇK-11	53.34	101.21	1.90
ÇK-12	53.39	101.50	1.90
ÇK-13	53.41	101.52	1.90
ÇK-14	53.38	101.42	1.90
ÇK-15	53.34	27.49	0.52
ÇK-16	53.31	27.45	0.51
ÇK-17	53.37	27.49	0.52
ÇK-18	53.41	27.56	0.52
ÇK-19	53.31	27.02	0.51
ÇK-20	53.45	27.56	0.52
ÇK-21	53.33	110.18	2.07
ÇK-22	53.37	109.94	2.06

Table A5.1 continues

Sample	D_{mean} (mm)	L_{mean} (mm)	L/D
ÇK-23	53.30	110.25	2.07
ÇK-24	53.31	110.74	2.08
ÇK-25.1	53.74	55.05	1.02
ÇK-25.2	53.43	54.08	1.01
ÇK-26	53.28	110.49	2.07
ÇK-27	53.38	109.82	2.06
ÇK-28	53.38	109.46	2.05
ÇK-29	53.39	57.48	1.08
ÇK-30	53.39	57.84	1.08
ÇK-31	53.39	57.71	1.08
ÇK-32	53.27	26.66	0.50
ÇK-33A.1	54.16	45.99	0.85
ÇK-33A.2	53.42	47.17	0.88
ÇK-33B	53.83	72.51	1.35
ÇK-34A.1	53.77	48.24	0.90
ÇK-34B.2	53.66	28.59	0.53
ÇK-34B.1	53.79	44.39	0.83
ÇK-34A.2	53.67	43.75	0.82
ÇK-35A	53.86	95.82	1.78
ÇK-35B.1	53.68	30.30	0.56
ÇK-35B.2	53.78	21.08	0.39
ÇK-35B.3	53.71	29.40	0.55
M-6	53.50	57.63	1.08
M-10	53.44	57.18	1.07
M-11	53.43	57.48	1.08
M-12.1	53.62	26.28	0.49
M-13.1	53.55	28.40	0.53
M-15	53.42	110.20	2.06
M-16	53.46	109.65	2.05
M-17	53.46	110.27	2.06
M-21	53.43	109.47	2.05
M-22	53.42	110.22	2.06
M-25	53.39	27.76	0.52
M-26	53.42	27.59	0.52
M-27	53.29	27.46	0.52
M-28	53.42	28.38	0.53
M-29	53.41	27.39	0.51
M-33.1	53.58	29.72	0.55
M-34	53.45	57.31	1.07
M-36	53.44	57.79	1.08
M-37	53.26	58.02	1.09
M-38	53.48	57.88	1.08
M-40	53.46	58.03	1.09
M-41	53.18	56.43	1.06
M-43.1	53.50	25.24	0.47
M-44	46.70	79.10	1.69
M-45	46.90	100.10	2.13
M-46	47.50	101.90	2.15
M-47	47.60	100.80	2.12
M-48	46.50	99.70	2.14
M-49	46.40	100.70	2.17
M-50	46.90	99.60	2.12

D_{mean} : Mean diameter; L_{mean} : Mean length; L/D : Length to diameter ratio

Table A5.2 The physical properties of the test specimens

Sample	W_{dry} (g)	W_{sat} (g)	W_{sat} in water (g)	n (%)	ρ_{dry} (g/cm^3)	ρ_{sat} (g/cm^3)	ρ_{grain} (g/cm^3)	S_w (%)
BK-1	549.41	553.99	329.51	2.04	2.45	2.47	2.50	0.83
BK-2	553.60	558.23	334.16	2.07	2.47	2.49	2.52	0.84
BK-3	544.52	552.44	326.22	3.50	2.41	2.44	2.49	1.45
BK-4	542.93	550.54	325.16	3.38	2.41	2.44	2.49	1.40
BK-5	554.81	557.94	333.38	1.39	2.47	2.48	2.51	0.56
BK-6	550.61	560.16	333.47	4.21	2.43	2.47	2.54	1.73
BK-7	563.56	569.57	342.38	2.65	2.48	2.51	2.55	1.07
BK-8	557.31	563.35	336.10	2.66	2.45	2.48	2.52	1.08
BK-9	556.07	559.65	334.42	1.59	2.47	2.48	2.51	0.64

Table A5.2 continues

Sample	W_{dry} (g)	W_{sat} (g)	W_{sat} in water (g)	n (%)	ρ_{dry} (g/cm^3)	ρ_{sat} (g/cm^3)	ρ_{grain} (g/cm^3)	S_w (%)
BK-10	554.13	563.39	336.37	4.08	2.44	2.48	2.54	1.67
BK-11	543.74	554.64	326.96	4.79	2.39	2.44	2.51	2.00
BK-12	565.79	570.04	345.64	1.89	2.52	2.54	2.57	0.75
BK-13	562.91	568.64	340.93	2.52	2.47	2.50	2.54	1.02
BK-14	138.40	149.88	89.21	18.92	2.28	2.47	2.81	8.29
BK-15	313.17	318.90	189.15	4.42	2.41	2.46	2.53	1.83
BK-16	317.52	323.29	193.67	4.45	2.45	2.49	2.56	1.82
BK-17	316.90	319.38	190.75	1.93	2.46	2.48	2.51	0.78
BK-18	321.95	325.65	195.23	2.84	2.47	2.50	2.54	1.15
BK-19	301.69	306.09	180.61	3.51	2.40	2.44	2.49	1.46
BK-20	134.32	142.02	81.86	12.80	2.23	2.36	2.56	5.73
BK-21	493.59	541.51	294.96	19.44	2.00	2.20	2.48	9.71
BK-22	503.22	548.43	301.76	18.33	2.04	2.22	2.50	8.98
BK-23	487.50	534.84	290.79	19.40	2.00	2.19	2.48	9.71
BK-24	256.52	280.33	154.27	18.89	2.03	2.22	2.51	9.28
BK-25	133.77	141.53	81.41	12.91	2.23	2.35	2.55	5.80
BK-26	144.64	149.68	89.20	8.33	2.39	2.47	2.61	3.48
BK-27	124.62	135.27	75.77	17.90	2.09	2.27	2.55	8.55
BK-28A	560.6	563.42	345.27	1.29	2.57	2.58	2.60	0.50
BK-28B	555.45	559.45	342.72	1.85	2.56	2.58	2.61	0.72
BK-29A	544.63	547.66	338.1	1.45	2.60	2.61	2.64	0.56
BK-29B	527.63	530.24	325.5	1.27	2.58	2.59	2.61	0.49
Ç-1	598.21	606.24	379.40	3.54	2.64	2.67	2.73	1.34
Ç-2	576.76	589.28	363.75	5.55	2.56	2.61	2.71	2.17
Ç-3	570.69	584.93	357.94	6.27	2.51	2.58	2.68	2.50
Ç-4	590.00	597.94	371.91	3.51	2.61	2.65	2.71	1.35
Ç-5	618.09	624.28	397.49	2.73	2.73	2.75	2.80	1.00
Ç-6	608.95	617.31	390.46	3.69	2.68	2.72	2.79	1.37
Ç-7	598.60	606.05	380.34	3.30	2.65	2.69	2.74	1.24
Ç-8	603.42	613.22	385.84	4.31	2.65	2.70	2.77	1.62
Ç-9	167.24	169.53	107.94	3.72	2.72	2.75	2.82	1.37
Ç-10	156.02	160.18	99.37	6.84	2.57	2.63	2.75	2.67
Ç-11	170.12	171.12	109.51	1.62	2.76	2.78	2.81	0.59
Ç-12	587.93	606.99	360.31	7.73	2.38	2.46	2.58	3.24
Ç-13	582.77	600.27	357.35	7.20	2.40	2.47	2.59	3.00
Ç-14	599.38	615.21	368.37	6.41	2.43	2.49	2.59	2.64
Ç-15	302.27	313.69	186.03	8.95	2.37	2.46	2.60	3.78
Ç-16	300.12	311.14	184.22	8.68	2.36	2.45	2.59	3.67
Ç-17	303.29	314.13	186.87	8.52	2.38	2.47	2.61	3.57

Table A5.2 continues

Sample	W_{dry} (g)	W_{sat} (g)	W_{sat} in water (g)	n (%)	ρ_{dry} (g/cm^3)	ρ_{sat} (g/cm^3)	ρ_{grain} (g/cm^3)	S_w (%)
Ç-18	301.49	312.60	184.50	8.67	2.35	2.44	2.58	3.69
Ç-19	146.01	151.63	90.96	9.26	2.41	2.50	2.65	3.85
ÇK-1	578.110	590.7	366.040	5.60	2.57	2.63	2.73	2.18
ÇK-2	599.400	607.630	380.410	3.62	2.64	2.67	2.74	1.37
ÇK-3	598.400	607.22	380.460	3.89	2.64	2.68	2.75	1.47
ÇK-4	606.430	612.700	385.330	2.76	2.67	2.69	2.74	1.03
ÇK-5	611.150	617.060	389.430	2.60	2.68	2.71	2.76	0.97
ÇK-6	611.210	616.260	388.930	2.22	2.69	2.71	2.75	0.83
ÇK-7	604.850	612.750	385.480	3.48	2.66	2.70	2.76	1.31
ÇK-8	603.490	611.620	383.680	3.57	2.65	2.68	2.75	1.35
ÇK-9	610.460	615.840	389.080	2.37	2.69	2.72	2.76	0.88
ÇK-10	613.600	618.530	391.030	2.17	2.70	2.72	2.76	0.80
ÇK-11	596.750	605.320	379.910	3.80	2.65	2.69	2.75	1.44
ÇK-12	608.530	614.750	387.770	2.74	2.68	2.71	2.76	1.02
ÇK-13	550.210	570.140	343.710	8.80	2.43	2.52	2.66	3.62
ÇK-14	549.950	570.650	344.030	9.13	2.43	2.52	2.67	3.76
ÇK-15	149.280	154.450	93.700	8.51	2.46	2.54	2.69	3.46
ÇK-16	140.780	147.930	87.860	11.90	2.34	2.46	2.66	5.08
ÇK-17	147.330	152.670	92.310	8.85	2.44	2.53	2.68	3.62
ÇK-18	162.370	164.080	103.330	2.81	2.67	2.70	2.75	1.05
ÇK-19	157.650	160.450	100.630	4.68	2.64	2.68	2.76	1.78
ÇK-20	164.000	165.570	104.230	2.56	2.67	2.70	2.74	0.96
ÇK-21	624.25	642.340	396.910	7.37	2.54	2.62	2.75	2.90
ÇK-22	614.76	636.550	391.100	8.88	2.50	2.59	2.75	3.54
ÇK-23	606.69	633.380	385.740	10.78	2.45	2.56	2.75	4.40
ÇK-24	602.8	631.760	383.060	11.64	2.42	2.54	2.74	4.80
ÇK-25	613	640.290	389.900	10.90	2.45	2.56	2.75	4.45
ÇK-26	606.23	632.640	385.420	10.68	2.45	2.56	2.75	4.36
ÇK-27	613.87	634.860	390.860	8.60	2.52	2.60	2.75	3.42
ÇK-28	617.63	636.370	392.810	7.69	2.54	2.61	2.75	3.03
ÇK-29	323.08	334.480	205.730	8.85	2.51	2.60	2.75	3.53
ÇK-30	322.66	333.880	205.210	8.72	2.51	2.59	2.75	3.48
ÇK-31	313.48	330.120	199.400	12.73	2.40	2.53	2.75	5.31
ÇK-32	144.82	151.150	92.180	10.73	2.46	2.56	2.75	4.37
ÇK-33A	543.8	556.04	339.25	5.65	2.51	2.56	2.66	2.25
ÇK-34A	536.3	548.29	334.51	5.61	2.51	2.56	2.66	2.24
ÇK-34B	505.7	519.92	315.57	6.96	2.47	2.54	2.66	2.81
ÇK-35A	537.98	549.67	335.42	5.46	2.51	2.57	2.66	2.17
ÇK-35B	521.64	535.9	325.67	6.78	2.48	2.55	2.66	2.73

Table A5.2 continues

Sample	W_{dry} (g)	W_{sat} (g)	W_{sat} in water (g)	n (%)	ρ_{dry} (g/cm^3)	ρ_{sat} (g/cm^3)	ρ_{grain} (g/cm^3)	S_w (%)
KÇ-1	607.23	616.56	379.04	3.93	2.56	2.60	2.66	1.54
KÇ-2	611.02	620.63	382.26	4.03	2.56	2.60	2.67	1.57
KÇ-3	596.06	612.33	374.33	6.84	2.50	2.57	2.69	2.73
KÇ-4	609.67	618.81	380.90	3.84	2.56	2.60	2.66	1.50
KÇ-5	602.53	615.85	378.07	5.60	2.53	2.59	2.68	2.21
KÇ-6	608.18	619.59	381.98	4.80	2.56	2.61	2.69	1.88
KÇ-7	598.18	610.51	373.20	5.20	2.52	2.57	2.66	2.06
KÇ-8	572.04	584.04	358.07	5.31	2.53	2.58	2.67	2.10
KÇ-9	159.21	162.02	100.04	4.53	2.57	2.61	2.69	1.76
KÇ-10	135.59	138.19	85.01	4.89	2.55	2.60	2.68	1.92
KÇ-11	136.23	138.96	85.67	5.12	2.56	2.61	2.69	2.00
KÇ-12	153.1	155.72	96.08	4.39	2.57	2.61	2.69	1.71
KÇ-13	151.38	154.95	95.25	5.98	2.54	2.60	2.70	2.36
KÇ-14	137.62	141.11	86.44	6.38	2.52	2.58	2.69	2.54
KÇ-15	150.44	153.09	94.46	4.52	2.57	2.61	2.69	1.76
KÇ-16	148.62	151.13	93.49	4.35	2.58	2.62	2.70	1.69
KÇ-17	162.38	165.60	102.00	5.06	2.55	2.60	2.69	1.98
KÇ-18	144.27	148.18	90.23	6.75	2.49	2.56	2.67	2.71
KÇ-19	148.11	151.21	93.28	5.35	2.56	2.61	2.70	2.09
KÇ-20	149.38	152.19	94.20	4.85	2.58	2.62	2.71	1.88
KÇ-21	151.44	155.57	95.39	6.86	2.52	2.59	2.70	2.73
KÇ-22	137.7	141.42	86.64	6.79	2.51	2.58	2.70	2.70
KÇ-23	155.58	159.63	97.76	6.55	2.51	2.58	2.69	2.60
KÇ-24	160.39	163.89	100.95	5.56	2.55	2.60	2.70	2.18
KÇ-25	144.64	148.60	91.11	6.89	2.52	2.58	2.70	2.74
KÇ-26	155.03	158.37	97.76	5.51	2.56	2.61	2.71	2.15
KÇ-27A	541.65	552.72	336.72	5.13	2.51	2.56	2.64	2.04
KÇ-27B	560.14	565.46	345.4	2.42	2.55	2.57	2.61	0.95
KÇ-28A	532.78	539.51	328	3.18	2.52	2.55	2.60	1.26
KÇ-28B	571.3	575.9	352.11	2.06	2.55	2.57	2.61	0.81
K-1	588.33	597.82	371.31	4.19	2.60	2.64	2.71	1.61
K-2	607.02	612.84	386.38	2.57	2.68	2.71	2.75	0.96
K-3	583.31	594.54	368.64	4.97	2.58	2.63	2.72	1.93
K-4	607.88	612.98	386.75	2.25	2.69	2.71	2.75	0.84
K-5	599.3	606.63	380.2	3.24	2.65	2.68	2.74	1.22
K-6	596.17	603.98	377.68	3.45	2.63	2.67	2.73	1.31
K7-A	525.61	541.91	329.71	7.68	2.48	2.55	2.68	3.10
K-7B	523.33	539.97	326.46	7.79	2.45	2.53	2.66	3.18
K-8A	556.06	571.74	348.5	7.02	2.49	2.56	2.68	2.82

Table A5.2 continues

Sample	W_{dry} (g)	W_{sat} (g)	W_{sat} in water (g)	n (%)	ρ_{dry} (g/cm^3)	ρ_{sat} (g/cm^3)	ρ_{grain} (g/cm^3)	S_w (%)
K-8B	548.45	562.11	344.9	6.29	2.52	2.59	2.69	2.49
K-9A	525.68	543.01	329.14	8.10	2.46	2.54	2.67	3.30
K-9B	531.13	547.24	331.47	7.47	2.46	2.54	2.66	3.03
K-11A	541.49	560.63	341.63	8.74	2.47	2.56	2.71	3.53
K-11B	533.93	550.58	339.07	7.87	2.52	2.60	2.74	3.12
K-13	365.07			12.20	2.35			
K-14	381.34				2.22			
K-15	344.5			17.20	2.23			
K-16	392.24			16.07	2.26			
K-17	392.92			9.60	2.30			
KKÇ-1	502.24	565.75	312.02	25.03	1.98	2.23	2.64	12.65
KKÇ-2	517.14	574.41	327.66	23.21	2.10	2.33	2.73	11.07
KKÇ-4	467.37	531.92	292.95	27.01	1.96	2.23	2.68	13.81
KKÇ-5	509.92	568.10	319.73	23.42	2.05	2.29	2.68	11.41
KKÇ-6	496.87	557.07	310.82	24.45	2.02	2.26	2.67	12.12
KKÇ-7	255.89	290.87	161.14	26.96	1.97	2.24	2.70	13.67
KKÇ-8	122.71	138.44	78.21	26.12	2.04	2.30	2.76	12.82
KKÇ-9	122.37	137.37	76.78	24.76	2.02	2.27	2.68	12.26
KKÇ-10	120.62	135.45	75.58	24.77	2.01	2.26	2.68	12.29
KKÇ-11	122.52	137.34	76.76	24.46	2.02	2.27	2.68	12.10
SK-1	581.92	591.54	363.99	4.23	2.56	2.60	2.67	1.65
SK-2	581.35	589.09	364.01	3.44	2.58	2.62	2.67	1.33
SK-3	582.35	593.1	365.03	4.71	2.55	2.60	2.68	1.85
SK-4	578.37	587.89	361.33	4.20	2.55	2.59	2.66	1.65
SK-5	582.55	591.17	364.59	3.80	2.57	2.61	2.67	1.48
SK-6	581.29	590.96	363.83	4.26	2.56	2.60	2.67	1.66
SK-7	584.46	592.99	365.79	3.75	2.57	2.61	2.67	1.46
SK-8	334.72	340.15	209.4	4.15	2.56	2.60	2.67	1.62
SK-9	338.18	342.66	211.94	3.43	2.59	2.62	2.68	1.32
SK-10	338.54	343.24	212.57	3.60	2.59	2.63	2.69	1.39
SK-11	152.73	156.78	95.28	6.59	2.48	2.55	2.66	2.65
SK-12	150.63	154.7	94.24	6.73	2.49	2.56	2.67	2.70
SK-13	309.01	320.53	190.14	8.84	2.37	2.46	2.60	3.73
SK-14	300.82	312.9	184.84	9.43	2.35	2.44	2.59	4.02
SK-15	299.11	314.44	183.32	11.69	2.28	2.40	2.58	5.13
SK-16	305.71	318.38	187.75	9.70	2.34	2.44	2.59	4.14
SK-17	307.49	320.7	190.27	10.13	2.36	2.46	2.62	4.30
SK-18	298.53	312.77	182.75	10.95	2.30	2.41	2.58	4.77
SK-19	312.26	323.41	192.46	8.51	2.38	2.47	2.61	3.57

Table A5.2 continues

Sample	W_{dry} (g)	W_{sat} (g)	W_{sat} in water (g)	n (%)	ρ_{dry} (g/cm^3)	ρ_{sat} (g/cm^3)	ρ_{grain} (g/cm^3)	S_w (%)
M-1	4887.76				2.38			
M-2	4281.08				2.09			
M-3	4391.84				2.06			
M-4	4321.47				2.07			
M-5	4450.73				2.22			
M-6	276.73	290.54	160.88	10.65	2.13	2.24	2.39	4.99
M-9	276.83	292.78	163.21	12.31	2.14	2.26	2.44	5.76
M-10	274.16	287.88	159.78	10.71	2.14	2.25	2.40	5.00
M-11	276.01	289.4	160.64	10.40	2.14	2.25	2.39	4.85
M-12	280.12	296.17	165.8	12.31	2.15	2.27	2.45	5.73
M-13	276.73	290.77	161.37	10.85	2.14	2.25	2.40	5.07
M-15	529.24	553.94	305.16	9.93	2.13	2.23	2.36	4.67
M-16	531.29	552.87	306.11	8.75	2.15	2.24	2.36	4.06
M-17	530.06	553.16	301.93	9.19	2.11	2.20	2.32	4.36
M-18	530.66	557.66	306.35	10.74	2.11	2.22	2.37	5.09
M-19	533.06	564.02	316.63	12.51	2.15	2.28	2.46	5.81
M-20	532.62	562.82	315.32	12.20	2.15	2.27	2.45	5.67
M-21	530.21	559.21	313.3	11.79	2.16	2.27	2.44	5.47
M-22	529.72	555.65	308.38	10.49	2.14	2.25	2.39	4.90
M-23	130.97	138.08	76.74	11.59	2.14	2.25	2.42	5.43
M-24	129.82	139.54	79.52	16.19	2.16	2.32	2.58	7.49
M-25	130.82	137.67	76.47	11.19	2.14	2.25	2.41	5.24
M-26	131.39	137.75	75.94	10.29	2.13	2.23	2.37	4.84
M-27	131.35	138.58	77.36	11.81	2.15	2.26	2.43	5.50
M-28	135.06	142.24	78.75	11.31	2.13	2.24	2.40	5.32
M-29	130.67	137.83	77.14	11.80	2.15	2.27	2.44	5.48
M-30	133.11	140.97	79.18	12.72	2.15	2.28	2.47	5.90
M-31	123.1	131.79	71.27	14.36	2.03	2.18	2.38	7.06
M-32	123.48	132	71.37	14.05	2.04	2.18	2.37	6.90
M-33	303.08	308.83	179.38	4.44	2.34	2.39	2.45	1.90
M-34	298.95	304.38	176.72	4.25	2.34	2.38	2.45	1.82
M-35	299.2	305.02	177.23	4.55	2.34	2.39	2.45	1.95
M-36	301.31	308.26	179.07	5.38	2.33	2.39	2.46	2.31
M-37	303.73	309.23	179.86	4.25	2.35	2.39	2.45	1.81
M-38	301.46	306.43	177.3	3.85	2.33	2.37	2.43	1.65
M-39	303.61	310.11	180.21	5.00	2.34	2.39	2.46	2.14
M-40	301.72	307.67	178.06	4.59	2.33	2.37	2.44	1.97
M-41	291.12	297.31	172.51	4.96	2.33	2.38	2.45	2.13
M-42	533.2	563.4	315.81	12.20	2.15	2.28	2.45	5.66

Table A5.2 continues

Sample	W_{dry} (g)	W_{sat} (g)	W_{sat} in water (g)	n (%)	ρ_{dry} (g/cm^3)	ρ_{sat} (g/cm^3)	ρ_{grain} (g/cm^3)	S_w (%)
M-43	534.27	563.77	315.64	11.89	2.15	2.27	2.44	5.52
M-44	306.37				2.26			
M-45	422.87			5.13	2.44			
M-46	396.29			3.10	2.19			
M-47	426.78				2.39			
M-48	334.86				1.98			
M-49	358.79			17.60	2.11			
M-50	438.11			1.38	2.55			

W_{dry}: Dry weight; W_{sat}: Saturated weight; n: Porosity; ρ_{dry}: Dry density; ρ_{sat}: Saturated density; ρ_{grain}: Grain density; S_w: Water absorption by weight

Table A5.3 P and S-wave velocities of the test specimens

Sample	Length (mm)	$V_{p\text{-}dry}$ (m/s)	$V_{s\text{-}dry}$ (m/s)	$V_{p\text{-}sat}$ (m/s)	$V_{s\text{-}sat}$ (m/s)
BK-1	101.07	5433.87	2307.53	5463.24	2323.45
BK-2	101.15	5438.17	2304.10	5619.44	2341.44
BK-3	101.49	5204.62	2301.36	5341.58	2343.88
BK-4	101.76	5355.79	2281.61	5355.79	2323.29
BK-5	101.08	5615.56	2323.68	5463.78	2339.81
BK-6	101.53	5343.68	2328.67	5488.11	2323.34
BK-7	101.65	5494.59		5647.22	
BK-8	101.61	5210.77		5492.43	
BK-9	101.51	5608.29		5487.03	
BK-10	101.53	5206.67		5206.67	
BK-11	101.53	5343.68	2312.76	5206.67	2323.34
BK-12	101.44	5763.64		5796.57	
BK-13	101.54	5488.65		5641.11	
BK-15	58.42	5080.00	1618.28	5263.06	1622.78
BK-16	58.26	5248.65	1631.93	5548.57	1636.52
BK-17	58.29	5025.00	1665.43	5499.06	1660.68
BK-18	58.4	5561.90		5509.43	
BK-19	56.65	5150.00		5395.24	
BK-20	26.89	4337.10	873.05	4408.20	873.05
BK-21	110.31	3897.88	2054.19	3764.85	2042.78

Table A5.3 continues

Sample	Length (mm)	$V_{p\text{-}dry}$ (m/s)	$V_{s\text{-}dry}$ (m/s)	$V_{p\text{-}sat}$ (m/s)	$V_{s\text{-}sat}$ (m/s)
BK-22	110.52	4004.35	2054.28	3905.30	2073.55
BK-23	110.39	3819.72		3780.48	
BK-24	57.16	4053.90	1432.58	3836.24	1432.58
BK-25	27.51	4509.84	876.11	4509.84	878.91
BK-26	27.45	4223.08	865.93	4223.08	868.67
SK-2	100.53	5263.35	2300.46	5263.35	2300.46
SK-3	101.58	5104.52	2094.43	5209.23	2272.48
SK-4	101.28	5193.85	2312.33	5302.62	2307.06
SK-5	101.7	5324.61	2327.23	5324.61	2316.63
SK-6	101.43	5201.54	2289.62	5338.42	2284.46
SK-7	101.26	5166.33	2322.48	5301.57	2317.16
SK-8	58.61	5280.18		5280.18	
SK-9	58.15	5485.85		5485.85	
SK-10	58.16	5287.27		5239.64	
SK-11	27.52	4511.48		4914.29	
SK-12	26.89	4801.79	884.54	4801.79	887.46
SK-13	57.74	4582.54	1556.33	4582.54	1552.15
SK-14	55.97	4477.60		4442.06	
SK-15	58.76	4320.59	1575.34	4320.59	1526.23
SK-16	57.34	4778.33	1541.40	4550.79	
SK-17	57.89	4594.44		4631.20	
SK-18	58.34	4453.44		4453.44	
SK-19	58.27	4815.70		4815.70	1562.20
KÇ-1	107.01	4864.09		4864.09	
KÇ-2	106.89	4750.67	2259.83	4971.63	2279.10
KÇ-3	106.35	4203.56	1933.64	4564.38	2161.59
KÇ-4	106.89	4548.51		4994.86	
KÇ-5	106.57	4279.92	2093.71	4633.48	2206.42
KÇ-6	106.67	4301.21		4762.05	
KÇ-7	106.66	4538.72	2190.14	4848.18	2231.38
KÇ-8	101.54	4835.24	2055.47	4953.17	2193.09

Table A5.3 continues

Sample	Length (mm)	$V_{p\text{-}dry}$ (m/s)	$V_{s\text{-}dry}$ (m/s)	$V_{p\text{-}sat}$ (m/s)	$V_{s\text{-}sat}$ (m/s)
KÇ-9	27.92	5474.51		4985.71	
KÇ-10	23.7	5152.17		4647.06	
KÇ-11	23.79	5171.74		5171.74	
KÇ-12	26.9	5274.51		5274.51	
KÇ-13	26.74	4775.00	876.72	4775.00	882.51
KÇ-14	24.68	4839.22		4839.22	
KÇ-15	25.2	4941.18		4941.18	
KÇ-16	26.15	5127.45	874.58	5127.45	877.52
KÇ-17	28.54	4324.24	903.16	4678.69	914.74
KÇ-18	26.24	4685.71		4685.71	
KÇ-19	25.86	4617.86		5070.59	
KÇ-20	25.99	4641.07	843.83	4641.07	852.13
KÇ-21	26.58	4746.43		4746.43	
KÇ-23	26.26	4040.00		3978.79	
KÇ-24	28.94	4744.26		5167.86	
KÇ-25	25.98	4639.29		4639.29	
KÇ-26	27.14	4846.43	886.93	4846.43	898.68
KÇ-27A	95.41	5048.15		5048.15	
KÇ-27B	98.05	5477.65	2280.23	5447.49	2274.94
KÇ-28A	94.42	5426.44	2211.24	5274.86	2211.24
KÇ-28B	98.88	5524.02		5373.91	
Ç-1	101.43	4923.79	2158.09	5071.50	2205.00
Ç-2	101.13	3904.63		4396.96	
Ç-3	101.47	4245.61		4697.69	
Ç-4	101.09	4746.01		5054.50	
Ç-5	101.61	5552.46		5522.28	
Ç-6	101.31	4348.07	2071.78	4734.11	2169.38
Ç-7	101.88	4652.05		4994.12	
Ç-8	101.73	4221.16	2088.91	4666.51	2169.08
Ç-9	27.69	4944.64	904.90	5429.41	904.90
Ç-10	27.35	3695.95		4273.44	

Table A5.3 continues

Sample	Length (mm)	$V_{p\text{-}dry}$ (m/s)	$V_{s\text{-}dry}$ (m/s)	$V_{p\text{-}sat}$ (m/s)	$V_{s\text{-}sat}$ (m/s)
Ç-11	27.83	6050.00		6050.00	
Ç-12	110.15	4388.45		4747.84	
Ç-13	111.05	4551.23		4745.73	
Ç-14	110.67	4918.67	2349.68	5195.77	2359.70
Ç-15	57.42	4416.92		4785.00	
Ç-16	56.79	4368.46		4543.20	
Ç-17	57.19	4236.30		4399.23	
Ç-18	57.56	3863.09	1439.00	4263.70	1460.91
Ç-19	27.45	4990.91		4575.00	
K-1	101.47	5637.22	2338.02	5798.29	2381.92
K-2	101.26	5473.51	2306.61	5594.48	2377.00
K-3	100.83	5420.97	2307.32	5601.67	2361.36
K-4	98.78	5310.75	2286.57	5487.78	2318.78
K-5	101.53	5488.11	2328.67	5609.39	2366.67
K-6	101.54	5316.23	2318.26	5641.11	2361.40
K7-A	94.29	4029.49		4209.38	
K-7B	97.13	4150.85	1970.18	4278.85	2019.33
K-8A	99.09	4234.62	1997.78	4408.30	2043.76
K-8B	96.28	4478.14		4742.86	
K-9A	95.3	4254.46		4161.57	
K-9B	96	4507.04	1991.70	4485.98	2091.50
K-11A	95.35	3557.84		3571.16	
K-11B	94.6	4042.74		4077.59	
K-14	99.7	3280.00	1804.00		
K-17	99.5	2196.00	1182.00		
KKÇ-1	110.58	2710.29		2565.66	
KKÇ-2	110.17	2661.11	1578.37	2782.07	1639.43
KKÇ-3					
KKÇ-4	106.5	2623.15	1589.55	2535.71	1568.48
KKÇ-5	109.75				
KKÇ-6	109.98	2624.82	1643.95	2493.88	1560.00

Table A5.3 continues

Sample	Length (mm)	$V_{p\text{-}dry}$ (m/s)	$V_{s\text{-}dry}$ (m/s)	$V_{p\text{-}sat}$ (m/s)	$V_{s\text{-}sat}$ (m/s)
KKÇ-7	58.53	2735.05	1229.62	2747.89	1242.68
KKÇ-8	27.45	2889.47	784.29	2889.47	773.24
KKÇ-9	27.32	2906.38		3035.56	
KKÇ-10	27.14	2634.95		2918.28	
KKÇ-11	27.3	2967.39		3067.42	
ÇK-1	100.14	3417.75		3973.81	
ÇK-2	101.57	3640.50	1912.81	4285.65	2094.23
ÇK-3	101.42	3841.67	1920.83	4352.79	
ÇK-4	101.66	4325.96	2087.47	4864.11	2210.00
ÇK-5	101.63	4324.68		4862.68	
ÇK-6	101.66	4420.00	2109.13	4840.95	2234.29
ÇK-7	101.43	4156.97	2012.50	4695.83	2195.45
ÇK-8	101.57	3640.50		4454.82	
ÇK-9	101.73	4328.94		4962.44	
ÇK-10	101.52	4413.91		4834.29	
ÇK-11	101.46	3994.49		4654.13	
ÇK-12	101.82	4089.16	2028.29	4649.32	2189.68
ÇK-13	101.41	2640.89		2991.45	
ÇK-14	101.46	2850.00		3283.50	
ÇK-15	27.45	2920.21		3709.46	
ÇK-16	27.16	1741.03		2301.69	
ÇK-17	27.35	2509.17		3295.18	
ÇK-18	27.14	4112.12	864.33	4846.43	892.76
ÇK-19	27.03	4431.15	858.10	4914.55	866.35
ÇK-20	28.13	4611.48		5023.21	
ÇK-21	110.19	3203.20	1877.17	3660.80	1926.40
ÇK-22	109.91	2954.57	1767.04	3402.79	1764.21
ÇK-27	109.93	3114.16		3640.07	
ÇK-28	109.49	3007.97	1732.44	3520.58	1830.94
ÇK-29	57.32	3098.38		3582.50	
ÇK-30	57.75	3300.00		3725.81	

Table A5.3 continues

Sample	Length (mm)	$V_{p\text{-}dry}$ (m/s)	$V_{s\text{-}dry}$ (m/s)	$V_{p\text{-}sat}$ (m/s)	$V_{s\text{-}sat}$ (m/s)
ÇK-31	57.62	2000.69	1059.19	2824.51	1132.02
ÇK-32	27.39	2883.16	765.08	3222.35	798.54
ÇK-33A	96.25	3730.62		4044.12	
ÇK-34A	94.86	4053.85	1893.41	4331.51	1817.24
ÇK-34B	89.89	3699.18	1762.55	3729.88	1725.34
ÇK-35A	94.82	3292.36	1699.28	3619.08	1775.66
ÇK-35B	93.59	3205.14		3492.16	
BK-28A	97.01	5301.09		5740.24	
BK-28B	97.83	5465.36		5788.76	
BK-29A	92.33	5463.31		5806.92	
BK-29B	91.18	5593.87		5920.78	
M-6	57.47	3569.57	1391.53	3380.59	1371.60
M-9	57.2	3788.08		3552.80	
M-10	56.57	3407.83	1363.13	3327.65	1337.35
M-11	57.21	3446.39	1381.88	3345.61	1358.91
M-12	58.43	3745.51		3629.19	
M-13	57.47	3462.05		3265.34	
M-15	110.22	3555.48		3391.38	
M-16	109.84	3531.83	1940.64	3328.48	1900.35
M-17	110.43	3550.80	1947.62	3346.36	1910.55
M-18	110.75	3504.75		3356.06	
M-19	110.48	3796.56	1987.05	3622.30	1945.07
M-20	110.33	3804.48		3665.45	
M-22	110.18	3486.71	1936.38	3338.79	1889.88
M-23	27.77	3428.40		3428.40	
M-24	27.63	3635.53		3411.11	
M-25	28.07	3465.43		3263.95	
M-26	27.79	3430.86	844.68	3430.86	842.12
M-27	27.45	3921.43		3388.89	
M-28	28.02	3459.26	846.53	3258.14	836.42
M-29	27.49	3871.83	851.08	3617.11	848.46

Table A5.3 continues

Sample	Length (mm)	$V_{p\text{-}dry}$ (m/s)	$V_{s\text{-}dry}$ (m/s)	$V_{p\text{-}sat}$ (m/s)	$V_{s\text{-}sat}$ (m/s)
M-30	28.72	3778.95		3778.95	
M-31	26.67	3509.21		3292.59	
M-32	27.05	3559.21		3339.51	
M-33	58.18	4126.24	1491.79	4126.24	1480.41
M-34	57.23	4058.87	1467.44	4058.87	1452.54
M-36	57.84	4131.43		3961.64	
M-37	58.41	4326.67	1501.54	4142.55	1493.86
M-38	58.01	4265.44	1495.10	4114.18	1487.44
M-39	58.09	4119.86		4119.86	
M-40	58.3	4134.75	1483.46	3993.15	1475.95
M-42	110.415	3730.24		3620.16	
M-43	110.58	3735.81	2014.21	3625.57	1981.72
M-46	101.9	3844.00	2364		
M-50	99.6	5185.00	2589.00		

$V_{p\text{-}dry}$: P-wave velocity under dry conditions; $V_{s\text{-}dry}$: S-wave velocity under dry conditions; $V_{p\text{-}sat}$: P-wave velocity under saturated conditions; $V_{s\text{-}sat}$: S-wave velocity under saturated conditions

Table A5.4 The dynamic elastic properties of the test specimens calculate from laboratory seismic velocities

Sample	Length (mm)	ρ_{dry} (g/cm^3)	ρ_{sat} (g/cm^3)	$E_{i\text{-}dyn\text{-}dry}$ (MPa)	$\nu_{i\text{-}dyn\text{-}dry}$	$G_{i\text{-}dyn\text{-}dry}$ (MPa)	$E_{i\text{-}dyn\text{-}sat}$ (MPa)	$\nu_{i\text{-}dyn\text{-}sat}$	$G_{i\text{-}dyn\text{-}sat}$ (MPa)
BK-1	101.07	2.45	2.47	36229.19	0.39	13032.12	37026.19	0.39	13322.64
BK-2	101.15	2.47	2.49	36479.51	0.39	13116.41	38105.25	0.39	13658.21
BK-3	101.49	2.41	2.44	35146.55	0.38	12748.30	37048.99	0.38	13416.06
BK-4	101.76	2.41	2.44	34840.83	0.39	12540.44	36498.79	0.38	13184.98
BK-5	101.08	2.47	2.48	37264.65	0.40	13340.25	37752.66	0.39	13602.48
BK-6	101.53	2.43	2.47	36426.17	0.38	13171.27	37102.93	0.39	13338.46
BK-11	101.53	2.39	2.44	35377.62	0.38	12773.98	36179.51	0.38	13149.59
BK-21	110.31	2.00	2.20	22094.95	0.31	8447.78	23671.54	0.29	9165.24
BK-22	110.52	2.04	2.22	22752.32	0.32	8609.12	24925.34	0.30	9559.43
SK-1	101.22	2.56	2.60	36993.03	0.38	13411.41	37713.99	0.38	13695.02

Table A5.4 continues

Sample	Length (mm)	ρ_{dry} (g/cm^3)	ρ_{sat} (g/cm^3)	$E_{i\text{-}dyn\text{-}dry}$ (MPa)	$\nu_{i\text{-}dyn\text{-}dry}$	$G_{i\text{-}dyn\text{-}dry}$ (MPa)	$E_{i\text{-}dyn\text{-}sat}$ (MPa)	$\nu_{i\text{-}dyn\text{-}sat}$	$G_{i\text{-}dyn\text{-}sat}$ (MPa)
SK-2	100.53	2.58	2.62	37778.53	0.38	13668.76	38281.51	0.38	13850.75
SK-3	101.58	2.55	2.60	31334.96	0.40	11200.80	37132.20	0.38	13429.54
SK-4	101.28	2.55	2.59	37574.69	0.38	13649.66	38208.76	0.38	13811.19
SK-5	101.70	2.57	2.61	38486.33	0.38	13924.85	38737.84	0.38	14002.44
SK-6	101.43	2.56	2.60	37025.58	0.38	13416.64	37691.45	0.39	13578.46
SK-7	101.26	2.57	2.61	38112.31	0.37	13875.52	38731.81	0.38	14013.67
KÇ-2	106.89	2.56	2.60	35443.08	0.35	13090.48	36974.12	0.37	13524.14
KÇ-3	106.35	2.50	2.57	25578.85	0.37	9364.03	32588.48	0.36	12021.35
KÇ-5	106.57	2.53	2.59	29829.57	0.34	11108.05	34128.93	0.35	12608.84
KÇ-7	106.66	2.52	2.57	32602.96	0.35	12090.97	34985.12	0.37	12809.26
KÇ-8	101.54	2.53	2.58	29727.04	0.39	10695.38	34261.63	0.38	12430.94
KÇ-27B	98.05	2.55	2.57	36929.85	0.40	13234.66	37085.87	0.39	13298.46
KÇ-28A	94.42	2.52	2.55	34497.26	0.40	12316.55	34757.38	0.39	12472.14
Ç-1	101.43	2.64	2.67	33925.69	0.38	12282.06	35953.04	0.38	12993.98
Ç-6	101.31	2.68	2.72	31181.89	0.35	11522.05	35015.89	0.37	12806.65
Ç-8	101.73	2.65	2.70	30984.36	0.34	11579.97	34569.01	0.36	12688.68
Ç-14	110.67	2.43	2.49	36254.58	0.35	13406.17	38027.27	0.37	13877.84
K-1	101.47	2.60	2.64	39644.56	0.40	14198.08	41882.19	0.40	14974.05
K-2	101.26	2.68	2.71	39704.30	0.39	14261.27	42502.17	0.39	15290.17
K-3	100.83	2.58	2.63	38198.90	0.39	13746.74	40854.69	0.39	14675.36
K-4	98.78	2.69	2.71	38949.32	0.39	14048.77	40539.21	0.39	14568.50
K-5	101.53	2.65	2.68	39905.95	0.39	14352.45	41768.24	0.39	15005.97
K-6	101.54	2.63	2.67	39150.42	0.38	14158.32	41485.53	0.39	14882.48
K-8A	99.09	2.49	2.56	26977.97	0.36	9941.36	29222.62	0.37	10697.63
K-9B	96.00	2.46	2.54	26924.42	0.38	9764.68	30201.79	0.36	11094.40
KKÇ-2	110.17	2.10	2.33	12829.84	0.23	5221.16	15441.82	0.23	6256.81
KKÇ-4	106.50	1.96	2.23	11957.29	0.21	4941.59	13034.34	0.19	5475.99
KKÇ-6	109.98	2.02	2.26	12839.57	0.18	5453.08	12977.04	0.18	5505.32
ÇK-2	101.57	2.64	2.67	25274.91	0.31	9651.88	31506.15	0.34	11728.44
ÇK-3	101.42	2.64	2.68	25964.10	0.33	9736.54	27250.88	0.38	9880.05

Table A5.4 continues

Sample	Length (mm)	ρ_{dry} (g/cm^3)	ρ_{sat} (g/cm^3)	$E_{i\text{-}dyn\text{-}dry}$ (MPa)	$\nu_{i\text{-}dyn\text{-}dry}$	$G_{i\text{-}dyn\text{-}dry}$ (MPa)	$E_{i\text{-}dyn\text{-}sat}$ (MPa)	$\nu_{i\text{-}dyn\text{-}sat}$	$G_{i\text{-}dyn\text{-}sat}$ (MPa)
ÇK-4	101.66	2.67	2.69	31339.05	0.35	11622.24	36060.27	0.37	13161.31
ÇK-6	101.66	2.69	2.71	32354.45	0.35	11960.24	36935.13	0.36	13532.71
ÇK-7	101.43	2.66	2.70	29037.16	0.35	10778.97	35351.00	0.36	12995.41
ÇK-12	101.82	2.68	2.71	29489.22	0.34	11029.43	35256.21	0.36	12985.88
ÇK-21	110.19	2.54	2.62	22199.98	0.24	8962.70	25417.95	0.31	9712.47
ÇK-22	109.91	2.50	2.59	19106.52	0.22	7820.53	21247.96	0.32	8071.75
ÇK-28	109.49	2.54	2.61	19054.90	0.25	7610.92	23029.42	0.31	8758.91
ÇK-35A	94.82	2.51	2.57	20805.42	0.35	7687.78	20659.43	0.36	7573.72
M-16	109.84	2.15	2.24	20818.83	0.28	8108.58	20360.69	0.26	8091.21
M-17	110.43	2.11	2.20	20565.60	0.28	8003.16	20224.45	0.26	8037.07
M-19	110.48	2.15	2.28	22313.34	0.31	8507.69	22381.70	0.30	8625.48
M-22	110.18	2.14	2.25	20515.45	0.28	8032.60	20294.09	0.26	8025.98
M-43	110.58	2.15	2.27	22626.53	0.30	8735.54	22967.11	0.29	8922.93

ρ_{dry}: Dry density; ρ_{sat}: Dry density; $E_{i\text{-}dyn\text{-}dry}$: Dynamic elastic modulus under dry conditions; $\nu_{i\text{-}dyn\text{-}dry}$: Dynamic Poisson's ratio under dry conditions; $G_{i\text{-}dyn\text{-}dry}$: Dynamic shear modulus under dry conditions; $E_{i\text{-}dyn\text{-}sat}$: Dynamic elastic modulus under saturated conditions; $\nu_{i\text{-}dyn\text{-}sat}$: Dynamic Poisson's ratio under saturated conditions; $G_{i\text{-}dyn\text{-}sat}$: Dynamic shear modulus under saturated conditions

Table A5.5 Brazilian test results of specimens

Sample	L/D	Failure load (kN)	Tensile Strength (σ_t) (MPa)
SK-8.1	0.54	19.543	8.08
SK-8.2	0.49	17.226	7.81
SK-9.1	0.54	23.943	9.74
SK-9.2	0.51	21.068	9.18
SK-12	0.51	24.27	10.57
SK-14.1	0.49	10.694	4.83
SK-14.2	0.52	20.074	8.59
KÇ-1.2	0.54	9.214	3.82
KÇ-1.3	1.05	4.437	0.95
KÇ-13	0.51	8.023	3.55
KÇ-15	0.50	6.924	3.11

Sample	L/D	Failure load (kN)	Tensile Strength (σ_t) (MPa)
KÇ-16	0.49	4.518	2.07
KÇ-18	0.49	6.964	3.15
KÇ-19	0.49	5.993	2.74
KÇ-20	0.49	3.916	1.79
KÇ-21	0.51	3.178	1.40
KÇ-24	0.53	4.097	1.72
KÇ-25	0.49	9.396	4.33
KÇ-26	0.51	7.258	3.17
BK-20	0.51	7.232	3.16
BK-21.1	0.59	3.175	1.22
BK-23.1	0.54	2.166	0.89

Table A5.5 continues

Sample	L/D	Failure load (kN)	Tensile Strength (σ_t) (MPa)
BK-23.2	0.57	4.802	1.85
BK-25	0.51	6.381	2.78
BK-26	0.51	5.696	2.49
BK-27	0.52	4.559	1.98
K-9A.1	0.53	2.792	1.16
K-9A.2	0.49	3.682	1.67
K-9A.3	0.51	4.703	2.03
K-11B.1	0.53	6.332	2.62
K-11B.2	0.55	5.332	2.14
K-11B.3	0.51	3.32	1.44
Ç-5.1	0.51	8.249	3.58
Ç-5.2	0.46	4.329	2.08
Ç-7.2	0.45	15.384	7.59
Ç-7.3	0.47	9.405	4.47
Ç-9	0.52	6.418	2.77
Ç-10	0.51	11.276	4.91
Ç-11	0.52	3.528	1.52
ÇK-15	0.52	18.266	7.92
ÇK-16	0.51	3.065	1.33
ÇK-17	0.52	1.851	0.80
ÇK-18	0.52	2.965	1.28
ÇK-19	0.51	9.866	4.36
ÇK-20	0.52	11.322	4.89
ÇK-32	0.50	8.298	3.72
ÇK-34B.2	0.53	1.97	0.82
ÇK-35B.1	0.56	4.391	1.72
ÇK-35B.3	0.55	3.516	1.42
KKÇ-7.1	0.52	2.888	1.24
KKÇ-7.2	0.52	0.839	0.36
KKÇ-8	0.52	1.54	0.67
KKÇ-9	0.51	2.55	1.11
KKÇ-10	0.51	2.718	1.19
KKÇ-11	0.52	1.396	0.61
M-12.1	0.49	6.163	2.78
M-13.1	0.53	10.385	4.34
M-25	0.52	8.172	3.51
M-26	0.52	6.988	3.02
M-27	0.52	0.912	0.40
M-28	0.53	5.394	2.26
M-29	0.51	3.199	1.39
M-43.1	0.47	2.979	1.40

Table A5.6 Point load test results of specimens

Sample	Type of test	L/D	Failure load (kN)	D_e^2 (mm^2)	Is (MPa)	F	$Is_{(50)}$ (MPa)
K-7A.1	2	0.88	4.489	3249.73	1.38	1.061	1.47
K-7A.2	2	0.82	3.362	3016.65	1.11	1.043	1.16
K-7B	1	1.82	4.105	9470.21	0.43	1.032	0.58
K-8A	1	1.17	5.530	3912.50	1.41	1.032	1.56
K-9B.1	2	0.56	2.301	2048.97	1.12	0.956	1.07
K-9B.2	2	0.58	0.746	2140.53	0.35	0.966	0.34
K-10A	2	0.54	5.885	2003.31	2.94	0.951	2.79
K-12	1	1.68	7.200	8112.24	0.89	1.031	1.16
BK-4.1	2	0.96	5.957	3478.23	1.71	1.077	1.84
BK-4.2	2	0.91	7.068	3333.76	2.12	1.067	2.26
BK-5.1	1	1.10	6.006	3452.74	1.74	1.031	1.87
BK-5.2	2	0.75	5.891	2729.01	2.16	1.020	2.20
BK-15	1	1.09	0.902	3379.97	0.27	1.030	0.29

Table A5.6 continues

Sample	Type of test	L/D	Failure load (kN)	D_e^2 (mm^2)	Is (MPa)	F	$Is_{(50)}$ (MPa)
BK-16	1	1.09	5.525	3405.01	1.62	1.029	1.74
BK-17	1	1.08	7.757	3327.56	2.33	1.030	2.49
BK-18	2	1.09	6.402	3969.07	1.61	1.110	1.79
BK-19	2	1.06	5.374	3841.76	1.40	1.101	1.54
BK-24	2	1.07	2.410	3853.84	0.63	1.102	0.69
SK-6	1	1.89	8.396	10230.31	0.82	1.031	1.13
SK-10	1	1.09	12.149	3382.59	3.59	1.031	3.84
SK-13	1	1.09	6.043	3389.28	1.78	1.031	1.91
SK-15	1	1.10	6.575	3435.13	1.91	1.031	2.06
SK-16	1	1.09	6.583	3372.12	1.95	1.031	2.09
SK-17	1	1.09	6.960	3401.81	2.05	1.031	2.19
SK-19	1	1.09	8.330	3398.89	2.45	1.031	2.63
KÇ-1.3	1	1.05	5.504	3101.38	1.77	1.029	1.86
KÇ-2.1	2	0.56	6.520	2024.28	3.22	0.954	3.07
KÇ-2.2	2	0.93	7.876	3363.33	2.34	1.069	2.50
KÇ-5.1	2	0.94	4.800	3407.22	1.41	1.072	1.51
KÇ-5.2	2	0.69	6.550	2526.32	2.59	1.002	2.60
KÇ-6.1	1	1.28	2.305	4670.36	0.49	1.029	0.57
KÇ-9	2	0.53	4.726	1899.36	2.49	0.940	2.34
KÇ-11	2	0.45	3.879	1629.42	2.38	0.908	2.16
KÇ-14	2	0.46	3.737	1678.70	2.23	0.914	2.04
KÇ-17	2	0.54	3.735	1944.60	1.92	0.945	1.82
KÇ-22	2	0.46	3.250	1675.61	1.94	0.914	1.77
M-6	1	1.08	1.586	3320.93	0.48	1.031	0.51
M-10	1	1.07	2.519	3268.98	0.77	1.030	0.82
M-11	1	1.08	3.312	3303.38	1.00	1.030	1.07
M-34	1	1.07	3.289	3284.15	1.00	1.030	1.06
M-36	1	1.08	2.143	3339.68	0.64	1.030	0.68
M-37	1	1.09	3.917	3365.74	1.16	1.029	1.24
M-38	1	1.08	6.530	3350.09	1.95	1.031	2.08
M-40	1	1.09	4.180	3366.90	1.24	1.031	1.33
M-41	1	1.06	4.716	3183.78	1.48	1.028	1.56
Ç-4.1	2	0.98	4.244	3546.15	1.20	1.082	1.29
Ç-4.2	2	0.43	2.344	1572.59	1.49	0.901	1.34
Ç-5.3	2	0.42	3.595	1533.15	2.34	0.896	2.10
Ç-5.4	2	0.43	4.318	1553.30	2.78	0.898	2.50
Ç-7.1	2	0.42	1.744	1544.74	1.13	0.897	1.01
Ç-7.4	2	0.35	1.016	1272.79	0.80	0.859	0.69

Table A5.6 continues

Sample	Type of test	L/D	Failure load (kN)	D_e^2 (mm^2)	Is (MPa)	F	$Is_{(50)}$ (MPa)
Ç-15	1	1.08	4.695	3292.46	1.43	1.029	1.52
Ç-16	1	1.07	5.584	3246.72	1.72	1.029	1.82
Ç-17	1	1.07	4.293	3269.27	1.31	1.030	1.39
Ç-18	1	1.08	1.229	3308.55	0.37	1.030	0.40
ÇK-24	1	2.08	1.795	12262.24	0.15	1.029	0.21
ÇK-25.1	1	1.02	0.581	3030.50	0.19	1.033	0.20
ÇK-25.2	1	1.01	1.712	2924.65	0.59	1.030	0.61
ÇK-29	1	1.08	2.692	3303.95	0.81	1.030	0.87
ÇK-30	1	1.08	1.263	3345.18	0.38	1.030	0.40
ÇK-31	1	1.08	1.207	3330.73	0.36	1.030	0.39
ÇK-33A.1	2	0.85	1.793	3173.02	0.57	1.055	0.60
ÇK-33A.2	2	0.88	0.341	3209.96	0.11	1.058	0.11
ÇK-33B	1	1.35	6.804	5257.70	1.29	1.034	1.53
ÇK-34A.1	2	0.90	1.465	3304.29	0.44	1.065	0.47
ÇK-34A.2	2	0.82	3.026	2991.16	1.01	1.041	1.05
ÇK-34B.1	2	0.83	2.465	3041.70	0.81	1.045	0.85

L/D: Length to diameter ratio; D_e: Equivalent core diameter; Is: Point load index; F: Correction factor; $Is_{(50)}$: Corrected point load index; 1: Diametral test; 2: Axial test

Table A5.7 Static uniaxial compressive test results of dry specimens

Dry Sample	L/D	Loading Conditions	σ_c (MPa)	Corrected σ_c (σ_{ci}) (MPa)	E_{avg} (MPa)	E_{sec} (MPa)	ν_i
BK-1	1.89	[a]1.2	28.56	28.37			
BK-7	1.90	[a]1.2	55.20	54.87			
BK-12	1.89	[a]1.2	52.04	51.67			
BK-6	1.90	[b]10^{-5}	34.78	34.56	7119.32	5144.97	
BK-11	1.90	[b]10^{-5}	51.63	51.31	10719.07	5776.28	
KKÇ-2	1.74	[b]10^{-5}	22.09	21.70	1726.56	2073.17	
KKÇ-6	2.06	[a]1.2	24.80	24.80			
K-4	1.85	[a]1.2	147.95	146.56			
K11A	1.76	[a]1.2	19.50	19.18			
K-2	1.90	[b]10^{-5}	107.28	106.62	10945.86	7859.24	
K-6	1.90	[b]10^{-5}	105.49	104.82	11299.67	7116.22	
K-13	1.90	[c]0.05	33.70	33.49	6710.55	9504.14	0.28
M-15	2.06	[a]1.2	49.91	49.91			
M-16	2.05	[b]10^{-5}	51.80	51.80	4795.11	3226.25	
M-17	2.06	[b]10^{-5}	80.69	80.69	5207.3	4017	
M-49	2.17	[c]0.05	55.44	55.44	5711.34	6059.9	0.34
SK-5	1.89	[a]1.2	105.37	104.63			

Table A5.7 continues

Dry Sample	L/D	Loading Conditions	σ_c (MPa)	Corrected σ_c (σ_{ci}) (MPa)	E_{avg} (MPa)	E_{sec} (MPa)	ν_i
SK-1	1.90	[b]10^{-5}	81.35	80.82	8410	5422.67	
SK-3	1.90	[b]10^{-5}	117.78	117.02	14561.67	8114.79	
Ç-2	1.90	[a]1.2	20.58	20.45			
Ç-13	2.09	[a]1.2	32.26	32.26			
Ç-1	1.90	[b]10^{-5}	42.05	41.78	5446.43	3835.77	
Ç-12	2.07	[b]10^{-5}	19.26	19.34	4776.83	2280.95	
KÇ-28A	1.70	[b]10^{-5}	79.77	78.11	14025.24	13333.33	
KÇ-28B	1.82	[a]1.2	81.34	80.37			
KÇ-27A	1.75	[a]1.2	28.96	28.47			
KÇ-3	2.00	[b]10^{-5}	46.06	46.06	8154	4767.63	
KÇ-7	2.00	[b]10^{-5}	52.53	52.53	7964.4	5568.66	
ÇK-1	1.88	[a]1.2	45.53	45.18			
ÇK-7	1.90	[a]1.2	72.89	72.45			
ÇK-8	1.90	[a]1.2	73.70	73.24			
ÇK-10	1.90	[a]1.2	104.58	103.92			
ÇK-11	1.90	[a]1.2	52.88	52.54			
ÇK-13	1.90	[a]1.2	22.51	22.37			
ÇK-22	2.06	[a]1.2	20.80	20.80			
ÇK-26	2.07	[a]1.2	26.89	26.89			
ÇK-2	1.90	[b]10^{-5}	59.85	59.48	6640	3707.5	
ÇK-21	2.07	[b]10^{-5}	58.23	58.23	4985.77	3914.98	
ÇK-27	2.06	[b]10^{-5}	29.90	29.90	3409.09	2205.88	

Table A5.8 Static uniaxial compressive test results of fully water saturated specimens

Saturated Sample	L/D	Loading Conditions	σ_c (MPa)	Corrected σ_c (σ_{ci}) (MPa)	E_{avg} (MPa)	E_{sec} (MPa)	ν_i
BK-3	1.90	[a]1.2	52.92	52.60			
BK-9	1.76	[a]1.2	46.17	45.42			
BK-10	1.91	[a]1.2	30.73	30.55			
BK-13	1.75	[a]1.2	51.57	50.69			
BK-22	2.08	[a]1.2	15.02	15.09			
BK-2	1.89	[b]10^{-5}	25.03	24.86	5125.9	2431.07	
BK-8	1.90	[b]10^{-5}	44.73	44.45	8356.154	3182.86	
KKÇ-4	1.78	[b]10^{-5}	10.19	10.04	2036	1913.53	
K-3	1.90	[b]10^{-5}	75.01	74.52	10593.22	7374.63	
K-5	1.72	[a]1.2	107.41	105.37			
K-1	1.90	[b]10^{-5}	36.21	35.98	4273.6		

Table A5.8 continues

Saturated Sample	L/D	Loading Conditions	σ_c (MPa)	Corrected σ_c (σ_{ci}) (MPa)	E_{avg} (MPa)	E_{sec} (MPa)	ν_i
K-8B	1.75	[b]10^{-5}	31.17	30.65	4455.96		
K-16	2.17	[c]0.05	10.28	10.28	591.48	369	0.44
M-18	2.07	[b]10^{-5}	37.21	37.21	3480.29	3101.67	
M-22	2.06	[b]10^{-5}	50.36	50.36	4535.6	4006.4	
SK-7	1.89	[a]1.2	134.66	133.73			
SK-2	1.88	[b]10^{-5}	48.11	47.75	3590	3745.31	
SK-4	1.89	[b]10^{-5}	98.66	97.97	13754.5	7762.2	
Ç-6	1.90	[a]1.2	34.59	34.38			
Ç-8	1.90	[b]10^{-5}	21.81	21.68	4231.7		
Ç-14	2.07	[b]10^{-5}	24.55	24.55	4883.5		
KÇ-27B	1.80	[b]10^{-5}	64.92	64.07	13638.65	13195.22	
KÇ-4	2.00	[b]10^{-5}	35.71	35.71	4845.2	3238.18	
KÇ-8	1.90	[b]10^{-5}	51.41	51.09	7783.75	7005.48	
ÇK-5	1.90	[a]1.2	63.03	62.64			
ÇK-6	1.90	[a]1.2	95.20	94.61			
ÇK-9	1.90	[a]1.2	54.87	54.53			
ÇK-12	1.71	[a]1.2	70.35	68.95			
ÇK-14	1.90	[a]1.2	6.17	6.13			
ÇK-23	2.07	[a]1.2	6.86	6.89			
ÇK-4	1.90	[b]10^{-5}	44.48	44.21	5984.75	3258.48	
ÇK-28	2.05	[b]10^{-5}	10.82	10.82	1180.18	731.57	
ÇK-35A	1.78	[b]10^{-5}	20.38	20.08	2045.29	1700.2	

Table A5.9 Cyclic uniaxial compressive test results of specimens

Sample	L/D	Loading Conditions	$\sigma_{c\text{-}dyn}$ (MPa)	Corrected σ_c ($\sigma_{ci\text{-}dyn}$) (MPa)	E_{avg} (MPa)	E_{sec} (MPa)	ν_{dyn}	$E_{avg\text{-}dyn}$ (MPa)
K-15	1.92	[c]0.005- 0.20	48.60	48.35	8000	8553.25	0.41	12685.71
K-17	2.13	[c]0.005- 0.20	36.56	36.56	4345.67	4444.44	0.48	16000
M-46	2.15	0.005- 0.20	102.43	102.43	20000	19915	0.35	26281
M-50	2.12	[c]0.005- 0.20	41.84	41.84	30066.11	28206.84	0.30	36787.29
M-45 (saturated)	2.13	[c]0.005- 0.20	66.27	66.27	10645	10000	0.48	26838.71

[a] Loading rate (kN/s); [b] Strain rate (s^{-1}); [c] Deformation rate (mm/min); σ_{ci}: Uniaxial compressive strength of intact rock; L/D: Length to diameter ratio; E_{avg}: Average elastic modulus; E_{sec}: Secant elastic modulus; ν_i : Poisson's ratio; $E_{avg\text{-}dyn}$: Average elastic modulus under dynamic conditions; ν_{dyn}: Poisson's ratio under dynamic conditions

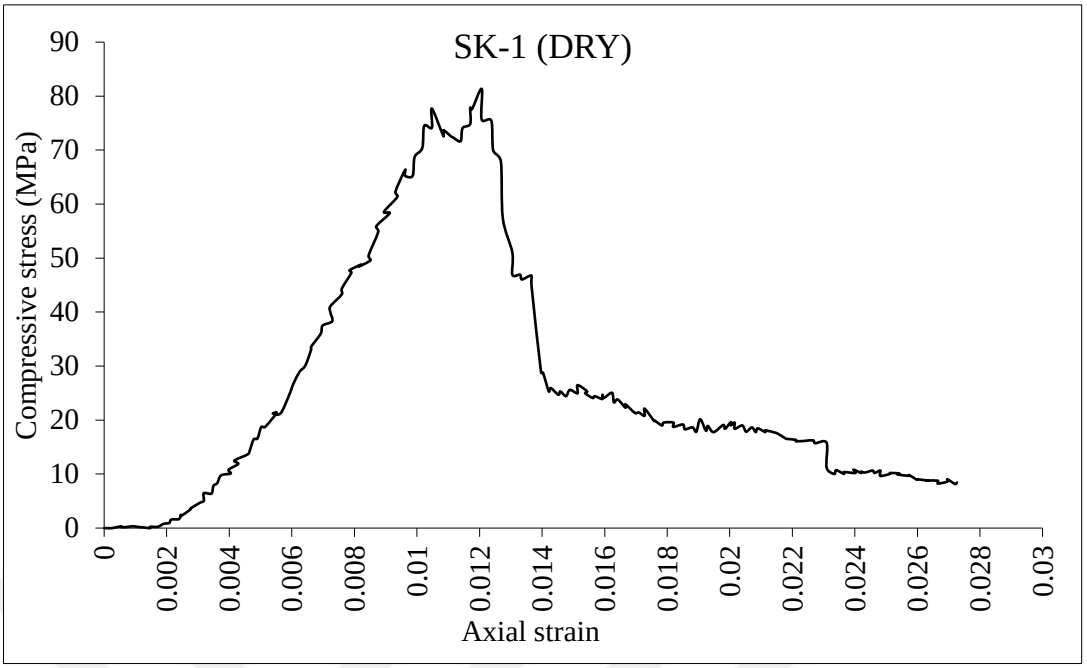


Figure A5.1 The stress-strain graph of SK-1 subjected to static uniaxial compressive strength test

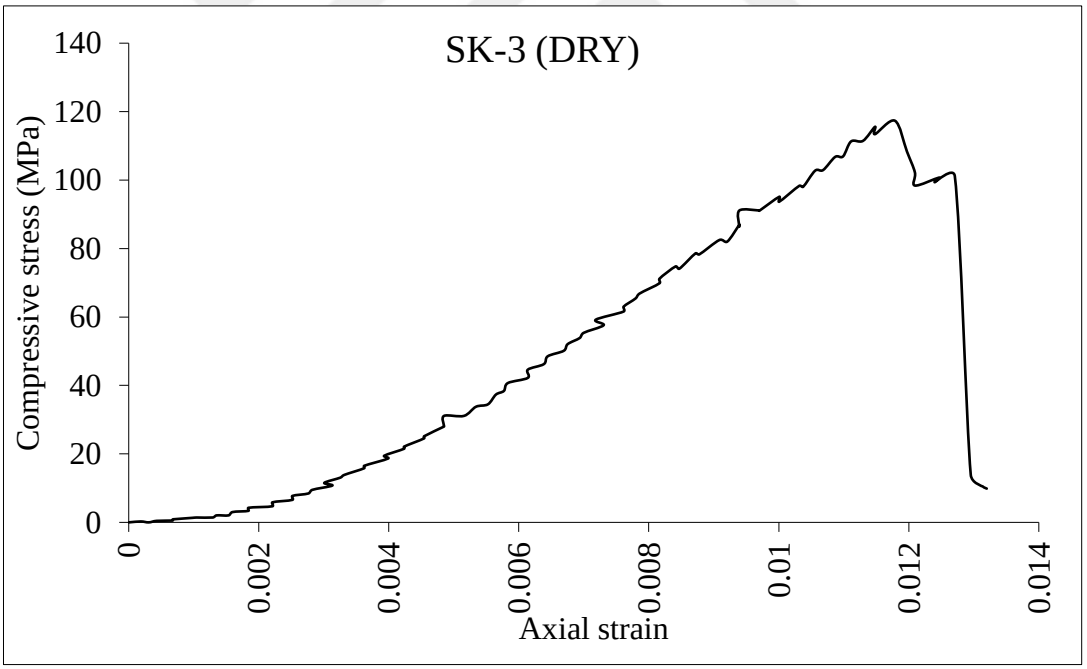


Figure A5.2 The stress-strain graph of SK-3 subjected to static uniaxial compressive strength test

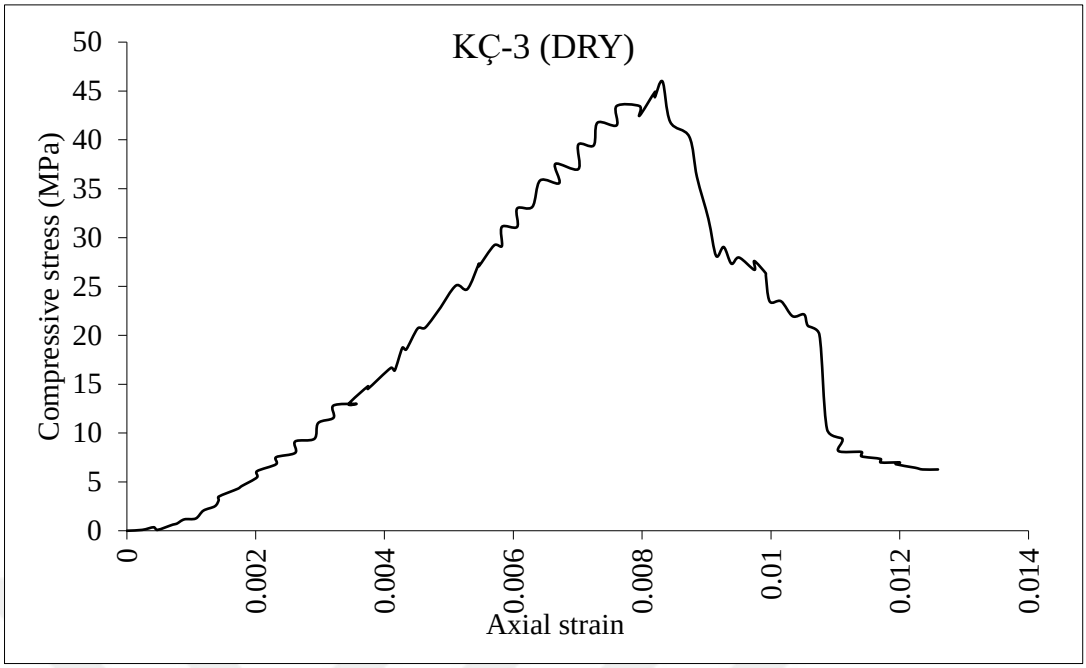


Figure A5.3 The stress-strain graph of KÇ-3 subjected to static uniaxial compressive strength test

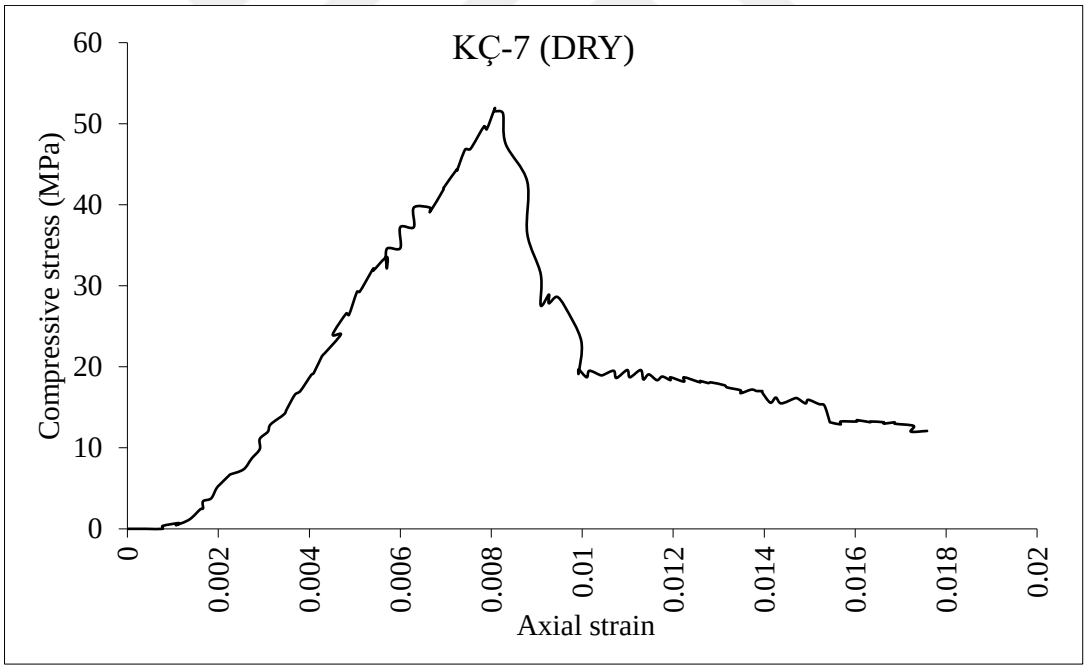


Figure A5.4 The stress-strain graph of KÇ-7 subjected to static uniaxial compressive strength test

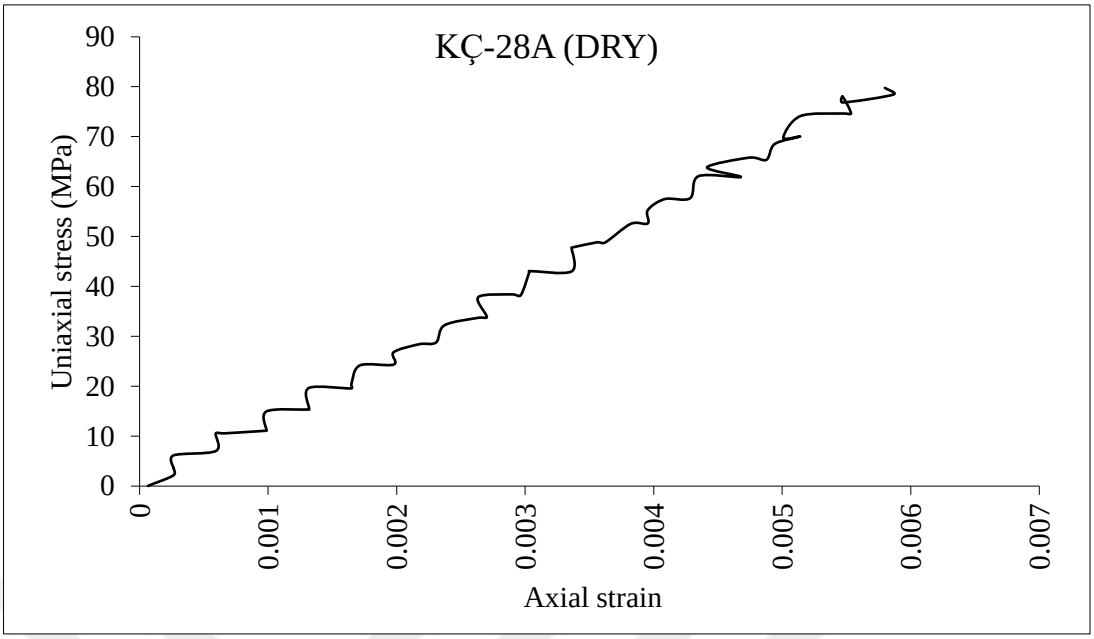


Figure A5.5 The stress-strain graph of KÇ-28A subjected to static uniaxial compressive strength test

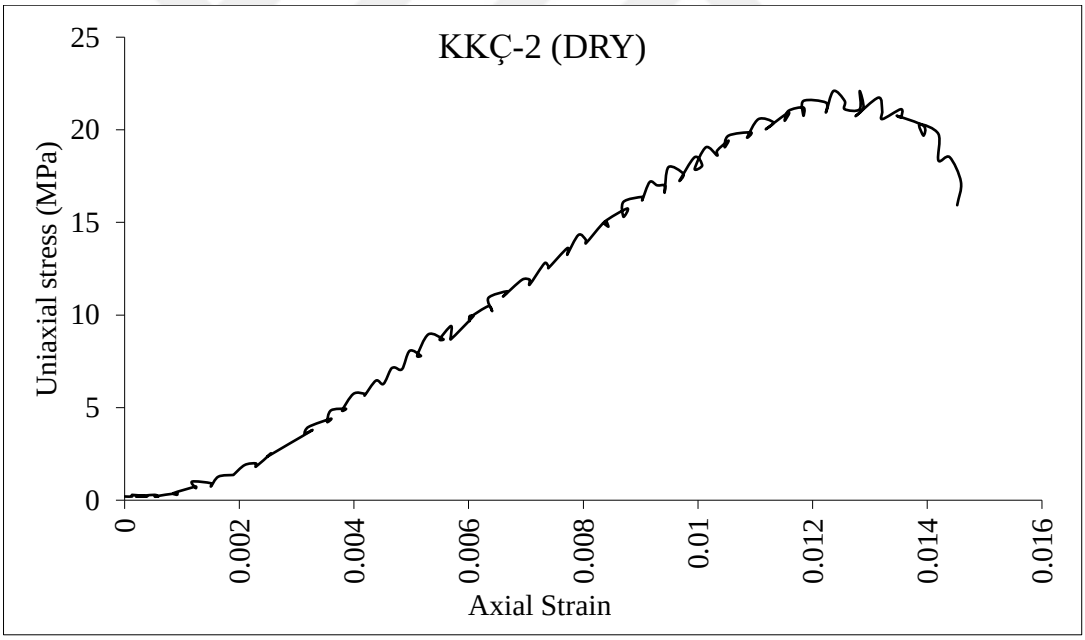


Figure A5.6 The stress-strain graph of KKÇ-2 subjected to static uniaxial compressive strength test

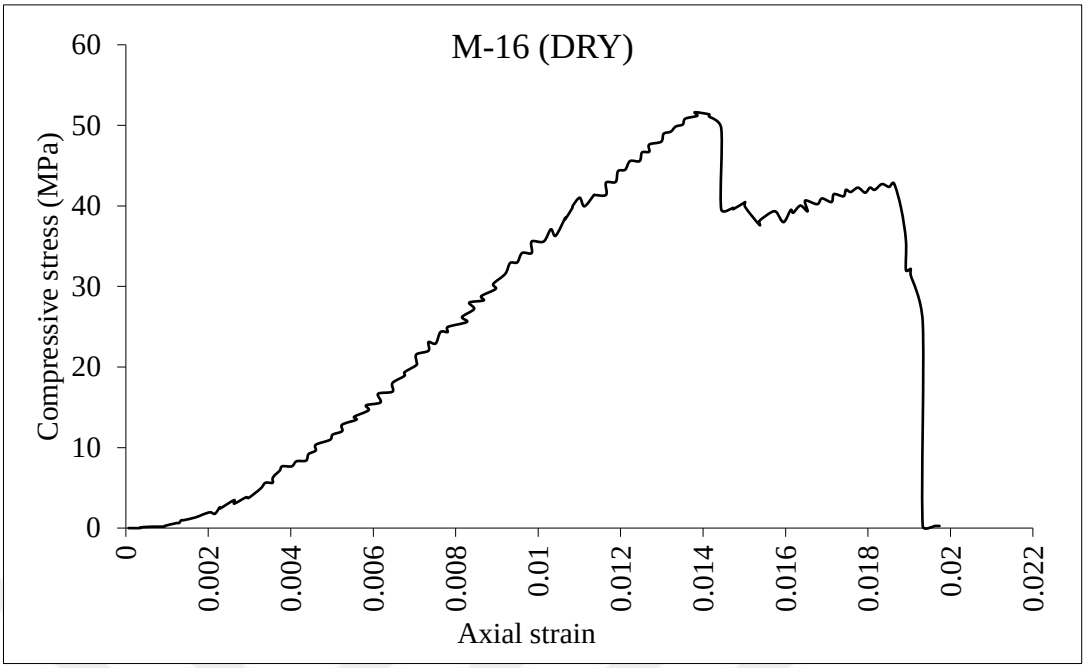


Figure A5.7 The stress-strain graph of M-16 subjected to static uniaxial compressive strength test

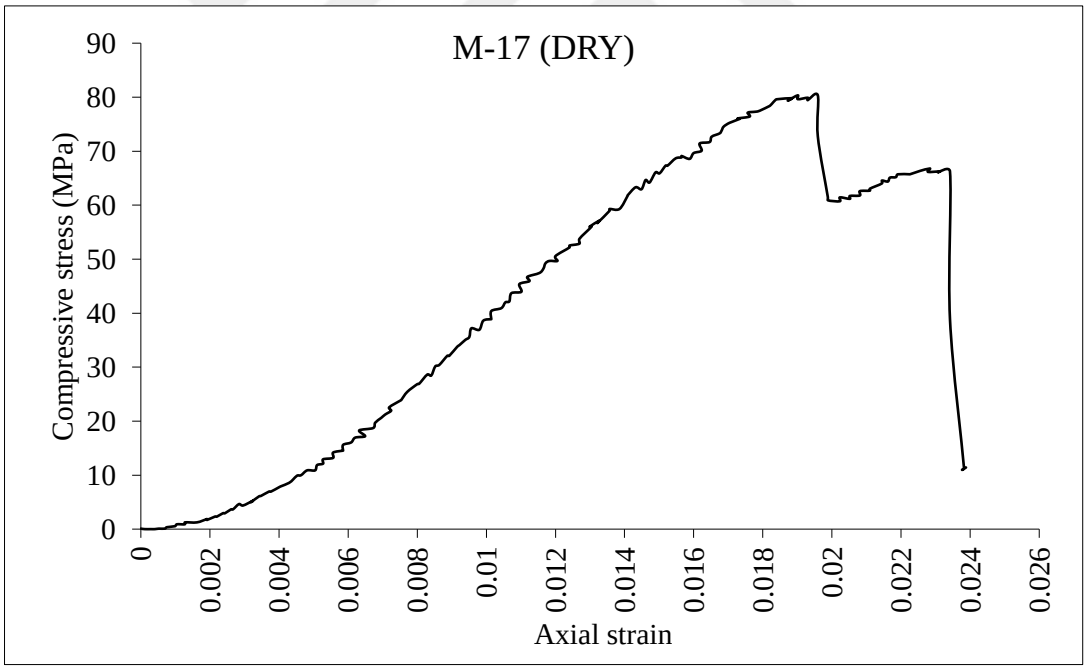


Figure A5.8 The stress-strain graph of M-17 subjected to static uniaxial compressive strength test

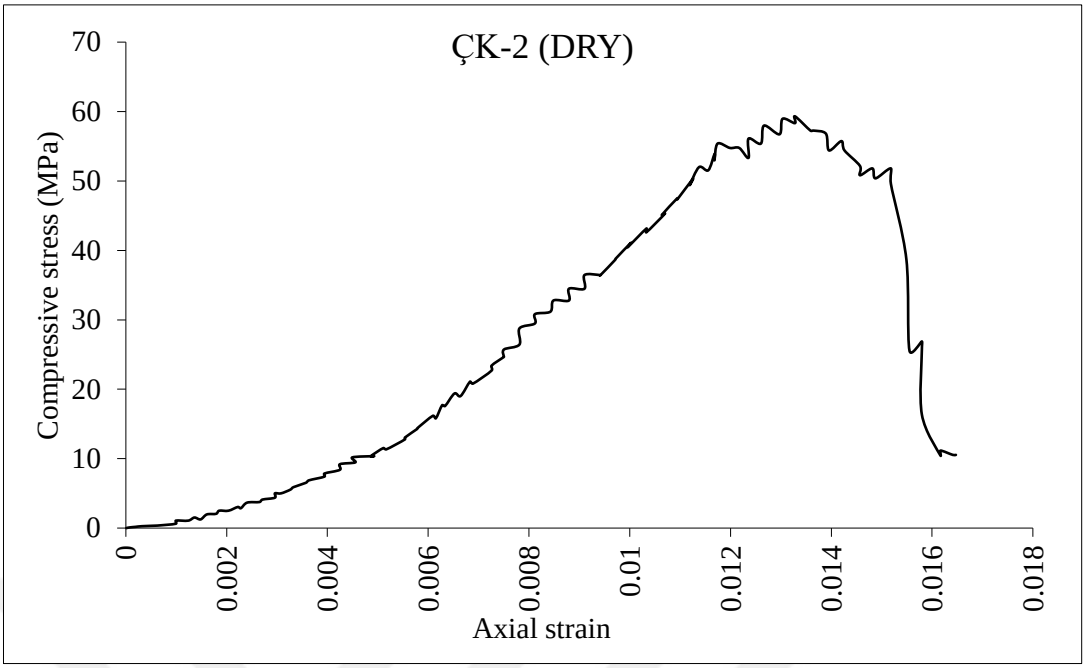


Figure A5.9 The stress-strain graph of ÇK-2 subjected to static uniaxial compressive strength test

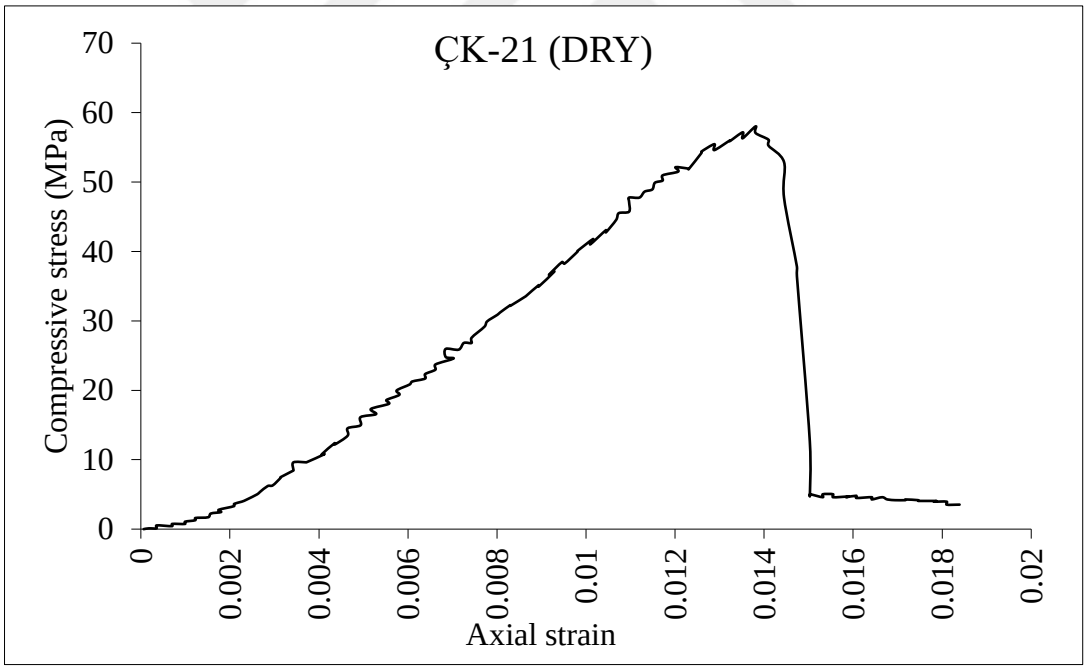


Figure A5.10 The stress-strain graph of ÇK-21 subjected to static uniaxial compressive strength test

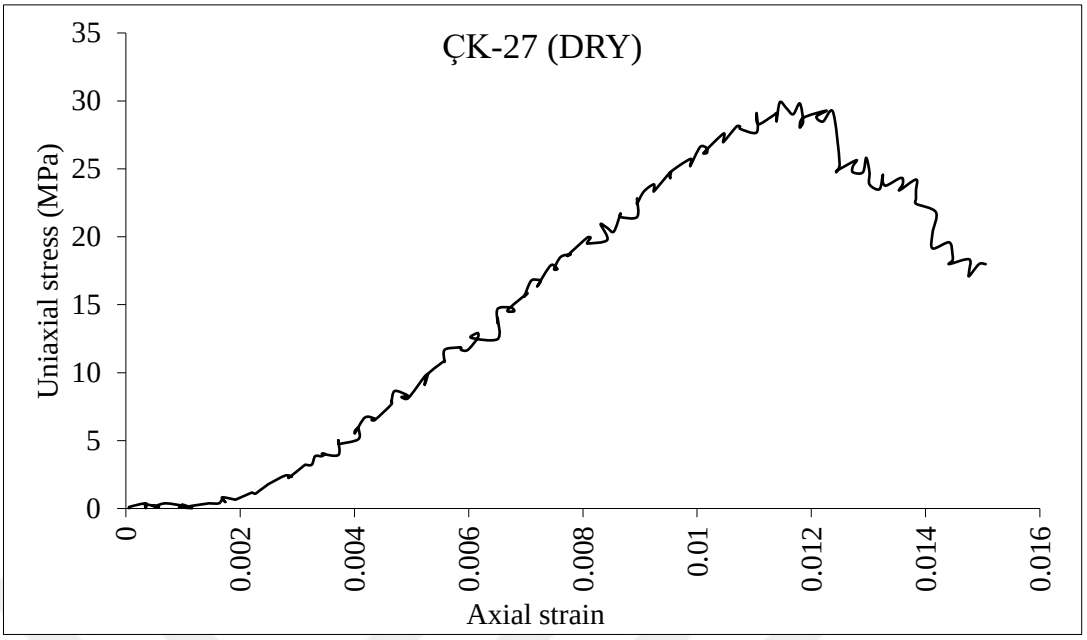


Figure A5.11 The stress-strain graph of ÇK-27 subjected to static uniaxial compressive strength test

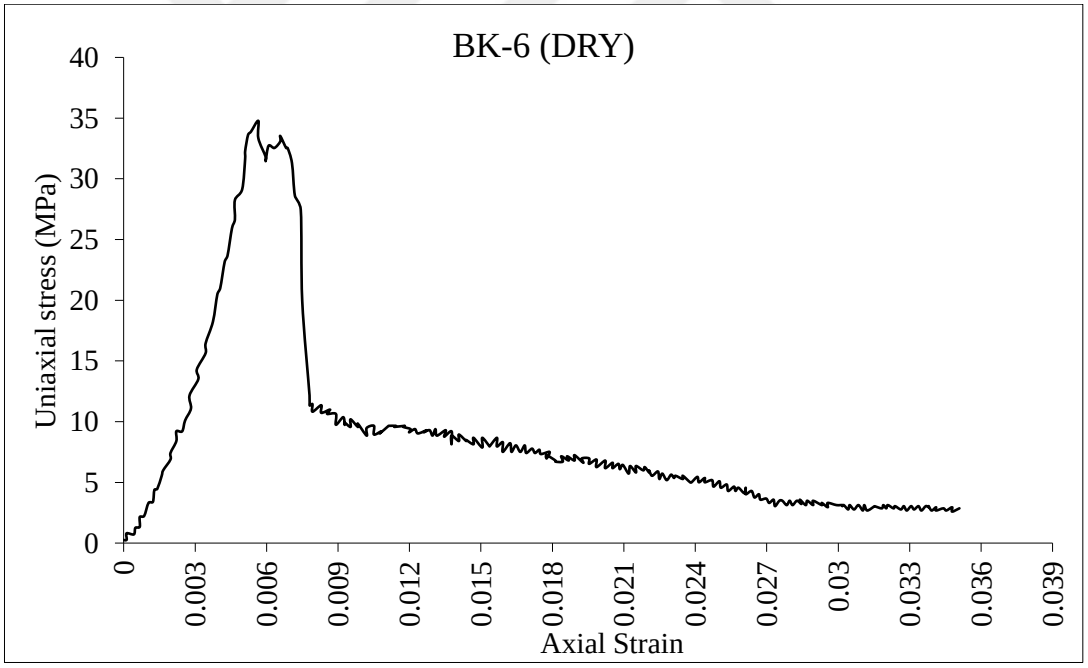


Figure A5.12 The stress-strain graph of BK-6 subjected to static uniaxial compressive strength test

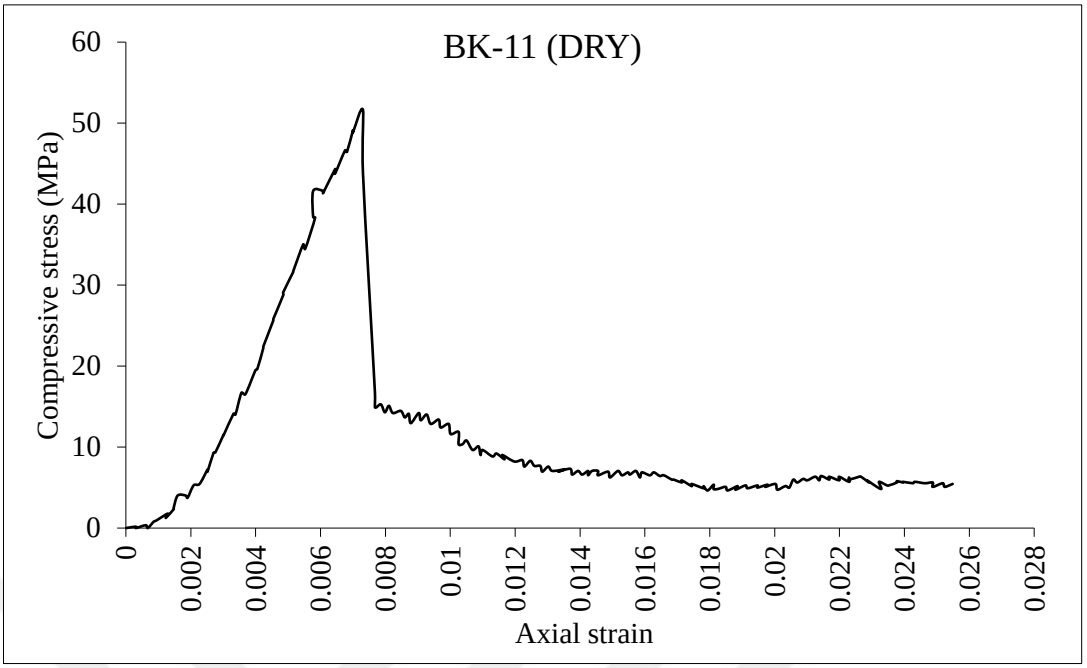


Figure A5.13 The stress-strain graph of BK-11 subjected to static uniaxial compressive strength test

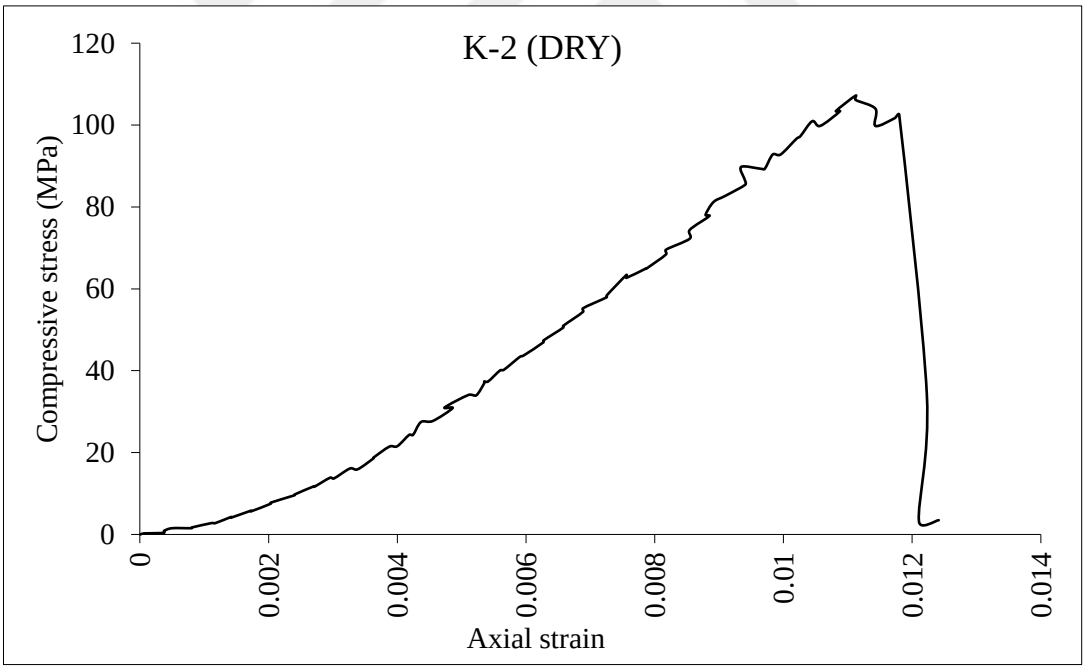


Figure A5.14 The stress-strain graph of K-2 subjected to static uniaxial compressive strength test

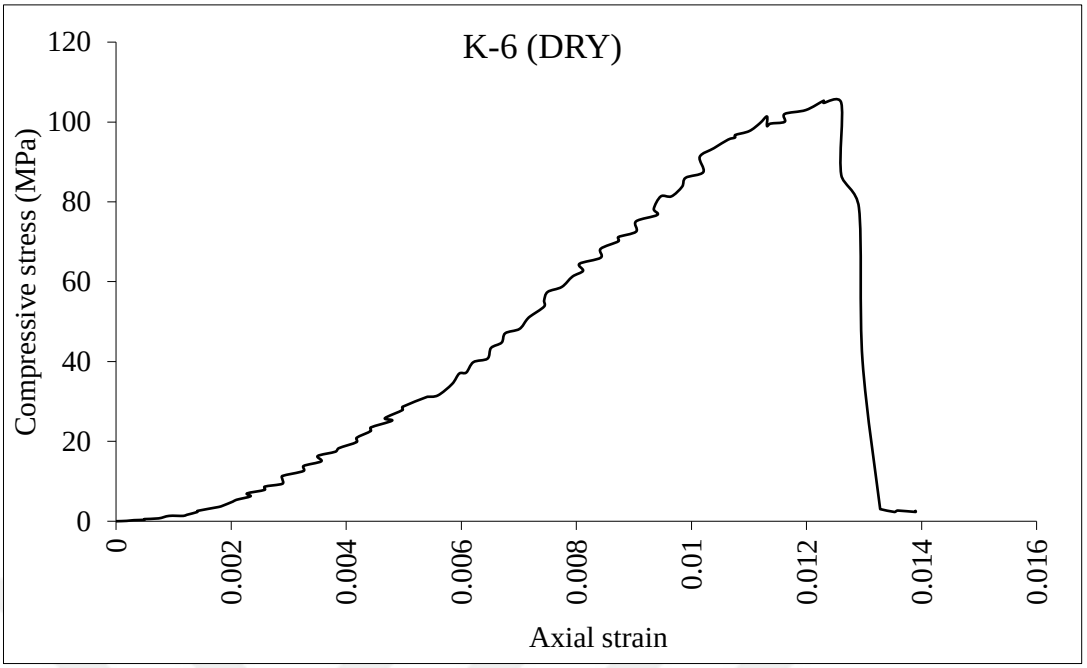


Figure A5.15 The stress-strain graph of K-6 subjected to static uniaxial compressive strength test

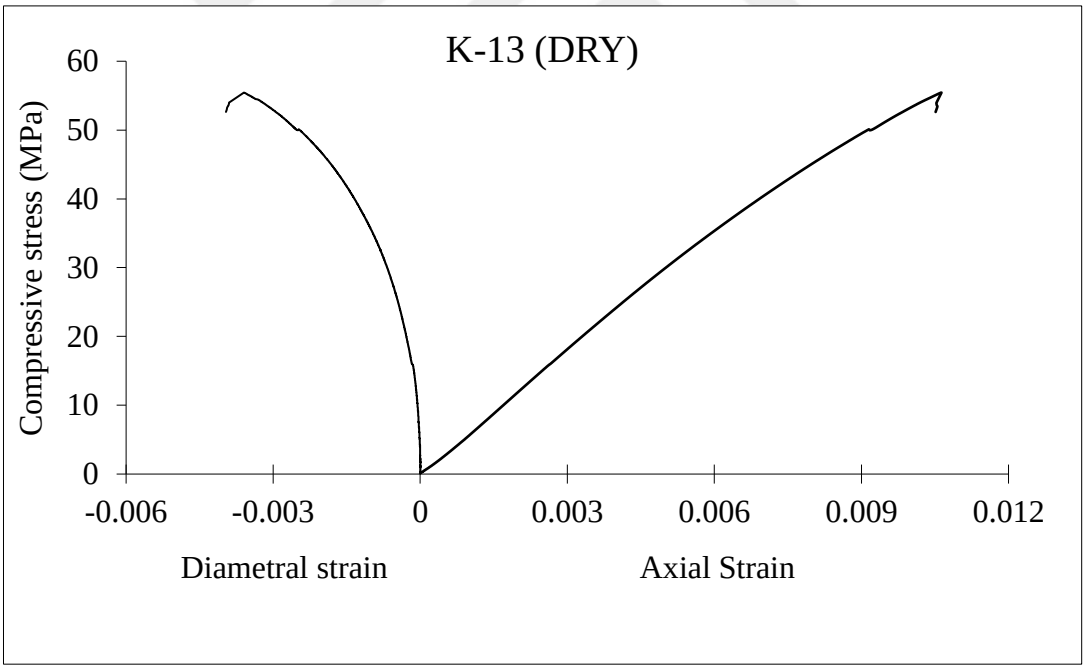


Figure A5.16 The stress-strain graph of K-13 subjected to static uniaxial compressive strength test

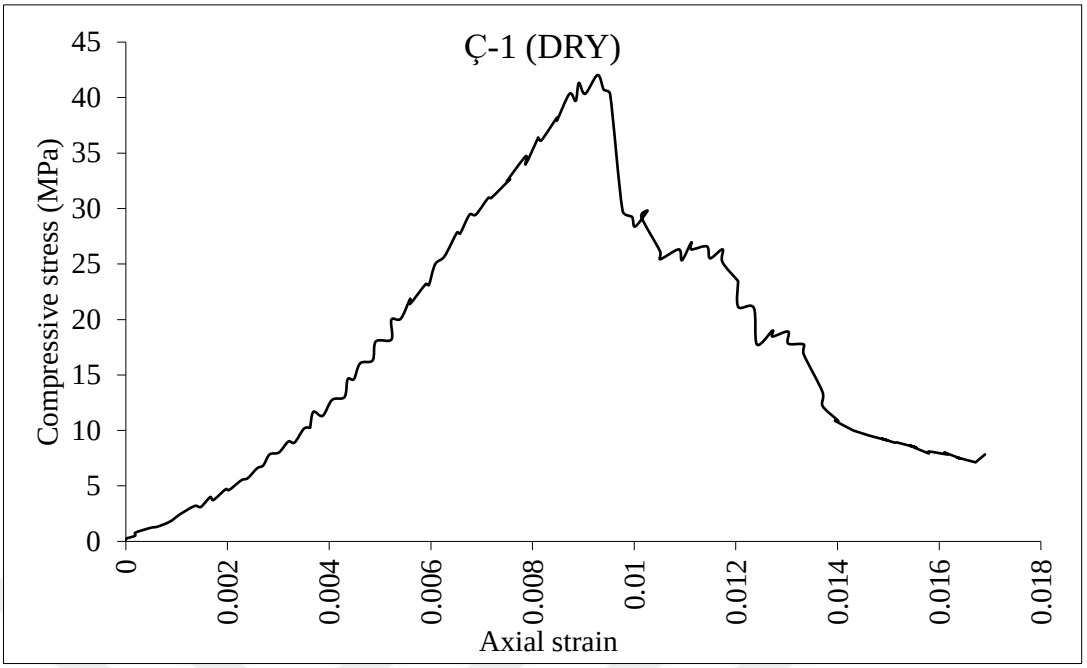


Figure A5.17 The stress-strain graph of Ç-1 subjected to static uniaxial compressive strength test

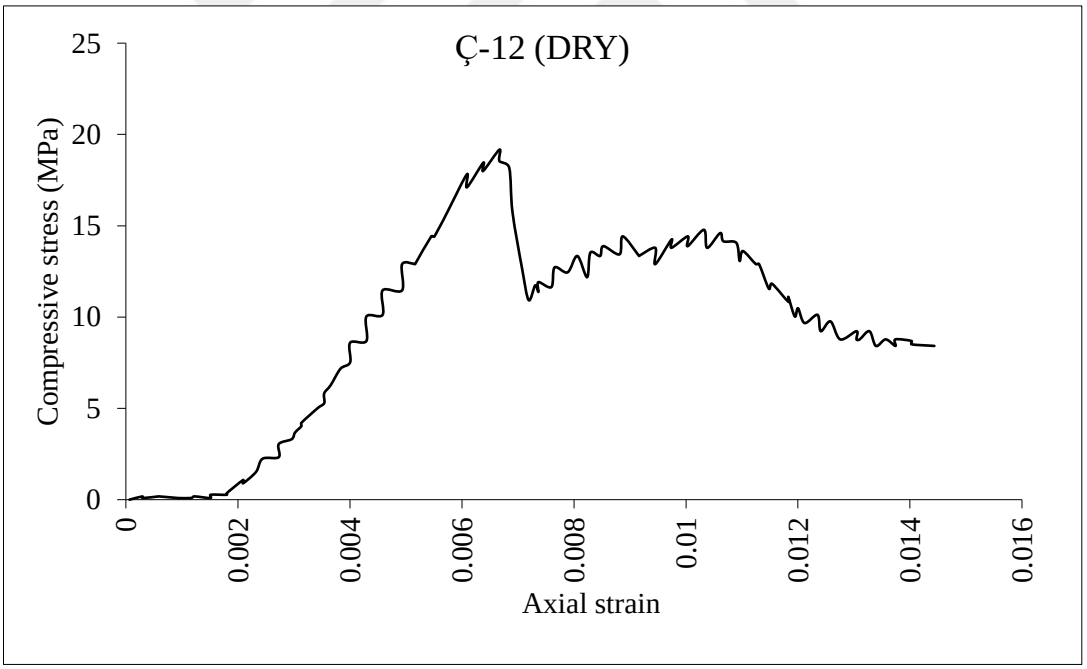


Figure A5.18 The stress-strain graph of Ç-12 subjected to static uniaxial compressive strength test

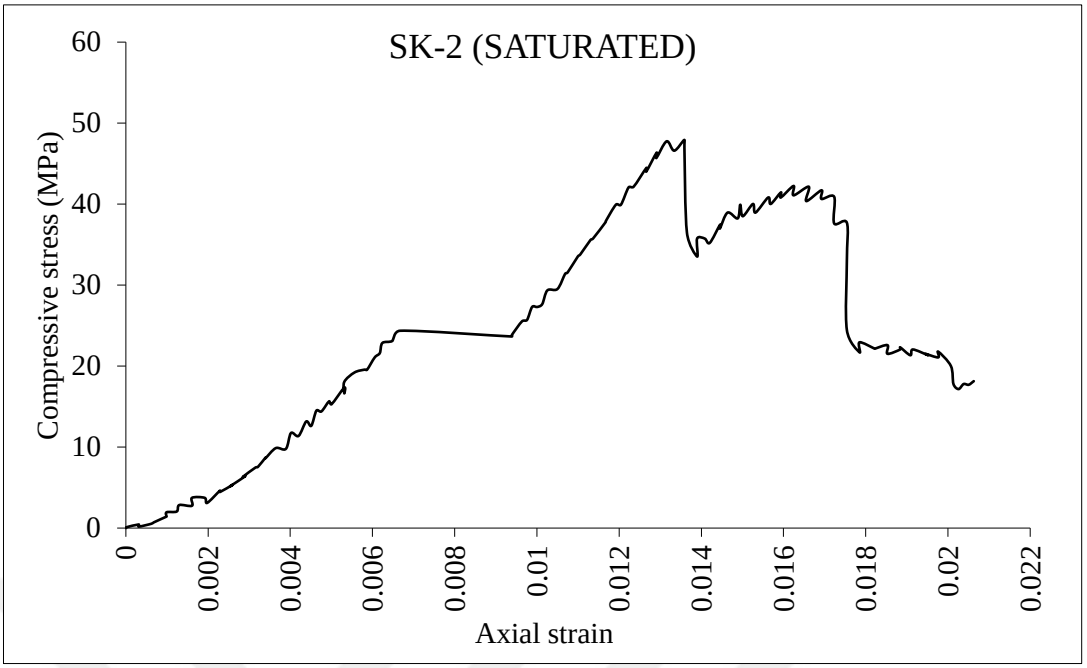


Figure A5.19 The stress-strain graph of SK-2 subjected to static uniaxial compressive strength test

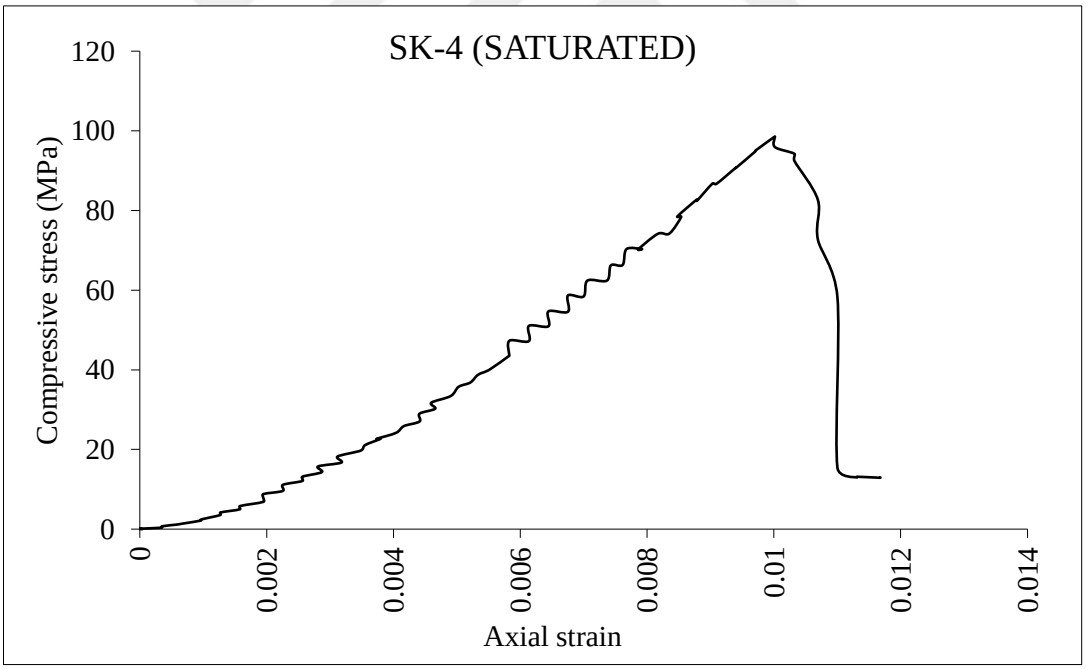


Figure A5.20 The stress-strain graph of SK-4 subjected to static uniaxial compressive strength test

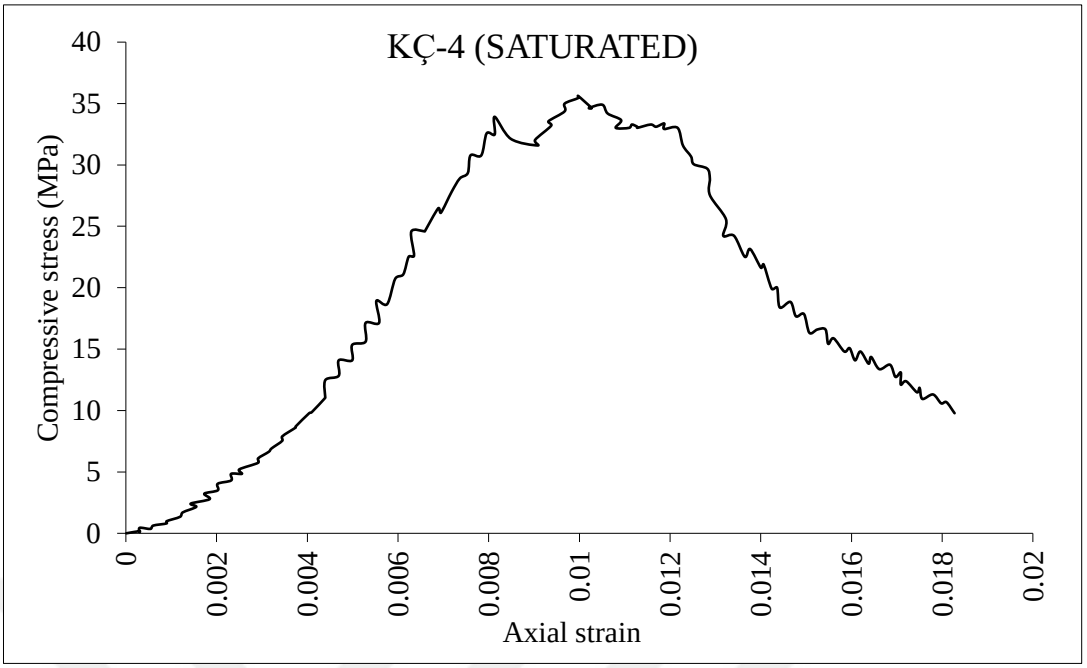


Figure A5.21 The stress-strain graph of KÇ-4 subjected to static uniaxial compressive strength test

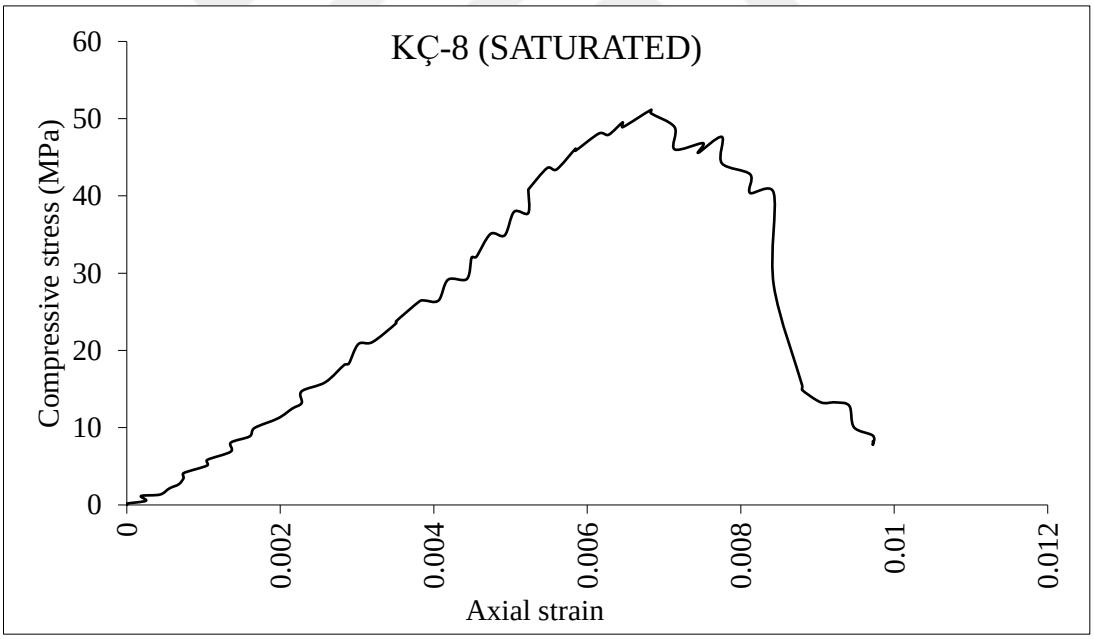


Figure A5.22 The stress-strain graph of KÇ-8 subjected to static uniaxial compressive strength test

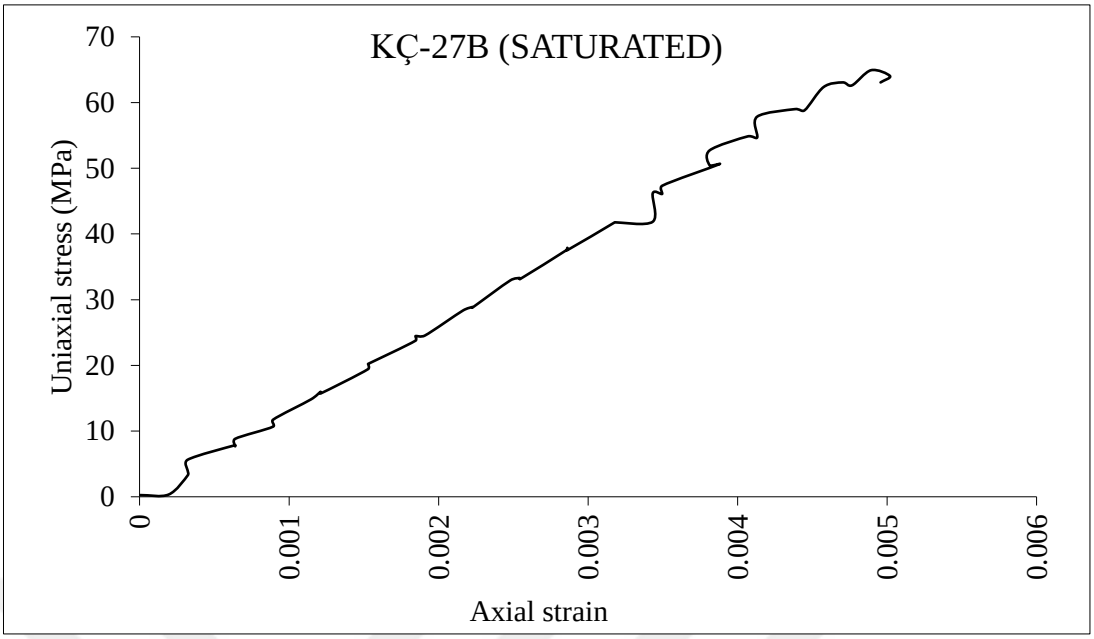


Figure A5.23 The stress-strain graph of KÇ-27B subjected to static uniaxial compressive strength test

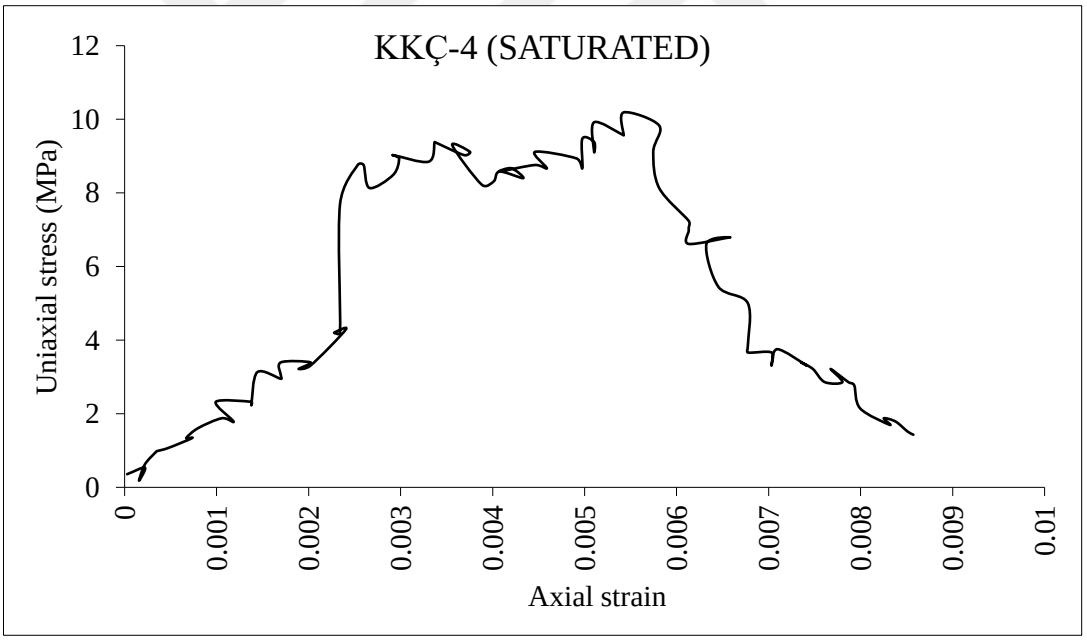


Figure A5.24 The stress-strain graph of KKÇ-4 subjected to static uniaxial compressive strength test

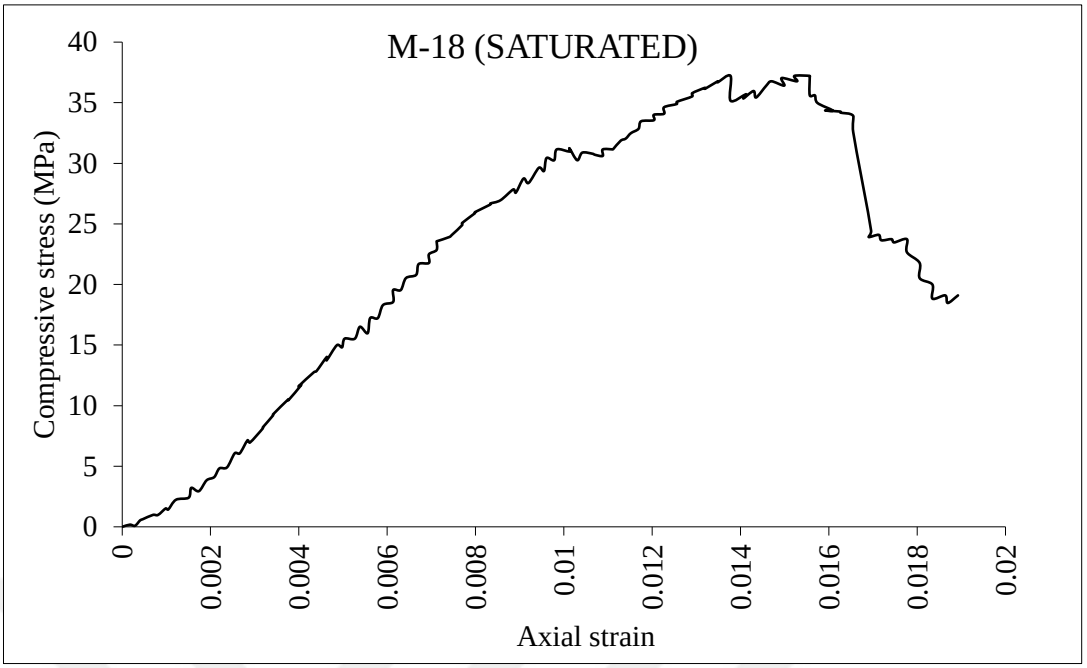


Figure A5.25 The stress-strain graph of M-18 subjected to static uniaxial compressive strength test

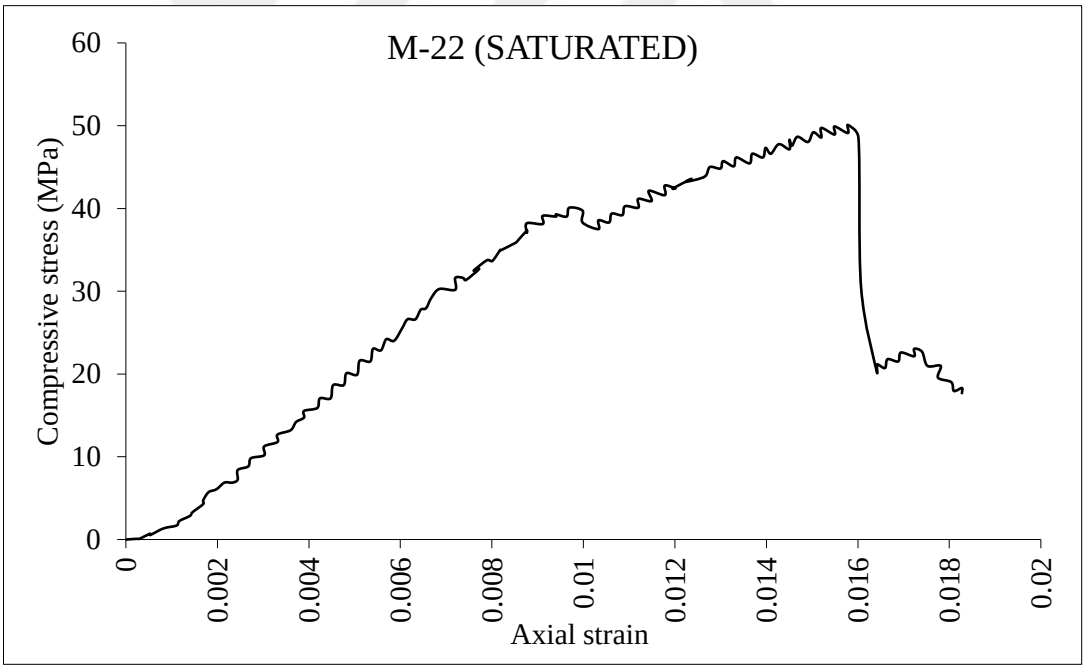


Figure A5.26 The stress-strain graph of M-22 subjected to static uniaxial compressive strength test

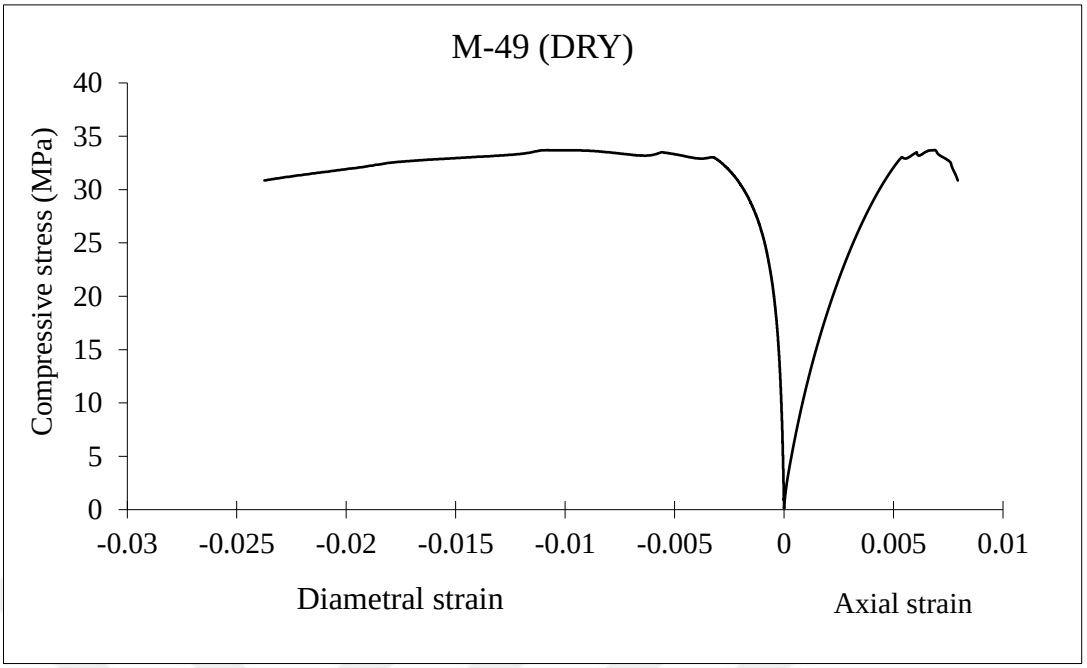


Figure A5.27 The stress-strain graph of M-49 subjected to static uniaxial compressive strength test

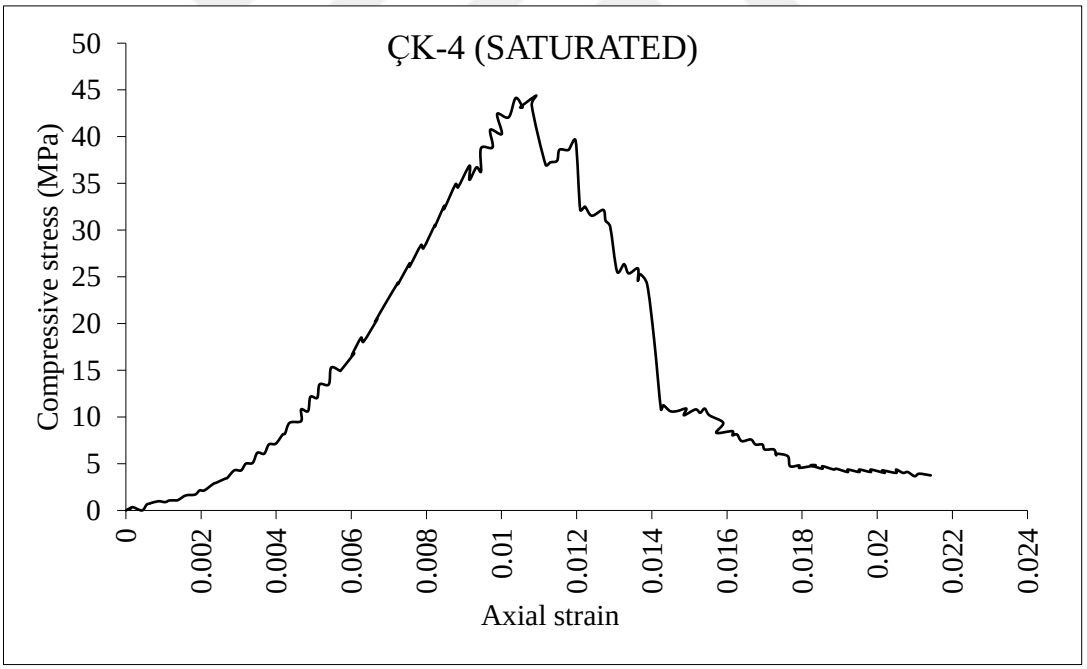


Figure A5.28 The stress-strain graph of ÇK-4 subjected to static uniaxial compressive strength test

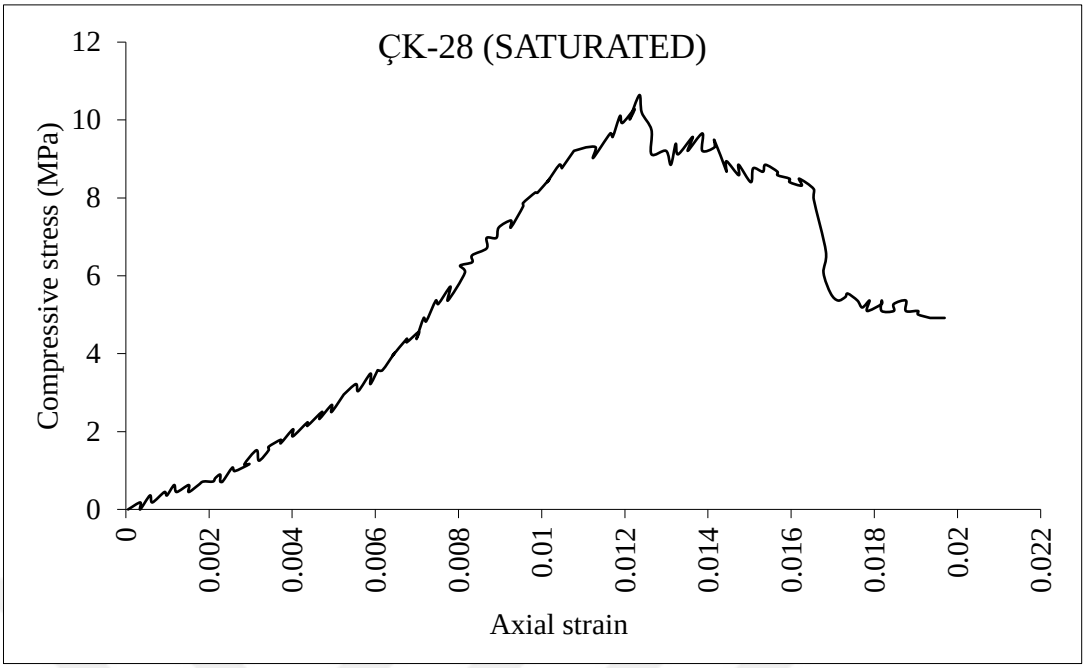


Figure A5.29 The stress-strain graph of ÇK-28 subjected to static uniaxial compressive strength test

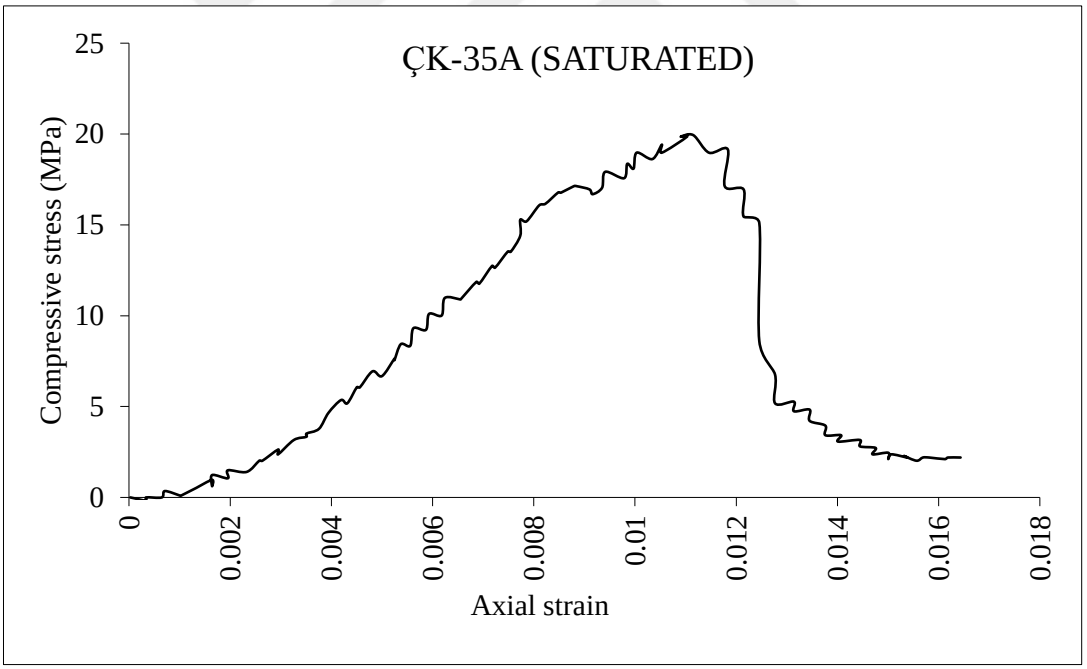


Figure A5.30 The stress-strain graph of ÇK-35A subjected to static uniaxial compressive strength test

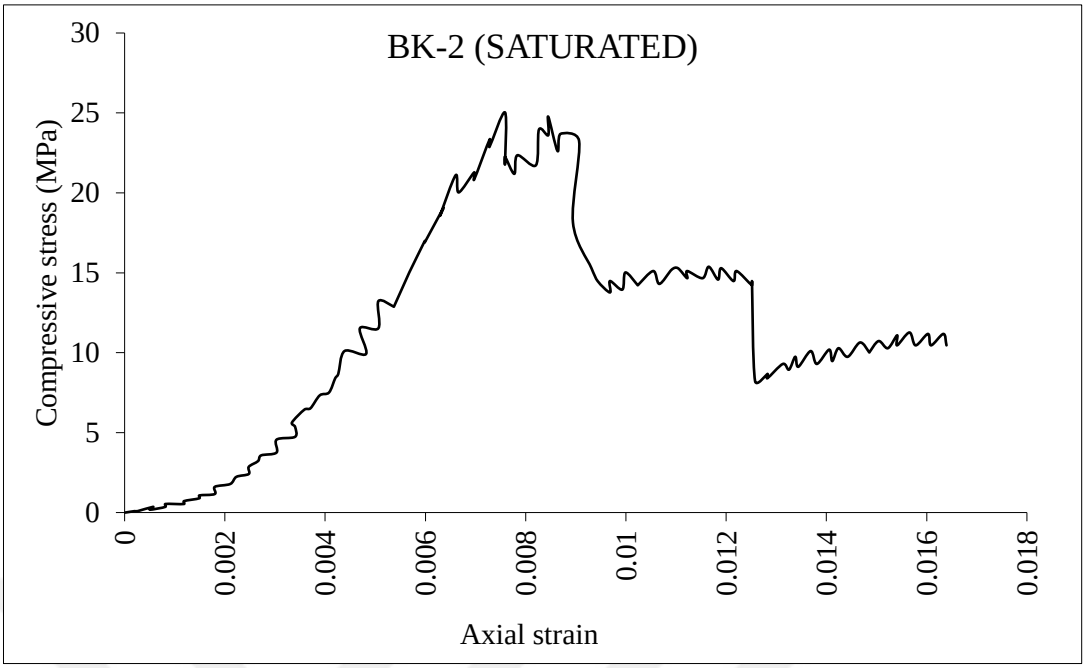


Figure A5.31 The stress-strain graph of BK-2 subjected to static uniaxial compressive strength test

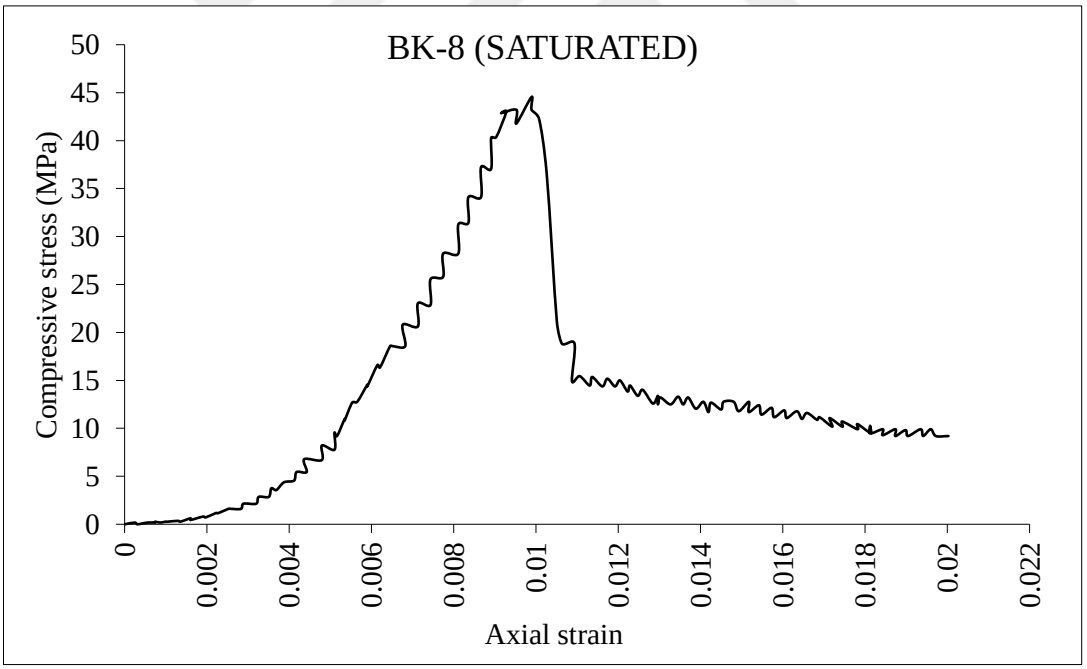


Figure A5.32 The stress-strain graph of BK-8 subjected to static uniaxial compressive strength test

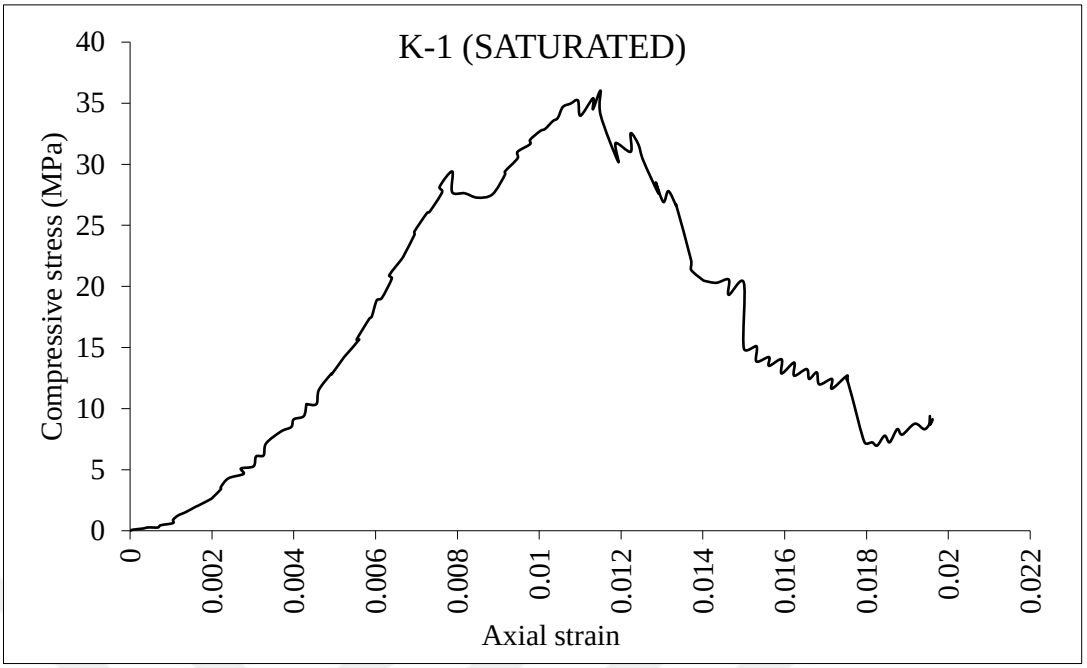


Figure A5.33 The stress-strain graph of K-1 subjected to static uniaxial compressive strength test

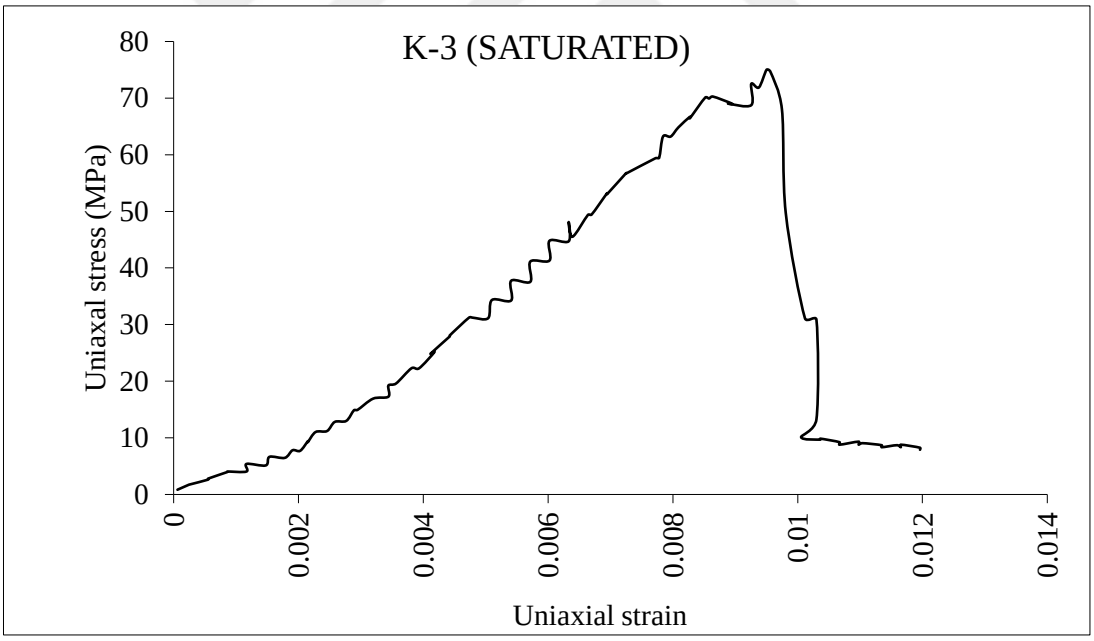


Figure A5.34 The stress-strain graph of K-3 subjected to static uniaxial compressive strength test

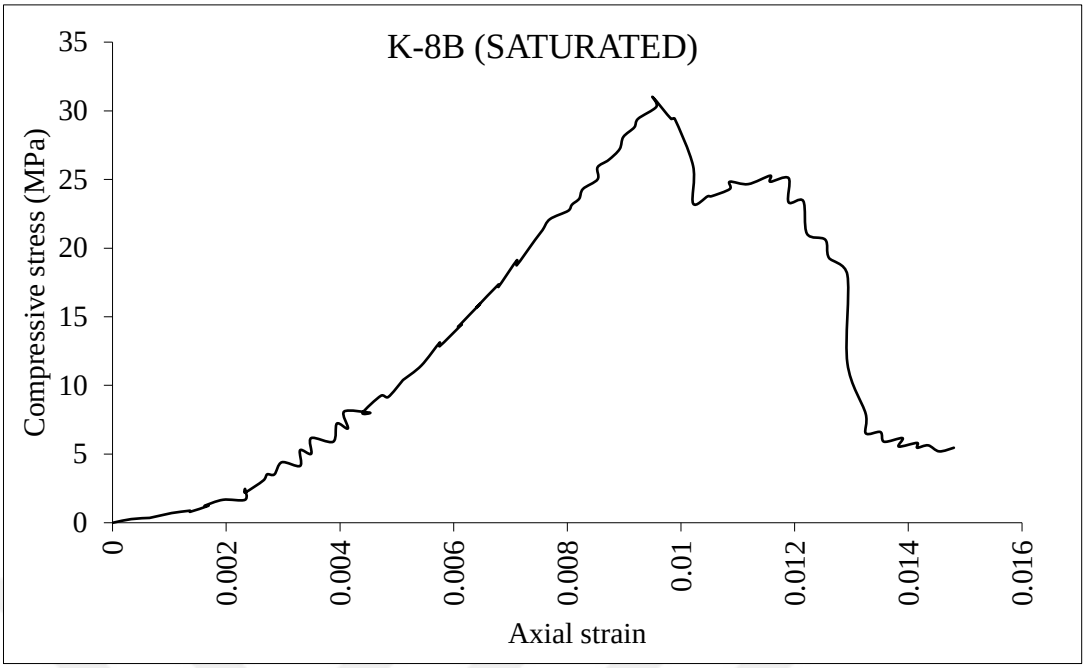


Figure A5.35 The stress-strain graph of K-8B subjected to static uniaxial compressive strength test

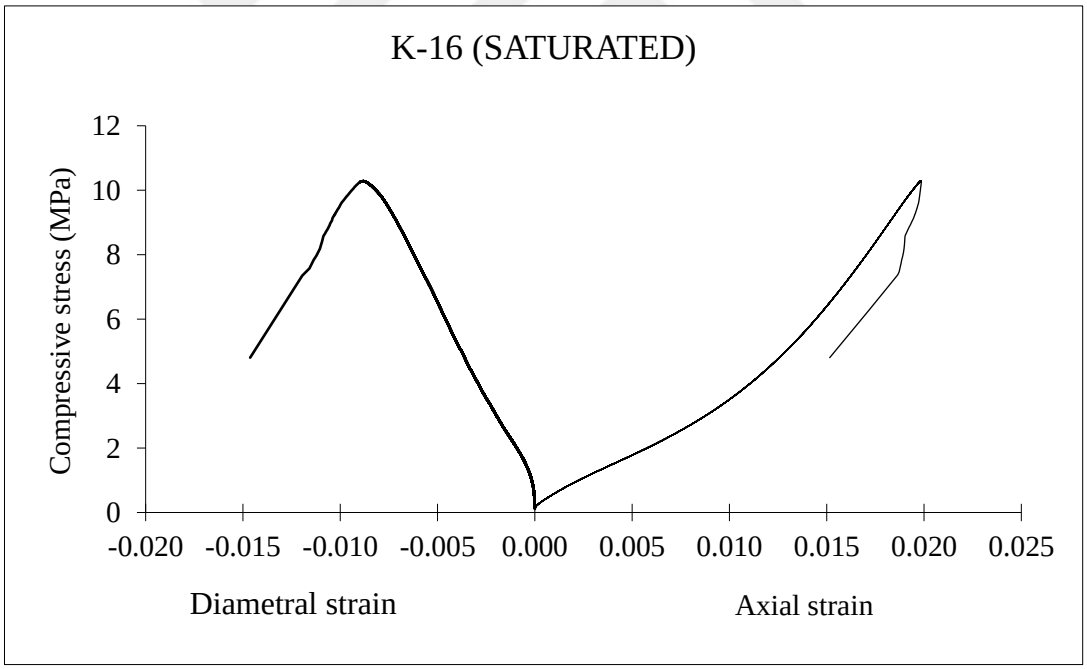


Figure A5.36 The stress-strain graph of K-16 subjected to static uniaxial compressive strength test

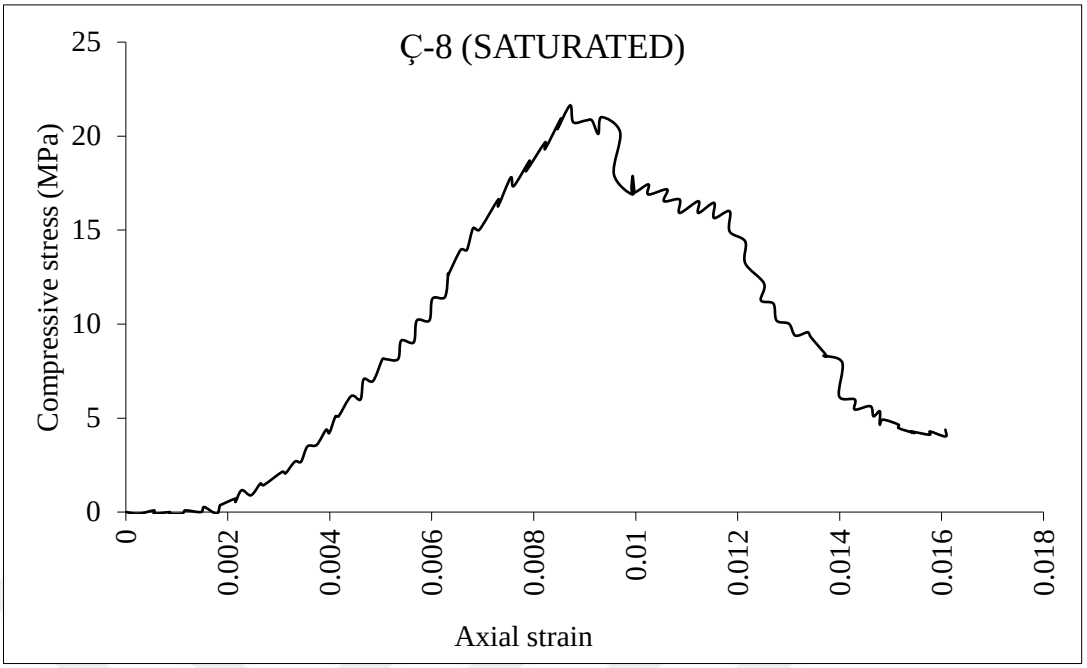


Figure A5.37 The stress-strain graph of Ç-8 subjected to static uniaxial compressive strength test

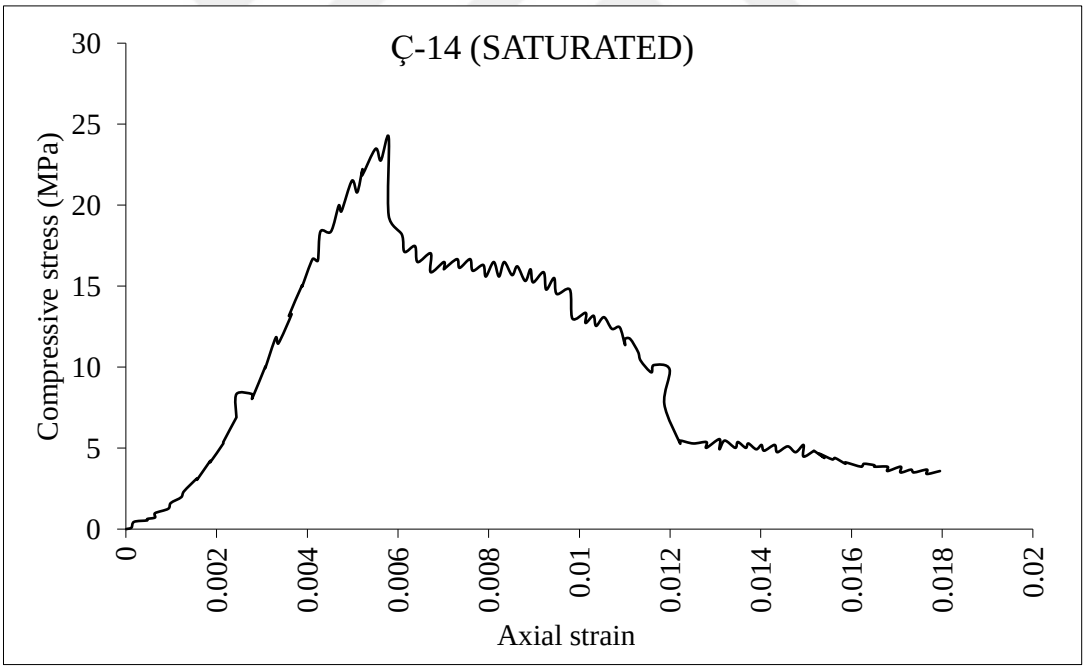


Figure A5.38 The stress-strain graph of Ç-14 subjected to static uniaxial compressive strength test

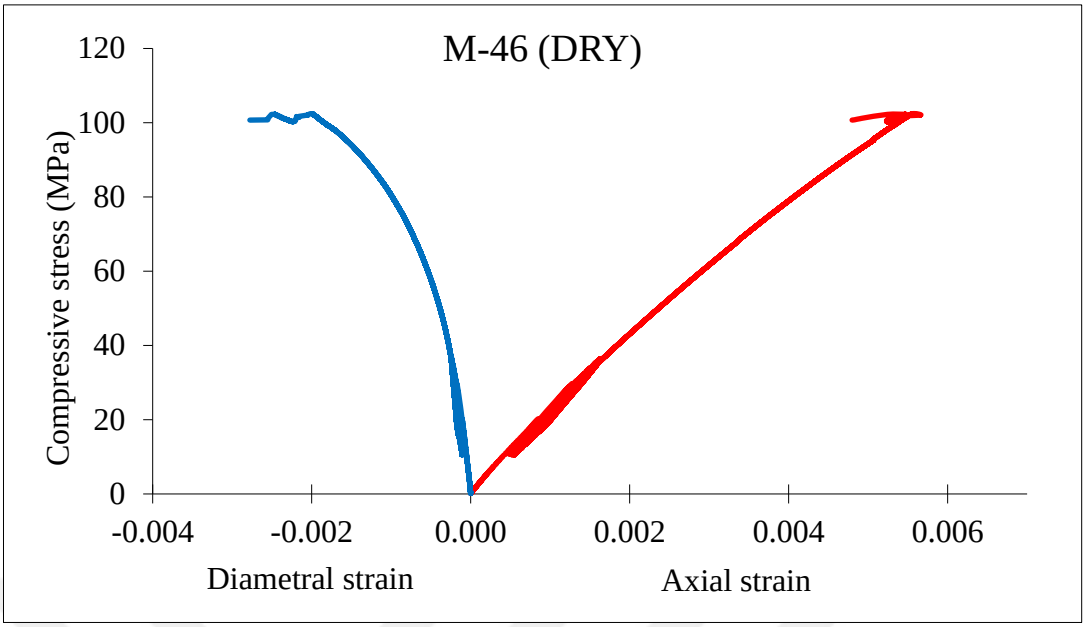


Figure A5.39 The stress-strain graphs of M-46 subjected to dynamic uniaxial compressive strength test

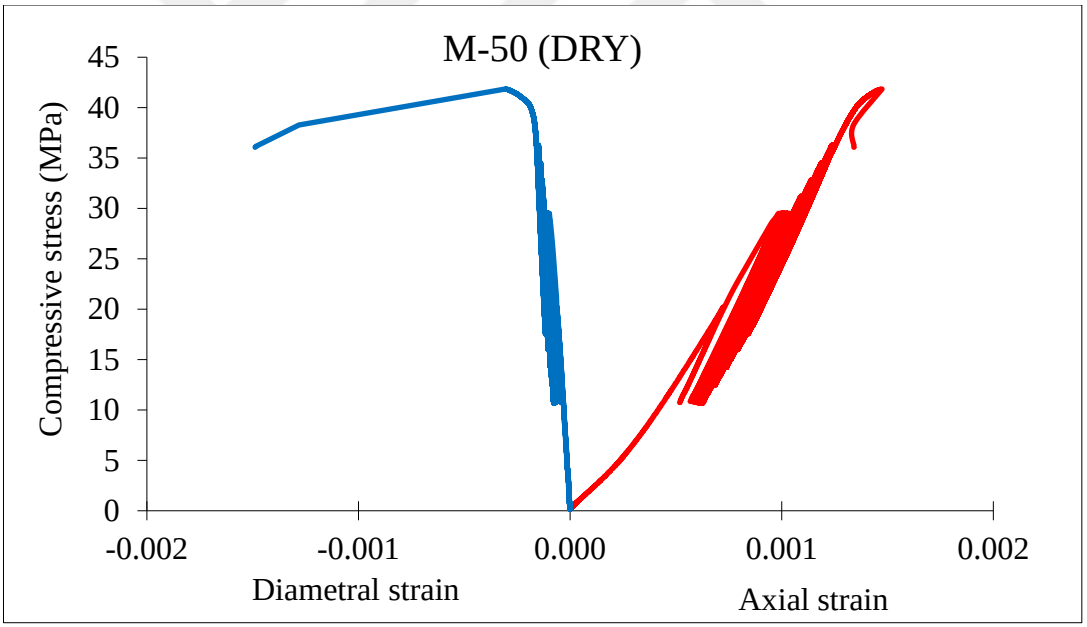


Figure A5.40 The stress-strain graphs of M-50 subjected to dynamic uniaxial compressive strength test

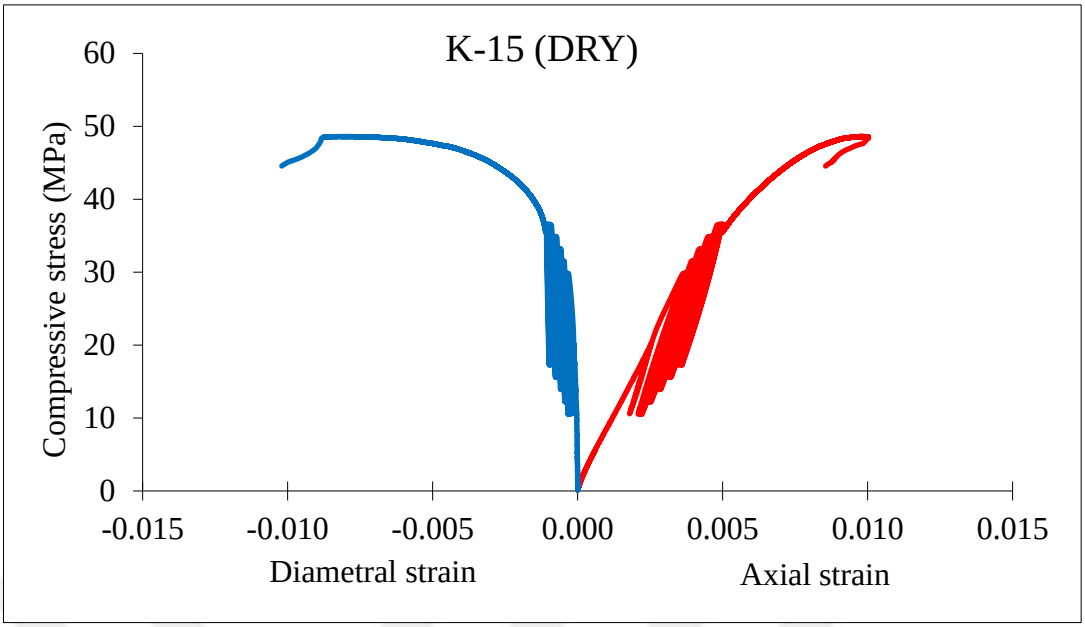


Figure A5.41 The stress-strain graphs of K-15 subjected to dynamic uniaxial compressive strength test

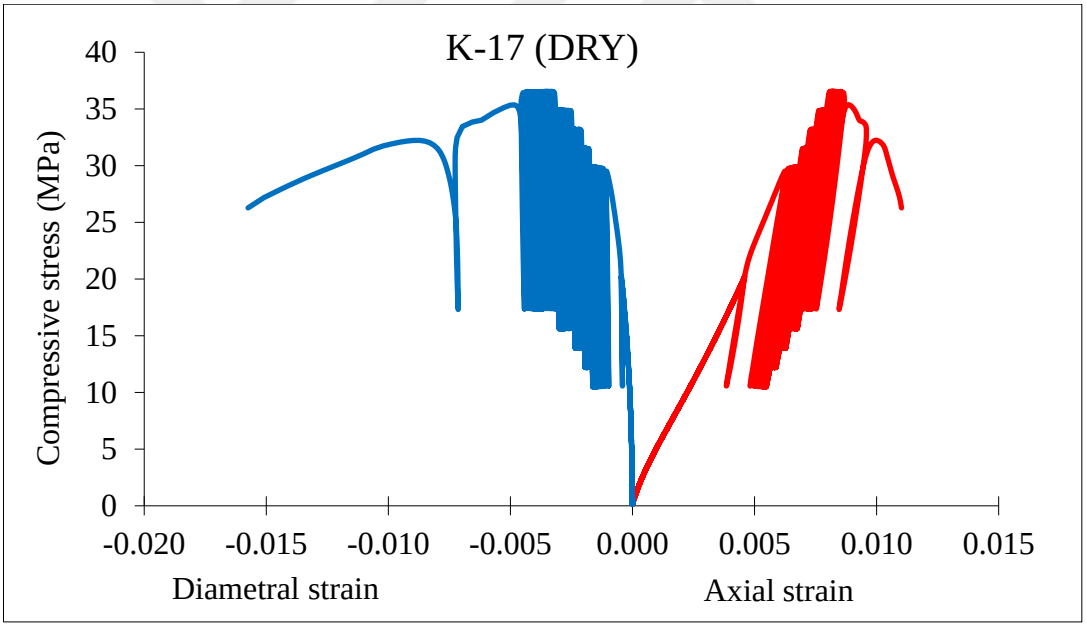


Figure A5.42 The stress-strain graphs of K-17 subjected to dynamic uniaxial compressive strength test

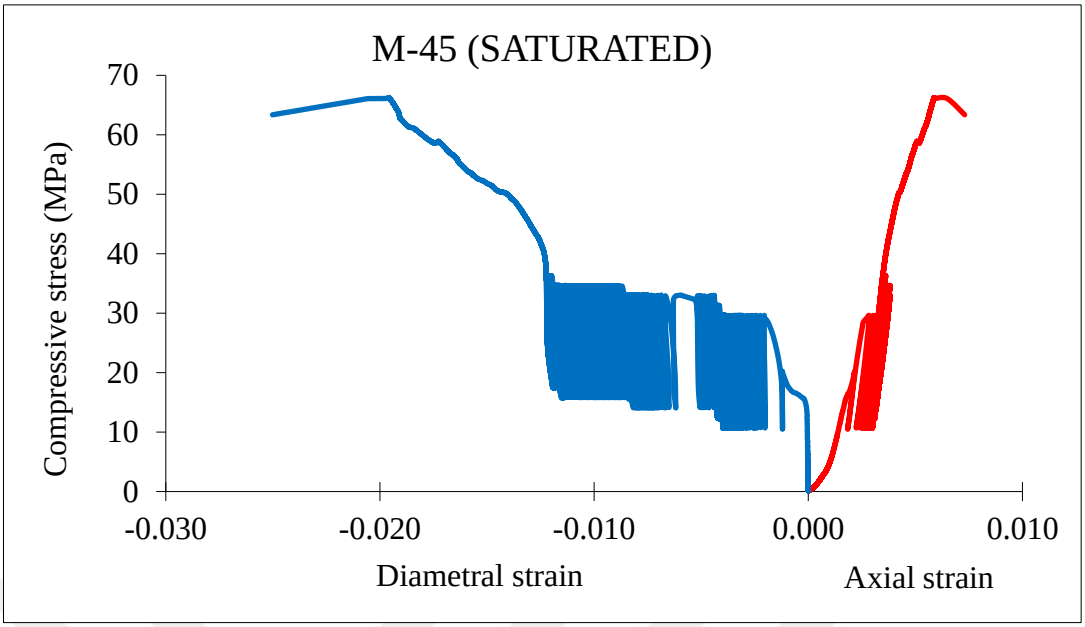


Figure A5.43 The stress-strain graphs of M-45 subjected to dynamic uniaxial compressive strength test

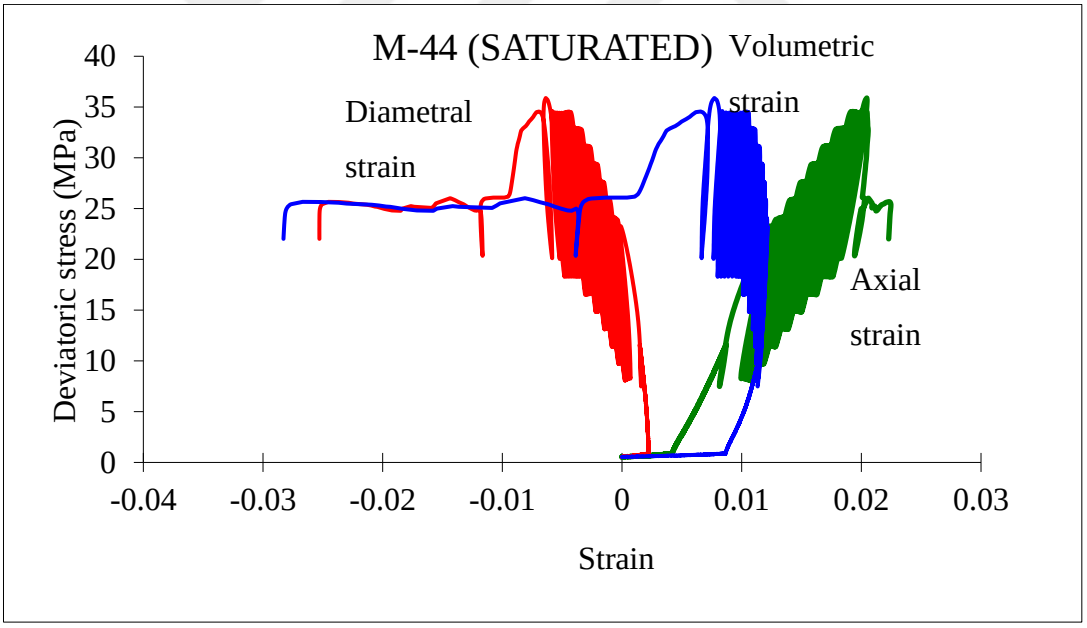


Figure A5.44 The stress-strain graphs of M-44 subjected to dynamic triaxial compressive strength test

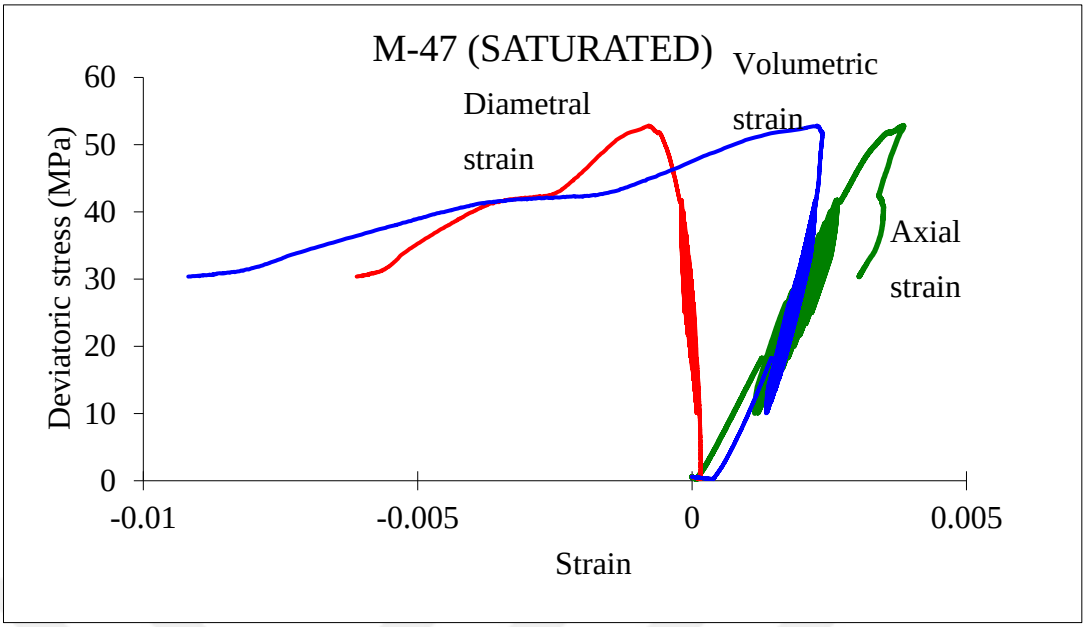


Figure A5.45The stress-strain graphs of M-47 subjected to dynamic triaxial compressive strength test

APPENDIX-6: SRF Values for Future Slope Stability Scenarios

Table A6.1 SRF values for various future slope conditions

Landslide-1				
CONDITION	TRIGGERING FACTOR	Critical SRF	Vertical Displacement at SRF=1 (cm)	Vertical Displacement at critical SRF (cm)
Before dam construction	Static-Ambient	1.87	13.13	17.04
	Seepage pressure	2.15	14.06	106.02
	Heavy rainfall	1.52	14.41	15.96
	Seismic activity	1.28	28.46	31.13
	Heavy rainfall+ Seismic activity	1.13	29.95	30.73
After dam construction (minimum water level)	Static-Ambient	1.90	14.22	41.03
	Seepage pressure	1.89	14.22	18.22
	Heavy rainfall	1.79	14.22	55.32
	Seismic activity	1.28	29.01	30.72
	Heavy rainfall+ seismic activity	1.18	29.67	30.67
After dam construction (maximum water level)	Static-Ambient	1.92	13.57	17.6
	Seepage pressure	1.90	13.59	17.08
	Heavy rainfall	1.90	13.52	18.05
	Seismic activity	1.29	28.31	30.86
	Heavy rainfall+ seismic activity	1.26	28.77	30.32
	Drawdown	1.80	14.58	40.22
	Drawdown+heavy rainfall	1.37	16.21	517.00
	Drawdown+ seismic activity	1.17	24.18	33.13
	Drawdown+heavy rainfall+ seismic activity	0.83	855.00	56.94

Table A6.1 continues

Landslide-2				
CONDITION	TRIGGERING FACTOR	Critical SRF	Vertical Displacement at SRF=1 (cm)	Vertical Displacement at critical SRF (cm)
Before dam construction	Static-Ambient	1.50	4.89	30.02
	Seepage pressure	1.75	4.92	18.64
	Heavy rainfall	1.29	32.74	50.30
	Seismic activity	1.20	110.00	79.40
	Heavy rainfall+ Seismic activity	1.00	-	188.00
After dam construction (minimum water level)	Static-Ambient	1.80	4.71	210.04
	Seepage pressure	1.75	5.94	51.71
	Heavy rainfall	1.70	65.60	88.55
	Seismic activit	1.20	79.70	79.79
	Heavy rainfall+ seismic activity	0.76	160.91	6.13
After dam construction (maximum water level)	Static-Ambient	1.49	5.74	55.99
	Seepage pressure	1.89	4.10	57.18
	Heavy rainfall	1.37	38.85	76.04
	Seismic activity	1.27	133	139.18
	Heavy rainfall+ seismic activity	0.75	175.81	5.58
	Drawdown	1.43	15.39	17.07
	Drawdown+heavy rainfall	1.10	90.23	92.17
	Drawdown+ seismic activity	1.03	25.15	156.05
	Drawdown+heavy rainfall+ seismic activity	1.00	-	143.00

Table A6.1 continues

Landslide-3				
CONDITION	TRIGGERING FACTOR	Critical SRF	Vertical Displacement at SRF=1 (cm)	Vertical Displacement at critical SRF (cm)
Before dam construction	Static-Ambient	2.50	4.38	8.27
	Seepage pressure	2.74	4.50	22.41
	Heavy rainfall	1.38	73.11	52.93
	Seismic activity	1.61	9.04	28.07
	Heavy rainfall+ Seismic activity	1.20	9.78	76.25
After dam construction (minimum water level)	Static-Ambient	2.50	4.34	8.07
	Seepage pressure	2.57	4.57	42.48
	Heavy rainfall	1.93	4.33	4.80
	Seismic activity	1.59	9.05	11.26
	Heavy rainfall+ seismic activity	1.50	9.13	109.49
After dam construction (maximum water level)	Static-Ambient	2.41	3.91	5.32
	Seepage pressure	2.84	4.92	429.16
	Heavy rainfall	1.75	3.91	5.91
	Seismic activity	1.58	8.50	10.39
	Heavy rainfall+ seismic activity	1.37	8.50	90.1
	Drawdown	2.53	4.30	18.94
	Drawdown+heavy rainfall	1.51	4.30	80.18
	Drawdown+ seismic activity	1.33	8.77	11.62
	Drawdown+heavy rainfall+ seismic activity	1.00	-	7.49

Table A6.1 continues

Landslide-4				
CONDITION	TRIGGERING FACTOR	Critical SRF	Vertical Displacement at SRF=1 (cm)	Vertical Displacement at critical SRF (cm)
Before dam construction	Static-Ambient	1.28	4.95	5.70
	Seepage pressure	1.48	4.94	6.54
	Heavy rainfall	1.00	-	11.22
	Seismic activity	0.94	359.99	9.90
	Heavy rainfall+ Seismic activity	0.72	572.54	9.26
After dam construction (minimum water level)	Ambient	1.24	4.94	5.39
	Seepage pressure	1.50	9.43	259.48
	Heavy rainfall	1.16	4.93	6.17
	Seismic activity	0.93	357.57	10.07
	Heavy rainfall+ seismic activity	0.92	411.52	11.13
After dam construction (maximum water level)	Static-Ambient	1.74	4.20	44.81
	Seepage pressure	1.49	31.17	228.13
	Heavy rainfall	1.82	4.19	153.24
	Seismic activity	1.40	14.80	160.18
	Heavy rainfall+ seismic activity	1.08	18.92	709.95
	Drawdown	1.18	10.21	162.48
	Drawdown+heavy rainfall	0.78	336.54	54.52
	Drawdown+ seismic activity	0.82	216.66	11.08
	Drawdown+heavy rainfall+ seismic activity	0.62	503.85	56.52